Characterisation of The Invasive Glioma Niche Using Astrocyte-Glioblastoma Organoids and Decellularised Human Brain (Gliomasphere matrices)

By

Dr. Mohammed Asaad Mohammed Diksin

Bachelor Degree in Medicine and surgery (M.B.Ch.B),

Stem Cell Technology (MSc).

Thesis submitted to the University of Nottingham for the degree of Doctor of Philosophy, July 2020

Supervisors:

Dr. Ruman Rahman

Dr. Stuart Smith

Abstract

Glioblastoma (GBM) therapeutic challenges are in considerable part due to myriad survival adaptations and mechanisms, which allow malignant cells to repurpose signalling pathways within discrete microenvironments. These Darwinian adaptations facilitate invasion into brain parenchyma and the perivascular space or promote evasion from repressive factors that represent anti-cancer defence mechanisms. While many large-scale studies and multiple innovative models have been focusing on the surgically-excised GBM tumour mass, inevitable deadly GBM recurrence usually originates from the non-resected/remaining tumour edge which is predominantly composed of astrocytes harbouring few, residual infiltrative GBM cells. This makes the GBM-infiltrated peri-tumour region more clinically-relevant to patient prognostic outcome. Furthermore, it is not yet known whether astrocytes located at the peri-tumour region can be malignantly transformed and/or can promote tumour re-population within brain parenchyma, via the effect of intercellular communications with GBM cells. We hypothesised that pre-clinical modelling of glioma invasion by recapitulating early events occurring immediately after surgery at the GBM invasive margin, could reveal the genetic cross-talk between malignant cells and the surrounding healthy astrocytes, which facilitates tumour recurrence.

We firstly generated transgenic H1-derived **N**eural **S**tem **C**ells (NSCs) using **C**lustered **R**egularly **I**nterspaced **S**hort **P**alindromic **R**epeats (CRISPR)/Cas9-mediated knock-in of a transgene, composed of a **Y**ellow **F**luorescent **P**rotein (YFP) reporter gene under the control of the **G**lial **F**ibrillary **A**cidic **P**rotein (GFAP) promoter, at the **A**deno-**A**ssociated **V**irus Integration **S**ite **1** (AAVS1) safe harbour locus, to facilitate viable astrocyte isolation/re-isolation and imaging. Reproducible ultrahigh-throughput 24-AggreWell™ plates (7200 mini-wells per plate; 300 microwells in each macrowell) were used to create astrocyte-GBM cerebral organoids, which we term 'Gliomasphere Matrices'. YFP-labelled astrocytes were co-cultured with each of 10 treatment-naïve patient-derived cell lines isolated from the **G**BM **IN**vasive (GIN lines) margin based on the fluorescence of 5-**A**mino**L**evulinic **A**cid (5-ALA) substrate that specifically labels cells with high activation of the heme synthesis pathway, (which includes GBM cells). Co-cultures were seeded upon on a sequentially constructed, **T**ime-**o**f-**F**light **S**econdary **I**on **M**ass **S**pectrometry (ToF-SIMS)-characterised 3D scaffold, composed of **d**ecellularised **h**uman **b**rain **E**xtra**C**ellular **M**atrix (dhb-ECM) with a bio-inert **P**oly**E**thylene **G**lycol **D**iacrylate (PEGDA) hydrogel. Based on

accurate spatially-controlled orientation of YFP-astrocytes within the model, two Gliomasphere Matrix phenotypes were created in line with the principles of good manufacturing practice, to provide an efficient platform for drug screening and cell-based therapy systems.

YFP-astrocytes were purified from each of the 10 Gliomasphere Matrices using **F**luorescent-**A**ctivated **C**ell **S**orting (FACS) after 6- and 10-days co-culture to assess transcriptomic alterations, whereby genetic cross-talk occurred in response to direct physical contact with GIN cells. **M**ulti-**D**imensional **S**caling (MDS) has shown the uniform clustering of our samples, which indicates the stringency of control on the biological conditions and technical aspects throughout the whole procedure starting from cellular differentiation, model creation, and transcriptome profiling. Additionally, gene expression changes intrinsic to tumour cells are discussed and validated in relation to RNA-sequencing data from 10 patient-derived 5ALA+ FACS-purified GBM invasive margin specimens. RNA-sequencing of the putatively reprogrammed YFP-astrocytes showed a characteristic expression of well-studied markers and molecular pathways known to be key regulators of glioma initiation and recurrence such as Notch and Akt/mTOR pathways respectively. Moreover, YFP-astrocytes upregulated an important neurodevelopmental genetic marker located at chromosome 1 (*c1orf61*), which has recently been shown to be associated with GBM stemness-acquirement/maintenance and epigenetic status, in addition to other cancers (especially liver cancer) in which *c1orf61* was hypothesised to act as a tumour initiator and associated with metastasis. We also revealed that *c1orf61* has a distinct high-expression in diffuse glioma as compared to all somatic cancers according to **T**he **C**ancer **G**enome **A**tlas (TCGA) RNA-NGS data analysis. However, the normally differentiated YFP-astrocytes also overexpressed the **ST**imulator of **I**nterferon **G**enes (STING) pathway, which is an innate immune pathway known to be involved in a defence mechanism and priming resistance against tumour cells and harmful microorganisms. The simultaneous co-expression of malignant and defence ultimately suggests a fluctuating state between malignant transformation imposed by the highly infiltrative glioma cells and/or the counter-action of the normal astrocytes to these deleterious invasive cells. Furthermore, our results encourage consideration of interferon therapy at the time of glioma diagnosis to enhance/augment the STING pathway expressed by peri-tumour astrocytes, which in turn may combat the progressive process of local invasion of glioma cells. Our findings also suggest a new viral therapeutic strategy involves targeting both GBM cells and peri-tumour

astrocytes, expressing the malignant neurodevelopmental marker *c1orf6*, that confers resistance to viral therapy.

Gliomasphere Matrix is a novel multi-faceted model which offers a unique opportunity to recapitulate early molecular cross-talk which facilitates GBM recurrence. This may influence future treatment approaches and may be utilised for high-throughput drug screening.

Acknowledgments

Initially, I would like to thank my supervisors Dr.Ruman Rahman and Dr.Stuart Smith, who believed in my abilities and trusted me to undertake such challenging multidisciplinary research. Many thanks for Dr.Smith who provided valuable advices at multiple pivotal periods of my research. No words can describe my gratitude for Dr.Ruman who provided scientific support and distinct encouragement throughout the research. Being under your kind supervision since coducting my master in 2014 to-date is a true gain for myself. You allowed me to learn many sophisticated research disciplines and to use various cutting-edge skills. I will envy myself forever for having you as supervisor. I truly enjoyed my PhD because of you.

Sincerest thanks to my father and mother to provide unlimited emotional and financial support throughout my life including this PhD, and without their prayers and financial support, this work would not be even possible. Thanks to my formidable wife who supported me through tough times. Equal thanks to my three lovely daughters for being polite and disciplined to allow me doing my own work. Thanks to my brothers for their kind supportive words during difficult times.

Big thanks for the colleagues at CBTRC especially Becky, Maria, Lisa, Helen, and Dawn. Special thanks for Jonathan Rowlinson who provided technical support, helped improving my English language fluency via discussing many scientific and philosophical topics. To my fellow PhD students/graduates James, Jasper, Sophie, Hannah, Alice, Macha, Huda, Phoebe, Catherine, Louisa, Josh and Tim, I enjoyed working next to all of you.

I would like to thank our internal and external collaborators; Alexandar Kondrashove, Jamie Hughes for providing gene-editing and cloning support respectively; Chris Denning and Wei Cui for offering two iPSC, and H1NSCs cell lines respectively; Tim Constantin-Teodo for facilitating the process lyophilisation of decellularised extracellular matrix; David Scurr for providing ToF-SIMS support; Omar Ahmed for providing RNA-extraction kit material; Christopher Gell for imaging; David Onion and Nicola Croxall for FAC-sorting of YFP-astrocytes. Without your expertise and kind scientific support, this work would not be accomplished.

Many thanks for the UK and the UK people who have been enormously kind and supportive with my family and myself, which I will appreciate throughout my entire life. Thanks to the university of Nottingham, including its members and staff for having me as MSc and then PhD student, I promise that I will continue to distribute the science, skills, research and knowledge that I have learned in this leading university. Thanks to the patients/deceased who unconditionally and nobly offered their tumour samples for the research.

To God be the glory!

List of contents

Abstract i
Acknowledgments iv
List of contents v
List of common Abbreviation xi
List of Figures xiii
List of Tables xvii
Chapter 1: Introduction 2
1.1. General Introduction 2
1.2. GBM Clinical aspects 3
1.2.1. Incidence and risk factors of GBM 3
1.2.2. Clinical presentation and diagnosis 3
1.2.3. GBM therapy 5
1.2.3.1. Treatment of newly diagnosed GBM patients 5
1.2.3.2. Treatment of patients with recurrent GBM 7
1.3. Histological classification of gliomas 9
1.4. Molecular classification of astrocytic and oligodendroglial gliomas in adults 14
1.4.1. Towards integrating gliomas genetic signature with characteristic histopathological features 14
1.4.2. Genetic markers of WHO grade II and III gliomas in adult patients 17
1.4.3. Genetic markers of WHO grade IV gliomas 18
1.4.4. GBM subtypes identified by large-scale transcriptome and (epi)genome profiling 20
1.5. Glioma invasive phenotype 23
1.6. GBM intra-tumour heterogeneity 24
1.7. Current scientific gaps which led to the project rationale and study aims ... 26
1.8. Rationale of *in-vitro* modelling objectives and design of study 28
Chapter 2 - Materials and methods 31
2.1 Guidelines for cryopreservation of cells (modified from Neurobiology protocol handbook from Gibco) 31
2.2 Guidelines for recovering frozen cells from liquid nitrogen (modified from Neurobiology protocol handbook from Gibco) 32
2.3 Guidelines of passaging cells (modified from Neurobiology protocol handbook from Gibco) 33

2.4 Immunofluorescence staining was performed according to standard operating protocols 34
2.5 Seeding cells inside Millicel ® EZ chambers slides (Millipore; PEZGS0816) for immunofluorescence imaging. 35
2.6 Agarose gel electrophoresis was conducted according to standard operating protocols 35
2.7 Preparing surface coating for the NSCs 37
2.7.1 Coating vessels surfaces with Geltrex™ LDEV-Free Reduced Growth Factor Basement Membrane Matrix (Gibco; A1413201) (modified from Neurobiology protocol handbook from Gibco). 37
2.7.2 Coating vessel surfaces with Corning® Matrigel® Basement Membrane Matrix, LDEV-free. (Corning; 354234) 38
Chapter 3 Creating a transgenic astrocytic reporter cell line using CRISPR/Cas9 technology 40
3.1 Introduction 40
3.2 Rationale for the transgenic strategy used to create the enhanced Yellow Fluorescent Protein (eYFP)- neural stem reporter cell line. 44
3.3 Materials and methods 50
3.3.1 Overview of molecular cloning strategy 50
3.3.2 Cloning of the HDR DNA template (agar plates, plasmid DNA extraction, gel electrophoresis, band extraction from gel, ligation protocols) 51
3.3.2.1 Making agar plates (modified from Addgene protocols): 51
3.3.2.2 Plasmid DNA purification using GeneJET Plasmid Miniprep. .. 53
3.3.2.3 Plasmid DNA purification using PureLink™ HiPure Plasmid Filter Midiprep Kit. 54
3.3.2.4 Plasmid DNA purification using PureLink™ Quick Gel Extraction Kit. (Thermofisher Catalogue number: K210025 (modified from manufacturer protocol) 55
3.3.2.5 Cloning strategy for 9733bp homology donor DNA 57
3.3.3 The assessment of sequencing and *in-vitro* transcription functionality of the HDR plasmid 66
3.3.4 NSCs transfection 67
3.3.5 NSCs colony selection 68
3.3.6 Identifying appropriate selection concentration of puromycin antibiotic using a dose-response curve 69

3.3.7 PCR screening for mutated clones and guidelines for extracting genomic DNA using GeneJET Genomic DNA Purification Kit; (Thermo Scientific™ *Catalogue number:* K0721) according to manufacturer protocol. 70
3.3.8 NSC differentiation 71
3.3.9 Astrocyte isolation using FACS 72
3.4 Results 73
3.4.1 Confirming the appropriate cloning of HDR donor DNA plasmid using restriction digestion. 73
3.4.2 Confirming the appropriate sequence and read-frame of the cloned HDR donor DNA plasmid using Sanger Sequencing and *in-vitro* functional experiment respectively. 74
3.4.3 PCR-based screening of genetically edited NSC clones 76
3.4.4 Confirming knock-in of the YFP transgenic construct into the AAVS1 safe harbour locus of NSCs using computational biology. 77
3.4.5 Confirming the stability of the genetic editing (KI) in H1AML NSCs via frequent passaging and differentiation 79
3.4.6 Confirmation of multi-potency and differentiation potentials of the genetically-edited H1AML NSC cell line 80
3.5 Discussion 82
Chapter 4 Huma brain ECM decellularisation 85
4.1 Introduction 85
4.1.1 Decellularisation of tissues 85
4.1.2 *In-vivo* applications of decellularised ECM 85
4.1.3 Decellularisation techniques and materials 87
4.1.4 Characterisation of decellularised ECM 88
4.1.5 Rationale for using dhb-ECM. 90
4.2 Materials and methods 93
4.2.1 Guidelines for mouse brain decellularisation 93
4.2.2 Guidelines of human brain tissue decelluarisation 95
4.2.3 Dissolving lyophilised human and mouse decellularised brain extra cellular matrix 96
4.2.4 Characterisation of decellularised brain ECM 96
4.2.4.1 TOF-SIMS characterisation of decellularised mouse and human brain ECMs 97
4.2.4.2 Blyscan colorimetric assay to assess the sulphated GAGs in the decellularised human brain ECM 98
4.2.4.3 SEM examination of the decellularised mouse brain ECM 99

4.2.4.4 Haematoxylin staining of the decellularised human and mouse brain materials 99
4.3 Results 100
4.3.1 Characterisation of the decellularised mouse brain ECM. 100
4.3.1.1 SEM reveals the ultra-structure of the decellularised mouse brain ECM. 101
4.3.1.2 Decellularised mouse brain ECM material has all essential components (proteins and non-sulphated GAGs) via thorough characterised using TOF-SIMS 102
4.3.1.3 Mouse brain ECM was efficiently decellularised 106
4.3.2 Characterisation of the dhb-ECM 107
4.3.2.1 dhb-ECM is composed of all essential components (proteins, sulphated-GAGs, non-sulphated GAGs) 107
4.3.2.2 Human brain tissue was efficiently decellularised 116
4.3.2.3 Decellularised human brain ECM material revealed sulfated GAGs using a Blyscan colorimetric assay 119
4.4 Discussion 120
Chapter 5 Generating Gliomasphere Matrices 123
5.1 Introduction 123
5.1.1 Current vision on models used to study GBM and microenvironmental communication 123
5.1.2 Chronological development of 3D GBM modelling 125
5.1.3 Overcoming technical challenges in the Gliomasphere Matrix system 128
5.1.4 Rationale of using PEGDA hydrogel and decellularised human brain ECM as components of the Gliomasphere Matrix 129
5.1.5 The rationale and objectives of creating models to study GIN-astrocyte intercellular communication 130
5.2 Materials and Methods 132
5.2.1 Guidelines to encapsulate the solubilised material of the dhb-ECM within PEGDA hydrogel to generate a 3D basement membrane. 132
5.2.2 Sequential-seeding protocols used to determine precise YFP-astrocyte location within the Gliomasphere Matrices. 134
5.2.2.1 Protocol used to seed YFP-astrocytes at the periphery of the Gliomasphere Matrices. 134
5.2.2.2 Protocol used to seed YFP-astrocytes at the centre of the Gliomasphere Matrices. 136

5.2.3 Novel protocol to transfer Gliomasphere Matrices onto WillCo dishes for imaging. 136
5.2.4 Novel protocol used to dissociate and isolate YFP-astrocytes from Gliomasphere Matrices after co-culture. 137
5.2.5 SEM examination of decellularised human brain ECM encapsulated within 3D PEGDA hydrogel 138
5.2.6 *In-vitro* proliferation 138
5.2.7 DeltaVision and confocal microscopic examinations 139
5.3 Results 140
5.3.1 3D reconstructed decellularised human brain ECM using PEGDA hydrogel is highly tuneable and reproducible. 140
5.3.2 SEM examination reveals the porosity and lamellar structure of the decellularised human brain matrix constructed within PEGDA hydrogel. 142
5.3.3 Generation of the high-throughput Gliomasphere Matrices in a reproducible manner. 144
5.3.4 Optimisation and creating the core of the Gliomasphere Matrices (GIN cell lines cultured on the decellularised human brain ECM-PEGDA) revealed that decellularised human brain ECM enhances aggregate formation of primary GBM invasive margin cells. 147
5.3.5 Decellularised human brain ECM within PEGDA hydrogel does not impair proliferation of invasive primary GBM cells. 149
5.3.6 Control of YFP-astrocyte location to ensure direct contact with GIN cells 152
5.4 Discussion 157
Chapter 6: Characterisation of astrocytic-GBM genetic communication at the invasive tumour edge 163
6.1 Introduction to RNA sequencing 163
6.2 Materials and methods for RNA sequencing 165
6.2.1. RNA Isolation 165
6.2.2. TapeStation 167
6.2.3. RNA library preparation, sequencing, and data analysis 168
6.3. Results of UPX RNA-sequencing 170
6.3.1. Confirming the integrity and concentration of mRNA isolated from the co-cultured astrocytes. 170
6.3.2. MDS of astrocytic genome-wide gene expression upon Gliomasphere Matrix. 174

6.3.3. UPX 3' RNA sequencing analysis reveals altered astrocytic gene expression induced by interaction with infiltrative GBM cells within Gliomasphere Matrix models. 178
6.3.3.1 Co-cultured YFP-astrocytes upregulate intercellular communication pathways. 197
6.3.3.2. Co-cultured YFP-astrocytes upregulate axon guidance pathways. 199
6.3.3.3. Co-cultured astrocytes upregulate Notch signalling. 201
6.3.3.4. Co-cultured astrocytes unregulated pathways triggered by oncogenic MAPK and PI3K/AKT signalling. 205
6.3.3.5. Co-cultured astrocytes and 5-ALA negative tumour associated astrocytes upregulate protein translation pathways. 209
6.3.3.7. The *c1orf61* gene identified as a novel putative determinant of astrocytic genetic response to GBM cross-communication 218
6.4 Discussion 224
Chapter 7: Conclusion 240
8. Appendix 246
Appendix of chapter four 246
Random fragmentation figures showing methods used to obtain ions of HA, and sulfated-GAGs (keratan sulfate and chondroitin sulfate). 246
Determining the unknown concentration of sulphated-GAGs in dhb-ECM using a Blyscan colorimetric assay. 251
Appendix of chapter five 252
Appendix of chapter six 253
PCA analysis performed by Qiagen show a variance of 26% and 12% between the co-cultured astrocytes and the astrocyte controls after 6 and 10 days co-culture respectively **(Figure 8. 5)**. 253
Outputs 270
References 272

List of common Abbreviation

AAVS1	Adeno-Associated Virus Integration Site 1
ABGIL	Adaptive Global Innovative Learning Environment
5-ALA	5-Aminolevulinic
bGH	Bovine Growth Hormone
CNS	Central nervous system
CRISPR	Clustered Regularly Interspaced Short Palindromic Repeats
CT	Computerised tomography
DBS	Double-stranded genomic break
DEG	Differentially expressed genes
dhb-ECM	Decellularised human brain extracellular matrix
ECM	Extracellular matrix
EDTA	Ethylenediaminetetraacetic acid
FACS	Fluorescent-Activated Cell Sorting
FBS	Foetal Bovine Serum
FDA	Food and Drug Administration
FDR	False detection rate
FPKM	Fragments Per Kilobase of Transcript per Million reads mapped
GAGs	Glycosaminoglycans
GBM	Glioblastoma
GIN	GBM INvasive
GSC	Glioma stem cells
GSEA	Gene set enrichment analysis
HA-L	Homology arm-Left
HA-R	Homology arm-Right
HA	Hyaluronic acid
HDR	Homology direct repair
HEV	Hepatitis E virus
HGG	High-grade glioma
hGH	Human Growth Hormone
iPSCs	Induced pluripotent stem cells
LGG	Low-grade glioma
MCS	Multiple cloning site
MDS	Multi-Dimensional Scaling
MRI	Magnetic resonance imaging
NADPH	Nicotinamide adenine dinucleotide phosphate
NGS	Next Generation Sequencing
NHEJ	Non-homologous end-joining
NMD	Nonsense-Mediated Decay
NS1	Non-viral structural protein S1
NSC	Neural Stem Cells
ORF3	Open read frame 3
PAM	Protospacer Adjacent Motif
PCA	Principle component analysis

PEGDA	Polyethylene glycol diacrylate
RT	Radiotherapy
RTK	Receptor tyrosine kinase
SA	Splice acceptor
SDS	Sodium dodecyl sulphate
SEM	Scanning electron microscopy
STING	Stimulator of interferon genes
TAA	Tumour associated astrocytes
TCGA	The Cancer Genome Atlas
TC-treated	Tissue culture treated
TMZ	Temozolomide
TOF-SIMS	Time-of-Flight Secondary Ion Mass Spectrometry
UMI	Unique molecular index
UPX	Ultraplex
WHO	World Health Organisation
WPRE	Woodchuck hepatitis virus post-translational regulatory element
YFP	Yellow Fluorescent Protein

List of Figures

Chapter 1 figures

Figure 1. 1. MRI radiographic features of GBM. 4
Figure 1. 2. Conventional decision tree followed by (neuro)pathologists to reach a diagnosis of central nervous system (CNS) tumours of glial and neuronal-glial origins. 12
Figure 1. 3. Typical gross and microscopic features of low- and high-grade astrocytoma. 13
Figure 1. 4. WHO classification of gliomas in 2016. 16
Figure 1. 5. Adult GBM classification according to DNA methylation profiles. 22

Chapter 3 figures

Figure 3. 1. Original discovery of CRISPR/Cas9 as part of the bacterial immune (S.pyogenes) system. 41
Figure 3. 2. Targeting strategies using Cas9 gRNA complexes. 42
Figure 3. 3. Cellular repair mechanisms acting upon Cas9-mediated DSB. 44
Figure 3. 4. The workflow and experimental schematic overview to generate the transgenic YFP-NSC line H1AML. 46
Figure 3. 5. Possible strategies for CRISPR/Cas9-mediated knock-in of a reporter gene. 49
Figure 3. 6. *In-silico* homology DNA template design. 57
Figure 3. 7. Preparing the backbone plasmid for the HDR DNA template. 58
Figure 3. 8. Obtaining the transgenic insert DNA fragments from plasmid 27054. ... 60
Figure 3. 9. Cloning assembly of the HDR DNA template. 64
Figure 3. 10. Confirmation of HDR sequences and transcription functionality. 75
Figure 3. 11. Screening of the YFP transgenic construct knock-in (KI) (edited NSCs clones) via PCR amplification. 76
Figure 3. 12. Confirmation of transgene KI within homozygously edited H1AML NSCs. 78
Figure 3. 13. Screening the H1AML transgenic line for neural-stem properties and differentiation potential after stringent puromycin selection. 81

Chapter 4 figures

Figure 4. 1. Workflow of the brain decellularisation process. 94
Figure 4. 2. SEM reveals the ultra-structure of the decellularised mouse brain ECM.. 101
Figure 4. 3. TOF-SIMS confirms the presence of amino acids, proteins, and non-sulphated GAGs in the decellularised mouse brain ECM. 106
Figure 4. 4. Microscopic examination confirms decellularisation of mouse brain ECM. 106
Figure 4. 5. TOF-SIMS confirms the presence of amino acids and proteins in the dhb-ECM. 111
Figure 4. 6. TOF-SIMS confirms the presence of non-sulfated-GAGs (HA) and sulfated-GAGs in the dhb-ECM. 116
Figure 4. 7. Human brain ECM was efficiently decellularised. 117
Figure 4. 8. Blyscan assay confirms the presence of sulfated GAGs in the dhb-ECM. 119

Chapter 5 figures

Figure 5. 1. DeltaVision and confocal microscopic examinations of Gliomasphere Matrices within WillCo dishes.. 139
Figure 5. 2. Reproducible and tuneable 3D decellularised human brain ECM using PEDGA hydrogel. 142
Figure 5. 3. SEM examination reveals the porosity and lamellar structure of the decellularised human brain matrix constructed within PEGDA hydrogel. 143
Figure 5. 4. Generation of the high-throughput Gliomasphere Matrices in a reproducible manner. 146
Figure 5. 5. 3D decellularised human brain ECM supports aggregate formation of invasive GBM cells. 148
Figure 5. 6. *In-vitro* growth assays revealed that dhb-ECM within PEGDA hydrogel did not impair proliferation of four GIN cell lines. 151
Figure 5. 7. Peri-tumoural astrocyte model using Gliomasphere Matrix ‘pheotype I’. 154
Figure 5. 8. Tumour-associated astrocyte model using Gliomasphere Matrix ‘pheotype II’ 156

Chapter 6 figures

Figure 6. 1. Intra-operative identification of the invasive margin using Stereotactic MRI. 169
Figure 6. 2. Screening RNA concentration and integrity across all experimental samples..... 172
Figure 6. 3. RNA concentration influences the number of the detectable genes of UPX sequencing. 173
Figure 6. 4. MDS analysis comparing *in-vitro* astrocytes (controls and co-culture) to the surgically resected and FACS-isolated 5-ALA (positive and negative) tissue specimens. 175
Figure 6. 5. MDS analyses of 5-ALA patient tumour samples in addition to the *in-vitro* samples (controls and co-culture astrocytes) at two different time points shown separately. 176
Figure 6. 6. In-house MDS analysis of all *in-vitro* samples included across both time points. 177
Figure 6. 7. Qiagen-generated volcano plots showing the results of differential gene analysis expressed by co-cultured astrocytes as compared to astrocyte-only controls. 181
Figure 6. 8. Qiagen MA-plots to showing the results of differential gene analysis expressed by the co-cultured astrocytes as compared to astrocyte-only controls. 184
Figure 6. 9. Volcano Plot showing the results of DEG of co-cultured astrocytes and 5-ALA negative primary tumour-associated astrocytes using EdgeR software. . 186
Figure 6. 10. MA-Plot showing DEG of co-cultured astrocytes and primary tumour-associated astrocytes using EdgeR software. 189
Figure 6. 11. Reactome pathway analysis depicted as a FoamTree showing the main molecular pathways significantly upregulated (highlighted in yellow) (highlighted in yellow) by co-cultured YFP-astrocytes upon FACS-isolation from each of 10 GIN cell lines, as compared to YFP-astrocyte-only controls after 10 days of co-culture. 194
Figure 6. 12. Reactome pathway analysis in a FoamTree showing the main molecular pathways significantly upregulated (Highlighted in yellow) by tumour-associated astrocytes (5-ALA negative cells) as compared to invasive GBM cells (5-ALA positive cells) from surgically resected and FACS-isolated tissue..... 196
Figure 6. 13. Cocultured astrocytes upregulated intercellular communications pathways. 199

Figure 6. 14. Co-cultured astrocytes upregulated axon guidance pathways in response to GIN cells. 201
Figure 6. 15. Co-cultured astrocytes unregulated Notch signalling in response to GIN cells. 204
Figure 6. 16. Co-cultured astrocytes unregulated oncogenic MAPK and PI3K/AKT1/mTOR signalling pathways in response to GIN cells. 206
Figure 6. 17. Co-cultured astrocytes unregulated cell senescence and apoptosis in response to GIN cells. 207
Figure 6. 18. Co-cultured astrocytes upregulated p53-dependent G1/S DNA damage response pathway in response to GIN cells. 208
Figure 6. 19. Co-cultured astrocytes upregulated protein translation pathways in response to GIN cells. 210
Figure 6. 20. Co-cultured astrocytes upregulated pathways involved in viral mRNA translation in response to GIN cells. 211
Figure 6. 21. Co-cultured astrocytes upregulated interferon gamma in response to GIN cells. 214
Figure 6. 22. Astrocytes upregulate interferon signalling in response to invasive GBM cells. 215
Figure 6. 23. TCGA RNA-sequencing data shows variable interferon pathway expression. 216
Figure 6. 24. Co-cultured astrocytes upregulated genes encode for CD28-costimulatory molecules in response to GIN cells. 217
Figure 6. 25. Astrocytes upregulate *c1orf61* in response to invasive GBM cells. ... 220
Figure 6. 26. Screening of the putative associations of C1orf61 in different immune pathways generated by IMMUNET. 221
Figure 6. 27. TCGA-based analysis and validation of *c1orf61* gene expression. ... 222
Figure 6. 28. TumorMap tool showed *c1orf61* gene expression in various subtypes of LGGs and GBMs. 223

Chapter 8 Figures (Appendix)

Figure 8. 1. Random Fragmentation method of the HA molecule. 248
Figure 8. 2. Random Fragmentation method of chondroitin sulfate molecules. 249
Figure 8. 3. Random Fragmentation method of keratan sulfate molecules. 250
Figure 8. 4. Determining the unknown concentration of dhb-ECM using Blyscan colorimetric assay. 251
Figure 8. 5. Qiagen PCA analysis of *in-vitro* all samples across both time points. . 253

List of Tables

Chapter 4 Tables

Table 4. 1. Characteristic amino acid ions that were detected at significantly higher levels in the decellularised mouse brain ECM relative to TC-treated glass slides. Two amino acids were not statistically significant (highlighted in red). 103

Table 4. 2 . HA ion fragments, predicted using a random fragmentation method via ChemDraw professional 16.0, were detected at significantly higher levels in the decellularised mouse brain ECM relative to TC-treated glass slides..... 104

Table 4. 3. The characteristic amino acid ions that were detected at significantly higher levels in dhb-ECM relative to TC-treated glass slides. 109

Table 4. 4. HA ions that were significantly higher in the dhb-ECM relative to TC-treated glass slides. 113

Table 4. 5. Sulfated-GAG ions that were significantly higher in the dhb-ECM relative to TC-treated glass slides. 114

Table 4. 6. Cell membrane lipid and nuclear TOF-SIMS markers were detected in the dhb-ECM at lower and higher levels relative to TC-treated glass slides respectively. 118

Chapter 6 Tables

Table 6. 1.The concentration and integrity of mRNA extracted from astrocytes prior to libtrary preparation and RNA sequencing. 171

Table 6. 2. GESA clinical annotations of events based on the DEG expressed by astrocytes after co-culturing them with primary GBM cell lines for 10 days..... 179

Chapter 8 Tables (Appendix)

Table 8. 1. Description of glioma invasive margin (GIN) cell lines utilised for Gliomasphere Matrix modelling 252

Table 8. 2. Reactome pathway analysis of DEG expressed by YFP-astrocytes after co-culture with primary GBM cells for 6 days. The DEG list has been generated using EdgeR software. 254

Table 8. 3. Reactome pathway analysis of DEG expressed by YFP-astrocytes after co-culture with primary GBM cells 10 days. The DEG list has been generated using EdgeR software. 256

Table 8. 4. Reactome pathway analysis of DEG by comparing all (20) co-cultured astrocyte samples to all six astrocyte-only controls of both time points. The DEG list has been generated using EdgeR software..... 261

Table 8. 5. Reactome pathway analysis of DEG expressed by 5-ALA negative samples (tumour associated astrocytes) when compared to 5-ALA positive (GBM cells). The DEG list has been generated using EdgeR software. 263
Table 8. 6. The association of C1orf61 in immune processes according to the IMMUNET website: 269

Chapter (1)

Introduction

Chapter 1: Introduction

1.1. General Introduction

Glioblastoma (GBM) remain one of the most aggressive and difficult to treat cancers in adults and children, with a very poor prognosis of 14 months median survival from diagnosis (Stupp *et al.*, 2005), despite all current multimodal therapeutic approaches. Unlike other solid tumours, GBM rarely metastasise outside the brain via haematological and lymphatic vessels (Beauchesne, 2011). However, local invasiveness of these tumours through normal brain tissue represents one of the major unmet clinical and scientific challenges for more efficacious treatment. The ability of glioma cells to infiltrate the surrounding parenchyma of the normal brain and along the nearby blood vessels, limits the surgical resection option, whereby complete resection is not safely possible (Nakada *et al.*, 2007). Moreover, the intra-tumoural genetic heterogeneity emerging from the dynamicity of clonal selection processes within spatially distinct intra-tumoural niches, allow glioma cells to acquire evolved adaptive phenotypes to escape conventional chemotherapeutic and radiotherapeutic treatments. Furthermore, temozolomide (standard-of-care chemotherapy) may confer a stringent selection pressure by which the acquisition of mutations in the AKT/mTOR, EGFR, PDGFR, JNK-ERK1/2 and Retinoblastoma pathways, can facilitate disease recurrence (Johnson, 2014a; Mazor *et al.*, 2015). Similarly, radiotherapy was shown to enrich for the stemness genotypes and phenotypes in some tumour subpopulations which might initiate tumour resistance and propagate disease progression (Suh and Lee, 2015).

Unfortunately, most glioma studies merely involve samples usually taken from tumour core regions, despite the intra-tumoural heterogeneity of genetic and epigenetic profiles shown within spatially distinct regions of these tumours at different time points (Sottoriva *et al.*, 2013; Suzuki *et al.*, 2015). Whereas glioma core regions are usually necrotic due to a rapidly growing tumour mass and inter-cellular competition for oxygen and nutrients, tumour edges represent a key hallmark of gliomas that are more clinically-relevant when considering next-generation therapy. Glioma invasive peripheries form a characteristic perivascular and perineural satellitosis. Ignoring these infiltrative tumour peripheries obscures the full biological profile of the invasive process, where residual infiltrating tumour cells which are left after maximal surgical removal, ultimately give rise to malignant glioma recurrence and the fatal incurable tumour.

1.2. GBM Clinical aspects

1.2.1. Incidence and risk factors of GBM

The mean GBM incidence rate with age-adjustment is 3.2 in 100,000 of the population (Ostrom *et al.*, 2014). Studies into risk factors putatively causal in the development of GBM have been found to be inconclusive and uncertain (Davis, 2016). It has been observed that less than 1% of GBM patients have hereditary diseases such as both types of neurofibromatosis, retinoblastoma, tuberous sclerosis, Li-Fraumeni and Turcot syndromes (Ellor, Pagano-Young and Avgeropoulos, 2014). Ionizing radiation was the only risk factor known to increase the risk of inducing GBM (Ellor, Pagano-Young and Avgeropoulos, 2014); however radiation can typically cause GBM after several years of radiotherapy indicated for another disease or tumour (Johnson *et al.*, 2015). Environmental and occupational risk factors such as the exposure to smoking, vinyl chloride, pesticides, petroleum derivatives at refineries and rubber manufacturing are similarly associated with development of GBM, whereas no association was found due to exposure to formaldehyde, electromagnetic fields and cell phone non-ionizing radiation (Alifieris and Trafalis, 2015).

1.2.2. Clinical presentation and diagnosis

The clinical presentation of GBM patients depends on the size and anatomic location of the tumour (Young *et al.*, 2015). Patients with GBM usually present with symptoms and signs of space occupying lesion, which are caused by tumoural invasion into native brain parenchyma and/or increased intracranial pressure due to the growing tumour mass. These symptoms includes seizure (in 25% of patients as the first presenting symptom and 50% of patients with advanced disease) (Perry *et al.*, 2006; Schiff *et al.*, 2015), behavioural changes, headaches, early morning nausea/vomiting, loss of consciousness, diplopia, weakness/paralysis, paraesthesia and speech difficulties, whereas signs including papilloedema as well as others, depend on the site of the tumour. Patients with a suspected brain tumour are urgently assessed using contrast computerised tomography (CT) or MRI. On MRI, the GBM tumour is enhanced with gadolinium contrast to show an irregular mass with a hyperintense rim and hypointense centre (Figure 1. 1). Necrosis is a pathognomonic feature of WHO grade IV glioma. The mass might be surrounded by haemorrhage or oedema and may be associated with ventricular shift wand (Ellor, Pagano-Young and Avgeropoulos, 2014; Johnson *et al.*, 2015). The definitive diagnosis is confirmed via a thorough histopathological examination of the surgical

excised biopsies (Davis, 2016), which now incorporates molecular pathological classification (Masui, Mischel and Reifenberger, 2016b).

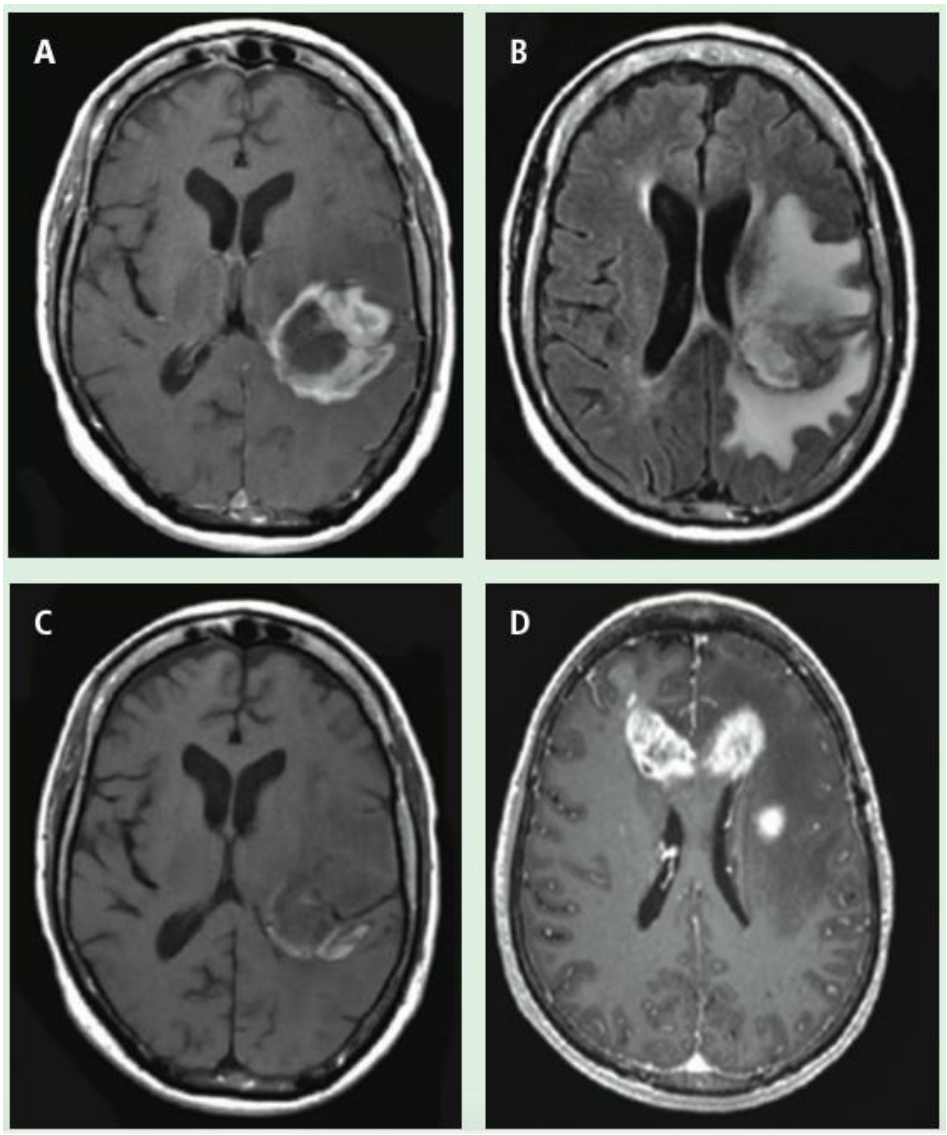


Figure 1. 1. MRI radiographic features of GBM. (A) T1 MRI image shows that the GBM rim appears as a hyperintense tumour edge post-gadolinium contrast enhancement.(B) MRI axial flair slice reveals the vasogenic oedema resulting in pressure effects on the left lateral ventricle. (C) T1 MRI section shows haemorrhagic lesion in the posterior edge of the tumour prior to gadolinium contrast enhancement. (D) Multiple GBM lesions with both cerebral hemispheres. The figure has been taken from (Davis, 2016).

1.2.3. GBM therapy

1.2.3.1. Treatment of newly diagnosed GBM patients

Upon confirming a new diagnosis of GBM, the treatment usually comprises a multidisciplinary approach, which includes surgery followed by chemoradiation approximately 4 weeks later (Stupp *et al.*, 2005). Complete surgical resection of a GBM tumour is impossible due to the highly infiltrative nature of GBM cells that usually invade through eloquent brain parenchymal areas involved in speech, motor and cognitive function. The residual tumour cells remain post-operatively and inevitably lead to disease progression or recurrence (Wilson, Karajannis and Harter, 2014). Extensive surgical resection was previously shown to be associated with better prognostic outcomes (Kuhnt *et al.*, 2011; Roder *et al.*, 2014), specifically, longer overall- and progression-free survival (Keles, Anderson and Berger, 1999; Lacroix *et al.*, 2001; Stummer *et al.*, 2006). Surgery was improved by pre-operative tumour mapping designed to achieve maximum resection, while maintaining brain functionality and improving the quality of life (Hayat, 2011). The utilization of advanced radiological methods and tools such as MRI and diffusion tensor imaging improved the pre-operative planning. Likewise, direct simulation during surgery using MRI, CT and ultrasound has allowed better “multimodal neuronavigation” and facilitated the integration of patient-specific anatomical and functional data.

Despite advancing surgical techniques, gross discrimination between normal and malignant cells during operation remain challenging, and the use of 5-ALA has been shown to have better efficiency (degree of gross total resection including infiltrative margins) in relation to conventional neuronavigation-guided surgery alone (Zhao *et al.*, 2013). Nevertheless, the prognosis for GBM remains dismal, with median overall survival of approximately 15 months (Thakkar *et al.*, 2014). In addition to the extension of surgical removal, other factors have a marked influence on overall survival, such as the performance status, patient age, tumour mass size, and location of the tumour. For example, elderly patients with low performance status and a tumour mass size of >5-6cm located at the midline, theoretically carries the worst prognosis (Ellor, Pagano-Young and Avgeropoulos, 2014).

The standard therapeutic approach for GBM until 2005 was appropriate surgical resection followed by radiotherapy (RT) only 4 weeks post-operatively (Davis, 2016). The conventional radiotherapeutic dose is 60Gy, in 1.8-2Gy fractions delivered for five days per each week for six consequative weeks. Next, the results of a phase III

trial showed that the external beam RT concurrently administered with temozolomide (TMZ), achieved better efficacy (2.5 months median survival advantage), compared to radiation monotherapy (Stupp *et al.*, 2005). This survival benefit was further corroborated when a large proportion of patients treated with TMZ and RT survived longer than patients treated with RT alone (Stupp *et al.*, 2009). The trial has also identified methylation of the *mgmt* gene promoter, located on chromosome 10q26, as a predictive marker of patient prognosis. The enzyme encoded by the *mgmt* gene is involved in DNA repair and in its inactivation state, (by methylation) confers a better prognosis for patients treated with TMZ, as DNA damage caused by chemoradiation cannot be fixed by the inactivated enzyme, leading to activation of apoptosis pathways within at least a sub-population of GBM cells.

The historical RT approach was performed by whole-brain RT, used to treat newly diagnosed patients with GBM. However, many complications such as neurocognitive toxicity, RT-induced leukoencephalopathy and endocrinopathy were associated with this treatment modality. This has led to the development of involved field RT to reduce toxicity, which aims to focus the RT on the tumour edge based on the observation that GBMs recur within 2cm from the original GBM site in 80-90% of cases (Narayana *et al.*, 2006). The involved field RT was shown to have similar or even better survival benefit over whole-brain RT, which in the latter case, caused normal brain parenchymal damage (Barani and Larson, 2015). Intensity-modulated and 3D conformal beam RT types are the current standard RT treatment (MacDonald *et al.*, 2007). Many trials including the utilization of 125 brachytherapy, stereotactic radiosurgery and radioimmunotherapy have been attempted to reduce therapeutic toxicity and to improve patient outcome (Barani and Larson, 2015).

In 2015, the Food and Drug Administration has approved Optune® device, that can deliver tumour-treating electrical fields intracranially, which is used concurrently with TMZ to treat patients with newly diagnosed supratentorial GBM, after surgery and standard-of-care treatment. Optune® can deliver low-intensity, moderate frequency alternating electrical fields to GBM cells to inhibit mitotic cell division, that in turn causes cell death. Optune® was shown to provide a 3.1 and 4.9 month progression-free and overall survival benefits respectively, when used concurrently with TMZ as compared to TMZ alone (Stupp *et al.*, 2015). Note, Optune® has been approved in the United States of America and yet to be approved in the United Kingdom. High cost is one the main reasons why it has not been approved in many countries.

1.2.3.2. Treatment of patients with recurrent GBM

Despite an optimal multimodal therapeutic approach including surgical resection followed by concurrent RT and TMZ, GBM inevitably recurs in all patients, with progression in 70% of cases within a year of diagnosis (Stupp *et al.*, 2005) and only <5% of patients surviving for five years (Ostrom *et al.*, 2014). Surgical re-excision/debulking to reduce the mass effect symptoms and signs is a possible treatment option in some patients with respect to tolerability. However, surgical options for removal of the recurrence have remained controversial. Evidence advocates for a survival benefit from surgical re-resection of GBM recurrence (McGirt *et al.*, 2009; Bloch *et al.*, 2012) is contradicted by other studies that found no extension of the overall survival (Brandes, Bartolotti and Franceschi, 2013; Franceschi *et al.*, 2015).

Similarly, additional RT is also an option for GBM recurrence; however limited tolerability of the native brain tissue to RT raises the risk of radiation-induced necrosis. A wide diversity of RT approaches including stereotactic surgery, brachytherapy and gamma knife can be used to treat GBM recurrence (Davis and Stoiber, 2011).

Chemotherapy and corticosteroids can be used to palliate the symptoms of GBM recurrence, which in turn can improve patients' quality of life. At this stage of GBM recurrence, the response is dismal and progression of disease is expected to occur after 3-6 months (Franceschi *et al.*, 2009). Several chemotherapeutic agents such as TMZ, irinotecan, etoposide, or nitrosourea-based medications can be utilized as individual or combination treatment regimens. Bevacizumab (Avastin®) is a monoclonal anti-vascular endothelial growth factor antibody (anti-angiogenesis) that was approved in 2009 as a treatment option in GBM recurrence. Although trials showed that Avastin has superior progression-free survival benefit, no substantial overall survival improvement was observed (Cohen *et al.*, 2009). Bevacizumab was found to reduce vasogenic oedema associated with GBM via reducing vascular permeability and to decrease radiation necrosis when delivered with RT (Niyazi *et al.*, 2016). However, it may cause serious side effects including haemorrhage, gastrointestinal perforation and blood clots (Salacz, Watson and Schomas, 2011; Taal *et al.*, 2014).

In 2011, Optune® was initially approved as a monotherapeutic treatment, when GBM recurrence is confirmed histologically or via imaging (only in supratentorial regions), as an alternative to standard chemotherapy options following surgery and radiation. Furthermore, a randomised clinical trial demonstrated that treatment with Optune® resulted in comparable overall survival to standard chemotherapy options following surgery and radiation, but with less haemorrhagic, gastrointestinal and infection side effects (Stupp *et al.*, 2012). Treatment using Optune® was also shown to improve patients' quality of life via, for example, the improvement of cognitive and emotional status of patients, as well as better tolerability due to a lack of serious adverse events (scalp irritation from array electrodes that deliver the tumour-treating electric fields is primarily the main side effect), as compared to patients receiving chemotherapy (Hottinger, Pacheco and Stupp, 2016; Mun *et al.*, 2018). Equally important to surgical and medicinal treatments, supportive care including psychological support and honest discussions should be started from diagnosis and maintained throughout the course of the disease.

1.3. Histological classification of gliomas

Until 2007, the World Health Organisation (WHO) has classified CNS tumours according to morphologic features. Gliomas were classified into astrocytic, oligodendroglial, mixed oligoastrocytic, or ependymal (Masui, Mischel and Reifenberger, 2016a). Histopathological diagnosis, using conventional haematoxylin and eosin staining of tissue sections, were considered the gold standard tool to classify gliomas, convey important information about course of disease and prognosis, which in turn could influence patient treatment and stratification (Perry and Wesseling, 2016). Furthermore, glioma histopathological grade is determined based on the mitotic activity, necrosis and microvascular proliferation, which reflects the progression from low- to high-grade neoplasm. However, glioma tumours often show a mixed phenotype when attempting to be classified during microscopic examination and are subjective to interpersonal variability (Van Den Bent *et al.*, 2010; Perry and Wesseling, 2016). Nevertheless, the (neuro)pathologists have to reach an accurate diagnosis after following a "decision tree" and "diagnostic algorithm" (Perry and Wesseling, 2016) **(Figure 1. 2)**. In addition, some clinical clues (patient age, the duration of signs and symptoms, previous treatment), and radiologic findings (the presence or absence of contrast enhancement), can provide valuable information to reach a diagnosis by excluding alternative possibilities through differential diagnosis (Perry and Wesseling, 2016). Although it is challenging to grossly identify glioma especially in cases of scarce samples or fragmented tissue, blurring of the sharp markings between grey and white matter could be an indicative sign of diffuse glioma. Additionally, necrosis and/or highly-vascularity may suggest **H**igh **G**rade **G**lioma (HGG) **(Figure 1. 3)**. Magnetic resonance imaging (MRI) remains the gold standard to assess CNS tumours (Vincentelli *et al.*, 2012).

Grade II and III gliomas are the commonest glial tumours in adult patients (Perry and Wesseling, 2016). In these astrocytoma tumours, neoplastic cells, characterised by pleomorphism, hyperchromasia and irregular large nuclei, gather around the blood vessels (peri-vascular satellitosis), neurons (peri-neuronal satellitosis), and just under the pia membrane (Perry and Wesseling, 2016). These neoplastic cell aggregates are called "Scherer's secondary structures" **(Figure 1. 3)**. The degree of mitotic activity, microvascular proliferation, and necrosis determine the grade of glioma. In this context, Grade IV (GBM) has the highest degree of necrosis, which is surrounded by densely packed, radially arranged neoplastic cells to form "pseudopalisading necrosis", and microvascular proliferation which is described as

multi-layered blood micro-vessels with hyperplasia of the endothelium and the pericytes (Perry and Wesseling, 2016) **(Figure 1. 3)**.

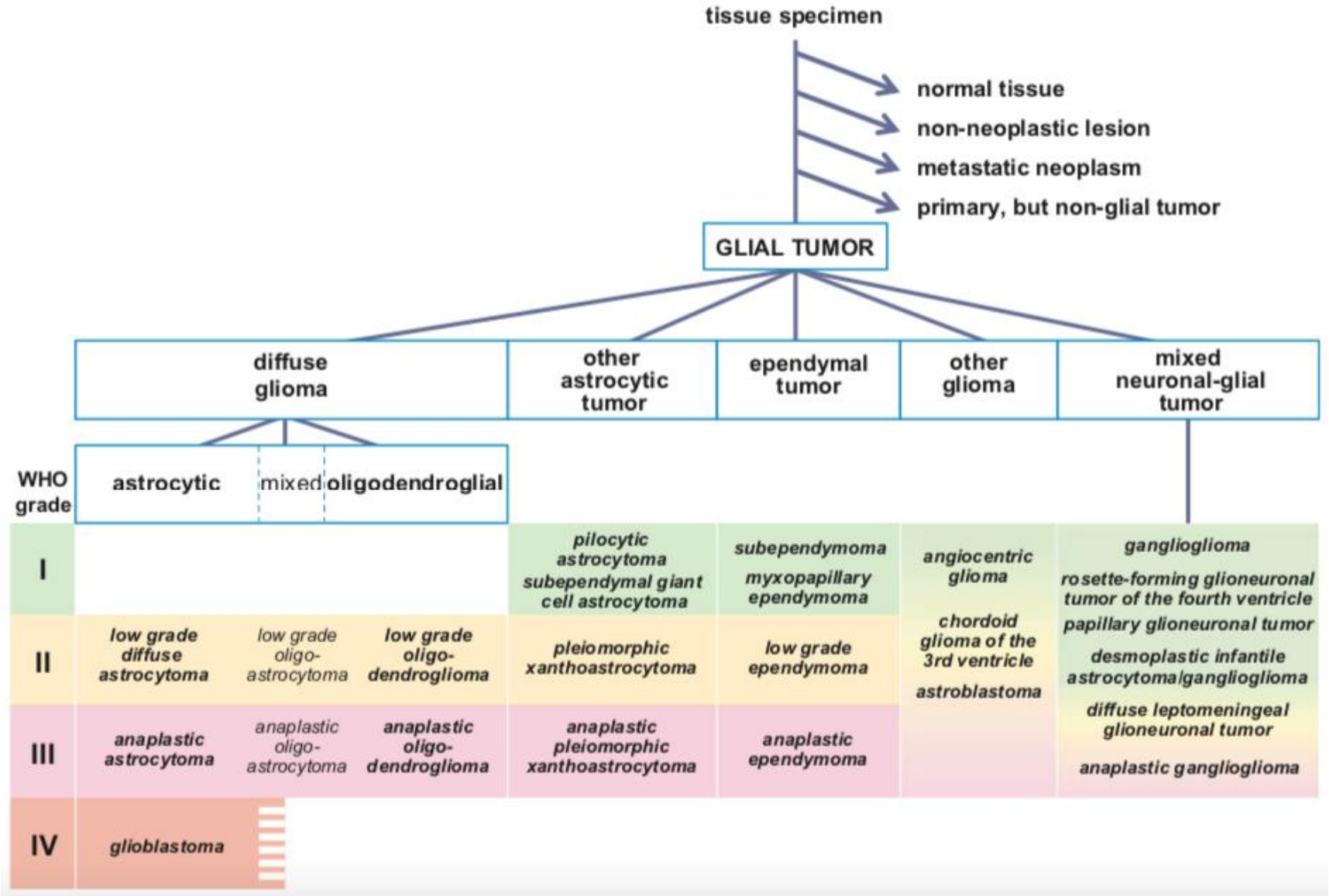

tissue specimen
normal tissue
non-neoplastic lesion
metastatic neoplasm
primary, but non-glial tumor
GLIAL TUMOR
diffuse glioma
other astrocytic tumor
ependymal tumor
other glioma
mixed neuronal-glial tumor
WHO grade
astrocytic
mixed
oligodendroglial
I
pilocytic astrocytoma
subependymal giant cell astrocytoma
subependymoma
myxopapillary ependymoma
angiocentric glioma
ganglioglioma
rosette-forming glioneuronal tumor of the fourth ventricle
II
low grade diffuse astrocytoma
low grade oligo-astrocytoma
low grade oligo-dendroglioma
pleiomorphic xanthoastrocytoma
low grade ependymoma
chordoid glioma of the 3rd ventricle
astroblastoma
papillary glioneuronal tumor
desmoplastic infantile astrocytoma/ganglioglioma
III
anaplastic astrocytoma
anaplastic oligo-astrocytoma
anaplastic oligo-dendroglioma
anaplastic pleiomorphic xanthoastrocytoma
anaplastic ependymoma
diffuse leptomeningeal glioneuronal tumor
anaplastic ganglioglioma
IV
glioblastoma

Figure 1. 2. Conventional decision tree followed by (neuro)pathologists to reach a diagnosis of CNS tumours of glial and neuronal-glial origins. For CNS neoplasms that present with an unclear picture of an individual categorical grade during microscopic examination, the above diagnostic algorithm is usually followed. Various glial tumour grades I, II, III, and IV are coloured with green, yellow, pink, and orange respectively. The grade of some malignant glial tumours, such as diffuse gliomas or ependymal neoplasms, are historically better understood compared to others which are labelled as 'other gliomas' and 'mixed neuronal-glial' malignancies. Consequently, the change in the colour of the columns of the later tumour types is gradual rather than abrupt as in cases of diffuse gliomas or ependymal neoplasms. With the integrated WHO classification of 2016, this decision tree can be further modified; for example, GBM with oligodendroglial component and anaplastic oligoastocytoma can be discriminated via assessing 1p/19q co-deletion, which reflects the importance of the integration of molecular markers (Molecular Pathology) with the histological examination to achieve an appropriate diagnosis. The figure was taken from (Perry and Wesseling, 2016).

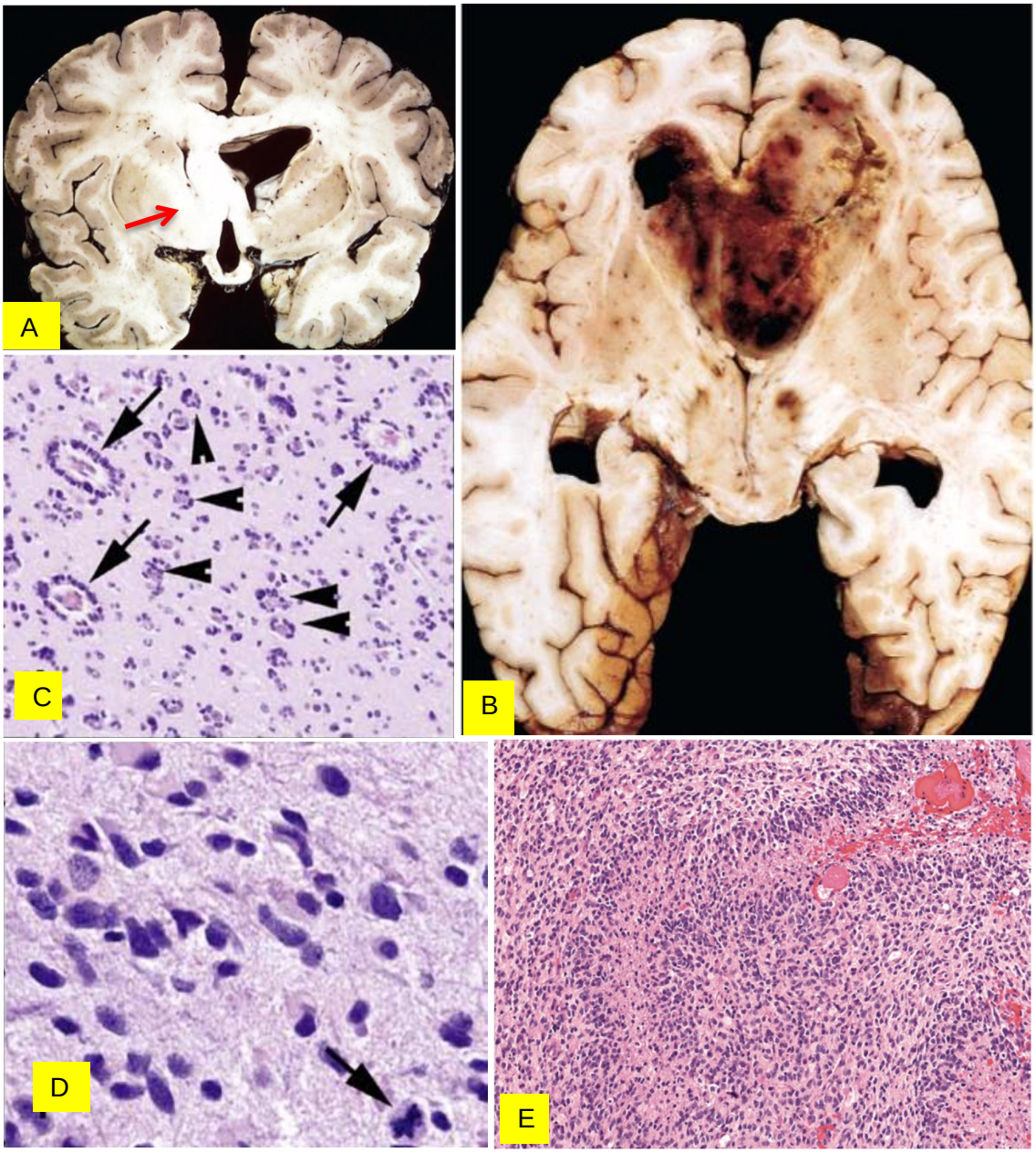


Figure 1. 3. Typical gross and microscopic features of low- and high-grade astrocytoma. Macroscopic (A, and B), and microscopic (C-E) images show the typical features of low- and high-grade gliomas. The disappearance of sharp demarcations between the white and grey matter (red arrow) is a characteristic gross appearance of **L**ow-**G**rade **G**lioma (LGG) (A), whereas necrosis, multiple haemorrhages, and inflammation within an infiltration mass, are features of WHO grade IV (GBM) (B). Secondary structures of Scherer can be seen in the perineuronal (black arrowheads) and perivascular (black arrows) satellitosis in low-grade astrocytoma (C). Toward progressive disease, the mitotic activity is increased (black arrowed) and the grade of glioma increases, as in this example of grade III anaplastic astrocytoma (D). The most progressive and aggressive grade is WHO grade IV glioma, which is characterised by pathognomonic pseudopalisading necrosis, dense cellularity, microvascular proliferation and haemorrhage (E). (A, B, and E), and (C, and D) were taken from and (Kumar, Abbas and Aster, 2013) and (Perry and Wesseling, 2016) respectively.

1.4. Molecular classification of astrocytic and oligodendroglial gliomas in adults

1.4.1. Towards integrating gliomas genetic signature with characteristic histopathological features

In the last two decades, extensive molecular intra-tumoural heterogeneity has been revealed within specially distinct regions within low-and HGG tumours (Sottoriva *et al.*, 2013; Suzuki *et al.*, 2015). Moreover, key driver genetic mutations of glioma were identified. Subsequently, new revision of the classification of CNS tumours was conducted by the WHO, which has led to the changing of definitions and taxonomy of CNS tumours (Scheithauer, Fuller and VandenBerg, 2008; Scheithauer, 2009). In 2016, the recent edition of WHO glioma classification has incorporated pathognomonic molecular markers surrogated by various glioma genotypes with different glioma phenotypes that have distinct histopathological features **(Figure 1.** 4**)**. In this integrated approach, distinct molecular markers of gliomas have been assessed using multiple laboratory techniques such as Immunohistochemistry which has thought to improve the accuracy of the diagnosis (Dunbar and Yachnis, 2010), by overcoming interpersonal variability, improving reproducibility, circumventing the ambiguity of the histological picture, and via identifying characteristic phenotypically-associated markers (Louis *et al.*, 2014; Masui, Mischel and Reifenberger, 2016b). For example, the ambiguity of the oligoastrocytic phenotype can be resolved by the identification of three genetic signatures and associated mutations such as the mutations in isocitrate dehydrogenase 1 or 2 (*idh1* or *idh2*) genes, the loss of expression in the nuclear alpha-thalassemia/mental retardation syndrome X-linked (*atrx*) gene and co-deletion of chromosome arms 1p and 19q, which can determine a given neoplasm is related to diffuse astrocytoma or oligodendroglioma (Sahm *et al.*, 2014). The integrative approach also provides valuable information that influences treatment plans and has enabled better stratification of patient prognosis (Reuss *et al.*, 2015).

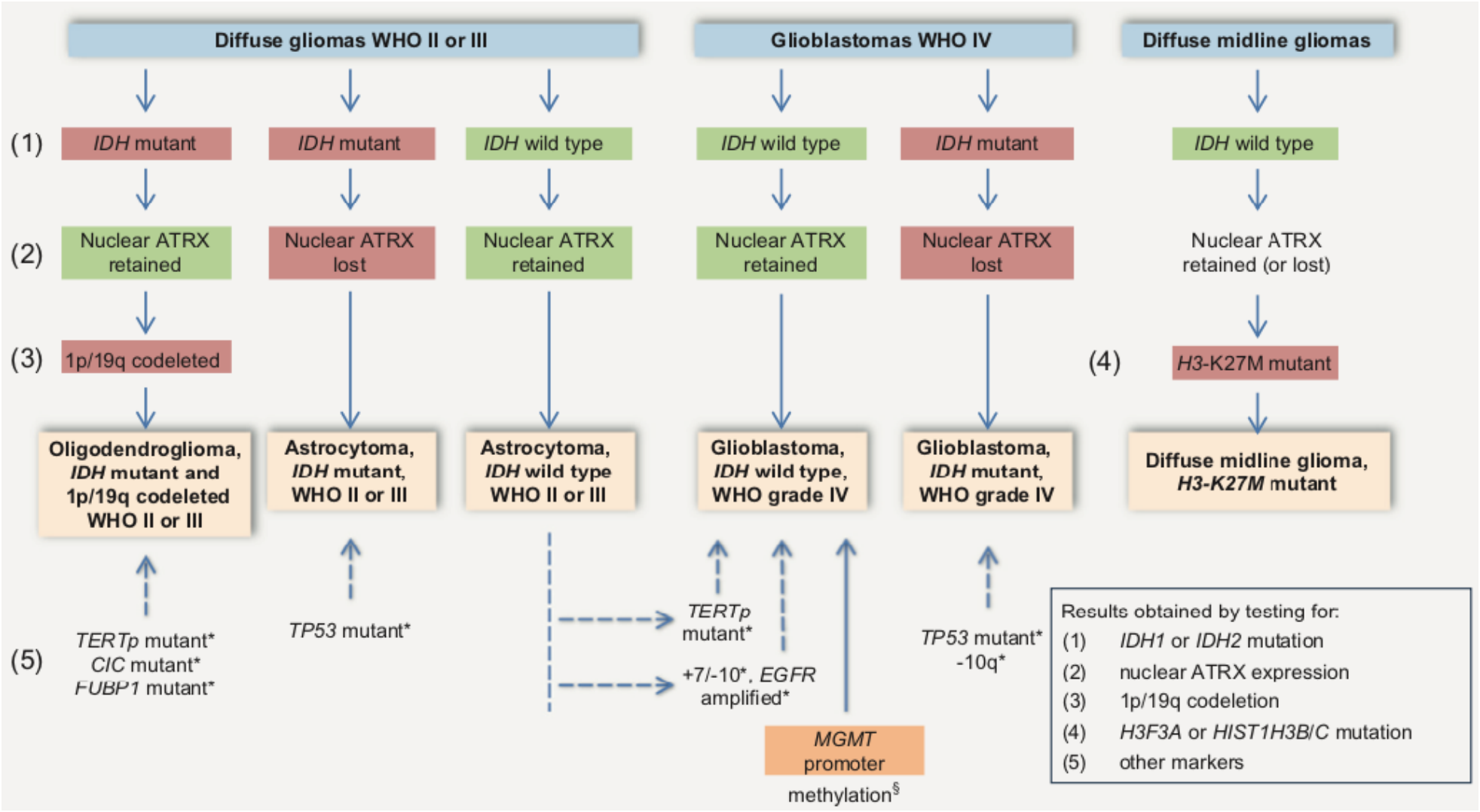

Diffuse gliomas WHO II or III
Glioblastomas WHO IV
Diffuse midline gliomas
(1)
IDH mutant
IDH mutant
IDH wild type
IDH wild type
IDH mutant
IDH wild type
(2)
Nuclear ATRX retained
Nuclear ATRX lost
Nuclear ATRX retained
Nuclear ATRX retained
Nuclear ATRX lost
Nuclear ATRX retained (or lost)
(3)
1p/19q codeleted
(4)
H3-K27M mutant
Oligodendroglioma, IDH mutant and 1p/19q codeleted WHO II or III
Astrocytoma, IDH mutant, WHO II or III
Astrocytoma, IDH wild type WHO II or III
Glioblastoma, IDH wild type, WHO grade IV
Glioblastoma, IDH mutant, WHO grade IV
Diffuse midline glioma, H3-K27M mutant
(5)
TERTp mutant*
CIC mutant*
FUBP1 mutant*
TP53 mutant*
TERTp mutant*
+7/-10*, EGFR amplified*
MGMT promoter methylation§
TP53 mutant*
-10q*
Results obtained by testing for:
(1) IDH1 or IDH2 mutation
(2) nuclear ATRX expression
(3) 1p/19q codeletion
(4) H3F3A or HIST1H3B/C mutation
(5) other markers

Figure 1. 4. WHO classification of gliomas in 2016. This latest WHO classification shows the integration of the typical genetic aberrations and molecular biomarker patterns associated with the most common types of diffuse gliomas. These typical mutations are *idh1* or *idh2* mutations, the loss of expression of *atrx*, co-deletion of 1p/19q and H3-K27M mutation. Additional genetic aberrations and chromosomal abnormalities are considered as extra diagnostic markers, such as mutations in *tert*p, *cic*, and *fubp1* in WHO grade II and III oligodendroglioma, tumour protein 53 (*tp53*) in low-grade diffuse glioma (WHO grade II and III), astrocytoma, or GBM with IDH mutation and ATRX loss. O6-methyltransferase (*mgmt*) promoter methylation acts as a prognostic marker via predicting the response to alkylating chemotherapeutic agents (e.g. temozolomide), rather than as a diagnostic marker, especially in elderly patients with grade IV GBM with wild-type *idh* and *atrx*. The figure has been taken from (Masui, Mischel and Reifenberger, 2016b).

1.4.2. Genetic markers of WHO grade II and III gliomas in adult patients

Grade II and III diffuse glioma (astrocytic and oligodendroglial) occur most commonly in cerebral hemispheres of young adults, can infiltrate through normal brain parenchyma, and has the genetic tendency for inevitable recurrence and transformation into malignant growth (Masui, Mischel and Reifenberger, 2016b). One of the key events that significantly influenced the classification of gliomas was the discovery of *idh* gene mutations which was originally identified in a subset of secondary GBM tumours which progressed from LGGs (Parsons *et al.*, 2008). *idh1*, and to a lesser extent, *idh2* have been detected in more than 70% of diffuse LGGs (WHO grade II and III) (Yan *et al.*, 2009). Gliomas with *idh* mutations have distinct molecular biology and clinical course of disease, reviewed in (Weller *et al.*, 2015). In normal conditions, the oxidative carboxylation of isocitrate is catalysed via IDH enzymes to produce α-ketoglutarate, which in turn reduces the nicotinamide adenine dinucleotide phosphate (NADP) into NADPH. Many mechanisms have been hypothesised to explain the relation of IDH mutations to gliomagenesis. Mutant IDH enzymes were hypothesised to increase DNA and histone methylation which could lead to an aberrant methylation of cytosine-phosphate-guanine dinucleotide-rich islands across the entire genome (epigenetic hallmark of glioma CPG island methylator phenotype; glioma G-CIMP) (Noushmehr *et al.*, 2010). This occurs via mutant-IDH-mediated conversion of α-ketoglutarate into 2-hydroxyglutarate, which inhibits α-ketoglutarate-dependent dioxygenases such as Jumonji-C domain-containing histone lysine demethylases, and ten-eleven-translocation family of 5-methylcytosine hydroxylases (Xu *et al.*, 2011). The alteration of the normal epigenetic mark may enhance the malignant transformation of neural stem or progenitors into glioma (Masui, Mischel and Reifenberger, 2016b).

Other proposed mechanisms are mediated by the increased production of 2-hydroxyglutarate which potentiates prolyl hydroxylase domain isoform 3 prolyl 4-hydroxylases, which in turn reduces hypoxia-induced factor and promotes human astrocyte proliferation (Koivunen *et al.*, 2012). Mutant IDH enzymes can also promote oncogenesis via increasing oxidative stress due to a reduction in the cellular endogenous NADPH, reviewed in (Molenaar *et al.*, 2014). However, it has became more evident that *idh* mutation is associated with favourable chemotherapeutic response and better prognostic outcome in patients with malignant gliomas, and this has been supported by several lines of evidence (Sanson *et al.*, 2009; Weller *et al.*, 2009; Wick *et al.*, 2009; Van Den Bent, 2010).

Although *idh* mutation seems to occur as an initial somatic aberration in diffuse and anaplastic LGG, evidence has showed that the mutation per se is not sufficient to initiate or induce tumour formation (Sasaki *et al.*, 2012). Alternatively, additional genetic aberrations such as those exclusively observed in diffuse and anaplastic astrocytoma (*tp53* and *atrx* genes), or oligodendroglioma (1p/19q co-deletion and telomerase reverse transcriptase promoter mutation; also known as *tert*), represent pathognomonic molecular markers that differentiates gliomas from astrocytic and oligdendroglial origins (Brat *et al.*, 2015; Suzuki *et al.*, 2015).

In oligodendroglioma, the co-deletion of 1p/19q is frequently associated with other mutations in *Drosophila* homolog of capicua (*cic*), and in the far upstream element-binding protein 1 (*fubp1*) genes (Yan *et al.*, 2009; Bettegowda *et al.*, 2011). However, these mutations are acquired while the glioma is progressing rather than stage of tumour initiation (Suzuki *et al.*, 2015). The co-deletion of 1p/19q typically refers to the deletion of both entire arms of chromosome 1 and 19, due to aberrant translocation [t(1;19)(q10;p10)] (Griffin *et al.*, 2006; Jenkins *et al.*, 2006). Incomplete deletions on one of the chromosomes is not diagnostic for oligodendroglioma, but can be found in WHO grade IV astrocytoma and are associated with poor prognostic outcome (Vogazianou *et al.*, 2010). Thus, if tumours with oligodendroglial histopathology show non-conclusive testing of IDH mutation or co-deletion of 1p/19q, or if testing is not possible, the diagnosis of “non-specified otherwise” (anaplastic) oligodenroglioma is made (Masui, Mischel and Reifenberger, 2016b; Perry and Wesseling, 2016). Likewise, astrocytoma diagnosis requires the identification of *idh* mutation with associated mutation/loss in the *atrx* gene (Jiao *et al.*, 2012; Reuss *et al.*, 2015).

1.4.3. Genetic markers of WHO grade IV gliomas

GBM is the most common high-grade, malignant sub-type of all gliomas, which can be subdivided into two main categories depending on the presence or absence of IDH mutation, and an additional entity (non-specified otherwise) in cases where *idh* mutation cannot be assessed (Masui, Mischel and Reifenberger, 2016b). About 90% of GBM patients have *idh*-wild-type GBM which has developed *de novo* in elderly patients; in contrast, *idh*-mutant GBM occurs most commonly in young adults and reflects progression from LGG (WHO grade II and III) (Ohgaki and Kleihues, 2013; Masui, Mischel and Reifenberger, 2016b).

In addition to the biological benefit of classifying GBM, *idh* mutation in GBM is associated with the clinical scenario of the disease including mean age and overall survival; i.e., longer overall survival was observed in patients with *idh* mutant GBM

(Sanson *et al.*, 2009; Weller *et al.*, 2009), which in some cases is superior even to WHO grade III anaplastic astrocytoma (Hartmann *et al.*, 2010). Immunostaining of the IDH-R132H mutant protein is considered to be a valid method when attempting to discriminate *idh* wild-type or mutant GBM in patients older than 55 years (Chen *et al.*, 2014), whereas DNA sequencing is recommended to be conducted in younger patients and patients with secondary GBM with negative immunostaining of the IDH-R132H mutant protein (Masui, Mischel and Reifenberger, 2016b).

idh wild-type GBM often display gains in copy numbers of chromosome 7, monosomy of chromosome 10, mutations in the phosphatase and tensin homolog (*pten*) tumour suppressor gene on chromosome 10, deletion of both alleles of cyclin-dependent kinase inhibitors (*cdkn2a/p14arf* and *cdkn2b*) on the 9p21 locus, and *tert* promoter mutations (Aldape et al., 2015). In more than 70% of IDH wild-type glioma, *tert* promoter mutation does exist and usually in association with the amplification of epidermal growth factor receptor (EGFR) and have been linked to poor survival outcome (Killela *et al.*, 2014; Labussière *et al.*, 2014; Eckel-Passow *et al.*, 2015). Contrastingly, *tert* promoter mutations which are detected in IDH-mutant type oligodendroglial tumours with 1p/19q co-deletion, are associated with better prognosis relative to GBMs with an *idh* mutation and wild-type *tert* (Arita *et al.*, 2013; Killela *et al.*, 2014). Finally, *tert* promoter mutations are associated with poor prognostic outcomes in GBMs with *idh* mutation and intact 1p/19q (Eckel-Passow *et al.*, 2015) **(Figure 1. 4)**.

In wild-type GBM, mutations frequently occur in more than 60 genes such as *tp53,* phosphatidylinositol 3-kinase regulatory subunit 1 (*pi3kr1*), phosphatidylinositol 3-kinase catalytic alpha (*pik3ca*) and neurofibromatosis type 1 (*nf1*) genes (Bhat *et al.*, 2013; Brennan *et al.*, 2013). Furthermore, proto-oncogene amplifications are common in adult GBM, particularly affecting platelet derived growth factor receptor A (*pdgfra*), *egfr* hepatocyte growth factor (*met)*, cyclin-dependent kinases 4 and 6 (*cdk4*, and *cdk6*), and murine double minute (*mdm2* and *mdm4*) genes (Aldape *et al.*, 2015). Of these, the amplification of *egfr* is the most common mutation, which is detected in more than 40% of wild-type GBMs. A deletion mutation of the external domain encoded by exons 2-7, also known as EGFR-vIII variant, can be found in approximately half of GBMs with an amplified *egfr*. Many other mutations in the intracellular and extracellular EGFR domains have been identified in GBM (Brennan *et al.*, 2013).

A limited (less than 5%) subset of *idh* wild-type GBM tumours exhibit BRAFv600E mutation (Knobbe, Reifenberger and Reifenberger, 2004; Brennan *et al.*, 2013), which is a potential target for BRAF inhibitors (Robinson, Orr and Gajjar, 2014). Rare IDH wild-type GBM exhibit oncogenic fusion mutations between fibroblast growth factor receptor and transforming acidic coiled coil-containing protein, which forms a hyperactive kinase that can be targeted by inhibitory medications (Singh *et al.*, 2012).

1.4.4. GBM subtypes identified by large-scale transcriptome and (epi)genome profiling

In the last decade, the availability of Next Generation Sequencing (NGS) data in TCGA (McLendon *et al.*, 2008a) has facilitated large-scale bio-molecular analyses that has allowed the classification of GBM tumours according to genetic signatures beyond IDH-based stratification. GBMs were classified into four main categories: classical, proneural, neural, and mesenchymal (Verhaak *et al.*, 2010). This has been clinically relevant, as GBM tumours with a mesenchymal genetic signature were shown to have poor response to radiotherapy and short overall survival as compared to other sub-types (Bhat *et al.*, 2013), whereas treatment with an anti-neo-angiogenic agent (Bevacizumab) has limited efficacy against *idh* wild-type GBM tumours with proneural molecular markers (Sandmann *et al.*, 2015).

However, diagnosis-based molecular signature and RNA expression profiles have some caveats that limit clinical benefit, due to technical issues such as the requirement of high quality RNA samples, and due to GBM cellular plasticity that is reflected by the intratumoural genetic heterogeneity caused by the dynamicity in GBM tumour evolution. For example, it has been shown that GSC with a proneural GBM genotype, can transform into a mesenchymal genotype when nuclear form kappa B (*nf-κb*) is activated (Bhat *et al.*, 2013). The vast majority of GBM clinical practice and research is usually based on surgical tissue taken from the core region of the tumour, which can lead to a misdiagnosis of the characteristic molecular signature of the entire tumour, caused by misrepresentation of the molecular diversity within distinct sub-clones of the tumour, as GBM intra-tumoural genetic heterogeneity has been proved to occur within spatially-distinct tumour regions (Sottoriva *et al.*, 2013), and even at single cell level (Patel *et al.*, 2014).

Conversely, epigenetic marks appear to be stable and persist throughout tumour evolution (Masui, Mischel and Reifenberger, 2016b). DNA methylation profiles and associated genetic mutations of GBM tumours were found to be highly reproducible

despite their underlying biological differences (Sturm, Witt, Hovestadt, Khuong-Quang, David T.W. Jones, *et al.*, 2012; Brennan *et al.*, 2013; Korshunov *et al.*, 2015). In these two studies, WHO grade IV gliomas were stratified into four groups according to DNA methylation and the most common associated molecular aberrations (Sturm *et al.*, 2012; Korshunov *et al.*, 2015) **(Figure 1. 5)**. Of these, two GBM groups were found to be prevalent in young adults and adolescents: one GBM category is characterised by *idh*(1/2)-mutations, G-CIMP, in addition to other genetic aberrations which usually occur in the proneural GBM mRNA expression profile such as *tp53, atrx,* and *cdkn2a/2b deletion*; whereas the second GBM category is referred to as "receptor tyrosine kinase I (RTKI)" and characterised by *pdgfra* amplification, in addition to mutations in the *tert* promoter. A further two GBM groups are prevalent in patients older than 50 years: one GBM category is designated as "receptor tyrosine kinase II (RTKII) or "classic" and is characterised by the amplification of *egfr*, *cdk4/cdk6*, and *mdm2/mdm4*, in addition to deletion in *cdkn2a/b* and other mutations in *pten, and tert*: whereas the final GBM category is known as "Mesenchymal" and is characterised by mutations in *nf1, pten*, and the *tert* promoter. Chromosome 10 loss is common in all four categories, whereas chromosome 7 gain can occur in RTKI, RTKII, and mesenchymal sub-types **(Figure 1. 5)**.

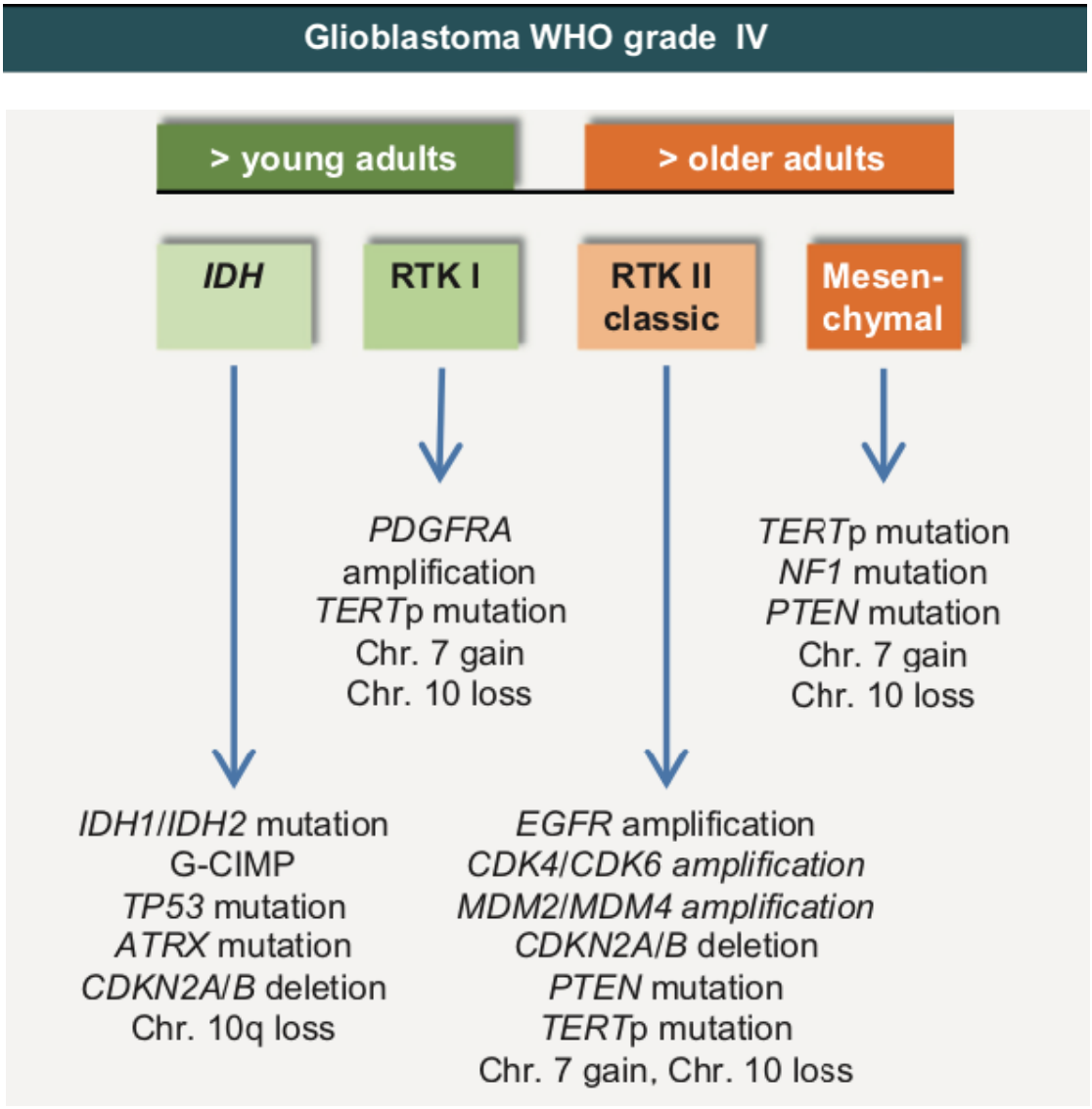


Figure 1. 5. Adult GBM classification according to DNA methylation profiles. Four adult GBM subgroups with distinct DNA methylation profiles are associated with common genetic aberrations; young adults are typically presented as “IDH” and “RTKI” GBM epigenetic subtypes, whereas patients who are older than 50 usually present with “RTKII; classic” and ”Mesenchymal” GBM epigenetic subtypes. The figure is adapted from (Masui, Mischel and Reifenberger, 2016b), which has been depicted according to the information described in (Sturm, Witt, Hovestadt, Khuong-Quang, David T.W. Jones, *et al.*, 2012; Brennan *et al.*, 2013; Korshunov *et al.*, 2015).

1.5. Glioma invasive phenotype

The invasive ability of gliomas has been the focus of pathologists since 1938, when German neuropathologist Hans Joachim Scherer suggested that the tumour cells of glioma malignancies can infiltrate the normal brain parenchyma with distinct morphological patterns (Scherer, 1938). Of these, Scherer categorised the secondary structures, which described the arrangement of the invading glioma cells in relation to neural and glial cells, or alongside the white matter tracts, blood vessels and meninges. In particular, perivascular satellitosis was described as the concentric arrangement of glioma cells outside the Virchow–Robin spaces of the pre-existing normal brain vessels. Scherer also described the predilection of invasive malignant glioma cells to capillaries and small blood vessels, as one of the distinctive features of gliomas, emerging from perivascular gliosis. In addition, Scherer observed that glioma cells can grow around blood vessels in areas of normal parenchymal brain tissue, at some distance from the original tumour mass. This view of the invasiveness of gliomas is still valid and accepted (Farin *et al.*, 2006; Zagzag *et al.*, 2008; Montana and Sontheimer, 2011), has been further corroborated by several recent studies and in considerable part contributes to the ineffectiveness of current chemotherapeutic treatments for HGG.

The attachment of migrating glioma cells is functionally associated with receptors expressed on the surface of tumour and non-tumour cells and on the ECM and is mediated through cell-cell and cell-matrix interaction by adhesion molecules such as integrins and cadherins. The detachment of these invading cells occurs mainly through the degradation and remodeling of the surrounding ECM by matrix metalloproteinases (Deryugina *et al.*, 1997; Demuth and Berens, 2004; D'Abaco and Kaye, 2007; Kwiatkowska and Symons, 2013; Wolfenson, Lavelin and Geiger, 2013). According to a related hypothesis, malignant glioma cells detach from the primary tumour mass, create new connections with surrounding parenchyma, destroy and remodel the ECM and finally migrate into healthy tissue (Rao, 2003). Similarly, some studies found that glioma cells undergo several complex morphological changes, which are mediated by the actin-myosin machinery, to enable migration into surrounding brain tissue (Christopher Beadle *et al.*, 2008; Lee, Lim and Kim, 2017). Additionally, significant volume and shape changes of glioma cells during the invasion process were observed by *in-vivo* and *ex-vivo* time-lapse imaging techniques (Farin *et al.*, 2006; Watkins and Sontheimer, 2011). For example, significant hydrodynamic glioma cell volume changes (that might result in 33% reduction of glioma cell volume) could facilitate invasion through small-sized

surrounding spaces. This was inferred from *in-vitro* observations where a one-third reduction in glioma cell volume preceded infiltration through transwell barriers with 3–8μm pore size (Watkins and Sontheimer, 2011). These periodic morphological changes were achieved by repurposing ion-channels that are normally used to control physiological neural excitability functions (Cuddapah *et al.*, 2014). Such complex sequential mechanisms promote the invasion of glioma cells into narrow compartments, such as the perivascular space which otherwise would be too small for the cells to infiltrate into (Cuddapah *et al.*, 2014).

In rodent-model studies, the perivascular space has been shown to be the major compartment where glioma cells invade and more than 85% of these invading malignant cells migrate around blood vessels to form the satellite tumour shape (Montana and Sontheimer, 2011; Watkins *et al.*, 2014). Furthermore, it could be argued that glioma cells invade the vascular compartment and co-opt pre-existing vessels (Watkins *et al.*, 2014), early during disease progression without the need for the neo-angiogenic factors produced by glioma cells. This may explain the failure of all anti-angiogenic drugs tested in clinical trials as a first line treatment option. For example, bevacizumab has failed to show any overall survival benefit in newly diagnosed glioma patients (Gilbert *et al.*, 2014). Moreover, at least some glioma cells retain or acquire the ability to create tumour-derived vascular networks toward late-stages of the disease, in a phenomenon termed ‘vascular mimicry’, shown by our group and others (El Hallani *et al.*, 2010; Smith *et al.*, 2015). El Hallani and colleagues showed that non-endothelial cells derived from GBM, which exhibited stem-like features, could secrete pro-angiogenic factors and express endothelial markers, mimicking features of vascular smooth muscle-like cells. Vascularity in gliomas was shown to be generated in both an oxygen-dependent and oxygen-independent manner via the master angiogenic regulators vascular endothelial growth factor (VEGF) and hypoxia induced factor-2α (HIF-2 α), or through fibroblast growth factor 1 (FGF1) signaling pathways respectively (Uriel, Brey and Greisler, 2006; Beenken and Mohammadi, 2009).

1.6. GBM intra-tumour heterogeneity

Many models have been proposed to better understand GBM heterogeneity. It is hypothesized that the ‘cancer stem cell theory’, ‘clonal evolution’, and ‘tumour cell plasticity’ hypotheses can in an inter-related manner, explain the initiation and/or the maintenance of cellular heterogeneity in GBM. The ‘cancer stem cell’ hypothesis states that GSC with self-renewal capacities can initiate tumour formation and

enhance tumour progression (Al-Hajj and Clarke, 2004). Furthermore, these cells can be influenced by different niches provided by distinct tumour micro-compartments and can ultimately differentiate into multi-lineage daughter cells with different morphological and genetic marks. On the contrary, the 'clonal evolution' model suggests that intra-tumour heterogeneity of GBM can be explained by the accumulation of genetic and epigenetic alterations within a single cell subpopulation (clonal), which can result in the acquisition of several mutations that leads to oncogenesis and GBM formation (Greaves and Maley, 2012). Although each individual model can explain GBM heterogeneity, these theories (cancer stem cells and clonal evolution) are not mutually exclusive to explain GBM evolution and cellular diversity. In other words, GSC with self-renewal capabilities have the capacity to persist and accumulate genetic and epigenetic alterations necessary for cancer initiation and progression, producing distinct transient amplifying cells which can further differentiate into many cell lineages within the same tumour. Transient amplifying cells can progressively acquire genetic mutations, but unless a mutation confers the emergence of self-renewal abilities, these alterations in cellular subpopulations may not promote cell survival and rapid proliferation, and will be eliminated from the tumour population. Recent evidence showed that signaling within the perivascular region of GBM can induce tumour cells to acquire stem-like characteristics. This study proposed an alternative model which suggests that most or all tumour cells, are liable to exhibit stem-like characteristics depending on distinct tumour microenvironments and/or the intrinsic status of the tumour cell itself (Charles *et al.*, 2010). This indicates that 'stemness' is a blurred concept which represents a dynamic cell state, rather a discreet cell entity. These findings highlight the elegant efforts performed to explain intra-tumour heterogeneity, whereby this cellular diversity contributes to a clinical hallmark of GBM by influencing tumour behaviours such as tumour invasiveness and recurrence, despite treatment multimodality (Yap *et al.*, 2012).

Intra-tumoural spatial and temporal heterogeneity has been one of the main challenges of GBM diagnosis and treatment. Historically, GBM samples are taken from the tumoral bulky mass, which is usually located within the core of the tumour, enhanced by radiological contrast, and hypercellular in microscopic examination. However, exclusively sampling the core of gliomas does not reflect the diversity and dynamicity of sub-clones within the tumour (Gerlinger *et al.*, 2012). This has led to the failure of the implementation of molecular targeted therapies due to the presence of malignant, invasive, and therapy-resistant subclones that evaded treatment

(Johnson, 2014b). Tumour evolution over disease-progression and the competition of between the founder clones and the emerging subclones, can profoundly alter the original clonal architecture, which in turn hampers the identification of predictive and prognostic molecular markers (Keats *et al.*, 2012). Intratumoural heterogeneity caused by spatial and temporal evolution of the tumour has been described as a "moving target", suggesting that next-generation treatment must aim to eradicate both founder clones and branching subclones (Ding *et al.*, 2012).

Leveraging the hypothesis of tumour clonal interdependencies led to the "adaptive therapy" approach. Unlike the Norton-Simon therapeutic approach which involves introducing maximum tolerable chemotherapeutic doses, the adaptive therapy is dynamically modulated to stabilize tumour burden via populating the outcompeting fitter chemo-sensitive subclones over the less-fit therapeutic-resistant subclones (Gatenby *et al.*, 2009); i.e., the utilization of initial high therapeutic doses at early stages of treatment aiming to kill the maximum number of cancer cells, will remove the predominant chemo-sensitive subclones that outcompete the less-abundant therapeutic-resistant subclones, and this according to Darwinian principles, means that the cancer microenvironment can enhance the rapid re-population of therapeutic-resistant subclones at early stages of treatment.

1.7. Current scientific gaps which led to the project rationale and study aims

HGG remain one of the most aggressive and difficult to treat cancers in adults and children, with a very poor prognosis of 14 months median survival from diagnosis (Stupp *et al.*, 2005), despite current multimodal therapeutic approaches. The ability of glioma cells to infiltrate the surrounding parenchyma of the normal brain and along the nearby blood vessels (Scherer, 1938; Cuddapah *et al.*, 2014; Diksin, Smith and Rahman, 2017), limits the surgical resection option, whereby true complete resection is not safely possible (Nakada *et al.*, 2007). Moreover, the intra-tumoural genetic heterogeneity emerging from the dynamicity of clonal selection processes within spatially distinct intra-tumoural niches, allow glioma cells to escape conventional chemotherapeutic and radiological treatments.

Unfortunately, most glioma studies and TCGA repository RNA sequencing data merely involve samples usually taken from tumour core regions, despite our increasing knowledge of genetic and epigenetic intra-tumoural heterogeneity (Sottoriva *et al.*, 2013; Suzuki *et al.*, 2015). Furthermore, the GBM tumour core is the part that is surgically resected with the bulky tumour mass, whereas approximately

80% of anaplastic astrocytoma recurrences occur within 2cm of the original peri-operative tumour (Wallner *et al.*, 1989; Pennington *et al.*, 2006; Konishi *et al.*, 2012; Petrecca *et al.*, 2013; Lemée, Clavreul and Menei, 2015; Rapp *et al.*, 2017).

Whereas glioma core regions are usually necrotic due to a rapidly growing tumour mass and inter-cellular competition for oxygen and nutrients, tumour edges (particularly the infiltrative margin) represent a key hallmark of gliomas that is more clinically-relevant when considering next generation therapy. Lack of an appropriate model and lack of a complete understanding of tumour complexity are the main reasons why it is not known whether or not the astrocytes are susceptible to malignant transformation when in contact with GBM invasive margin residual disease cells, or how peri-tumour astrocytes may promote re-growth of infiltrative disease within the recurrent tumour microenvironment. Specifically, it is not known whether or not the cell-to-cell contact between GBM cells and the surrounding reactive astrocytes can enhance the malignant transformation of astrocytes and thereby provide the tumour with newly recruited neoplastic astrocytic cells (Broekman *et al.*, 2018). Literature evidence shown so far, advocates for a strong supportive role of astrocytes in GBM invasion and resistance to therapy; for example, astrocytes were described as the “rising stars of the GBM microenvironment”; i.e., astrocytes were thought to support/enhance GBM cells proliferation, migration, invasion, cell survival, and antagonizing apoptotic pathways aimed to be activated via multi-model therapeutic approaches, reviewed in (Brandao *et al.*, 2019). Literature evidence also suggests that tumour associated astrocytes are key enhancers for GBM survival, immune-protection and chemo-resistance, reviewed in (Venkataramani *et al.*, 2019; Venkatesh *et al.*, 2019). Astrocytes can be transformed into malignant GBM using various oncogenes such as MYC, RAS, and EGFRVIII, confirming astrocytes as cell-of-origin for these neoplasms (Jahani-As *et al.*, 2016; Li *et al.*, 2016). Furthermore, normal astrocytes have been reported to reduce p53 tumour suppressor expression through an unknown mechanism after exposure to GBM conditioned medium and can enrich the ECM with laminin and fibronectin, which enhances glioma cell survival (Biasoli *et al.*, 2014). However, it is also not known if the astrocytes located adjacent to the periphery of GBM tumours, are involved in immune/defense mechanisms against GBM cells, and indeed astrocytes are thought to enhance the immune-suppressive microenvironment of GBM (Henrik Heiland *et al.*, 2019).

Therefore, we hypothesized that the infiltrative malignant glioma cells that are left post-operatively within the invasive margin of GBM, can interact with the surrounding healthy astrocytes and induce important alterations in their genetic signitures. Our

overarching aim was to model the invasive margin of GBM tumours to recapitulate the reprogramming events which occur immediately after surgical removal of the bulk tumour mass and to ultimately reveal the genetic cross-talk between malignant and non-malignant astrocytes. If successful, this approach may unravel intricate and non-canonical molecular pathways promoting disease recurrence from the invasive tumour margin, and also facilitate the identification of an optimal therapeutic approach against this clinically-relevant tumour sub-population.

1.8. Rationale of *in-vitro* modelling objectives and design of study

To model the GBM invasive edge accurately, the environment of the entire model, must resemble the normal human brain niche as closely as possible. In this context, the most abundant cell type that is present in normal human brain tissue (astrocytes), was derived from multi-potent NSCs using a well-characterised and reproducible differentiation protocol. These astrocytes were co-cultured with each of 10 distinct low-passage primary GBM cell lines that were surgically isolated from the GBM invasive margin. Upon a period of 6 and 10 days of co-culture, astrocytes were proposed to be isolated, RNA extracted and transcriptomic profiles analysed. However, there is no definitive molecular marker which can distinguish normal astrocytes from malignant astrocytoma cells. This adds a considerable scientific challenge, which requires the creation of genetically-stable astrocytic-lineage-labelled NSCs, using CRISPR/Cas9 technology, which may facilitate fluorescence-based isolation of fluorescently-tagged astrocytes after NSCs differentiation, and upon re-isolation after co-culturing with invasive GBM cells (chapter 3).

Another important component of the invasive model is the ECM, which should hypothetically provide native physiological human brain ECM signals. However, human brain ECM composition and the proportions of these components are yet to be properly characterised, which makes the construction of a 3D human brain ECM from appropriately characterised synthetic materials extremely challenging. Additionally, commercially available ECM products include animal materials as a major component, which are usually derived from or abundantly found in tumours. For example, Matrigel, which is derived from the Engelbreth-Holm-Swarm Sarcoma, contains collagen and laminin as essential elements, whereas all such fibrillar proteins are present in only minuscule amounts in the normal human brain ECM (Ruoslahti, 1996) and also abundant in tumours such as gliomas (Zheng *et al.*, 2004; Hu *et al.*, 2008). Thus, preparing ECM derived from a human brain donor using a decellularised process was one of the corner-stone objectives of the project (chapter

4), in order to recapitulate a physiologically-accurate brain microenvironment (chapter 5). Additionally, reconstructing the decellularised human brain material into a 3D structure using a bio-inert PEGDA hydrogel was anticipated to provide the required 3D cellular niche without introducing unnecessary signals that may bias the results (chapter 5).

Collectively, this original multi-component model (transgenic astrocytes, invasive GBM cells, human brain decellularised ECM) was termed ‘Gliomasphere Matrices’ and was investigated here as a 3D cellular model which represents the immediate post-surgical microenvironment where residual disease remains. Gliomasphere Matrices thereby presents a molecular snapshot of astrocyte-GBM cellular interactions which promotes tumour recurrence, a current ‘black box’ in understanding of this deadly disease.

In summary, our objectives to create a co-culture model include:

- Creating genetically modified NSCs with a knocked-in reporter gene, which requires cloning of cutting and HDR vectors and using CRISPR-Cas9 technology to knock-in the specificallt designed transgenic segment into the NSCs genome (Chapter 3).
- Decellularising Human brain ECM and characterise its components using highly sensitive TOF-SIMS tool according (chapter 4)
- Preparing a physiologically-accurate scaffold by the 3D reconstruction of the decellularised human bain ECM (derived in chapter 4) using bioinert 3D material called PEGDA, which allows performing co-culture of genitically-labelled astrocytes with GBM cells derived from the invasive margin of GBM (chapter 5),
- Analysing RNA-sequencing data of astrocytes isolated from co-culture experiments and validate these results with patient samples and TCGA, to reveal genetic alerations caused by by direct cell-cell interaction with glioma cells (chapter 6).

Chapter (2)

General Materials and Methods

Chapter 2 - Materials and methods

2.1 Guidelines for cryopreservation of cells (modified from Neurobiology protocol handbook from Gibco)

1. The cryomedium (in general, the growth culture medium deprived of growth factors with the addition of 10% DMSO) was always pre-chilled on ice for at least 15 minutes to minimize cytotoxicity from DMSO to reduce the time needed for the cryomedium to cool down. The growth medium used for the propagation of NSCs was StemPro NSC SMF (Gibco Catalogue number: A1050901), Astrocyte medium (ScienCell, Catalogue number: 1801) was used for propagation of astrocytes, and DMEM/F12, GlutaMAX (Gibco Catalogue number: 31331093) plus 10-20% foetal Bovine Serum for propagation of primary GIN cell lines.
2. The empty pre-chilled cryovials were labelled with the name of the cell line, number of cells, date, freezing medium, and gene edits where applicable.
3. The cryovials were rinsed with the cryomedium prior to the addition of the cells to avoid the adherence of the cells to the plastic surfaces.
4. Mr. Frosty freezing containers were checked to have 250ml of 100% propanol and pre-chilled to (4°C) prior to the addition of the cryovials containing the cells.
5. The cells were harvested from culture surfaces using StemPro™ Accutase™ Cell Dissociation Reagent (Thermofisher scientific; catalogue number: A1110501), which was mainly used for passaging astrocytes throughout differentiation. However, TryplE Express (TrypLE™ Express Enzyme (1X), phenol red; Gibco catalogue number: 12605010) was utilized to passage NSC or whenever single cell suspensions were required; for example, prior to cell sorting using FACS. The volume used for the dissociation reagents was 1ml per each 25cm^2 culture surface. These reagents were used for 30 seconds to a maximum of 2 minutes at (37°C) and then deactivated (diluted 1/10) using the appropriate growth medium.
6. Cells were resuspended in the culture medium before taking 10µl of each single cell suspension to be counted using a haemocytometer, in order to determine the total cell number of the stock solution and to label the cryovial.
7. The cells were centrifuged at 200-220 x g for 4-5 minutes and the supernatant aspirated.

8. The pre-chilled (4°C) cryomedium was added in a drop-wise fashion and cells gently resuspended in the cold medium at a concentration of 1.0-2.0 x 10^6 cells/ml and 1ml transferred into the cryovial to be frozen at -80°C for short-term storage and liquid nitrogen for long-term storage.

2.2 Guidelines for recovering frozen cells from liquid nitrogen (modified from Neurobiology protocol handbook from Gibco)

1. The growth media was prepared and warmed to 37°C.
2. The cryovials were removed from liquid nitrogen and immediately kept on dry ice prior to being transferred to a 37°C water bath.
3. The frozen vials rapidly (<2minutes) thawed at 37°C after which the cryomedium was pipetted up and down gently before moving the cells with preservative medium (0.5-1ml) into 15ml falcon tubes.
4. The pre-warmed cryovial was then rinsed with 1ml of medium and the 1ml rinse medium moved into15ml falcon tubes.
5. Another 2ml of the corresponding medium was added drop-wise to a total of 4ml.
6. Using a pre-rinsed P10 tip, 10µl of the single cell suspension was gently mixed with another 10µl of 0.4% trypan blue in a microcentrifuge tube.
7. The number of viable cells was determined using a haemocytometer and manual counting method.
8. The 15ml tube was centrifuged at 200-220 x *g* for 4-5 minutes to pellet the cells. This wash ensured that DMSO was removed from the cells.
9. The supernatant was aspirated and cells were resuspended in a variable volume of growth medium depending on experimental need.
10. The resuspended cells were plated onto pre-coated culture surfaces at different seeding densities depending on experimental need, but usually 25000cells/cm^2.

2.3 Guidelines of passaging cells (modified from Neurobiology protocol handbook from Gibco)

1. Growth medium was aspirated and attached cells were washed twice with DPBS without Ca^{+2} and Mg^{+2}, to remove growth medium that may inactivate the dissociation reagent or reduce its efficiency.
2. 1ml of TryplE Express or Stem Pro Accutase per 25cm^2 culture surface was added to harvest the cells. The choice of TryplE Express or Accutase was dependent on experimental need as TryplE Express generates a single cell suspension, whereas Accutase typically removes the cells as clumps. Also, the nature and type of cells was an important consideration; for example, TryplE Express was used for NSCs, whereas Accutase was used for astrocytes and primary GBM cell lines.
3. Culture vessels were then incubated at 37°C for 30 seconds to detach cells grown as a monolayer.
4. The cells were gently pipetted up and down to dissociate large clumps of cells. It is important to note that cells were not incubated with dissociation reagents for more than 3 minutes, to maintain a high proportion of cell viability.
5. The dissociation reagents were neutralized (inactivated) by a 5-10-fold dilution using pre-warmed growth medium.
6. Using a haemocytometer, the cells were counted to determine the concentration of cells per each ml of medium.
7. The total volume of cell suspension was then transferred into a 15ml tube and centrifuged at 200-220 x *g* for 4-5 minutes to pellet the cells.
8. The supernatant was aspirated and discarded to avoid any residual passaging of reagents in the growth medium.
9. The cells are resuspended to the required concentration using fresh pre-warmed growth medium.
10. The cells were then appropriately plated on pre-coated culture surfaces; for example, Geltrex for NSCs and Matrigel for astrocytes.

2.4 Immunofluorescence staining was performed according to standard operating protocols

1. The growth medium was removed and NSCs were washed twice with DPBS without Ca^{+2} and Mg^{+2}.
2. The NSCs were fixed using 0.4% paraformaldehyde for 20 minutes at room temperature.
3. The paraformaldehyde was removed and cells were washed using DPBS without Ca^{+2} and Mg^{+2}.
4. NSCs were permeabilised using a PBS-T solution composed of 0.1%Tween, 0.25% Triton-X in 10mlPBS.
5. The chamber slide was placed in a humidity chamber
6. The PBS-T was replaced by 5% normal goat serum in DPBS (blocking solution) for 60 minutes at room temperature.
7. The 5% normal goat serum was removed and cells were washed with PBS-T three times for 5 minutes.
8. Primary antibodies Nestin (abcam; ab220335), and SOX2 (abcam; ab92494) were diluted using 2% normal goat serum (200µl normal goat serum in 9.8 ml PBS-T) at a concentration of 1:200.
9. The primary antibodies were applied on NSCs and incubated overnight at 4°C.
10. NSCs were then washed three times using DPBS without Ca^{+2} and Mg^{+2} to wash the cells thoroughly and to remove unbound primary antibodies.
11. The appropriate secondary antibodies (Alexa fluor 488nm or 555nm) were applied for 2 hours in the dark at room temperature.
12. The slide was washed thoroughly three times, air-dried and mounted using Vectasheild mounting medium with DAPI (Vector Laboratories; H-1800-10). Slides were kept in the dark at 4°C until examination using microscopy.

2.5 Seeding cells inside Millicel ® EZ chambers slides (Millipore; PEZGS0816) for immunofluorescence imaging.

1. The chamber slide was firstly coated with Geltrex™ LDEV-Free Reduced Growth Factor Basement Membrane Matrix (Gibco; A1413201), according to manufacturer guidelines (section 2.7.1).
2. NSCs were cultured on Geltrex™ and passaged using TryplE Express or StemPro Accutase. The cells were counted using a haemocytometer or EVE automatic cell counter (Cambridge Bioscience).
3. 4-5 x10^4 NSCs were suspended in 700µl StemPro medium and seeded in each well. Cells were incubated in standard cell culture conditions.
4. Growth medium was changed every day until immunofluorescence imaging.

2.6 Agarose gel electrophoresis was conducted according to standard operating protocols

1. An appropriate weight of agarose was prepared depending on the percentage of agarose gel, which usually has a range of 0.7-1%. The choice of agarose percentage depends on the physical distance expected between gel bands and thus the resolution required, particularly whenever the bands need to be excised. The physical approximation between bands on different agarose percentages was best anticipated using NEB cutter V2 (http://nc2.neb.com/NEBcutter2/).
2. 0.7-1g of agarose was dissolved in 100ml 1X TAE buffer by heating using a microwave at interrupted intervals of 1 minute with the container lid open.
3. The lid was then closed and the container cooled under running tap water, until it could be held with gloved hands.
4. 4µl/100ml of ethidium bromide was next added to the soluble agarose still warm to the touch.
5. A casting tray was sealed using tape and an appropriate comb was placed before pouring the gel, to create gel lanes. Any bubbles were burst or moved to the side of the gel using a P1000 tip.
6. The tape was removed once the agarose gel solidified and the casting tray placed inside the electrophoresis tank.
7. 1X TAE buffer was poured into the electrophoresis tank ensuring the gel was submerged, before removing the lane comb.

8. 6x Gel loading dye (NEB; catalogue number: B7024) was mixed with the total DNA reaction volume and sterile DNase-free water until 1x of dye was obtained.
9. 10µl of 2-Log DNA ladder (NEB; catalogue number: N3200S) was loaded in one well, and 10-12µl of the DNA reaction plus 1X purple dye was loaded into the remaining wells.
10. The wells containing DNA samples were at the side of the negative electrode to allow negatively charged DNA to travel through the gel toward the positive electrode.
11. DNA samples and ladder were run at 90 volts for 40 minutes. Higher voltages were not used, to avoid shearing forces which may have led to DNA damage, as DNA was often required to be extracted from the gel during molecular cloning experiments.
12. The gel was removed from the casting tray and transferred to a UV platform to be either imaged or for gel bands to be excised.

2.7 Preparing surface coating for the NSCs

2.7.1 Coating vessels surfaces with Geltrex™ LDEV-Free Reduced Growth Factor Basement Membrane Matrix (Gibco; A1413201) (modified from Neurobiology protocol handbook from Gibco).

1. In preparation for NSC propagation, a 1ml Geltrex™ tube was thawed on ice and stored at 4°C overnight to avoid polymerisation. 10x 100µl aliquots were prepared in 0.2ml tubes and frozen at -20°C until further use. All work was performed on ice. Geltrex™ was not kept at room temperature for more than 1-2 minutes throughout the coating procedure, to avoid polymerisation.
2. When required, a 100µl aliquot was thawed on ice and diluted in 9.9ml pre-chilled (4°C) advanced DMEM (Gibco; 12491015), to a final concentration of 0.1mg/10ml. The mixing process was very gentle and on ice to avoid gelling of the Geltrex™. Vortexing was avoided.
3. 5ml of the diluted Geltrex™ was applied to the entire culture surface of a T25 flask (2.5ml for each well of 6-well plate), which was then kept at 37°C for 1 hour to polymerise and to ensure coverage of the entire culture surface with a thin Geltrex coating layer. Alternatively, T25 flasks could be sealed with parafilm and stored at 4°C for a maximum of 2 weeks until further use. The culture vessels were kept at a horizontal plane to ensure even distribution of the Geltrex™.
4. After incubating the culture vessel, all Geltrex™ dilute was removed and the vessel immediately washed once using DPBS without Ca^{+2} and Mg^{+2}. It was critical to quickly add DPBS once Geltrex dilute was removed to avoid drying of the Geltrex™ coating. In addition, touching the coated surface was avoided when aspirating the supernatant, as this may have caused the NSC to differentiate.
5. Cell suspensions in pre-warmed complete StemPro medium was finally applied onto the Geltrex™-coated surface.

2.7.2 Coating vessel surfaces with Corning® Matrigel® Basement Membrane Matrix, LDEV-free. (Corning; 354234)

1. 10ml Matrigel (Corning; 354234) was thawed on ice overnight to avoid polymerisation. Aliquots of 0.5ml from the original stock were prepared in 1.5ml tubes and frozen at -20°C until further use. All work was performed on ice. Matrigel was not kept at room temperature for more than 1-2 minutes throughout the coating procedure to avoid polymerisation.
2. When required, a 0.5ml aliquot was thawed on ice (approximately 30-40 minutes) and diluted in 24.5ml of pre-chilled (4°C) advanced DMEM (Gibco; 12491015), to a final concentration of 4mg/ml. The mixing process was very gentle and on ice to avoid gelling of the Matrigel. Vortexing was avoided to avoid Matrigel polymerisation.
3. 2.5ml of the diluted Matrigel was applied to the entire culture surface of a T25 flask (1.25ml for each well of 6-well plate), which was then stored at 37°C for 1 hour to polymerise and to ensure coverage of the entire culture surface. Alternatively, T25 could be sealed with parafilm and stored at 4°C for a maximum of 2 weeks until further use. The culture vessels were kept at a horizontal plane to ensure even distribution of the Matrigel on the culture-wares.
4. After incubating the culture vessel, all Matrigel dilute was removed and immediately washed twice using DPBS without Ca^{+2} and Mg^{+2}. It was critical to quickly add DPBS once Matrigel dilute was removed to avoid drying of the Matrigel coating. In addition, touching the coated surface was avoided when aspirating the supernatant.
5. Cell suspension in pre-warmed complete astrocyte medium was finally applied onto the Matrigel-coated surface.

Chapter (3)

Creating a transgenic astrocytic reporter cell line using CRISPR/Cas9 technology

Chapter 3 Creating a transgenic astrocytic reporter cell line using CRISPR/Cas9 technology

3.1 Introduction

In human stem cells, stable gene-editing strategies using homology recombination represents a considerable technical challenge across laboratories (Tiyaboonchai *et al.*, 2014). Most of these genomic modifications are mediated by either viral transduction, lipofection or plasmid electroporation. However, these methods lead to random integration of transgenes within the stem cell genome. Transgene integration at a random locus in the genome may lead to silencing of the transgene expression, referred to as position effect variegation (Hatzistavrou *et al.*, 2009). Thus, choosing the knock-in genomic site is critical for stability of reporter gene expression in the edited cell line. The induction of a **D**ouble **S**trand **B**reak **(**DSB) using CRISPR and **C**RISPR-**as**sociated (Cas) 9 (CRISPR/Cas9) system at the AAVS1, located within intron 1 of the protein phosphatase 1 regulatory subunit 12C (PPP1R12C) gene, is essential for stable long-term transgene expression due to this genomic region being insulated (Ogata, Kozuka and Kanda, 2003). CRISPR/Cas9 was originally discovered as an endogenous component of bacterial (*S.pyogenes*) immune systems **(Figure 3. 1)** and recently developed as a versatile gene-editing tool with many potential applications in molecular biology **(Figure 3. 2)**.

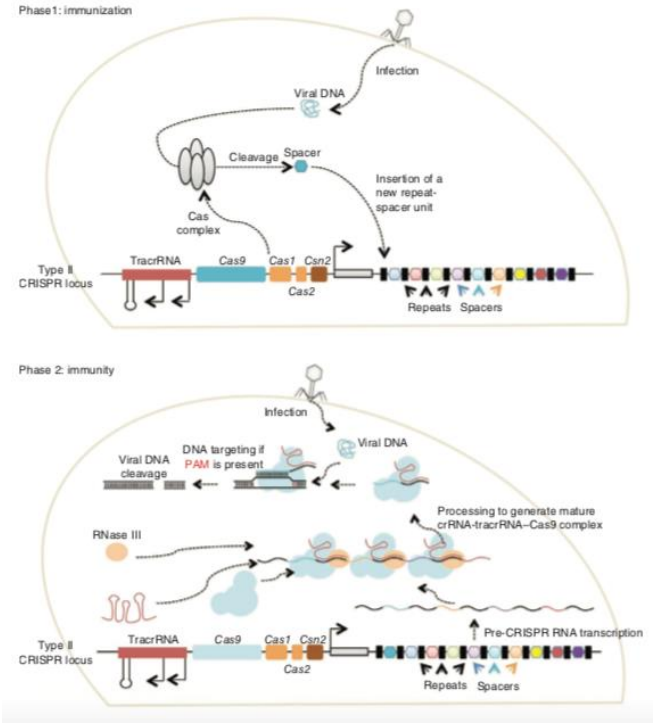


Figure 3. 1. Original discovery of CRISPR/Cas9 as part of the bacterial immune (*S.pyogenes*) system. The figure was taken from (Mali *et al.,* 2013). In the immunization step (phase I), the CRISPR system stores the genetic signature of the invading phage or plasmid DNA as "spacers" within the CRISPR locus. In the immunity phase (Phase II), the bacterium activates the transcription of the CRISPR loci using the stored information to produce CRISPR RNAs (crRNAs) that lead the nuclease to locate the cleavage sites at the invader/foreign nucleic acids that match the sequences of the spacers. This enables the bacterium to defend against invading pathogens such as viruses. Initially, the repeat regions of pre-crRNAs are hybridized by the tracrRNAs. Next, the intrinsic RNaseIII cleaves the hybridized crRNA-tracrRNA followed by a second event of removing the 5'end of the spacer to yield a mature crRNAs bound to tracr and Cas9. The complexes cut through the complementary sequence "protospacers" merely if a Protospacer Adjacent Motif (PAM) sequence is present.

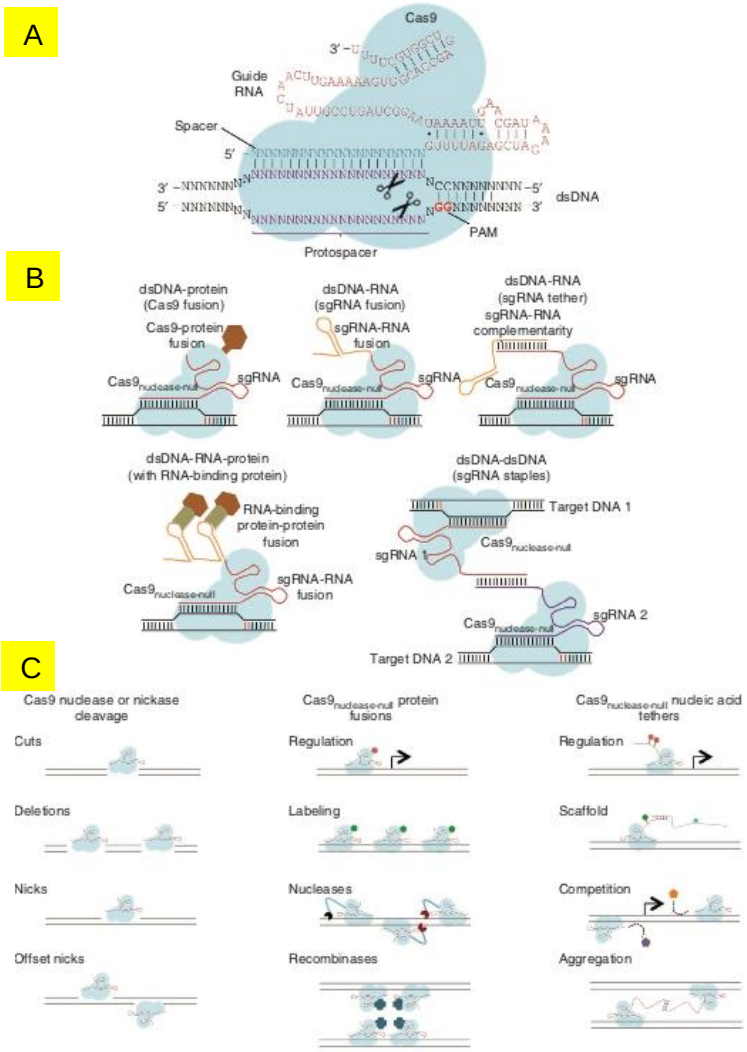


Figure 3. 2. Targeting strategies using Cas9 gRNA complexes. The figure was taken from (Mali *et al.,* 2013). (a) The basic components of the bacterial Cas9 protein plus its RNA guide holding the spacer sequence that is complementary to a specific DNA site within a particular eukaryotic genome. (b) Cas9 can be used to precisely locate dsDNA, RNA and RNA-binding proteins. Proteins can be fused to Cas9 (nuclease-null) to target dsDNA sequences. An extra RNA can be fused to the terminal region of the guide RNA without compromising the binding efficiency of the Cas9 protein (nuclease-null). This can also provide an extra hybridization site to recruit further RNAs. The binding sites of the attached RNAs can provide further recruitment sites for other RNAs or RNA-binding proteins. Hypothetically, Cas9 can also tether two distinct DNA sequences by binding their guide RNAs. Thus, it can bind and fuse to proteins, RNAs (natural or fused), and/or dsDNA loci at any specific genomic site of interest. (c) The diversity of potential uses and applications of Cas9 technology in genome engineering.

CRISPR/Cas9 technology (Mali *et al.*, 2013; Mali, Esvelt and Church, 2013; Ran *et al.*, 2013) uses short guided RNA to edit specific protein-coding genomic sites (Horvath and Barrangou, 2010; Bhaya, Davison and Barrangou, 2011; Wiedenheft, Sternberg and Doudna, 2012). CRISPR/Cas9-Induced DNA breakage at these sites triggers the intrinsic DNA repair machinery by either **H**omology **D**irect **R**epair (HDR) or **N**on-**H**omology **E**nd **J**oning (NHEJ) mechanisms (O'Driscoll and Jeggo, 2006; Sakuma and Woltjen, 2014), to either create targeted integration or gene knock-out respectively. NHEJ occurs when the DSB is fixed with random mismatched nitrogen bases or deletion (indels) of various DNA length around the break, which results in mutations and ultimately gene inactivation (Chang *et al.*, 2017). This is a strategy that is commonly used to cause gene disruptions (i.e. point mutation or knock-down; one allele is targeted) and/or knockouts (both alleles are targeted) as, for example, the formation of indels within a coding sequence can lead to frameshift mutations and ultimately mRNA degradation or a non-functional protein (Lieber *et al.*, 2014). NHEJ is considered to be easier to harness experimentally than HDR as it does not need a DNA repair template and unlike HDR, occurs throughout the cell cycle (Delacôte and Lopez, 2008). In contrast, HDR occurs when a rapidly proliferating cell repairs its DSB using a homologous DNA fragment provided from an exogenous source or from the other unaffected endogenous allele **(Figure 3. 3)**. This has been widely used to create precise mutations within *in-vitro* models by providing the properly designed repair templates flanked by the sequences identical to those located at both sides of the DSB, thereby creating site-specific mutation correction or new sequence insertion (Kim and Kim, 2014; Verma and Greenberg, 2016).

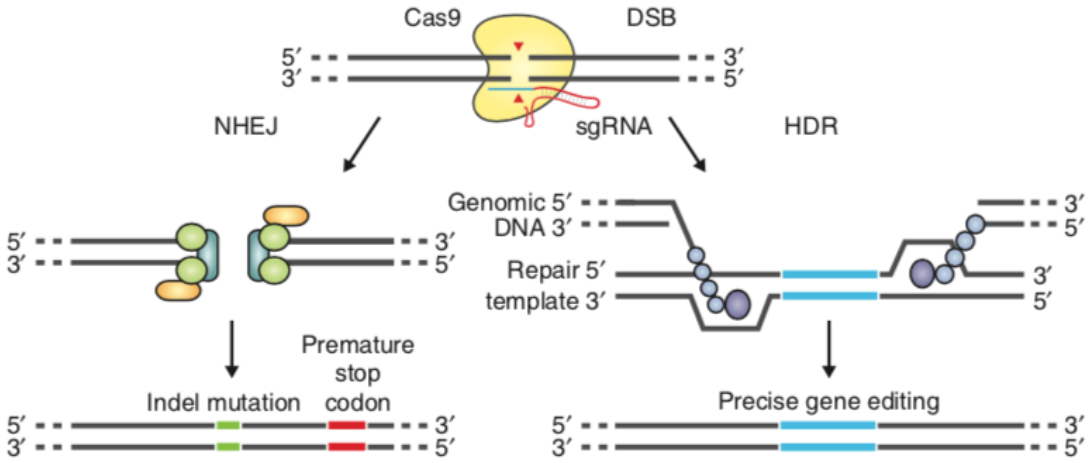


Figure 3. 3. Cellular repair mechanisms acting upon Cas9-mediated DSB. The figure has been taken from (Ran *et al.,* 2013). The DSB mediated by the Cas9 (yellow) protein can be repaired by two methods. (Left) In the NHEJ is an error-prone mechanism, in which the ends of the DSB are re-joined by the endogenous repair machinery using random DNA sequences. This generates indel mutations and premature stop codons, which can knockout the gene if it is located within the coding region. (Right) The alternative mechanism is HDR, which occurs when an exogenous template HDR DNA in the form of a plasmid DNA, is provided to cells to enhance the activation of the high-fidelity homology recombination repair process.

3.2 Rationale for the transgenic strategy used to create the enhanced Yellow Fluorescent Protein (eYFP)- neural stem reporter cell line.

In the experiments presented in this chapter, the AAVS1 locus was chosen as the site for transgene integration, which has determined the donor DNA template design. Thus, the HDR DNA structure had to have a robust selection marker gene (puromycin), which was designed to be transcribed by the intrinsic promoter of the PPP1R12C gene of the multi-potent (neural) and pluripotent stem cells. This was followed respectively in the 3' direction by **b**ovine **G**rowth **H**ormon (bGH) polyA tail to terminate the transcription and the intrinsic human glial fibrillary acidic protein (GFAP) promoter sequence that was aimed to be transcriptionally activated upon directed differentiation of the stem cells towards the astrocytes lineage. The reporter eYFP gene was designed to be in the read frame with the human GFAP promoter and to be co-transcribed upon stimulated activation during differentiation towards the astrocyte lineage. The transcriptional stability of the eYFP reporter gene was essential for enhancing brighter fluorescence, and thus a DNA segment known as **W**oodchuck hepatitis virus **P**ost-translational **R**egulatory **E**lement (WPRE), was

added at the 3' end of the YFP gene. This can increase the fluorescence of the YFP 5-8 fold in a transgene-, promoter-, and vector-independent manner (Zufferey *et al.*, 1999). The final DNA fragment was the **h**uman **G**rowth **H**ormon (hGH) polyA tail to terminate the transcription performed by the GFAP promoter after its constitutional activation. This transgenic construct within the donor HDR DNA template was flanked by right (530bp) and left (804bp) homologous DNA fragments that have sequences identical to the DNA sequences flanking the genomic breakage site induced by the CRISPR/Cas9 plasmid **(Figure 3. 4)**. The rationale behind creating a DSB via CRISPR/Cas9 technology and repairing this break using a purposely-designed donor HDR DNA fragment, was to knock-in a transgene containing YFP into the AAVS1 site of stem cells to ultimately creating reporter stem cell lines which can, hypothetically, propagate long-term in cultures and continuously provide viable YFP-fluorescing astrocytes whenever stem cells are precisely differentiated towards the astrocytic lineage.

We were successful in generating all three reporter cell lines; the first was a homozygously-edited H1-derived human neural stem cell line (H1NSCs), which we called (H1AML) in addition to two heterozygously-edited induced pluripotent stem cells (iPSCs) lines. The H1AML will be the focus in our study, whereas the generation and characterisation of the two iPSCs cell lines will not be discussed as we could not use them in this study due to financial issues. The schematic workflow of creating reporter cell lines is shown in **(Figure 3. 4)**. The labelling technique allowed transgenic YFP-astrocytes to be co-cultured with primary GBM cell lines, which were derived from the invasive region of ten distinct patient GBMs, within a 3D model (termed 'Gliomasphere Matrices'; see Chapter 6) and then re-isolated to reveal the genome-wide transcriptional changes induced by the malignant cells. This engineered model provides a unique opportunity to study complex molecular mechanisms occurring within astrocytes at the invasive GBM edge, which may influence future treatment options during recurrence.

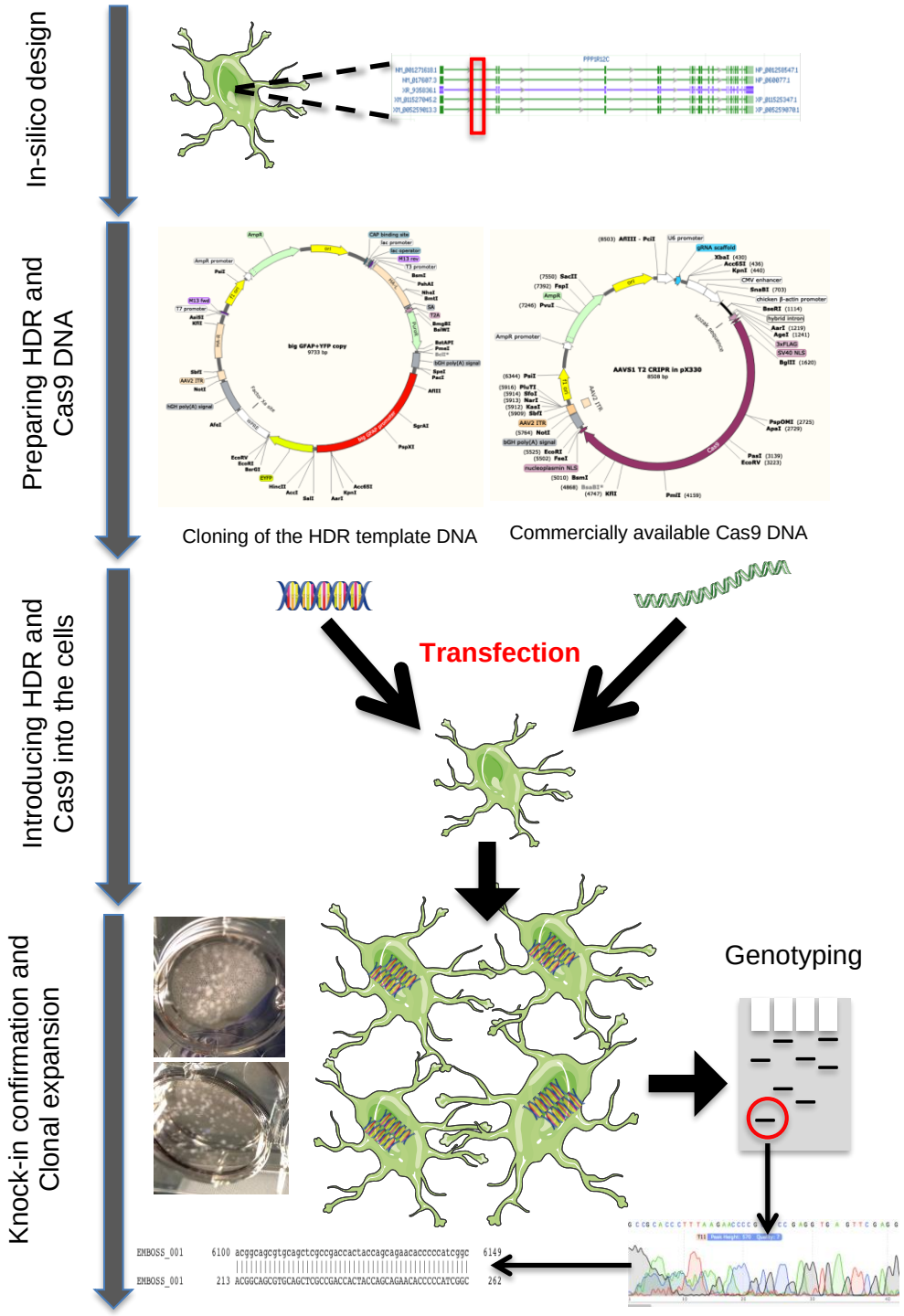


Figure 3. 4. The workflow and experimental schematic overview to generate the transgenic YFP-NSC line H1AML. The reporter cell line generation starts with designing of the experiment and identifying the site for knock-in, which influences the HDR DNA template design in the next step. Furthermore, it determines the RNA guide. Preparing the reagents and DNAs constitutes the next step followed by HDR and CRISPR DNAs transfer into the cells via lipid-based or electroporation approaches. The surviving clones upon antibiotic selection are screened using PCR and excised DNA bands are sequenced to confirm presence of the transgene knock-in.

Several methods can be used to create stable genetically-edited mammalian cell lines. These include the use of viral and electroporation methods to randomly knock-in a construct with a constitutive promoter (such as EIF1-alpha, beta-globin, and CMV), that can transcriptionally activate transgene and reporter expression regardless of differentiation status. However, this strategy is not compatible with our main objective of creating a reporter stem cell line which displays YFP expression only upon astrocytic differentiation, i.e. a gene edited YFP-H1AML NSC reporter line. In contrast, the strategy described above will label NSC, and all derived differentiated cells (astrocytes, oligodendrocytes and neurons), which exhibit YFP expression upon NSC differentiation, which in turn, hampers the fluorescence-activated cell sorting (FACS)-based isolation of the astrocytic population proposed to be co-cultured with multiple GIN cells, and the re-isolation upon co-culture to profile their transcriptome. By using CRISPR/Cas9 to stably introduce YFP under the control of the GFAP promoter in NSC (or iPSC), cell lineage-specific expression of YFP upon directed differentiation to the astrocytic lineage can be achieved. We chose to label NSC rather than GBM cells, to offer flexibility of isolation, and ultimately testing, the astrocytes co-cultured with multiple (ten) GIN cell lines. Had we aimed to label tumour (GIN) cells instead of astrocytes, a total of ten experimental GIN lines would be required to be stably labelled instead of just one NSC line.

Other method involves CRISPR/Cas9-mediated knock-in of a construct composed of the YFP gene, WPRE segment and polyA tail, can be sub-cloned downstream to, and in-frame with, the endogenous promoter of the GFAP gene. This can be either between the endogenous GFAP promoter and the first exon, or distal to the last exon but proximal to the ployA tail of the GFAP gene **(Figure 3. 5A)**. However, YFP fusion at the beginning (N-terminal) or end (C-terminal) of the GFAP protein may adversely affect this protein integrity which is extremely critical for astrocytes to regulate their structure and vital functions at health and disease states (Middeldorp and Hol, 2011; Sullivan, 2014). This, in turn, may bias the results of our study, as we aim to reveal the transcriptomic alterations of normal astrocytes upon co-culture with primary GBM cells. Furthermore, this method may be associated with technical challenges as it may hamper the FACS-based isolation/re-isolation of YFP astrocytes, due to reduction of the YFP fluorescence, as the YFP gene will not be transcribed within all GFAP transcript isoforms; i.e., not all GFAP transcripts contain the nine exons of the gene. The intensity of fluorescence is crucial in our experiment as GBM cells can express high auto-fluorescence with wavelengths which may

overlap with YFP fluorescence emitted from astrocytes. This would negatively impact on the ability to FACS-isolate YFP-astrocytes upon co-culture with GBM cells, prior to measuring transcriptomic profiles. Finally, the removal of the antibiotic resistance selection cassette is required in this method after knock-in confirmation and thus, the selection gene and its preceding promoter must be flanked by, for example, (LoxP) sites, to allow the excision after overexpressing Cre in the mutated clones. This is another significant disadvantage, as it requires extra labour, time and money.

The safe harbour locus AAVS1 of the PPP1R12C gene on chromosome 19 (position 19q13.42) was found to be the most frequent site where the wild-type adeno-associated virus integrates into the human genome (Kotin, Linden and Berns, 1992), with no significant detrimental effects on cellular structure or function (Kotin, Linden and Berns, 1992; Ogata, Kozuka and Kanda, 2003; Smith *et al.*, 2008; Hockemeyer *et al.*, 2009, 2011; DeKelver *et al.*, 2010). The AAVS1 site was therefore chosen as a strategic target for CRISPR/Cas9-mediated knock-in, to avoid any gain or loss of function in any vital genes due to iatrogenic mutations that are usually caused by random integration methods such as viral transduction or lipid-based transfection (**Figure 3. 5B**) (Tenzen, Zembowicz and Cowan, 2010). Furthermore, the insulating properties of this specific site, prevents silencing of the transgenic construct that may occur with random integration method. Stem cells can silence transgenes due to a highly dynamic epigenome; for example, a transgene containing a beta globin promoter was silenced in embryonic stem cell lines when a random integration method was used (Hatzistavrou *et al.*, 2009). Thus, targeting the AAVS1 site allows stable expression of the YFP transgene via maintaining an open chromatin confirmation, an important consideration to potentially investigate alterations to epigenetic marks upon co-culture of astrocytes with GBM cells (Ogata, Kozuka and Kanda, 2003). Ultimately this will ensure the integrity of the transcriptome within the transgenic astrocytic line.

Saving time and labour could be another advantage as confirming stable knock-in of a randomly integrated transgene within an unknown genomic site, requires exceptional efforts and time to screen for the transgene in the entire genome. Furthermore, the availability of many ready-to-use cutting, and construct-carrying vectors designed specifically for the AAVS1 site is another approach to reduce time, labour, and costs required for cloning.

Hypothesis:

CRISPR/Cas9-mediated knock-in of a construct containing the puromycin gene, GFAP promoter, YFP gene, WPRE segment and polyA tail at the AAVS1 safe harbour locus, within neural (and iPSCs) stem cells, can generate transgenic lines which stably express the YFP reporter upon directed differentiation to the astrocytic lineage.

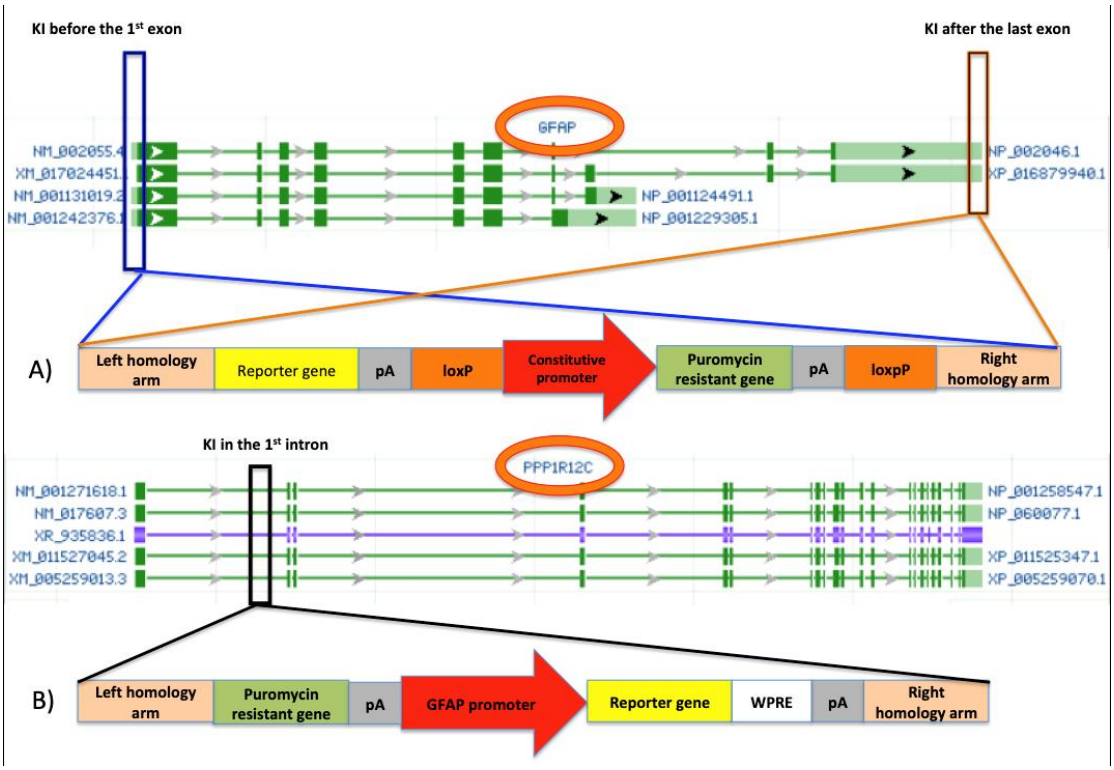


Figure 3. 5. Possible strategies for CRISPR/Cas9-mediated knock-in of a reporter gene. The knock-in site determines the HDR template design. (A) The first approach is to knock-in the construct at the 5' end of the first exon or the 3' end of the last exon. The transgene in this strategy contains LoxP sites surrounding the antibiotic resistance selection marker to facilitate removing of the selection cassette after knock-in confirmation. The reporter gene is transcribed by the endogenous promoter of GFAP. (B) Reporter gene knock-in into the AAVS1 safe harbour locus (the first intron of the PPP1R12C gene). This is the chosen strategy in which the antibiotic resistance selection marker is upstream of the exogenous GFAP promoter which is activated upon astrocyte lineage commitment during directed differentiation.

3.3 Materials and methods

3.3.1 Overview of molecular cloning strategy

To engineer the YFP-GFAP transgenic construct and generate the YFP-H1AML NSC line, two plasmid DNA vectors were required; a CRISPR/Cas9 plasmid DNA vector to induce DSB and a vector containing the puromycin-polA-GFAP promoter-YFP-WPRE-polyA cassette flanked by homology arms, with DNA sequences identical to those flanking the breakage site (first intron of AAVS1 safe harbour locus) **(Figure 3. 4)**. The length of the right (0.4kb) and left (0.8kb) homology arms was purposely designed to increase the efficiency of the homology recombination process and ultimately the integration of the transgenic segment into the host NSC genome (Byrne *et al.*, 2015). Fortunately, the first CRISPR/Cas9 vector is readily available in the market (Addgene number 72833) as it was previously used in (Natsume *et al.*, 2016) to generate protocols for consistent and scalable transgene expression at the AAVS1 site. This considerably reduced the costs, time and labour of the cloning process. More importantly, the guide RNA has been previously assessed to have 92% targeting efficiency and low off-target effects (Oceguera-yanez *et al.*, 2016). However, the HDR DNA template was required to be cloned from different plasmid DNA (Addgene) purchased as bacterial stabs. These competent bacteria were grown using a double streaking method on penicillin selection agar plates and followed by bacterial expansion using an agitated liquid broth method. Plasmid DNA was extracted from the bacteria using mini- and midi-plasmid preparation kits. These plasmids were digested using high-fidelity restriction enzymes, run on agarose gel using electrophoresis and gel bands with correct sizes excised using a surgical knife prior to extraction of plasmid DNA segments using a gel extraction kit. As the DNA yield from this step is generally low, DNA segments were amplified using conventional PCR via specially designed primers which have two segments; the first part (leading sequence) is composed of 20-25bp of complementary DNA sequence to the beginning (5') or end (3') of the required DNA segment, whereas the second part (overlapping sequence) has 20-25bp designed to be identical to the sequence of the adjacent DNA fragment amplified using the same method. This is to assemble the amplified DNA fragments using a recent high-fidelity approach based on the traditional New England Biolab Gibson Assembly® cloning guidelines. The assembled plasmid DNA was inoculated into chemical competent bacteria and double streaked on penicillin selection agar plates followed by bacterial expansion using agitated liquid broth method. This leads to plasmid DNA yield amounts that are sufficient to be used for the gene editing purposes we initially aimed for. Both CRISPR/Cas9 and HDR plasmids were introduced into the NSC and iPSC cell lines

using lipofection and electroporation methods respectively. The mutated clones were selected using puromycin, PCR-screened, and expanded to ultimately be differentiated into astrocytes. The detailed protocols are listed below:

3.3.2 Cloning of the HDR DNA template (agar plates, plasmid DNA extraction, gel electrophoresis, band extraction from gel, ligation protocols)

3.3.2.1 Making agar plates (modified from Addgene protocols):

1. Agar media was prepared according to laboratory standard procedures and sterilised by the CBTRC laboratory technicians.
2. Pouring station was prepared according to the following:
    I. Empty station on laboratory bench with a Bunsen burner.
    II. The bench was sprayed with a 70% ethanol solution and wiped with a paper towel before igniting the flame to ensure a safe working station, as ethanol is highly flammable.
    III. The plates were stacked upside down on the sterile working station.
    IV. The plates were labeled with the date and the medium including the antibiotic (ampicillin as the plasmids contained the ampicillin resistant gene and thus 5-alpha competent bacteria containing our plasmids were grown on these plates).
3. The bottom 3/4 of the bottle containing molten gel mixture was submerged in a 60°C water bath to dissolve the solid agar.
4. Ampicillin was added to the molten agar at a concentration of 100ug/mL after cooling it down to approximately 60°C or less to avoid damage to the chemical structure of the antibiotics, while maintaining its liquid state to ensure equal distribution of the antibiotics within the agar.
5. The agar bottle was swirled to mix the antibiotic throughout the agar evenly.
6. Bunsen flame was ignited at the plate pouring station before any bacterial work.
7. Next to the flame, liquefied agar was poured onto plates one at a time. Alternatively, 20ml agar can be measured and added to each plate using a serological pipette controller. However, the procedure should be performed quickly as the agar will start to solidify and re-melting is inappropriate as re-heating may affect the integrity of the antibiotics.
8. The plates were swirled to ensure equal distribution of agar on the plates surfaces and to avoid the formation of air bubbles that may generate at the bottom of the plates. Superficial bubbles can be quickly burned using the flame. It is important to remove and air bubbles, as they resemble bacterial colonies when they develop.

9. The plates were left for approximately 30 minutes at room temperature to solidify the agar, before overnight storage at room temperature to get rid of condensations on plate lids. Plates were kept in a sealed plastic bag with absorbent material at 4°C until further use (the plates were not kept more than 2 weeks before use). The plates were kept in a clean working station for 3-4 hours at room temperature before use.
10. A test for each batch was conducted to test antibiotic function and to ensure that the batch was not contaminated. Two plates were streaked, the first with a bacterial strain that is known to be resistant to ampicillin (Addgene bacteria with the inoculated plasmid inside), whereas the second plate was streaked with a strain that is sensitive to the antibiotic (D5-alpha bacteria from NEB). A third plate was left as a control without streaking to screen for environmental contamination.
11. The two streaked and the control plates were incubated overnight at 37°C for 16-24 hours to check for bacterial growth. Colonies appeared only on the plate with bacteria containing the plasmid DNA.
12. After confirming the functionality of the plates and strict culture conditions, the inoculated bacteria with plasmids (Addgene numbers 27054, 80488, and 723833) were cultured on ampicillin agar plates to obtain colonies.
13. All selected colonies were re-streaked as most bacteria develop resistance to antibiotics within 8 hours.
14. The plasmid colonies were further expanded in LB broth containing 100µg/ml ampicillin, which was made according to standard procedures and sterilised by the CBTRC technicians.
15. The competent bacteria were centrifuged at maximum speed for 10 minutes to obtain plasmid DNA which was isolated using the GeneJET Plasmid Miniprep Kit (Thermofisher Catalogue number: K0502) and PureLink™ HiPure Plasmid Filter Midiprep Kit (Thermofisher Catalogue number: K210015) according to the manufacturer protocols below.

3.3.2.2 Plasmid DNA purification using GeneJET Plasmid Miniprep.

1. The pelleted cells were resuspended in 250µl of the resuspension solution after adding RNase A to the solution. Cell suspension was transferred into a microcentrifuge tube, which was vortexed vigorously for 2 minutes.
2. Another 250µl of lysis solution was added to the initial volume of cell suspension. The tube was inverted 4-6 times (but not vortexed) to avoid damage to the supercoiled plasmid DNA. During this step, the solution turns into more viscous and becomes clearer.
3. Additional 350µl of neutralizing solution was added immediately and the microcentrifuge tube inverted 4-6 times. It is important to mix the solution gently but thoroughly to avoid localised neutralization of lysis solution and localised precipitation of bacterial lysate, which is cloudy at this stage.
4. Chromosomal DNA and cell debris were pelleted by centrifugation at ≥12000 x *g* for 5 minutes.
5. The supernatant was aspirated and transferred into a GeneJET spin column. The precipitated white pellet should not be transferred to the column.
6. The column was balanced and centrifuged at ≥12000 x *g* for 1 minute and the flow-through discarded.
7. The column was washed with 500µl wash solution, which was diluted with ethanol before the first use.
8. The column was balanced and spun at ≥12000 x *g* for 1 minute and the flow-through was discarded.
9. The GeneJET spin column was transferred to a fresh microcentrifuge tube.
10. Without touching the column membrane, the elution buffer was added to the centre of the membrane of the column using a volume ≤ 20µl to increase DNA concentration and incubated for 2 minutes at room temperature.
11. The column was finally centrifuged at ≥12000 x *g* for 2 minutes and the flow-through containing purified plasmid DNA was stored at -20°C.

3.3.2.3 Plasmid DNA purification using PureLink™ HiPure Plasmid Filter Midiprep Kit.

The purified DNA using this kit was used in cell cultures and introduced to cells using lipid-based or electroporation methods.

1. The column holder is used to stabilize the HiPure filter Midi Column on top of conical flask.
2. 15ml of equilibration buffer was applied directly to the cartridge of the HiPure filter Midi Column and left to be drained by the effect of gravity.
3. While the column equilibrated, the competent bacterial cells were harvested by centrifugation of the overnight LB at 4000x *g* for 10 minutes and the supernatant LB medium was removed.
4. 4ml of resuspension buffer (R3) with RNase A was applied and gently mixed with a pellet of competent cells until a homogeneous solution was obtained.
5. Another 4 ml of lysis buffer (L7) was added to the mixture, the tube was recapped and inverted 6-10 times It is important to mix (not vortex) the solution gently but thoroughly to avoid localised neutralization of lysis solution and localised precipitation of bacterial lysate, which is cloudy at this stage.
6. The lysate solution incubated at room temperature for exactly 5 minutes.
7. 4ml of precipitation buffer (N3) was added and mixed immediately by inverting the tube gently but thoroughly until homogeneity was obtained.
8. The mixture was then centrifuged at 12000x *g* for 10 minutes at room temperature.
9. The supernatant was loaded into the HiPure filter Midi Column, the lysate drained by gravity (10-15 minutes) and the column washed with 10ml wash buffer (W8). The flow-through was discarded.
10. The column was washed by 10ml wash buffer (W8) and the washing buffer was allowed to pass through the filter by gravity. This step is important as the final DNA yield will be increased. The flow-through was discarded.
11. A sterile 15ml tube (elution tube) was placed under the column and plasmid DNA eluted by applying 5ml elution buffer (E4) to the column.
12. Isopropanol (3.5ml) was added to the elution flow-through to precipitate the DNA. The mixture was then incubated for 2 minutes at room temperature.

13. The JA-25.50 fixed angle rotor and chamber of the of Avanti J-25 High Performance centrifuge from Beckman Coulter, was pre-chilled to (4°C) 15 minutes before use. Next, the total volume of 8.5ml was transferred into a pre-chilled (4°C) 50ml polyethylene (HDPE) sterile Beckman coulter tube mixture was centrifuged at 14000 x *g* for 30 minutes at 4°C. The supernatant was carefully aspirated and discarded. The tube was chosen with satisfactory compatibility to chemicals (especially isopropanol) of the kit, according to chemical resistance for Beckman Coulter centrifugation products manual.
    The DNA pellet resuspended in 3ml of 70% ethanol and centrifuged at 14000 x *g* for 30 minutes at 4°C. The supernatant was carefully aspirated and discarded.
14. The DNA pellet was air-dried for approximately 10 minutes, resuspended in 100µl of TE buffer (TE) and stored at -20°C.

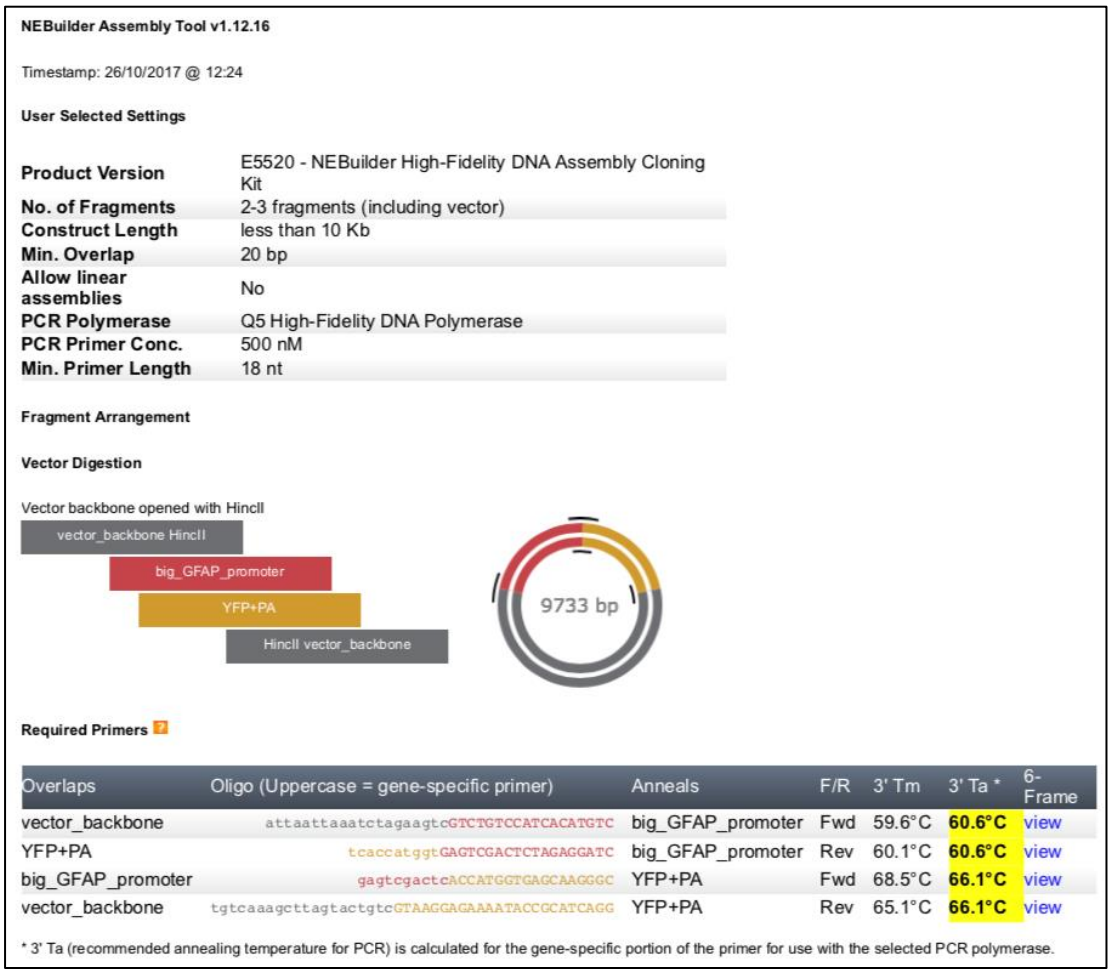
3.3.2.4 Plasmid DNA purification using PureLink™ Quick Gel Extraction Kit. (Thermofisher Catalogue number: K210025 (modified from manufacturer protocol)

1. The linear or circular DNA fragments with various sizes were separated using agarose gel electrophoresis.
2. The required DNA bands that had the appropriate sizes were physically excised using a surgical blade with minimal agarose surrounding the band.
3. Polypropylene microcentrifuge 2ml tubes were weighed before adding the excised pieces of agarose, using scale sensitive to 0.001g.
4. The agarose slices were transferred into the 2ml microcentrifuge tubes and weighed again to find the net weight of the agarose slice. Most excised slices ranged between 240-290mg.
5. Three volumes of gel solubilisation buffer (L3) were added to one volume of agarose gel. For example, 750µl of gel solubilisation buffer (L3) was added to a slice of 250mg agarose gel.
6. The 2 ml polypropylene microcentrifuge tubes were then submerged in a pre-heated water bath or placed in a heat block at 50°C for 10 minutes. The tube was inverted several times every 3-5 minutes. At this step, the gel was completely solubilized.
7. Once the gel was completely solubilized, the tube was incubated for an additional 5 minutes.

8. One volume of isopropanol was also added to the mixture to maximize the final DNA yield.
9. The dissolved gel was then transferred into a Quick Gel Extraction column placed inside the wash tube. The loading volume of the dissolved gel did not exceed 700µl into the column, however the procedure was repeated but after discarding the flow-through of the previous step.
10. The columns were balanced and centrifuged at ≥12000 x *g* for 1minute and the flow-through was discarded.
11. 500µl of wash buffer was applied to the centre of the column filter prior to centrifugation at ≥12000 x *g* for 1minute and discarding of flow-through.
12. The centrifugation step was repeated at 24000 x *g* for 2 minutes to remove the residual ethanol and washing buffer and columns placed in a fresh recovery tube.
13. The elution buffer (20µl) was added to the centre of the column membrane, and the tubes were incubated at room temperature for 1-2 minutes prior to centrifugation at ≥12000 x *g* for 2 minutes.
14. Flow-through containing the purified plasmid DNA was stored at -20°C.

3.3.2.5 Cloning strategy for 9733bp homology donor DNA

The homology plasmid backbone was taken from the plasmid provided by Addgene and deposited by Knut Woltjen (Addgene plasmid # 80488) and the transgenic insert has been taken from Karl Deisseroth (Addgene plasmid # 27054). The in-silico design is depicted in **(Figure 3. 6)**.



NEBuilder Assembly Tool v1.12.16

Timestamp: 26/10/2017 @ 12:24

User Selected Settings

Product Version	E5520 - NEBuilder High-Fidelity DNA Assembly Cloning Kit
No. of Fragments	2-3 fragments (including vector)
Construct Length	less than 10 Kb
Min. Overlap	20 bp
Allow linear assemblies	No
PCR Polymerase	Q5 High-Fidelity DNA Polymerase
PCR Primer Conc.	500 nM
Min. Primer Length	18 nt

Fragment Arrangement

Vector Digestion

Vector backbone opened with HincII

Required Primers

Overlaps	Oligo (Uppercase = gene-specific primer)	Anneals	F/R	3' Tm	3' Ta *	6-Frame
vector_backbone	attaattaaatctagaagtcGTCTGTCCATCACATGTC	big_GFAP_promoter	Fwd	59.6°C	**60.6°C**	view
YFP+PA	tcaccatggtGAGTCGACTCTAGAGGATC	big_GFAP_promoter	Rev	60.1°C	**60.6°C**	view
big_GFAP_promoter	gagtcgactcACCATGGTGAGCAAGGGC	YFP+PA	Fwd	68.5°C	**66.1°C**	view
vector_backbone	tgtcaaagcttagtactgtcGTAAGGAGAAAATACCGCATCAGG	YFP+PA	Rev	65.1°C	**66.1°C**	view

* 3' Ta (recommended annealing temperature for PCR) is calculated for the gene-specific portion of the primer for use with the selected PCR polymerase.

Figure 3. 6. *In-silico* homology DNA template design. This design was performed using the NEB assembly tool v1.12.16. The tool shows the potentially assembled DNA segments; the grey segment is the vector backbone, the red segment is the GFAP promoter and the yellow fragment includes the YFP, WPRE, and hGH ployA tail. Primers used in the cloning process are shown and which are located around (black dashes) the designed vector (coloured ring). These primers are coloured according to the origin of the sequence. All primers were initially designed to amplify the corresponding DNA fragments using Q5 polymerase, and thus all estimated annealing temperatures of the primers are highlighted.

The backbone vector (pAAVS1-P-MCS) contained the AAVS1 left homology arm (HA-L) followed by the splice acceptor (SA) and linker protein sequences (T2A), puromycin resistant gene (for clonal selection), bGH polyA tail (to terminate the transcription of the puromycin resistant gene (PuroR), the multiple cloning site (MCS) where the insert was ligated and the right homology arm (HA-R) in the distal 3' end **(Figure 3. 7)**. The backbone plasmid DNA also contained an origin of replication and an ampicillin resistant promoter and gene for bacterial selection on agar plates. The transgene insert is composed of a GFAP promoter (2052bp), eYFP, WPRE, and hGH polyA tail **(Figure 3. 5A)**.

1. The backbone plasmid was digested using HincII restriction enzyme to create blunt ends. Thus, for each microgram of DNA of 80488 plasmid DNA, the following reaction was prepared by adding:
    - 5µl cutsmart or (3.1) buffer
    - 1µl (10 units) HincII restiction enzyme
    - Shrimp alkaline phosphatase and nuclease free water up to 50µl per reaction.

This is to linearize the vector backbone **(Figure 3. 7)**. The shrimp alkaline phosphatase was added to remove the phosphate group from the blunt ends of the backbone, which prevents re-ligation of both blunt ends of the vector backbone.

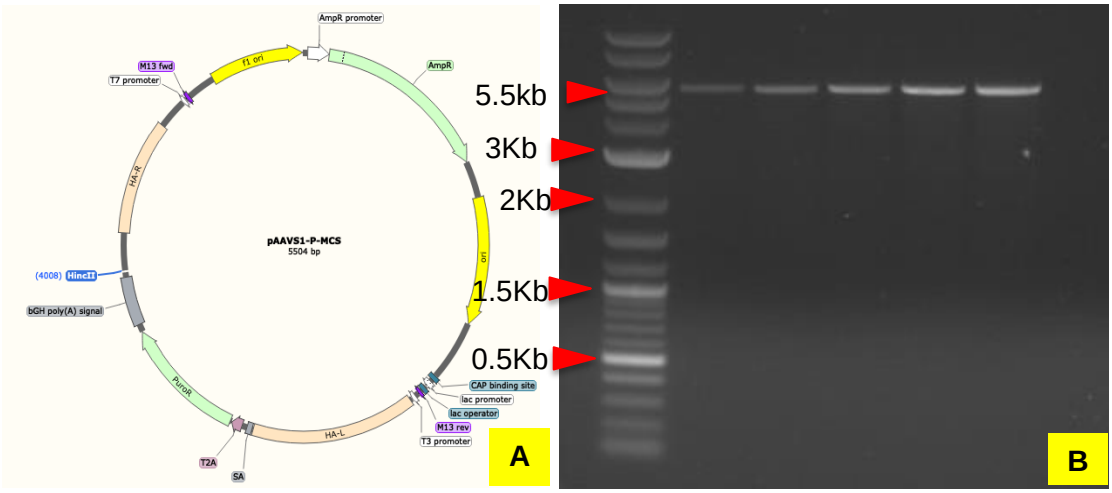


Figure 3. 7. Preparing the backbone plasmid for the HDR DNA template. (A) The backbone vector contains the AAVS1 HA-L followed by SA, T2A sequences, PuroR, bGH polyA tail and MSC where the insert was planned to be ligated, followed by the AAVS1 HA-R. The backbone vector (Addgene plasmid number 80488) was linerized using HincII restriction enzyme (which is located at the MSC and highlighted with blue). (B) The lineaerised insert DNA segment was electrophoresed on agarose gel to obtain the appropriate size band (5504bp) to be extracted for further cloning steps. Lanes 1-5 represent five clones. *DNA ladder is a 2-log DNA ladder from NEB (0.1-10Kb).*

2. To obtain the linear insert, the plasmid 27054 was digested with SbfI-HF restriction enzyme. Thus, for each microgram of plasmid DNA the following reaction was prepared by adding:
    - 5µl cutsmart buffer
    - 0.5µl SbFI-HF
    - Nuclease free water up to 50 µl per reaction

    This generated a 5353bp fragment composed of the GFAP promoter, human Channelrhodopsin-2 (optogenetic gene), YFP, WPRE and hGH polyA tail **(Figure 3. 8)**.
3. Next, both restriction digestions were then electrophoresed on agarose 1% gel and the appropriately sized bands were purified using PureLink™ Quick Gel Extraction Kit. The transgenic segment contains human Channelrhodopsin-2 (~900bp), which is not required for our experiment, as the segment will increase the size of the homology plasmid and may reduce the efficiency of lipofection. Thus, we planned to remove this unnecessary DNA fragment by, first, separate PCR-amplification of both the DNA segments flanking both sides of Channelrhodopsin-2 (5' end; GFAP promoter) and (3' end; YFP, WPRE, and hGH polyA tail) to generate two DNA segment entities excluding Channelrhodopsin-2 DNA. Next, both of these two DNA fragments were ligated within the MCS of the carrying vector 80488 backbone in a transcriptional order (GFAP promoter-eYFP-WPRE-hGH polyA tail) when performing the final assembly reaction.

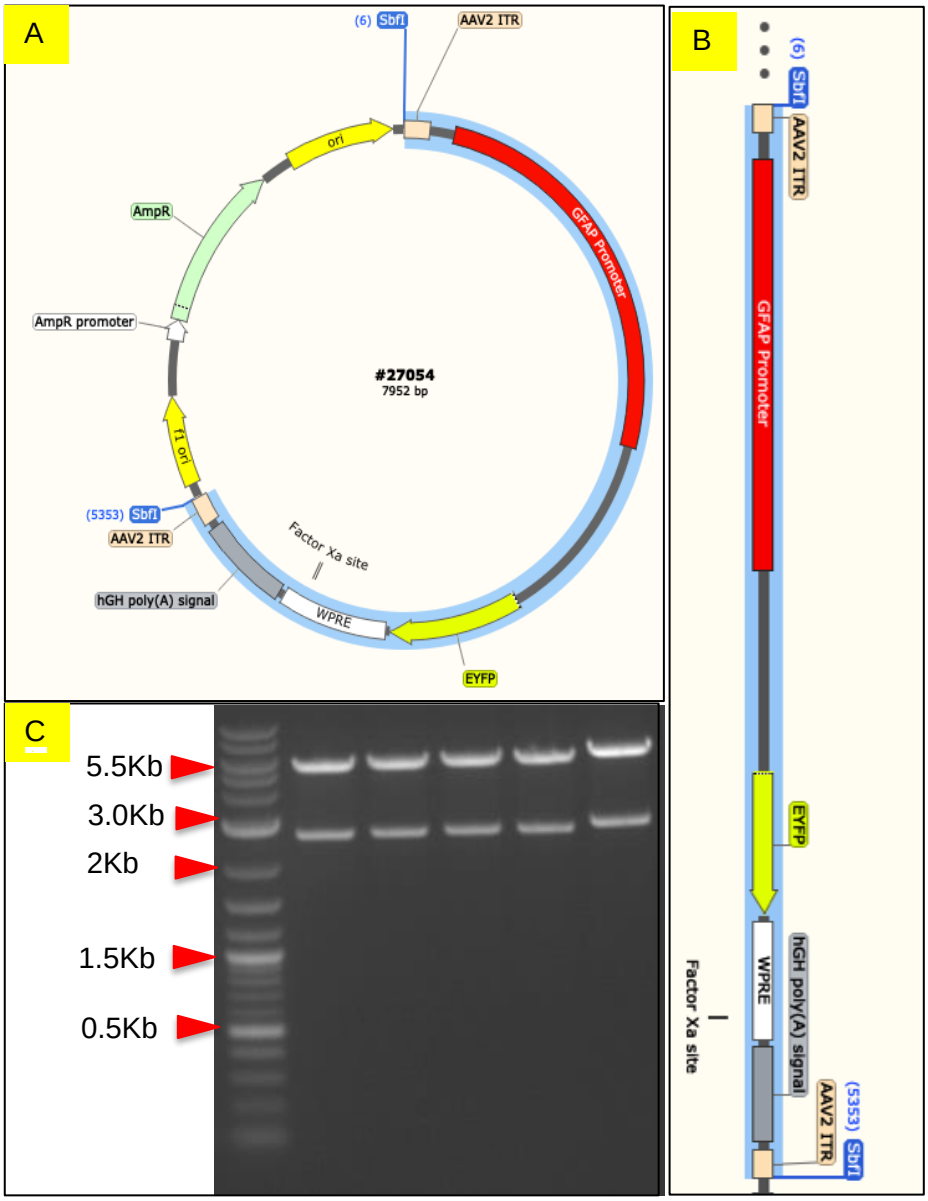


Figure 3. 8. Obtaining the transgenic insert DNA fragments from plasmid 27054. (A) The transgene insert is highlighted in blue in both circular and linear plasmid shapes. It is composed of a big GFAP promoter (red), YFP gene (Yellow), WPRE (white), and hGH polyA tail (Grey). The non-labelled part located between the GFAP promoter and the YFP gene is the optogenetic gene (human Channelrhodopsin-2). The circular plasmid was digested using a high-fidelity dual-cutter (sbfI-HF), which is highlighted in blue (A-B) to generate a linearized DNA fragment (B). This restriction digestion of plasmid 27054 has resulted in two linear DNA fragments (the bands are replicates); the first segment, which is the top 5347bp band in the agarose gel image (the required insert); the second fragment (2605bp) band of the plasmid backbone that is located slightly below the 3kb bright band (C). *DNA ladder is a 2-log DNA ladder from NEB (0.1-10Kb).*

4. The GFAP promoter was successfully amplified using Q5 high-fidelity polymerase via conventional PCR using the forward primer (5'-gtattaattaaatctagaagtcGTCTGTCCATCACATGTC-3') and the reverse primer (5'-tcaccatggtGAGTCGACTCTAGAGGATC-3'), according to PCR reactions and conditions set below and shown in **Figure 3. 9**. The primers were designed to have two parts; (i) the leading and (ii) the overlapping sequences.

- Mastermix reaction for 6 X 12.5µl or 3 X 50µl reactions (in order and on ice to avoid non-specific bindings). The mastermix contained 94.5µl neuclease free water, 30µl Q5 reaction buffer, 3µl dNTPs (10mM concentration), 1.5µl Q5 Polymerase, 6µl template DNA (1ng/µl product of digestion from 27054 plasmid DNA), 7.5µl FW primer and 7.5µl RV primer.
- The PCR thermal cycles included:
  - Initial denaturation 98°C for 10minutes
  - 3 cycles (for the leading sequences) of:
    98°C for 15 sec
    60°C for 10 sec
    59°C for 30 sec
    72°C for 3min: 30 sec
  - 29 cycles (for ligation of the overlapping sequence) of
    98°C for 15 sec
    70°C for 30 sec
    72 °C for 3min: 30 sec
  - Final extension on 72 °C for of 7minutes: 30 sec
  - Final hold on 4°C forever

However, as Q5 polymerase usually works at high temperatures, it was not feasible to use this polymerase for the amplifications of the second DNA segment (YFP, WPRE, hGH polyA tail), as this is a GC-rich region. We therefore used One*Taq*® polymerase (One*Taq*® 2X Master Mix with Standard Buffer NEB; catalogue number: M0482S) which works at temperatures 3-5°C less than the Q5 polymerase. This polymerase successfully led to the amplification of the linear DNA segment (YFP, WPRE, hGH polyA tail) which was cut from the 27054 plasmid, using forward primer (5'-gagtcgactcACCATGGTGAGCAAGGGC-3') and reverse primer (5'-tgtcaaagcttagtactgtcGTAAGGAGAAAATACCGCATCAGG-3') according to PCR reactions and conditions set below and shown in **Figure 3. 9**

- Mastermix reaction for 6X 12.5 µl or 3X 50µl reactions (in order and on ice to avoid non-specific bindings). The master mix contained 44µl,neuclease free water 75µl One*Taq*® mastermix, 16µl template DNA (1ng/µl product of digestion from 50473 plasmid DNA), 7.5µl FW primer, and 7.5µl RV primer.
- The PCR thermal cycles included:
  - Initial denaturation 94°C for 2minutes
  - 3 cycles (for the hybridizing sequence) of:
    94°C for 15 sec
    60°C for 10 sec
    55°C for 60 sec
    68 °C for 3min: 30sec
  - 29 cycles (for ligation of the leading sequence) of
    94°C for 15 sec
    67°C for 60 sec
    68°C for 3min: 30 sec
  - Final extension on 68 °C for of 15minutes
  - Final hold on 4°C forever

The resulting amplified PCR fragment was not appropriate to be assembled directly onto other DNA segments because One*Taq*® polymerase usually adds dNTA at the 3' end to the amplified fragments. Thus, we blunted this fragment using DNA polymerase I (DNA Polymerase I, Large (Klenow) Fragment; NEB catalogue number M0210S) to remove the 3' overhang.

5. To remove this dNTA at the 3' end of the linear DNA segment, we set up the reaction below:

- 1µg of the DNA segment amplified by PCR, which was excised from agarose gel
- 1µl NEB buffer
- 3 µl dNTP
- 1 µl DNA polymerase I

The reaction was incubated at 25°C for 15 minutes. This was followed by adding 10mM **E**thylene**D**iamine**T**etraacetic **A**cid (EDTA) and heating at 75°C for 20 minutes to stop the reaction.

This resulted in the generation of a blunted segment (YFP, WPRE, and hGH polyA), which had 20bp overlapping sequences with the GFAP DNA segment. Thus, the segment contained sequences (5'-GAGTCGACTCACCATGGTGA-3') at its 5' end that are complementary to the 3' end (3'-CTCAGCTGAGTGGTACCACT-5') of the GFAP promoter. Both the 3' end of this segment and the 5' end of the GFAP promoter contained 21bp that are identical to the edges of the HincII cleavage site within the vector backbone (Addgene plasmid ♯ 80488).

6. The final assembly **(Figure 3. 9)** of the two inserts (GFAP promoter) and (YFP, WPRE and hGH polyA tail) to the vector backbone at the HincII cleavage site (Linearized plasmid 80488) was performed using the NEBuilder® HiFi DNA Assembly Cloning Kit (New England Biolabs *Catalogue Number* E5520S) according to the NEB assembly protocol below:

- 10µl NEB HiFi DNA Assembly Master mix
- 2.5µl of vector with a total amount of of 125ng (concentration 50ng/µl)(0.035 pmol of ends)
- 1.5µl of GFAP promoter DNA insert with a total amount of 165ng (concentration 110ng/ µl) (0.1237pmol of ends)
- 1µl of the DNA segment (YFP, WPRE and hGH polyA tail) (187ng/µl) (0.1397pmol of ends)
- 6 µl of Neuclease Free Water
- The pmols of the assembeled fragments were calculated accoding to the equation: pmols = (wieght in ng) x 1000 / (base pairs X 650).
- The mixture was incubated at 50°C for 60 minutes and the reaction was immediately chilled on ice.

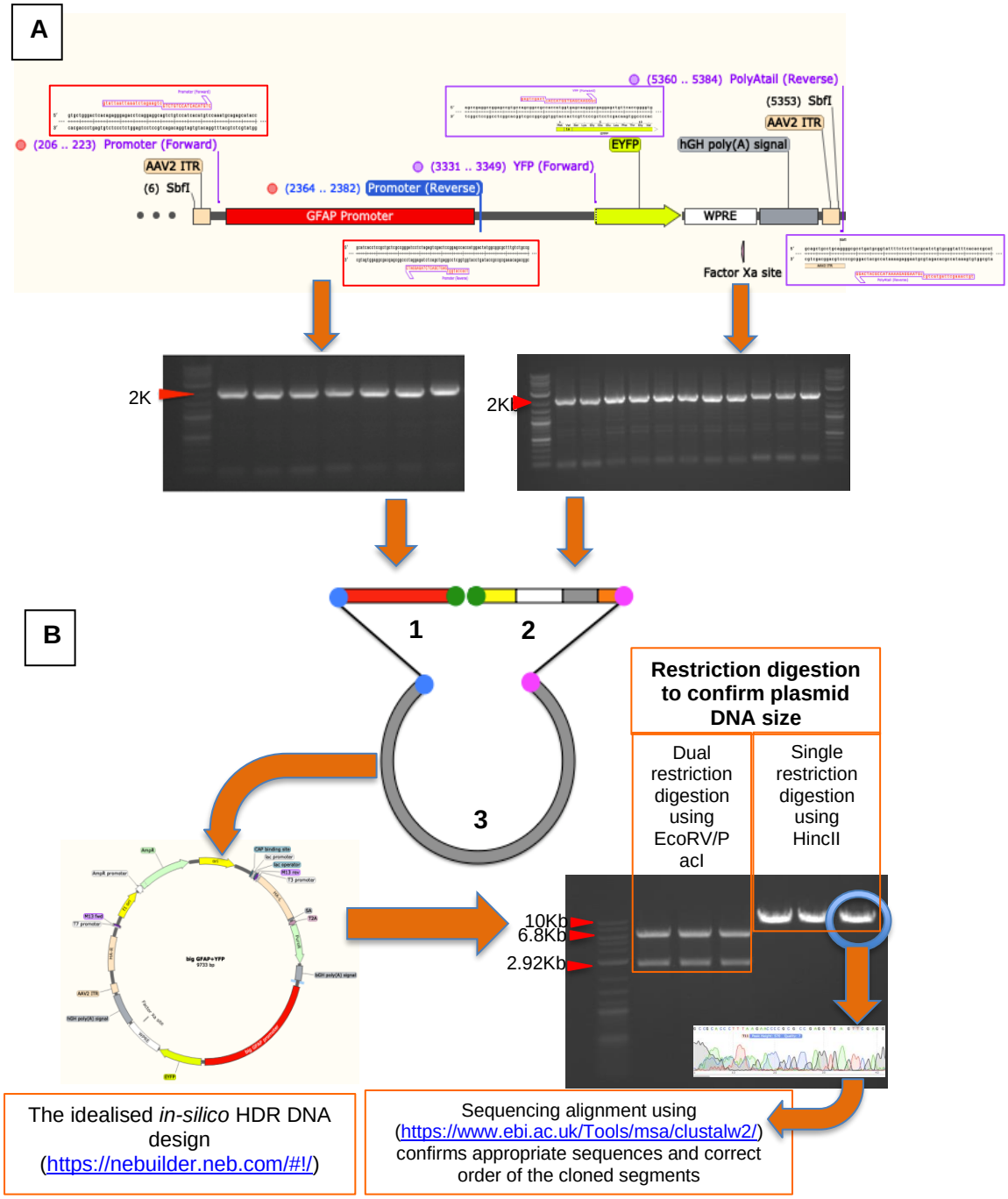


Figure 3. 9. Cloning assembly of the HDR DNA template. (A) *In-silico* primer design to amplify two segments from the restricted insert of plasmid 27054 to remove the human Channelrhodopsin-2 segment (thick black line between the GFAP promoter (red box) and the YFP gene (yellow arrow)), which is located between the required (amplified) DNA segments. Schematic generated from: https://www.snapgene.com/snapgene-viewer/. Primer design and PCR amplification products of the two required insert DNA segments (GFAP promoter; forward and reverse primers show in red rectangles) and (YFP, WPRE, and hGH polyA tail; forward and reverse primers shown in purple rectangles), which surround the dispensable (Channelrhodopsin-2) segment are shown. (B) The two amplified segments (1 and 2) were assembled with the vector backbone (3). Single (blue circle), dual restriction digestion, and Sanger-sequencing of these excised band replicates confirmed a match with the *in-silico* designed HDR DNA.

Immediately following the assembly reaction above, the chemically competent bacterial cells were next prepared to be transformed with approximately 1.5µg DNA from the assembly reaction according to a protocol modified from NEB instruction guidelines:

1. The chemically competent cells (5D alpha-Ecoli provided with the NEBuilder® HiFi DNA Assembly Cloning Kit, were thawed on ice for one hour before the transformation process. The SOC medium was kept in room temperature for 2 hours prior to the transformation process.
2. 5µl from the assembly reaction was chilled and added to the competent bacteria then mixed gently by pipetting and placed on ice for 30 minutes.
3. The chemically competent bacterial cells were heat-shocked at exactly 42°C for 35 seconds and quickly transferred to be placed on ice for 2 minutes.
4. 950ul of room temperature SOC medium was added to the 50µl assembly reaction, tubes shaken vigorously (250 rpm) in the SOC medium and Incubated at 37°C for 60 minutes without antibiotics.
5. Ampicillin selection plates were warmed to 37°C to avoid cold shock to the transformed bacteria.
6. 100µl of the cells were spread onto the ampicillin selection plates and incubated overnight (16 hours) at 37°C.
7. On the next day, colonies were formed and another selection plates were re-streaked to get the next generation of bacterial colonies to reduce the risk of populating bacterial colonies that acquired ampicillin-resistance due to adaptation capabilities, rather than from the ampicillin-resistant gene in the cloned vectors.
8. These Ampicillin-resistant colonies containing the homology plasmid were inoculated into LB medium and extracted using PureLink™ HiPure Plasmid Filter Midiprep Kit (Thermofisher Catalogue number: K210015) according to modified manufacturer protocols.

3.3.3 The assessment of sequencing and *in-vitro* transcription functionality of the HDR plasmid

Although the cloned homology DNA plasmid was assembled using the high-fidelity NEB HiFi DNA Assembly kit, Sanger sequencing was performed at multiple sites including junction sites between the insert(s) and the vector backbone. In addition, transcriptional activation of the YFP reporter gene under the control of a GFAP promoter, was tested *in-vitro* using lipid-based transfection of U87 GBM cells, a malignant astrocytic cell line which exhibits GFAP expression. The protocol was as follows:

1. U87 Cells were washed twice with DPBS after removing the medium and passaged using DMEM+10% **F**etal **B**ovine **S**erum (FBS). U87 were initially seeded at a density of 80,000 cells in 2ml DMEM+10%FBS per each well of a 24-well plate.
2. The transfection was performed 24 hours after the initial plating. For each well of the 24-well plate, two tubes were prepared; the first containing 1µl Lipofectamine Stem reagent diluted in 25µl Opti-MEM I medium, and the second containing 1.5µg of the cloned HDR DNA plasmid diluted in 25µl Opti-MEM I.
3. The tubes were mixed and incubated at room temperature for 10 minutes.
4. 50µl of the stock mixture was added to each well.
5. After 24 hours, the growth medium containing Lipofectamine Stem was replaced with fresh 2ml DMEM+10%FBS and cells were imaged to assess YFP expression.

3.3.4 NSCs transfection

The H1-NSCs were transfected with both the cutting plasmid (AAVS1 T2 CRISPR in PX330; Addgene plasmid ♯ 72833) (Natsume *et al.*, 2016) and the cloned HDR plasmid, using Lipofectamine™ Stem DNA transfection reagent (Invitrogen; STEM00003) according to the modified manufacturer protocol below:

1. A 24-well plate was coated with 1:100 diluted Geltrex.
2. The H1-NSCs were cultured in 3 X T25 flasks until 90% confluence for at least 3-4 passages before the final transfection passage to enhance the enrichment for neural stem populations that favour the of neural stem culture condition (StemPro NSCs SFM plus Geltrex matrix); i.e., to reduce the undifferentiated pluripotent or multi-potent progenitors which may have persisted throughout the differentiation process, as there is no ideal differentiation protocol that produces NSC with 100% efficiency, while obtaining a healthy and rapidly growing NSCs population.
3. Cells were washed twice with DPBS after removing the medium and passaged using StemPro Accutase to form a single cell suspension. It is important to make a single cell suspension to maximize the efficiency of the transfection. The NSCs were initially seeded at a density of 80,000 cells in 2ml StemPro medium per each well of a 24-well plate.
4. The transfection was performed 24 hours after the initial plating. For each well of the 24-well plate, two tubes were prepared; the first containing 1µl Lipofectamine Stem reagent diluted in 25µl Opti-MEM I medium, and the second containing both plasmid DNAs (0.5µg CRSIPR plasmid, and 1µg of the cloned HDR DNA plasmid) diluted in 25µl Opti-MEM I.
5. The tubes were mixed and incubated at room temperature for 10 minutes.
6. 50µl of the stock mixture was added to each well and the plate swirled gently to ensure even distribution of the DNA-lipid complexes throughout each well.
7. After 24 hours, the growth medium containing Lipofectamine Stem was replaced with the NSC selection medium (StemPro plus puromycin), as the lipotransfection regaent is toxic to the NSCs used.

3.3.5 NSCs colony selection

1. The selection medium used was StemPro NSC SFM with puromycin antibiotic at a concentration of 0.25µg/ml.
2. The selection medium was changed every other day for approximately 21 days to obtain microscoppically-visible NSC colonies, which indicate their puromycin resistance. Several NSC colonies survived the selection process and a proportion (approximately 20-30%) of these survived colonies were individually screened for transgene knock-in using PCR amplifcation and Sanger Sequencing, prior to passaging the remaining monolayer proportion (approximately 70-80%). PCR amplification was conducted using the following PCR primers: forward primer 5'-TATGTCCACTTCAGGACAGCAT-3', and reverse primer 5'-TTAGAGGTTCTGGCAAGGAGAG-3'. The medium was changed prior to physical transferring (using a p200 pippette set to 20µl) of the colony samples into a microtube containing 180µl DPBS. Colony DNA was purified using GeneJET Genomic DNA Purification Kit (Thermo Scientific™ *Catalogue number:* K0721), to allow further PCR amplification and Sanger Sequencing to screen for the knock-in transgenic insert.
    - Reaction Master mix contained 44µl Neuclease Free Water, 75µl One*Taq*® mastermix, 16µl template DNA (1µg/µl extracted DNA), 7.5µl FW primer and 7.5µl RV primer.
    - Thermal cycles were according to the protocol below:
        - Initial denaturation 94°C for 2 minutes
        - <u>30 cycles of:</u>

          94°C for 15 sec

          62.3°C for 60 sec

          68°C for 5 minutes
        - Final extension on 68 °C for of 15 minutes
        - Final hold on 4°C forever
3. The remaing adherent homozygously edited colonies were washed with DPBS twice and also picked using 200µl yellow tip under stereomicroscope to be passaged onto Geltrex pre-coated 6-well plate for further expansion using NSC selection medium.
4. The selection medium was maintained for a further four days after the first passage of the selected NSCs colony, to avoid possible propagation of non-edited NSC colonies. Following, the cells were washed twice with DPBS and fresh StemPro medium was applied for further expansion.

3.3.6 Identifying appropriate selection concentration of puromycin antibiotic using a dose-response curve

The determination of the optimal antibiotic concentration to select the genetically edited clones 24 hours after transfection, is a necessary first step for the generation of a stable cell line. In this dose-response experiment, a variable range of antibiotic concentrations was used to identify the lowest antibiotic concentration which kills all cells within 4-7days. However, it is difficult to choose the optimal puromycin concentration that kills 95%-100% of the NSCs as the cell line may have multiple sub-populations caused due to the persistence of pluripotent (H1 embryonic stem cells) or multi-potent progenitors that remained in culture after differentiation from pluripotent stem cells to neural progenitors, which is one of the major technical challenges that blocks the generation of mutated NSC clones and ultimately edited NSC lines. Choosing the proper concentration for selecting genetically edited-NSCs was conducted as follows:

1. At Day 0, approximately 80,000 H1-derived NSCs were plated in each well of a Geltrex pre-coated 24-well plate. StemPro NSC SFM was used as a growth medium. Two plates were used as duplicates for each concentration.
2. The growth medium was changed every 24 hours into StemPro NSC SFM plus puromycin dihydrochloride (Gibco; catalogue number: A1113803) at a variable range of concentrations; i.e., the puromycin concentration started from 0µg (as controls) and was increased by 0.1µg/ml up to 1µg/ml, by 0.25µg/ml up to 2 µg/ml, and by 0.5 µg/ml up to 5µg/ml from Day 1 onward, with the culture medium changed every 48hours.
3. The selection was continued for 5 days and a manual cell count using a haemocytometer was performed at day 5 to determine the number of viable cells.
4. The initial experiment to identify the optimal concentration of the minimum puromycin concentration required to kill ≥ 95% of the cells was not accurately conclusive. However, it was helpful in identifying a puromycin range of concentrations (0.2-0.3 µg/ml) that could kill the NSCs within +/-5 days. Thus, the experiment was repeated in a 6-well plate with a larger number of cells (350,000 cells) in the same culture system. The closely selected puromycin range of concentrations was 0.15µg/ml, 0.2 µg/ml, 0.25 µg/ml, 0.3µg/ml, and two control wells, in a 6-well plate. Results showed that the most appropriate puromycin concentrations to be used for NSCs selection were 0.2-0.25µg/ml. We chose to use 0.25µg/ml for selecting chimeric clones to enrich for homozygously edited NSCs clones which hypothetically express the

transgene 2-fold more than the heterozygously edited colonies. We have not performed kill curves for the remaining two iPSCs cell lines as these concentrations were previously determined by Prof. Chris Denning's group (University of Nottingham).

3.3.7 PCR screening for mutated clones and guidelines for extracting genomic DNA using GeneJET Genomic DNA Purification Kit; (Thermo Scientific™ *Catalogue number:* K0721) according to manufacturer protocol.

1. The cells were transferred into 180µl DPBS.
2. 200µl lysis buffer containing 20µl of protien K Solution was added to cells and the mixture was vortexed to ensure even distribution throughout the microtube.
3. The suspension was incubated at 56°C for 10 minutes while vortexing using a rocking heat block.
4. 20µl RNase A solution was added and mixed by vortexing. The mixture was incubated at room temperature for 10 minutes.
5. 400µl of 50% ethanol was added and mixed by pipetting.
6. The cell lysate was transferred into the GeneJET Genomic DNA Purification Column that was inserted into a collection tube. The mixture was cetrifuged at 6000 x *g* for 1 minute and the collecttion tube containing the flow-through was discarded and replaced by a new 2ml collection tube.
7. 500µl of washing buffer I (with the ethanol added before the first use) was loaded into the column and centrifuged at 8000 x *g* for 1 minute and wash buffer I flow-through discarded.
8. 500µl of washing buffer II (with the ethanol added before the first use) was loaded into the column and centrifuged 14000 x *g* for 3 minute and wash buffer II flow-through discarded. The column was centrifuged for an additional minute at 23000 x *g* to avoid any residual buffers and ethanol and the column transferred to a new 1.5ml microtube.
9. Only 15µl of ellution buffer was loaded into the center of the column and incubated for 10 minutes at room temperature, followed by centrifugation at at ≥12000 x *g* for 2 minutes. Flow-through containing purified DNA was stored at -20°C.

3.3.8 NSC differentiation

P8 H1AML NSCs were differentiated into mature astrocytes according to guidelines modified from a previously reported protocol (TCW *et al.*, 2017). NSCs were cultured using Geltrex™ LDEV-Free Reduced Growth Factor Basement Membrane Matrix (Gibco; A1413201) and complete StemPro growth medium (Gibco Catalogue number: A1050901), and passaged (section 2.3, Chapter 2) at a ratio of 1:3 every 3-4 days using StemPro™ Accutase™ Cell Dissociation Reagent (Gibco; catalogue number: A1110501). After the final passage before starting the differentiation, the healthy growing NSCs were seeded as single cells at 25,000 cells/cm^2 on Matrigel (Corning; Fisher catalogue number 11593620) coated vessels and left to grow in StemPro NSC SFM medium for 24 hours, to adapt the NSCs onto the new basement membrane. On the next day, the medium was replaced with astrocyte medium (Sciencell Catalogue number: 1801), which is composed of astrocyte basal medium (1801-b), 2% foetal bovine serum (ScienCell, Catalogue number: 0010), astrocyte growth supplement (ScienCell Catalogue number: 1852) and penicillin/streptomycin solution (ScienCell Catalogue number: 0503). Astrocyte medium was changed every other day for 40-45 days. Morphological changes (cellular body enlargement and prominent cell processes) of NSCs appeared from Day 2-3 and intensified as differentiation progressed.

3.3.9 Astrocyte isolation using FACS

Astrocytic cells isolation was performed independently three times: the first cell sorting was performed when NSCs differentiated into astrocytes; astrocytes were then isolated on two further occasions after these astrocytes were co-cultured with each of ten primary glioma cell lines derived from the infiltrative margin GIN for six and ten days respectively. In all occasions, astrocytes were washed from medium using DPBS (without calcium and magnesium) and passaged from coated surfaces using TryplE Express to create single cell suspensions. The washing step is critical to remove any residual serum that causes cells to form clumps. Cells were next centrifuged at 200-250 x *g* for 5 minutes and the supernatant was completely removed. Astrocytes were re-suspended in room temperature FluoroBrite ™ DMEM (Gibco; A1896701) and kept on ice for cell sorting. It is important to keep FluoroBrite DMEM medium at room temperature for 60 minutes to allow the medium to warm up to room temperature before applying it onto the cells, as this may reduce the possibility of causing a cold shock to the cells. Cell sorting was performed using a Beckman coulter MoFlo XPD and Astrios EQ. Blue laser (488nm) at maximum intensity (100%) was used for YFP excitation. While sorting differentiated YFP-astrocytes, the undifferentiated NSCs were used as a negative control for astrocyte cell enrichment. To collect astrocytes from co-cultures at both time points of the experiment, the primary GIN cell lines were used as controls for their corresponding co-culture to determine the setting of the gates, the double-enrichment process and the re-collection of the co-cultured YFP-astrocytes.

3.4 Results

To study the effect of malignant glioma cells on the surrounding reactive astrocytes and explore whether these astrocytes have been reprogrammed by malignant signals, a yellow fluorescent astrocytic reporter cell line was generated as described above. Labelling NSCs facilitated fluorescence-based cell sorting after differentiation and co-culture with GBM cells. GFAP marks the astrocyte lineage, and thus the GFAP promoter was purposely constructed to be in-frame with the upstream 5' end of YFP gene to initiate YFP transcription when NSCs were differentiated towards the astrocytic lineage. To create this stable genetically-edited cell line, both CRISPR/Cas9 and HDR template donor DNAs were lipofected and electroporated into NSCs and two iPSCs cell lines respectively. A CRISPR/Cas9 plasmid carried a guide RNA sequence (GGGCCACTAGGGACAGGAT) that was previously used to make a DSB in the AAVS1 safe harbour locus of the PPP1R12C gene within these stem cell lines (Kotin, Linden and Berns, 1992; Ogata, Kozuka and Kanda, 2003; Smith *et al.*, 2008; Hockemeyer *et al.*, 2009, 2011; DeKelver *et al.*, 2010). In addition, the HDR DNA was designed to contain a transgenic insert composed from the GFAP promoter, eYFP gene, WHPTE, and hGH polyA tail. This transgene must be successfully integrated into the stem cell genome by the homologous recombination process after creating the break using CRISPR/Cas9 DNA. The CRISPR/Cas9 DNA was purchased, whereas the HDR was cloned during this project as described previously.

3.4.1 Confirming the appropriate cloning of HDR donor DNA plasmid using restriction digestion.

We used the NEBuilder® HiFi DNA Assembly Cloning Kit to clone the HDR vector which has high fidelity and precision to seamlessly assemble several DNA fragments by scar-less joining of their overlapping sequences. However, it was important to assess the direction and sequence of the cloned HDR vector. We used the conventional restriction digestion methods to confirm the appropriate size of the plasmid, and thus the HDR plasmid was electrophoresed on 1% agarose gel after linearization using a single restriction digestion reaction mediated by the HincII restriction enzyme. This correctly identified the appropriate HDR DNA band size of 9733bp **(Figure 3. 9)**. To further confirm the HDR DNA sequences according to the *in-silico* homology donor DNA construct, double restriction digestion of the HDR template DNA was conducted using high fidelity restriction enzymes EcoRV-HF and PacI. This successfully resulted in two linear DNA fragments of 2923bp and 6810bp **(Figure 3. 9)**. The single and double restriction digestion reactions successfully

indicated that the homology HDR DNA vector was correctly sub-cloned. However, the direction of full-length sequences of the cloned DNA fragments (such as the direction of the YFP gene) cannot be confirmed with this method.

3.4.2 Confirming the appropriate sequence and read-frame of the cloned HDR donor DNA plasmid using Sanger Sequencing and *in-vitro* functional experiment respectively.

The HDR template DNA was cloned from three distinct DNA fragments from three separate plasmids. These segments are the vector backbone, the human GFAP promoter, and a DNA fragment that consists of three segments (eYFP gene, WPRE, and hGH polyA tail). HDR Plasmids of correct size as determined by restriction digestion, were sent for Sanger Sequencing to confirm the alignment of the assembled DNA segments. Primers were designed to assess the junction between the 5' end of the human GFAP promoter and the puromycin 3' end of the vector backbone, specifically the forward primer (GTGGTTCCTGGCCACCGTC) and the reverse primer (CTGAATAGAGCCTTGTTCTCCACCG). Similarly, the junction between the HA-R and the hGH polyA tail was assessed using the reverse primer (GCTACTGGCCTTATCTCACAGG). This alignment of the sequence reads was performed using multi-sequence aligner (https://www.ebi.ac.uk/Tools/msa/clustalw2/) **(Figure 3. 10)**. However, the most important junction located between the promoter and the eYFP gene could not be assessed with the designed primers, as they possibly required high annealing temperatures. To address this, a more robust functional experiment was conducted to assess this sequence based on the functionality of the GFAP promoter and whether the eYFP gene was located within the reading frame of this promoter. The human protein atlas (https://www.proteinatlas.org) provided valuable information that glioma cell lines exhibit relatively high expression of GFAP, which prompted us to conduct *in-vitro* testing of the generated HDR plasmid that contained the GFAP promoter. The HDR donor DNA was transfected into the established U87 glioma line using Lipofectamine Stem. The transfected glioma cells were examined under fluorescent microscopy which confirmed the expression of the YFP reporter gene **(Figure 3. 10)**. Thereby this result indirectly confirmed that the eYFP gene was located within the reading frame of the GFAP promoter. Most importantly, the result confirms the success of the entire cloning procedure and an acceptance of the hypothesis that this CRISPR/Cas9-mediated knock-in strategy can generate a transgenic line which stably express the YFP reporter upon directed differentiation to the astrocytic lineage.

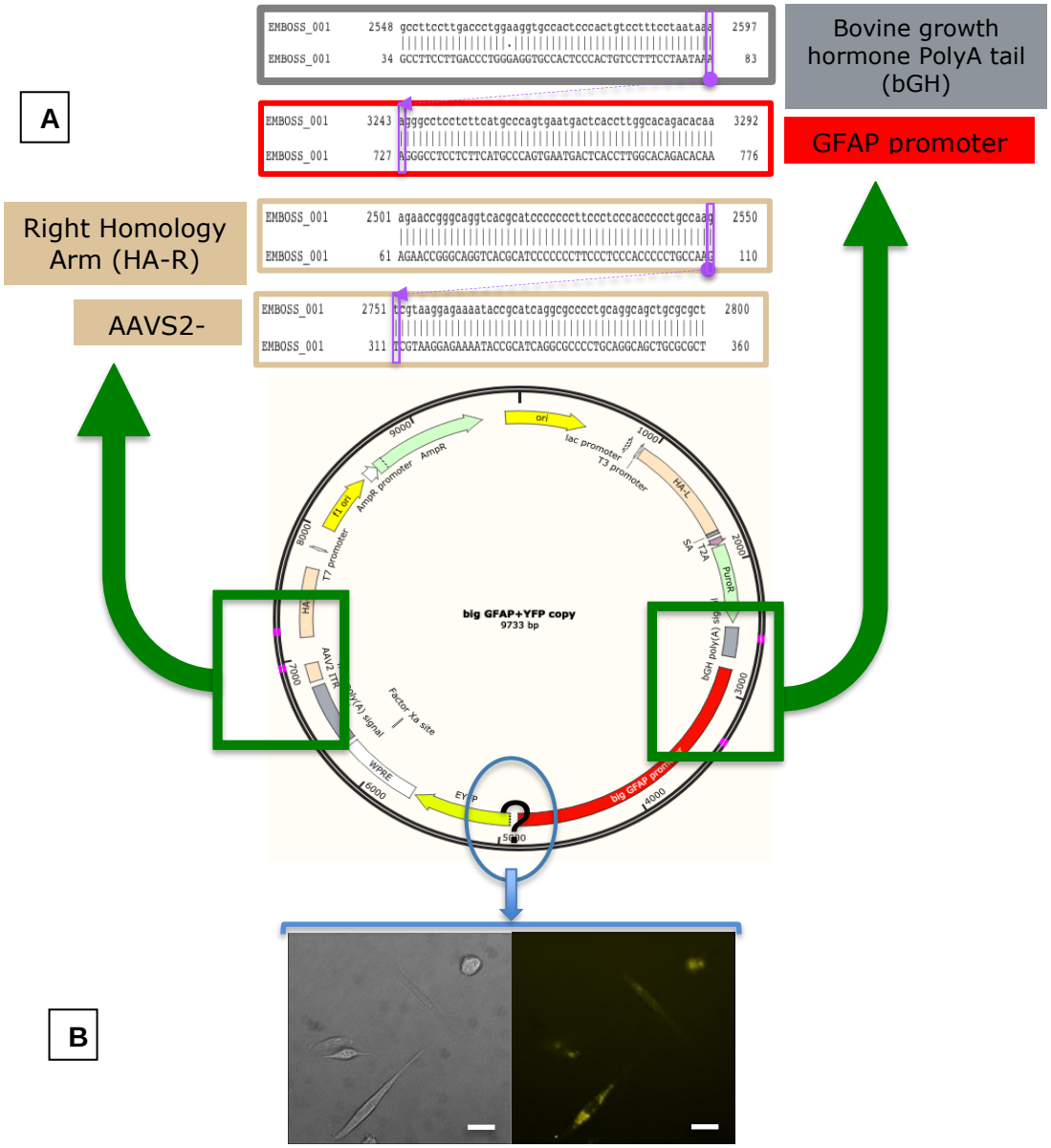


Figure 3. 10. Confirmation of HDR sequences and transcription functionality. (A) Within the green rectangle (left), the magenta coloured spots represent the ends of the sequenced DNA fragment that surround the distal junction between AAVS2 (part of the plasmid which the insert was taken from) and the vector adjacent to the HA-R. Sanger Sequences for these two regions are shown in light brown boxes above the vector schematic. Within the green rectangle (right), the magenta coloured spots represent the proximal junction that was designed *in-silico* to occur between the bGH polyA tail of the vector backbone and the large GFAP promoter of the insert, for which Sanger Sequences are shown in grey and red boxes above the vector schematic respectively. The segment flanking the eYFP gene and GFAP promoter (circled) could not be sequenced. (B) However, *in-vitro* transcriptional activity was confirmed by lipid-based transfection of the cloned HDR plasmid into a GFAP expressing glioma cell line (U87). Visible eYFP expression directly confirmed the functional activity of the cloned GFAP promoter and indirectly confirmed the correct sequence alignment, where the YFP gene has been successfully cloned within the reading frame of the promoter. Scale bar is 20µm.

3.4.3 PCR-based screening of genetically edited NSC clones

Extracted DNA from mutated NSC clones that survived the puromycin selection was purified and two primers (forward primer; TATGTCCACTTCAGGACAGCAT and backward primer; TTAGAGGTTCTGGCAAGGAGAG) were designed that can precisely amplify the entire transgenic construct (5535bp), extending between the homology arms **(Figure 3. 11)**. The homozygously edited clone was selected and expanded as this would hypothetically exhibit higher expression of the YFP reporter (i.e. both alleles contain the YFP transgenic knick-in) within astrocytes, relative to a heterozygously edited clone. However, we performed sequencing on the amplified DNA fragment to confirm transgene knock-in.

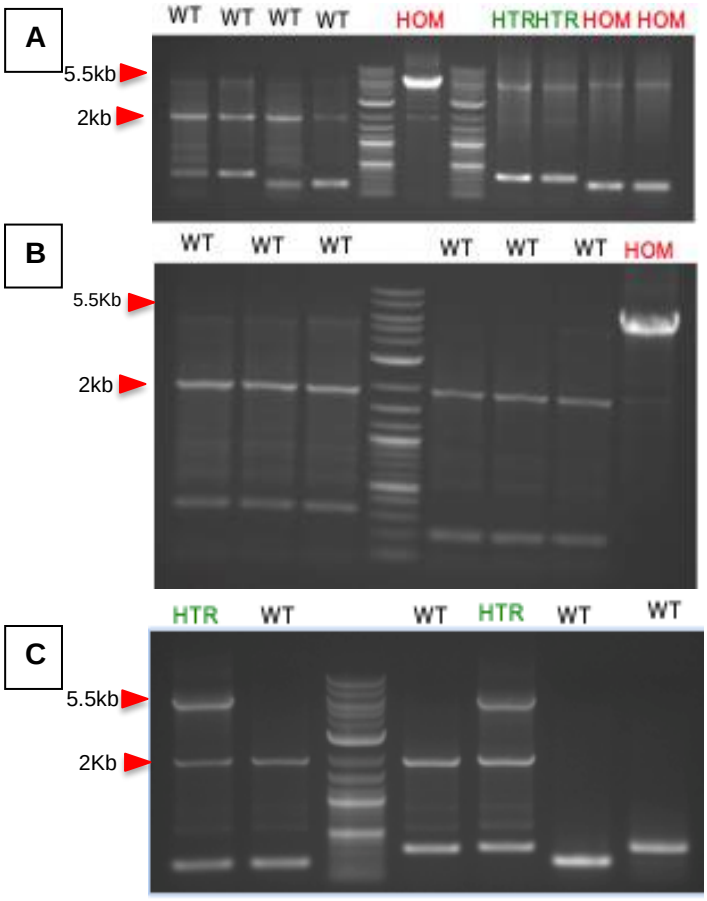


Figure 3. 11. Screening of the YFP transgenic construct knock-in (KI) (edited NSCs clones) via PCR amplification. (A-C) The screening process for mutated NSC colonies shows that 8 NSCs colonies were homozygously (HOM)- or heterozygously (HTR)-edited. The optimised primers either amplified the wild-type (WT) genomic region of the AAVS1 site (approximately 2kb), or the KI construct flanked by the WT region (approximately 5.5kb).

3.4.4 Confirming knock-in of the YFP transgenic construct into the AAVS1 safe harbour locus of NSCs using computational biology.

The PCR-amplified DNA fragment generated appropriate bands using the optimised primers **(Figure 3. 12A)**. These bands were excised and extracted DNA outsourced for Sanger Sequencing to screen several transgenic sites not endogenous to the human genome, such as the YFP reporter sequence **(Figure 3. 12)**. Sequences were aligned with the designed HDR template DNA using Snapgene (https://www.snapgene.com/snapgene-viewer/) and pairwise genomic DNA sequence aligner (https://www.ebi.ac.uk/Tools/msa/clustalw2/). These computational tools clearly showed the presence of the YFP sequence under control of the GFAP promoter in the amplified DNA fragment from the chimeric clones, confirming KI of the transgenic insert **(Figure 3. 12)**. However, this was to screen for genomic integration only; i.e., the function of this knocked-in construct had to be further elucidated, as transgenes are highly subjected to epigenetic silencing. This can be appropriately confirmed by differentiating the multi-potent NSCs into astrocytes to transcriptionally activate the GFAP promoter within the construct to express the eYFP gene.

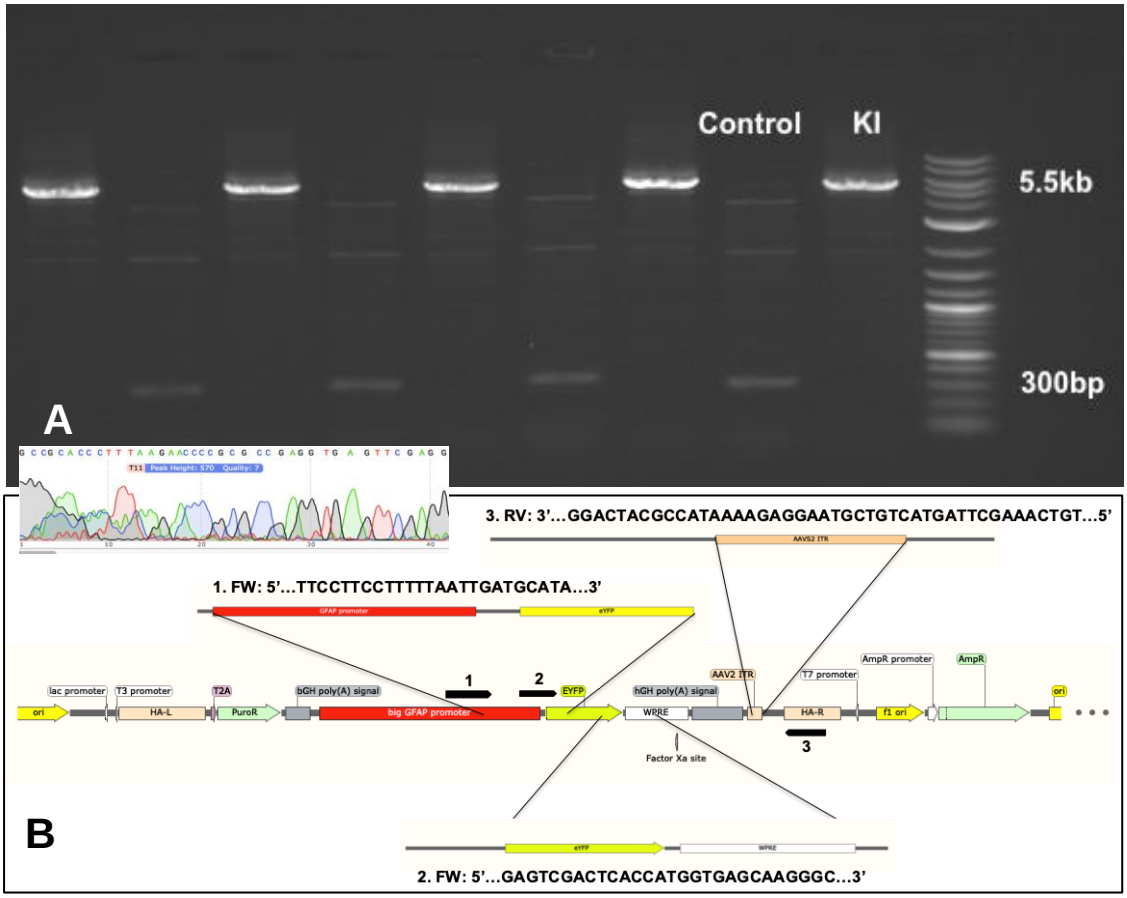


Figure 3. 12. Confirmation of transgene KI within homozygously edited H1AML NSCs. (A) PCR amplification bands of selected mutated NSCs colonies, composed of the entire transgene construct (3.95kb) flanked by ~0.75kb of vector genomic sequences either up- and down-stream to the AAVS1 genomic cleavage site. The bands shown were excised using a DNA gel purification kit and sequenced by the Sanger Sequencing method. (B) The sequences were aligned to the *in-silico* designed HDR and human genome sequence using Snapgene and ClustlW2 computational tools. Three primers (1, 2 and 3) were used and locations are shown (black arrows). Two were forward primers (1) and (2) which start at the GFAP promoter and the YFP gene respectively, whereas reverse primer (3) was designed to start at the HA-R. These primers were used to identify characteristic mutated sites located at the AAVS1 to confirm the KI in the human genome. For example, forward primers (1) and (2) revealed the positive (5' to 3') strand sequences of the GFAP promoter followed by the YFP gene as well as the presence of the WPRE segment followed by the AAVS2 ITR site (part of the vector backbone) respectively. The reverse primer showed the negative (3' to 5') strand sequences of AAVS2 ITR. The fact that DNA fragment sequences such as the eYFP gene and WPRE are not present in the native human genome, or are present but not in this spatial orientation (the GFAP gene is not normally followed by YFP), confirmed the presence of the KI of the entire transgene within the NSCs genome.

3.4.5 Confirming the stability of the genetic editing (KI) in H1AML NSCs via frequent passaging and differentiation

To exclude the possibility that the entire amplified DNA segment originated from the amplification of a non-integrated HDR DNA template (false positive), eYFP transgene transcriptional activity was confirmed by differentiating the multipotent NSCs into astrocytes, thus in principle activating the GFAP promoter within the construct and consequent express the eYFP gene. Demonstrating stability of transgene expression and with frequent passaging is an important objective in our study. Thus, a further confirmatory step was performed by taking samples from the homozygously-mutated clones of H1AML NSCs and expanding them. Next, these expanded clones were propagated for 20 passages. DNA from these expanded clones was extracted and PCR performed to confirm the integration of the genetic insert within the human genome. In addition, the function of the GFAP promoter within the construct was assessed by directed differentiation of the passaged clones into astrocytes for 42 days, after which the astrocytes were sorted and imaged based on fluorescence, to ensure confirm YFP expression and differentiation efficiency.

3.4.6 Confirmation of multi-potency and differentiation potentials of the genetically-edited H1AML NSC cell line

The H1AML cell line has gone through robust clonal selection process using puromycin drug. Thus, assessing characteristic neural-stem markers and the differentiation capacities of H1AML cell line were essential before conducting our experiment. The characterisation included immunostaining of the neural stem markers Nestin and SOX2 **(Figure 3. 13)**. The differentiation capacities of this cell line was assessed for several reasons; firstly, it was crucial to know if this cell line could generate mature astrocytes, according to the protocol previously described in (TCW *et al.*, 2017), as these transgenic astrocytes are one of the essential components of our Gliomasphere Matrix model (see Chapter 5). Secondly, differentiating the H1AML cells would confirm whether the construct is transcriptionally active, as the entire integrated cassette is susceptible to epigenetic silencing. Finally, the differentiation of H1AML cells at this stage allowed the optimisation of the differentiation conditions and isolation via FACS, a requirement for co-culture transcriptomic experiments using Gliomasphere Matrices (see Chapter 6). Thus, H1AML NSCs were cultured using Geltrex basement membrane and StemPro medium for rapid healthy growth, followed by Matrigel and astrocyte medium for 45 days to achieve successful directed differentiation. The cells started to show morphological changes from the characteristic neural stem-shaped cells into the star-like astrocytic appearance by Day 3 after being exposed to astrocyte medium. Multi-branching, stellate YFP-expressing cells started to express the YFP transgene at Days 14-16 of differentiation and were sorted after 40-45 days using FACS **(Figure 3. 13)**. The enhanced YFP reporter gene under the control of the transgenic GFAP promoter, was intensely expressed at 45 days, indicative of transcriptional activation via endogenous transcription factors. The differentiation protocol previously described in (TCW *et al.*, 2017) was successfully reproduced, and optimised to our laboratory culture standards, to achieve 78% efficiency (78% of FACS-isolated cells were YFP-positive astrocytes). The YFP-astrocytes were double-gated during FACS to ensure maximum purity and enrichment.

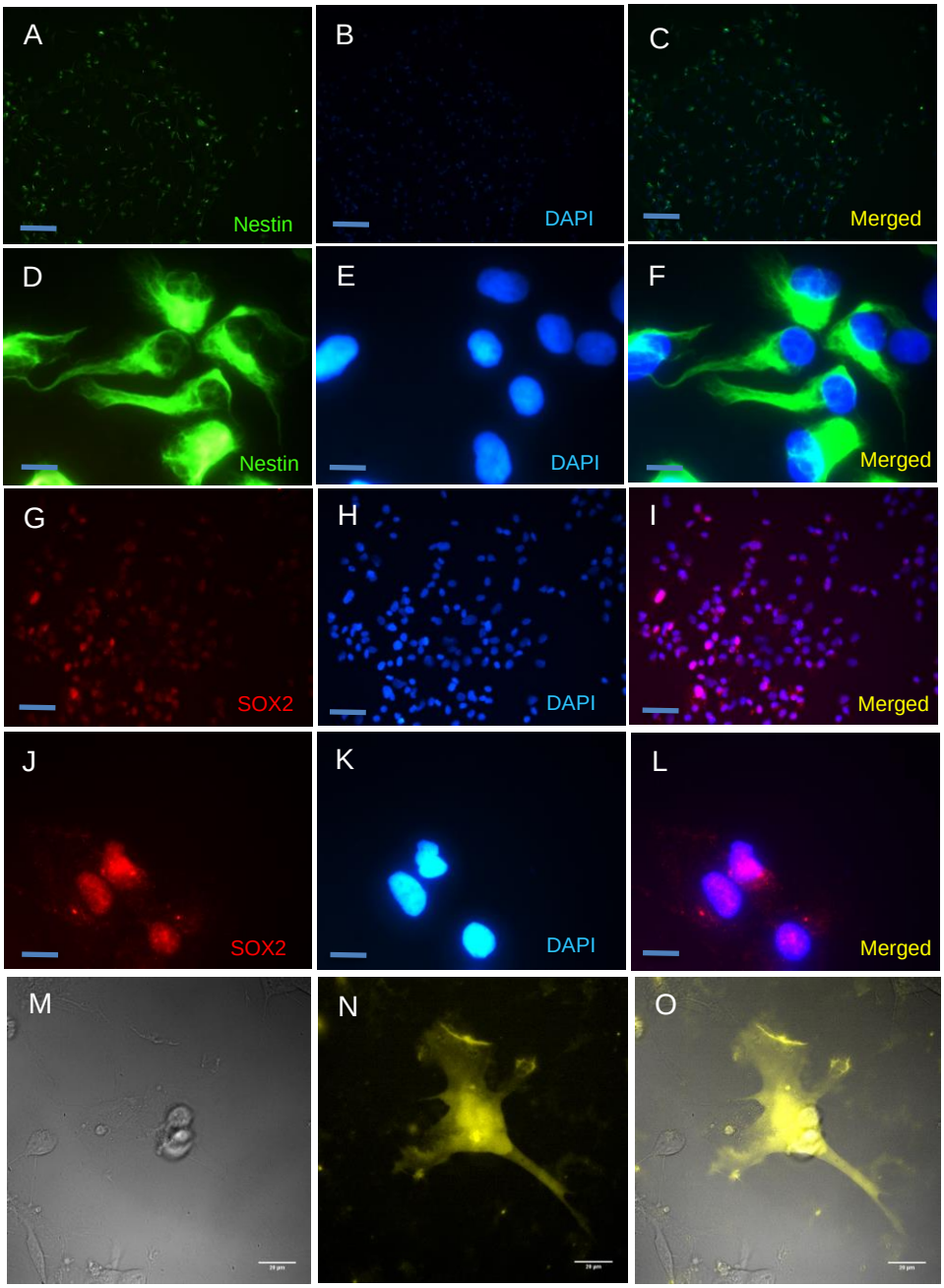


Figure 3. 13. Screening the H1AML transgenic line for neural-stem properties and differentiation potential after stringent puromycin selection. (A-L) The homozygously-edited H1AML cells were fixed and stained for the neural-stem markers Nestin (A-F) and SOX2 (G-L) which are shown at high (D-F; J-L) (100X; oil lens) and low (20X) (A-C; G-I) magnification by fluorescent microscopy respectively. (M-O) Mature differentiated astrocytes (viable) expressing the YFP transgene whereas H1-differentiated cells other than astrocytes (neurons, oligodendrocytes, and stem cells) do not express YFP (marked with blue triangle). *Scale bar is 20nm in (D-F; J-L) and 100nm in (A-C; G-I; and M-O).*

3.5 Discussion

We successfully achieved our objective of creating three transgenic YFP reporter lines, in which a cloned construct composed of the puromycin selection gene, GFAP promoter, YFP gene, WPRE and hGH polyA tail, was knocked-in at the AAVS1 safe harbour locus. For practical purposes and brevity of thesis, only data related to the H1 NSCs is shown, whilst data related to the two iPSC cell lines are not shown. The GFAP promoter in this construct is constitutionally activated upon astrocyte lineage specialisation and maturation during directed differentiation of NSCs. This allowed us to isolate a pure population of astrocytes after differentiation and was applicable methodology for the generation of Gliomasphere Matrices and investigating of molecular cross-talk between astrocytes and invasive GBM cells after re-isolation of YFP-astrocytes after 3D co-culture (See Chapters 5 and 6). Despite the successful generation of three reporter cell lines, we only used YFP-astrocytes derived from the homozygously edited H1AML NSC line, as YFP expression level was highest in this line relative to both iPSC lines (data not shown). Furthermore, the high costs required for cell culture, differentiation and RNA-sequencing, was a severely limiting factor. Future studies could incorporate these transgenic cell lines to increase the stringency of the experiment via eliminating the normal variability of human astrocyte transcriptomes from different donors

To the best of our knowledge, H1-AML NSC reporter cell line is the first cell line to be generated by knocking-in a construct directly into the AAVS1 site of NSCs, instead of the classical approach of labelling pluripotent stem cells and differentiating them into NSCs such as (Zhang *et al.*, 2015). Slower growth rates of NSCs compared to pluripotent stem cells, the choice of culture system, and the heterogeneous populations of progenitors within NSC lines, could individually or collectively have been the reason(s) of failure of generating transgenic NSC lines. We have identified several approaches that allowed us to successfully achieve this: firstly, the lipofection of plasmid DNAs on poly-L-Laminin is not an efficient transfection method, whereas the use of an alternative culture system (StemPro growth medium and Geltrex surface coating) allowed successful lipofection efficiency of ~40-50%; secondly, adapting the NSC cell line to StemPro growth medium and Geltrex surface coating enhanced the enrichment of neural progenitor populations. Thirdly, frequently passaging (at least four passages) NSCs using StemPro growth medium and Geltrex basement membrane was a key step to overcome the challenge of heterogeneous progenitor populations within the same NSC cell line. Finally, choosing the AAVS1 site for KI, which influenced the HDR plasmid cloning design, was extremely

important to achieve successful creation of the transgenic NSC-reporter cell line. In this context, designing the location of the puromycin selection gene to be at the beginning of the insertion cassette of the HDR plasmid, to be transcribed by the endogenous AAVS1 promoter, was a successful method to visually (via microscopic examination) indicate edited NSC clones after puromycin selection.

The sub-cloning of the HDR DNA and the genetic labelling of H1NSCs (and two iPSCs lines) via CRISPR/Cas9 technology, allowed us to save a considerable amount of research funding which otherwise would have been incurred if commercially outsourced. Furthermore, using labelled NSCs allowed us to avoid the laborious and expensive process of differentiating pluripotent stem cells into NSCs and then subsequently into astrocytes. Such an approach usually takes 7-21 days to obtain the NSCs, followed by approximately 45 days for astrocyte differentiation. The use of transgenic NSCs also reduced the costs allocated for primary antibodies to FACS-isolate astrocytes, that would otherwise have been required if alternative labelling strategies were used. Labelling NSCs included chemical and physical selection to generate a pure transgenic population of NSCs, whereas labelling and differentiating iPSCs would result in undifferentiated progenitors that may outcompete NSCs and NSC-derived differentiated cells. Collectively, labelling NSCs reduces costs, time and require less laboratory technical skills. The generation of the H1AML transgenic cell line permitted the re-isolation of astrocytes co-cultured with invasive GBM cells, based on YFP reporter expression. Without this transgenic approach, it would be extremely challenging to separate healthy astrocytes from glioma cells, due to lack of discriminative markers, as glial markers such as GFAP cannot discriminate these cell types. Moreover, stably introducing the YFP transgene into NSCs provides flexibility to co-culture and re-isolate astrocytes at different stages of astrocytic differentiation and maturation. Furthermore, our approach facilitated live cell tracking and imaging of YFP-astrocytes within the core and the peripheral regions of the invasive co-culture model (see Chapter 5).

The genetic labelling method could have been substituted by the use of cell tracing dyes. However, cellular tracking using these expensive cell tracing dyes could only persist for few days, limiting the period within which to assess altered astrocytic transcriptomic profiles upon physical interaction with invasive GBM cells. Indeed, profound transcriptome alterations occurred in co-cultured YFP-astrocytes which were FACS-isolated at Day 10 compared to those isolated at Day 6 (see Chapter 6).

Chapter (4)

Decellularising human brain extracellular matrix (ECM)

Chapter 4 Huma brain ECM decellularisation

4.1 Introduction

4.1.1 Decellularisation of tissues

The ECM for a given tissue exerts distinct regulatory influences on various cellular processes such as growth (Koochekpour, Merzak and Pilkington, 1995; Williams *et al.*, 2008), differentiation, maturation and survival (Bosnakovski *et al.*, 2006; Chastain *et al.*, 2006), as well as a critical role in controlling developmental stages (Simon-Assmann *et al.*, 1995). Despite the complexity of ECM molecular composition, which is the major contributing factor for distinct cellular behaviours, many studies can measure cellular phenotypes directly on polystyrene surfaces or on an individual purified protein (Dequach *et al.*, 2011). However, these culture surfaces do not physiologically resemble the extracellular microenvironment, nor the complex nature of the native ECM, which may bias experimental results and hamper the translation of findings from *in-vitro* studies to *in-vivo* models (Koochekpour, Merzak and Pilkington, 1995; Everitt, Malik and Hendey, 1996). Thus, it is important to provide a platform that resembles the native niche and which allow cells to behave and function naturally while retaining physiologically-relevant phenotypes. Decellularisation of brain ECM offers an approach to recapitulate the tissue-specific brain microenvironment. In principle, decellularised brain ECM retains the suite of extracellular ligands which are involved in receptor-mediated biochemical signalling within neural cells (Dequach *et al.*, 2011). Furthermore, decellularised brain ECM is amenable for incorporation into multi-component cerebral organoid models, such as the novel Gliomasphere Matrices described in Chapter 5.

4.1.2 *In-vivo* applications of decellularised ECM

The ECM is conserved among species and contains similar components of mainly proteins and polysaccharides (Bernard *et al.*, 1983), but where the unique combination of these compositions determines the specificity to an individual tissue (Lutolf and Hubbell, 2005; Uriel *et al.*, 2009). Classical cell culture coating materials either lack sufficient protein composition complexity required to regulate physiologically-accurate cellular behaviour, or are derived from poorly characterised sarcomatas materials (Dequach *et al.*, 2011). Tissue decellularisation methods have been developed to recapitulate the native tissue microenvironment, comprising a

combination of the proteins and polysaccharides specific to each individual tissue. The use of decellularisation techniques is not new, being first reported in 1973 when porcine skin was decellularised to provide dressings for burned skin of patients (Elliott and Hoehn, 1973). Recently, many decellularised matrices such as skin, pericardium, heart, muscle, liver, and fat, have been assessed as viable cell culture coatings (Blaisdell, 2002; Hackam, Goodman and Anand, 2005). For example, neurons differentiated from pluripotent stem cells were successfully cultured on decellularised 2D human brain ECM coating (DeQuach *et al.*, 2011). These scaffolds provided a native *in-vivo* microenvironment mimic to allow proper cellular behaviours (DeQuach *et al.*, 2010, 2011). As ECM is conserved among species (Bernard *et al.*, 1983), many xeno-derived decellularised ECM materials (such as small intestine submucosa, skin, pericardium, heart valves) from porcine and bovine origins were approved by the Food and Drugs Agency (FDA) for clinical purposes, due to favourable tolerability and lack of immunogenicity (Badylak, Freytes and Gilbert, 2009). In brain *in-vivo* studies, heterologous urinary bladder ECM hydrogels were assessed for the study of two brain conditions; stroke (Massensini *et al.*, 2015; Ghuman *et al.*, 2016) and traumatic brain injuries (Zhang *et al.*, 2013). Two further studies were conducted by Badylak and colleagues assessing the use of urinary bladder ECM hydrogel for chronic stroke in a small animal model. Various concentrations (1-8mg/ml) of hydrogel were delivered for two weeks after inducing the stroke by occluding the middle cerebral artery of the rat. It was found that hydrogels with a concentration of < 3mg/ml diffused to the surrounding tissue and interfaced with the stroke cavity rim within 24 hours. Cells accumulated at the cavity edge as there was no media to infiltrate through. However, the urinary bladder hydrogel with a concentration of > 3mg/ml successfully formed gels within approximately 3 minutes after its application and was infiltrated with various brain and immune cells after only 24 hours. Thus, the authors suggested that the urinary bladder hydrogel showed ideal properties for an injectable therapy (Massensini *et al.*, 2015; Ghuman *et al.*, 2016). Likewise, the urinary bladder ECM hydrogel was daily delivered at a concentration of 5mg/ml to an impact-induced cortical brain injury rat model. The hydrogel improved the area of tissue damage, reduced the lesion size and mitigated the vestibular-motor function; however no cognitive improvement was observed (Zhang *et al.*, 2013). The urinary bladder ECM hydrogel for these brain applications was shown to be safe, as no adverse effects occurred when this ECM hydrogel was injected into the normal brain. Moreover, no reactive astrocytes nor neuronal damage was observed at three time points within one week of the experiment (Zhang *et al.*, 2013). In addition, previous applications of the various

ECM hydrogels did not induce immunogenic responses within various host tissues such as brain (Zhang *et al.*, 2013; Massensini *et al.*, 2015; Ghuman *et al.*, 2016), liver (Lee *et al.*, 2014), heart (Singelyn *et al.*, 2009, 2012; Seif-Naraghi *et al.*, 2011, 2012, 2013; Wassenaar, Braden, *et al.*, 2016; Wassenaar, Gaetani, *et al.*, 2016), skeletal muscles (DeQuach *et al.*, 2012; Wolf *et al.*, 2012; Fu *et al.*, 2016; Ungerleider *et al.*, 2016), tendon (Fisher *et al.*, 2012; Farnebo *et al.*, 2014; Kim *et al.*, 2014), fat (Uriel *et al.*, 2008; Cheng *et al.*, 2010; Young *et al.*, 2011; Poon *et al.*, 2013; Kim *et al.*, 2016), spinal cord (Tukmachev *et al.*, 2016), lung (Pouliot *et al.*, 2016), cartilage (Wua *et al.*, 2015), or colon (Keane, Dziki, Castelton, *et al.*, 2017; Keane, Dziki, Sobieski, *et al.*, 2017). Note, these studies utilized ECM hydrogels of both heterologous and homologous tissues.

4.1.3 Decellularisation techniques and materials

Biologic scaffolds obtained by successful decellularised of tissue ECMs have great potential to be used in clinical applications as it is hypothesised that decellularised tissues enhance and foster “constructive remodelling” (Keane, Swinehart and Badylak, 2015). The constructive remodelling includes multiple mechanisms of repair and reconstruction by recruiting and differentiating stem or progenitor cells, in addition to favourably modifying the native immune microenvironment. The active molecules within tissue ECM are exposed when cells are removed during decellularisation (Keane, Swinehart and Badylak, 2015). Robust decellularisation is critical for the outcome consequences. Improper decellularisation and the retention of cellular components can induce unwanted strong inflammatory and damage responses within host cells (Keane *et al.*, 2012). The major aim of tissue decellularisation is to remove all cells and cellular components. However, there have been no decellularisation protocols to date which can remove all cellular components while preserving ECM architecture and signalling ligands (Keane, Swinehart and Badylak, 2015). Multiple optimised methods and materials have been designed to specifically decellularise various tissues which have different densities of cells and matrix, reviewed in (Keane, Swinehart and Badylak, 2015). These decellularised approaches are physical, chemical or combinatorial methods involving both physical and chemical methods. For example, the immersion of tissues in detergents and enzymatic solutions with agitation/stirring, is one of the most commonly used approaches, reviewed in (Keane, Swinehart and Badylak, 2015). In this approach, the agitation step enhances the ability of chemicals to remove cellular adhesions and to maximise the permeation and penetration into tissues. The chemical reagents can

include enzymatic and hypertonic solutions, ionic and non-ionic detergents, alcohols, and acids. Some of these materials were used in our decelullarisation protocols, reviewed in (Keane, Swinehart and Badylak, 2015; Tomlins, 2015) (see Materials and Methods and Results sections). For example, trypsin protease enzymatic solution plays a role in the selective cleavage of cellular adhesion at the carboxyl sides of lysine and arginine, which facilitates the release of cells from their ECM substratum. Proteases are effective decellularisation adjuvants, but long exposure to trypsin is known to cause damage to collagen, Glycosminogycans (GAGs), and elastin fibres. Trypsin is usually used with a chelating agent such as EDTA to bind the divalent metal cations at cell-ECM adhesion sites, which results in cell-sequestration, which in turn releases cells from their ECM. Triton-X-100 is an example of a non-ionic detergent that gently allows the solubilisation of proteins, while preserving native enzymatic activity and structure of the ECM proteins. However, it can also cause damage to GAGs and proteoglycans. Hypertonic solutions such as sucrose can enhance cell shrinkage and detachment from the ECM, but can also damage GAGs. Alcohols such as ethanol dissolve lipids and lyse cells by dehydration when the cell membranes are permeated. Ethanol is used during the final steps of the decellularisation process to wash and remove the nucleic acids. The materials thus far described, are effective as adjuvant decellularisation materials when utilized with additional decellularisation materials such as sodium dodecyl sulphate (SDS) or sodium deoxycholate, which can enhance solubilisation of DNA, lipids, and cytoplasmic membranes, but which may reduce the number of ECM GAGs, damage collagen and increase the extensibility of ECM (i.e. cause ECM stretching). The final step of decellularisation utilises acids for two purposes: firstly, acids can solubilize cytoplasmic contents and disrupt the nucleic acids; secondly, acids, such as peracetic acid, are effectively used to terminally sterilise the decellularised tissue ECMs as required by guidelines outlined by the FDA (Yoganarasimha *et al.*, 2014).

4.1.4 Characterisation of decellularised ECM

The complete removal of all cellular components from the ECM is unlikely to occur despite using robust combinatorial decellularisation approaches (Crapo, Gilbert and Badylak, 2011). The presence of residual cellular material in the decellularised tissue ECM may lead to cellular incompatibility issues *in-vitro* and trigger adverse host reactions *in-vivo* (Brown *et al.*, 2009; Manfredi *et al.*, 2009; Nagata, Hanayama and Kawane, 2010; Zhang *et al.*, 2010). Yet, there has been no regulation or criteria

identifying efficient decellularisation methods for both *in-vitro* studies and clinical use (Keane, Swinehart and Badylak, 2015). One study suggested three criteria depending on the quantity (<50ng) of DNA present within 1mg of dry decellularised tissue, the length of DNA segments (<200bp), and the presence of visible stained nuclei within the decellularised tissue (Crapo, Gilbert and Badylak, 2011). However, the vast majority of decellularisation studies in the literature do not follow these criteria. In addition, the same study suggested that these criteria are susceptible for edition or modification with advancement of techniques to enhance the reproducibility, consistency and quality of decellularisation for clinical use (Crapo, Gilbert and Badylak, 2011). In our study, we first used conventional methods to assess the decellularised brain chemical compositions and decellularisation efficiency. In addition, we conducted thorough analytical analysis and semi-quantification of decellularised human brain ECM (dhb-ECM) biochemical components to evaluate the efficiency of the decellularisation process, using Time-of-Flight Secondary Ion Mass Spectrometry (TOF-SIMS). This cutting-edge technique has been widely used to conduct highly-sensitive characterisation analyses of the chemical composition of surfaces, within distinct research areas: in biology (proteins, and lipids in cells and tissues) (Touboul *et al.*, 2004; Fletcher *et al.*, 2008; Passarelli and Winograd, 2011; Kraft and Klitzing, 2014; Bodzon-Kulakowska and Suder, 2016); materials science (McPhail, 2006); pharmaceutical chemistry (Belu *et al.*, 2000; Barnes, Kempson and Prestidge, 2011; Meeus *et al.*, 2012; Meeus, Lenaerts, *et al.*, 2015; Meeus, Scurr, *et al.*, 2015). The TOF-SIMS mechanism of action involves the bombardment of surfaces using ion guns (Ar+, Cs+, Bi3+), within an extremely high-vacuumed chamber. The kinetic energy of these primary ions leads to the release of atoms, electrons, ions, molecular fragments and whole molecules. Only ionized molecular signatures are detected by TOF-SIMS. The resulting secondary ions are accelerated and collected by the analyser part of the TOF-SIMS instrument. The time required for the secondary ions to travel and reach the TOF-SIMS detector is represented by the (*m*/*z*) ratio and results in positive and negative mass spectra based on the original charge of the collected molecular fragment (Brown and Vickerman, 1984; Belu *et al.*, 2000; Barnes, Kempson and Prestidge, 2011; Jesson and Watts, 2012; Lietz, Gemperline and Li, 2013). TOF-SIMS has the capability for high resolution (0.2µm), high sensitivity and extremely low detection limits (Prestidge, Barnes and Skinner, 2007). TOF-SIMS is therefore considered a suitable analytical tool for surface chemical identification and characterisation of dhb-ECM in our study.

4.1.5 Rationale for using dhb-ECM.

Brain ECM is critical for many cellular phenotypes and proper functionality (Crapo, Gilbert and Badylak, 2011). The nature and complexity of the ECM considerably influences cellular processes such as chemotaxis and differentiation (Bornstein and Sage, 2002; Cheng *et al.*, 2009; Stern *et al.*, 2009; Allen *et al.*, 2010; Barkan, Green and Chambers, 2010; Cortiella *et al.*, 2010; Vorotnikova *et al.*, 2010). Several studies have suggested that the decellularised tissue-specific ECM maintains specific function and phenotype of specialised cells (Wicha *et al.*, 1982; Karabekmez, Duymaz and Moran, 2009; Flynn, 2010; Ott *et al.*, 2010; Petersen *et al.*, 2010; Sellaro *et al.*, 2010; Uygun *et al.*, 2010). Although different tissues may have similar protein and polysaccharide ECM components (Bernard *et al.*, 1983), the combinatorial ratios of these components determines its uniqueness to a specific tissue (Lutolf and Hubbell, 2005; Uriel *et al.*, 2009). This has unfortunately been ignored by many studies evaluating different cellular behaviours upon plastic-wares or when using a single ECM protein component. For example, a single matrix protein that is adsorbed onto cell culture surfaces has been shown to modify and even alter cellular behaviour, due to the alteration of the microenvironment (Dequach *et al.*, 2011). In stem cell culture systems, plastics treated with inactivated fibroblasts has been widely used (Ueno *et al.*, 2001; Cooper *et al.*, 2004; Luo *et al.*, 2006; Flaim *et al.*, 2008; Radisic *et al.*, 2008). However, this method has many disadvantages as the fibroblasts need to be cultured for several days in advance to lay (secrete) ECM. In addition, the inactivated fibroblasts can either be removed prior to cell culture using reagents that may substantially alter the chemical composition of the substrate, or they can be left with a high risk of animal product carry over. Likewise, the use of more complex matrices, that have multiple proteins such as collagens, fibronectin, vitronectin, and laminin, can provide combinatorial molecular signals, but this can also result in considerable changes in cellular behaviours and function (Flaim *et al.*, 2008; Brafman *et al.*, 2009). Additionally, they do not recapitulate the *in-vivo* tissue-specific niche as they have different protein to polysaccharide ratios present than what is present in the native microenvironment (Dequach *et al.*, 2011). Matrigel (Kleinman and Martin, 2005) is an appropriate example of this, as its chemical component has yet to be accurately characterised. Also, the known predominant composition in Matrigel laminin has recently been found to promote malignant features of glioma stem-like cells by modulating cellular adhesion, differentiation, proliferation and resistance to chemotherapeutic agents (Yu *et al.*, 2018). Generally, cell-derived matrices (inactivated fibroblasts and Matrigel) can provide better *in-vivo*-

like support. Thus, materials derived from decellularised tissues could be a competitive approach to be used in cell culture.

In our major experiment (see Chapter 6), we aim to reveal the molecular cross-talk between normal human astrocytes and malignant glioma cells derived from the invasive margin GIN of 10 different primary GBMs. We thereby aim to reconstruct a molecular snapshot of the early stages of GBM invasion through normal brain parenchyma post-surgery, which represents the critical region where the glioma recurrence will inevitably occur. To precisely study the impacts of these GIN cells on the astrocytic transcriptome profiles, we had to create an animal-free invasion model (Gliomasphere Matrices; see Chapters 5 and 6) that can recapitulate the normal brain-specific niche with only one malignant element; the presence of GIN cells in the 3D co-culture model. Therefore, the dhb-ECM is a critical element for providing the maximum possible resemblance of the human brain microenvironment for both astrocytes and GIN cells. Matrigel in contrast, can hypothetically favour the malignant environment as it is derived from the Engelbreth-Holm-Swarm (EHS) mouse Sarcoma cell line. Indeed it has been shown to increase the risk of tumour formation (Albini *et al.*, 1992; Yue and Brodie, 1993) . Whereas fibrillar proteins are a character of glioma ECM (Zheng *et al.*, 2004; Hu *et al.*, 2008), Matrigel is known to be enriched with laminin and collagen to form its major components, with laminin recently found to enhance the malignant features of glioma stem-like cells via alteration of cellular adhesions and behaviour (Yu *et al.*, 2018). This could potentially lead to the alteration of the astrocytic transcriptome and be a confounding factor for any precise experiments attempting to elucidate induced gene expression changes upon co-culture with invasive GBM cells. Similarly, fibroblast-derived matrices are known to provide growth factors that maintain stem-properties which may influence the cellular behaviour of astrocytes and/or GIN lines. Based on previous evidence, a single protein can alter the transcriptome of normal astrocytes due to the alteration of the tumour microenvironment (Dequach *et al.*, 2011). Moreover, astrocytes cannot survive on tissue-culture treated polystyrene surfaces. Another advantage of using the dhb-ECM is the biocompatibility with both astrocytes and astrocytoma cells without activating immunogenic reactions triggered by various cellular antigens (Gilbert, Sellaro and Badylak, 2006).

Initially, we successfully decellularised mouse brains to optimise the decellularisation method and conducted thorough analysis of the data generated by TOF-SIMS, to robustly characterise the dhb-ECM components. However, the protocol used for

decellularisation of mouse brains could not be successfully replicated in human brain due to the frail texture of the human brain, as compared to mouse brains which were encapsulated within their meningeal layers. Thus, we modified a previously described protocol for human brain decellularisation and characterised the dhb-ECM to ensure efficient and complete decellularisation, while maintaining physiologically-accurate brain ECM composition. To our knowledge, this is the first thorough characterisation of decelullarised human and mouse brain. Ultimately, the dhb-ECM was dissolved and encapsulated within a bio-inert PEGDA hydrogel to reconstruct the 3D scaffold structure, which facilitates direct cell-cell and cell-matrix contact. The overarching hypothesis for the decellularisation of human and mouse brains states that:

- Decellularised human brain ECM retains essential chemical components of native human (mouse) brain tissue, required for normal cellular function.

4.2 Materials and methods

The workflow of mouse and human brain decellularisation and characterisation has been depicted in **Figure 4. 1**.

4.2.1 Guidelines for mouse brain decellularisation

Mouse brain decellularisation protocol was modified from (DeQuach *et al.*, 2010, 2011) as follows:

1. Metal forceps and beakers (500ml and 100ml) were autoclaved prior to use.
2. Mouse brains were sectioned into small pieces (each hemisphere was cut into two equal pieces) of approximately similar sizes and washed using PBS.
3. The decellularisation solution was prepared by adding 4ml (400mg) of UltraPure SDS, 10% (Invitrogen; Thermofisher Scientific catalogue number 15553027) and 4ml penicillin/streptomycin, to 392ml of PBS.
4. Mouse brain pieces were stirred in the 400ml decellularisation solution.
5. The supernatant containing cellular materials was decanted every 24 h and refilled with fresh 400ml decellularisation solution. The entire process was repeated for 4 days until the yellowish-brown brain tissue became white to transparent.
6. The slurry material was stirred in deionized sterile-filtered water overnight to remove the detergents, followed by final washings with PBS and deionized water.
7. The decellularised materials were then lyophilized at -40°C overnight.
8. The lyophilized mouse brain ECM was finally stored at -80°C until further use (solubilisation step).

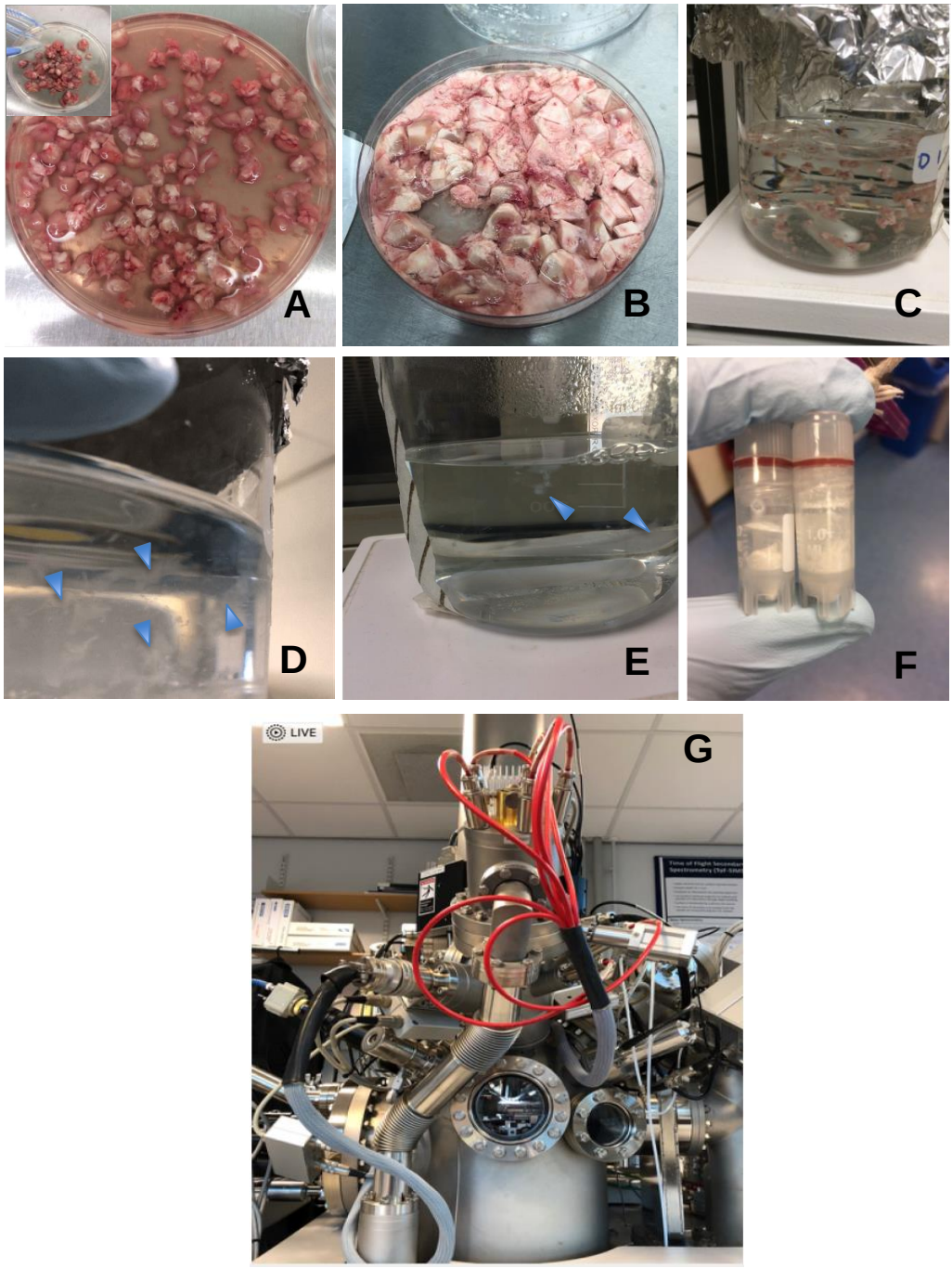


Figure 4. 1. Workflow of the brain decellularisation process. The mouse (A) and human (B) brains were sectioned to obtain approximately equal-sized pieces of tissue. The sectioned specimens were stirred using a sterile beaker (C) until the tissue became transparent (blue arrows), which visually indicated successful decellularisation of human and mouse brain tissue (D-E) respectively. The slurry of decellularised materials were collected and lyophilized (freeze-dried) to produce ECM powder (F) that could be used for surface coating after dissolving in acids. The decellularised and lyophilized human and mouse brains were characterised using different methods, including the highly sensitive TOF-SIMS instrument (G).

4.2.2 Guidelines of human brain tissue decelluarisation

The human brain was obtained from donor autopsy according to Nottingham University Hospitals Trust guidelines (Ethical approval reference: 11/EM/0076) and the protocol for human brain decellularisation was modified from guidelines previously described in (Crapo et al., 2012). The optimisation of the decellularisation process was performed using mouse brain tissue according to the protocol described in (DeQuach et al., 2011). However, the human brain has a frail texture as compared to the mouse brain, which was enclosed within the meninges. We could therefore not replicate the work of the mouse brain decellularisation with the human brain tissue, as the critical vigorous stirring step destroyed the entire tissue and human brain ECM could not be recovered. A modified gentler protocol, that has a shorter stirring time, previously described in (Crapo et al., 2012), was instead used to conduct human brain decellularisation as follows:

1. The brain specimens were completely thawed from -80°C. The dura was removed and samples washed using PBS without calcium or magnesium.
2. Approximately 30g of cadaver human brain was sectioned into pieces (~ 0.5cm x 0.5cm x 0.5cm) while the brain tissue was kept cold.
3. The sectioned brain fragments were stirred in sterile-filtered ultra-pure water at 4°C for 16 hours, at 60 rpm. The water contained penicillin/streptomycin antibiotic (Gibco; catalogue number: 15240062)
4. Tissue fragments were then agitated in 0.025% trypsin/0.05%EDTA (Sigma; 59418C) at 90rpm for 60 minutes. The temperature (37°C) used for this step is critical for enzymatic activity.
5. The enzymatic reagent was replaced by 3% Triton X-100 and brain fragments were stirred at 90rpm for 60 minutes.
6. The brain tissue pieces were then stirred at room temperature at 90rpm in 1M sucrose (Sigma; catalogue number S9378) (15 minutes), water (15 minutes), 4% deoxycholate (Sigma; catalogue number 30970) (60 minutes) and 4% ethanol/0.1% peracetic acid (Darrent chemicals; DC0096) (20 minutes).
7. The slurry material of the decellularised human brain was centrifuged in sterile 50ml polyethylene (HDPE) Beckman coulter tubes, using an Avanti J-25 High Performance centrifuge at 10,000 x *g* for a final series of washes at room temperature using high quality DPBS (Gibco; catalogue number 10010023) (15 minutes), sterile-filtered water (x2 15 minutes) and DPBS again (15 minutes).
8. The decellularised human brain tissue was lyophilized and stored at -80°C until further use.

4.2.3 Dissolving lyophilised human and mouse decellularised brain extra cellular matrix

The lyophilized powder of the decellularised human and mouse brain ECM was solubilised using a enzymatic digestion method previously reported in (Freytes *et al.*, 2008; Singelyn *et al.*, 2009; DeQuach *et al.*, 2010, 2011):

1. Pepsin solution was prepared by dissolving 100mg of porcine pepsin (Sigma; catalogue number: 77151) into100ml of 0.01M HCL and the mixture was then sterile-filtered using Sartorius 0.22 blue filters.
2. Each 20mg of lyophilized human brain ECM was dissolved in 1ml of the pepsin solution (20mg/ml). The mixture was stirred at 100rpm for 48 hours at 38°C.

4.2.4 Characterisation of decellularised brain ECM

Current decellularisation protocols of various tissues, including brain, are unlikely to achieve 100% removal of all cells and cellular components from corresponding ECMs. Furthermore, health-regulatory bodies such as the Human Tissue Authority (HTA) and FDA have no current guidelines (quantitative metric methods) defining optimal decellularisation (Keane, Swinehart and Badylak, 2015). Thus, the definition of effective decellularisation is highly subjective and varies across the literature. However, few methods have been used to characterise decellularised matrices. We utilized a cutting-edge sensitive technique (TOF-SIMS) to conduct robust characterisations of human and mouse brains for the first time, to the best of our knowledge. This was to allow semi-quantitative measurement of various decellularised human and mouse brain components (e.g. non-sulphated GAGs and fibrillar proteins). A colorimetric biochemical testing kit was used to measure the sulphated-GAGs component within decellularised human brain ECM. The efficacy of the decellularisation technique was assessed by semi-quantitating both cellular membrane and nuclear markers using TOF-SIMS. Haematoxylin dye was also used to screen for residual nuclei within the decellularised brain tissues. **S**canning **E**lectron **M**icroscopy (SEM) was used to study the topography of the mouse brain ECM at high resolution. Finally, the functionality of the decellularised human brain ECM were assessed using basic *in-vitro* proliferation assays by culturing GIN cells derived from the invasive margin of primary GBMs on the decellularised matrices.

4.2.4.1 TOF-SIMS characterisation of decellularised mouse and human brain ECMs

The lyophilized materials of the decellularised brain matrices were firstly dissolved according to section (4.2.4) and adsorbed onto sterilized non-tissue culture (TC) treated glass slides. The controls were manufactured standard TC-treated culture wares; TC-treated plates and TC-treated chamber slides (Millicel ® EZ chambers slides (Millipore; PEZGS0816) for mouse and human decellularised brain ECM materials respectively. Three replicates for each treated and control sample were created. The adsorbed materials first air-dried and then gently washed using ultra-pure deionised water (Milli-Q) to remove salts, such as Na^+ and K^+, and finally dried using compressed nitrogen. The treated and control samples on their respective surfaces were mounted onto the TOF-SIMS (ION-TOF GmbH, Münster, Germany) stage using double-sided sticker tape. The analysed surface area for all samples was 3mm X 3mm. We used a protocol previously described in (Canavan *et al.*, 2007; Baki *et al.*, 2017; Dereymaker *et al.*, 2017; White *et al.*, 2017). TOF-SIMS has a liquid bismuth metal gun (Bi_3^+) and an individual platform reflectron analyser. The 25keV Bi_3^+ beam was angulated at 45° to the samples. The current of the primary ion beam was 0.8pA and appropriately kept below 10^{12} per each squared centimetre to maintain the static conditions required by the SIMS segment of the instrument. The positive surface charges produced from the primary ion beam were compensated using an electron-generating flood gun. Each 1µm x 1µm area analysed consisted of 1.28 x 1.28 pixels. The mass/charge range (*m*/*z*) of the positive and negative spectra was 0-800 and collected and analysed by software provided by ION-TOF GmbH. However, the positive ion spectrum, where most of the amino acids and GAGs can be detected, was the main focus in this project (Wagner, Tyler and Castner, 2002). Measured positive secondary ion spectra of all samples were calibrated to total ion intensity using C_2H_4+ (*m*/*z* = 28.03), C_3H_6+ (*m*/*z* = 42.046), C_4H_8+ (*m*/*z* = 56.062), and C_7H_7+ (*m*/*z* = 91.054), to allow semi-quantative compasisions between samples. We used previously described amino acids peaks (Wagner and Castner, 2001; Wagner, Tyler and Castner, 2002; Wagner, Horbett and Castner, 2003; Canavan *et al.*, 2007) to assess the adsorption of the decellularised ECM fibrillar proteins such as collagen, fibronectin and laminin on the culture surfaces. The non-sulphated GAGs, particularly **H**yaluronic **A**cid (HA) of the decellularised ECM, was assessed according to peaks previously characterised in (Shard *et al.*, 1997) as well as predicted ions generated by random bond breaking of the HA compound molecule using ChemDraw professional software 16.0

(https://www.cambridgesoft.com/Ensemble_for_Chemistry/ChemDraw/ChemDrawProfessional/Default.aspx) (Appendix **Figure 8. 1**). The sulphated GAGs were assessed using prediction tools as described above (Appendix **Figure 8. 2**, and **Figure 8. 3**) and via biochemical colorimetric assay (section 4.2.5.2).

4.2.4.2 Blyscan colorimetric assay to assess the sulphated GAGs in the decellularised human brain ECM

Blyscan assay (bio-color life science assays; B1000) was utilized to assess the total sulphated GAGs in the decellularised human brain ECM as follows:

1. GAGs reference standards (1, 2, 3, 4, 5µg) and ultra-pure deionised water (Milli-Q) (0.0 µg) as a blank reagent, were prepared before the start of the experiment. Blank and GAGs standards were adjusted with Milli-Q water to a volume of 100µl.
2. The original stock of decellularised human brain ECM sample with a concentration of 2mg/100µl was diluted 10X and 100µl was used in the following steps.
3. 1ml of Blyscan dye reagent was added to the samples and gently shook for 30 minutes.
4. The samples were centrifuged at 12000 x *g* for 10 minutes and the supernatant was drained according to manufacturer instructions.
5. 0.5ml of Dissociation reagent was added to each sample, vortexed and incubated for 10 minutes at room temperature.
6. After a second centrifugation as above, 100µl was transferred to a 96-well transparent pate to measure absorbance at 656nm. Rat tail collagen was used as a negative control.

4.2.4.3 SEM examination of the decellularised mouse brain ECM

The surface morphology of the matrices was examined using JEOL 6060LV SEM (JEOL, Peabody, MA, USA). The topology of the lyophilized materials of the decellularised brain matrices was directly scanned using JEOL 6060LV. Alternatively, the lyophilized materials were firstly dissolved according to section (4.2.4) and adsorbed onto sterilized non-tissue culture (TC)-treated glass slides. The mounted matrices were then air-dried and coated with gold using a Polaron SC7640 sputter-coater according to standard operating procedures provided by the Nanoscale and Microscale Research Centre at the university of Nottingham. To coat the culture surface with the mouse decellularised brain material, a 6-well culture plate was treated with 20 µg/mL poly-L-ornithine (Sigma; p4957) at 37°C for 2 hours (alternatively it can be incubated at 4°C overnight until further use). The wells were rinsed twice with sterile deionized water to remove unattached poly-L-ornithine as it is toxic to cells. The decellularised mouse brain ECM (methods section 4.3.2) was solubilized, diluted and coated onto the culture-ware at a concentration of 24µg/cm^2.

4.2.4.4 Haematoxylin staining of the decellularised human and mouse brain materials

Haematoxylin staining was conducted according to standard operating procedures in our laboratory. The slurry tissues were fixed, preserved in paraffin, and sectioned. The wax sections (on glass slides) were dehydrated using xylene for 10 minutes, ethanol 100% for 10 minutes, and ethanol 95% for 10 minutes before thorough washes using tap water. The sections were placed in 1% Gills III haematoxylin for 5 minutes, followed by 1% lithium carbonate, 1% acid alcohol, and 1% lithium carbonate briefly. Washes with tap water interrupted these steps before each transition. The sections were then rehydrated using a reverse order of dehydration (ethanol 95%, ethanol 100% for 10 minutes, and xylene for 10 minutes) and mounted.

4.3 Results

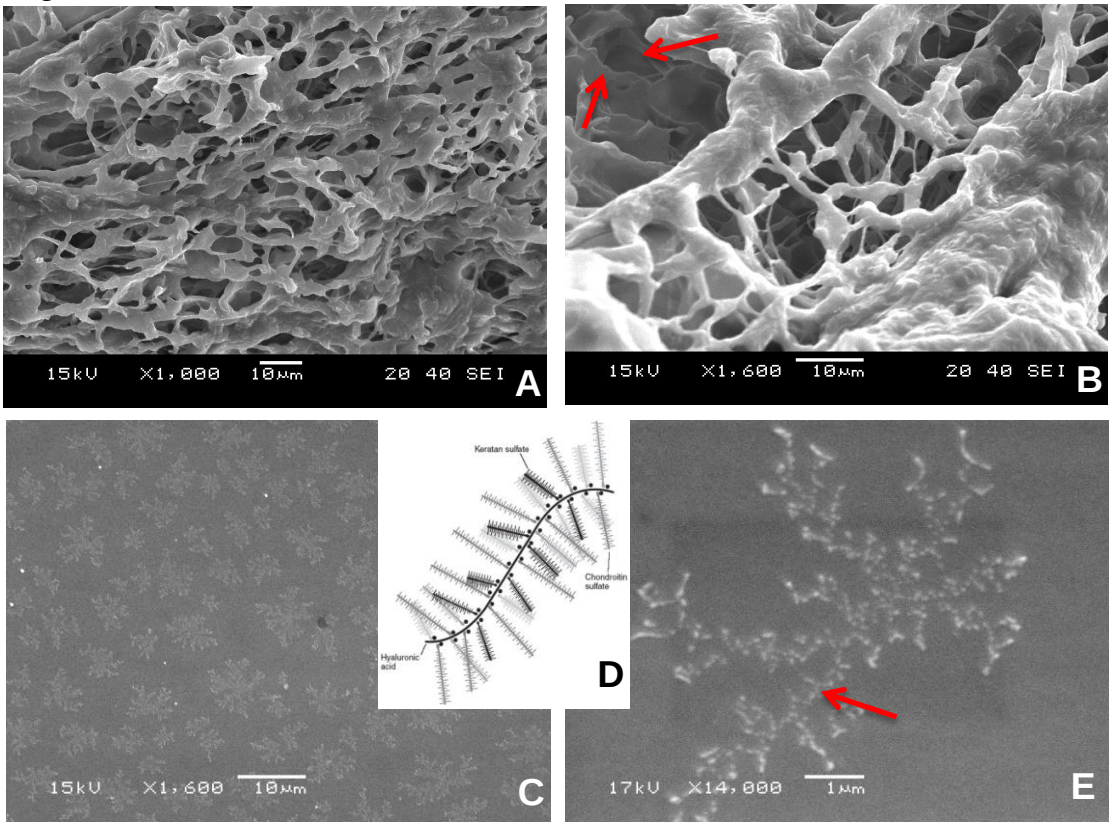
4.3.1 Characterisation of the decellularised mouse brain ECM.

Mouse brain was decellularised according to a protocol previously described in (DeQuach *et al.*, 2010, 2011). Although the decellularisation process was replicated under strict biological conditions, robust characterisation was required to assess the efficiency of the decellularisation, surface morphology, and essential components of the slurry material. The surface topology of the lyophilised mouse brain materials was examined using SEM. Thorough characterisation of the essential brain components was conducted using the highly sensitive TOF-SIMS to identify essential brain components such as proteins and GAGs. Finally, the decellularisation efficinecy was assessed using conventional haematoxylin staining.

4.3.1.1 SEM reveals the ultra-structure of the decellularised mouse brain ECM.

The topological scanning of ultra-structure of the decellularised mouse brain ECM reveals the native highly-porous scaffold, which contains a wide range of pore sizes (most commonly 10μm) and lamellar structures (with a lumen width of 10μm). The pores were formed by the cross-linking of nano- and microfibers (possibly the fibrillar proteins). In addition, it shows the uniform distribution of what is believed to be the adsorbed GAGs on the culture surface **(Figure 4. 2)**.

Figure 4. 2. SEM reveals the ultra-structure of the decellularised mouse brain



ECM. Highly porous structure of the decellularised ECM of mouse brain is shown in (A). The sizes of the pores are variable (A, and B), whereas the average pore size is approximately 10μm. The porous mouse brain ECM shows lamellar structure (B; red-arrowed) with a lumen width of approximately 10μm. The pores were formed by the cross-linking of nano- and microfibers covered with brain ECM materials. The SEM allowed the visualisation of the uniform distribution of the solubilized ECM materials onto the culture-ware (C), in addition to the visualisation of the characteristic feathery-like structure which we believe, based on previously reported evidence (image copy right of Anne Neville, Adrian Morina, Tomasz Liskiewicz, and Yu Yan) (D), to be part of GAGs, particularly lecticans (E). The hyaluronic acid backbone of proteoglycans is red-arrowed (E).

4.3.1.2 Decellularised mouse brain ECM material has all essential components (proteins and non-sulphated GAGs) via thorough characterised using TOF-SIMS

TOF-SIMS was used to confirm the presence of the main components of the decellularised mouse brain ECM including the non-sulfated GAGs (HA), and the fibrillar proteins (Collagen I, Laminin and Fibronectin). The final product of the decellularised mouse brain material was solubilized (section 4.2.3) and adsorbed onto non-TC-treated ordinary sterile glass slides. The control surfaces were manufacturer standard TC-treated glass surfaces designed to grow and image cells (Millicel ® EZ chambers slides). For each sample, four regions of interests (ROI) were selected and the total ion intensity reading was obtained from each ROI to increase the power of statistical significance. The focus of the screening was mainly on the identification of key mouse brain ECM proteins by the recognition of characteristic amino acid ion fragments in the positive TOF-SIMS spectra, as well as the detection of the ions of the non-sulfated GAGs (HA). The unique amino acid fragments of the brain ECM proteins that were previously described in (Wagner and Castner, 2001; Wagner, Tyler and Castner, 2002; Wagner, Horbett and Castner, 2003; Canavan *et al.*, 2007), were found to be significantly higher in the decellularised mouse brain ECM samples as compared to the TC-treated glass surface control, except for two ions; Asparagine (C_4H_4NO_2+) (*p-value* 0.279578), and Cysteine (C_2H_6SNO+) (*p-value* 0.476514) which showed no statistical significance (Table 4. 1) and **(Figure 4. 3A)**. Previous studies categorised the amino acid ionic fragments according to standard reference proteins using principal component analyses (PCA). Based on these studies, the amino acid ions identified in our analyses were categorised according to corresponding proteins of origin (collagen, fibronectin, and laminin) **(Figure 4. 3B-D)**. TOF-SIMS amino acid ions from brain ECM proteins were previously studied by the Wagner and Castner groups (Wagner and Castner, 2001; Wagner, Tyler and Castner, 2002; Wagner, Horbett and Castner, 2003; Canavan *et al.*, 2007); however the ions generated from HA and sulphated GAGs were poorly studied in the literature. Therefore, we utilized ChemDrawprofessional 16.0 software to predict HA ion fragments, generated from the bombardment of the original HA molecule (http://pubchem.ncbi.nlm.nih.gov), which was observed to be significantly higher in the decellularised mouse brain ECM samples, relative to the TC-treated glass surface control (Table 4. 2) and **(Figure 4. 3E)**. One of these ions ($C_{14}H_{22}NO_{12}$), which forms half of the entire HA compound ($C_{33}H_{54}N_2O_{23}$), was also found to be significantly higher (*p-value* <0.0001) in the

decellularised human brain samples as compared to the TC-treated control **(Figure 4. 3F)**.

Table 4. 1. Characteristic amino acid ions that were detected at significantly higher levels in the decellularised mouse brain ECM relative to TC-treated glass slides. Two amino acids were not statistically significant (highlighted in red). *p-value indicates the level of confidence. m/z represents the mass/charge ratio determined by measuring the time required for the secondary ions to reach the TOF-SIMS detector.*

Amino acid	*m/z*	Ion fragment	p-value
Alanine/Cystine	44.0521	C_2H_6N+	<0.000001
Arginine	73.0569	C_2H_7N_3+	<0.000001
Arginine	100.085	C_4H_10N_3+	<0.000001
Arginine	127.0453	C_5H_11N_4+	0.000498
Arginine	43.0201	CH_3N_2+	<0.000001
Arginine/Histidine	110.0804	C_5H_8N_3+	<0.000001
Arginine/Proline/Leucine	70.0669	C_4H_8N+	<0.000001
Asparagine	70.029	C_3H_4NO+	<0.000001
Asparagine	98.0243	C_4H_4NO_2+	0.279578
Asparagine/ Glysine	87.0913	C_3H_7N_2O+	<0.000001
Asparagine/Aspartate	88.0391	C_3H_6NO_2+	<0.000001
Cysteine	76.0247	C_2H_6NS+	0.476514
Glutamate E	102.0444	C_4H_8NO_2+	0.000079
Glutamine	84.0448	C_4H_6NO+	<0.000001
Glycine	30.0342	CH_4N+	<0.000001
Histidine	81.0677	C_4H_5N_2+	<0.000001
Histidine	82.0652	C_4H_6N_2+	<0.000001
L-Serine	60.0524	C_2H_6NO+	<0.000001
L-Serine	71.0103	C_3H_3O_2+	<0.000001
Leucine/ Isoleucine	86.1041	C_5H_12N+	<0.000001
Lysine	84.0843	C_5H_10N+	<0.000001
Methionine	61.0057	C_2H_5S+	0.000808
Phenylalanine	120.0859	C_8H_10N+	<0.000001
Phenylalanine	132.0872	C_9H_8O+	<0.000001
Proline	68.0508	C_4H_6N+	<0.000001
Threonine	74.0596	C_3H_8NO+	<0.000001
Threonine	69.0321	C_4H_5O+	<0.000001
Tryptophan	145.1006	C_10H_11N+	<0.000001
Tryptophan	170.0595	C_11H_8NO+	<0.000001
Tryptophan	130.0632	C_9H_8N+	<0.000001
Tyrosine	107.0426	C_7H_7O+	<0.000001
Tyrosine	136.0776	C_8H_10NO+	<0.000001
Valine	72.0817	C_4H_10N+	<0.000001
Valine	83.051	C_5H_7O+	<0.000001

Table 4. 2. HA ion fragments, predicted using a random fragmentation method via ChemDraw professional 16.0, were detected at significantly higher levels in the decellularised mouse brain ECM relative to TC-treated glass slides. *p-value indicates the level of confidence. m/z represents the mass/charge ratio determined by measuring the time required for the secondary ions to reach the TOF-SIMS detector.*

Ion fragment	*m/z*	p-value
CH_3O+	31.0163	1.81487E-06
C_2H_4N+	42.0386	7.77257E-09
C_2H_4No+	58.0279	8.56556E-07
C_3H_4O+	56.0204	7.63075E-06
C_3H_5No+	71.0386	5.1559E-09
C_3H_8N+	58.0678	2.13233E-07
C_4H_7No_2+	101.0566	1.30553E-08
C_4H_7No_3+	117.0566	1.81597E-08
C_5H_6No_4+	146.0407	1.40029E-07
C_5H_8No_2+	114.0507	4.93072E-09
C_6H_11No_4+	161.0896	2.60776E-07
C_7H_9No_2+	139.0705	3.95177E-08
C_8H_13No_4+	187.1045	5.24302E-08
C_14H_22No_12+	396.1182	0.001699646

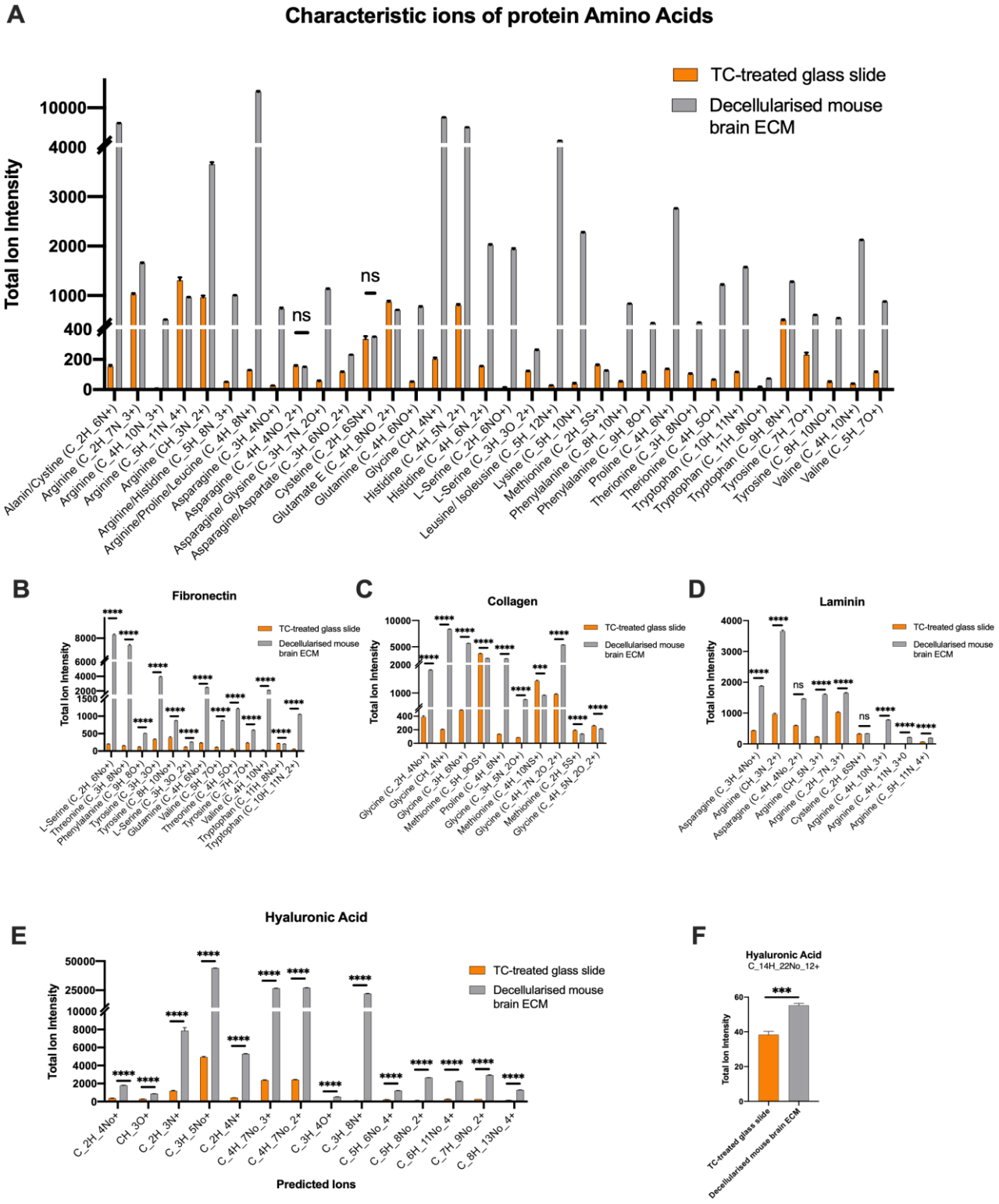

A
Characteristic ions of protein Amino Acids
TC-treated glass slide
Decellularised mouse brain ECM
Total Ion Intensity
ns
B
Fibronectin
C
Collagen
D
Laminin
E
Hyaluronic Acid
Predicted Ions
F
Hyaluronic Acid
C_14H_22No_12+

Figure 4. 3. TOF-SIMS confirms the presence of amino acids, proteins, and non-sulphated GAGs in the decellularised mouse brain ECM. TOF-SIMS showed that characteristic amino acid ions are detected at significantly higher levels in the decellularised mouse brain ECM relative to TC-treated glass slides (A), except for two amino acid ions (Asparagine (C_4H_4NO_2+), and Cysteine (C_2H_6SN+), which showed no statistical significance and indicated with (ns). Previous PCA studies attributed these amino acids to corresponding native fibrillar proteins, which was used here to assess the adsorption of entire proteins such as fibronectin (B), collagen (C), and laminin (D) onto blank slides. All ions are detected at significantly levels in the decellularised mouse brain ECM relative to TC-treated glass slides, unless denoted by (ns). A random fragmentation method was used to predict the secondary ions generated from HA (E) and identified as significantly higher in the decellularised mouse brain ECM. The C_14H_22No_12+ ion, forming half of the HA compound, was similarly found to be significantly higher in the decellularised mouse brain ECM (E), despite its low intensity signal. *Multiple t-test was used to obtain significance. *,**,***,and **** equal to p-value of 0.05, 0.01,0.001, and ≥ 0.0001 respectively*.

4.3.1.3 Mouse brain ECM was efficiently decellularised

The efficiency of mouse brain decellularisation was assessed visually by staining of the slurry of decellularised mouse brain material with haematoxylin, to identify residual nuclei within the decellularised matrix. Generally, the brain tissue appeared to be completely decellularised with no visible nuclei observed by light microscopy examination **(Figure 4. 4)**.

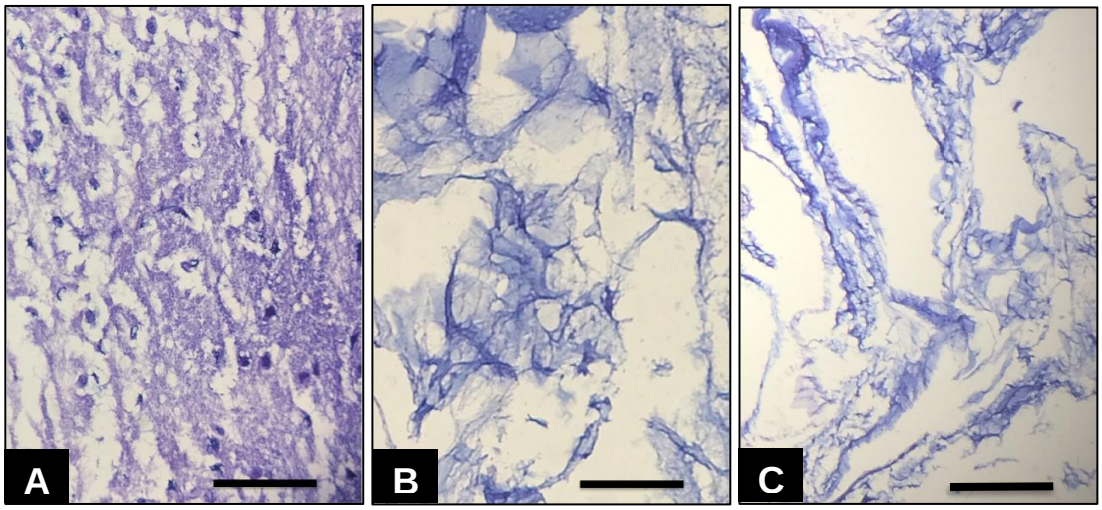


Figure 4. 4. Microscopic examination confirms decellularisation of mouse brain ECM. The mouse brains were partially decellularised after 36 hours (cell nuclei can still be seen; however, they are disproportionally distributed in the section) (A), whereas nuclei were completely absent after 4 days (B, and C).

4.3.2 Characterisation of the dhb-ECM

TOF-SIMS was used to detect the solubilised and adsorbed brain components (protein and GAGs), and to assess decellularisation efficiency of the human brain ECM. The efficiency of decellularisation was also assessed using the standard method of haematoxylin nuclear staining. To ensure that the dhb-ECM contains sulphated-GAGs, we quantified the sulphated-GAGs using a biochemical assay.

4.3.2.1 dhb-ECM is composed of all essential components (proteins, sulphated-GAGs, non-sulphated GAGs)

TOF-SIMS was used to confirm the presence of the main components of the dhb-ECM including non-sulfated GAGs (HA), sulfated GAGs (keratan sulfate and chondroitin sulfate), and the fibrillar proteins (Collagen I, Laminin and Fibronectin). The TOF-SIMS spectra of the dhb-ECM samples were semi-quantatively compared to the spectra obtained from an empty chamber of the TC-treated glass slide control. The final product of the decellularised human brain material was solubilized (section 4.2.3) and adsorbed onto non-TC-treated sterile glass slides. The control surfaces were manufacturer standard TC-treated glass surfaces, designed to grow and image cells (Millicel ® EZ chambers slides). TOF-SIMS semiquantative comparison of the unknown biochemicanl components in the dhb-ECM to a brand standards of TC treated slides (known to grow and support various types of cells) may predicts a successful cell-culture outcome (containing the components required for cells to grow) on the newly developed dhb-ECM which was derived and created by complex methods, if the tested samples has equal or more the biochemical components relative to the TC-treated samples. However, this comparison cannot accurately determine/indicate the proportion of biochemical components to each others in the dhb-ECM (tested samples) as the control sample (TC-treated slide) has a variabl one or more component(s) determined by the manufacture to support cells growth and do not represent the native EMC materials. Comparing experimental samples to a blank glass slide will bias the result toward successful cell-culture outcome. However, this may give more accurate picture of the proportions of different biochemical components of the dhb-ECM. For each sample, four ROI were selected and the total ion intensity reading was obtained from each ROI to increase statistical power. The focus of the screening was mainly on the identification of main human brain ECM proteins by the recognition of their characteristic amino acid ion fragments in the positive TOF-SIMS spectra, as well as the detection of ions of the non-sulfated GAGs (e.g. HA), due to the functional relevance of these molecules for the GBM

invasive phenotype (J. W. E. Chen *et al.*, 2018). The unique amino acid fragments of the brain ECM proteins that were previously characterised in (Wagner and Castner, 2001; Wagner, Tyler and Castner, 2002; Wagner, Horbett and Castner, 2003; Canavan *et al.*, 2007), were observed to be significantly higher in the dhb-ECM samples relative to the TC-treated glass surface control, except one glycine residue (C_3H_5N_2O+) (Table 4. 3) **(Figure 4. 5A)**. Previous studies categorised the amino acid ionic fragments according to corresponding standard reference standard proteins using PCA. Based on these past studies, the amino acid ions identified by our TOF-SIMS analyses were categorised according to the corresponding protein of origin (collagen, fibronectin, and laminin) **(Figure 4. 5B-D)**.

Table 4. 3. The characteristic amino acid ions that were detected at significantly higher levels in dhb-ECM relative to TC-treated glass slides. One amino acid was found to be statistically not significant (highlighted in red). *p-value indicates the level of confidence. m/z represents the mass/charge ratio determined by measuring the time required for the secondary ions to reach the TOF-SIMS detector.*

Amino acid	Ion fragment	*m/z*	p-value
Alanine	C_2H_6N+	44.0494	0.0028
Arginine	CH_3N_2+	43.0173	0.003558
Arginine	C_2H_7N_3+	73.0514	0.001528
Arginine	C_4H_10N_3+	100.0783	0.003824
Arginine	C_4H_7SN+	101.0267	0.004305
Arginine	C_5H_11N_4+	127.0409	0.007459
Arginine	CH_5N_3+	59.0553	0.004395
Asparagine	C_3H_4NO+	70.0257	0.003111
Asparagine	C_4H_4NO_2+	98.0108	0.004441
Asparagine/Aspartic acid	C_3H_6NO_2+	88.0372	0.004336
Asparagine/Glycine	C_3H_7N_2O+	87.0857	0.002539
Cystine	C_2H_6NS+	76.0209	0.004508
Glutamic acid GluQ	C_4H_8NO_2+	102.0395	0.003188
Glutamine Gluq, Glutamic acid Glu E	C_4H_6NO+	84.0411	0.003814
Glycine	CH_4N+	30.0349	0.003161
Glycine	C_2H_4NO+	58.0651	0.00468
Glycine	C_3H_5N_2O+	85.0196	0.297382
Histidine	C_4H_5N_2+	81.0665	0.003413
Histidine	C_4H_6N_2+	82.0634	0.003737
Histidine	C_6H_5N_2O+	121.0154	0.010001
Histidine, Arginine	C_5H_8N_3+	110.0739	0.004439
Isoleucine, leucine	C_5H_12N+	86.0987	0.00272
L-Serine	C_2H_6NO+	60.0491	0.003557
L-Serine	C_3H_3O_2+	71.0127	0.019078
Lysine	C_5H_10N+	84.0798	0.003669
Lysine	C_3H_7N+	57.0705	0.004055
Methionine	C_5H_9OS+	117.0162	0.041941
Methionine	C_4H_10NS+	104.0499	0.003169
Methionine	C_2H_5S+	61.0252	0.0052
Phenylalanine	C_8H_10N+	120.0769	0.002348
Phenylalanine	C_9H_8O+	132.08	0.003161
Proline	C_4H_6N+	68.0528	0.004622
Proline/Leucine/Arginine	C_4H_8N+	70.065	0.00369
Threonine	C_4H_5O+	69.029	0.002404
Threonine	C_3H_8NO+	74.0552	0.002682
Tryptophan	C_9H_8N+	130.0477	0.005042
Tryptophan	C_11H_8NO+	170.0565	0.003076
Tryptophan	C_10H_11N_2+	159.084	0.004163

Tyrosine	C_7H_7O+	107.0378	0.003286
Tyrosine	C_8H_10NO+	136.0711	0.002821
Tyrosine	C_3H_3O+	55.0175	0.003129
Valine	C_4H_10N+	72.0764	0.002621
Valine	C_5H_7O+	83.045	0.002949

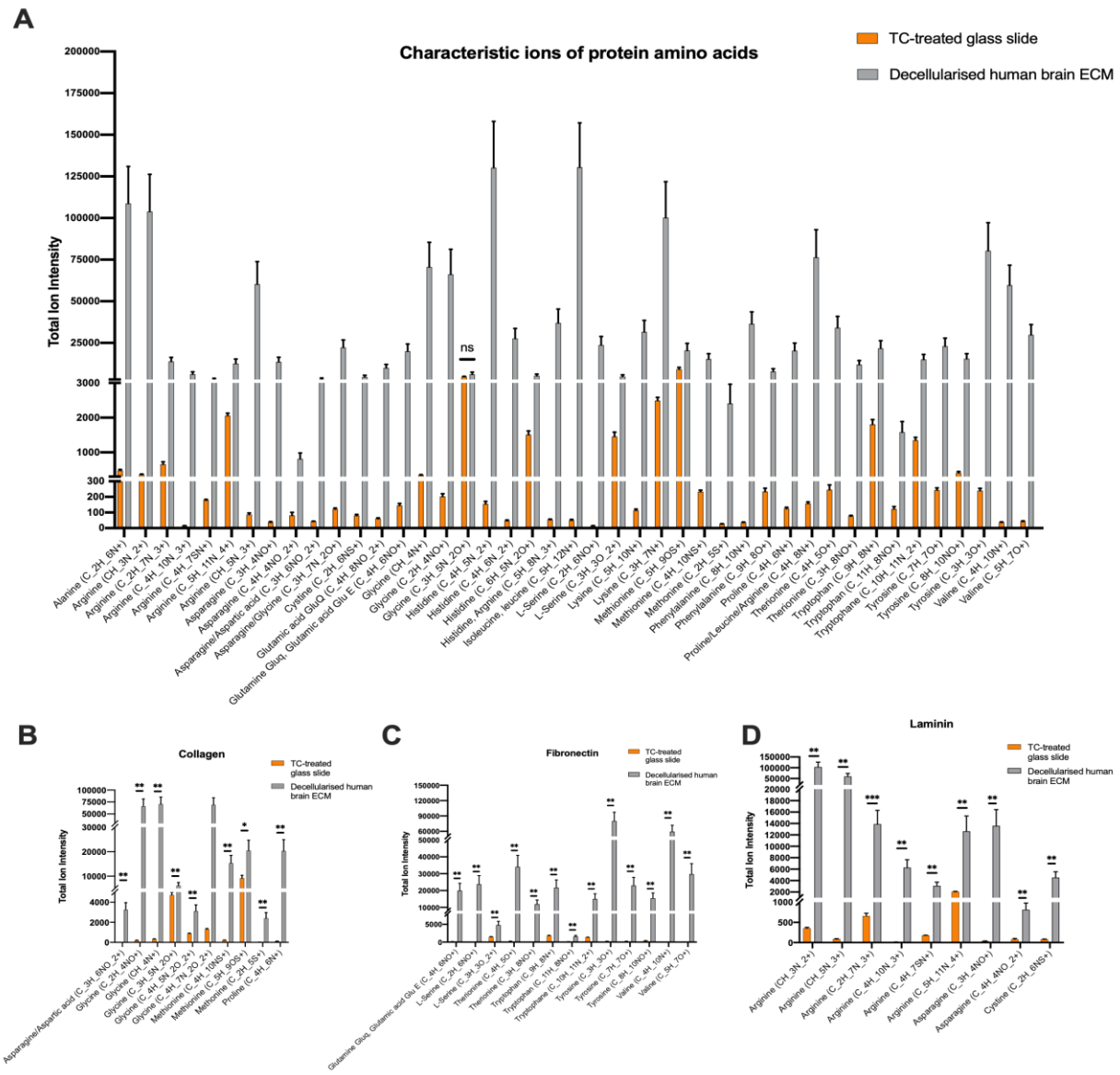


Figure 4. 5. TOF-SIMS confirms the presence of amino acids and proteins in the dhb-ECM. TOF-SIMS showed that characteristic amino acid ions are detected at significantly higher levels in the dhb-ECM relative to TC-treated glass slides (A), except for one amino acid ion (Glycine (C_3H_5N_2O+)), which showed no statistical significance and is indicated with (ns). Previous studies reported PCA to attribute these amino acids to corresponding native fibrillar proteins, which was used here to assess the adsorption of entire proteins such as collagen (B), fibronectin (C) and laminin (D) onto blank slides. *Multiple t-test was used to obtain significance. *,**,***,and **** equal to p-value of 0.05, 0.01,0.001, and ≥ 0.0001 respectively*.

TOF-SIMS ions for amino acids of brain ECM proteins were robustly studied by the Wagner and Castner groups (Wagner and Castner, 2001; Wagner, Tyler and Castner, 2002; Wagner, Horbett and Castner, 2003; Canavan *et al.*, 2007); however the ions of HA and sulfated GAGs were poorly studied. Therefore, we utilized ChemDraw Professional 16.0 software to predict HA ion fragments, generated from the bombardment of the original HA molecule (http://pubchem.ncbi.nlm.nih.gov), which were also found to be significantly higher relative to controls (Table 4. 4) and **(Figure 4. 6A)**. One of these ions, ($C_{14}H_{22}NO_{12}$), which forms half of the entire HA compound ($C_{33}H_{54}N_2O_{23}$), was also found to be significantly higher (*p-value* <0.0001) in the decellularised human brain samples as compared to TC-treated control **(Figure 4. 6B)**. Similarly, the total ion intensity of HA sodium salt molecule (Poly(β-glucuronic acid-[1→3]-β-N-acetylglucosamine-[1→4]), alternating; also referred to as $C_{14}H_{21}NaNO_{11}$), which is present natively *in-vivo* and has been used commercially for different cell-ECM applications such as (Sigma; catalogue number H7630), was also found to be significantly higher (*p-value* 0.0388) in the decellularised human brain samples relative to TC-treated control **(Figure 4. 6C)**. To our knowledge, only one previous study has described HA TOF-SIMS ions (Shard *et al.*, 1997). These HA ions previously described in Shard *et al.* were also significantly higher in the dhb-ECM samples relative to TC-treated surface controls (Table 4. 4) and **(Figure 4. 6D)**. The sulfated-GAGs (chondroitin sulfate and keratan sulfate) ions were predicted by the random fragmentation process using ChemDraw Professional 16.0 software. Six and four predicted ions were generated form the random fragmentation of keratan sulfate and chondroitin sulfate respectively. These ions were also found to be significantly higher in the dhb-ECM samples relative to TC-treated surface controls (Table 4. 5) and **(Figure 4. 6E, and F)**. Further confirmation of the preservation of sulfated GAGs within the dhb-ECM was conducted using biochemical testing (section 4.3.5).

Table 4. 4. HA ions that were significantly higher in the dhb-ECM relative to TC-treated glass slides. *p-value indicates the level of confidence. m/z represents the mass/charge ratio determined by measuring the time required for the secondary ions to reach the TOF-SIMS detector.*

Predicted HA ions	*m/z*	p-value
C_2H_4No+	58.0283	0.00001
CH_3O+	31.0168	<0.000001
C_3H_5No+	71.0379	<0.000001
C_2H_4N+	42.0359	<0.000001
C_4H_7No_2+	117.0555	<0.000001
C_4H_7No_3+	117.0555	<0.000001
C_3H_4O+	56.0508	<0.000001
C_3H_8N+	58.0647	<0.000001
C_5H_6No_4+	146.0491	<0.000001
C_5H_8No_2+	114.0596	<0.000001
C_6H_11No_4+	161.0754	<0.000001
C_7H_9No_2+	139.0666	0.000001
C_8H_13No_4+	187.0987	0.000003
C_14H_21NaNO_11+	402.2768	0.048723168
C_14H_22No_12+	396.11	<0.0001
HA ions (Reported by Shards et al 1997)	m/z	p-value
C_2H_3+	27.0184	0.008489
C_2H_5+	29.0347	0.00533
CH_2OH+	31.0174	0.004446
CHO+	29.0347	0.00533
CH_3CO+	43.0123	0.003584
C_7H_7+	91.039	0.003929

Table 4. 5. Sulfated-GAG ions that were significantly higher in the dhb-ECM relative to TC-treated glass slides. *p-value indicates the level of confidence. m/z represents the mass/charge ratio determined by measuring the time required for the secondary ions to reach the TOF-SIMS detector.*

Keratan sulfate predicted ions	m/z	p-values
CH_3O_4S+	111.0696	0.003395
C_3H_6O_6S+	170.0592	0.004509
C_8H_13NO_8S+	282.2415	0.007175
C_8H_13NO_7S+	264.2499	0.005746
C_6H_11O_9S+	257.1744	0.008199
C_5H_8O_4+	132.0713	0.002802
Chondroitin sulfate predicted ions	m/z	p-values
C_6H_9O_6+	178.035	0.004051
C_7H_12NO_9S+	287.1173	0.021533
C_7H_12NO_8S+	273.1849	0.012539
C_6H_9O_9+	225.0851	0.030863

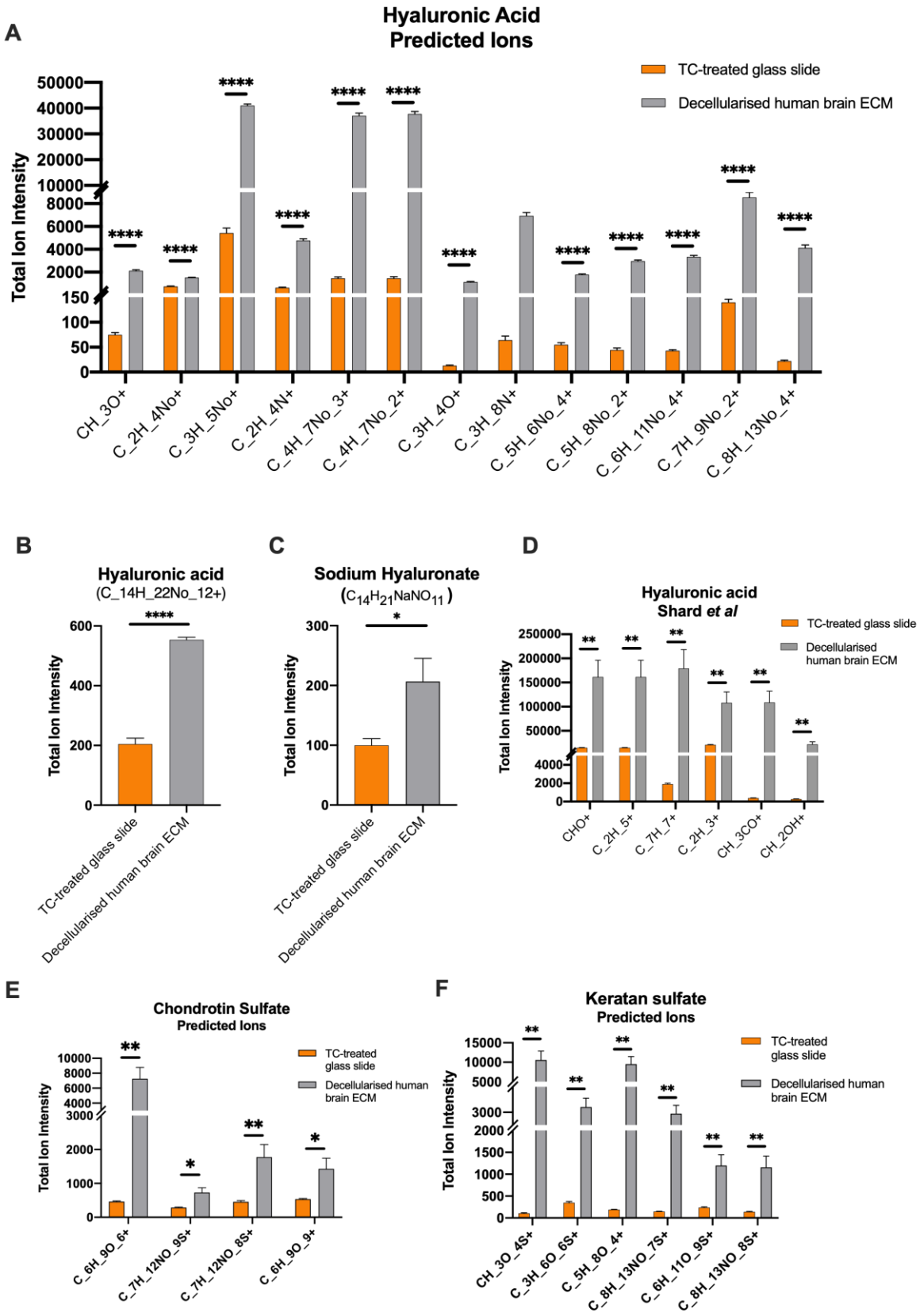

A
Hyaluronic Acid
Predicted Ions
TC-treated glass slide
Decellularised human brain ECM
Total Ion Intensity
CH_3O+
C_2H_4No+
C_3H_5No+
C_2H_4N+
C_4H_7No_3+
C_4H_7No_2+
C_3H_4O+
C_3H_8N+
C_5H_6No_4+
C_5H_8No_2+
C_6H_11No_4+
C_7H_9No_2+
C_8H_13No_4+
B
Hyaluronic acid
(C_14H_22No_12+)
C
Sodium Hyaluronate
(C14H21NaNO11)
D
Hyaluronic acid
Shard et al
CHO+
C_2H_5+
C_7H_7+
C_2H_3+
CH_3CO+
CH_2OH+
E
Chondrotin Sulfate
Predicted Ions
C_6H_9O_6+
C_7H_12NO_9S+
C_7H_12NO_8S+
C_6H_9O_9+
F
Keratan sulfate
Predicted Ions
CH_3O_4S+
C_3H_6O_6S+
C_5H_8O_4+
C_8H_13NO_7S+
C_6H_11O_9S+
C_8H_13NO_8S+

Figure 4. 6. TOF-SIMS confirms the presence of non-sulfated-GAGs (HA) and sulfated-GAGs in the dhb-ECM. We used random a fragmentation method to predict the secondary ions generated from HA (A), which were found to be significantly higher in the dhb-ECM relative to TC-treated glass controls. Despite its low intensity signal, the large ion (C_14H_22No_12+) forming half of the HA compound and the sodium hyaluronate ion (C_14H_21NaNo_11+), were found to be significantly higher in the dhb-ECM relative to TC-treated glass slides (B-C). Likewise, HA ions previously described by Shards and colleagues were significantly higher in dhb-ECM relative to TC-treated glass controls (D). The predicted ions of keratan sulfate and chondroitin sulfate, which forms the major component of sulfated-GAGs, were found to be to be significantly higher in the dhb-ECM relative to TC-treated glass controls. (E-F). *Multiple t-test was used to obtain significance and results were validated by Two-Way ANOVA (Sidak's multiple comparison tests). *,**,***,and **** equal to p-value of 0.05, 0.01,0.001, and ≥ 0.0001 respectively*.

4.3.2.2 Human brain tissue was efficiently decellularised

The efficiency of human brain decellularisation was assessed visually by staining the slurry of decellularised human brain tissue with haematoxylin to identify residual nuclei within the decellularised matrix **(Figure 4. 7A and B)**. Generally, the brain tissue seemed to be completely decellularised with no visible nuclei observable by light microscopy examination. Although haematoxylin staining is considered to be the conventional method for visual assessment of decellularisation, TOF-SIMS has high sensitivity in detecting cell membrane and nuclear remnants within the solubilised and adsorbed dhb-ECM **(Figure 4. 7C and D)**. The total ion intensities of cell membrane lipid components (choline, phosphocholine and glycerophosphocholine) (Table 4. 6), which were previously described in (Ostrowski *et al.*, 2005; White *et al.*, 2017), were found to be significantly lower in the dhb-ECM relative to TC-treated surface controls **(Figure 4. 7C)**. However, phosphates (PO^-_2, and PO^-_3) which were identified as nuclear TOF-SIMS markers in (Hashimoto *et al.*, 2004; Sakata, Kamahori and Miyahara, 2004; Samuel and Castner, 2004; White *et al.*, 2017) (Table 4. 6), were found to be significantly higher in the dhb-ECM relative to TC-treated surface controls (*p-values* <0.0001 for both) **(Figure 4. 7D)**.

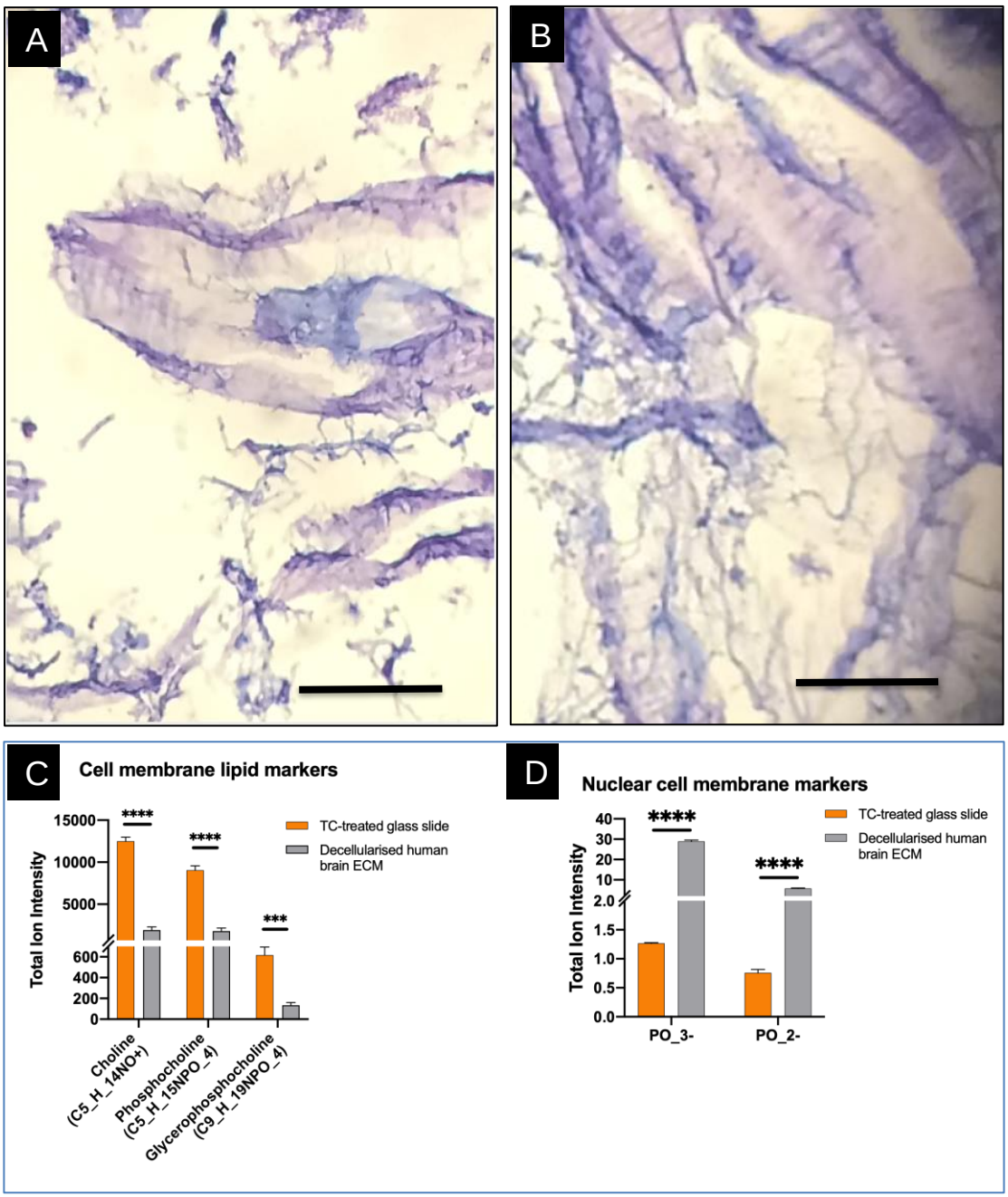


Figure 4. 7. Human brain ECM was efficiently decellularised. The ECM was confirmed to be efficiently decellularised using a conventional method of screening for haematoxylin-stained nuclei using light microscopy (A-B). TOF-SIMS demonstrated that cell membrane lipid markers (choline, phosphocholine and glycerophosphocholine) were significantly lower in the dhb-ECM relative to TC-treated glass slides (C). In contrast, phosphates (PO^-_2, and PO^-_3) were found to be significantly higher in the dhb-ECM relative to TC-treated surface controls (D). *Multiple t-test was used to obtain significance and results were validated by Two-Way ANOVA (Sidak's multiple comparison tests). *,**,***,and **** equal to p-value of 0.05, 0.01,0.001, and ≥ 0.0001 respectively*.

Table 4. 6. Cell membrane lipid and nuclear TOF-SIMS markers were detected in the dhb-ECM at lower and higher levels relative to TC-treated glass slides respectively. *P-value indicates the level of confidence. m/z represents the time required for the secondary ions to reach the TOF-SIMS detector.*

Cell membrane ions	*m/z*	p-values
Choline (C5_H_14NO+)	103.9847	0.000002
Phosphocholine (C5_H_15NPO_4)	184.9568	0.000026
Glycerophosphocholine (C9_H_19NPO_4)	234.836	0.001086
Nuclear ions	*m/z*	p-values
PO_2-	62.9654	<0.000001
PO_3-	78.9644	<0.000001

4.3.2.3 Decellularised human brain ECM material revealed sulfated GAGs using a Blyscan colorimetric assay

The absorbances of the reference standards were measured at 656nm. The absorbances were plotted against concentrations to obtain the standard curve to determine the concentration of the total sulfated GAGs (chondroitin sulfates, keratan sulfates, dermatan sulfates and heparin sulfates), present in the dhb-ECM (Appendix **Figure 8. 4**). The sulfated GAGs were measured as 42.75µg ±6.76µg in 1mg dry weight of dhb-ECM and the presence of sulfated GAGs confirmed by a Blyscan colorimetric assay **(Figure 4. 8)**.

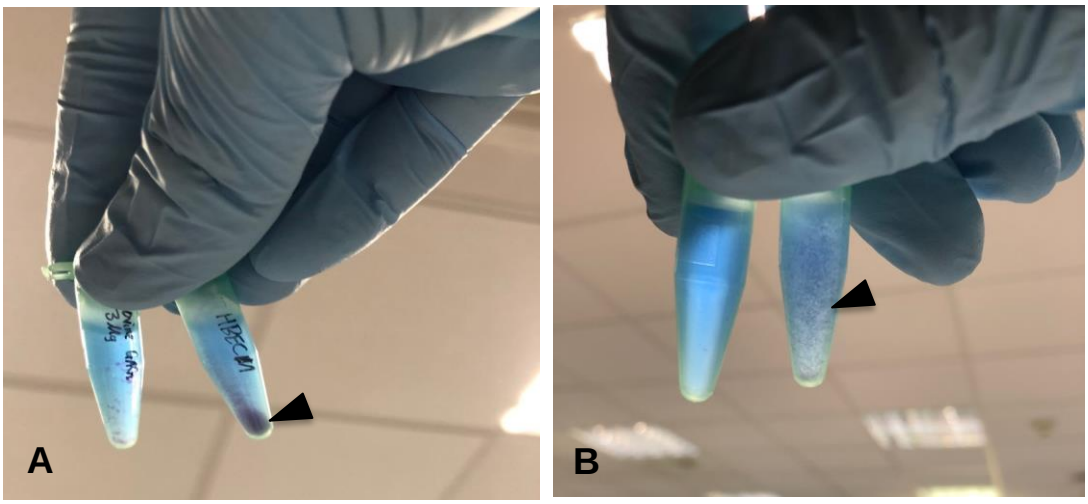


Figure 4. 8. Blyscan assay confirms the presence of sulfated GAGs in the dhb-ECM. Blyscan colorimetric assay revealed the amounts of sulfated-GAGs in 2mg (A; black arrow) dhb-ECM relative to 3µg bovine sulfated-GAGs control. The amounts of sulphated-GAGs in 0.2mg dhb-ECM relative to rat-tail collagen control (B; black arrow).

4.4 Discussion

Brain-specific ECM is critical for neural phenotypes and functionality (Crapo, Gilbert and Badylak, 2011). Previous evidence showed that the nature and complexity of the ECM chemical composition is required for different cellular behaviours. Although various tissue ECMs contains similar compositions (Bernard *et al.*, 1983), tissue-specific ECM recapitulates the native biological microenvironment required for preserving phenotype and function of specialised cells within a particular niche (Wicha *et al.*, 1982; Karabekmez, Duymaz and Moran, 2009; Flynn, 2010; Ott *et al.*, 2010; Petersen *et al.*, 2010; Sellaro *et al.*, 2010; Uygun *et al.*, 2010). Studies have reported that currently available surface coatings involve either single purified proteins or poorly-characterised highly complex sarcomata materials. However, these mimetics cannot accurately recapitulate the native physiological brain niche. Many decellularised matrices have been approved by the FDA and successfully translated for clinical purposes. Thus, decellularisation of human brain ECM can provide a more physiologically-relevant alternative to current surface coating methods.

In our study, we conducted a thorough characterisation of surface chemical compositions of human and mouse brain decellularised ECM, using the highly sensitive TOF-SIMS instrument. Previous studies by others have typically utilised immunofluorescent-staining immediately after the decellularisation step, to assess ECM protein composition. However, the freeze-dried decellularised matrices need to be solubilised prior to adsorbing them onto culture surfaces and this involves acids which can cause damage to the brain ECM. Whereas the solubilisation process can adversely affect the integrity of the ECM chemical composition, we have conducted thorough characterisation steps using TOF-SIMS and other methods to overcome this. A TOF-SIMS-based analytical approach permitted assessment of completely solubilised ECM materials adsorbed onto the culture surfaces, to accurately determine the chemical compositions of human and mouse brain ECM. Furthermore, we compared the adsorbed decellularised ECM samples to slides that represented manufacture standards used for growing and imaging cells.

The characteristic amino acids fragments were previously well studied using reference standards by leading TOF-SIMS laboratories (Wagner and Castner, 2001; Wagner, Tyler and Castner, 2002; Wagner, Horbett and Castner, 2003; Canavan *et al.*, 2007). To the best of our knowledge, we have conducted the first thorough TOF-SIMS characterisation of decellularised human and mouse brain ECM components. We revealed that almost all known ECM components including various fibrillar

proteins, sulfated GAGs, and non-sulfated GAGs (HA) were adsorbed onto blank culture surfaces. Furthermore, the quantity of the chemical compositions (i.e. ion intensities) of the decellularised human and mouse brain matrices that were adsorbed onto non-treated blank slides, were remarkably higher relative to manufacturer-standard tissue culture treatment. Specifically, we semi-quantified ion intensities of previously described characteristic amino acids fragments as well as predicted GAGs ions, using TOF-SIMS, in the decellularised brain ECM (adsorbed onto blank slides) samples relative to TC-treated slide surfaces (Millicel ® EZ chambers slides; Millipore; PEZGS0816). We additionally utilized random fragmentation methods to identify characteristic TOF-SIMS ions of HA and sulfated GAGs, which bridges a scientific gap in the literature, which currently lacks characteristic TOF-SIMS ion fragment data for these important brain ECM components.

Although the efficiency of decellularisation was confirmed using conventional microscopy to screen for stained residual nuclei within the decellularised matrices, nuclear residual phosphates (PO^-_2, and PO^-_3) were detected by TOF-SIMS. However, identifying these markers was perhaps inevitable, as an absolute decellularisation process with 100% efficiency is yet to be achieved, even with clinically translated matrices (Crapo, Gilbert and Badylak, 2011). The decellularised human brain matrix ultra-structure was not shown in our study, as the ultra-high centrifugations steps required at the final stages of the optimised decellularisation protocol to collect the ECM, in addition to salt deposition caused by DPBS washes, collectively distorted the SEM images. In contrast to decellularised human brain matrix, studying the ultra-structure of mouse brain using SEM revealed important features concerning the porosity and size of interconnected pores, in addition to wafer-like structures which need to be taken into consideration when designing 3D culture matrices, such as the novel 3D matrix we generated and described (see Chapter 5). The distribution of the mouse ECM lecticans were shown to be successfully adsorbed onto the culture surfaces in a uniform pattern, and future work with this method could be valuable.

In summary, we have generated well-characterised human and mouse decellularised brain ECMs, which exhibit essential chemical components of native human brain tissue, known to be required for normal cellular behaviours.

Chapter (5)

Generating Gliomasphere Matrices

Chapter 5 Generating Gliomasphere Matrices

5.1 Introduction

5.1.1 Current vision on models used to study GBM and microenvironmental communication

Although many models have recently been developed to study the interaction of GBM cells with surrounding non-cancerous cell types, the lack of appropriate representation of the glioma microenvironment is yet to be addressed (Broekman *et al.*, 2018). One method of *in-vitro* model development is to isolate cells from GBM resected tissue and propagating them as neurospheres in serum-free medium to retain genetic heterogeneity and tumour initiating capabilities when implanted orthotopically in immune-compromised mice (Kim, Pirollo and Chang, 2015; Hubert *et al.*, 2016). Other studies have used embryonic and glioma stem cells to "retro-engineer" patient-specific GBM (Linkous *et al.*, 2019), which can be implanted in immune-compromised patient-derived xenograft mouse models (William *et al.*, 2017; Xu *et al.*, 2018). Similarly, micro-dissected GBM samples were recently grown and expanded to generate bio-banks for derived cerebral (tumour) organoids (Jacob *et al.*, 2020). The use of syngeneic mouse models, in which tumours can be induced using chemicals or viruses to generate cell lines that can be re-implanted back into mouse brains, permits immune therapies to be evaluated as these models are immune-competent (Oh *et al.*, 2014). The induction of spontaneous brain tumours *de novo*, can be achieved using well characterised driver mutations in engineered GBM models (Hambardzumyan *et al.*, 2011). Despite these remarkable efforts to recapitulate GBM tumour microenvironments, physiologically-accurate representation of the *in-vivo* malignant niche, remains a challenging unmet scientific need due to several reasons (Broekman *et al.*, 2018). For example, the genetic engineering of GBM mouse models results in only a few driver mutations and displays limited antigens, which are the current focus of several developing immunotherapies (Broekman *et al.*, 2018). Furthermore, neurosphere culture systems and patient-derived xenografts are vulnerable to genetic instability (Ben-David *et al.*, 2017) which can be caused by the extensive passaging of glioma cell lines (Bigner, Mark and Bigner, 1987), which may consequently express artefactual immune profiles (Beutler *et al.*, 1999). Furthermore, patient derived cell lines typically exhibit a low degree of invasiveness into adjacent parenchyma (Broekman *et al.*, 2018) and may harbour altered genomic methylation and transcriptome profiles (Baysan *et al.*, 2014). Thus, the lack of an ideal model(s) to study GBM cell molecular communications with the

surrounding cells within the tumour microenvironment requires further exploration. Indeed, this is the reason RNA sequencing results from our tumour co-culture modelling were extensively validated against high-depth read RNA sequencing data obtained from surgically resected patient samples (see Chapter 6).

Understanding the molecular cross-talk at the tumour periphery between glioma cells and adjacent neural tissue, is of high clinical relevance, as residual tumour cells within the infiltrative tumour margins that are inevitably left post-operatively, are responsible for the re-growth of the recurrent tumour, whereas the bulk tumour mass is usually excised surgically. This renders the GBM invasive margin/brain parenchyma interface of clinical interest to identify genetic targets and for designing/repurposing therapies to impair GBM recurrence.

One of the main aims of our experiment is to study the reprogramming events imposed on the co-cultured astrocytes by GBM cells at the infiltrative margin, where GBM recurrence is hypothesised to occur. To accomplish this in an accurate manner, we hypothesised that sophisticated co-culture methods could be a valuable approach to assess the cross-talk between the astrocytes and GIN cells, derived from primary tumours after debulking surgery at Queen's Medical Centre, Nottingham. Furthermore, the entire co-culture microenvironment should be hypothetically normal or the closest possible state to the *in-vivo* native brain niche, except for the presence of the invasive GBM cells. With the rationale of having no known distinctive astrocytic molecular markers from GBM cells which can effectively discriminate tumour from healthy astrocytes, we utilised CRISPR/Cas9 gene editing technology to genetically label NSC to obtain YFP-astrocytes upon differentiation (see Chapter 3), which can be re-isolated from the co-culture with GIN cells by FACS (see Chapter 6). These YFP-astrocytes were co-cultured with each of ten different GIN lines. These GIN cells were also selected to be chemo- and radio-naïve cells, and to have a low passage number ranging from 4-6 passages, to hypothetically preserve the original malignant genetic and epigenetic marks. In addition, GIN cell lines were chosen as those having no 1p/19q co-deletion and which retain wild type IDH, and ATRX expression. This ensures that despite well-documented inter-patient heterogeneity manifest in GBM, the 10 cell lines chosen are relatively homogeneous with regards to genetic background, thereby effectively offering ten independent repeats to assess induced changes within the YFP-astrocytic cell line upon co-culture. These ten GIN lines have the classical genetic signatures presented in primary grade IV astrocytoma patients, which we aim to investigate. However, this will limit the scope

of the study to a certain GBM category and future studies incorporating other cell lines with different genetic signatures will be required to investigate the intercellular communication in other GBM categories such as the secondary GBM or grade IV oligodendroglioma. Complete selection criteria are described in (Appendix Table 8. 1). In the co-culture invasion model, the cellular components (astrocytes and GIN cells) were allowed to communicate and held within a 3D cultured native brain niche, which was recapitulated using decellularised human brain material (from an ethically approved autopsy donor) and reconstructed within a defined, bio-inert material, called PEGDA hydrogel (see Chapter 4). We herein refer to this novel multi-component co-culture model as “Gliomasphere Matrix”. Although Gliomasphere Matrices can potentially provide an original approach to study intercellular molecular communication, some of the technical challenges and scientific rationales must be highlighted.

5.1.2 Chronological development of 3D GBM modelling

Many studies have described the isolation GSC from primary GBM tumours (Ignatova *et al.*, 2002; Hemmati *et al.*, 2003; Galli *et al.*, 2004; Sheila K. Singh *et al.*, 2004; Tunici *et al.*, 2004; Yuan *et al.*, 2004; Fael Al-Mayhani *et al.*, 2009; Pollard *et al.*, 2009; Vukicevic *et al.*, 2010). Furthermore, GSC are propagated in NSC culture conditions, which reflects the relationship and similarities between these cell-type (Conti *et al.*, 2005; Pollard *et al.*, 2006, 2009), and can be cultured in 2D and 3D culture conditions as neurospheres that represent the earliest forms of 3D GBM models (Galli *et al.*, 2004; Azari *et al.*, 2011). However, these models contain necrotic cores when 3D spheroids reach ~300μm in diameter, and the cells within the central regions of these 3D models can lose the interaction with the ECM component, which renders them different from *in-vivo* GSC (Reynolds and Weiss, 1992; Svendsen *et al.*, 1998; Reynolds and Rietze, 2005). In 2016, minced GBM samples were embedded in Matrigel and allowed to grow to 3-4mm in diameter within 2 months to form GBM organoids, which can be further propagated in culture for over a year (Hubert *et al.*, 2016). These 3D organoids recapitulated the stem-associated hypoxic gradient found in GBM tumours. The cells at the organoids’ peripheral region expressed SOX2, whereas this stem marker was less abundant in the core regions. In addition, cells isolated from distinct organoids regions showed different molecular markers and exhibited distinct cellular behaviour, suggesting the influence of different microenvironmental cues. In 2018-2019, GBM 3D modelling has

been revolutionised and several elegant studies have utilized CRISPR/Cas9 technology to develop genetically-engineered organoids attempting to model GBM tumours. In one study, well-characterised GBM oncogenic drivers were tagged with green fluorescent protein and overexpressed in embryonic stem cells (ESC) at the initial stages of neuroectodermal differentiation, to screen for tumour-inducing/promoting genetic aberrations in the generated 'neoplastic Cerebral Organoids', abbreviated as neoCOR". This has led to the identification of four genetic mutations (MYC^{OE}, $CDKN2A^{-/-}/CDKN2B^{-/-}/EGFR^{OE}/EGFRvIII^{OE}$, $NF1^{-/-}/PTEN^{-/-}/p53^{-/-}$ and $EGFRvIII/PTEN^{-/-}/CDKN2A^{-/-}$) which confers a proliferative advantage and results in tumorigenesis, producing GBM-like or Central Nervous System-Primitive NeuroEctodermal Tumour (CNS-PNET) (Bian *et al.*, 2018). Furthermore, RNA sequencing showed that MYC expression led to the creation of a CNS-PNET tumour phenotype, whereas other genetic aberrations resulted in GBM-like tumour identity, suggesting that distinct genetic mutations can lead to various tumour phenotypes (Bian *et al.*, 2018).

Two further studies have sought to model GBM invasion via the isolation of GSC from patient specimens and propagating them in 2D monolayers to be genetically labelled with reporter genes to facilitate GSC tracing when allowed to co-culture/invade through ESC-derived neuroectodermal cerebral organoids (Ogawa *et al.*, 2018; Linkous *et al.*, 2019), also obtained by a similar method described in (Bian *et al.*, 2018). Many 3D GBM modelling studies highlighted the importance of incorporating multi-cellular lineages within synthetic biomaterials (with porcine-derived ECM) to form 3D bio-printed GBM-on-a-chip (Yi *et al.*, 2019). Many other similar studies were reviewed in (Robertson *et al.*, 2019; Wolf *et al.*, 2019). Recently in 2020, a novel protocol has been developed to rapidly (within 1-2 weeks) obtain GBM organoids; termed as GBO (Jacob *et al.*, 2020). The protocol allows smaller fragments generated by macroscopic dissection of GBM specimens to grow on orbital shakers in culture conditions deprived of Matrigel and growth factors such as Epidermal Growth Factor (EFG) and Fibroblast Growth Factor (FGF). The study showed that GBOs can preserve GBM inter- and intra-tumour heterogeneity, in addition to hypoxic gradients which can be controlled by re-cutting the GBOs when propagating them. Moreover, GBOs were shown to maintain the genomic profiles of the original GBM tumours from which they were derived. Furthermore, the study showed that GBOs can be cryopreserved and successfully recovered to continue proliferation, which is an important step to create 'biobanks' that facilitate subsequent recovery of GBOs for future studies and which may open new avenues for

personalised medicine. Remarkable clinical translational has been revealed when GBOs with a high percentage of EGFRvIII expression, showed a response to CAR-T cells, which has been tested in clinical trials to date (O'Rourke *et al.*, 2017; Goff *et al.*, 2019), directed against the EGFRvIII mutational variant (Jacob *et al.*, 2020).

5.1.3 Overcoming technical challenges in the Gliomasphere Matrix system

Studying the cross-talk between GBM cells and the surrounding astrocytes at the invasive tumour edge is challenging due to several technical issues, for example, the choice of culture medium and identifying the appropriate numbers and ratios between the co-cultured cell types, previously reviewed in (Battiston *et al.*, 2014). The co-culture system in our model contains two types of cells that require two different media; normally differentiated astrocytes and invasive GIN cell lines, which are respectively cultured in astrocyte medium containing 2% FBS, and DMEM/F12 medium that contains 10%FBS. It has been challenging to address the question of whether choosing one medium type or combining two media is optimal for this co-culture model. However, we chose to use the astrocyte medium for both cell types (astrocytes and GBM cells) in the co-culture system, as it was previously shown that this medium allowed the generation of human astrocytes with normal transcriptome expression profiles from 42 neural progenitor cell lines (TCW *et al.*, 2017). Furthermore, excessive serum in the culture media can itself induce a reactive astrocytic genotype (Prah *et al.*, 2019), which in turn may obscure the molecular cross-talk with GBM cells and bias the results. It is also known that serum has an inhibitory effect on sphere formation using GBM cells (Hong, Chedid and Kalkanis, 2012) or astrocytes. However, we have conducted optimisations which showed that four different GBM cell lines can efficiently grow (normal lag and log phases) and form glioma spheroids for ten days in low serum conditions (including astrocyte medium containing 2% FBS), when cultured on our novel PEGDA plus decellularised human brain matrix. This was maximised by treating the polystyrene surface of the wells of an AggreWell™ plate with anti-adherence solution (Results section 5. 3. 4). Thus, astrocyte medium with 2% FBS was chosen for the co-culture, hypothesising that it can potentially provide a normal environment for the astrocytes, while maintaining the normal growth rate of GIN cells. Identifying astrocytes to GBM cell numbers and co-culture ratios was another technical challenge, as proliferating GBM cells could potentially stress non-proliferative, differentiated astrocytes, by outcompeting for nutrients contained within the 2ml medium volume of each well of an AggreWell™ plate during the time-frame of experiment. However, the utilization of GIN cell lines at low passage numbers ensured that proliferation rate was low and would not markedly hamper the experimental set-up.

5.1.4 Rationale of using PEGDA hydrogel and decellularised human brain ECM as components of the Gliomasphere Matrix

The use of collagen gelling methods to reconstruct various decellularised matrices, such as myocardium, bladder and brain, into 3D structures is not new (Freytes *et al.*, 2008; Singelyn *et al.*, 2009; DeQuach *et al.*, 2010, 2011; Dequach *et al.*, 2011; Wang and Christman, 2016). Based on this, the few experiments to date, conducting 3D culture modelling using GBM cell lines, usually involve the encapsulation of glioma cells within a constructed scaffold with collagen as a main component (Koh *et al.*, 2018; Sood *et al.*, 2019). However, the collagen that was used in these studies is a type 1 collagen, derived from rat tails. Furthermore, the amount of collagen that is needed for the gelling reaction to occur and create the 3D structure, is approximately ten times the volume of the decellularised ECM. In addition, it has been hypothesised that collagen type 1 is highly associated with an inflammatory reactive astrocytic niche; for example, elegant work showed that collagen type I can induce astrocytic scar formation via the integrin-beta-cadherin pathway (Hara *et al.*, 2017). Another study showed that reactive astrocytes within the glial scar can produce collagen (Chen and Swanson, 2003). More importantly, the native brain ECM has low levels of fibrillar proteins such as collagen, laminin, and fibronectin (Ruoslahti, 1996), and these proteins are present in the brain during development or predominantly located around blood vessels, basement membranes and white matter tracts in the adult brain (Liesi, 1984). Alternatively, these fibrillar proteins are mainly present in tumour ECM (Zheng *et al.*, 2004; Hu *et al.*, 2008) and therefore it was argued that “oncology recapitulates ontology” (Dwyer and Mattews, 2011). Thus, collagen was not used in our invasive Gliomasphere Matrix model to avoid biasing the transcriptomic profile of the co-cultured YFP-astrocytes, towards a reactive astrocytic type by providing inappropriate inflammatory, developmental or malignant microenvironments. Likewise, any product that is derived from sarcoma material and/or enriched with collagen and other fibrillar proteins such as Matrigel, was not used based upon the same rationale. Furthermore, Matrigel was shown to (inappropriately) enhance the acquisition of invasive properties in glioma cell lines by altering the cadherin-catenin adhesion pathway (Perego *et al.*, 2002). We therefore used the bio-inert PEGDA hydrogel to encapsulate the decellularised brain ECM molecules, which was thoroughly characterised using TOF-SIMS (see Chapter 4), to deliver the normal native brain signals. PEGDA is a well-defined material which has been used previously in a sensitive experiment to study brain development (Karzbrun *et al.*, 2018) and has been extensively used with gelatine or collagen in the commercially available Hystem™, HA-based hydrogel products.

5.1.5 The rationale and objectives of creating models to study GIN-astrocyte intercellular communication

In our study, we aimed to unravel the genetic cross-talk between GIN cells and astrocytes at the invasive tumour margin, where residual infiltrative GBM cells are left post-operatively and which inevitably manifests in tumour recurrence. This requires appropriate modelling and recapitulation of the required niche for the astrocytes at the tumour edge. This can be conducted using a co-culture model that includes GIN cell lines co-cultured with YFP-astrocytes on a 3D constructed decellularised human brain ECM (dhb-ECM) using PEGDA hydrogel (collectively termed Gliomasphere Matrices). Next, the co-cultured YFP-astrocytes can be isolated and astrocytic transcriptome profiles analysed. Whereas tumour-associated astrocytes located within the MRI contrast-enhanced tumour core and exposed to various stresses (hypoxia, pH alteration, and physical pressure), peri-tumoural astrocytes which surround the invasive satellitotic GBM processes at the infiltrative tumour margin, are hypothetically residing within a normal native human brain niche. These astrocytes maintain molecular communication with invasive margin GBM cells (e.g. GIN cells) via direct physical contact or a paracrine route. We hypothesised that modelling the peri-tumoural astrocytic niche surrounding invasive glioma cells requires an intricate design which can provide the following appropriate biological and technical aspects:

- Biological aspects
  - The entire model must recapitulate the *in-vivo* physiological native brain niche within which infiltrative GBM cells can be directly exposed.
  - Direct physical contact between GIN cells with YFP-astrocytes must be ensured to obtain an accurate representation of intercellular communication occurring at the infiltrative GBM edge.
  - The model should avoid/minimise the unnecessary microenvironmental stresses induced by proliferating GBM cells; i.e., hypothetically, the YFP-astrocytes should not be exposed to any kind of microenvironmental stress such as hypoxia (unlikely to be prominent in the infiltrative microenvironment immediately post-surgery) which may lead to pH alteration, and physical pressure effects caused by the proliferating tumour cells.
- Technical perspectives
  - The model should recapitulate the 3D microenvironment.
  - The model should be tuneable and adjustable to accommodate various concentrations of dhb-ECM

- Scalability.
- Reproducibility.
- Multifaceted and broad applicability to studies involving other somatic tissues.
- Spatially-controllable; i.e., the location of the YFP-astrocytes can be preferentially controlled. This is to provide an efficient platform to assess intercellular communication resulting from different conditions within GBM rim and core regions.
- High-throughput to overcome the low-throughput technical challenge of organ-on-chip models (Horvath *et al.*, 2016).

5.2 Materials and Methods

5.2.1 Guidelines to encapsulate the solubilised material of the dhb-ECM within PEGDA hydrogel to generate a 3D basement membrane.

1. The stock of the photo-initiator solution was made by dissolving 20mg of 2,2-dimethoxy-2-phenylacetophenone (Sigma; catalogue number 196118) in 1ml of 70% ethanol at room temperature. PEGDA solution (Sigma; catalogue number 729094) was prepared by dissolving 200mg PEGDA in 900µl of sterile-filtered deionized water (Milli-Q ultrapure water) (modified from Karzbrun et al., 2018). PEGDA was dissolved in water at 90°C for 5 minutes on a heat block until complete disappearance of PEGDA particles. At this stage, the solution became light yellow without particles. The solution was kept at temperature ranging from 35-40°C as the PEGDA starts to polymerise again if the surrounding temperature drops below that range.
2. Both solutions were sterile filtered using 0.22µm blue syringe filters to remove residual none-dissolved particles.
3. dhb-ECM at a concentration of 20µg/1µl was filtered through a reversible strainer with 37µm pore size (STEMCELL TECHNOLOGIES; catalogue number 27215) to avoid any ECM particles larger than 37µm to pass through the strainer.
4. The dhb-ECM solution was neutralised by adding 5-10µl 10X DPBS for each 100µl of the dhb-ECM. The DPBS did not compromise the concentration of the dissolved dhb-ECM and was kept at 20µg/1µl. If large volumes are required for the neutralisation step, the same volume should be deducted from the volume of the deionised water in which the PEGDA will be disolved. The pH of the decellularised human brain matrix solution ranged between 7-8, to avoid PEGDA cross-linking. The pH was frequently checked by applying 2-3µl of the mixture directly on pH strips. Using other methods such as the pH meter was unnecessary as buffering was later performed and the use of a PH meter could potentially increase the risk of contamination.
5. 100µl of soluble dhb-ECM at a concentration of 20µg/1µl (acid-solubilized dhb-ECM lyophilized material in chapter 4) was added to 900µl of the sterile filtered PEGDA solution and mixed thourghly via gente pipetting. Vortexing or vigrous shaking was avoided to prevent crystalisation of the dissolved PEGDA. Also, the ECM was added to the PEGDA hydrogel after cooling down to 35-40°C as high temperatures could have caused ECM protein denaturation.

6. The first solution of 1ml water containing PEGDA and 2mg dhb-ECM was mixed with the second solution. The tube was covered with opaque wrap to prevent crystalisation.
7. The wells of an AggreWell^{TM}800 plate (STEMCELL TECHNOLOGIES; catalogue number 27215) were rinsed each with 2ml anti-adherence rinsing solution (STEMCELL TECHNOLOGIES; catalogue number 07010) and the plate was appropriately balanced and centrifuged at 2000 x *g* for 10 minutes to remove any bubble at the base of the microwells. Next, the plate was checked under the microscope for any bubble formation at the bottom of the microwells of the AggreWell™ plate. The anti-adherence rinsing solution was then removed. This is a very critical step to prevent GIN cells, which are highly adherent, from attaching and travelling to the bottom of microwells of the AggreWell™ plate.
8. 250µl of the mixture solution was applied into each well of an AggreWell^{TM}800 plate (STEMCELL TECHNOLOGIES; catalogue number 27215). The AggreWell™ plate was then gently shaken at two perpendicular planes horizontally (to ensure even distribution of the dhb-ECM), where swirling movements of the pate were avoided as this can bring the dhb-ECM into the centre of the well; i.e., the centrally located microwells within the large well will be covered with the decellularised human brain material, whereas the peripherally located microwells will not be coated.
9. Before PEGDA crosslinking, the plates were left for 5-7 minutes on the benchtop to allow the dhb-ECM to precipitate within the entire depth of the microwell. Alternatively, the pates can be centrifuged at 100 *g* for 30 seconds to bring the dhb-ECM towards the centre of the microwells.
10. Thorough visual examination was conducted using a light microscope to ensure even distribution of the dhb-ECM within the microwells before crosslinking of the PEGDA hydrogel, an essential step to ensure consistency and reproducibility of Gliomasphere Matrices.
11. The PEGDA hydrogel containing the dhb-ECM was cross-linked using a UV light source (UVP mini UV lamps; Fisher catalogue: 100155274) on top and below the plate for a total of 10 minutes (5 minutes for each side).
12. Thorough visual examination was conducted using a light microscope to ensure PEGDA setting after UV-mediated crosslinking. This can be tested by gently tapping on the side of the plate, while microscopically observing the shaking movement of the ECM particles. Although air bubble formation is considered harmful to the experiment, visualising a trapped bubble that is not

close to the bottom of the well is highly suggestive of successful crosslinking, as this indicates the media has solidified.

13. After cross-linking, the generated 3D matrix containing PEGDA hydrogel and dhb-ECM was washed gently using DPBS without calicum and magnisium, followed by DMEM/F12 (Gibco; catalogue number 10565018) twice. This ensured that biomaterials that are not held within the 3D scaffold structure are washed out and that the niche was buffered to prevent unnecessary pH alteration that may adversely affect cells.
14. The basment mambrane ECM was thoroughly examined under light microscopy to ensure consistency of the distribution of the dhb-ECM within the microwells of the AggreWell™ plate.
15. The astrocytes and GIN cells were added immediately according to the protocol below.

5.2.2 Sequential-seeding protocols used to determine precise YFP-astrocyte location within the Gliomasphere Matrices.

5.2.2.1 Protocol used to seed YFP-astrocytes at the periphery of the Gliomasphere Matrices.

1. Culture surfaces of AggreWell™ microwells were prepared by encapsulating the dhb-ECM within the PEGDA 3D hydrogel according to the protocol described above (section 5.2.1).
2. 1ml of astrocyte medium was added to each well of the AggreWell™ plate.
3. 10 primary GIN cell lines were harvested and cultured in DMEM/F-12 media containing 10%FBS within T75 TC-treated flasks (Corning 430641U), using TryplE Express for 2 minutes.
4. The TryplE Express was then neutralised using 10% FBS in DMEM/F-12 and the cells were centrifuged at 300 x *g* for 5 minutes. Cells were manually counted using haemocytometer and cell count was validated using an EVE Automatic cell counter. The supernatant was then removed and 150,000 cells from each GIN cell line was resuspended in 1ml of astrocyte medium and added to 1ml of astrocyte medium kept in each large macrowell of the AggreWell™ plate. Each macrowell contains 300 miniwells within a single AggreWell™ plate, permittig high-throughput, reproducibel analyses. The cells were thoroughly mixed by pipetting using a 10µl tip, to ensure even dirtribution of cells throughout the microwells while maintaining the integrity of the ECM basment membrane. It is noteworthy to mention that with high cell

numbers, the 1ml cell suspension can be added to the medium inside the large macrowell and centrifuged at 100 x *g* for 3 minutes, to precipitate the cells evenly throughout the microwells. .

5. Primary GIN cells were left for 30 minutes until complete precipitation at the bottom of the microwells and checked under a microscope for even distribution of cells.
6. The process was repeated for all GIN lines and the AggreWell™ plate was incubated overnight at 37°C with 5% CO2 and 95% humidity to form small aggregates of approximately 500 cells per microwell.
7. All GIN lines formed small aggregates of approximately 500 cells within each microwell. Microscopic examination was conducted to ensure consistent aggregate formation throughout microwells prior to seeding of the YFP-astrocytes onto GIN aggregates, to mimic interactions between peri-tumour astrocytes and invasive GBM cells. Seeding YFP-astrocytes onto non-aggregated GIN cells within microwells was avoided as this could potentially lead to a random heterogeneous mixture of YFP-astrocytes with GIN cells and thus poorly mimic peri-tumour astrocytes.
8. 1 ml of the astrocyte medium was removed gently to avoid any dislodgment of GIN aggregates.
9. The YFP-astrocytes were next harvested using StemPro Accutase and counted using a haemocytometer. Cell count was validated using an EVE Automatic cell counter. The supernatant was then removed and each population of 350,000 YFP-astrocytes was resuspended in 1ml astrocyte medium and added to the 1ml of astrocyte medium kept in each large well of the AggreWell™ plate. The total 2ml of astrocyte medium was thoroughly mixed by moving a 10µl pipette tip in two perpendicular zigzag planes to avoid dislodgment of GIN aggregates. It is noteworthy to mention that with high cell numbers, the 1ml cell suspension can be added to the medium inside the macrowell and centrifuged at 100 x *g* for 3 minutes to precipitate the cells evenly throughout the microwells.
10. Three quarters (1.5ml) of the total medium volume was changed daily until cells were dissociated at Days 6 and 10.

5.2.2.2 Protocol used to seed YFP-astrocytes at the centre of the Gliomasphere Matrices.

The YFP-astrocytes were seeded onto the centre of Gliomasphere Matrices in a controlled manner by repeating the same protocol described above (section 5.2.2.1), with the following modification; the YFP-astrocytes were seeded first and left overnight to form the aggregates, prior to primary GIN cells being seeded onto YFP-astrocyte aggregates the following day. GIN cells were then centrifuged at 100 x *g* for 3 minutes to precipitate the cells evenly throughout the microwells.

5.2.3 Novel protocol to transfer Gliomasphere Matrices onto WillCo dishes for imaging.

1. WillCo dishes were rinsed each with 2ml anti-adherence rinsing solution (STEMCELL TECHNOLOGIES; catalogue number 07010) to avoid cellular attachment. The anti-adherence rinsing solution was then removed and the WillCo dish (GWSt-3522) was rinsed with DMEM/ F-12, GlutaMAX media (Gibco Catalogue number: 31331093).
2. A reversible strainer with 37µm pore size (STEMCELL TECHNOLOGIES; catalogue number 27215) was placed onto a 15ml tube with its arrow pointing upward; i.e., the aperture of the lower chamber facing upward (vertically-inverted position).
3. The attached co-culture aggregates were dislodged from the 3D scaffold by aspirating 1ml of astrocyte medium from each macrowell of the AggreWell™ plate and re-flushing the media once firmly using a standard narrow p1000 tip.
4. The standard p1000 tip was immediately changed to an ART™ wide-bore filtered pipettep1000 tip (Thermo Scientific ™; catalogue number 2079G) to aspirate 1ml of astrocyte medium which included the aggregates. This is a critical step as the aggregates could be fragmented if a standard narrow tip is used. The wide-bore tips were rinsed with medium or DPBS before aspirating the aggregates to ensure that the aggregates did not stick to the walls of the tip.
5. The aggregates within the aspirated 1ml medium were filtered through a reversible strainer with 37µm pore size (STEMCELL TECHNOLOGIES; catalogue number 27215), leaving the spheroids/matrices, harvested from multiple wells, on top of the filter mesh.

6. The process was repeated until no aggregates were left in the microwells of the AggreWell™ plate. The aggregates were frequently washed to prevent dryness.
7. The aggregates on top of the filter mesh were then washed gently using DMEM/F-12 or DPBS to get rid of the detached single cells.
8. The reversible strainer was inverted (the arrow should be pointed down) and aggregates were flushed into WillCo dishes using 1.5ml astrocyte medium (3 x 0.5ml to remove all aggregates).

5.2.4 Novel protocol used to dissociate and isolate YFP-astrocytes from Gliomasphere Matrices after co-culture.

1. The attached co-cultured aggregates were dislodged from the 3D matrices by aspirating 1ml of astrocyte medium from each macrowell of the AggreWell™ plate and re-flushing once firmly using a standard narrow p1000 pipette tip.
2. The standard p1000 tip was immediately changed to an ART™ wide-bore filtered pipettep1000 tip (Thermo Scientific ™; catalogue number 2079G) to aspirate 1ml of astrocyte medium which included the aggregates. This is a critical step as the aggregates may block the tip if standard narrow-tip is used. Equally important, the wide-bore tips should be rinsed with medium or DPBS before aspirating the aggregates to ensure that they will not stick to the walls of the tip.
3. The aggregates within the aspirated 1ml medium were next transferred into a 15ml tube and the process was repeated until no aggregates were left in the microwells of the AggreWell plate.
4. The tube containing the aggregates was centrifuged at 300 x *g* for 5 minutes to physically dissociate the aggregates. The supernatant was aspirated and 0.5ml TryplE Express was applied onto the fragmented aggregates.
5. The tube was then incubated at 37°C for a total of 3 minutes, after which the spheroids were further disaggregated physically by gentle pipetting for 15-20 seconds every minute until full dissociation and disappearance of visible cell clumps was achieved. The standard p1000 tips should be rinsed with medium or DPBS before use to minimize the adherence of aggregates and cells to the walls of the tip.
6. TryplE Express was neutralised by the addition of 4.5ml astrocyte medium and the tube was centrifuged at 300 x *g* for 5 minutes.

7. The supernatant was then aspirated, and single cells re-suspended in FluoroBrite ™ DMEM (Gibco; A1896701) for FACS-isolation of YFP-astrocytes from primary GIN cells (details of FCAS-isolation has been described in Chapter 3).

5.2.5 SEM examination of decellularised human brain ECM encapsulated within 3D PEGDA hydrogel

The dhb-ECM encapsulated within the PEGDA hydrogel matrix, was mixed and set according to the protocols described. The mounted matrix was then allowed to air-dry and coated with gold using a sputter-coater (Polaron SC7640) and examined according to standard operating procedures, provided by the Nanoscale and Microscale Research Centre at the University of Nottingham. The surface morphology of the dhb-ECM encapsulated within the PEGDA hydrogel matrix was examined using JEOL 6060LV SEM (JEOL, Peabody, MA, USA).

5.2.6 *In-vitro* proliferation

Four GIN cell lines (GIN5, GIN8, GIN28, and GIN31) with passage numbers >20, were cultured in three conditions: i) without basement membrane in advanced DMEM media (reduced serum) supplemented with GlutaMAX 1%; ii) without basement membrane in astrocyte medium (2% FBS); iii) in astrocyte medium (2% FBS) on dhb-ECM encapsulated within PEGDA hydrogel. Three-hundred thousand cells from each GIN cell line were passaged into separate macrowells of an AggreWell™ plate, centrifuged at 100 X *g* for 30 seconds and allowed to form spheres within 24 hours. The culture duration was 10 days and a manual cell count was conducted at three points; Day 3, Day 7 and Day 10.

5.2.7 DeltaVision and confocal microscopic examinations

The images and z-stacks of Gliomasphere Matrices were collected and resolved using a DeltaVision Elite microscope (applied Precision/GH Healthcare Life Sciences Buckinghamshire, UK) at x20 (numerical aperture 0.85, PlanApo; Olympus) or x100 (numerical aperture 1.4, UPlanApo Olympus, South-end-on-sea, UK) magnifications. Images were recorded using a Photometric CoolSnap HQ2 camera (Photometrics, Arizona, USA). The excitement and emission of YFP wavelengths were 513nm (Bandwidth 17) and 559 (Bandwidth 38) respectively. The live cell filter wheel was used with the C/YFP/mCH Polychroic. A series of (x-y) images or z-slices through the sample were acquired. Widefield-restoration was conducted as spheroids/matrices contained dark regions and due to the anticipated movement of spheroids/matrices within the culture media of the WillCo imaging wells **(Figure 5. 1)**. For high-resolution images confirming the location of the YFP-astrocytes at the peripheral, peri-tumour location, a Zeiss LSM880 confocal laser scanning microscope was used.

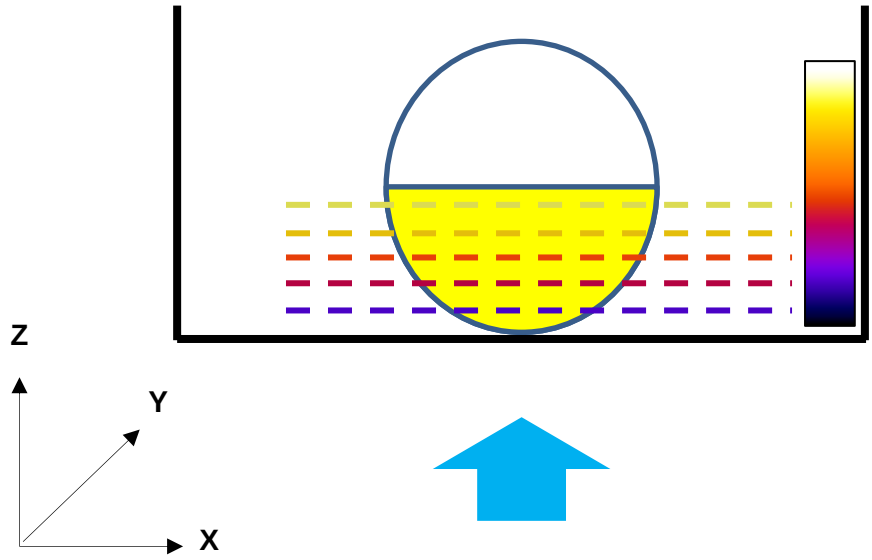


Figure 5. 1. DeltaVision and confocal microscopic examinations of Gliomasphere Matrices within WillCo dishes. Gliomasphere Matrices were z-stacked and the depth of the images of z-stack slices was colour coded as shown by the colour scale, where slices of increasing depth are shown in the order of yellow > orange > red > purple. The blue arrow represents the direction of visualisation of the spheroids/matrices along the z-axis.

5.3 Results

5.3.1 3D reconstructed decellularised human brain ECM using PEGDA hydrogel is highly tuneable and reproducible.

The dhb-ECM was encapsulated within the PEGDA hydrogel to form a 3D ECM that covers all microwells within the AggreWell™ plate. Despite the vigorous solubilisation step when preparing dhb-ECM, residual large particles appeared in the transparent PEGDA hydrogel **(Figure 5. 2A-D)**. Although dhb-ECM was uniformly distributed across microwells of the AggreWell™ plates and throughout the depth of each microwell, large residual dhb-ECM particles were observed. This was assumed to be a potential source of technical error, which could negatively affect the reproducibility and consistency of the Gliomasphere Matrices model. The initial experimental design included the creation of a co-culture model composed of relatively small numbers of both YFP-astrocytes and GIN cells, to ensure viability and avoidance of potential environmental stress which may have been caused by using a high number of cells and a small volume (2ml) of growth medium (the capacity of each macrowell within the AggreWell™ plate). Moreover, an optimal direct physical contact between YFP-astrocytes and GIN cells within dhb-ECM was also required to reveal transcriptomic alterations in the tumour-associated astrocytes induced by molecular cross talk with GIN cells. However, this optimal physical contact cannot be achieved when a small number of both cell types are provided. In addition, the presence of large ECM particles may act as a physical separating barrier in the case where small cell numbers are already limited by the volume capacity of macrowells of the AggreWell™ plate. Thus, the presence of large ECM residues may bias the results in our study by preventing the cross-talk assumed to occur between YFP-astrocytes and GIN cells; nevertheless large ECM particles can be efficiently utilized for various experimental purposes if high numbers of cells need to be used.

Upon further optimisation to remove ECM large particles, an essential filtration step was included, and ECM material centrifuged at the lowest possible centrifugal speed to allow homogenous dispersion throughout the entire depth of each microwell on the AggreWell™ plate **(Figure 5. 2E-H)**. This was confirmed by light microscopy which showed the ECM at different depths within the mircowells. The air bubble confirms the appropriate gelling of the transparent PEGDA hydrogel, which holds the dhb-ECM **(Figure 5. 2H)**. Moreover, filtration reduced the size (to ≤ 37nm) of the individual ECM particles upon which the small numbers of astrocyte and GIN cells could be seeded, thereby facilitating cellular contact with ECM ligands **(Figure 5. 2E-H).**

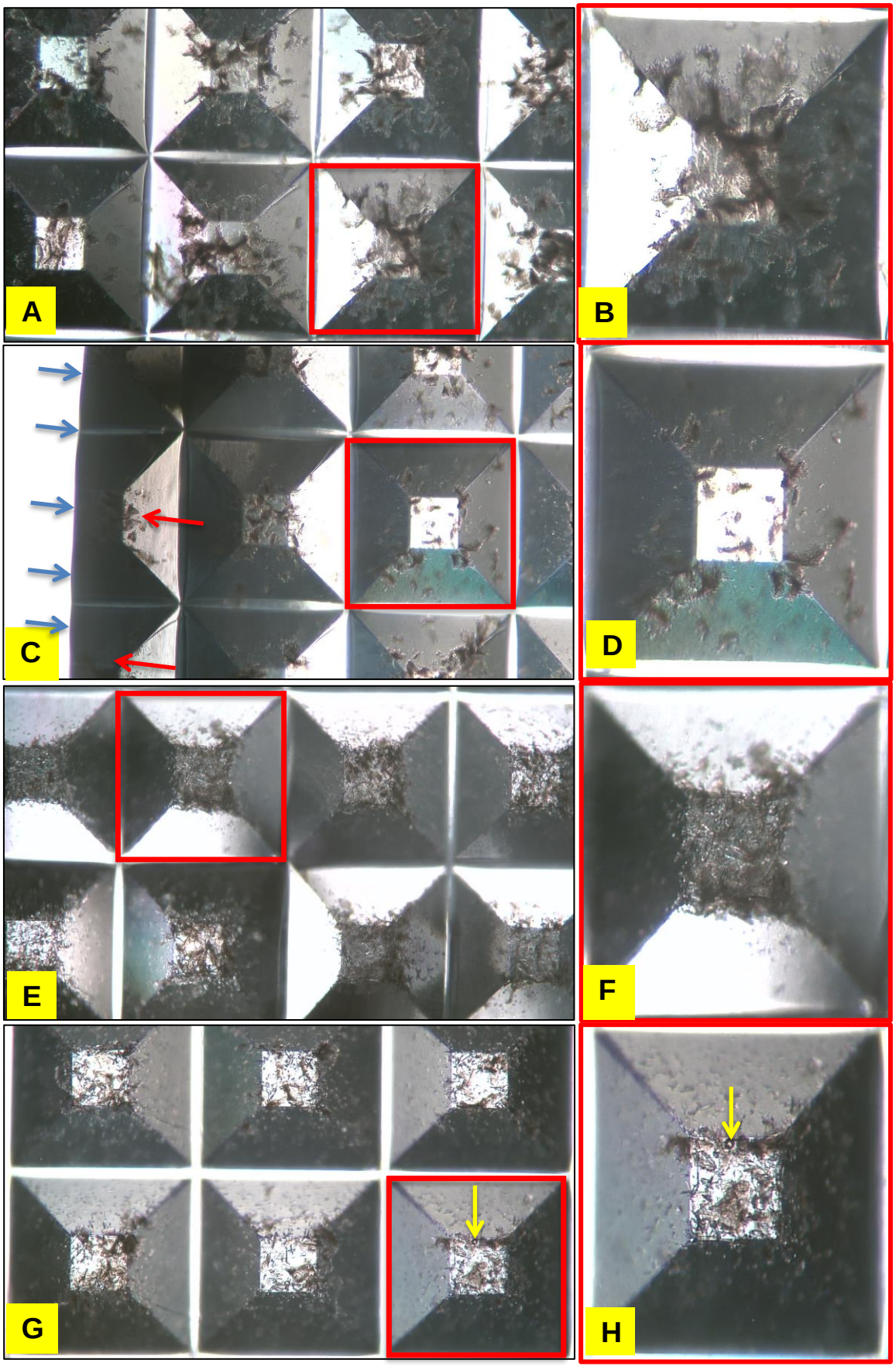

A
B
C
D
E
F
G
H

Figure 5. 2. Reproducible and tuneable 3D decellularised human brain ECM using PEDGA hydrogel. The images represent the microwells of the AggreWell™ plate, where optimisation of the 3D reconstructed dhb-ECM within PEGDA hydrogel was conducted (A-H). (A, C, E, and G) were visualised at x10 magnification, whereas (B, D, F, and H) were magnified at x40 (red squares in A, C, E, and G). The microwells measure 800µm in size. The dhb-ECM was created using a highly reproducible approach and visually shown to be evenly distributed across microwells and well dispersed throughout the depth of each microwell (red arrows) including microwells located at the edge of the macrowell (blue arrows). Initially, 2000µg of the solubilised dhb-ECM was directly encapsulated within PEGDA hydrogel without filtration, which produced relatively large particles within the microwells (A-B). Likewise, similar ECM particles were observed despite reduction of the concentration of dhb-ECM to 250µg (C-D). Next, a filtration step through a 37µm strainer was added, and 500µg (E-F) or 250µg (G-H) dhb-ECM was used. This resulted in the disappearance of large ECM particulates within the microwells, thus more suitable to incorporate small numbers of cells in the co-culture experiment. The small bubbles which formed within the microwell (yellow arrows) are an indicator of proper gelling of the PEDA hydrogel.

5.3.2 SEM examination reveals the porosity and lamellar structure of the decellularised human brain matrix constructed within PEGDA hydrogel.

The topography of the scaffold composed from the decellularised human brain matrix constructed within PEGDA hydrogel, shows important ECM features known to be essential properties when manufacturing biomaterial-based ECM. The scaffold was highly porous and multi-lamellar **(Figure 5. 3A-D)**. Although the sizes of these pores were variable within these lamellae, the prevalent pore size range was 5-20µm **(Figure 5. 3A-D)**. The pores formed slit-like lumens and were compacted due to possible dehydration of the hydrogel occurred duing processing of samples to be imaged by SEM **(Figure 5. 3A-D)**. A particle of dhb-ECM was shown to be encapsulated within the lamellae of the surface of PEGDA hydrogel **(Figure 5. 3A)**. However, the dhb-ECM particles were not abundantly distributed within the PEGDA hydrogel uppermost ECM surface due to SEM limitation, but were visulalised to be distrubuted throughout the depth of AggreWell™ microwells as seen by light microscopy in **(Figure 5.2)**, however future confirmation analysis using transaction electron microscopy is recommended. It is important to note that the scaffold pores were interconnected **(Figure 5. 3D)**.

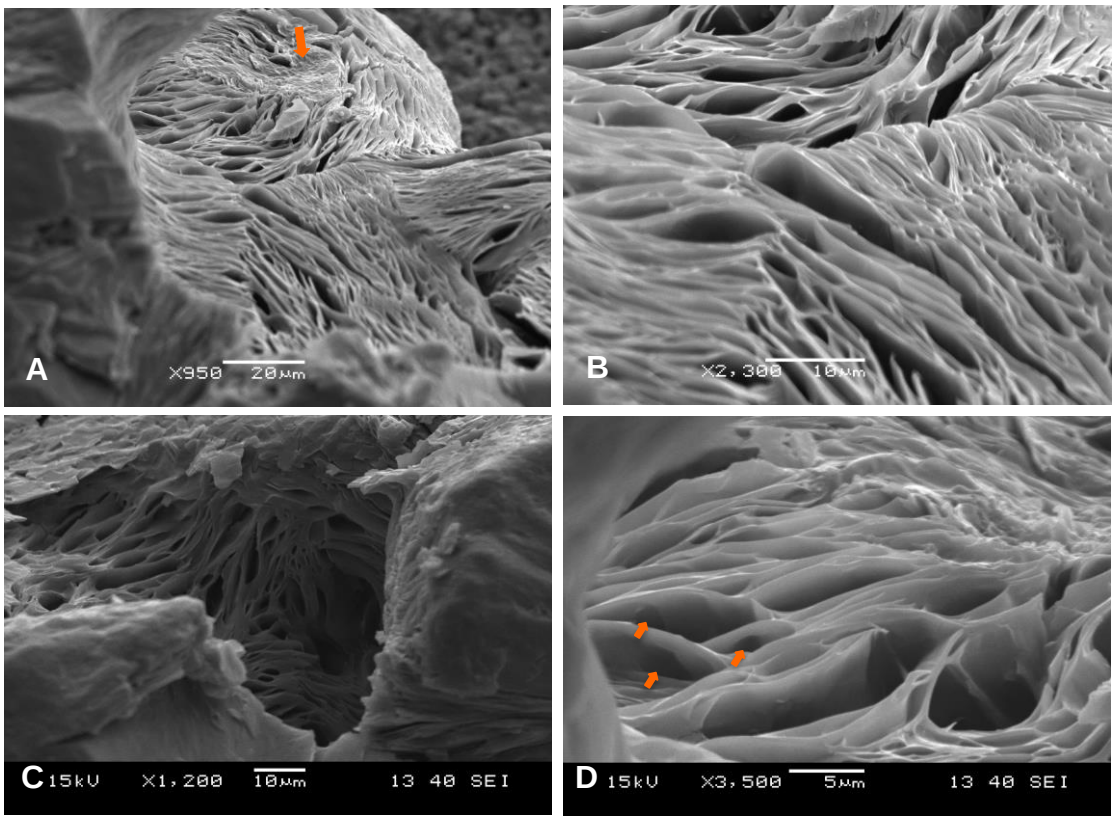


Figure 5. 3. SEM examination reveals the porosity and lamellar structure of the decellularised human brain matrix constructed within PEGDA hydrogel. The scaffold was highly porous and multi-lamellar (A-D). Although the pore sizes were variable within these lamellae, the prevalent pore size range was 5-20µm (A-D). The pores formed slit-like lumens and were compacted due to effects of hydrogel dehydration(A-D). Approximately 20-30µm sized particles of dhb-ECM was shown to be encapsulated within the surface of the lamellae of PEGDA hydrogel (A, arrow). The scaffold pores were also interconnected (D, arrows).

5.3.3 Generation of the high-throughput Gliomasphere Matrices in a reproducible manner.

The 24-well AggreWell™800 plates and novel protocol to encapsulate dhb-ECM within PEGDA hydrogel, have worked synergistically to maintain consistency and reproducibility of the creation of astrocyte-GBM aggregates within the Gliomasphere Matrices **(Figure 5. 4A-I)**. The AggreWell™800 plate facilitated the generation of 300 reproducible technical replicates (i.e. 300 microwells within each macrowell of a 24-well plate) for each GIN-YFP-astrocyte co-culture (10 distinct GIN lines in total). To determine whether our Gliomasphere Matrices are fit-for-purpose and the multi-component model is reproducible and scalable, light microscopy was first used to assess the overall integrity, consistency and distribution of the dhb-ECM within the microwells of the AggreWell™800 plate **(Figure 5. 4A-C)**. Cross-linking of the PEGDA hydrogel to encapsulate the dhb-ECM within PEGDA and construction of the 3D matrices, was achieved via applying UV light **(Figure 5. 4D-F)**. Sequential cell seeding of GIN cells (150,000 cells) followed by YFP-astrocytes (300,000 cells) generated co-culture aggregates with an approximate size of 300μm diameter **(Figure 5. 4F-G)**, whereas seeding approximately double the number of each cell-type generated aggregates with an approximate size of 500μm diameter **(Figure 5. 4H-I).** Although aggregates formed in both conditions, the edges of the aggregates with 300μm size were relatively irregular as compared to aggregates with 500μm size. This may be explained by the physical flexibility of this novel 3D matrix (dhb-ECM held within PEGDA hydrogel), which can be spatially modified by the proliferating GIN cells. That is to say, doubling GIN cell number did not result in doubling of spheroid size, which reflects the flexible rheological modulus of this matrix. This assumes that physical pressure applied by double the number of GIN cells, led to forceful encasing/enclosure of the dhb-ECM with PEGDA hydrogel, to generate more spatially accurate spheroids. The protocol can potentially be further scaled-up by increasing the initial cell seeding density to increase the size of Gliomasphere Matrices within the 300 microwells, and further scaled-out (increasing the areas of culture surfaces) by using a 6-well plate that contains 1200 microwells to increase the number of Gliomasphere Matrices **(Figure 5. 4D)**, and/or a combination of both.

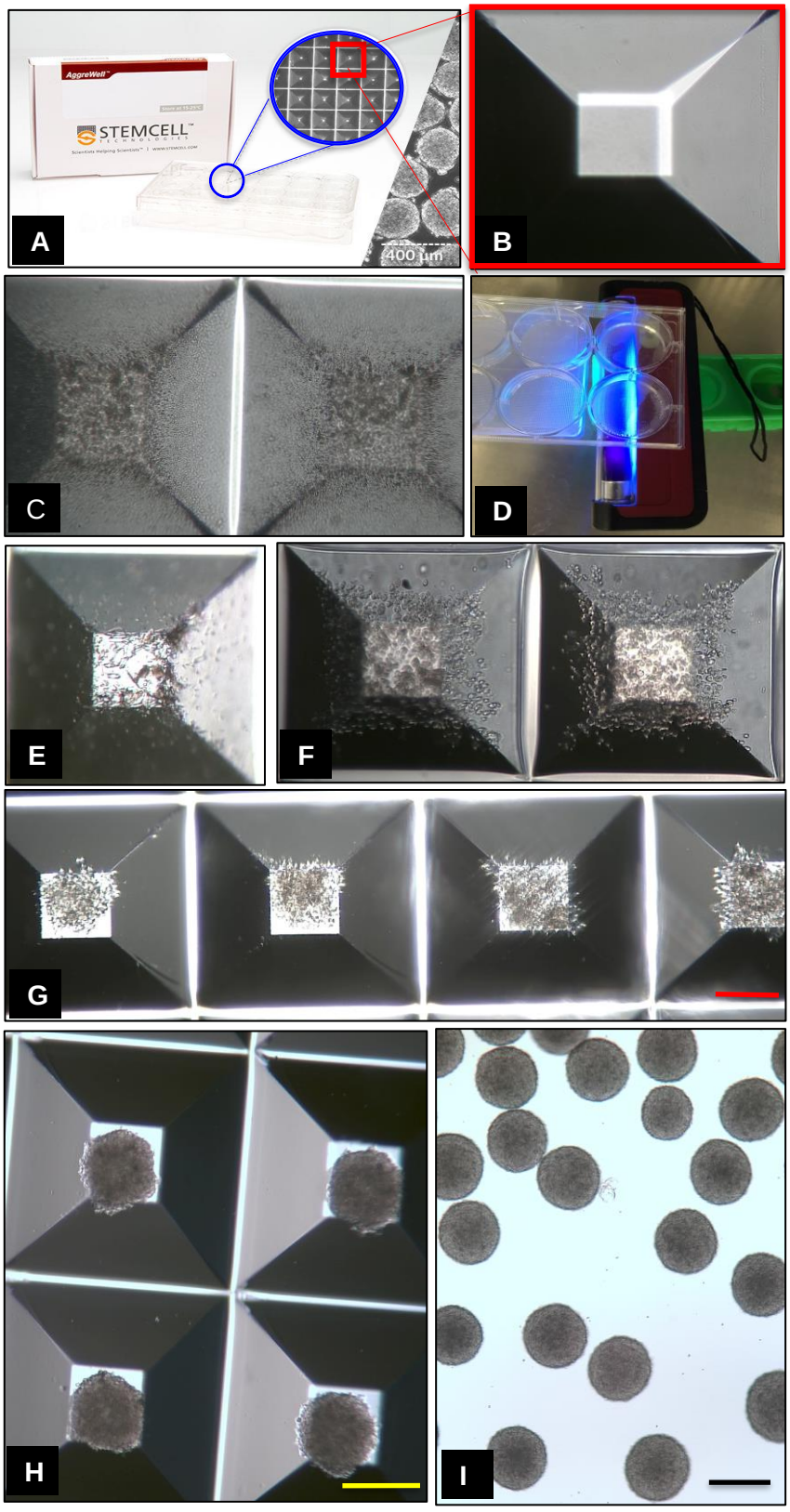

AggreWell
STEMCELL
A
400 µm
B
C
D
E
F
G
H
I

Figure 5. 4. Generation of the high-throughput Gliomasphere Matrices in a reproducible manner. An individual magnified macrowell (dark blue) of 24-well AggreWell™800 plates (STEMCELL TECHNOLOGIES) (A), which consist of 300 microwells (red sequares; 800 µm diameter) per each macrowell (B), were used as a platform to generate Gliomasphere Matrices. The novel protocol of encapsulating dhb-ECM within PEGDA hydrogel, was first examined using light microscopy to assess the overall structural integrity, consistency across each miniwell, and distribution of the dhb-ECM within the microwells (C). Application of UV light (D) led to crosslinking of the PEGDA hydrogel and thereby encapsulation of the dhb-ECM within PEGDA, to generate a 3D matrix (E). Sequential cell seeding of GIN cells followed by YFP-astrocytes (F), resulted in the generation of co-cultured aggregates with an approximate size of 300µm (G). Note, the image of the aggregates in (G) were taken from Day 10 co-culture of GIN28 (150,000 cells) and YFP-astrocytes (300,000 cells). This novel protocol is feasible for scale-up, as increasing the number of seeded cells; GIN28 (250,000 cells) and YFP-astrocytes (550,000 cells) resulted in larger aggregates (500µm), with an encapsulated dhb-ECM core (H-I). The edges of the aggregates of 300µm size (G) were relatively irregular (G) as compared to aggregates of 500µm size (H-I). The protocol can be further scaled-up by using a 6-well AggreWell™ plate that contains 1200 microwells (D). Aggregates can be efficiently produced at larger scale when number of cells are increased or created using larger wells for different applications (e.g. metabolic viability/drug screening assays) without any disruption of structural integrity (I). *Red scale bar = 300µm; black and yellow scale bars = 500 µm*.

5.3.4 Optimisation and creating the core of the Gliomasphere Matrices (GIN cell lines cultured on the decellularised human brain ECM-PEGDA) revealed that decellularised human brain ECM enhances aggregate formation of primary GBM invasive margin cells.

Efficient creation of the Gliomasphere Matrices required optimising the ECM and cellular aggregates. After the optimisation of the dhb-ECM within PEGDA hydrogel, optimising spheroid formation for different GIN cell lines (derived from the invasive GBM margin) was required **(Figure 5. 5)**. Three culture systems were used to asses four GIN cell lines (GIN5, GIN8, GIN28, and GIN31); advanced DMEM without ECM **(Figure 5. 5A, D, G, and J)**, astrocyte medium with PEGDA hydrogel only **(Figure 5. 5B, E, H, and K)**, and astrocyte medium plus 3D reconstructed dhb-ECM using PEGDA hydrogel **(Figure 5. 5C, F, I, and L)**. The advanced medium is widely known to enhance cellular aggregate formation due to a lack of serum (whereas the astrocyte medium contained 2% serum). Evident GIN cellular predilection to the dhb-ECM was clearly observed for all GIN cell lines, despite only a small number of cells attaching to the culture plastic surface of the AggreWell™ plate **(Figure 5. 5C, F, I, and L)**. Furthermore, cellular aggregates of all GIN cell lines were centrally located and physically non-motile within the microwells, when moving the pate for different purposes **(Figure 5. 5C, F, I, and L)**. This may be due to the presence of the dhb-ECM what has been designed to be held at the centre of each microwell by PEGDA hydrogel. GIN5 cells formed a mesh-like structure within PEGDA hydrogel with no evident sphere formation when dhb-brain ECM was absent **(Figure 5. 5A-B).** GIN8 and GIN31 also attached to the culture plastic surface of the AggreWell™ plate and formed aggregates with variable size **(Figure 5. 5D, E, J, and K)**. Cellular aggregates of GIN8 and GIN31 fused across neighbouring microwells **(Figure 5. 5D-E and J-K)**. GIN28 formed spheroids in a similar manner; however they also exhibited a highly migratory phenotype and fusion of aggregates was widely disseminated across various microwells **(Figure 5. 5G-H).**

Collectively, these properties could potentially introduce variability in the results. In all conditions, especially in the absence of the dhb-ECM, varying percentages of GIN cells tended to attach to the culture plastic surface. Therefore, pre-culture treatment of the AggreWell™ plates with anti-adherence material, prior to the preparation of the ECM, was extremely critical for the integrity of the spheroids and used in the final optimised protocol of co-culture experiments to produces Gliomasphere Matrices **(Figure 5. 4G, and H)**.

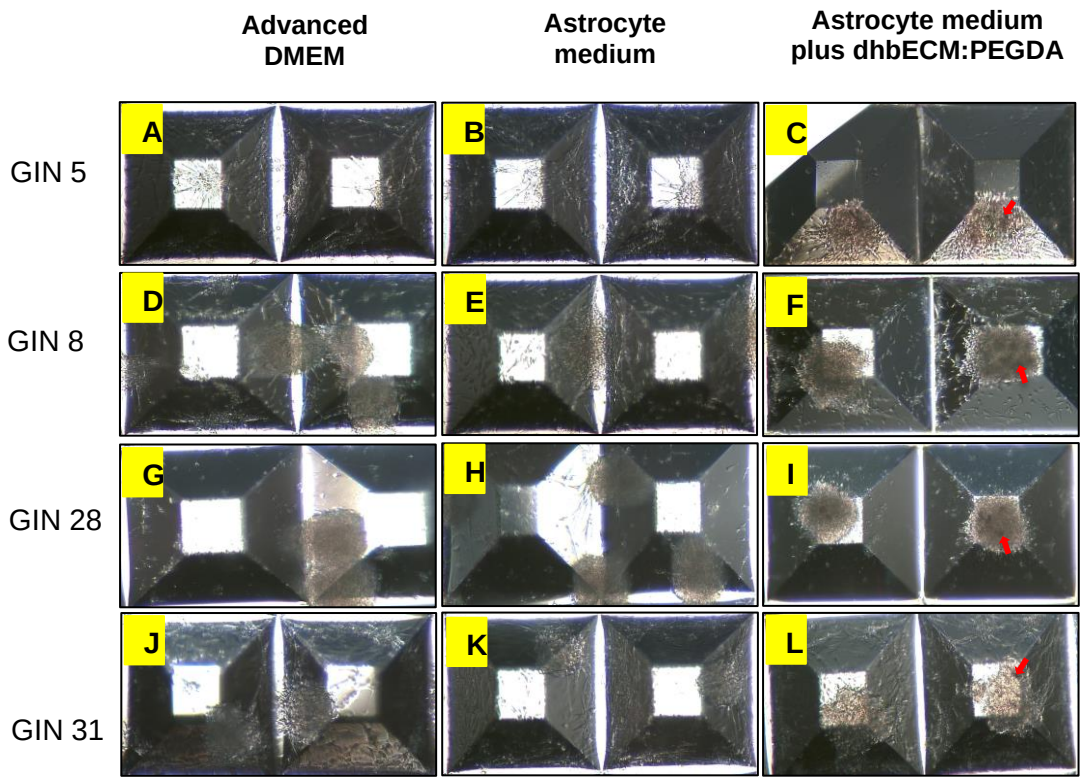


Figure 5. 5. 3D decellularised human brain ECM supports aggregate formation of invasive GBM cells. Three culture systems were tested on four GIN cell lines (GIN5, GIN8, GIN28, and GIN31); advanced DMEM without ECM (A, D, G, and J), astrocyte medium with PEGDA hydrogel only (B, E, H, and K), and astrocyte medium plus 3D reconstructed dhb-ECM using PEGDA hydrogel (C, F, I, and L). Astrocyte medium with 3D reconstructed dhb-ECM using PEGDA hydrogel, was shown to effectively enhance the creation of the Gliomasphere Matrices for all GIN cell lines, as compared to all other conditions (C, F, I, and L). The dhb-ECM can be seen in the centre of the aggregates (red arrows). GIN cells from all four lines, exhibited a predilection to the dhb-ECM, despite a small number of cells attaching to the plastic culture surface of the AggreWell™ plate (C, F, I, and L). Furthermore, cellular aggregates of all GIN cell lines were centrally located and physically-stable within the microwells (C, F, I, and L). GIN5 cells formed a mesh-like structure within PEGDA hydrogel, with no evident sphere formation when dhb-ECM was absent (A-B). GIN8 and GIN31 cells also attached to the culture plastic surface and formed aggregates with variable size (D-E and J-K). Cellular aggregates of GIN8 and GIN31 fused across neighbouring microwells (D-E and J-K). GIN28 formed spheroids in all culture conditions; however, GIN28 spheroids had highly migratory properties and fusion of aggregates was widely disseminated across various microwells (G-H). Note, the microwell is 800μm in size.

5.3.5 Decellularised human brain ECM within PEGDA hydrogel does not impair proliferation of invasive primary GBM cells.

Having optimised a method to ensure that the GIN cells could be maintained within the core of the Gliomasphere Matrices, we next assessed tumour cell viability and growth potential, in comparison to standard conditions for spheroid culture. Four representative GIN cell lines (GIN5, GIN8, GIN28, and GIN31) were cultured in three conditions: (i) without basement membrane in advanced DMEM media; (ii) without basement membrane in astrocyte medium (AM); (iii) astrocyte medium with dhb-ECM encapsulated within PEGDA hydrogel. The dhb-ECM/PEGDA hydrogel/AM did not impair GIN cellular viability and growth (for any of the four cell lines tested), relative to GIN cells cultured with PEGDA hydrogel/AM in the absence of dhb-ECM **(Figure 5. 6A-D)**. A comparison of culture conditions of all GIN cell lines grown in Advanced DMEM media or in PEGDA hydrogel/AM, was conducted to reveal if there is an impact on GIN cellular behaviour caused by the absence of serum in these culture conditions. The number of GIN5 cells was found to be significantly higher in PEGDA hydrogel/AM relative to GIN5 cultured in Advanced DMEM at Day 10 **(Figure 5. 6E)**. No significant difference in total number of cells was observed for GIN8 and GIN28 cells grown in Advanced DMEM or PEGDA hydrogel/AM **(Figure 5. 6F-G),** whereas the number of GIN31 cells were significantly higher in Advanced DMEM relative to PEGDA hydrogel/AM at Day 7 and Day 10 **(Figure 5. 6H).** This may be explained by the variable requirement of GIN cells to serum present in AM and reduced in Advanced DMEM. However, culturing GIN cells on dhb-ECM encapsulated with PEGDA hydrogel and using AM, revealed no significant difference in the number of cells in all four GIN cell lines, relative to serum-containing Advanced DMEM **(Figure 5. 6I-L)**. Culture conditions for Gliomasphere Matrices appear to compensate for the lack of serum and are likely a more physiologically-accurate growth response. All four GIN cells (GIN5, GIN8, GIN28, and GIN31) with passage number >20, exhibited a doubling time of approximately 3 days, which is a relatively faster growth rate compared to the 10 low passage (passage 4-6) primary GIN cells that were used in the Gliomasphere Matrix co-culture experiments (data not shown). This may indicate that the presence of serum (in the AM) combined with the presence of the dhb-ECM within the PEGDA hydrogel in the provided culture conditions, allowed a gradual transition from lag to log growth phases across all four GIN cell lines, relative to conditions where basement membrane or serum was absent. In summary, the dhb-ECM and PEGDA hydrogel did not have any detrimental effect on the viability nor propagation of GIN cells.

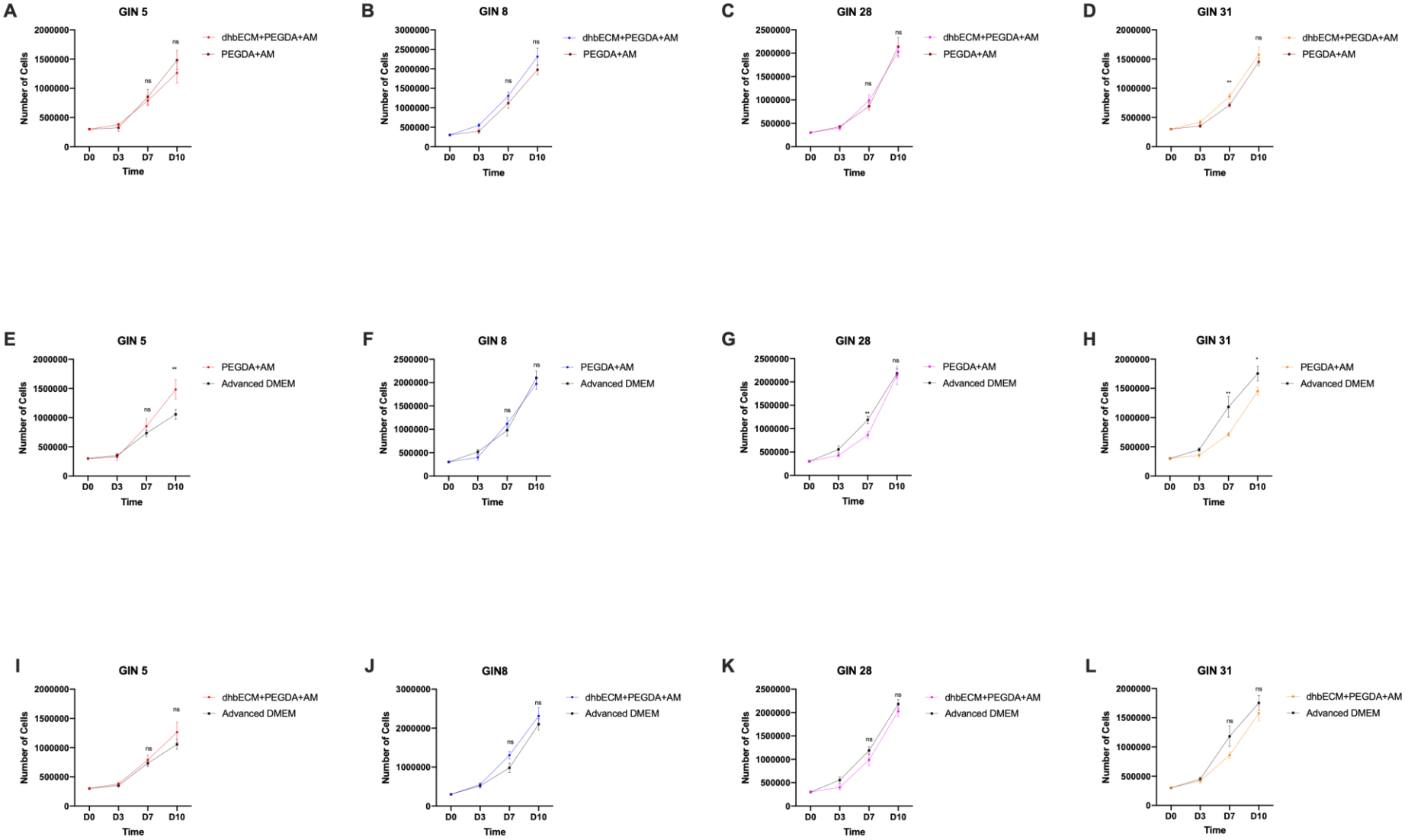

A
GIN 5
dhbECM+PEGDA+AM
PEGDA+AM
Number of Cells
Time
D0
D3
D7
D10
ns
B
GIN 8
C
GIN 28
D
GIN 31
**
E
GIN 5
PEGDA+AM
Advanced DMEM
F
GIN 8
G
GIN 28
H
GIN 31
*
I
GIN 5
J
GIN8
K
GIN 28
L
GIN 31

Figure 5. 6*. In-vitro* growth assays revealed that dhb-ECM within PEGDA hydrogel did not impair proliferation of four GIN cell lines. *Three culture conditions tested were: Advanced DMEM without ECM or PEGDA; PEGDA + astrocyte medium (AM); dhb-ECM + PEGDA + AM*. No significant difference in GIN cellular viability and growth was observed between dhb-ECM + PEGDA + AM and PEGDA + AM (A-D). The number of GIN5 cells was significantly higher in PEGDA+AM relative to Advanced DMEM at Day 10 (E), whereas no significant difference was observed for GIN8 and GIN28 (F-G). GIN31 cell numbers in contrast, were significantly higher in Advanced DMEM relative to PEGDA+AM at Day 7 and Day 10 (H). No significant difference in GIN cellular viability and growth was observed between dhb-ECM and Advanced DMEM (I-L).

5.3.6 Control of YFP-astrocyte location to ensure direct contact with GIN cells

Modelling the peri-tumoural astrocytic niche surrounding invasive glioma cells (similar to the invasive GBM margin), ideally requires a design that is devoid of excessive stress signals which may be induced by the outcompeting glioma cells. The rationale here is that our model aims to mimic the immediate molecular snapshot post-surgery or following GBM cellular infiltration into native brain tissue, whereby only micro-deposits of residual disease remain within infiltrative margin brain parenchyma. It is the molecular cross-talk that constitutes early events which we are modelling, rather than astrocytic interactions within the core region of the tumour mass which presumably recapitulates hypoxic and angiogenic microenvironments. Consequently, controlling the position of YFP-astrocytes to be located at the peripheral regions of the GIN cellular aggregates, was critical for our experimental design. A novel sequential cell seeding protocol, which involved seeding the YFP-astrocytes on top of pre-formed GIN aggregates, allowed the YFP-astrocytes to preferentially occupy the peripheral rim of Gliomasphere Matrices, which we termed 'phenotype I', and confirmed using a DeltaVision Ultra High resolution microscope **(Figure 5. 7)**. Alternatively, reversing the sequential seeding of GIN cells on top of pre-formed YFP-astrocytes aggregates or mixing both cell types and seeding them simultaneously, resulted in YFP-astrocytes preferentially occupying the central regions within Gliomasphere Matrices, termed 'phenotype II' **(Figure 5. 8)**. Notably, the YFP-astrocytes located at peripheral regions of Gliomasphere Matrices (phenotype I) displayed elongated astrocytic processes and a characteristic starry appearance **(Figure 5. 7)**. In contrast, centrally-located YFP-astrocytes within Gliomasphere Matrices (phenotype II) displayed less pronounced processes amid GIN cells **(Figure 5. 8)**. The establishment of direct physical contact between YFP-cells and GIN cells was confirmed in both Gliomasphere Matrix phenotype I **(Figure 5. 7)** and phenotype II **(Figure 5. 8),** using a Z-stacking technique obtained by the DeltaVision/confocal microscope. We also observed that the translated YFP was internalised by the surrounding non-fluorescent GIN cells for both Gliomasphere Matrices phenotypes **(Figure 5. 7)**, and **(Figure 5. 8)**. In summary, we created two multifaceted co-culture models that can be used for various applications, such as interrogation of molecular communication (see Chapter 6) in the central and peripheral regions of tumours.

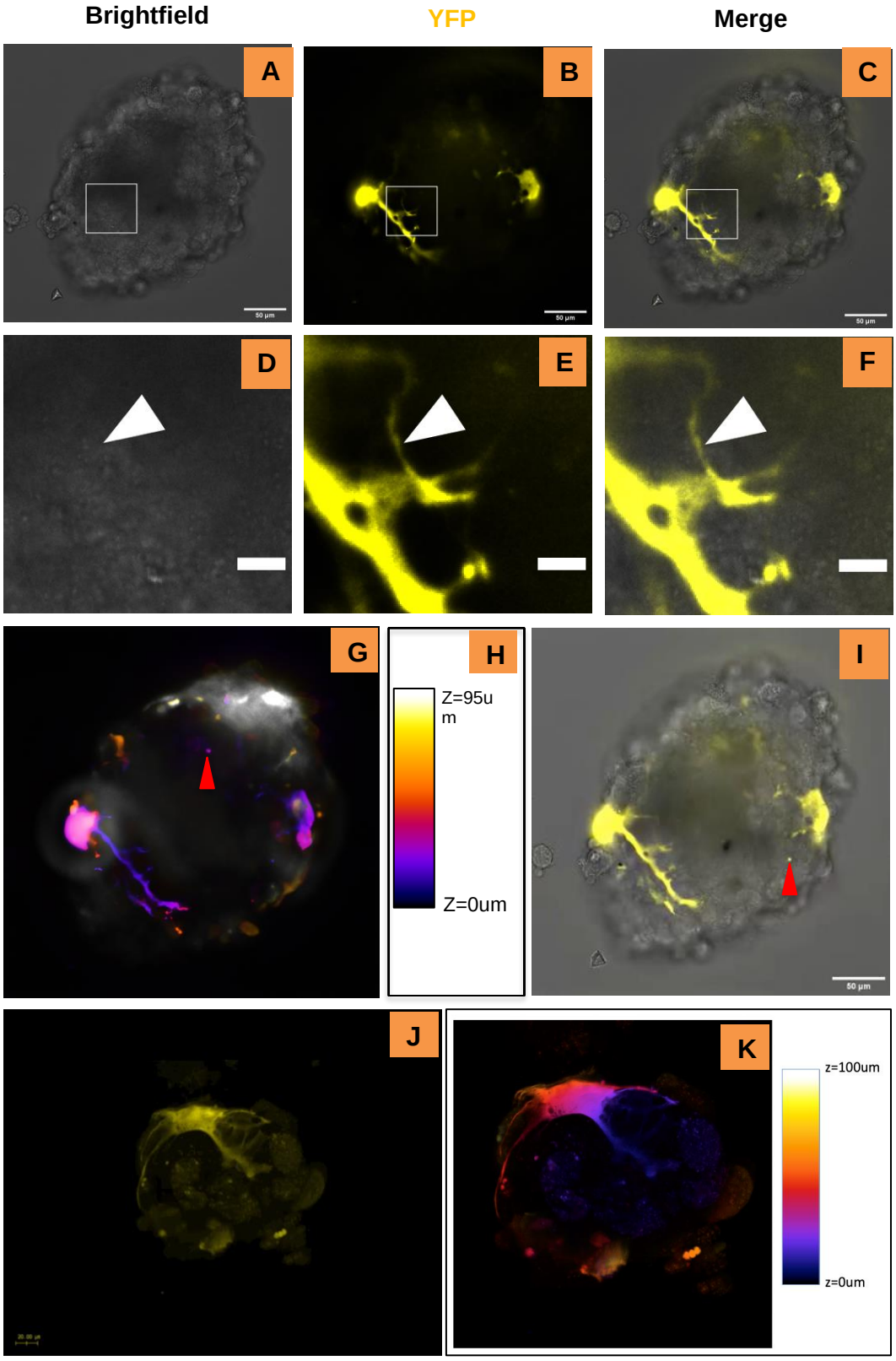

Brightfield
YFP
Merge
A
B
C
D
E
F
G
H
Z=95um
Z=0um
I
J
K
z=100um
z=0um

Figure 5. 7. Peri-tumoural astrocyte model using Gliomasphere Matrix 'pheotype I'. This model was used in the co-culture experiments at both time points (Day 7 and 10) of the study. The brightfield images (A and D) and YFP images (B and E) were merged in (C and F) respectively. YFP-astrocytes within Glioamsphere Matrices were imaged using maginifications of x20 (A-C) and x100 (D-F). YFP-astrocytes were confirmed to only occupy the peripheral rim of Glioamsphere Matrices as shown in the representative image (C). Furthermore, direct physical contact between YFP-astrocytes and the non-fluorscent neighbouring GIN cells was confirmed on low- (C) and high- (D-F) magnification, revealing characteristic astrocytic processes to emerge. YFP-particles were observed to be internalised by the surrounding non-fluorscent GIN cells, which indicates the intercellular communications between these two cell types (G and I, red arrows). DeltaVision microscopy was utlized to z-stackthe bottom 95µm (G-H) of the GIiomasphere Matrix shown in (A). All YFP signals were colour-coded by depth (G-H). YFP signal originatingnear the top (farthest from glass of dish) of the spheroid (C and G) is coloured white; YFP signal originating near the bottom of the spheroid is coloured black accorging to the colour scale (H). According to this scale, it was evident that YFP-astrocytes were colour-coded purple. This indicates that YFP-astrocytes were located within the first series of z-stacks of the Gliomasphere Matrix, representing the peripheral rim (G). YFP-astrocytes located at peripheral regions of Gliomasphere Matrices (phenotype I), display elongated astrocytic processes and the characteristic starry appearance of normal astrocytes, confirmed using DeltaVision microscopy (C, E, F and I) and confocal microscopy (J-K). *Scale bars for D, E, and F= 10 µm. All other scale bars = 50 µm*.

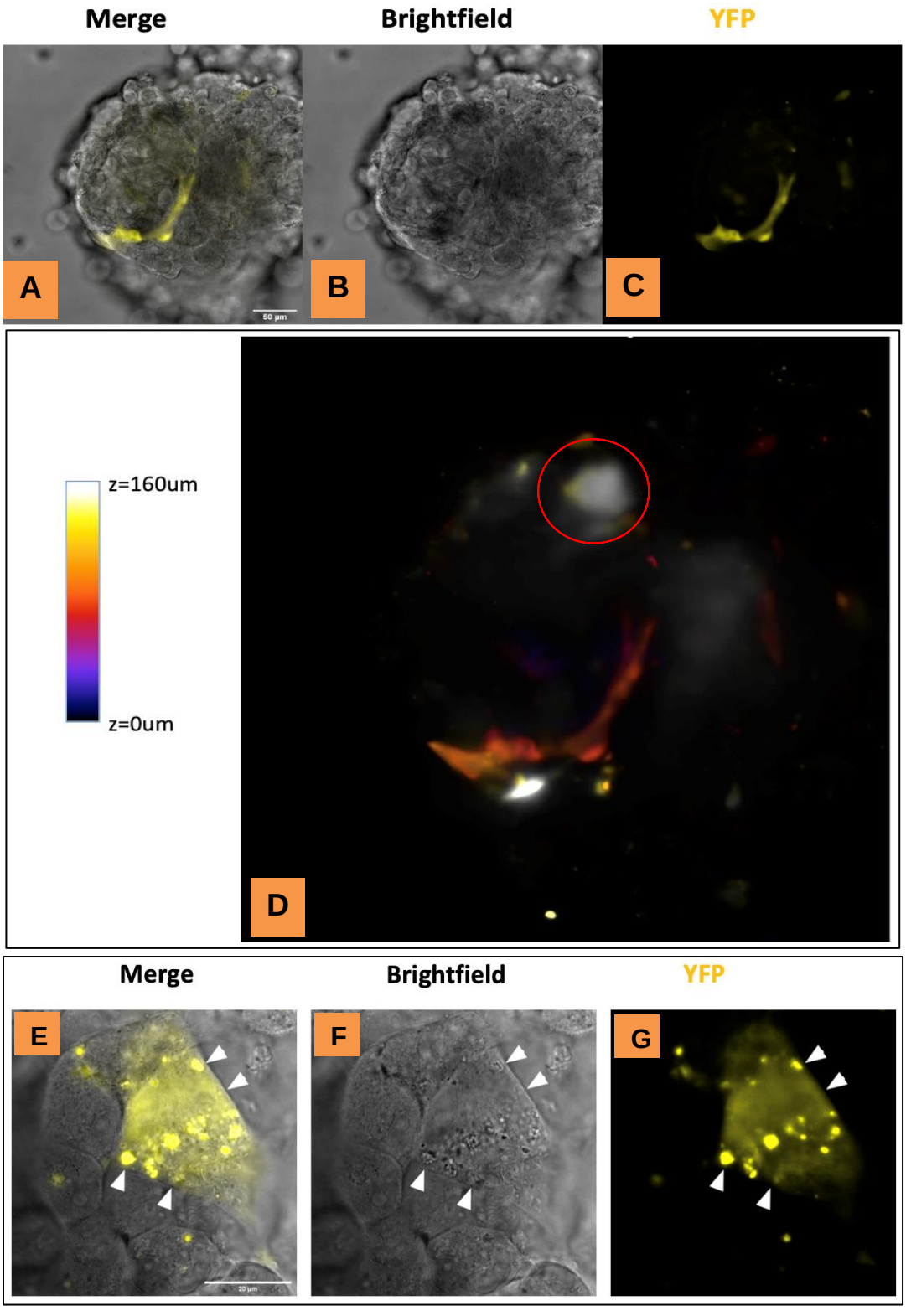

Merge
Brightfield
YFP
A
B
C
z=160um
z=0um
D
Merge
Brightfield
YFP
E
F
G

Figure 5. 8. Tumour-associated astrocyte model using Gliomasphere Matrix 'pheotype II'. This model was used for studies requiring astrocytes to be centrally locted within tumours. YFP-astrocytes within Gliomasphere Matrices were imaged at x20 magnification (A-C) and precisely controlled to be in the centre of the Glioamsphere matrices, as shown in the representative image. YFP-astrocytes within the red circle (coloured white due to being located at the top of the z-stack) (D) was magnified at x100 using DeltaVision microscopy (E-G). Direct physical contact between elongated YFP-astrocytic processes and non-fluorscent neighbouring GIN cells, can be clearly observed at low (x20) and high (x100) magnification (A-C, E-G). White arrowheads indicate the borders of the YFP-astrocytes amid the non-fluorscent GIN cells (E-G). Furthermore, centrally-located YFP-astrocytes within Gliomasphere Matrix phenotype II, appears to display shorter processes and are fewer in number (E-G), relative to YFP-astrocytes observed in Gliomasphere Matrix phenotype I **(Figure 5. 7)**. YFP-particles also appeared internalised by the surrounding non-fluorscent GIN cells, indicatingintercellular communications between these two cell types (E-G). DeltaVision microscopy was used to z-stack the bottom 160µm of the GIiomasphere Matrix shown in (A). All YFP signals were colour-coded by depth. YFP signal originating near the top (farthest from glass of dish) of the spheroid is coloured white;YFP signal originating from near the bottom of the spheroid is coloured black accorging to the colour scale (D). It is clear that YFP-astrocytes were colour-coded red, orange and white (D), indicating that YFP-astrocytes were located within the final series of z-stacks, near the middle of the Gliomasphere Matrix. This confirms a centralised location of YFP-astrocytes within the Gliomasphere Matrix (E). *scale bar in (A) = 50nm and applies to (A-C), whereas scale bar = 20nm in (E) and applies to (E-G)*.

5.4 Discussion

Historically, *in-vitro* models for investigating the molecular cross-talk between glioma cells and astrocytes are usually conducted using a Transwell system, which permits the study of paracrine signalling only; alternative models have sought to simulate direct *in-vivo* cell-to-cell contact in both 2D and 3D culture systems (Chekhonin *et al.*, 2018). The currently available co-culture models cannot fulfil the requirement of our study needs for several reasons. For example, astrocytes and glioma cells cannot be initially seeded at 100% confluence on 2D culture surfaces, to ensure sufficient and appropriate direct physical contact for all YFP-astrocytes to reveal their transcriptomic changes caused by the intercellular communication with GIN cells, due to the effect of contact inhibition that may bias the results by increasing death signals. Furthermore, 2D monolayers permit only an acute, short-term co-culture period, where astrocytes may struggle to survive amid the rapidly proliferating glioma cells. Similarly, the current practice of co-culturing these cell-types within 3D scaffolds usually involves resuspending co-cultured cells within a pre-set matrix, followed by setting the matrices (Koh *et al.*, 2018), or alternatively cells are seeded onto porous matrices (Sood *et al.*, 2019). However, these models do not ensure all astrocytes will be in direct physical contact with GBM cells. Furthermore, this may subject some of the cell colonies to hypoxic conditions, which may negatively impact transcriptome profiling. Our study required direct physical contact between peripherally located astrocytes and core GBM cells, to recapitulate of the infiltration of GBM cells through native human brain parenchyma. In particular, we aimed to unravel the genetic cross-talk between the infiltrative GBM cells and astrocytes located within the normal brain parenchyma. Indeed, many canonical malignant pathways that initiate, maintain or regulate gliomagenesis, such as Notch signalling and tumour tunnelling, depend on direct cell-to-cell communication (see Chapter 6).

In line with the general principles of good manufacturing practice, we have provided detailed protocols to create an accurate, highly reproducible and novel co-culture model (Gliomasphere Matrices), that ensures optimal direct contact between two different cell types and which is flexible for scaling up. In this context, we addressed important issues and technical challenges commonly experienced in current GBM co-culture models; for example, we have generated novel protocols to direct all cells types (GIN tumour cells and YFP-astrocytes) towards the microwells of the AggreWell™ plate to form multilayer spheroids, which ensure direct cell-to-cell physical contact for all YFP-astrocytes for which transcriptomes were profiled and analysed. Indeed, RNA sequencing analysis corroborated this hypothesis as the

mechanical receptor (in-trans) NOTCH1 was found to be upregulated in the YFP-astrocytes (discussed in chapter 6). Had YFP-astrocytes not been in direct contact with GIN cells, this key genetic trigger could have been obscured.

Unlike what has been suggested before (Horvath *et al.*, 2016), this brain-on-a-chip model has high-throughput properties. For example, this protocol allowed high-throughput analyses in a consistent and reproducible manner; i.e., 300 technical replicates were used for each experimental co-culture or control cultures, while maintaining cost-effectiveness as 300 Gliomasphere Matrices are generated in one large well of a 24-well Aggrewell™ plate. The consistency and reproducibility of spheroids has been clearly reflected in the multi-dimensional scaling analysis of RNA-sequencing data, which shows close proximity of samples in relation to independent datasets (discussed in chapter 6). To our knowledge, this original approach of incorporating dhb-ECM within defined PEGDA hydrogel, has been used for the first time in a neuro-oncological study to create a 3D structured native brain matrix. This multifaceted model can be tuned for other decellularised tissue matrices and therefore may have broad applicability to the oncology field in general.

Controlling the location of the astrocytes within Gliomasphere Matrices allowed the creation of two distinct phenotypes. Gliomasphere Matrix phenotype I was efficiently utilised in our study to recapitulate the niche of peri-tumoural astrocytes located within normal brain parenchyma. Any alterations in the transcriptome of the peripherally located YFP-astrocytes within this model are hypothesised to be induced directly by cell-to-cell physical contact (with GIN cells) and paracrine signalling, since this model has theoretically reduced possible detrimental effects caused by proliferating tumour cells such as hypoxia, pH changes, and physical pressure effects. However, Gliomasphere Matrix phenotype II was designed to recapitulate the microenvironment of tumour-associated astrocytes located within the centre of the tumour mass, amenable for future studies (to reveal hypoxic niche that may induce stem-features and/or angiogenesis) where astrocytes are co-cultured with GBM cells derived from the MRI contrast-enhanced core. Increasing or decreasing the number of cells (scaling) and spatial control of the cellular location shows the degree of precision tuning of this multifaceted model for various research purposes. genetic labelling of the astrocytes with YFP using CRISPR/Cas9 technology allowed propagating the co-culture experiment for ten days and hypothetically, could have been propagated for longer. The accuracy, reproducibility and scalability of this novel model may provide further innovative research avenues to study intercellular

communication and to identify new genetic targets which allow the design of novel therapeutic modalities for GBM tumour cells residing within the core and rim regions.

Many elegant and field-changing studies were reviewed in this chapter (section 5.1.1, and 5.1.2) to reveal the tremendous work and efforts that have been made, especially in the last 3 years, to create 2D and 3D models which recapitulate the phenotypes and genotypes of GBM tumours. This will likely allow future identification and targeting of the initiators/promoters involved in GBM tumourigenesis. To our best knowledge however, none of these studies have aimed to model peri-tumour human brain tissue surrounding the GBM tumour mass, infiltrated by GBM cells, to reveal the molecular cross-talk which occurs at the tumour invasive edge. This has resulted in a considerable scientific gap in the understanding of molecular events which lead to tumour recurrence after tumour debulking surgery. Furthermore, it has not yet known whether the astrocytes in the peri-tumour region can transform to acquire a malignant genotype. To corroborate this statement, Broekman *et al.* (2018) in an elegant review, focused on the intercellular communication within different GBM microenvironments, and has raised the question of "whether the communication between glioblastoma and the surrounding reactive astrocytes can promote the process of transformation and thereby feed the tumour with newly recruited oncogenic cells", which has yet to be addressed (Broekman *et al.*, 2018).

In addition to this scientific gap, the plateauing in efficacious treatment approaches and the dismal patient prognostic outcome, (which has only marginally improved by the use of tumour-treating fields), reveal the real life clinical practice challenge to treat GBM and its inevitable recurrence. To address this knowledge gap and aiming to reach a better patient prognostic outcome, many studies have been trying to achieve an appropriate human-specific GBM model which may allow future identification and therapeutic targeting of the major genetic drivers involved in GBM tumourigenesis.

Two elegant reviews exposed the lack of an appropriate model that provides an authentic representation of the genetic and phenotypic properties of human GBM (Chekhonin *et al.*, 2018; Broekman *et al.*, 2018). Whilst several sophisticated models have recently been created which better represent GBM tumourigenesis (Bian *et al.*, 2018; Ogawa *et al.*, 2018; Linkous *et al.*, 2019; Yi *et al.*, 2019; Jacob *et al.*, 2020), no study has appropriately attempted to study the intercellular communication at the peri-tumour infiltrative edge, which composed of predominant normal human brain

parenchymal cells and few residual GBM invasive cells. As stated in our hypothesis (described in the 'study rationale and aims'), modelling the invasive margin of GBM tumour and unravelling the complex molecular cross talk may lead to a better understanding of GBM recurrence.

Unlike the currently available GBM modelling methodologies, our model has the advantage of providing an efficient platform to assess molecular intercellular communication between both co-cultured cell types (astrocyte and WHO grade IV astrocytoma cells), which recapitulates early stages of GBM recurrence when few residual GBM cells are left post-operatively within predominantly normal human brain parenchyma.

For example, we explore the transcriptomic alterations in the normal YFP-labelled astrocytes induced by the co-cultured infiltrative GBM cells (Chapter 6); conversely the induced molecular changes in GBM cells can in principle also be assessed after co-culture with normal astrocytes in future studies, particularly as many studies have suggested an essential role for reactive astrocytes to promote GBM resistance. However, studying the molecular cross-talk in the cellular component representing the GBM-infiltrated normal peri-tumour region in other existing models will be scientifically and technically challenging for multiple reasons. For instance, genetically-engineered cerebral organoid studies typically introduce common oncogenic mutations into pluripotent stem cells or multipotent NSC prior to differentiation, which are then expressed in embryonal (neuroectodermal) tissue (Bian *et al.*, 2018; Ogawa *et al.*, 2018; Linkous *et al.*, 2019). This cellular compartment cannot be considered comparable to GBM-infiltrated normal brain parenchyma, which is comprised mainly of mature, differentiated cells. Furthermore, direct physical contact cannot be ensured to all non-malignant (neuroectodermal) cells in the genetically-engineered models, as oncogenic cells invaded these cerebral organoids in a random manner (Bian *et al.*, 2018; Ogawa *et al.*, 2018; Linkous *et al.*, 2019). Likewise, direct physical contact to all co-cultured cells cannot be achieved when their initial seeding occurs on top of a set porous 3D matrix (Sood *et al.*, 2019).

Methods used to generate current 3D GBM spheroid models include: i)low-attachment 96-well plates (Bian *et al.*, 2018; Ogawa *et al.*, 2018; Linkous *et al.*, 2019); ii) GBM cells cultured on Matrigel (Hubert *et al.*, 2016); iii) macroscopically-dissected GBM tissue propagated as organoids. These methods permit long-term culture (months up to a year) of 3D models to reach gross sizes. However, this raises

the question of whether or not the core region of these spheroids and organoids develop hypoxic and necrotic regions, which represent the conditions of the centre region of a primary GBM and unlikely to represent the tumour invasive margin post-surgery or at early invasion. This may resemble ‘Gliomasphere phenotype II’ in our model, which was designed to study the intercellular communications under conditions (↓O_2, ↓pH, ↑physical pressure) found in the primary GBM core, in contrast to ‘Gliomasphere phenotype I’ in our model, where YFP-astrocytes are located at the exterior edge of the spheroid to avoid such microenvironmental pressures.

Although recent GBM 3D spheroid and organoid models were intricately designed to unravel genetic aberrations in the GBM cell-of-origin which can initiate and progress the tumour, they are not appropriate candidates to study early stages of GBM invasion or recurrence (post-operatively), usually originating within 2-3cm of the peri-tumour region where terminally differentiated astrocytic cells predominate (Wallner *et al.*, 1989; Pennington *et al.*, 2006; Konishi *et al.*, 2012; Petrecca *et al.*, 2013; Lemée, Clavreul and Menei, 2015; Rapp *et al.*, 2017). Furthermore, the current models generally lack the presence of ECM to provide physiological niche cues for various normal cellular behaviours; where models have incorporated ECM, this is either derived from animal brains (Yi *et al.*, 2019) or sarcomas (Hubert *et al.*, 2016).

Several studies have attempted to model the 3D microenvironment of GBM via incorporating multicellular lineages within a bio-printed scaffold, reviewed in (Robertson *et al.*, 2019; Wolf *et al.*, 2019). However, such techniques are expensive and require special equipment/training and tools not necessarily available in all laboratories. Moreover, the throughput and scalability of methods used to generate these models have yet to be developed.

None of the models created so far, offer the capability of reproducible, high-throughput scale-up (i.e. 7200 mini-wells per plate), capable with our Gliomasphere Matrix model. This exposes how our multifaceted novel 3D model can provide an efficient platform to accurately assess the astrocyte-GBM intercellular communication at tumour core and invasive margin regions, while maintaining the general principles of good manufacturing practice, including reasonable costs and defined technical specifications.

Chapter (6)

Characterisation of astrocytic-GBM genetic communication at the invasive tumour edge

Chapter 6: Characterisation of astrocytic-GBM genetic communication at the invasive tumour edge

6.1 Introduction to RNA sequencing

Understanding the transcriptome is a powerful tool to interpret the functional entities of the genome, which in turn facilitates studying the molecular components within tissues and cells, or to assess developmental processes and disease conditions (Wang, Gerstein and Snyder, 2009). Transcriptome analysis can involve studying various species of RNAs such as mRNAs, microRNAs, non-coding RNAs, and small RNAs (microRNA and small interfering RNA). Several approaches were invented to study the transcriptome such as hybridisation-based methods (microarray) and nucleotide sequencing. Unlike hybridization methods, sequencing approaches directly reveal cDNA sequences (Wang, Gerstein and Snyder, 2009). Sequencing technology is not reliant on genomic sequences in most cases and has low background noise. Its applications allow a wider range to quantify gene expression level (>8000 fold), whereas the hybridization method has less dynamicity and can quantify gene expression level up to only a few hundred-fold (Wang, Gerstein and Snyder, 2009). Hybridization methods have limited capacity in detecting different transcript isoforms, as well as low distinguishing ability for allelic expression as compared to sequencing methods (Wang, Gerstein and Snyder, 2009). Moreover, some technical challenges, such as the requirement of high amounts of concentrated RNA and relatively higher costs for genome mapping, are more associated with the microarray method. Initially, cDNA or expressed sequence tag libraries were sequenced using Sanger sequencing. However, this approach has a relatively high cost, is low throughput, and requires higher RNA concentrations as compared to next generation sequencing (NGS). More importantly, it does not provide quantitative assessment for gene expression changes (Wang, Gerstein and Snyder, 2009).

NGS is a robust approach to quantify and profile transcriptomes. Currently it is widely used to assess the abundance and the relative changes gene expression (Han *et al.*, 2015) as it provides high throughput results. Although it is an expensive approach, its costs has been decreasing substantially over the past two decades, facilitated by the exponential advances in computational capability to analyse large datasets, which has allowed greater flexibility in performing various investigations in molecular biology in an accurate and comprehensive manner (Han *et al.*, 2015). In general, NGS includes fragmentation of cDNA or RNA to generate a library of small fragments

of cDNA from the long RNA segments. Small adaptor sequences are added to each small cDNA fragment. The generated segments are sequenced, and the resulting reads are aligned with a genomic or transcriptomic reference (Wang, Gerstein and Snyder, 2009). Many library preparation methods and sequencing platforms are currently available commercially (Ma *et al.*, 2019). Of these, Ultraplex (UPX) sequencing (Qiagen) has an innovative advantage during reverse transcription, which is the tagging of each cell with a sample ID and each RNA molecule with a **U**nique **M**olecular **I**ndex (UMI). This allows the processing of the library preparation steps in one tube, which reduces the labour and costs. More importantly, it prevents mixing errors of samples which usually occurs during laborious library preparation steps. Thus, we aimed to use this method, mainly to reveal the changes which occur in the astrocyte transcriptome after co-culturing them with each of ten different primary GBM cell lines derived from the infiltrative tumour margin of GBM tumours in our innovative Gliomasphere Matrix invasion model. The model aims to mimic gene expression changes within reactive astrocytes surrounding residual infiltrative GBM cells post-surgery, thus recapitulating human astrocytes genetic events which facilitate GBM recurrence. The disruptions of this cross-talk may thereby reveal new therapeutic avenues.

Hypothesis:

- Astrocytic co-culture with infiltrative GBM cells upon human decellularised brain ECM, induces transcriptomic changes and activation of signalling pathways, which are putative processes to facilitate and foster GBM recurrence.

6.2 Materials and methods for RNA sequencing

6.2.1. RNA Isolation

miRNeasy micro kit (Qiagen; 217084) was used to purify mRNA from the Fluorescence-activated cell (FAC)-sorted YFP-astrocytes after being co-cultured at the two time points (6 and 10 days), according to modified manufacturer guidelines below:

1. The YFP-astrocytes were directly sorted into 700µl QIAzol lysis reagent. This was a very critical step to preserve the integrity where mRNA was isolated from very low cell numbers. This is a very critical step to maintain the transcriptome picture obtained by the influence of the GBM cells.
2. The tube was flicked several times to ensure appropriate mixing and YFP-astrocytes were spun down at 500 x *g* for 5 minutes.
3. The sorted cells within the QIAzol were immediately frozen on dry ice and transferred into a -80°C freezer until further mRNA isolation.
4. Upon further isolation, the tubes were thawed on ice (approximately 20-30minutes) and cells were homogenised by vortexing for 1 minute.
5. The lysates were placed on the benchtop at room temperature (25 °C) for 5 minutes and 140µl chloroform was added to the tube containing the homogenate and re-capped safely. The tubes were shaken vigrously for 15 seconds.
6. The tubes containing the homogenate were placed on a benchtop for 2 minutes and then centrifuged at 12000 x *g* at 4°C. At this step, the samples were separated into three phases; the upper (colourless) aqueous phase (~350µl and contains the RNA), the white intermediate phase, and the lower (red) organic phase.
7. The aqueous phase was transferred into a fresh sterile microtube and 1.5 volumes (525µl) of 100% ethanol was added and mixed robustly by pipetting several times.
8. 700µl of the sample solution was loaded into an RNeasy MinElute spin column placed in a 2ml tube, and centrifuged at 12000 x *g* for 15 seconds at room temperature and the flow-through was discarded. This step was repeated for the reminder of the sample.
9. The DNA digestion step was performed in the same column using the RNase-free DNase set (Qiagen; catalogue number 79254) according to the following steps:

I. 350µl of Buffer RWT (prepared with isopropanol instead of ethanol) was loaded into the RNeasy MinElute spin column and centrifuged at 12000 x *g* for 15 seconds to wash the membrane. The flow-through was discarded.

II. DNase I solution for each sample reaction was prepared by the addition of 10µl of DNase I stock solution into 70µl Buffer RDD and mixed by gentle pipetting.

III. 80µl from the DNase I solution was loaded into the center of the membrane of an RNeasy MinElute spin column for each sample and incubated at benchtop (25 °C) for 15 minutes.

IV. 500µl of buffer RTW (prepared with isopropanol instead of ethanol) was applied onto the membrane of an RNeasy MinElute spin column and centrifuged at 12000 x *g* for 15 seconds with this step being repeated with the flow-through.

V. Continue to the next step.

10. 500µl of Buffer RPE was loaded onto the RNeasy MinElute spin column and centrifuged at 12000 x *g* for 15 seconds, with flow-through discarded.
11. 500µl of 80% ethanol was added onto the RNeasy MinElute spin column and centrifuged at 12000 x *g* for 2 minutes. The collection tube, with flow-through discarded.
12. The RNeasy MinElute spin column was placed in a new 2 ml tube and centrifuged at 23000 x *g* while the lid of the column was open to dry the membrane. Flow-through was discarded. At this stage, the tubes were labelled on side to anticipate any damage that may occur to columns' lids.
13. The RNeasy MinElute spin column was placed into a new 1.5ml tube and 10µl RNase-free water was directly applied into the center of the membrane of the column, followed by centrifugation at 23000 x *g* for 1 minute to elute RNA.

6.2.2. TapeStation

1. The RNA sample buffer was equilibrated at room temperature for 30 minutes before use.
2. Agilent 4200 TapeStaion controller software was launched and selected to assess RNA. The rest of the instruments were checked before starting the preparation of the tested samples.
3. The reagents were vortexed before use
4. 5µl of the RNA sample buffer and 1µl of purified sample RNA were pipetted into a tube strip (401428).
5. The tube was vortexed at 2000 rpm for 1 minute, and then spun down.
6. RNA samples were denatured by heating to 72°C for 3 minutes, then placed immediately on ice for 2 minutes, followed by a final brief centrifugation step to bring the evaporated liquids to the bottom of the tubes strip.
7. Samples were loaded into Agilent 4200 TapeStaion and an electronic ladder option was selected for the analysis.

6.2.3. RNA library preparation, sequencing, and data analysis

Library preparation was accomplished by using a QIA UPX 3' Transcriptome Kit (Qiagen). Approximately 170pg RNA from each sample was purified and reverse transcribed into cDNA of the NGS libraries. Each cell was tagged with a unique ID. During reverse transcription, each UMI was individually tagged to a single RNA molecule. The RNA was then converted into cDNA that ultimately amplified using PCR. During PCR to amplify the cDNA, the indices were added, and samples were purified. Quality control of the generated Libraries was assessed using TapeStation 4200 (Agilent) or Agilent Bioanalyzer. The libraries were pooled in equimolar ratios, quantified using qPCR and sequenced using NextSeq500 sequencer according to the manufacturer instructions. Using bcl2fastq software (Illumina), the FASTQ files were generated by de-multiplexing the raw data. The FASTQC tool allowed the assessment of the quality of FASTQ files. The cells were de-multiplexed by the extraction of the UNIs and cell index sequences from R2 reads. The splice aware aligner STAR software was used to align the reads to a reference human genome (GRCh38) (Dobin *et al.*, 2013). Next, the aligned reads of each gene regions were annotated and counted across different cell indices. Qiagen provided analyses of differentially expressed genes (DEG) using the DESeq2 bio-conductor package (Love, Huber and Anders, 2014). However, we have additionally and independently conducted a thorough, in-house, analysis using the EdgeR computational and statistical package which has superior accuracy when less than 12 biological replicates are used (Schurch *et al.*, 2016). The results were further validated against a higher-depth read RNA sequencing dataset from the primary GBM invasive margin of 10 patients (Smith *et al.*, 2020). In this related study from our laboratory, the tissues from the invasive margin of 10 GBM patients were dissociated and isolated by FACS using 5-ALA fluorescence, a metabolic substrate that facilitates the guidance of GBM resection during surgery as it is specifically taken up by GBM cells (Stummer *et al.*, 2006; Kaneko and Kaneko, 2016). The 10 GIN cell lines were derived from 10 distinct primary tumours with no neoadjuvant treatment prior to surgery and were wild-type for both IDH-1 and ATRX. The dissociated tumour samples were sorted into 5-ALA positive (GBM) and 5-ALA negative cells. The 5-ALA negative group is predominantly composed of tumour-associated astrocytes (TAA), with likely minor populations of vascular-related and inflammatory cells. The 5-ALA negative cells were the focus of interest as they represent populations of cells that surround the infiltrative glioma cells at the invasive margin of the tumour **(Figure 6. 1)**. We further validated genes of interest against TCGA publicly accessible dataset. TCGA enabled comparisons of genes of interest from our study, against the

transcriptomes of a comprehensive panel of somatic tumours including high- and low-grade glioma (approximately 18500 cases). It also facilitates the comparison between low- and HGG as compared to non-malignant/normal brain. This thorough analysis was performed using the TCGA bioinformatics tool; Xena software (UCSC, University of California, Santa Cruz).

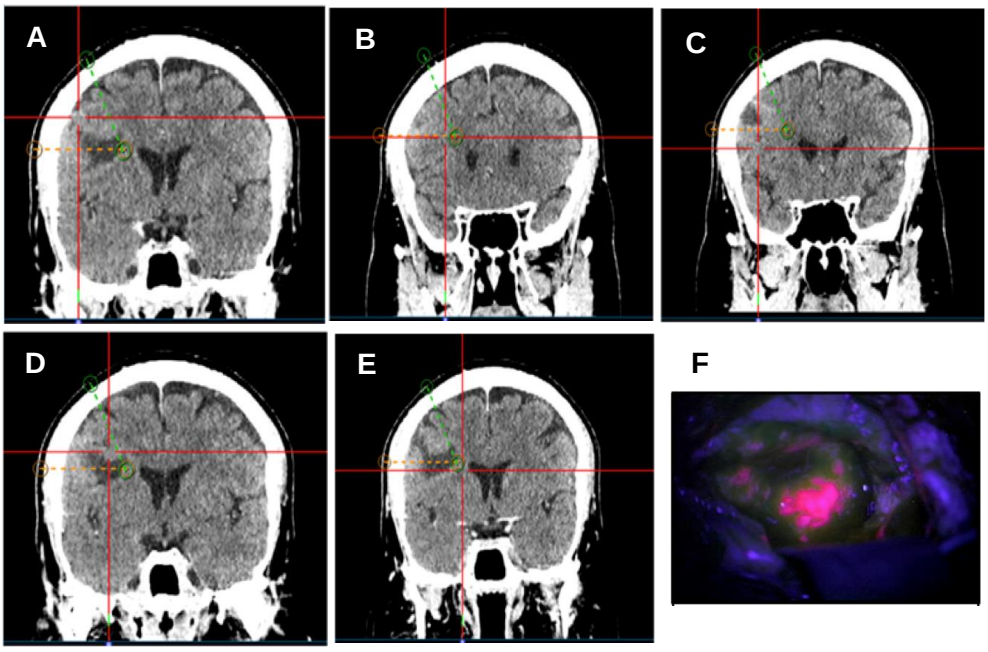


Figure 6. 1. Intra-operative identification of the invasive margin using Stereotactic MRI. The StealthStation™ neuro-navigation tool was used to identify multiple spatially- and morphologically-distinct intra-tumour GBM regions during surgery. The exact locations of each region are from a representative GBM case are indicated by the red cursor. Different regions of GBM are shown; (A), (B), and(C) regions are the superficial-, anterior-, and inferior-enhancement regions respectively. The contrast-enhanced core area is indicated as (D), whereas the invasive GBM margin is represented by (E). 5ALA is converted to a pink fluorescence-emitting metabolic product within GBM cells based on high activation of the heme synthesis pathway; this surgical adjunct enables fluorescence-guided resection of the invasive margin. (F). *Adapted from PhD thesis (James Wood, 2019)*

6.3. Results of UPX RNA-sequencing

6.3.1. Confirming the integrity and concentration of mRNA isolated from the co-cultured astrocytes.

The RNA integrity and concentration were measured from astrocytes cultured alone and astrocytes isolated upon co-culture with each of 10 distinct GIN cell lines (Table 6. 1) and **(Figure 6. 2)**. RINe value of most of the samples was above 8 except few samples which showed RINe value ranging between 6-7. However, the accuracy of these results was questionable as TapeStation 4200 (Agilent) is not accurate for concentrations below 100pg/µl. The concentration of the RNA was standardised for all samples to a maximum possible of 170pg/µl except for a few samples which had lower concentrations. The total amount of RNA provided to Qiagen for RNA sequencing was approximately 1.2ng for all samples. This was required to approximately obtain more than 7000 detectable genes **(Figure 6. 3)**.

Table 6. 1.The concentration and integrity of mRNA extracted from astrocytes prior to library preparation and RNA sequencing. *YFP_control_1.1-1.3-astrocytes alone after 7 days culture; CO_58.1- CO_40.1-astrocytes co-culture with each of 10 GIN lines for 6 days; YFP_control_2.1-2.3-astrocytes alone after 10 days culture; CO_58.2-CO_40.2-astrocytes co-culture with each of 10 GIN lines for 10 days;*

Sample Description	RINe	28S/18S (Area)	Conc. [pg/µl]
YFP control_1.1	10.0	2.5	175
YFP control_1.2	8.7	2.5	346
YFP control_1.3	8.9	2.4	272
CO_58_1	9.2	3.1	341
CO_41_1	9.5	2.9	161
CO_46_1	8.9	2.9	432
CO_52_1	6.2	-	87.2
CO_55_1	8.8	2.7	417
CO_39_1	9.6	3.2	1360
CO_37_1	-	-	57.9
CO_28_1	9.7	3.2	1320
CO_38_1	9.4	3.1	700
CO_40_1	9.5	3.0	399
YFP_CONTROL_2.1	9.9	3.2	79.0
YFP_CONTROL_2.2	6.7	1.5	199
YFP_CONTROL_2.3	8.4	2.5	563
CO_58_2	9.4	3.0	377
CO_41_2	9.4	3.2	616
CO_46_2	9.5	3.5	392
CO_52_2	9.3	3.0	1240
CO_55_2	8.4	2.2	167
CO_39_2	9.5	3.2	478
CO_37_2	8.8	3.1	315
CO_28_2	10.0	3.5	2910
CO_38_2	9.4	3.2	183
CO_40_2	-	-	56.7

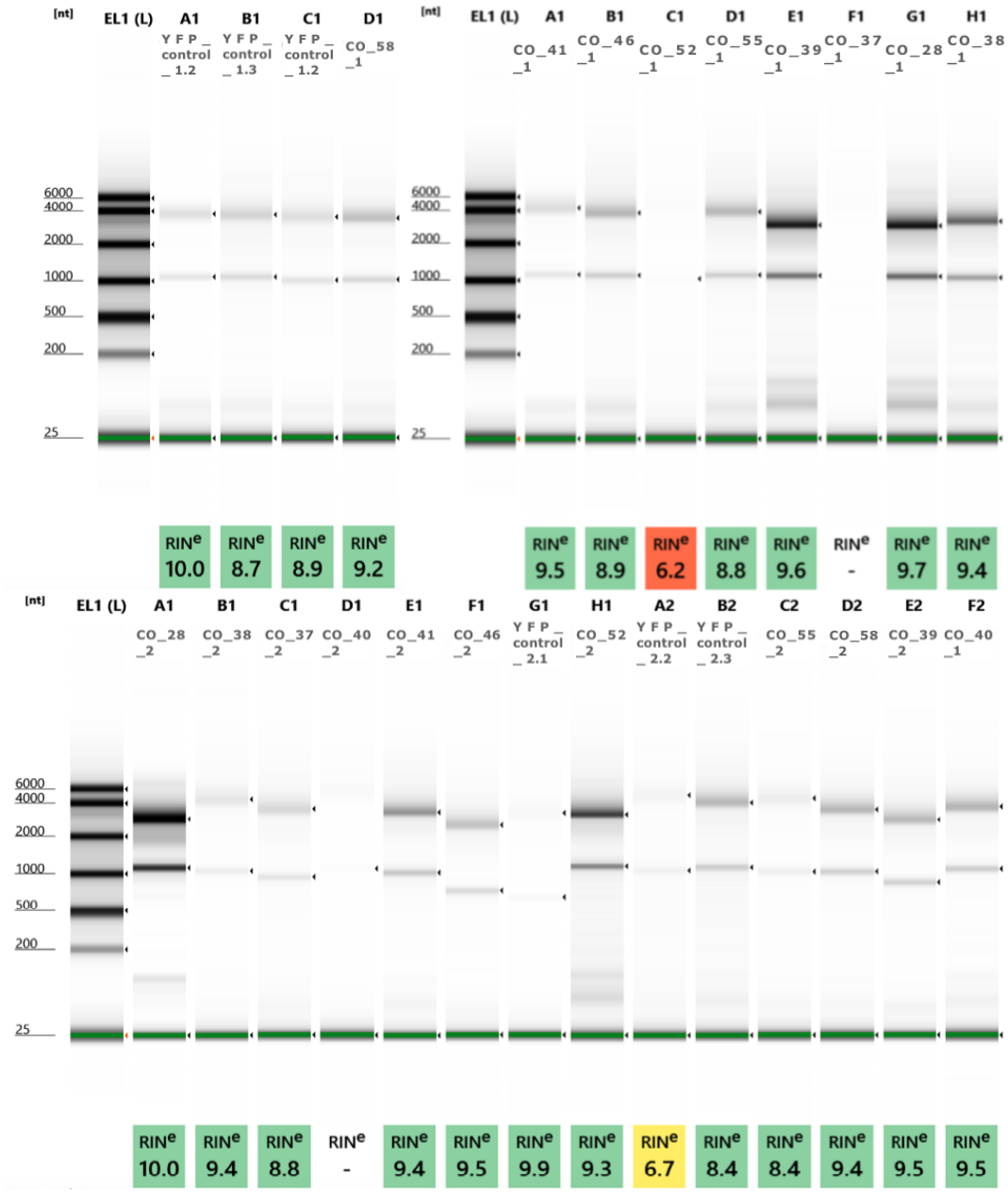


Figure 6. 2. Screening RNA concentration and integrity across all experimental samples. Generally, the RNA did not exhibit any smearing, which is indicative of RNA integrity preservation. The RNA integrity was suitable library preparation as the RINe values were generally above 8 except four samples. Two (YFP_control_2.2, and CO_52_1) of these four samples had RINe value of 6.7 and 6.2 respectively, whereas the CO_40_2 and CO_37_1 were not detectable.

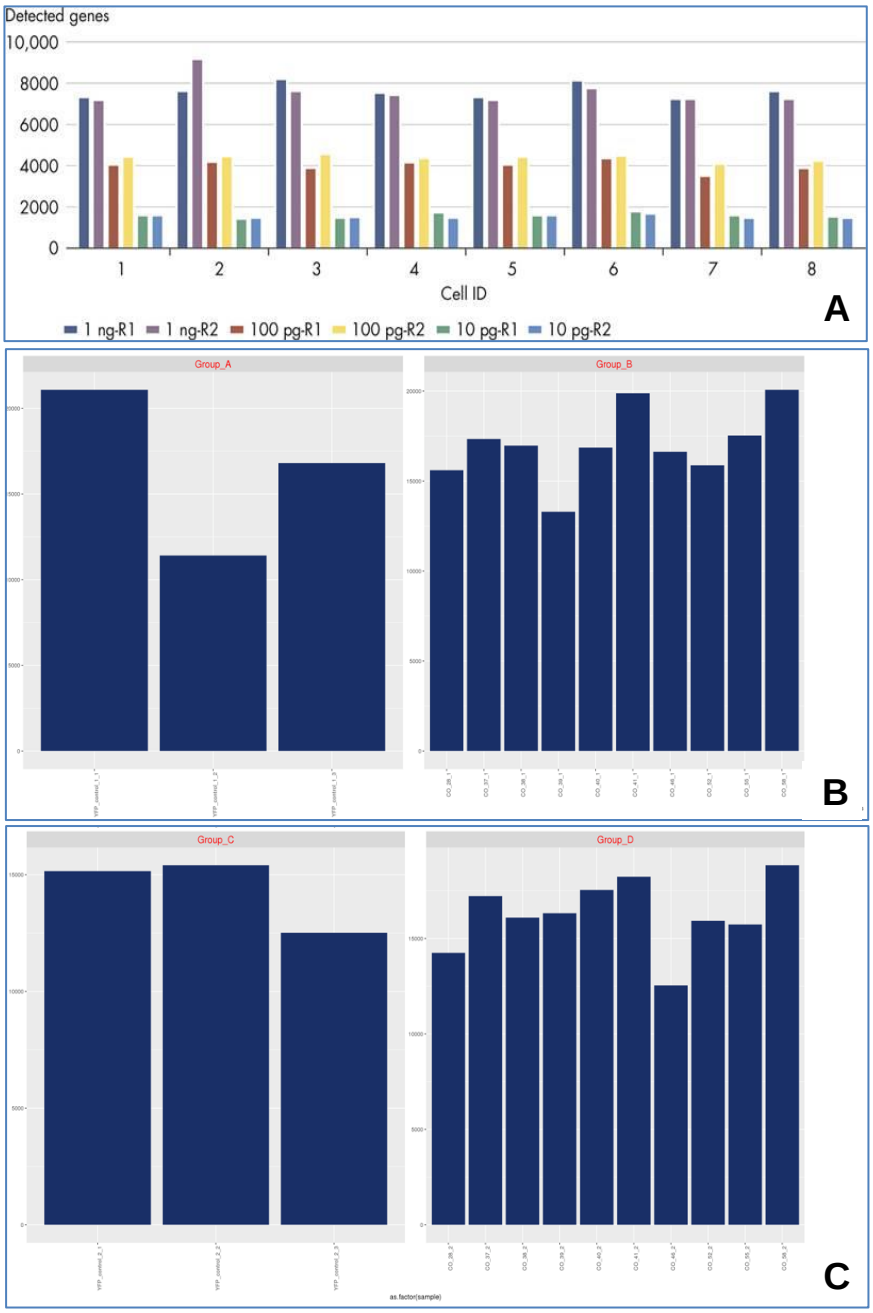


Figure 6. 3. RNA concentration influences the number of the detectable genes of UPX sequencing. The figure (A) was generated by Qiagen R&D which shows the variability of detectable genes in eight samples depending on the RNA concentration. Despite the low yield of the RNA concentration extracted from small numbers of cells after FACS re-isolation from the astrocyte-GIN co-culture models, the number of detectable genes for all samples was not less than 11000 genes across both time points (B, and C). This allowed thorough analysis of DEG and pathway analysis between tested (CO_X_1 or 2) and control (YFP_control_X) samples. Group_A and *Group_B represent the first time point of the experiment (day 6) respectively, whereas Group_C and Group_D are the number of the detectable genes in the second time point (day 10).* Group_A and Group_C are controls (monocultured astrocytes) for their respective astrocytes-GIN co-cultures (Group_B and Group_D).

6.3.2. MDS of astrocytic genome-wide gene expression upon Gliomasphere Matrix.

We first assessed the physiological relevance of our Gliomasphere Matrices by validating wholistic transcriptomic profiles of *in-vitro* experimental samples (YFP-astrocyte controls and astrocytes co-cultured with GIN cells and then isolated) against surgically resected and FACS-isolated 5-ALA positive (invasive GBM cells) and 5-ALA negative (reactive astrocytes within brain parenchyma harbouring invasive GBM cells) specimens by MDS using the EdgeR computational tool. Significant variance (more than 47%) was observed between both sets of samples **(Figure 6. 4A)**. All twenty co-cultured astrocytes (with each of 10 GIN cell lines and at two time-points) and six astrocyte-only controls, were clustered more closely compared to the 5-ALA negative and positive patient specimens **(Figure 6. 4A)**. This reflects the reproducibility and consistency of the ultra-high throughput methods and biological conditions used to create our Gliomaspehre Matrix model. Genome-wide gene expression of the six YFP-astrocyte controls from both time points were compared to 5-ALA negative and positive patient specimens, revealing a slight shift towards the 5-ALA negative tissue samples (as compared to the astrocyte co-cultures) **(Figure 6. 4B)**, whereas astrocytes isolated from co-cultures with GIN cells are cluster more closely to 5-ALA positive tissue samples **(Figure 6. 4C)**. The YFP-astrocyte control group have variances of 43% and 61% from 5-ALA negative and positive groups respectively, whereas the co-cultured astrocyte group have variances of 50% and 55% from 5-ALA negative and positive groups respectively. This strongly indicates that astrocytes cultures alone exhibit a transcriptomic profile similar to 5-ALA negative GBM tissue, whereas astrocytes co-cultured with GIN cells exhibit a transcriptomic shift towards a gene expression profile more comparable to 5-ALA positive GBM tissue. MDS of the 5-ALA negative and positive patient specimens shows variance of about 38% **(Figure 6. 5A)**. The MDS of all *in-vitro* experimental samples at day six shows 40% variance **(Figure 6. 5B)**, whereas it is 22% at day ten **(Figure 6. 5C)**. Our In-house MDS analysis comparing all 20 co-cultured astrocyte samples against all 6 YFP-controls, showed a clear separation with variance of approximately 75% **(Figure 6. 6)**. Qiagen Company performed PCA with less details on all samples using the DESeq2 transformed counts of all genes **(Figure 8. 5)**.

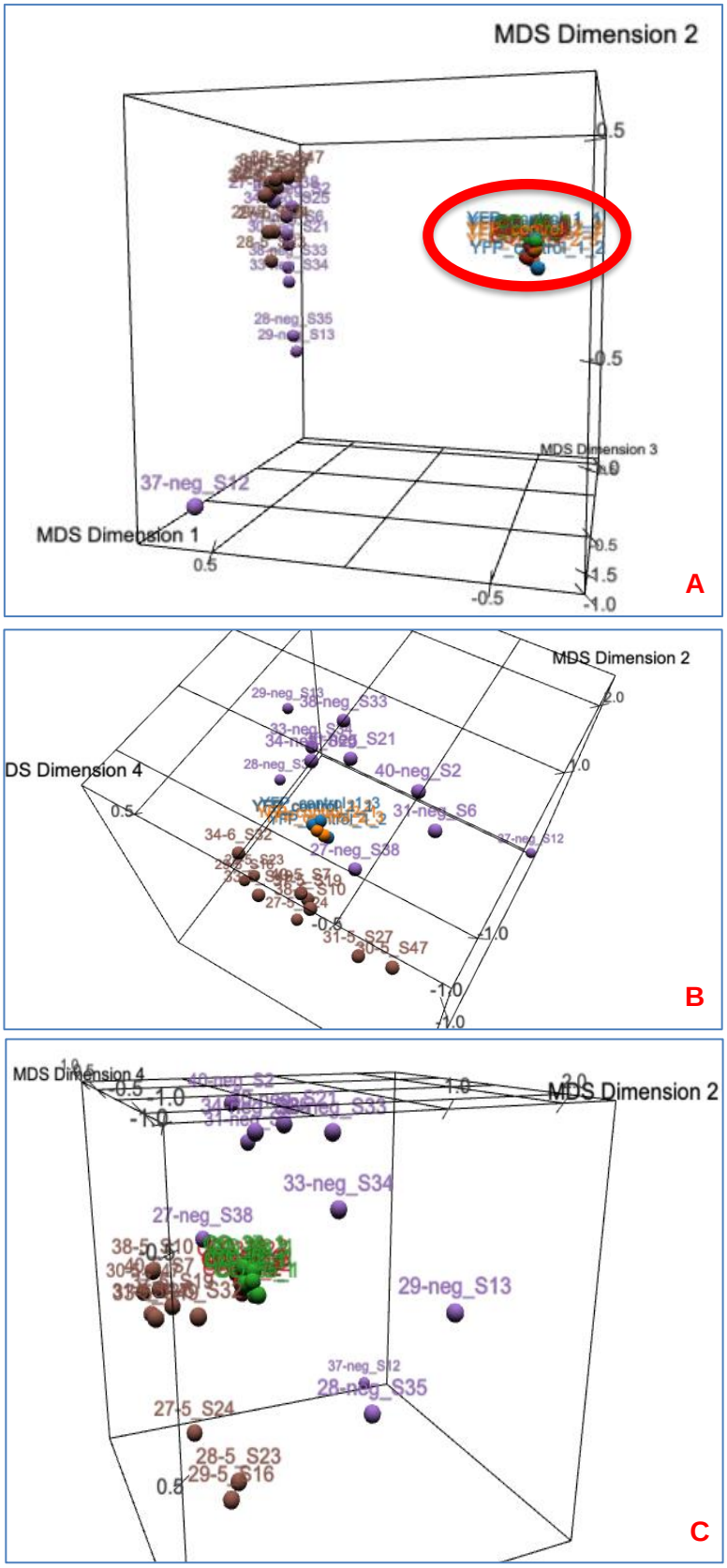


Figure 6. 4. MDS analysis comparing *in-vitro* astrocytes (controls and co-culture) to the surgically resected and FACS-isolated 5-ALA (positive and negative) tissue specimens. The *in-vitro* samples show clear separation from patient samples with a variance of more than 47% (A). The superimposition of all experimental samples (red circled) is evident, which reflects the consistency and reproducibility of the biological and technical conditions within Gliomasphere Matrices. Comparing the astrocytes-only controls (blue and orange) to the 5-ALA negative tumour-associated astrocytes (purple) and positive (invasive GBM cells; brown) patient samples shows *in-vitro* experimental controls (blue and orange) cluster more closely to the 5-ALA negative tumour-associated astrocyte (purple) tissue samples (B), whereas the co-cultured astrocytes isolated from co-culture with GIN cells (green and red) cluster more closely to the 5-ALA positive GBM cells (brown) (C). *MDS, multidimensional scaling*.

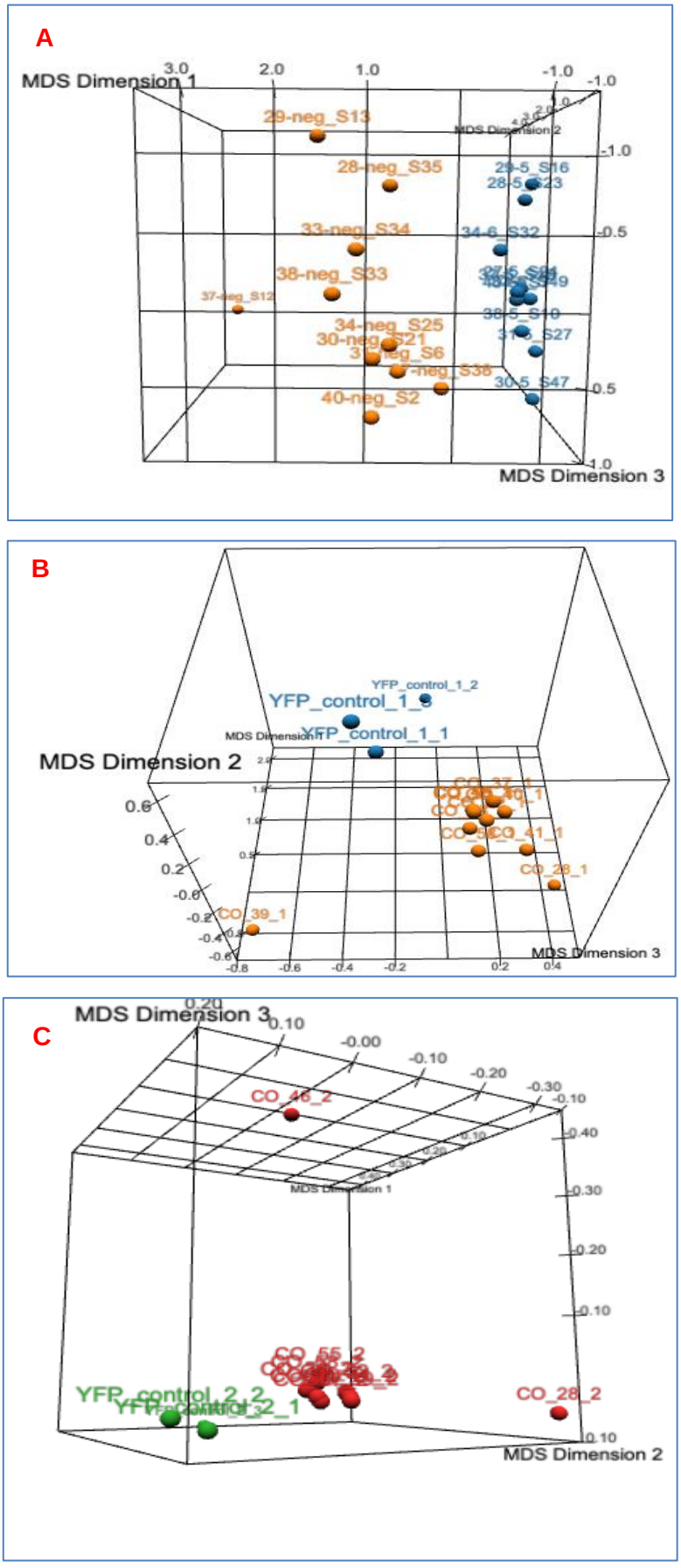


Figure 6. 5. MDS analyses of 5-ALA patient tumour samples in addition to the *in-vitro* samples (controls and co-culture astrocytes) at two different time points shown separately. 5-ALA positive (invasive GBM cells; blue) and 5-ALA negative (tumour-associated astrocytes; orange) shows clear separation with regards to transcriptomic profile with 45% variance distinct (A). The co-cultured astrocytes were compared to the YFP-astrocyte controls at two different points; at six days (B) and at ten days (C) with variances of 40% and 22% respectively. The YFP-astrocyte controls are shown in blue and green in the first (B) and second (C) time points respectively. Likewise, the co-cultured astrocytes are coloured with orange and red in the first (B) and second (C) time points respectively. *MDS, multidimensional scaling*.

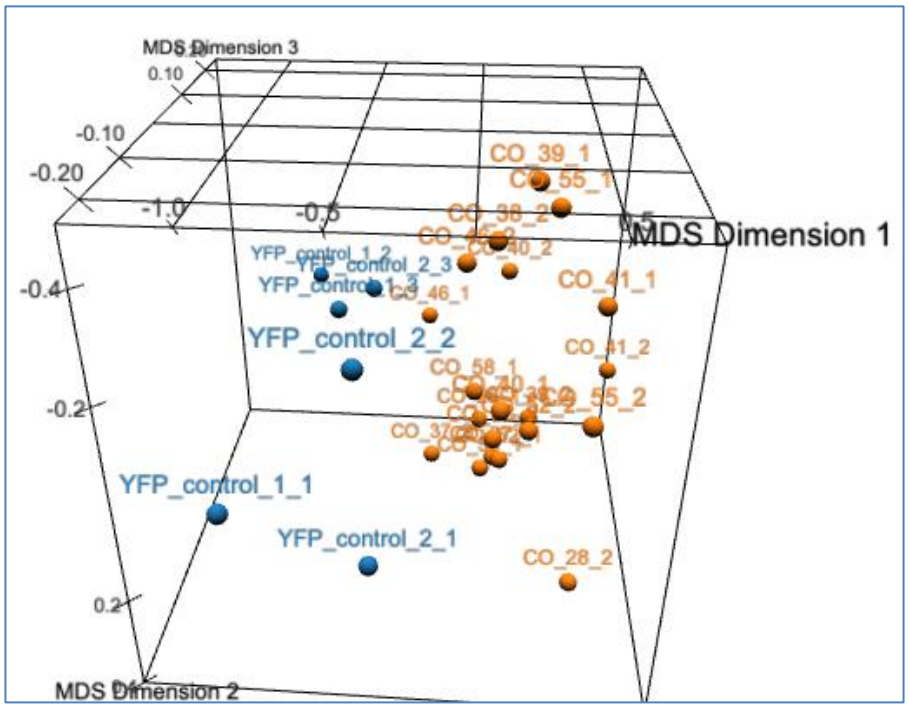


Figure 6. 6. In-house MDS analysis of all *in-vitro* samples included across both time points. The figure shows the significant variance (75%) and clear separation between 20 co-cultured astrocyte samples (orange) and 6 astrocyte-only controls group (blue) over two time points. *MDS, multidimensional scaling*.

6.3.3. UPX 3' RNA sequencing analysis reveals altered astrocytic gene expression induced by interaction with infiltrative GBM cells within Gliomasphere Matrix models.

Transcriptome profiling and pathway analysis of ten co-cultured YFP-astrocyte/GIN (i.e. each of ten distinct GIN lines) samples were compared to three YFP-astrocyte monoculture control samples at two time points; 6 and 10 days. Furthermore, these results were validated with high- depth read RNA-sequencing data (previously generated in our laboratory) of tumour-associated astrocytes that were surgically obtained from ten different primary GBMs using 5-ALA guidance and FACS isolation of 5-ALA positive (purified invasive GBM cells) and 5-ALA negative (tumour-associated astrocytes) populations. There were common trends and similarities in the differentially expressed genes (DEG) and molecular pathways between the two distinct data sets, despite different computational packages (DESeq2 and EdgeR) used for the analysis, different read-depth of the RNA-sequencing data and different operators who analysed the data. We used Reactome (https://reactome.org) and gene set enrichment analysis (GSEA) (https://www.gsea-msigdb.org/gsea/index.jsp) tools to reveal gene enrichment for specific molecular pathways. GSEA clinical annotation of the DEG of YFP-astrocytes, isolated upon co-culture with each of ten GIN lines after 10 days, significantly enriched for events which occur in CNS tumours (GBM), as well as stimulated immune responses (Table 6. 2). RNA-sequencing data analysis conducted by Qiagen includes three comparisons; one for each experimental time point (Day 6 and Day 10), and a final comparison of all 20 co-cultured astrocyte samples and all 6 astrocyte monoculture controls at both time points.

Table 6. 2. GESA clinical annotations of events based on the DEG expressed by astrocytes after co-culturing them with primary GBM cell lines for 10 days.

Clinical annotation	Category	P-value	Hits	Hits(%)	Module hits in category	Arrays in annotation	Arrays
Prostate (Prostate cancer*)	Prostate cancer*	3.2e-18	38	24.5	155	101	1945
Hematologic cancer and cell line (Stimulated immune*)	Stimulated immune*	1.3e-16	26	17.6	147	53	1945
Hematologic samples and cell lines (Stimulated immune*)	Stimulated immune*	1.3e-16	26	17.6	147	53	1945
Macrophages (Stimulated immune*)	Stimulated immune*	1.3e-16	26	17.6	147	53	1945
Monocytes (Stimulated immune*)	Stimulated immune*	1.3e-16	26	17.6	147	53	1945
CNS cancer or cell line (Neuro tumors*)	Neuro tumors*	6.0e-10	25	16.1	155	81	1945
CNS tumor (Neuro tumors*)	Neuro tumors*	6.0e-10	25	16.1	155	81	1945
CNS tissue, cancer or cell line (Neuro tumors*)	Neuro tumors*	1.8e-09	25	16.1	155	85	1945
Cancer and cell line (Neuro tumors*)	Neuro tumors*	2.4e-09	25	16.1	155	86	1945
Cancer (Neuro tumors*)	Neuro tumors*	2.4e-09	25	16.1	155	86	1945
Prostate (Prostate cancer*)	Prostate cancer*	6.1e-09	26	17.6	147	101	1945
CNS cancer or cell line (Various tumors)	Various tumors	1.2e-08	11	57.8	19	16	154
CNS tumor (Various tumors)	Various tumors	1.2e-08	11	57.8	19	16	154
Hematologic cancer and cell line (Stimulated immune*)	Stimulated immune*	3.6e-08	18	11.6	155	53	1945
Hematologic samples and cell lines (Stimulated immune*)	Stimulated immune*	3.6e-08	18	11.6	155	53	1945
Macrophages (Stimulated immune*)	Stimulated immune*	3.6e-08	18	11.6	155	53	1945
Monocytes (Stimulated immune*)	Stimulated immune*	3.6e-08	18	11.6	155	53	1945
CNS tissue, cancer or cell line (Various tumors)	Various tumors	4.0e-08	12	63.1	19	21	154
Malignant glioblastoma (Various tumors)	Various tumors	9.7e-08	8	42.1	19	9	154
Adenocarcinoma (Prostate cancer)	Prostate cancer	4.3e-07	24	92.3	26	52	102
Cancer and cell line (Prostate cancer)	Prostate cancer	4.3e-07	24	92.3	26	52	102
Cancer (Prostate cancer)	Prostate cancer	4.3e-07	24	92.3	26	52	102
Prostate cancer or cell line (Prostate cancer)	Prostate cancer	4.3e-07	24	92.3	26	52	102
Prostate cancer (Prostate cancer)	Prostate cancer	4.3e-07	24	92.3	26	52	102
Cancer and cell line (Liver cancer)	Liver cancer	2.5e-06	24	100	24	126	207
Atypical teratoid/rhabdoid tumour - CNS and other origin (Neuro tumors)	Neuro tumors	4.6e-06	7	63.6	11	10	90
Breast tissue or cancer (NCI60)	NCI60	9.0e-05	3	60	5	4	139
Female hormonal tissue or cancer (NCI60)	NCI60	9.0e-05	3	60	5	4	139
Breast tissue, cancer or cell line (NCI60)	NCI60	0.0004	5	100	5	31	139

We chose to compute the significance values of DEG using both volcano and MA plots. Volcano plots reveal statistical significance (p-values) versus magnitude of change (fold change); this is complemented by MA plots which visualises the differences in gene expression between control and experimental samples, by transforming data onto M (log ratio) and A (mean) scales. Comparing the co-cultured astrocytes at two time points (6 and 10 days) to their corresponding controls, using DESeq2, resulted in DEG lists and pathways and are depicted in the volcano- **(Figure 6. 7A, and Figure 6. 7B)** and the MA-plots **(Figure 6. 8A, and Figure 6. 8B)**. Note, DEG shown in **Figures 6.8 and 6.9** represent the combined significant genes identified from each distinct astrocyte-GIN co-culture, relative to astrocyte-only controls. Furthermore, the stringent comparison of all 20 co-cultured astrocyte samples collectively against all six controls, at both time points (6, and 10 days), has resulted in the identification of the *c1orf61* gene as differentially upregulated, strongly suggesting the importance of *c1orf61* induction in reactive human astrocytes in response to molecular cross-talk with invasive GBM cells **(Figure 6. 7C, and Figure 6. 8C).** This comparison has also resulted in DEG and molecular pathways. The differential gene expression for all analyses was calculated to have statistical significance (*p-value* <0.05) of at least-2 fold change or more as shown in the volcano- **(Figure 6. 7)** and MA-plots **(Figure 6. 8)**.

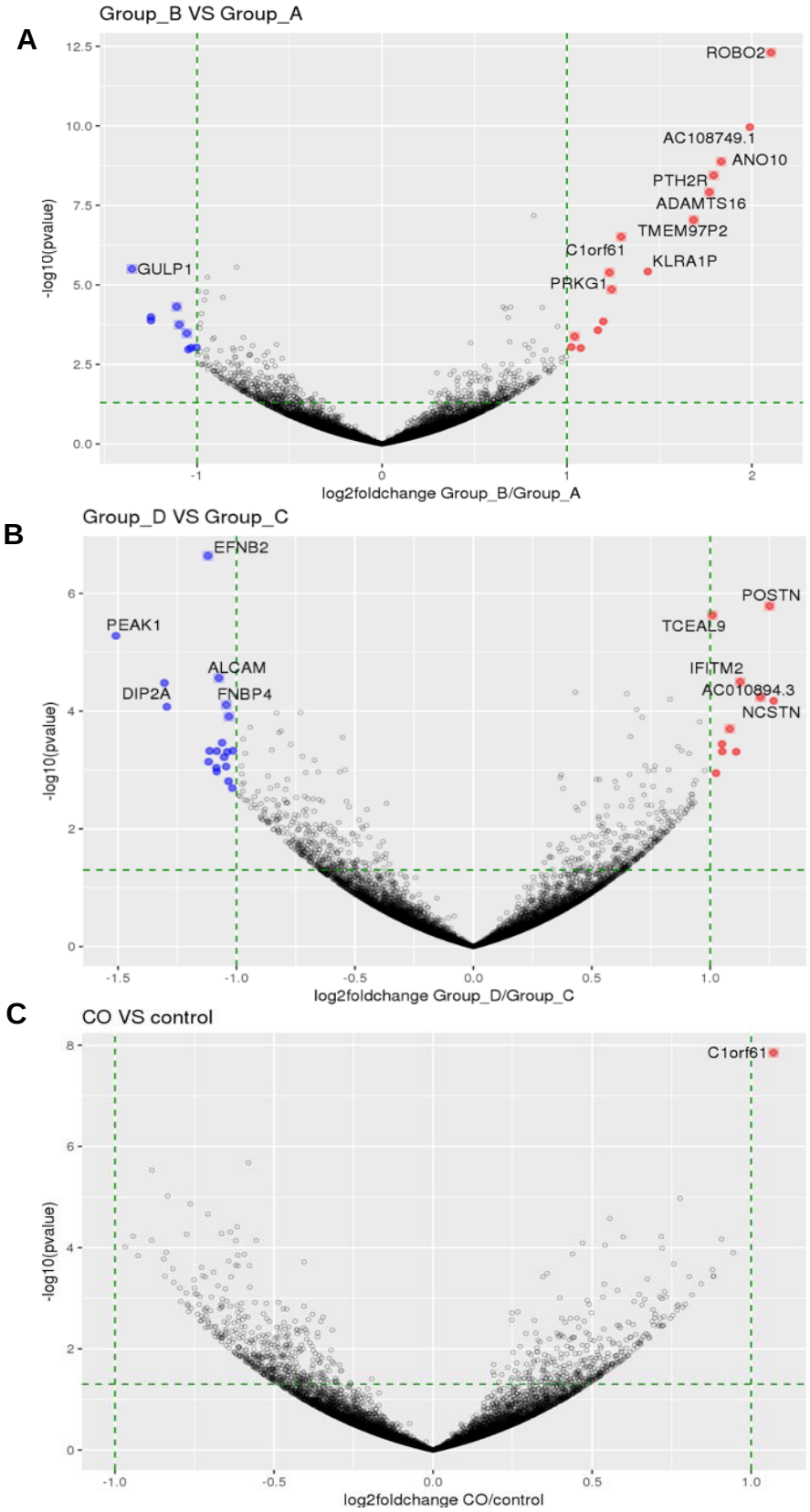

A
Group_B VS Group_A
ROBO2
AC108749.1
ANO10
PTH2R
ADAMTS16
TMEM97P2
C1orf61
KLRA1P
PRKG1
GULP1
-log10(pvalue)
log2foldchange Group_B/Group_A
B
Group_D VS Group_C
EFNB2
POSTN
TCEAL9
PEAK1
ALCAM
IFITM2
DIP2A
FNBP4
AC010894.3
NCSTN
-log10(pvalue)
log2foldchange Group_D/Group_C
C
CO VS control
C1orf61
-log10(pvalue)
log2foldchange CO/control

Figure 6. 7. Qiagen-generated volcano plots showing the results of differential gene analysis expressed by co-cultured astrocytes as compared to astrocyte-only controls. Group_B VS Group_A and Group_D VS Group_C represent the comparison of the co-cultured astrocytes in relation to their corresponding controls at day 6 and day 10 respectively (A-B), whereas (CO VS control) represent the comparison of all (20) co-cultured astrocyte samples (with each of 10 GIN lines and at both time points) versus six astrocyte-only controls across both time points (C). Each volcano plot shows the relationship between the -log10 (p-values) and the log2 fold change values obtained from analysis using DESeq2 software. The genes above the 0.05 p-value and log2 fold change threshold (horizontal green dashed line) are shown. Upregulated (red) and downregulated (blue) genes with ≥ -1 and ≥ 1-fold differences are shown (beyond vertical green dashed line). Coloured red and blue circles correspond to genes with **F**alse **D**etection **R**ate (FDR) less than 0.05. The top 10 significant genes of each comparison, which have the lowest *p-value* were labelled in the plot.

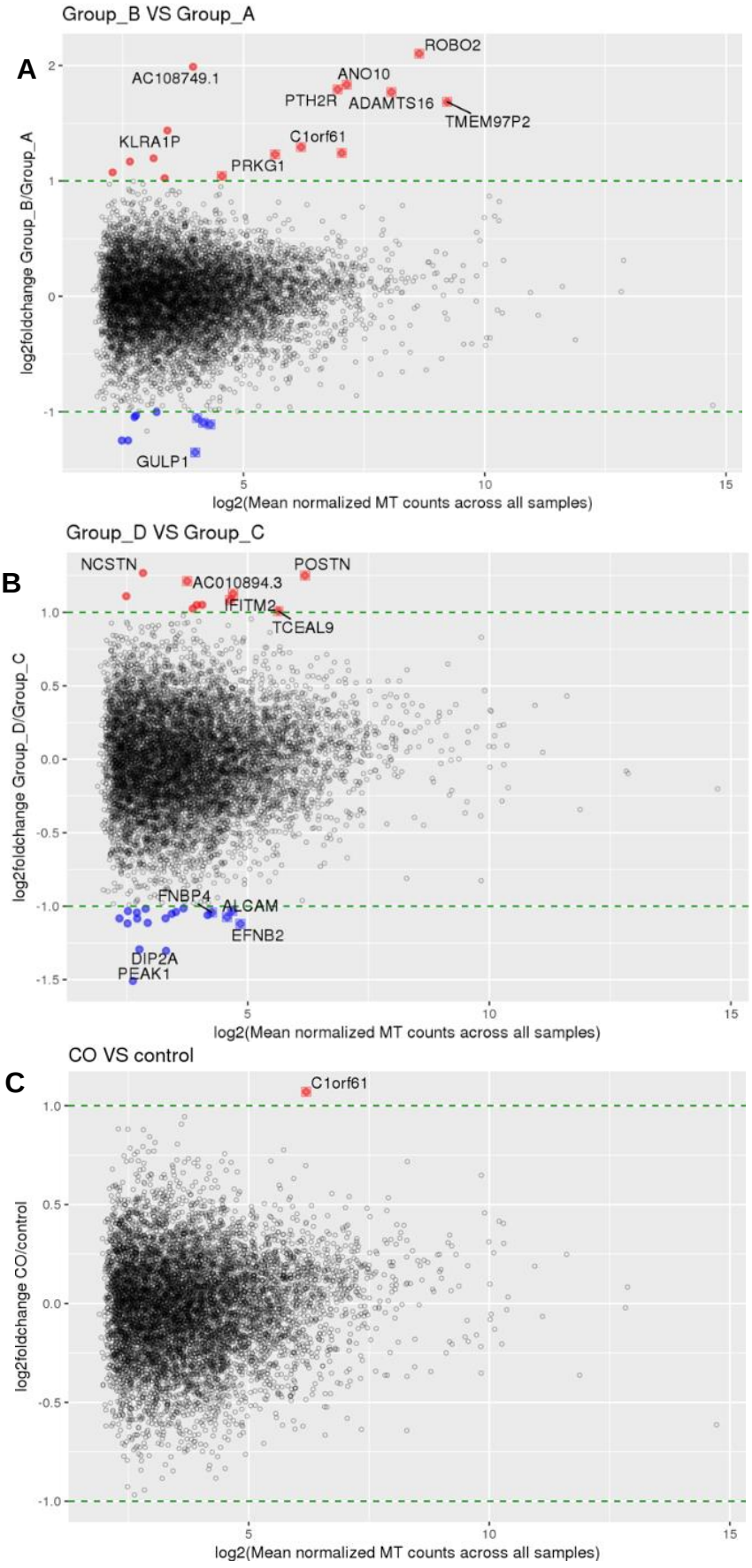
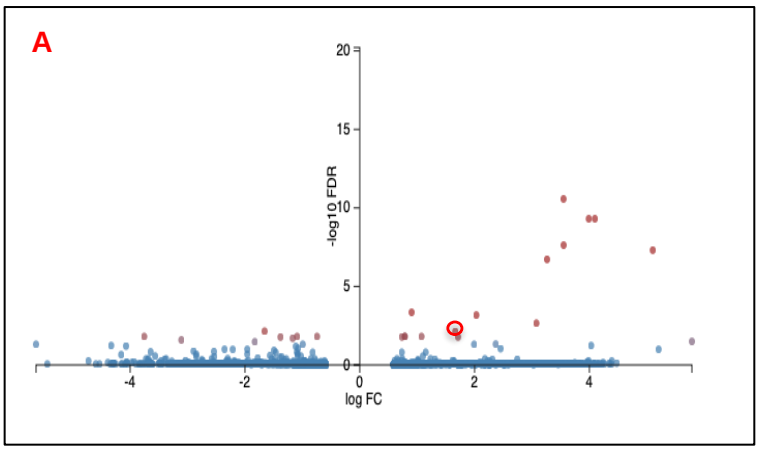
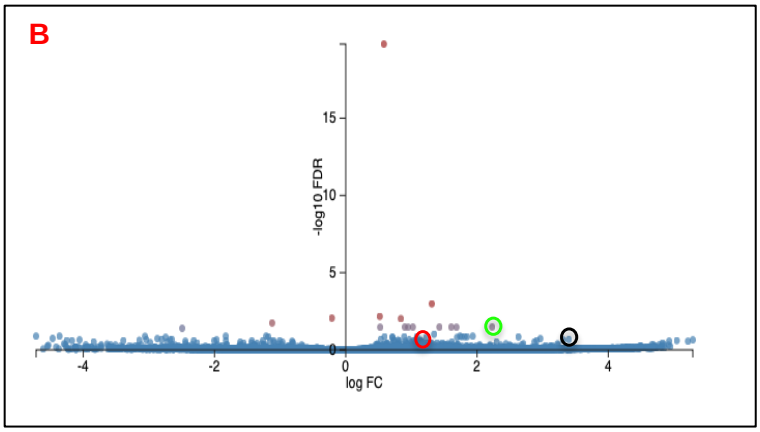
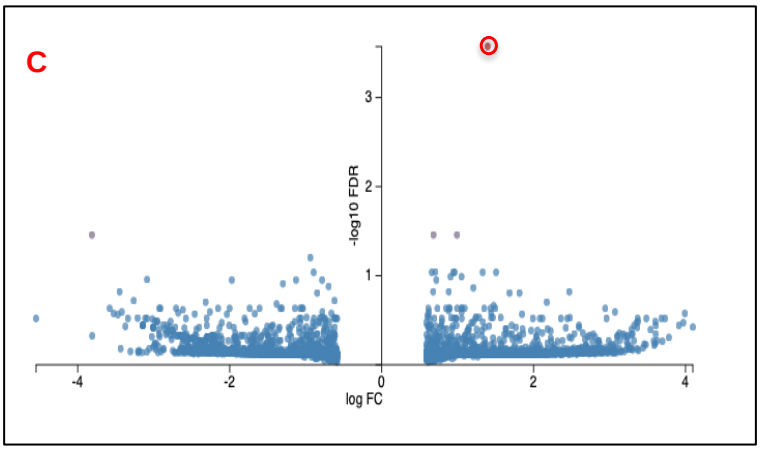

A
Group_B VS Group_A
ROBO2
AC108749.1
ANO10
PTH2R
ADAMTS16
TMEM97P2
KLRA1P
C1orf61
PRKG1
GULP1
log2foldchange Group_B/Group_A
log2(Mean normalized MT counts across all samples)
B
Group_D VS Group_C
NCSTN
POSTN
AC010894.3
IFITM2
TCEAL9
FNBP4
ALCAM
EFNB2
DIP2A
PEAK1
log2foldchange Group_D/Group_C
log2(Mean normalized MT counts across all samples)
C
CO VS control
C1orf61
log2foldchange CO/control
log2(Mean normalized MT counts across all samples)

Figure 6. 8. Qiagen MA-plots showing the results of differential gene analysis expressed by the co-cultured astrocytes as compared to astrocyte-only controls. Group_B VS Group_A and Group_D VS Group_C represent the comparison of the co-cultured astrocytes in relation to their corresponding controls at day 6 and day 10 respectively (A-B), whereas CO VS control represent the comparison of all (20) co-cultured astrocyte samples (with each of 10 GIN lines and at both time points) versus six astrocyte-monoculture controls across both time points (C). Each MA-plot shows the relationship between the -log10 (p-values) and the log2 fold change values obtained from DESeq2 software. The genes above the p-value threshold (0.05) and log2 fold change threshold (horizontal green dashed lines, depicting upregulated (red) and downregulated (blue) genes with ≥ -1 and ≥ 1-fold differences are shown. Coloured red and blue circles correspond to genes with FDR less than 0.05. The top 10 significant genes of each comparison, which have the lowest *p-value* were labelled in the plot.

To ensure greater confidence to our data, we independently conducted further comprehensive in-house RNA-sequencing data analysis using EdgeR software. This analysis has revealed the up- and down-regulated DEG expressed by the co-cultured astrocytes at two time points in relation to their corresponding controls (at 6 and 10 days) shown in the volcano- **(Figure 6. 9A, and Figure 6. 9B)** and MA-plots **(Figure 6. 10A, and Figure 6. 10B)** respectively. The same analysis has also revealed molecular pathways (Appendix Table 8. 2 and Table 8. 3). Note that similar to the Qiagen analyses, DEG shown in Figures 6.10 and 6.11 represent the combined significant genes identified from each distinct astrocyte-GIN co-culture, relative to astrocyte-only controls (at 6 and 10 days). A similar comparison between all 20 co-cultured astrocyte samples collectively and all 6 astrocytes-only controls has resulted in the differential gene regulation and distinct molecular pathways (Appendix Table 8. 4) depicted in the volcano- **(Figure 6. 9C)** and MA-plots **(Figure 6. 10C)**. A final RNA sequencing comparison was conducted for tumour-associated astrocytes (5-ALA negative) versus GBM cells (5-ALA positive) from ten patient-derived surgically resected and FACS isolated samples as previously described. This analysis has resulted in DEG and molecular pathways (Appendix Table 8. 5) that are shown in the volcano- **(Figure 6. 9D)** and MA-plots **(Figure 6. 10D)** respectively. The parameters of our statistical analysis were reduced, as we were searching for subtle changes in gene expression, and ultimately molecular pathways, in the co-cultured astrocytes as compared to the controls for each experimental time point and contrasting these results with tumour-associated astrocytes derived from 5-ALA negative patient samples. Thus, the DEG lists generated by our analysis of the co-cultured astrocytes and tumour associated astrocytes, were calculated to have statistical significance (*p-value* <0.05) of at least 1.5 fold change or more as shown in the volcano- **(Figure 6. 9)** and MA-plots **(Figure 6. 10)**.


A
20
15
10
5
0
-log10 FDR
-4
-2
0
2
4
log FC


B
15
10
5
0
-log10 FDR
-4
-2
0
2
4
log FC


C
3
2
1
-log10 FDR
-4
-2
0
2
4
log FC

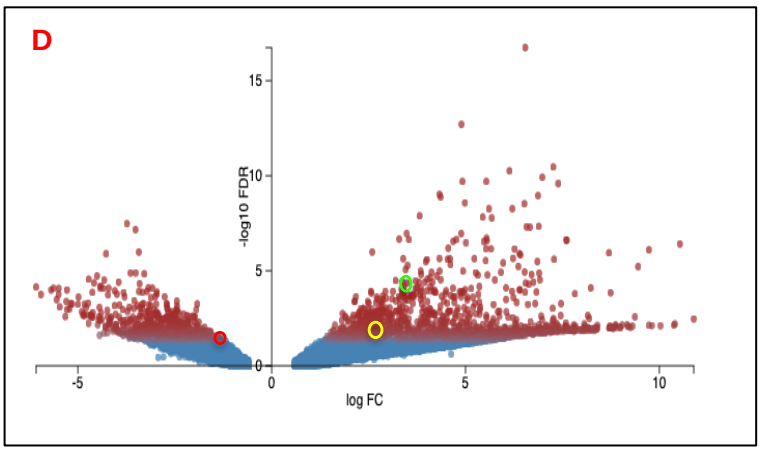

D
15
10
5
0
-log10 FDR
-5
0
5
10
log FC

Figure 6. 9. Volcano Plot showing the results of DEG of co-cultured astrocytes and 5-ALA negative primary tumour-associated astrocytes using EdgeR software. DEG were used to conduct pathway analysis using Reactome pathway analysis tool for astrocytes co-cultured with each of 10 GIN lines and shown relative to astrocyte-only cultures at Day 6 (A), Day 10 (B) and when all 20 co-cultured astrocytes at both time-points were analyzed collectively (C). All volcano plots depict the relationship between the log2 fold change values (LogFC) and the –log10 FDR (significance). The genes with *p-value* <0.05 and log2 fold change threshold (≥0.0585 & ≤-0.585) were included, whilst genes with LogFC between these values or a *p-value* >0.05 were ignored, which explains the presence of a white area around the 0 value on the significance axis. Brown dots represent genes with the lowest false detection rate genes (0.05). Genes of interest are annotated such as C1orf61 which is significantly upregulated (red circle) at Day 6 time point (A), Day 10 time-point (B), and when collectively comparing all 20 co-cultured astrocyte samples versus all six astrocyte-only controls (C). Interferon genes including *ifitm2* (green circle) and *ifitm2* (black circle) were significantly upregulated within 10 days. Higher depth read RNA-sequencing data analysis of patient-derived tumours were performed to compare 5-ALA negative relative to 5-ALA positive patient samples (D). Interferon genes IFITM2 (green circle) and *ifitm2* (black circle) were significantly upregulated in 5-ALA negative samples, whereas *c1orf61* was significantly downregulated (red circle).

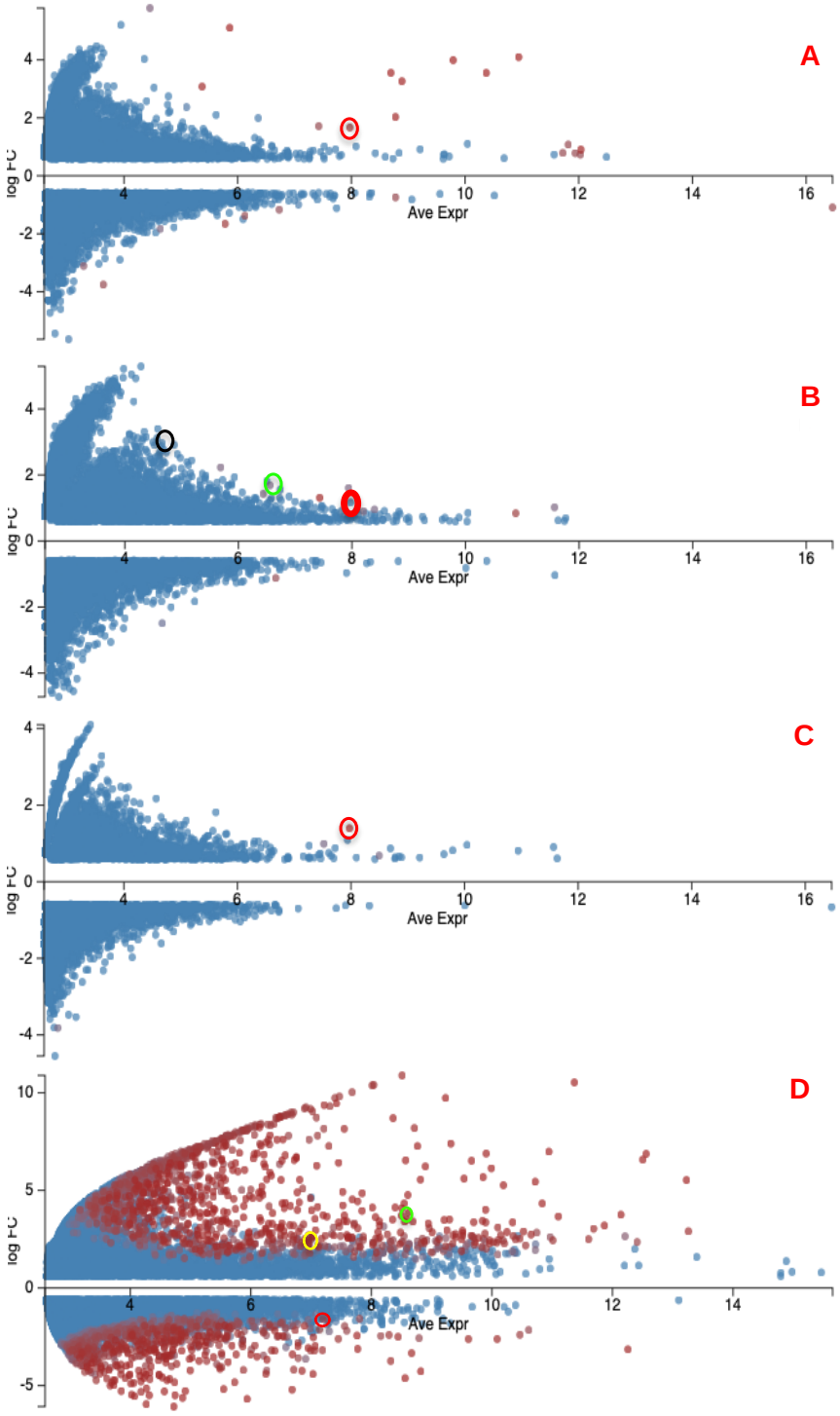

A
B
C
D
Ave Expr
Ave Expr
Ave Expr
Ave Expr

Figure 6. 10. MA-Plot showing DEG of co-cultured astrocytes and primary tumour-associated astrocytes using EdgeR software. Significant genes differentially expressed were used to conduct the pathway analysis using Reactome pathway analysis tool for astrocytes co-cultured with each of 10 GIN lines and shown relative to astrocyte-only cultures at Day 6 (A), Day 10 (B) and when all 20 co-cultured astrocytes at both time-points were analysed collectively (C). All MA-Plots depict the relationship between the log2 fold change values (LogFC) and the –log10 FDR (significance). The genes with *p-value* <0.05 and log2 fold change threshold (≥0.585 and ≤-0.585) were included and genes having LogFC between these values or *p-value* >0.05 were ignored, which explains the presence of a white area around the baseline 0 value in the average expression axis. Brown dots represent genes with high false detection rates. *c1orf61* is significantly upregulated (red circle) at the Day 6 time-point (A), Day 10 time-point (B), and when comparing all 20 co-cultured astrocyte samples versus all six astrocyte-only controls (C). Higher depth read RNA-sequencing data analysis of patient-derived tumours were performed to compare 5-ALA negative relative to 5-ALA positive patient samples (D). Interferon genes *ifitm2* (green circle) and *ifitm2* (black circle) were significantly upregulated in 5-ALA negative samples by Day 10, whereas *c1orf61* was significantly downregulated (red circle).

To interpret the RNA sequencing data in a more systemic manner and to further validate co-cultured astrocytes from our Gliomasphere Matrices against putative counterpart 5-ALA negative primary tumour associated astrocytes, the Reactome Pathway Database and bioinformatic tool was used to analyse the inter-connectedness of DEG. Reactome generates FoamTrees (JavaScript) which aid animated visualisation of pathway-based interactions. Reactome pathway analysis of the DEG expressed by the co-cultured astrocytes at both time points and of the clinical tumour-associated astrocytes from surgically resected and FACS-isolated clinical samples, utilising both the DESeq2 and EdgeR computational tools are provided in the (Appendix Table 8. 2, Table 8. 3, Table 8. 4, and Table 8. 5). The significance threshold of pathway analysis using Reactome was properly adjusted (*p-value* <0.05). Although transcriptomic analysis results by both bioinformatic tools showed considerable similarities, gene clustering using Reactome pathway analysis tool was more robust and more accurate with DEG results generated by EdgeR software as compared to DESeq2, and thus we shall focus more on these results.

The co-cultured astrocytes from Gliomaspehre Matrices, which were isolated from GIN cells by FACS based on YFP after 6 days, significantly upregulated 24 pathways. In particular, co-cultured astrocytes upregulated genes involved in intercellular communications such as the intra-flagellar and Gap-junction pathways, in addition to other pathways which were upregulated in the co-cultured astrocytes after 10 days and upregulated in the surgically resected and FACS isolated 5-ALA negative tumour-associated astrocytes. These common molecular pathways will be the primary focus here. Co-cultured astrocytes from Gliomasphere Matrices show significant upregulation of 64 pathways (Appendix Table 8. 3), whereas the 5-ALA negative clinical samples show significant upregulation of 72 pathways, with no statistical significance found for the downregulated genes (Appendix Table 8. 5). Twenty-four pathways were common between these two datasets. However, more genes were clustered in each pathway in the samples that were obtained from patients as RNA-sequencing data from that study had higher-read depth as compared to UPX sequencing performed for the Gliomasphere Matrix samples. FoamTrees simplify the visualisation of upregulated functional pathways within the co-cultured YFP-astrocytes (FAC-isolated from GIN cells at 10 days) from Gliomasphere Matrices relative to astrocyte-only cultures **(Figure 6. 11)**. Similarly, FoamTrees aid the visualisation of upregulated functional pathways within 5-ALA negative tumour-associated astrocytes relative to 5-ALA positive invasive GBM cells, derived from surgically resected tissue **(Figure 6. 12)**. Visual comparison between both **(Figure 6. 11)** and **(Figure 6. 12)** reveals the pathway trend similarities between

the co-cultured YFP-astrocytes (FACS-isolated from GIN cells at 10 days) in the *in-vitro* experiment and tumour-associated astrocytes that were derived from GBM tumours of patients.

Transcriptomic profiles for the co-cultured YFP-astrocytes (at Day10) and 5-ALA negative tumour associated astrocytes reveal comparable up-regulation of genes involved in: axon guidance (signalling by roundabout (ROBO) receptors, Regulation of expression of SLITs and ROBOs, Semaphorin interactions and Ephrin signalling); translation (L13a-mediated translational silencing of Ceruloplasmin expression, Ribosomal scanning and start codon recognition, Activation of the mRNA upon binding of the cap-binding complex and eIFs and subsequent binding to 43S, Formation of a pool of free 40S subunits, Formation of the ternary complex, and subsequently the 43S complex, GTP hydrolysis and joining of the 60S ribosomal subunit, Eukaryotic Translation Initiation, Cap-dependent Translation Initiation, Peptide chain elongation, Eukaryotic Translation Elongation, Eukaryotic Translation Termination, and SRP-dependent co-translational protein targeting to membrane); rRNA processing (Major pathway of rRNA processing in the nucleolus and cytosol, AUF1 (hnRNP D0) binds and destabilizes mRNA, Nonsense Mediated Decay (NMD) independent of the Exon Junction Complex (EJC), Nonsense-Mediated Decay, and Nonsense Mediated Decay enhanced by the Exon Junction Complex); influenza life cycle (Influenza viral mRNA translation, Influenza Viral RNA Transcription and Replication); cell response to stress (response of EIF2AK4 (GCN2) to amino acid deficiency; Selenocysteine synthesis; transcriptional regulation by RUNX3; and Oncogene induced senescence triggered by Oncogenic MAPK signalling **(Figure 6.12 and 6.13).** After 10 days, the co-cultured astrocytes showed up-regulation of certain cell cycle pathways and cell cycle check points including SCF(Skp2)-mediated degradation of p27/p21, Stabilization of p53, p53-Dependent G1/S DNA damage checkpoint, p53-Dependent G1 DNA Damage Response, Cyclin E associated events during G1/S transition, G1/S DNA Damage Checkpoints, Cyclin A:Cdk2-associated events at S phase entry, The role of GTSE1 in G2/M progression after G2 checkpoint, and Ubiquitin-dependent degradation of Cyclin D. Moreover, the co-cultured astrocytes revealed molecular pathways involved in diseases such as diseases of cellular senescence (evasion of the oncogene- and stress-induced apoptosis due to p14ARF defect), and signalling by NOTCH1 in cancer **(Figure 6. 11)**. In general, the co-cultured astrocytes significantly expressed in-trans activation of Notch signalling pathways at Day 6 and Day 10 and when collectively comparing all 20 co-cultured YFP-astrocytes to all six astrocytes-only controls of both time

points. However, Notch signalling pathways were not significantly expressed in 5-ALA negative tumour-associated astrocytes. Although the co-cultured astrocytes showed significant upregulation of many pathways that are usually linked to malignant processes, they significantly upregulated immune pathways such as interferon signalling after 10 days of directly interaction with invasive GBM cells. Comparably, the interferon signalling pathway was also significantly upregulated in 5-ALA negative tumour-associated astrocytes, suggesting a similar immune response is induced in the invasive niche post-GBM surgery **(Figure 6. 22)**. Further validation of the results was conducted using TCGA dataset, which will be discussed below in section 6.3.3.6. Also, the comparison of all 20 co-cultured astrocyte samples of the two time points with all 6 YFP- astrocyte-only controls at both time points, showed consistent upregulation of Notch signalling in addition to the identification of a previously poorly-studied, developmental gene known as *c1orf61* (*p-value* 7.27e-9; FDR 2.68e-4) **(Figure 6. 7C, Figure 6. 8C, Figure 6. 9C, and Figure 6. 10C)**, which has recently been linked to many cancers including glioma (Verhaak *et al.*, 2010, Carro *et al.*, 2010; Bhat *et al.*, 2011, Cai *et al.*, 2018, Meyer *et al.*, 2015, Marziali *et al.*, 2016; Taiwo, Mahlokozera and Kim, 2018, Jung *et al.*, 2017, Cosset *et al.*, 2017). This important result was also validated against TCGA data as shown below in section 6.3.3.7.

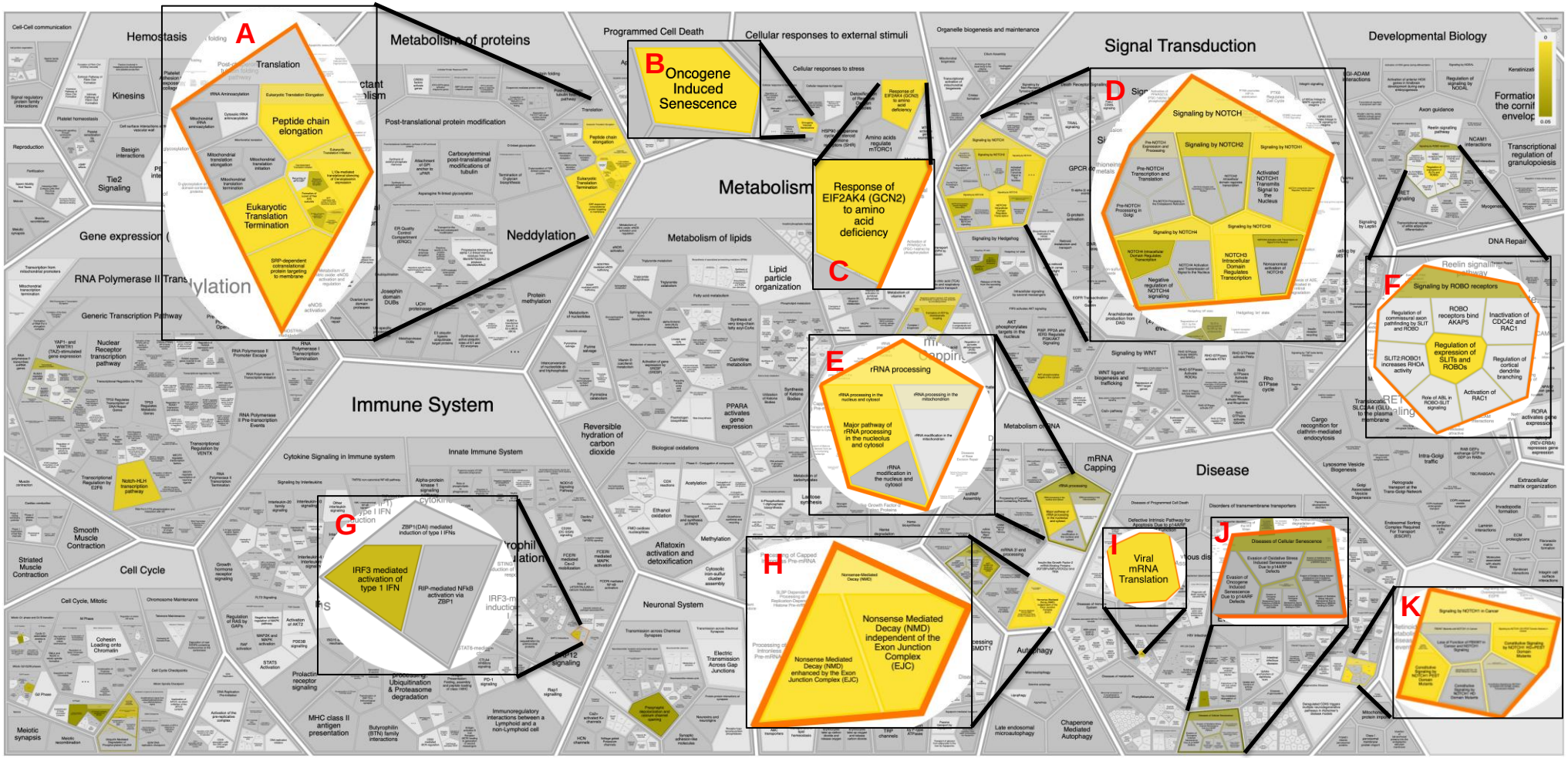

A
Translation
Peptide chain elongation
Eukaryotic Translation Termination
SRP-dependent cotranslational protein targeting to membrane
B
Oncogene Induced Senescence
C
Response of EIF2AK4 (GCN2) to amino acid deficiency
D
Signaling by NOTCH
Signaling by NOTCH2
Signaling by NOTCH1
Activated NOTCH1 Transmits Signal to the Nucleus
Signaling by NOTCH4
Signaling by NOTCH3
NOTCH3 Intracellular Domain Regulates Transcription
Pre-NOTCH Transcription and Translation
Pre-NOTCH Processing in Golgi
Negative regulation of NOTCH4 signaling
E
rRNA processing
rRNA processing in the nucleus and cytosol
rRNA processing in the mitochondrion
Major pathway of rRNA processing in the nucleolus and cytosol
rRNA modification in the nucleus and cytosol
rRNA modification in the mitochondrion
F
Signaling by ROBO receptors
ROBO receptors bind AKAP5
Inactivation of CDC42 and RAC1
Regulation of expression of SLITs and ROBOs
SLIT2:ROBO1 increases RHOA activity
Regulation of cortical dendrite branching
Activation of RAC1
Role of ABL in ROBO-SLIT signaling
G
IRF3 mediated activation of type 1 IFN
ZBP1(DAI) mediated induction of type I IFNs
RIP-mediated NFkB activation via ZBP1
H
Nonsense Mediated Decay (NMD) independent of the Exon Junction Complex (EJC)
Nonsense Mediated Decay (NMD) enhanced by the Exon Junction Complex (EJC)
I
Viral mRNA Translation
J
Diseases of Cellular Senescence
Evasion of Oncogene Induced Senescence Due to p14ARF Defects
K
Signaling by NOTCH1 in Cancer
Hemostasis
Metabolism of proteins
Programmed Cell Death
Cellular responses to external stimuli
Organelle biogenesis and maintenance
Signal Transduction
Developmental Biology
Metabolism
Gene expression (
Neddylation
Metabolism of lipids
Lipid particle organization
Immune System
Cytokine Signaling in Immune system
Innate Immune System
Reversible hydration of carbon dioxide
Metabolism of RNA
mRNA Capping
Disease
Cell Cycle
Cell Cycle, Mitotic
Neuronal System
Autophagy
Late endosomal microautophagy
Chaperone Mediated Autophagy
Meiotic synapsis
Meiotic recombination
Smooth Muscle Contraction
Striated Muscle Contraction
Kinesins
Tie2 Signaling
Reproduction
Basigin interactions
Cell-Cell communication
RNA Polymerase II Trans
Generic Transcription Pathway
Nuclear Receptor transcription pathway
Notch-HLH transcription pathway
Transcriptional Regulation by E2Fs
Transcriptional Regulation by VENTX
Cohesin Loading onto Chromatin
Chromosome Maintenance
Aflatoxin activation and detoxification
Ethanol oxidation
Methylation
Biological oxidations
PPARA activates gene expression
Carnitine metabolism
Synthesis of very long-chain fatty acyl-CoAs
Synthesis of Ketone Bodies
Fatty acid metabolism
Triglyceride metabolism
Triglyceride catabolism
Metabolism of nucleotides
Pyrimidine catabolism
Pyrimidine salvage
Josephin domain DUBs
UCH proteinases
ER Quality Control Compartment (ERQC)
Attachment of GPI anchor to uPAR
Carboxyterminal post-translational modifications of tubulin
Post-translational protein modification
Protein methylation
Translocation of SLC2A4 (GLUT4) to the plasma membrane
Cargo recognition for clathrin-mediated endocytosis
Lysosome Vesicle Biogenesis
Golgi Associated Vesicle Biogenesis
Intra-Golgi traffic
Retrograde transport at the Trans-Golgi-Network
Endosomal Sorting Complex Required for Pol Transport (ESCRT)
Extracellular matrix organization
Invadopodia formation
ECM proteoglycans
Fibronectin matrix formation
Integrin cell surface interactions
Laminin interactions
Signaling by WNT
WNT ligand biogenesis and trafficking
Rho GTPase cycle
RHO GTPases Activate ROCKs
RHO GTPases Activate Formins
RHO GTPases Activate PAKs
RHO GTPases Activate WASPs and WAVEs
RHO GTPases Activate NADPH Oxidases
RHO GTPases Activate PKNs
RHO GTPases Activate IQGAPs
RHO GTPases Activate CIT
RHO GTPases Activate RHOBTB3
RHO GTPases Activate Rhotekin and Rhophilins
RHO GTPases Activate Myosins
RHO GTPases Activate CIT
RHO GTPases Activate RHOBTB3
RHO GTPases Activate Rhotekin and Rhophilins
RHO GTPases Activate Myosins
Signaling by Hedgehog
Hedgehog 'on' state
Hedgehog 'off' state
GPCR
G-protein activation
Signaling by Leptin
DNA Repair
Reelin signaling pathway
Axon guidance
NCAM1 interactions
Transcriptional regulation of granulopoiesis
Keratinization
Regulation of signaling by NODAL
Formation of the cornified envelope
Translocation of SLC2A4 (GLUT4) to the plasma membrane
RET signaling
RORA activates gene expression
(REV-ERBA) represses gene expression
RAB GEFs exchange GTP for GDP on RABs
TBC/RABGAPs
Translation
Eukaryotic Translation Elongation
Mitochondrial tRNA aminoacylation
Cytosolic tRNA aminoacylation
Mitochondrial translation elongation
Mitochondrial translation initiation
Mitochondrial translation termination
L13a-mediated translational silencing of Ceruloplasmin expression
Eukaryotic Translation Initiation
Formation of a pool of free 40S subunits
Eukaryotic Translation Termination
Peptide chain elongation
Translation of Replicase and Assembly of the Replication Transcription Complex
Viral mRNA Translation
Nonsense-Mediated Decay (NMD)
Nonsense Mediated Decay (NMD) enhanced by the Exon Junction Complex (EJC)
Nonsense Mediated Decay (NMD) independent of the Exon Junction Complex (EJC)
Response of EIF2AK4 (GCN2) amino acid deficiency
Amino acids regulate mTORC1
Cellular responses to stress
Cellular response to hypoxia
HSP90 chaperone cycle for steroid hormone receptors (SHR)
Signaling by NOTCH
Signaling by NOTCH2
Signaling by NOTCH1
Activated NOTCH1 Transmits Signal to the Nucleus
Signaling by NOTCH4
Signaling by NOTCH3
NOTCH3 Intracellular Domain Regulates Transcription
Pre-NOTCH Transcription and Translation
Pre-NOTCH Processing in Golgi
Negative regulation of NOTCH4 signaling
NOTCH4 Activation and Transmission of Signal to the Nucleus
Nonsynonymous SNPs affecting NOTCH3
NOTCH4 Intracellular Domain Regulates Transcription
Signaling by ROBO receptors
ROBO receptors bind AKAP5
Inactivation of CDC42 and RAC1
Regulation of expression of SLITs and ROBOs
SLIT2:ROBO1 increases RHOA activity
Regulation of cortical dendrite branching
Activation of RAC1
Role of ABL in ROBO-SLIT signaling
Regulation of commissural axon pathfinding by SLIT and ROBO
Diseases of Cellular Senescence
Evasion of Oncogene Induced Senescence Due to p14ARF Defects
Evasion of Oxidative Stress Induced Senescence Due to p14ARF Defects
Signaling by NOTCH1 in Cancer
Loss of Function of PBRM1 in Cancer
Constitutive Signaling by NOTCH1 HD+PEST Domain Mutants
Constitutive Signaling by NOTCH1 PEST Domain Mutants
Constitutive Signaling by NOTCH1 HD Domain Mutants
IRF3 mediated activation of type 1 IFN
ZBP1(DAI) mediated induction of type I IFNs
RIP-mediated NFkB activation via ZBP1
Cytokine Signaling in Immune system
Interferon Signaling
Interferon alpha/beta signaling
Interferon gamma signaling
Interleukin-10 signaling
Interleukin-20 family signaling
Interleukin-35 Signalling
Interleukin-4 and Interleukin-13 signaling
Interleukin-37 signaling
Interleukin-1 signaling
Interleukin-1 family signaling
Interleukin-2 family signaling
Interleukin-3, Interleukin-5 and GM-CSF signaling
Interleukin-6 family signaling
Interleukin-7 signaling
Interleukin-9 signaling
Other interleukin signaling
Signaling by Interleukins
Innate Immune System
Neutrophil degranulation
Antigen Processing: Ubiquitination & Proteasome degradation
MHC class II antigen presentation
Immunoregulatory interactions between a Lymphoid and a non-Lymphoid cell
Butyrophilin (BTN) family interactions
PD-1 signaling
CD22 mediated BCR regulation
FCERI mediated MAPK activation
FCERI mediated NF-kB activation
FCGR activation
FCGR3A-mediated IL10 synthesis
FCGR3A-mediated phagocytosis
Fc epsilon receptor (FCERI) signaling
Fcgamma receptor (FCGR) dependent phagocytosis
Regulation of actin dynamics for phagocytic cup formation
Phagocytosis
Phagocytosis of apoptotic cell
Phagocytosis of bacteria
Phagocytosis of fungus
Phagocytosis of virus
Phagocytosis of yeast
Phagocytosis, recognition of bacteria and bacterial toxins
Phagocytosis, recognition of fungus
Phagocytosis, recognition of virus
Phagocytosis, recognition of yeast
Phagocytosis, recognition of apoptotic cell
Phagocytosis, recognition of bacteria

Figure 6. 11. Reactome pathway analysis depicted as a FoamTree showing the main molecular pathways significantly upregulated (highlighted in yellow) (highlighted in yellow) by co-cultured YFP-astrocytes upon FACS-isolation from each of 10 GIN cell lines, as compared to YFP-astrocyte-only controls after 10 days of co-culture. Reactome computational tool can cluster the significant pathways according to major hierarchical pathway families such as cell cycle pathways, protein metabolism, signalling, development or pathways involved in disease pathway. The pathways of interest that are uniquely upregulated in co-cultured astrocytes in response to GIN cell lines or commonly upregulated in both co-cultured astrocytes after FACS-isolation at Day 10 and 5-ALA negative tumour-associated astrocytes were magnified in the black frame squares. The pathways are protein translation (A), Oncogene induced senescence (B), Response of EIF2AK4 (GCN2) to amino acid deficiency (C), Signalling by NOTCH (D), rRNA processing in the nucleus and cytosol (E), Regulation of expression of SLITs and ROBOs (F), IRF3 mediated activation of type I interferon (G), Nonsense-Mediated Decay (NMD) (H), viral mRNA translation (I), Disease of cellular senescence (J), and Signalling by NOTCH1 in Cancer (K). *The black thick lines indicate the position of the pathway in the pathway family within the FoamTree.*

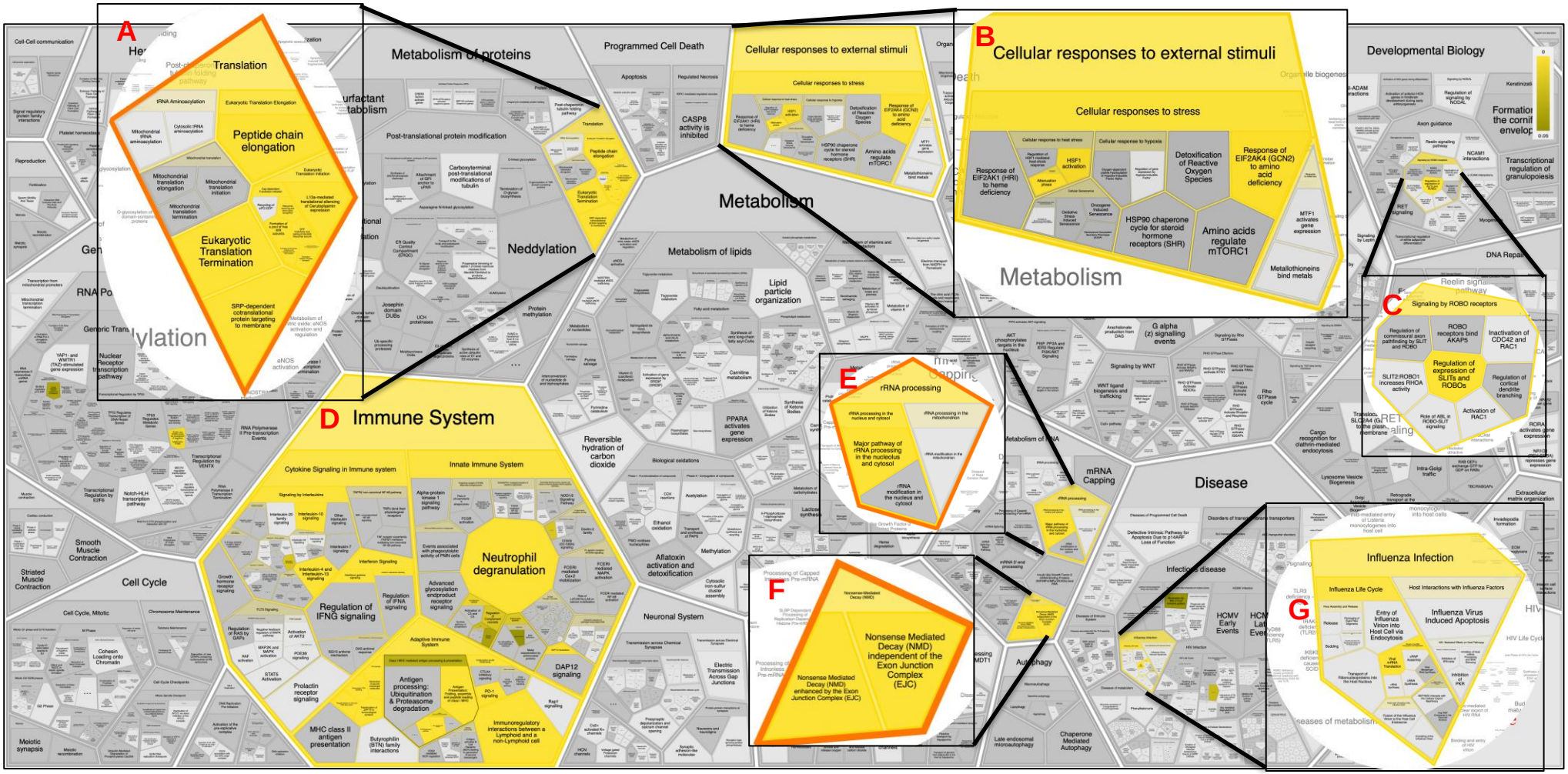

A
Translation
Peptide chain elongation
Eukaryotic Translation Termination
SRP-dependent cotranslational protein targeting to membrane
B
Cellular responses to external stimuli
Cellular responses to stress
Response of EIF2AK1 (HRI) to heme deficiency
HSF1 activation
Detoxification of Reactive Oxygen Species
Response of EIF2AK4 (GCN2) to amino acid deficiency
HSP90 chaperone cycle for steroid hormone receptors (SHR)
Amino acids regulate mTORC1
MTF1 activates gene expression
Metallothioneins bind metals
Metabolism
C
Signaling by ROBO receptors
ROBO receptors bind AKAP5
Inactivation of CDC42 and RAC1
Regulation of expression of SLITs and ROBOs
SLIT2:ROBO1 increases RHOA activity
Activation of RAC1
D
Immune System
Cytokine Signaling in Immune system
Innate Immune System
Neutrophil degranulation
Regulation of IFNG signaling
Adaptive Immune System
Antigen processing: Ubiquitination & Proteasome degradation
MHC class II antigen presentation
DAP12 signaling
E
rRNA processing
Major pathway of rRNA processing in the nucleolus and cytosol
F
Nonsense Mediated Decay (NMD) independent of the Exon Junction Complex (EJC)
Nonsense Mediated Decay (NMD) enhanced by the Exon Junction Complex (EJC)
G
Influenza Infection
Influenza Life Cycle
Host Interactions with Influenza Factors
Influenza Virus Induced Apoptosis
Entry of Influenza Virion into Host Cell via Endocytosis
Metabolism of proteins
Programmed Cell Death
Cellular responses to external stimuli
Metabolism
Neddylation
Metabolism of lipids
Lipid particle organization
Reversible hydration of carbon dioxide
PPARA activates gene expression
Aflatoxin activation and detoxification
Neuronal System
Disease
mRNA Capping
Developmental Biology
Cell-Cell communication
Cell Cycle
Smooth Muscle Contraction
Striated Muscle Contraction
Meiotic synapsis
Cohesin Loading onto Chromatin
Cell Cycle, Mitotic
Chromosome Maintenance
Notch-HLH transcription pathway
Nuclear Receptor transcription pathway
Transcriptional Regulation by E2F6
Transcriptional Regulation by MITF
Transcriptional Regulation by NEUROD1
Transcriptional Regulation by NEUROG3
Transcriptional Regulation by NOTCH4
Transcriptional Regulation by RUNX1
Transcriptional Regulation by RUNX2
Transcriptional Regulation by RUNX3
Transcriptional Regulation by TBX21
Transcriptional Regulation by TCF7
Transcriptional Regulation by TCF7L2
Transcriptional Regulation by VENTX
Transcriptional Regulation by ZBTB7A
Transcriptional Regulation by ZNF281
Transcriptional Regulation by ZNF423
Transcriptional Regulation by ZNF503
Transcriptional Regulation by ZNF516
Transcriptional Regulation by ZNF518A
Transcriptional Regulation by ZNF521
Transcriptional Regulation by ZNF524
Transcriptional Regulation by ZNF526
Transcriptional Regulation by ZNF527
Transcriptional Regulation by ZNF528
Transcriptional Regulation by ZNF529
Transcriptional Regulation by ZNF530
Transcriptional Regulation by ZNF531
Transcriptional Regulation by ZNF532
Transcriptional Regulation by ZNF533
Transcriptional Regulation by ZNF534
Transcriptional Regulation by ZNF535
Transcriptional Regulation by ZNF536
Transcriptional Regulation by ZNF537
Transcriptional Regulation by ZNF538
Transcriptional Regulation by ZNF539
Transcriptional Regulation by ZNF540
Transcriptional Regulation by ZNF541
Transcriptional Regulation by ZNF542
Transcriptional Regulation by ZNF543
Transcriptional Regulation by ZNF544
Transcriptional Regulation by ZNF545
Transcriptional Regulation by ZNF546
Transcriptional Regulation by ZNF547
Transcriptional Regulation by ZNF548
Transcriptional Regulation by ZNF549
Transcriptional Regulation by ZNF550
Transcriptional Regulation by ZNF551
Transcriptional Regulation by ZNF552
Transcriptional Regulation by ZNF553
Transcriptional Regulation by ZNF554
Transcriptional Regulation by ZNF555
Transcriptional Regulation by ZNF556
Transcriptional Regulation by ZNF557
Transcriptional Regulation by ZNF558
Transcriptional Regulation by ZNF559
Transcriptional Regulation by ZNF560
Transcriptional Regulation by ZNF561
Transcriptional Regulation by ZNF562
Transcriptional Regulation by ZNF563
Transcriptional Regulation by ZNF564
Transcriptional Regulation by ZNF565
Transcriptional Regulation by ZNF566
Transcriptional Regulation by ZNF567
Transcriptional Regulation by ZNF568
Transcriptional Regulation by ZNF569
Transcriptional Regulation by ZNF570
Transcriptional Regulation by ZNF571
Transcriptional Regulation by ZNF572
Transcriptional Regulation by ZNF573
Transcriptional Regulation by ZNF574
Transcriptional Regulation by ZNF575
Transcriptional Regulation by ZNF576
Transcriptional Regulation by ZNF577
Transcriptional Regulation by ZNF578
Transcriptional Regulation by ZNF579
Transcriptional Regulation by ZNF580
Transcriptional Regulation by ZNF581
Transcriptional Regulation by ZNF582
Transcriptional Regulation by ZNF583
Transcriptional Regulation by ZNF584
Transcriptional Regulation by ZNF585
Transcriptional Regulation by ZNF586
Transcriptional Regulation by ZNF587
Transcriptional Regulation by ZNF588
Transcriptional Regulation by ZNF589
Transcriptional Regulation by ZNF590
Transcriptional Regulation by ZNF591
Transcriptional Regulation by ZNF592
Transcriptional Regulation by ZNF593
Transcriptional Regulation by ZNF594
Transcriptional Regulation by ZNF595
Transcriptional Regulation by ZNF596
Transcriptional Regulation by ZNF597
Transcriptional Regulation by ZNF598
Transcriptional Regulation by ZNF599
Transcriptional Regulation by ZNF600
Transcriptional Regulation by ZNF601
Transcriptional Regulation by ZNF602
Transcriptional Regulation by ZNF603
Transcriptional Regulation by ZNF604
Transcriptional Regulation by ZNF605
Transcriptional Regulation by ZNF606
Transcriptional Regulation by ZNF607
Transcriptional Regulation by ZNF608
Transcriptional Regulation by ZNF609
Transcriptional Regulation by ZNF610
Transcriptional Regulation by ZNF611
Transcriptional Regulation by ZNF612
Transcriptional Regulation by ZNF613
Transcriptional Regulation by ZNF614
Transcriptional Regulation by ZNF615
Transcriptional Regulation by ZNF616
Transcriptional Regulation by ZNF617
Transcriptional Regulation by ZNF618
Transcriptional Regulation by ZNF619
Transcriptional Regulation by ZNF620
Transcriptional Regulation by ZNF621
Transcriptional Regulation by ZNF622
Transcriptional Regulation by ZNF623
Transcriptional Regulation by ZNF624
Transcriptional Regulation by ZNF625
Transcriptional Regulation by ZNF626
Transcriptional Regulation by ZNF627
Transcriptional Regulation by ZNF628
Transcriptional Regulation by ZNF629
Transcriptional Regulation by ZNF630
Transcriptional Regulation by ZNF631
Transcriptional Regulation by ZNF632
Transcriptional Regulation by ZNF633
Transcriptional Regulation by ZNF634
Transcriptional Regulation by ZNF635
Transcriptional Regulation by ZNF636
Transcriptional Regulation by ZNF637
Transcriptional Regulation by ZNF638
Transcriptional Regulation by ZNF639
Transcriptional Regulation by ZNF640
Transcriptional Regulation by ZNF641
Transcriptional Regulation by ZNF642
Transcriptional Regulation by ZNF643
Transcriptional Regulation by ZNF644
Transcriptional Regulation by ZNF645
Transcriptional Regulation by ZNF646
Transcriptional Regulation by ZNF647
Transcriptional Regulation by ZNF648
Transcriptional Regulation by ZNF649
Transcriptional Regulation by ZNF650
Transcriptional Regulation by ZNF651
Transcriptional Regulation by ZNF652
Transcriptional Regulation by ZNF653
Transcriptional Regulation by ZNF654
Transcriptional Regulation by ZNF655
Transcriptional Regulation by ZNF656
Transcriptional Regulation by ZNF657
Transcriptional Regulation by ZNF658
Transcriptional Regulation by ZNF659
Transcriptional Regulation by ZNF660
Transcriptional Regulation by ZNF661
Transcriptional Regulation by ZNF662
Transcriptional Regulation by ZNF663
Transcriptional Regulation by ZNF664
Transcriptional Regulation by ZNF665
Transcriptional Regulation by ZNF666
Transcriptional Regulation by ZNF667
Transcriptional Regulation by ZNF668
Transcriptional Regulation by ZNF669
Transcriptional Regulation by ZNF670
Transcriptional Regulation by ZNF671
Transcriptional Regulation by ZNF672
Transcriptional Regulation by ZNF673
Transcriptional Regulation by ZNF674
Transcriptional Regulation by ZNF675
Transcriptional Regulation by ZNF676
Transcriptional Regulation by ZNF677
Transcriptional Regulation by ZNF678
Transcriptional Regulation by ZNF679
Transcriptional Regulation by ZNF680
Transcriptional Regulation by ZNF681
Transcriptional Regulation by ZNF682
Transcriptional Regulation by ZNF683
Transcriptional Regulation by ZNF684
Transcriptional Regulation by ZNF685
Transcriptional Regulation by ZNF686
Transcriptional Regulation by ZNF687
Transcriptional Regulation by ZNF688
Transcriptional Regulation by ZNF689
Transcriptional Regulation by ZNF690
Transcriptional Regulation by ZNF691
Transcriptional Regulation by ZNF692
Transcriptional Regulation by ZNF693
Transcriptional Regulation by ZNF694
Transcriptional Regulation by ZNF695
Transcriptional Regulation by ZNF696
Transcriptional Regulation by ZNF697
Transcriptional Regulation by ZNF698
Transcriptional Regulation by ZNF699
Transcriptional Regulation by ZNF700
Transcriptional Regulation by ZNF701
Transcriptional Regulation by ZNF702
Transcriptional Regulation by ZNF703
Transcriptional Regulation by ZNF704
Transcriptional Regulation by ZNF705
Transcriptional Regulation by ZNF706
Transcriptional Regulation by ZNF707
Transcriptional Regulation by ZNF708
Transcriptional Regulation by ZNF709
Transcriptional Regulation by ZNF710
Transcriptional Regulation by ZNF711
Transcriptional Regulation by ZNF712
Transcriptional Regulation by ZNF713
Transcriptional Regulation by ZNF714
Transcriptional Regulation by ZNF715
Transcriptional Regulation by ZNF716
Transcriptional Regulation by ZNF717
Transcriptional Regulation by ZNF718
Transcriptional Regulation by ZNF719
Transcriptional Regulation by ZNF720
Transcriptional Regulation by ZNF721
Transcriptional Regulation by ZNF722
Transcriptional Regulation by ZNF723
Transcriptional Regulation by ZNF724
Transcriptional Regulation by ZNF725
Transcriptional Regulation by ZNF726
Transcriptional Regulation by ZNF727
Transcriptional Regulation by ZNF728
Transcriptional Regulation by ZNF729
Transcriptional Regulation by ZNF730
Transcriptional Regulation by ZNF731
Transcriptional Regulation by ZNF732
Transcriptional Regulation by ZNF733
Transcriptional Regulation by ZNF734
Transcriptional Regulation by ZNF735
Transcriptional Regulation by ZNF736
Transcriptional Regulation by ZNF737
Transcriptional Regulation by ZNF738
Transcriptional Regulation by ZNF739
Transcriptional Regulation by ZNF740
Transcriptional Regulation by ZNF741
Transcriptional Regulation by ZNF742
Transcriptional Regulation by ZNF743
Transcriptional Regulation by ZNF744
Transcriptional Regulation by ZNF745
Transcriptional Regulation by ZNF746
Transcriptional Regulation by ZNF747
Transcriptional Regulation by ZNF748
Transcriptional Regulation by ZNF749
Transcriptional Regulation by ZNF750
Transcriptional Regulation by ZNF751
Transcriptional Regulation by ZNF752
Transcriptional Regulation by ZNF753
Transcriptional Regulation by ZNF754
Transcriptional Regulation by ZNF755
Transcriptional Regulation by ZNF756
Transcriptional Regulation by ZNF757
Transcriptional Regulation by ZNF758
Transcriptional Regulation by ZNF759
Transcriptional Regulation by ZNF760
Transcriptional Regulation by ZNF761
Transcriptional Regulation by ZNF762
Transcriptional Regulation by ZNF763
Transcriptional Regulation by ZNF764
Transcriptional Regulation by ZNF765
Transcriptional Regulation by ZNF766
Transcriptional Regulation by ZNF767
Transcriptional Regulation by ZNF768
Transcriptional Regulation by ZNF769
Transcriptional Regulation by ZNF770
Transcriptional Regulation by ZNF771
Transcriptional Regulation by ZNF772
Transcriptional Regulation by ZNF773
Transcriptional Regulation by ZNF774
Transcriptional Regulation by ZNF775
Transcriptional Regulation by ZNF776
Transcriptional Regulation by ZNF777
Transcriptional Regulation by ZNF778
Transcriptional Regulation by ZNF779
Transcriptional Regulation by ZNF780
Transcriptional Regulation by ZNF781
Transcriptional Regulation by ZNF782
Transcriptional Regulation by ZNF783
Transcriptional Regulation by ZNF784
Transcriptional Regulation by ZNF785
Transcriptional Regulation by ZNF786
Transcriptional Regulation by ZNF787
Transcriptional Regulation by ZNF788
Transcriptional Regulation by ZNF789
Transcriptional Regulation by ZNF790
Transcriptional Regulation by ZNF791
Transcriptional Regulation by ZNF792
Transcriptional Regulation by ZNF793
Transcriptional Regulation by ZNF794
Transcriptional Regulation by ZNF795
Transcriptional Regulation by ZNF796
Transcriptional Regulation by ZNF797
Transcriptional Regulation by ZNF798
Transcriptional Regulation by ZNF799
Transcriptional Regulation by ZNF800
Transcriptional Regulation by ZNF801
Transcriptional Regulation by ZNF802
Transcriptional Regulation by ZNF803
Transcriptional Regulation by ZNF804
Transcriptional Regulation by ZNF805
Transcriptional Regulation by ZNF806
Transcriptional Regulation by ZNF807
Transcriptional Regulation by ZNF808
Transcriptional Regulation by ZNF809
Transcriptional Regulation by ZNF810
Transcriptional Regulation by ZNF811
Transcriptional Regulation by ZNF812
Transcriptional Regulation by ZNF813
Transcriptional Regulation by ZNF814
Transcriptional Regulation by ZNF815
Transcriptional Regulation by ZNF816
Transcriptional Regulation by ZNF817
Transcriptional Regulation by ZNF818
Transcriptional Regulation by ZNF819
Transcriptional Regulation by ZNF820
Transcriptional Regulation by ZNF821
Transcriptional Regulation by ZNF822
Transcriptional Regulation by ZNF823
Transcriptional Regulation by ZNF824
Transcriptional Regulation by ZNF825
Transcriptional Regulation by ZNF826
Transcriptional Regulation by ZNF827
Transcriptional Regulation by ZNF828
Transcriptional Regulation by ZNF829
Transcriptional Regulation by ZNF830
Transcriptional Regulation by ZNF831
Transcriptional Regulation by ZNF832
Transcriptional Regulation by ZNF833
Transcriptional Regulation by ZNF834
Transcriptional Regulation by ZNF835
Transcriptional Regulation by ZNF836
Transcriptional Regulation by ZNF837
Transcriptional Regulation by ZNF838
Transcriptional Regulation by ZNF839
Transcriptional Regulation by ZNF840
Transcriptional Regulation by ZNF841
Transcriptional Regulation by ZNF842
Transcriptional Regulation by ZNF843
Transcriptional Regulation by ZNF844
Transcriptional Regulation by ZNF845
Transcriptional Regulation by ZNF846
Transcriptional Regulation by ZNF847
Transcriptional Regulation by ZNF848
Transcriptional Regulation by ZNF849
Transcriptional Regulation by ZNF850
Transcriptional Regulation by ZNF851
Transcriptional Regulation by ZNF852
Transcriptional Regulation by ZNF853
Transcriptional Regulation by ZNF854
Transcriptional Regulation by ZNF855
Transcriptional Regulation by ZNF856
Transcriptional Regulation by ZNF857
Transcriptional Regulation by ZNF858
Transcriptional Regulation by ZNF859
Transcriptional Regulation by ZNF860
Transcriptional Regulation by ZNF861
Transcriptional Regulation by ZNF862
Transcriptional Regulation by ZNF863
Transcriptional Regulation by ZNF864
Transcriptional Regulation by ZNF865
Transcriptional Regulation by ZNF866
Transcriptional Regulation by ZNF867
Transcriptional Regulation by ZNF868
Transcriptional Regulation by ZNF869
Transcriptional Regulation by ZNF870
Transcriptional Regulation by ZNF871
Transcriptional Regulation by ZNF872
Transcriptional Regulation by ZNF873
Transcriptional Regulation by ZNF874
Transcriptional Regulation by ZNF875
Transcriptional Regulation by ZNF876
Transcriptional Regulation by ZNF877
Transcriptional Regulation by ZNF878
Transcriptional Regulation by ZNF879
Transcriptional Regulation by ZNF880
Transcriptional Regulation by ZNF881
Transcriptional Regulation by ZNF882
Transcriptional Regulation by ZNF883
Transcriptional Regulation by ZNF884
Transcriptional Regulation by ZNF885
Transcriptional Regulation by ZNF886
Transcriptional Regulation by ZNF887
Transcriptional Regulation by ZNF888
Transcriptional Regulation by ZNF889
Transcriptional Regulation by ZNF890
Transcriptional Regulation by ZNF891
Transcriptional Regulation by ZNF892
Transcriptional Regulation by ZNF893
Transcriptional Regulation by ZNF894
Transcriptional Regulation by ZNF895
Transcriptional Regulation by ZNF896
Transcriptional Regulation by ZNF897
Transcriptional Regulation by ZNF898
Transcriptional Regulation by ZNF899
Transcriptional Regulation by ZNF900
Transcriptional Regulation by ZNF901
Transcriptional Regulation by ZNF902
Transcriptional Regulation by ZNF903
Transcriptional Regulation by ZNF904
Transcriptional Regulation by ZNF905
Transcriptional Regulation by ZNF906
Transcriptional Regulation by ZNF907
Transcriptional Regulation by ZNF908
Transcriptional Regulation by ZNF909
Transcriptional Regulation by ZNF910
Transcriptional Regulation by ZNF911
Transcriptional Regulation by ZNF912
Transcriptional Regulation by ZNF913
Transcriptional Regulation by ZNF914
Transcriptional Regulation by ZNF915
Transcriptional Regulation by ZNF916
Transcriptional Regulation by ZNF917
Transcriptional Regulation by ZNF918
Transcriptional Regulation by ZNF919
Transcriptional Regulation by ZNF920
Transcriptional Regulation by ZNF921
Transcriptional Regulation by ZNF922
Transcriptional Regulation by ZNF923
Transcriptional Regulation by ZNF924
Transcriptional Regulation by ZNF925
Transcriptional Regulation by ZNF926
Transcriptional Regulation by ZNF927
Transcriptional Regulation by ZNF928
Transcriptional Regulation by ZNF929
Transcriptional Regulation by ZNF930
Transcriptional Regulation by ZNF931
Transcriptional Regulation by ZNF932
Transcriptional Regulation by ZNF933
Transcriptional Regulation by ZNF934
Transcriptional Regulation by ZNF935
Transcriptional Regulation by ZNF936
Transcriptional Regulation by ZNF937
Transcriptional Regulation by ZNF938
Transcriptional Regulation by ZNF939
Transcriptional Regulation by ZNF940
Transcriptional Regulation by ZNF941
Transcriptional Regulation by ZNF942
Transcriptional Regulation by ZNF943
Transcriptional Regulation by ZNF944
Transcriptional Regulation by ZNF945
Transcriptional Regulation by ZNF946
Transcriptional Regulation by ZNF947
Transcriptional Regulation by ZNF948
Transcriptional Regulation by ZNF949
Transcriptional Regulation by ZNF950
Transcriptional Regulation by ZNF951
Transcriptional Regulation by ZNF952
Transcriptional Regulation by ZNF953
Transcriptional Regulation by ZNF954
Transcriptional Regulation by ZNF955
Transcriptional Regulation by ZNF956
Transcriptional Regulation by ZNF957
Transcriptional Regulation by ZNF958
Transcriptional Regulation by ZNF959
Transcriptional Regulation by ZNF960
Transcriptional Regulation by ZNF961
Transcriptional Regulation by ZNF962
Transcriptional Regulation by ZNF963
Transcriptional Regulation by ZNF964
Transcriptional Regulation by ZNF965
Transcriptional Regulation by ZNF966
Transcriptional Regulation by ZNF967
Transcriptional Regulation by ZNF968
Transcriptional Regulation by ZNF969
Transcriptional Regulation by ZNF970
Transcriptional Regulation by ZNF971
Transcriptional Regulation by ZNF972
Transcriptional Regulation by ZNF973
Transcriptional Regulation by ZNF974
Transcriptional Regulation by ZNF975
Transcriptional Regulation by ZNF976
Transcriptional Regulation by ZNF977
Transcriptional Regulation by ZNF978
Transcriptional Regulation by ZNF979
Transcriptional Regulation by ZNF980
Transcriptional Regulation by ZNF981
Transcriptional Regulation by ZNF982
Transcriptional Regulation by ZNF983
Transcriptional Regulation by ZNF984
Transcriptional Regulation by ZNF985
Transcriptional Regulation by ZNF986
Transcriptional Regulation by ZNF987
Transcriptional Regulation by ZNF988
Transcriptional Regulation by ZNF989
Transcriptional Regulation by ZNF990
Transcriptional Regulation by ZNF991
Transcriptional Regulation by ZNF992
Transcriptional Regulation by ZNF993
Transcriptional Regulation by ZNF994
Transcriptional Regulation by ZNF995
Transcriptional Regulation by ZNF996
Transcriptional Regulation by ZNF997
Transcriptional Regulation by ZNF998
Transcriptional Regulation by ZNF999
Transcriptional Regulation by ZNF1000

Figure 6. 12. Reactome pathway analysis depicted as a FoamTree showing the main molecular pathways significantly upregulated by tumour-associated astrocytes (5-ALA negative cells) as compared to invasive GBM cells (5-ALA positive cells) from surgically resected and FACS-isolated tissue. Reactome computational tool can cluster the significant pathways (highlighted in yellow) according to major hierarchical pathway families such as cell cycle pathways, protein metabolism, signalling, development or pathways involved in disease pathway. The pathways of interest that are uniquely upregulated in 5-ALA negative tumour-associated astrocytes or commonly upregulated in both co-cultured astrocytes after FACS-isolation at Day 10 and 5-ALA negative tumour-associated astrocytes were magnified in the black frame squares. The pathways are protein translation (A), cell response to stresses including response of EIF2AK4 (GCN2) to amino acid deficiency (B), Regulation of expression of SLITs and ROBOs (C), Immune signalling (D), rRNA processing in the nucleus and cytosol (E), Nonsense-Mediated Decay (NMD) (F), and Influenza infection including viral mRNA translation pathway (G. *The black thick lines indicate the position of the pathway family within the FoamTree.*

6.3.3.1 Co-cultured YFP-astrocytes upregulate intercellular communication pathways.

Visualising the evidence of the YFP within the primary invasive GBM cells in our Gliomasphere Matrix model indicates the establishment of intercellular communicating channels (Figure 5. 7G-I, and 5. 8E-G), which have allowed the transfer of secreted proteins from the YFP-labelled astrocytes into the GBM cells. This was corroborated by the results of the RNA sequencing data, which showed the significant up-regulation of intra-flagellar transport pathway (*p-value* 1.01e-02; FDR 6.99e-01), which may be responsible for this protein exchange. The significant genes clustered in this pathway are *dynlrb1* (*p-value* 9.21e-03), *tubb2a* (*p-value* 0.03), *tuba1a* (*p-value* 4.31e-04), *tubb2b* (*p-value* 9.36e-03), *ttc30a* (*p-value* 0.04), and *dynll1* (*p-value* 0.04). These genes, in addition to *actg1* (*p-value* 1.62e-3), and *ap2m1* (*p-value* 0.02), were annotated by Reactome analyses as important genes that mediate the gap junction trafficking of ions and small molecules **(Figure 6. 13)**. Comparing all twenty co-cultured YFP-astrocytes samples to all six astrocyte monoculture controls at both time points reveals significant upregulation of *gap43* (*p-value* 3.55e-6; FDR 0.03) **(Figure 6. 13I)** and *c1orf61* (*p-value* 7.27e-9; FDR 2.68e-4) **(Figure 6. 25C)**, which are both known to be involved in microtubule formation and enhancement of microtubules functionality (Osswald *et al.*, 2015; Jung *et al.*, 2017). This indicates the functional enhancement of channelling and communication processes between GIN cells and YFP-astrocytes cells in our Gliomasphere Matrix model.

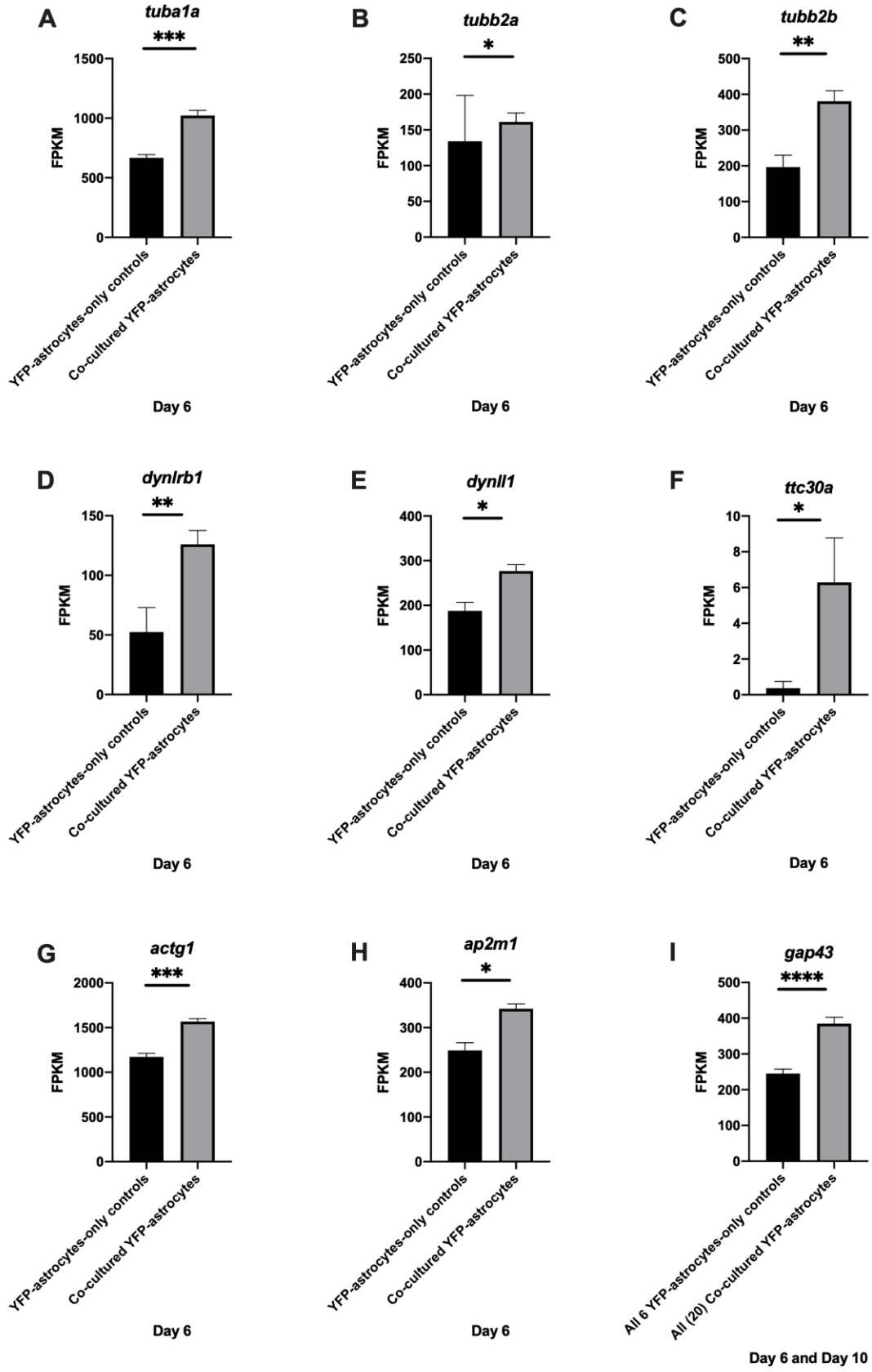

A
tuba1a
***
FPKM
1500
1000
500
0
YFP-astrocytes-only controls
Co-cultured YFP-astrocytes
Day 6
B
tubb2a
*
FPKM
250
200
150
100
50
0
YFP-astrocytes-only controls
Co-cultured YFP-astrocytes
Day 6
C
tubb2b
**
FPKM
500
400
300
200
100
0
YFP-astrocytes-only controls
Co-cultured YFP-astrocytes
Day 6
D
dynlrb1
**
FPKM
150
100
50
0
YFP-astrocytes-only controls
Co-cultured YFP-astrocytes
Day 6
E
dynll1
*
FPKM
400
300
200
100
0
YFP-astrocytes-only controls
Co-cultured YFP-astrocytes
Day 6
F
ttc30a
*
FPKM
10
8
6
4
2
0
YFP-astrocytes-only controls
Co-cultured YFP-astrocytes
Day 6
G
actg1
***
FPKM
2000
1500
1000
500
0
YFP-astrocytes-only controls
Co-cultured YFP-astrocytes
Day 6
H
ap2m1
*
FPKM
400
300
200
100
0
YFP-astrocytes-only controls
Co-cultured YFP-astrocytes
Day 6
I
gap43
****
FPKM
500
400
300
200
100
0
All 6 YFP-astrocytes-only controls
All (20) Co-cultured YFP-astrocytes
Day 6 and Day 10

Figure 6. 13. Cocultured astrocytes upregulated intercellular communications pathways. The co-cultured astrocytes showed upregulation of channelling pathways in response to GIN cells (A-I). Genes involved in the intra-flagellar transport pathway (A-H) were upregulated in the co-cultured astrocytes in relation to astrocyte-only controls at Day 6. In addition, collective comparison of all 20 co-cultured astrocytes to astrocyte monocultures of both time points (Day 6 and Day 10) revealed significant upregulation of *gap43* (I), which is the only known gene so far to be functionally involved in the formation of microtubules (Osswald *et al.*, 2015). *FPKM; Fragments Per Kilobase of Transcript per Million reads mapped. *, **, ***, and **** equal to p-value of 0.05, 0.01,0.001, and ≥ 0.0001 respectively*.

6.3.3.2. Co-cultured YFP-astrocytes upregulate axon guidance pathways.

Both of the co-cultured astrocytes (after 6 and 10 days of co-culture with GBM cells) and 5-ALA negative tumour associated astrocytes from surgically resected samples, significantly upregulated gene families (relative to YFP-astrocyte-only controls and 5-ALA positive primary GBM cells respectively) that are known to regulate axon growth and migration at early stages of development. During embryo development, these groups of ligands and associated receptors provide attractive and repulsive signals to alter the axon cytoskeleton and guide the highly motile axon cone (at the axon tip) through different microenvironments to reach their ultimate spatial developmental targets (Chédotal, 2019; Suter and Jaworski, 2019). Axon path-finding processes are also known to be associated with cancer progression (Biankin *et al.*, 2012), where they may enhance cell migration and new vessel formation (Mehlen, Delloye-Bourgeois and Chédotal, 2011). For example, co-cultured astrocytes upregulated the following gene families relative to YFP-astrocyte-only controls; Semaphorins (*cfl1* (*p-value* 0.03)*, myl6* (*p-value* 0.01)*, plxnd1* (*p-value* 0.02)*, gsk3a* (*p-value* 0.02)*, rhob* (*p-value 5.11e-3*), Ephrins (*actg1* (*p-value* 1.62e-3) **(Figure 6. 13G)**, *ap2m1* (*p-value* 0.02), *cfl1, myl6, ephb4* (*p-value* 0.02), *ephb2* (*p-value* 0.02), *kalrn* (*p-value* 8.59e-3), *sdc2* (*p-value* 0.04), and *pak3* (*p-value* 0.04), and associated receptors known as Roundabouts (ROBO2 (*p-value* 1.45e-15; FDR 2.68e-11) **(Figure 6. 14A-K)**. Astrocytes (co-cultured with GBM cells for 10 days) significantly downregulated *enfb2* (*p-value* 2.96e-6; FDR 0.02) which is a receptor of Ephrins **(Figure 6. 14L)**.

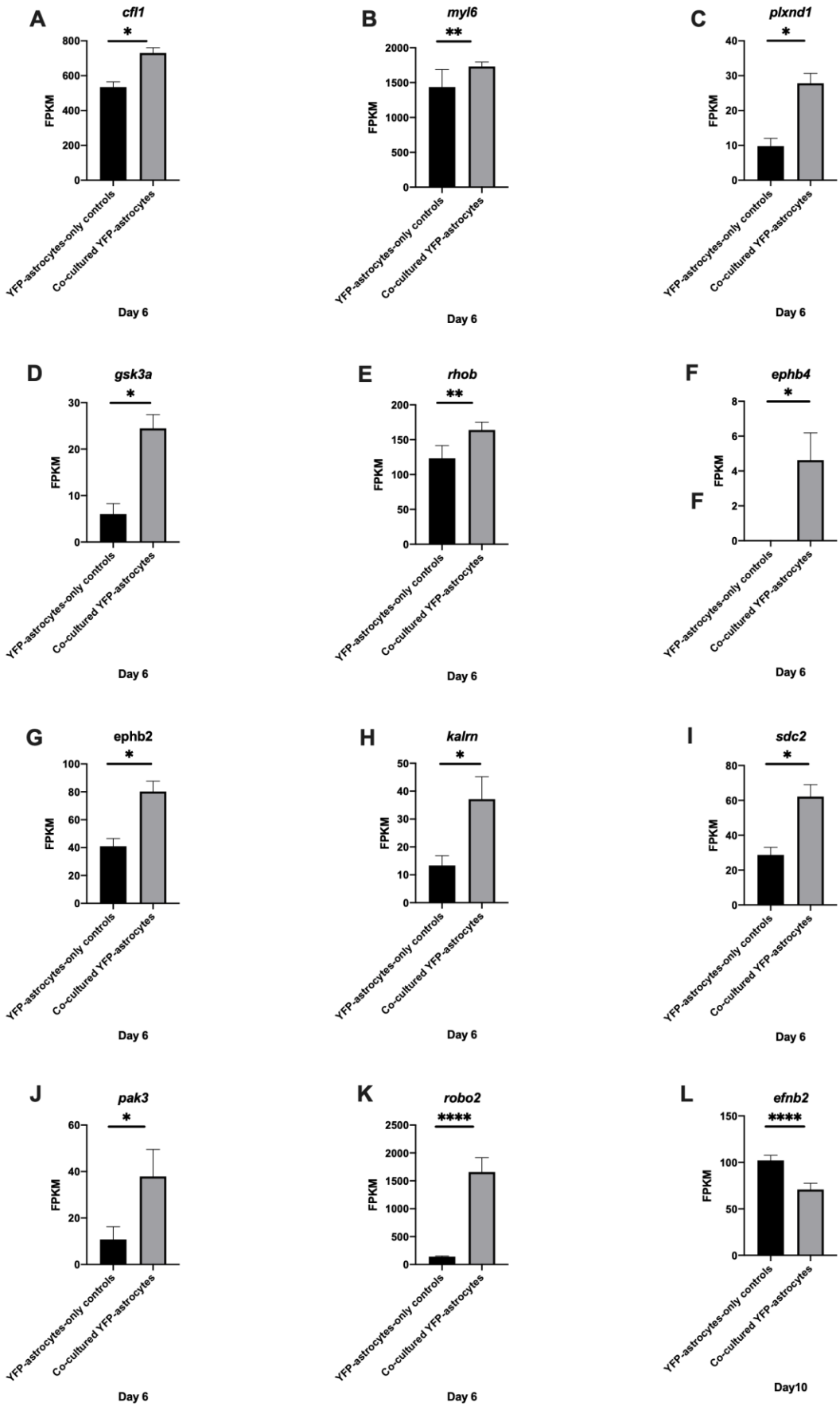

A
cfl1
*
FPKM
800
600
400
200
0
YFP-astrocytes-only controls
Co-cultured YFP-astrocytes
Day 6
B
myl6
**
FPKM
2000
1500
1000
500
0
YFP-astrocytes-only controls
Co-cultured YFP-astrocytes
Day 6
C
plxnd1
*
FPKM
40
30
20
10
0
YFP-astrocytes-only controls
Co-cultured YFP-astrocytes
Day 6
D
gsk3a
*
FPKM
30
20
10
0
YFP-astrocytes-only controls
Co-cultured YFP-astrocytes
Day 6
E
rhob
**
FPKM
200
150
100
50
0
YFP-astrocytes-only controls
Co-cultured YFP-astrocytes
Day 6
F
ephb4
*
FPKM
8
6
4
2
0
F
YFP-astrocytes-only controls
Co-cultured YFP-astrocytes
Day 6
G
ephb2
*
FPKM
100
80
60
40
20
0
YFP-astrocytes-only controls
Co-cultured YFP-astrocytes
Day 6
H
kalrn
*
FPKM
50
40
30
20
10
0
YFP-astrocytes-only controls
Co-cultured YFP-astrocytes
Day 6
I
sdc2
*
FPKM
80
60
40
20
0
YFP-astrocytes-only controls
Co-cultured YFP-astrocytes
Day 6
J
pak3
*
FPKM
60
40
20
0
YFP-astrocytes-only controls
Co-cultured YFP-astrocytes
Day 6
K
robo2
****
FPKM
2500
2000
1500
1000
500
0
YFP-astrocytes-only controls
Co-cultured YFP-astrocytes
Day 6
L
efnb2
****
FPKM
150
100
50
0
YFP-astrocytes-only controls
Co-cultured YFP-astrocytes
Day10

Figure 6. 14. Co-cultured astrocytes upregulated axon guidance pathways in response to GIN cells. Day 6 Co-cultured astrocytes upregulated groups of genes (A-L) know to be gene families activated during brain development to guide the axon tip to reach spatially determined sites, relative to YFP-astrocyte-only controls; Semaphorins (A-E), Ephrins (A, B, and, and F-G), and associated roundabout receptor (K). However, Co-cultured astrocytes (isolated at Day 10) downregulated *enfb2. FPKM; Fragments Per Kilobase of Transcript per Million reads mapped. *, **,* ***, and **** *equal to p-value of 0.05, 0.01,0.001, and ≥ 0.0001 respectively*.

6.3.3.3. Co-cultured astrocytes upregulate Notch signalling.

The co-cultured astrocytes have shown to consistently upregulate the Notch signalling pathway (NSP) throughout the co-culture experiments at both time points (Day 6 and Day 10). The cell-cell communication is crucial to stimulate this pathway. NSP is well known to be involved in many cellular functions such as differentiation, proliferation and regulating pluripotency such as the maintenance of stem properties in NSCs (Nagao, Sugimori and Nakafuku, 2007). In general, NSP is activated when Delta-like and Jagged ligands attach to their corresponding receptors. Biochemical activation downstream of ligand-receptor coupling is referred to as in-trans Notch activation, whereas the activation from the side of the ligand is referred to as Cis activation (Bazzoni and Bentivegna, 2019). In our Gliomasphere Matrix model, Notch within co-cultured YFP-astrocytes was activated in an in-trans fashion where the ligands on GIN cells have likely activated Notch receptors on the neighbouring co-cultured astrocytes. Notch1 is a transmembrane receptor on cell surfaces which also regulates the process of transcription. The intracellular domain of NOTCH1 is cleaved and translocated into the nucleus, where it displaces the co-repressor complex genes such as *ncor2* (*p-value* 0.04), *hdac2* (*p-value* 0.02), *hdac6* (*p-value* 0.049), and *hdac10* (*p-value* 0.02) **(Figure 6. 15A-D)**. In the nucleus, after removing the repressor complexes, NOTCH1 combines with RBPJ (also known as CSL or CBF) and mastermind-like proteins, such as *maml1* which is significantly upregulated (*p-value* 4.38e-3) **(Figure 6. 15E)** to form NOTCH1 co-activator complexes that actives crucial transcription regulators such as *hes-1* (*p-value* 1.06e-3) **(Figure 6. 15H)** and related YRPW protein motifs (Hey) such as *hey2* (*p-value* 0.03) **(Figure 6. 15I)**. The other important master transcription regulator is *myc* which showed no statistical significance despite the possible binding of NOTCH1 to its promoter, with 117 interactions from the DEG list identified by Reactome analyses **(Figure 6. 15J**). *myc* can also transcriptionally-activate master regulatory genes such as the stem and development gene *sox2* (*p-value* 1.5e-4) **(Figure 6. 15M)**, cell cycle master regulator *cdkn2a* (*p-value* 3.62e-3) **(Figure 6. 15L)**, and some immune/inflammatory-

modulatory genes such as *nf-κb* (*p-value* 7.5e-4) **(Figure 6. 15K)**. NSP usually terminates by the ubiquitination of the NOTCH1 intracellular domain mediated by *cdk8* **(Figure 6. 15F)** and *fbxw7* **(Figure 6. 15G)**, which showed no statistical significance (*p-values* 0.13, and 0.69) respectively. This means that *Notch1* is continuously expressed without its cessation signals. The Notch3 signalling pathway is also important for transcription with similar target genes to the Notch1 pathway; for example, *plxnd1* (*p-value* 3.80e-3) **(Figure 6. 15N)** and *fabp7* (*p-value* 7.74e-5) **(Figure 6. 15O)** were significantly upregulated in co-cultured astrocytes. Physiological neurodevelopment of mouse brain and in cancer conditions can be mediated by the synergistic action between *notch1* and *notch3* which was found to be significantly upregulated (*p-value* 0.01) in the co-cultured astrocytes at Day10 in relation to YFP-astrocytes only controls) **(Figure 6. 15P).** It can also transcriptionally-activate the genes discussed above.

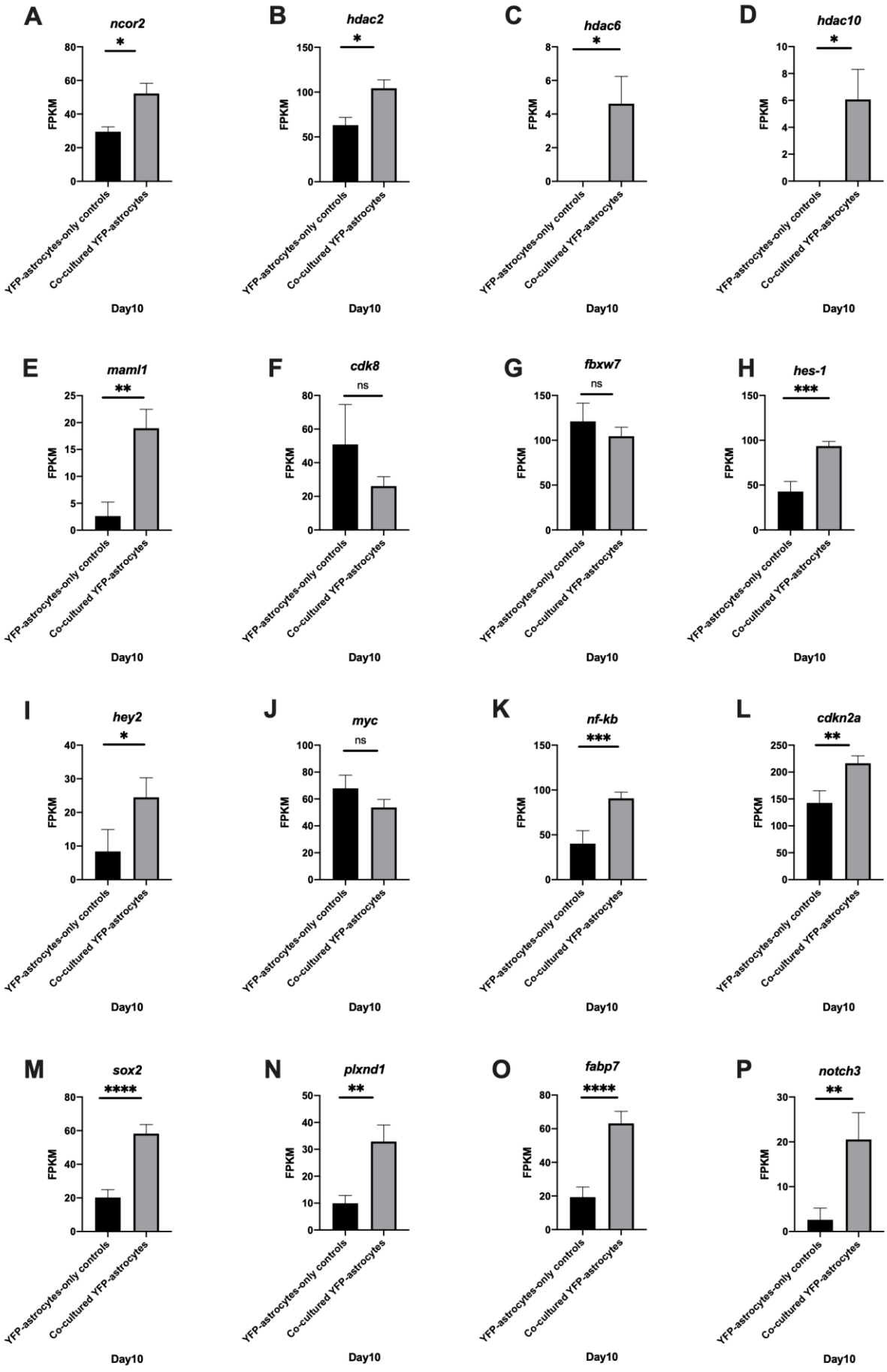

A
ncor2
*
FPKM
80
60
40
20
0
YFP-astrocytes-only controls
Co-cultured YFP-astrocytes
Day10
B
hdac2
*
FPKM
150
100
50
0
YFP-astrocytes-only controls
Co-cultured YFP-astrocytes
Day10
C
hdac6
*
FPKM
8
6
4
2
0
YFP-astrocytes-only controls
Co-cultured YFP-astrocytes
Day10
D
hdac10
*
FPKM
10
8
6
4
2
0
YFP-astrocytes-only controls
Co-cultured YFP-astrocytes
Day10
E
maml1
**
FPKM
25
20
15
10
5
0
YFP-astrocytes-only controls
Co-cultured YFP-astrocytes
Day10
F
cdk8
ns
FPKM
80
60
40
20
0
YFP-astrocytes-only controls
Co-cultured YFP-astrocytes
Day10
G
fbxw7
ns
FPKM
150
100
50
0
YFP-astrocytes-only controls
Co-cultured YFP-astrocytes
Day10
H
hes-1
***
FPKM
150
100
50
0
YFP-astrocytes-only controls
Co-cultured YFP-astrocytes
Day10
I
hey2
*
FPKM
40
30
20
10
0
YFP-astrocytes-only controls
Co-cultured YFP-astrocytes
Day10
J
myc
ns
FPKM
100
80
60
40
20
0
YFP-astrocytes-only controls
Co-cultured YFP-astrocytes
Day10
K
nf-kb
***
FPKM
150
100
50
0
YFP-astrocytes-only controls
Co-cultured YFP-astrocytes
Day10
L
cdkn2a
**
FPKM
250
200
150
100
50
0
YFP-astrocytes-only controls
Co-cultured YFP-astrocytes
Day10
M
sox2
****
FPKM
80
60
40
20
0
YFP-astrocytes-only controls
Co-cultured YFP-astrocytes
Day10
N
plxnd1
**
FPKM
50
40
30
20
10
0
YFP-astrocytes-only controls
Co-cultured YFP-astrocytes
Day10
O
fabp7
****
FPKM
80
60
40
20
0
YFP-astrocytes-only controls
Co-cultured YFP-astrocytes
Day10
P
notch3
**
FPKM
30
20
10
0
YFP-astrocytes-only controls
Co-cultured YFP-astrocytes
Day10

Figure 6. 15. Co-cultured astrocytes upregulated Notch signalling in response to GIN cells. Pathway analysis using the Reactome pathway computational tool showed upregulation of Notch1 and Notch3 signalling particularly at Day 10 (A-P). Co-cultured astrocytes upregulated genes known to remove the co-repressor complexes that inhibit downstream NOTCH1 signalling (A-D). Additionally, *maml1* (E) is known to be part of NOTCH1 co-activator complexes. Co-cultured astrocytes did not show significant upregulation of genes responsible for NOTCH1 ubiquitination (F, and G). The upregulation of genes enhancing the formation of NOTCH1 co-activator complexes and removal of the co-repressor complexes, with lack of NOTCH1 ubiquitination, leads to persistent activation of NOTCH1, and in turn activation of crucial transcription regulators such as *hes-1* (H) and *hey2* (I). Although *myc* (J) did not show significant upregulation, other downstream NOTCH1 effector genes were significantly upregulated (K-O). *notch3* (P), which is known to synergistically act with *Notch1*, was also found to be upregulated. FPKM; Fragments Per Kilobase of Transcript per Million reads mapped. *, **, ***, and **** equal to p-value of 0.05, 0.01,0.001, and ≥ 0.0001 respectively.

6.3.3.4. Co-cultured astrocytes unregulated pathways triggered by oncogenic MAPK and PI3K/AKT signalling.

NSP is known to activate other malignant pathways such as the activation of MAPK and PI3K/AKT pathways (Merlo, 2003; Raghu *et al.*, 2011). In the pathway analyses using the Reactome computational tool, both oncogenic MAPK and PI3K/AKT pathways were not significantly upregulated according to DEG generated by EdgeR. However, the oncogenic MAPK pathway was shown to be significantly upregulated (*p-value* 7.43e-03; FDR 5.49e-02), when DEG generated by DESeq2 at the first time point (Day 6) was analysed using Reactome pathway analysis tool, evidenced by several key regulatory DEG which clustered in this pathway; *snd1* (*p-value* 1.63e-07), *actg1* (*p-value* 1.62e-3) **(Figure 6. 13G)**, *vasp* (*p-value* 0.04), and *calm1* (*p-value* 0.02) **(Figure 6. 16A-C)**, Furthermore, a subset of master regulatory genes within the PI3K/AKT/mTOR pathways was significantly upregulated, such as *akt1* (*p-value* 3.09e-3), *lamtor2* (*p-value* 1.86e-3), and *lamtor5* (*p-value* 0.02) at Day 10 **(Figure 6. 16D-F)**. Notably, all genes discussed above were found to be upregulated by both EdgeR and DESeq2. EdgeR and DESeq2 both showed similar upregulation pattern of MAPK and PI3K/AKT genes, whereas Reactome only showed significant upregulation of these pathways when the analysis conducted on DEG generated by DESeq2. This can be explained by mainly the ranking of these genes, and their association with other genes, within various DEG lists generated by different software packages (EdgeR and DESeq2). The AKT/mTOR pathway genes are likely essential for the significant activation of translation pathway DEG identified, by both EdgeR and DESeq2 in the co-cultured astrocytes at Day 10, which were validated against 5-ALA negative tumour-associated astrocytes from patient samples.

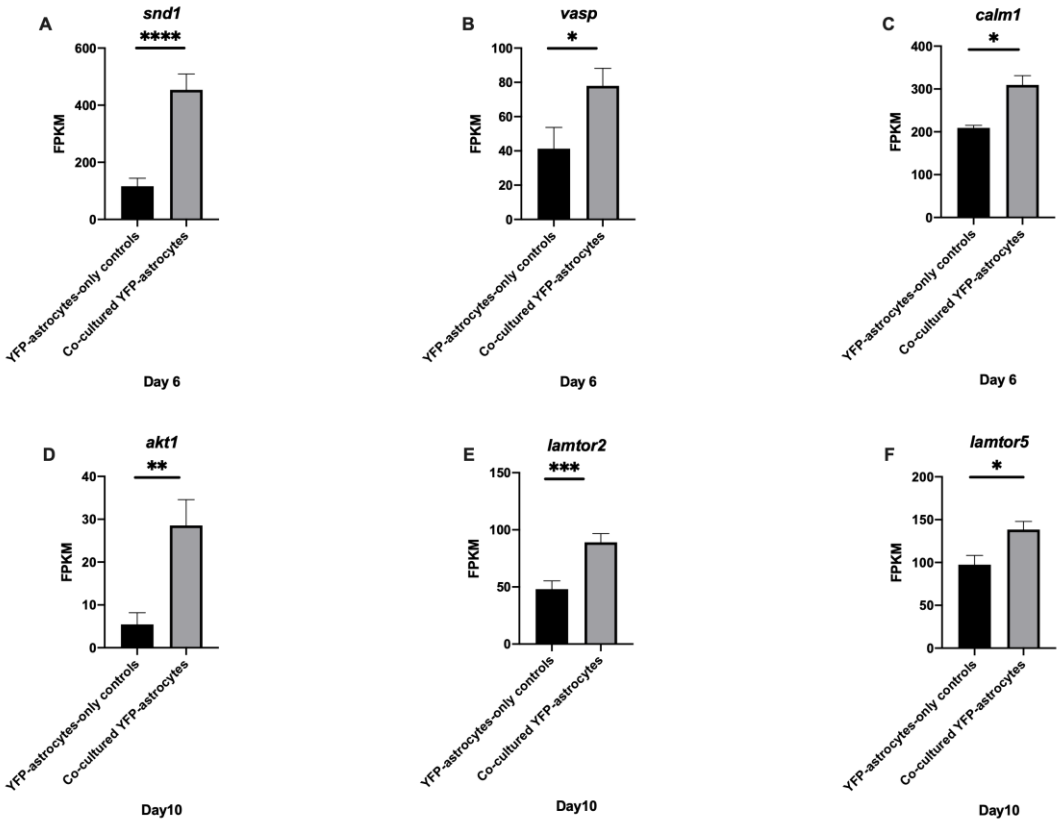


Figure 6. 16. Co-cultured astrocytes upregulated oncogenic MAPK and PI3K/AKT1/mTOR signalling pathways in response to GIN cells. The MAPK pathway key genes *snd1* (A), *vasp* (B), and *calm1* (C) were significantly upregulated in the co-cultured astrocytes at Day 6. Likewise, essential PI3K/AKT1/mTOR pathway regulatory genes were significantly upregulated at Day 10 according to both EdgeR and DESeq2 computational tools, such as *akt1* (D), *lamtor2* (E), and *lamtor5* (F)*. FPKM; Fragments Per Kilobase of Transcript per Million reads mapped. *, **, ****, and ***** equal to p-value of 0.05, 0.01,0.001, and ≥ 0.0001 respectively*.

The oncogenic MAPK pathway leads to the activation of other pathways such as the oncogene-induced cell senescence pathway, mediated by the activation of *cdkn2a* (*p-value* 3.62e-3) (**Figure 6. 15L)**, *mdm4* (*p-value* 8.81e-3), *sp1* (*p-value* 0.02), *fam192a* (*p-value* 0.02), *tfdp2* (*p-value* 3.04e-3), and *tnrc6b* (*p-value* 0.02) (**Figure 6. 17A-E**). Additionally, the activation of oncogenic MAPK signals can also induce the initiation of apoptosis intrinsic pathways via the *diablo* (*p-value* 1.85e-3) (**Figure 6. 17F**), in addition to cell senescence genes as described above.

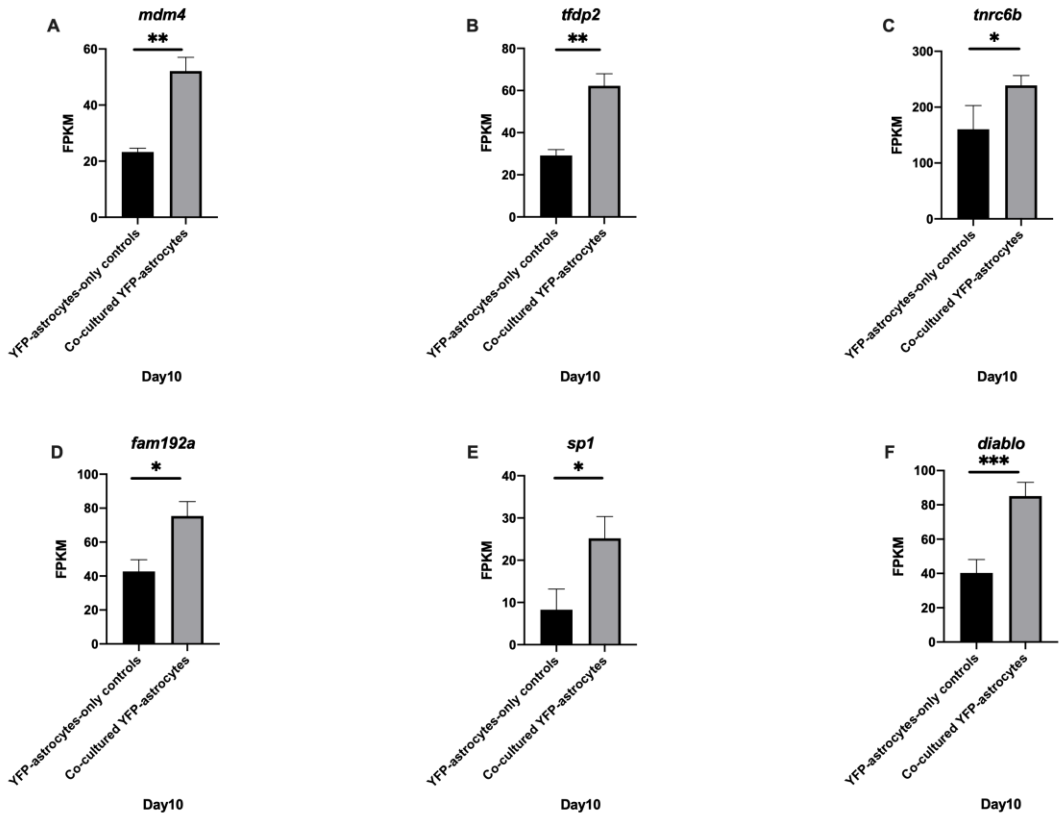


Figure 6. 17. Co-cultured astrocytes upregulated cell senescence and apoptosis genes in response to GIN cells. Co-cultured astrocytes significantly upregulated genes; *mdm4, tfdp2, tnrc6b, fam192a, and sp1* (A-E) that are known to induce endogenous cell senescence intrinsic apoptotic pathways mediated by the *diablo* gene (F). These genes (A-F) are induced in response to the activation of oncogenic MAPK signalling pathways. *FPKM; Fragments Per Kilobase of Transcript per Million reads mapped. *, **, ***,* and **** *equal to p-value of 0.05, 0.01,0.001, and ≥ 0.0001 respectively*.

The co-cultured astrocytes showed significant activation of these apoptotic and senescence genes, likely in response to oncogenic MAPK signalling, which suggests the activation of an acute cellular protective response to malignant signals from GIN cells. However, upregulation of the cell cycle master stimulator *cdkn2a* **(Figure 6. 15L)**, and downregulation of the cell cycle inhibitor *cdkn2b* (*p-value* 1.01e-3) **(Figure 6. 18A)**, may prime the co-cultured astrocytes to re-enter the cell cycle and evade senescence/apoptosis genes and pathways (**Figure 6. 17A-E**), especially *tp53* **(Figure 6. 18B)** and *rb1* **(Figure 6. 18C)** showed no statistical significance (*p-values* 0.19 and 0.86 respectively). The respective upregulation and downregulation of *cdkn2a and cdkn2b* genes in co-cultured astrocytes led to the upregulation of checkpoint genes, such as p53-dependent G1/S DNA damage response genes; *sem1* (*p-value* 6.70e-3), *psmb4* (*p-value* 3.43e-4), *psma4* (*p-value* 0.02), *psmb5* (*p-value* 9.47e-3), and *psmb7* (*p-value* 6.42e-4), *sort1* (*p-value* 0.04), *znhit3* (*p-value* 0.01), *pdia4* (*p-value* 0.02), *thrb* (*p-value* 0.02) **(Figure 6. 18D-L)**.

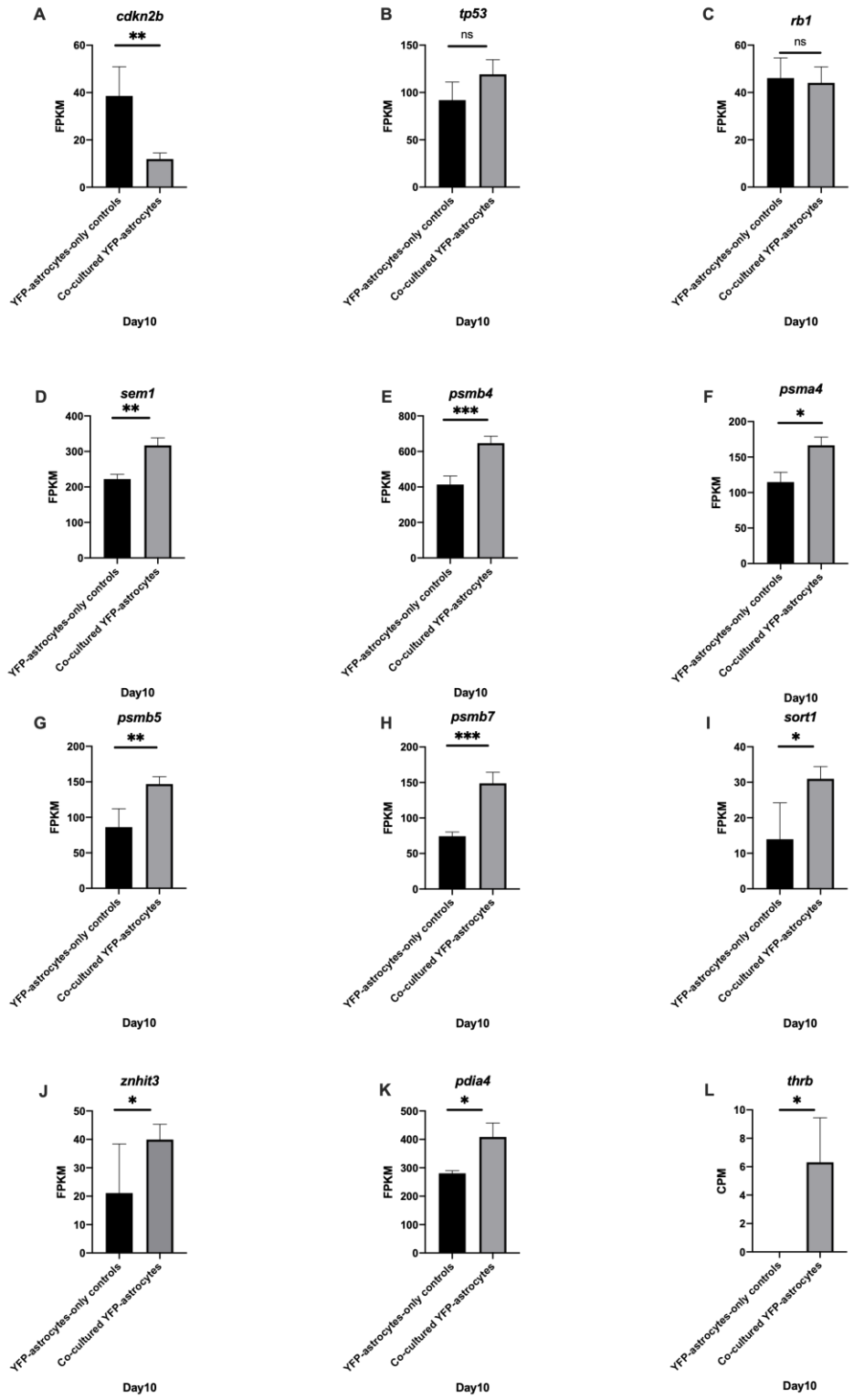


Figure 6. 18. Co-cultured astrocytes upregulated p53-dependent G1/S DNA damage response pathway in response to GIN cells. Co-cultured astrocytes showed significant downregulation of the master cell cycle inhibitor *cdkn2b* (A). The major tumour suppressors *tp53* (B) and *rb1* (C) were not differentially regulated from astrocyte-only controls. However, G1/S DNA damage response genes (D-L) were significantly upregulated in the co-cultured astrocytes in relation to astrocyte monocultures. *FPKM; Fragments Per Kilobase of Transcript per Million reads mapped. *, **, ***,* and ***** equal to p-value of 0.05, 0.01,0.001, and ≥ 0.0001 respectively.*

6.3.3.5. Co-cultured astrocytes and 5-ALA negative tumour associated astrocytes upregulate protein translation pathways.

The co-cultured astrocytes showed increased transcription mediated by Notch signalling and activation of the PI3K/AKT/MTOR pathway, involved in protein translation. Approximately, 26 genes (referred to as entities in the Appendix Table 8. 3) upregulated in the co-cultured YFP-astrocytes (Day10) were aligned to translation initiation (*p-value* 2.67e-3; FDR 4.73e-1), elongation (*p-value* 5.65e-3; FDR 4.73e-1) and termination (*p-value* 7.98; FDR 4.91e-1) in Reactome pathway analysis tool. Notably, the total entities of the translation pathway in Reactome pathway analysis tool are 120 genes. Likewise, our EdgeR analysis of the 5-ALA negative tumour associated astrocytes, with greater RNA-sequencing read depth showed similar results with more stringent gene clustering within the protein translation pathways (FDR 1.87e-4); 66 entities out of 120 were linked to translation initiation (*p-value* 1.11e-16; FDR 6.77e-15), elongation (*p-value* 1.11e-16; FDR 6.77e-15), and termination (*p-value* 1.11e-16; FDR 6.77e-15) (Appendix Table 8. 5). Twenty-six and 66 genes were clustered in the translation pathways of the co-cultured astrocytes (Day 10) and tumour-associated astrocytes respectively. Most of these significantly upregulated genes were *rpl-*, *rps-*, and *eif-related genes*. Twelve key protein translation genes were found to be upregulated in the co-cultured astrocytes and in the 5-ALA surgical specimens **(Figure 6. 19)**. Protein biosynthesis in humans via these genes can also be utilised by viruses to translate their viral mRNA in the cytoplasm using human's ribosomal translational machinery (reviewed in Kash et. al., 2006), especially for the activation of *ivns1abp* (*p-value* 0.03) **(Figure 6. 20A)** which encodes for NS1 protein, initially reported to be a viral protein (Kash et. al., 2006). Two genes, (hspb1 (*p-value* 8.88e-3), smarcb1 (*p-value* 0.03) known to be involved in viral translation were also found to be significantly upregulated in the co-cultured astrocytes **(Figure 6. 20)**. The RPL and RPS genes may be responsible for the significant activation of the GCN2 cellular stress response (*p-value* 1.6e-2; FDR 5.28e-1), and non-sense mediated decay (NMD) (*p-value* 1.52e-2; FDR 5.28e-1) pathways in the co-cultured astrocytes and tumour-associated astrocytes (*p-value* 1.11e-16; FDR 6.77e-15 for both pathways).

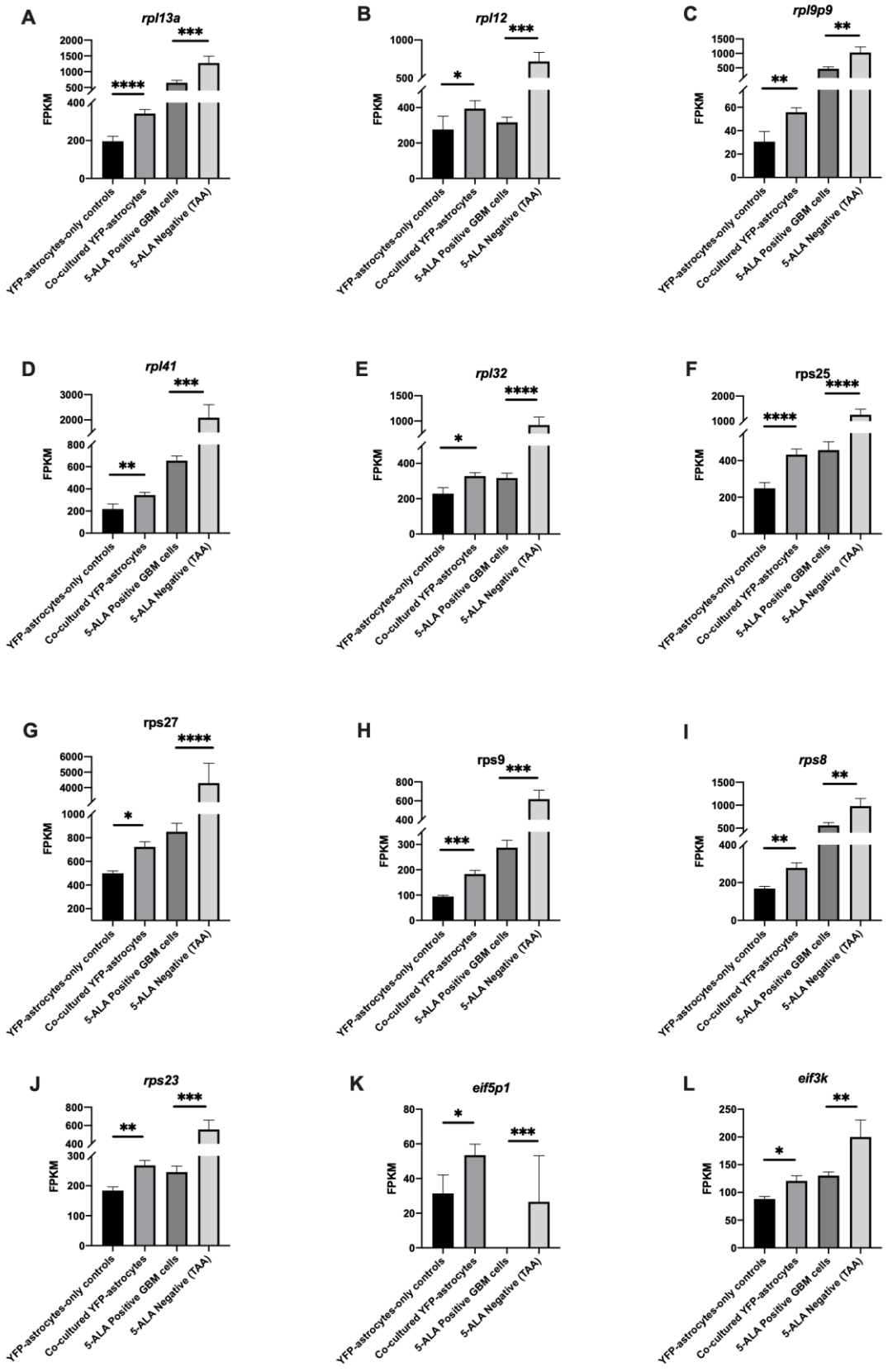

A
rpl13a
FPKM
2000
1500
1000
500
400
200
0
****
***
B
rpl12
1000
500
400
200
0
*
***
C
rpl9p9
1500
1000
500
60
40
20
0
**
**
D
rpl41
3000
2000
800
600
400
200
0
**
***
E
rpl32
1500
1000
400
200
0
*
****
F
rps25
2000
1000
400
200
0
****
****
G
rps27
6000
5000
4000
1000
800
600
400
200
*
****
H
rps9
800
600
400
300
200
100
0
***
***
I
rps8
1500
1000
500
400
200
0
**
**
J
rps23
800
600
400
300
200
100
0
**
***
K
eif5p1
80
60
40
20
0
*
***
L
eif3k
250
200
150
100
50
0
*
**
YFP-astrocytes-only controls
Co-cultured YFP-astrocytes
5-ALA Positive GBM cells
5-ALA Negative (TAA)

Figure 6. 19. Co-cultured astrocytes upregulated protein translation pathways in response to GIN cells. The co-cultured astrocytes and 5-ALA negative tumour-associated astrocytes significantly upregulated 26 and 66 genes involved in protein translation respectively. Twelve of these genes were found to be upregulated in both co-cultured astrocytes (isolated at Day 10) and in the 5-ALA negative surgical specimens. Five of these were *rpl*-related genes (A-E), five genes were *rps*-related (F-J) and two were *eif*-related genes (K-L). *Y-axes were segmented in some of the panels depicted above as the FPKM were generated from different datasets (co-cultured astrocytes and 5-ALA negative surgical samples). FPKM; Fragments Per Kilobase of Transcript per Million reads mapped. *, **, ***, and **** equal to p-value of 0.05, 0.01,0.001, and ≥ 0.0001 respectively.*

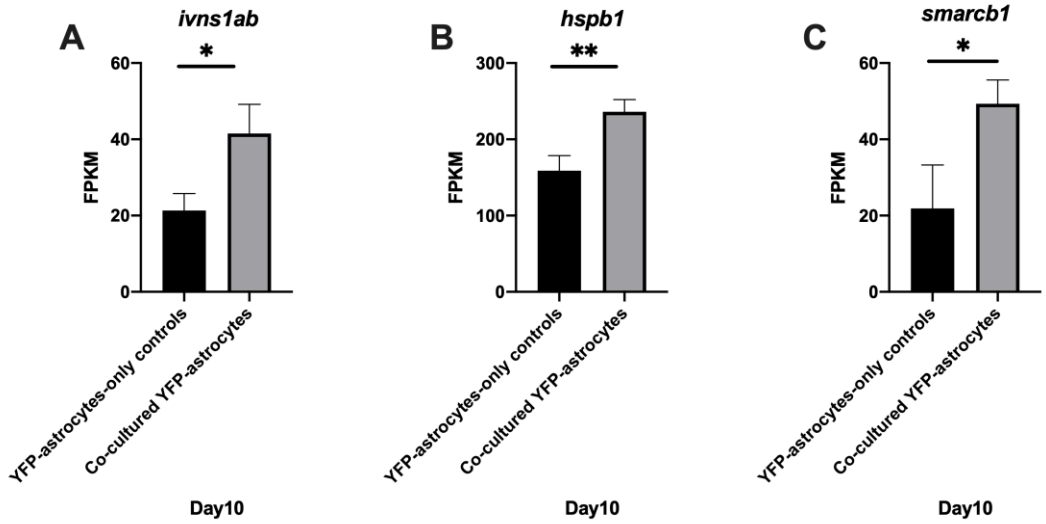


Figure 6. 20. Co-cultured astrocytes upregulated pathways involved in viral mRNA translation in response to GIN cells. The co-cultured astrocytes showed significant upregulation of *ivns1ab* (A), *hspb1* (B), and *smarcb1* (C), which are known to encode for proteins involved in viral mRNA translation. *FPKM; Fragments Per Kilobase of Transcript per Million reads mapped. *, **, ***, and **** equal to p-value of 0.05, 0.01,0.001, and ≥ 0.0001 respectively*.

6.3.3.6. Co-cultured astrocytes upregulate innate immune genes

5-ALA negative tumour-associated astrocytes showed significant activation of immune pathways (*p-value* 5.46e-6; FDR 1.37e-4) (Appendix Table 8. 5). However, these clinical samples were sorted based on 5-ALA fluorescence, specific GBM cells. A caveat is that this means that immune cells were likely captured in the 5-ALA negative FACS-isolated samples. Although the presence of immune cells is unlikely to represent a substantial sub-population, within the GBM invasive margin samples (as the predominant cellular population is tumour associated astrocytes), this minor population of cells may bias the results of 5-ALA negative samples towards immune hyperactivation. Therefore, our analyses on the immune-related genes have focused on the interferon and CD28 co-stimulation pathways, as both were upregulated by the co-cultured astrocytes and tumour-associated astrocytes. The isolated co-cultured astrocytes at Day 6 significantly upregulated interferon gamma genes such as *socs1* (*p-value* 0.02), *socs2* (*p-value* 6.28e-3) and *socs3* (*p-value* 0.04), in addition to the upregulation of genes regulating alpha and beta interferon such as the master regulator *irf3* (*p-value* 0.04) **(Figure 6. 21)**. This is consistent with the upregulation of *socs1* (*p-value* 2.03e-4) and *socs3* (*p-value* 2.74e-3) genes noticed in the 5-ALA tumour associated astrocytes **(Figure 6. 21)**. Although type 1 interferon master regulator *irf3* was significantly activated in Day6 co-cultured YFP-astrocytes, no alpha and/or beta interferon genes showed statistical significance. However, the entire *irf3* pathway and some its downstream typ1 interferon genes were significantly activated at Day 10 (*p-value* 2.40e-02; FDR 7.36e-01) (Appendix Table 8. 3). Cytosolic sensors of the co-cultured astrocytes were induced the activation of type 1 interferon via the STING pathway which is mediated by the master regulator *irf3* (*p-value* 4.15e-4) and *tbk1* (*p-value* 0.02) **(Figure 6. 22)**. Additionally, co-cultured astrocytes significantly upregulated the master inflammatory marker *nf-κb* (*p-value* 7.57e-4) **(Figure 6. 15K)**. This is consistent with the significant upregulation of *ifitm2* (*p-value* 1.23e-5; FDR 0.03) and *ifitm10* (*p-value* 1.99e-4; FDR 0.19), which were amongst the top DEG genes after 10 days of co-culture with GIN cells. Moreover, *ifitm1* (*p-value* 0.02), *ifitm2* (*p-value* 2.35e-3), and *ifitm10* (*p-value* 1.37e-4) are significantly upregulated when collectively comparing all 20 co-culture astrocyte samples versus all six astrocyte monoculture controls. In addition, *ifitm1* (*p-value* 6.24e-4; FDR 0.02), and *ifitm2* (*p-value* 4.50e-5; FDR 7.61e-8) were also upregulated in 5-ALA negative tumour-associated astrocytes of 10 GBM samples relative to 5-ALA positive invasive GBM cells, upon FACS-isolation of 10 surgically resected samples **(Figure 6. 22)**. Indeed, the entire interferon pathway was significantly upregulated (*p-value* 1.97e-11; FDR 6.9e-10). Furthermore, RNA

sequencing data analysis of the low- and high-grade gliomas deposited in TCGA shows that the expression of *ifitm1*, and *iftim2*, in non-tumour brain samples is significantly higher than LGG samples whereas, it is significantly lower than expression in relation to GBM samples (*p-value* <0.0001) **(Figure 6. 23)**. Reactome pathway analysis of the DEG generated by the collective comparison of all 20 co-cultured astrocyte samples versus all six astrocyte monoculture controls revealed an additional significantly upregulated T-cell mediated immune response via receptor (CD28) co-stimulation (*p-value* 2.37e-02; FDR 8.33e-01). Three genes were significantly upregulated and clustered in this pathway; *trib3* (*p-value* 0.04), *pak3* (*p-value* 0.03), *prr5* (*p-value* 0.03), in addition to *akt1* (*p-value* 3.07e-3) **(Figure 6. 24)**. Similarly, 5-ALA negative tumour-associated astrocytes showed significant upregulation of CD28 co-stimulation pathway (*p-value* 1.42e-8; FDR 4.68e-7) with important regulatory genes such as *cd28* (*p-value* 0.02), *icos* (*p-value* 3.88e-4), *ctla4* (*p-value* 5.11e-4) and PD-1 signalling pathway (*p-value* 5.91e-14; FDR 2.60e-12) (which includes *cd247* (PD1) as one of its entities (*p-value* 1.42e-8; FDR 0.01), significantly upregulated **(Figure 6. 24)**.

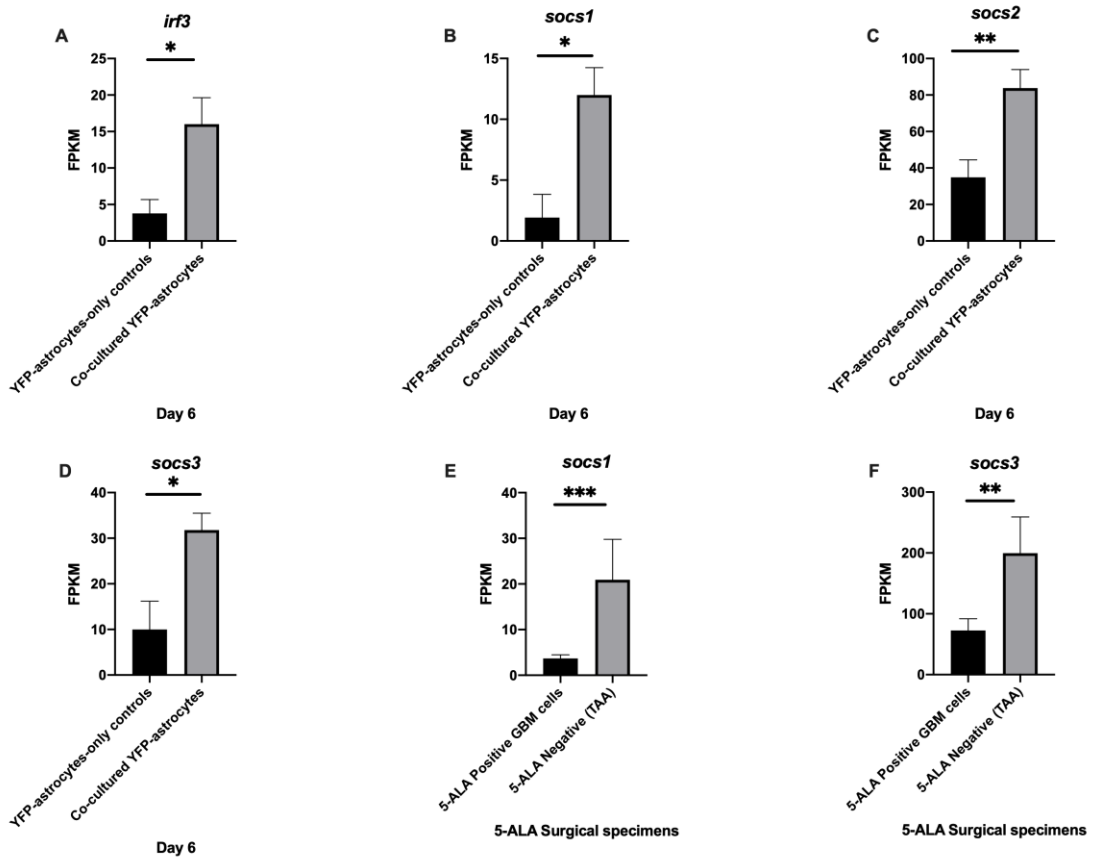


Figure 6. 21. Co-cultured astrocytes upregulated interferon gamma in response to GIN cells. Co-cultured astrocytes isolated at Day 6 showed significant upregulation of the interferon master regulator gene *irf3* (A), in addition to *socs1, socs2,* and *socs3* (B-D), genes which are known to be involved in interferon gamma signalling. Similarly, tumour-associated astrocytes (TAA) showed significant interferon gamma pathway overexpression due to the upregulation of several genes including *socs1* (E), and *socs3* (F)*. FPKM; Fragments Per Kilobase of Transcript per Million reads mapped. *, **, ***,* and **** *equal to p-value of 0.05, 0.01,0.001, and ≥ 0.0001 respectively*.

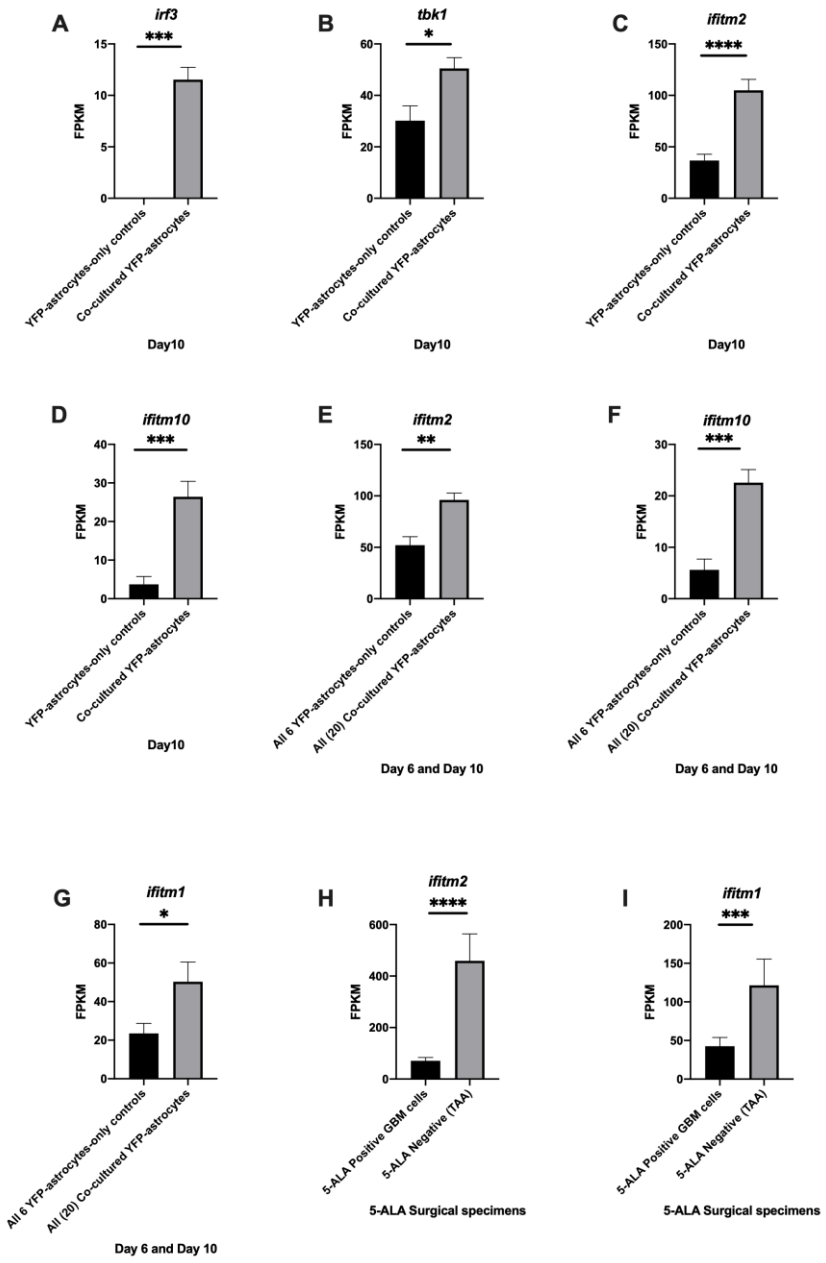


Figure 6. 22. Astrocytes upregulate interferon signalling in response to invasive GBM cells. Tumour associated astrocytes, either those co-cultured with GIN cells (A-G) or constituting brain parenchyma harbouring infiltrative GBM cells (H-I), show significant activation of the interferon pathway. The co-cultured astrocytes isolated at Day 10 significantly upregulated the STING pathway including the master interferon regulators *irf3*, and *tbk1* in addition to several key interferon markers such as *ifitm2*, and *ifitm10*, relative to astrocyte-only controls (A-D). Comparing all 20 co-cultured astrocytes and astrocyte-only controls (Day 6 and Day 10) reveals the significant upregulation of the same interferon genes in addition to *ifitm1* (E-G). These results were validated using RNA sequencing data from 5-ALA negative cells tumour associated astrocytes obtained from surgically-resected and FACS-isolated invasive GBM tissue from 10 patients. 5-ALA negative tumour-associated astrocytes significantly upregulated interferon markers *ifitm1* and *ifitm2* relative to 5-ALA positive invasive GBM cells (H, and I). *FPKM; Fragments Per Kilobase of Transcript per Million reads mapped. *,**,***,and **** equal to p-value of 0.05, 0.01,0.001, and ≥ 0.0001 respectively*.

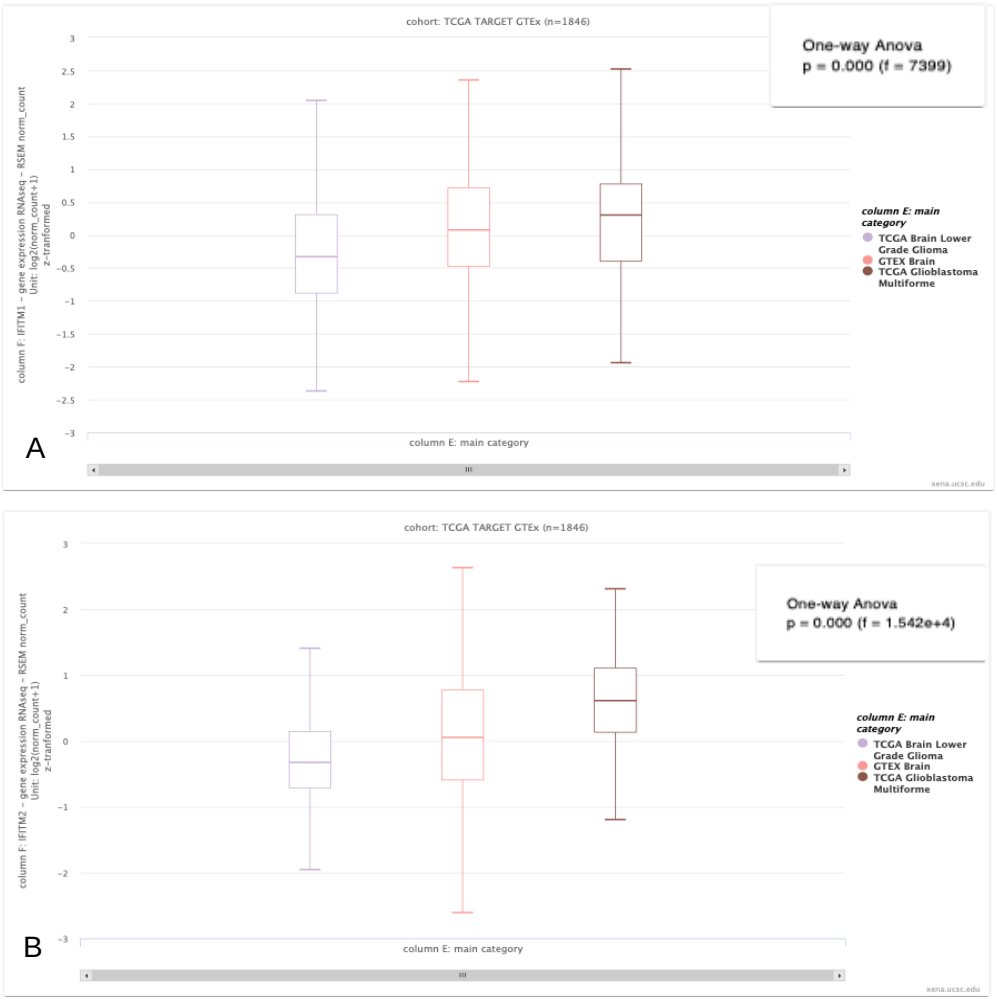


Figure 6. 23. TCGA RNA-sequencing data shows variable interferon pathway expression. Analysis of gene expression from 1846 glioma cases reveals that *ifitm1* (A), and *ifitm2* (B) are significantly upregulated in GBM relative to LGG and to non-tumour brain (GTEX brain dataset), whereas both GBM and non-tumour brain show significant upregulation of *ifitm1/2* relative to LGG. *P-value was stated as equal to 0.000 due to significance of more than 0.0001.*

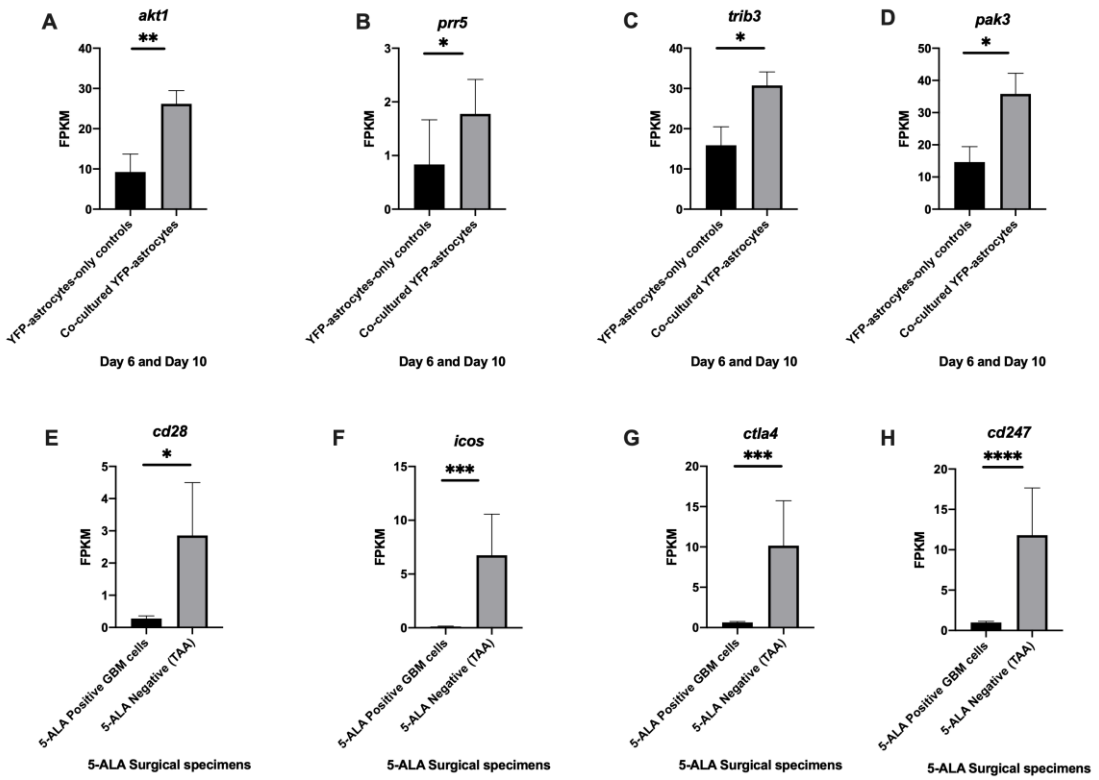


Figure 6. 24. Co-cultured astrocytes upregulated genes encoding for CD28-costimulatory molecules in response to GIN cells. Collective comparison of all 20 co-cultured astrocyte samples versus all six astrocyte-monoculture controls of both time points (Day6 and Day 10), revealed upregulation of CD28 co-stimulatory genes (A-D). These results were validated against 5-ALA negative tumour-associated astrocytes isolated from surgical specimens, which revealed the upregulation of genes encoding for CD28 co-stimulation factors such as *cd28* (E) and *icos* (F), in addition to genes involved in CD28 inhibition such as *ctla4* (G) and *cd247* (H). *FPKM; Fragments Per Kilobase of Transcript per Million reads mapped. *, **, ****, and ***** equal to p-value of 0.05, 0.01,0.001, and ≥ 0.0001 respectively*.

6.3.3.7. The *c1orf61* gene identified as a novel putative determinant of astrocytic genetic response to GBM cross-communication

The combined consideration of all YFP-astrocytes co-cultured with each of 10 distinct patient-derived GIN cell lines within Gliomasphere Matrices and at both Day 6 and Day 10, presents a stringent selection of significant RNA sequencing-based DEG despite inter-tumour genetic heterogeneity (i.e. identifying mean astrocytic DEG in response to 10 GIN lines). The comparison of all 20 co-cultured astrocyte samples relative to all 6 YFP-controls at both Day 6 and Day 10, showed significant upregulation of Notch3 (*p-value* 1.36e-03; FDR 8.33-01), Notch4 (*p-value* 4.05e-02; FDR 8.33-01) and WNT signalling pathways (*p-value* 2.89e-02; FDR 8.33-01) pathways (Appendix Table 8. 4). In addition, a developmental gene not well characterised in the context of brain tumour biology, *c1orf61*, revealed significant upregulation in co-cultured astrocytes at both Day 6 and Day 10 (**Figure 6. 25**) and was identified as the only gene that was significantly upregulated > 2-fold relative to astrocyte monocultures (*p-value* 7.27e-9; FDR 2.68e-4) **(Figure 6. 7C, Figure 6. 8C, Figure 6. 9C, and Figure 6. 10C, and Figure 6. 25)**. Moreover, the comparison has also revealed one, poorly studied, significantly downregulated gene known as *ac098934.2* (*p-value* 2.19e-6; FDR 0.03). These two genes were identified to have significant fold changes when the FDR was adjusted to <0.05, and log2 fold change to 1 (2-fold change). However, reducing the log2 fold change to >0.585 (1.5-fold change) reveals significant upregulation of *gap43* (*p-value* 3.55e-6; FDR 0.03) **(Figure 6. 13l)**, and *igfbp7* (*p-value* 3.06e-6; FDR 0.03). The *c1orf61* has recently been linked into many cancers including HGG. However, *c1orf61* was also shown to be involved in several immune mechanisms listed in (Appendix Table 8. 6) according to the immuNet computational tool (http://immunet.princeton.edu). We computationally probed *c1orf61* further for assumed immune functions and possible malignant association using the Immunet website and Xena TCGA bioinformatics online tools respectively. Thus, *c1orf61* was screened across all pathways in Table 8. 6 described by Immunet and only four immune mechanisms were found to be associated: antigen processing and presentation; complement and coagulation cascades; haematopoietic cell lineage; and intestinal immune network for IgA production **(Figure 6. 26)**. Large immune gene networks linking *c1orf61* to these four immune pathways were next generated. Statistical adjustment of the relationship (between *c1orf61* and genes in these different immune networks) confidence interval to ≥ 95%, enhanced the refinement of many genes in these immune genetic trees **(Figure 6. 26)**. This analysis was conducted to reveal any association between

C1orf61 and any immune mechanism. However, the identified genes in each immune network were screened against our data and none showed statistical significance (data not shown). This suggests poor association of *c1orf61*, which was expressed in the co-cultured YFP-astrocytes in our Gliomasphere matrix model, with any proposed immune function. Screening of *c1orf61* in publicly accessible TCGA data revealed upregulation in both GBM and LGG as compared to all other human somatic cancers **(Figure 6. 27)**, which suggests an essential role within gliomas. We utilized UCSC TumorMap tool (https://tumormap.ucsc.edu), previously described in (Hoadley *et al.*, 2018) to classify 10000 tumours from 33 cancer types, to assess *c1orf61* expression in various subtypes of GBMs and LGGs **(Figure 6. 28)**. TumorMap analysis was consistent with the analysis conducted using Xena computational tool as it showed that *c1orf61* is uniquely upregulated in low- and high-grade gliomas as compared to other somatic tumours **(Figure 6. 28B)**. Furthermore, TumorMap showed that *c1orf61* is upregulated in various subtypes of LGGs; IDH wild-type, IDH mutant-codel and IDH mutant-non-codel **(Figure 6. 28C)**. Moreover, *c1orf61* was shown to be unregulated in IDH wild-type, and IDH mutant-non-codel GBM tumours **(Figure 6. 28D)**.

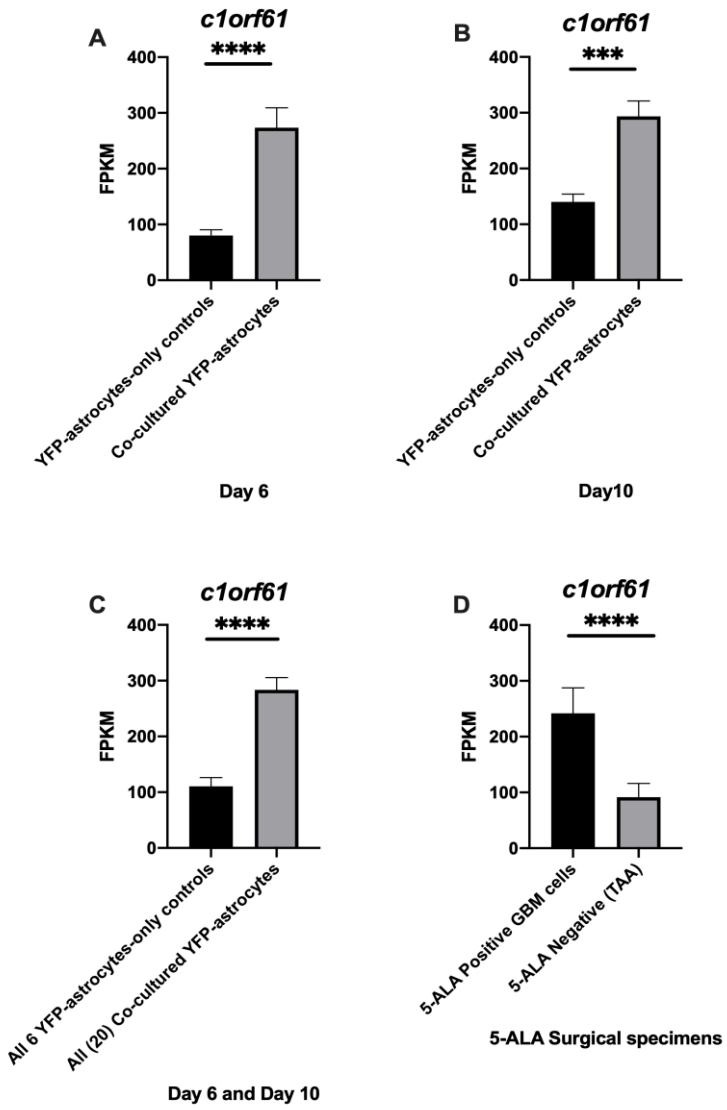


Figure 6. 25. Astrocytes upregulate *c1orf61* in response to invasive GBM cells. C1orf61 was identified as a novel gene significantly upregulated by astrocytes upon co-culture with each of 10 GIN cell lines at Day 6 and Day 10 (A-B). *c1orf61* was the only gene identified which was significanly upregulated > 2-fold by co-cultured astrocytes when comparing all 20 astrocyte-GIN co-cultures relative to all 6 control YFP-astrocyte-only samples (C). The *c1orf61* gene was also significanly upregulated in 5-ALA positive cells (GBM invasive cells) relative to 5-ALA negative cells (tumour associated astrocytes), determined from 10 samples obtained using 5-ALA guided surgery followed FACS-isolation of both sub-populations.

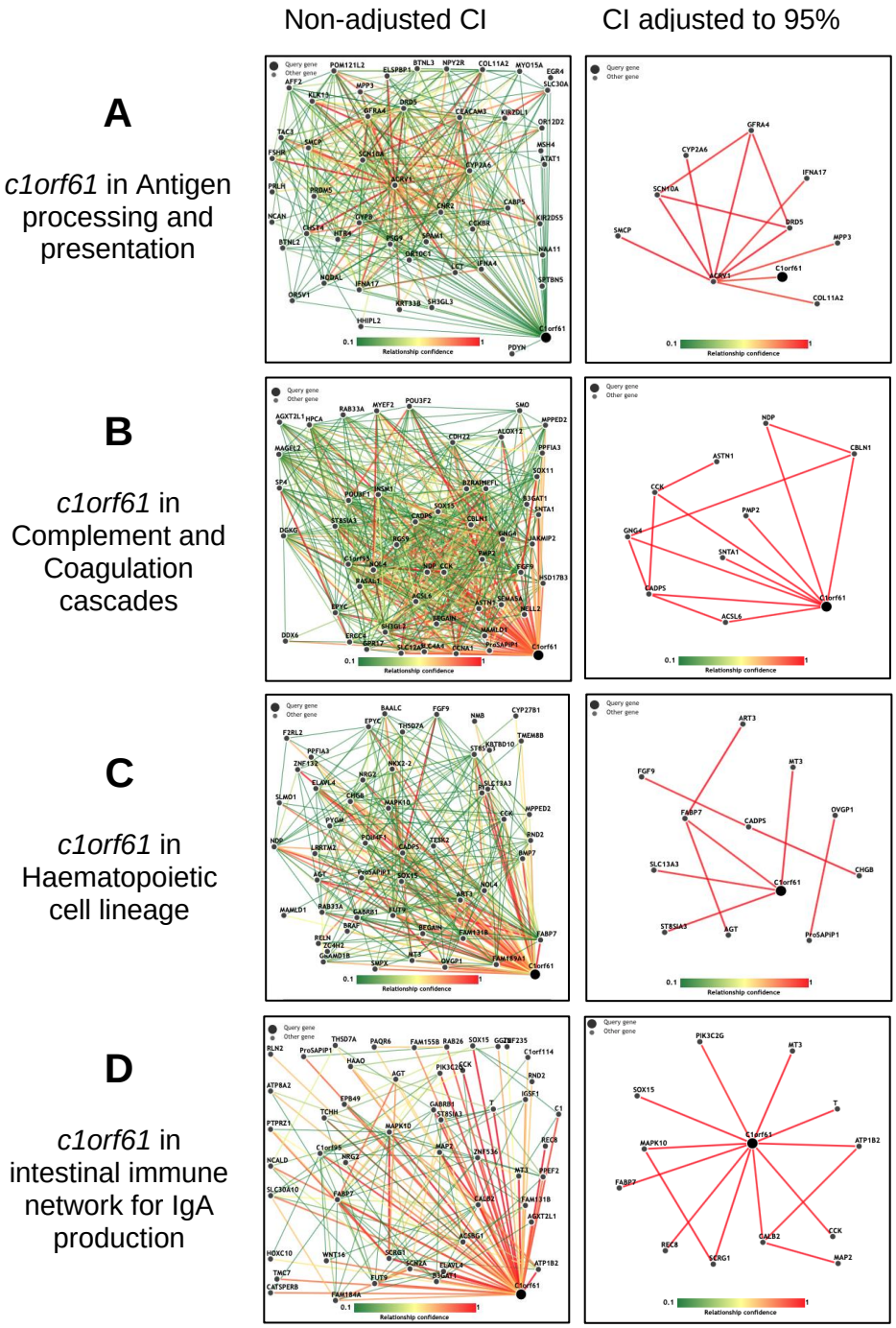


Figure 6. 26. Screening of the putative associations of C1orf61 in different immune pathways generated by IMMUNET. The *c1orf61* gene was studied in all pathways listed in (Appendix Table 8. 6) and identified to be strongly associated with gene networks within four immune pathways (A-D). The confidence interval (CI) for the relationship of *c1orf61* with other genes was adjusted to ≥ 95%. Next, all genes generated after statistical adjustment of the CI, were screened against our data and none were identified as statistically significant, indicating that *c1orf61* expressed by co-cultured astrocytes in our experiment is unlikely to be associated with immune function.

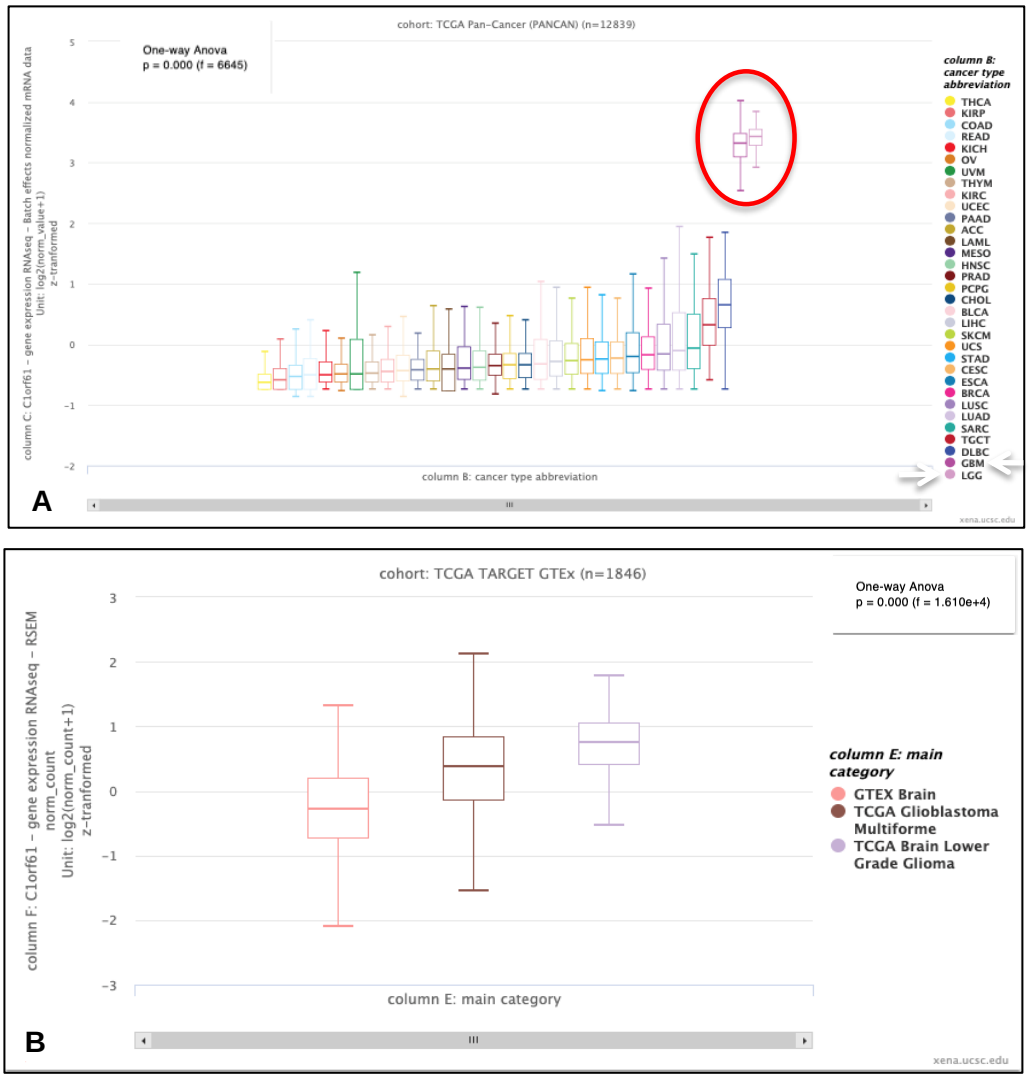


Figure 6. 27. TCGA-based analysis and validation of *c1orf61* gene expression. RNA sequencing data deposited in TCGA Pan-Cancer genome atlas was analysed to determine *c1orf61* expression for healthy brain, gliomas and somatic cancers. Analysis of RNA sequencing data from 12839 cases using a TCGA bioinformatics tool, reveals that *c1orf61* is expressed at significantly elevated levels in LGG and GBM as compared to all other body tumours (red circle) (A). Of 1846 gliomas, LGG have significantly higher *c1orf61* expression as compared to GBM and both LGG and GBM have significantly higher expression than non-malignant brain (GTEX Brain) (C). *p-values* are indicated within each figure. *P-value was stated as equal to 0.000 due to significance of more than 0.0001.*

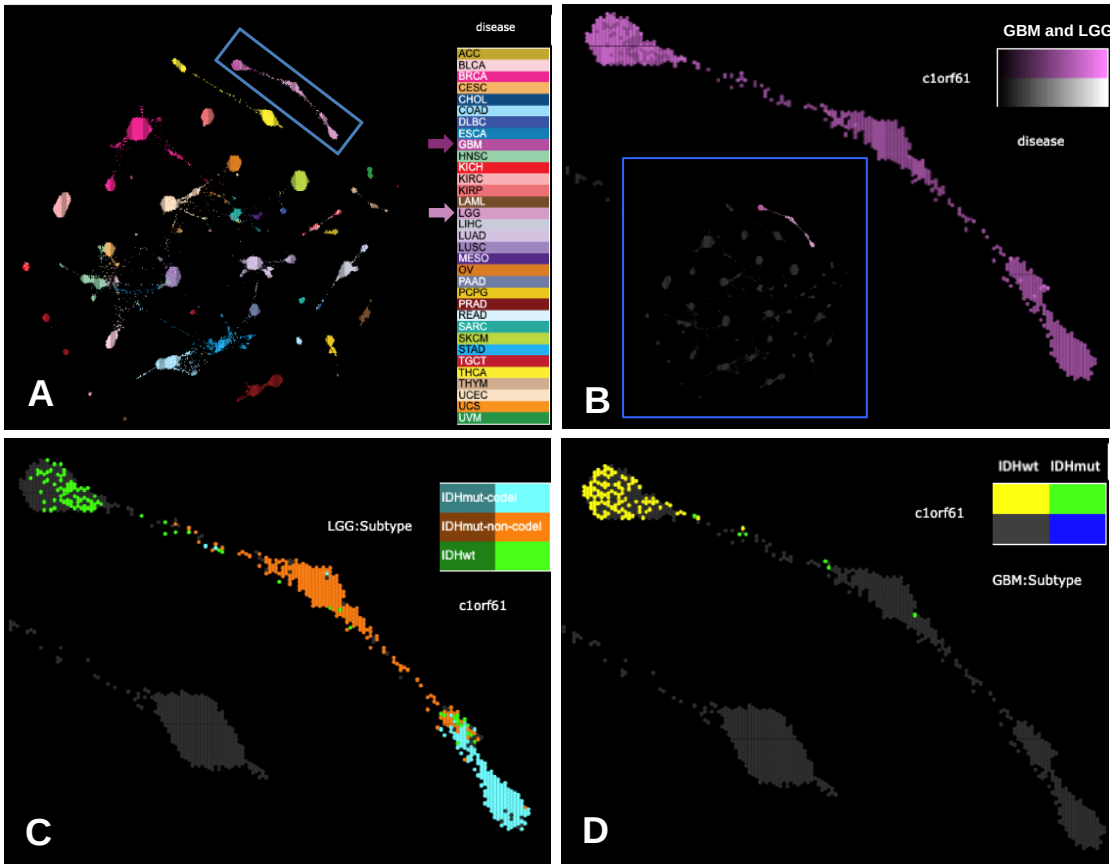


Figure 6. 28. TumorMap reveals *c1orf61* gene expression in various subtypes of LGGs and GBMs. RNA sequencing data of 10000 cases deposited in TCGA Pan-Cancer database was analysed to determine C1orf61 expression in 33 cancer types including high- and low-grade gliomas and other somatic cancers (A). Analysis of RNA sequencing data also reveals unique upregulation in LGG and GBM as compared to all other body tumours, which is shown inside the blue rectangle (A) and magnified in panel (B). TumorMap showed that *c1orf61* is upregulated in various subtypes of LGGs (C); IDH wild-type, IDH mutant-codel and IDH mutant-non-codel. Furthermore, *c1orf61* was shown to be upregulated in IDH wild-type, and IDH mutant-non-codel GBM tumours (D).

6.4 Discussion

Astrocytes are the most abundant cellular subtype in the brain. Moreover, they represent one of the major cellular subtypes, which can give rise to malignant gliomas. Literature evidence suggests that tumour associated astrocytes are key enhancers for GBM survival, proliferation, invasion, immune-protection and chemo-resistance, reviewed in (Brandao *et al.*, 2019; Venkataramani *et al.*, 2019; Venkatesh *et al.*, 2019). Astrocytes can be transformed into malignant GBM using various oncogenes such as MYC, RAS, and EGFRVIII, suggesting astrocytes as cell-of-origin for these neoplasms (Jahani-As *et al.*, 2016; Li *et al.*, 2016). Furthermore, normal astrocytes have been reported to reduce p53 tumour suppressor expression through an unknown mechanism after exposure to GBM conditioned medium and can enrich the ECM with laminin and fibronectin, which enhances glioma cell survival (Biasoli *et al.*, 2014). However, the intercellular molecular cross-talk between infiltrative GBM cells and surrounding astrocytes is yet to be fully unravelled, with a lack of physiologically-accurate *in vitro* models a major impediment. The complex heterogeneity of GBM and the surrounding brain parenchyma must be faithfully recapitulated to address how astrocytes may facilitate a permissive microenvironment for the recurrent growth of GBM (Broekman *et al.*, 2018). Most of the current GBM/astrocyte co-culture 2D and 3D models reviewed in (Chekhonin *et al.*, 2018) have several limitations which hamper attempts to address this question: (i) do not ensure 100% contact between the two types of cells; (ii) typically use commercial high-passage GBM cell lines isolated from the MRI contrast-enhanced core; (iii) incorporate an ECM mimic. In this study, we tried to address these issues by generating a novel multi-faceted 3D invasion model incorporating decellularised human ECM, that simulates the communication between astrocytes and GBM cells isolated from the 5-ALA positive infiltrative edge, which we term ‘Gliomasphere Matrix’. The creation of genetically engineered YFP-labelled astrocytes enabled the isolation of these cells upon periods of co-culture with invasive GBM cells and subsequent analyses of transcriptomic changes induced. Our in-house MDS analyses of the RNA-sequencing data using EdgeR showed clustering of all 26 samples (6 YFP-astrocyte-only controls and 20 YFP-astrocytes co-cultured with GIN cells) at two time points, when independently compared to a different dataset containing 20 specimens (10 5-ALA negative tumour-associated astrocytes and 10 5-ALA positive invasive GBM cells) which were surgically obtained and FACS-isolated. This reflects the stringency of controlling the biological conditions within this 3D culture system, in addition to the technical consistency and reproducibility amongst all 26 samples at two different time points (Day 6 and Day 10). Assessing the

variance between all 26 Gliomasphere Matrix cultures and the 20 5-ALA patient specimens, reveals that all 26 YFP-astrocyte samples are generally located in a closer plane to 5-ALA negative tumour-associated astrocytes than 5-ALA invasive GBM cells. This can be explained by the transcriptome profile of the normally differentiated YFP-astrocytes, which resembles the transcriptome of native 5-ALA tumour-associated astrocytes. However, once monocultures and co-cultures are analysed separately, MDS analysis showed that the plane of all 6 YFP-astrocyte-only controls and all 20 YFP-astrocytes co-cultured with invasive GIN cells, are closer to planes of 5-ALA negative tumour-associated astrocytes and 5-ALA positive (GBM) cells respectively. This indicates the remarkable effect of invasive GIN cells on the astrocyte transcriptome.

Within Gliomasphere Matrices, the co-cultured astrocytes upregulated gene expression profiles consistent with genetic events know to occur in GBM, within only ten days. In particular, the direct physical contact between GBM primary invasive cell lines and astrocytes within Gliomasphere Matrices highlighted the importance of receptor-mediated communications between these two different cell types as represented by Notch signalling, which may be associated with tumour promoting genotypes and phenotypes within GBM invasive margins post-surgery. Despite the upregulation of the RUNX3 transcription regulatory pathway, which has inhibitory effects on Notch signalling, co-cultured astrocytes within Gliomasphere Matrices continued to upregulate all genes of the Notch molecular pathway. The enhanced activation of all Notch pathway genes in the co-cultured astrocytes suggests the activation of a genetic response analogous to events which are known to occur during oncogenic transformation of astrocytes. Supporting this theory, Notch was previously hypothesised to function as an oncogene in cell lineages that require Notch to preserve an undifferentiated (stem-like) state (Stockhausen, Kristoffersen and Poulsen, 2010). For example, activated Notch1 was firstly described to promote cancer initiation in T-cell acute lymphoblastic leukaemia, where hyper-activated Notch1 signalling due to the chromosomal translocation of the Notch1 C-terminus with the T-cell receptor locus, leads to the expansion of an immature T-cell pool and ultimately the development of this type of leukaemia (Ellisen *et al.*, 1991; Weng *et al.*, 2004). Similarly, mutations were found in the PEST domain of Notch2 in B-cell lymphoma (Lee *et al.*, 2009). Notch signalling is also associated with GBM pathogenesis through multiple pathways as reviewed in (Stockhausen, Kristoffersen and Poulsen, 2010; Teodorczyk and Schmidt, 2014; Bazzoni and Bentivegna, 2019)

and Notch pathway genetic or pharmacological inhibition shows promising evidence to inhibit GBM (Gersey *et al.*, 2019).

YFP-astrocytes upregulated the NOTCH signalling pathway, which is historically known to be associated with GBM pathogenesis through multiple pathways, as reviewed in (Stockhausen, Kristoffersen and Poulsen, 2010; Teodorczyk and Schmidt, 2014; Bazzoni and Bentivegna, 2019), as well as the AKT/mTOR pathway which was previously found to be a key genetic driver for GBM recurrence in patients whose primary tumours were treated with TMZ (Johnson, 2014b). Particularly, YFP-astrocytes upregulated *lamtor2* and *nf-κb* genes upon co-culture with GIN cells. The *lamtor2* gene encodes mTOR2 which is overexpressed in 64% of gliomas and found to enhance the proliferation and survival of GBM cells (Tanaka *et al.*, 2011). Moreover, the activated mTOR2/NF-κB signalling axis was previously described to mediate GBM resistance to chemotherapeutic agents designed to cause DNA damage (Tanaka *et al.*, 2011; Weiler *et al.*, 2014). Evidence also showed that mTOR2 can reprogram GBM cell metabolism to mediate resistance to targeted therapies (Masui *et al.*, 2013, 2015; Masui, Cavenee and Mischel, 2014).

It has been shown that NSP can activate EGF tyrosine kinase signalling and promote cell proliferation via the PI3K-AKT-mTOR pathway (Merlo, 2003; Raghu *et al.*, 2011), the most frequent genetic aberration in GBM (Lino, Merlo and Boulay, 2010). Although our study showed significant upregulation of oncogenic AKT1 and related signalling genes such as GSK3A, MDM4, mTOR2, SOS1 and mTOR5, the entire PI3K-AKT-mTOR pathway was not shown to be significantly overexpressed as determined by Reactome pathway analyses, based upon DEG generated by EdgeR. However, the PI3K-AKT-mTOR signalling axis was significantly upregulated according to DEG analysed by DESeq2. The effect of dysregulated PI3K-AKT-mTOR signalling on protein translation in GBM is reviewed in (Marina *et al.*, 2019). The upregulation of EIF, a downstream PI3K-AKT-mTOR pathway effector, in both co-cultured astrocytes and 5-ALA negative tumour associated astrocytes, suggests activation of translation processes, known to be essential for GBM cell survival (Obacz *et al.*, 2017; Wang, Gundelach and Bram, 2017).The activation of translation pathways via EIF genes can recruit stress response mediators such as EIF2AK4 (GCN2) (Marina *et al.*, 2019), but can also can activate mRNA non-sense mediated decay (NMD).

Whereas upregulation of this process could be part of a physiological mechanism to prevent mRNA abundance and remove mutated mRNAs to preserve overall mRNA quality (Behm-Ansmant *et al.*, 2007; Chang, Imam and Wilkinson, 2007; Isken and Maquat, 2007; Neu-Yilik and Kulozik, 2008; Rebbapragada and Lykke-Andersen, 2009; Bhuvanagiri *et al.*, 2010; Nicholson *et al.*, 2010). The NMD pathway could be activated due to mutated transcripts being transferred from the neighbouring GBM cells via microvesicles (Valadi *et al.*, 2007; Minciacchi *et al.*, 2015; Tkach and Théry, 2016; Maas, Breakefield and Weaver, 2017), gap junction proteins (Hong *et al.*, 2015), and microtubules network channels which is prevalently expressed in GBM (Osswald *et al.*, 2019). The other hazardous aspect is that the NMD pathway can also be activated by cancer cells to selectively deplete mRNAs of tumour suppressor genes such as myc via either chromosomal loss/deletion, or Haplo depletion of the wild-type gene (Popp and Maquat, 2018). The NMD pathway could also be activated by up-regulation of developmental axon guidance (SLITs and associated ROBO receptors) molecules (Colak *et al.*, 2013), which are involved in the formation of many cancers including GBM (reviewed in Chédotal, Kerjan and Moreau-Fauvarque, 2005; Angelucci, Lama and Sica, 2019). Likewise, Semaphorins have a remarkable role in gliomas (Law and Lee, 2012). This is consistent with the observation that after only 6 days of co-culturing astrocytes with invasive GBM cells, the astrocytes showed significant upregulation of genes encode for ephrin receptors (*ephb*2 and *ephb*4). These receptors are a type of developmental (axon guidance molecules) tyrosine kinase molecules which were previously known to mediate glioma cell invasiveness via forward signalling (Nakada *et al.*, 2005). These ephrin receptors can also increase cyclin D1 expression (observed in the co-cultured YFP-astrocytes isolated at Day 10) (Genander *et al.*, 2009), and in turn leads to cell proliferation, reviewed in (Pasquale, 2010). However, ephrin ligands mediate bidirectional signalling that exerts a tumour suppressor effect (Pasquale, 2010). Thus, the down-regulation of gene encode for ephrin ligands (such as *efnb*2; the top downregulated gene) observed in the co-cultured YFP-astrocytes isolated at Day 10 and also in 5-ALA negative tumour-associated astrocytes, may lead to the abrogation of tumour suppressive function within healthy brain parenchyma at the infiltrative margin of GBM. In a disease setting, this may promote cancerous invasion due to loss of the tumour-confinement barrier around tumour edges (Pasquale, 2010; Depner *et al.*, 2016).

Reactome pathway analysis showed that oncogenic MAPK and Notch3 signalling pathways have stimulatory effects on the master regulators of cell cycle genes (i.e.,

CDKN2A), that have been shown to be upregulated in the co-cultured YFP-astrocytes isolated at Day10. This is consistent with the upregulation of cell cycle pathways, via regulation of cyclin D, A, and E (Hydbring, Malumbres and Sicinski, 2016), in the co-cultured astrocytes, which were terminally differentiated for 45 days, relative to the astrocyte-only controls. Reactome also showed that priming the co-cultured differentiated astrocytes to re-enter the cell cycle, mediated by oncogenic MAPK, has led to the activation of two protective (apoptotic) mechanisms; the intrinsic death signals mediated by the *diablo* gene and the upregulation of the cell cycle checkpoint mediated by the *tp53* tumour suppressor gene (overexpression trend with no statistical significance). As co-cultured astrocytes showed a significant induction of oncogene cell senescence pathway genes which typically respond to oncogenic MAPK signalling, this finding may indicate that astrocytes are responding to intrinsic neoplastic processes manifest in GIN cells.

However, Reactome also showed that co-cultured astrocytes isolated at Day 10 have upregulated evasion to these oncogene- and stress-induced senescence/apoptosis pathways due to a p14ARF defect. This is due to the upregulation of the master cell cycle inducer (*cdnk2a*), and downregulation of the cell cycle inhibitor (*cdnk2b*), in addition to the (non-statistically significant) regulation of tumour suppressors *tp53* and *rb1*, which are assumed to be upregulated in response to cell cycle priming to induce apoptosis as a protective mechanism in normal differentiated cells. This is possibly mediated by either defective binding of p16INK4A with CDK4 and CD6 or due to failure of translocation of p14ARF into the nucleus (Kamb *et al.*, 1994; Herman *et al.*, 1995; Merlo *et al.*, 1995; Ruas *et al.*, 1999; Zhang and Xiong, 1999; Becker *et al.*, 2005; Itahana and Zhang, 2008; Witkiewicz *et al.*, 2011; Jeanblanc *et al.*, 2012; LaPak and Burd, 2014; Childs *et al.*, 2015; Baek and Ryeom, 2017; He and Sharpless, 2017), which is a process that was previously described in many cancers such as medulloblastoma (Tamayo-Orrego *et al.*, 2016), meningioma (Boström *et al.*, 2001), pancreatic cancer (Bartsch *et al.*, 1995), melanoma (Castellano *et al.*, 1997; Liu *et al.*, 1999; Harland *et al.*, 2000; Harland, 2001; Haferkamp *et al.*, 2008), lymphoma (Eischen *et al.*, 1999; Schmitt *et al.*, 1999; Pinyol *et al.*, 2000), colorectal cancer (Shima *et al.*, 2011), and oesophagus cancer (Wong *et al.*, 1997). This may explain why we were only able to FACS-isolate small numbers of YFP-astrocytes after co-culturing with GIN cell lines, as the resistant sorted cells may have evaded and survived the apoptotic signals, whereas the rest of the cells initially seeded died from the endogenous activation of protective mechanisms.

The upregulation of protein translation pathways within both co-cultured astrocytes and 5-ALA negative tumour associated astrocytes could be a consequence of the activation of EIFs mediated by oncogenic MAPK signalling. However, an alternative theory is that activation of translation pathways in both experimental settings could be due to the significant overexpression of pathways that are usually involved in intracellular influenza virus replication and translation within the host cell after virus endocytosis. These pathways could be recruited via the non-viral structural protein S1 (NS1) encoded by the *ivns1abp* gene, which is significantly upregulated. NS1 can induce selective translational pressure and increase the efficiency of foreign mRNA translation within host astrocytic cells via activation of EIF2α through modulating the inhibitory signals of PKR. In addition to this translation function modulation, NS1 can recruit stress response pathways to increase the efficiency of translation, such as the upregulation of EIF2AK4 (GCN2) (Kash *et al.*, 2006; Ye *et al.*, 2010; Adam *et al.*, 2018; Marina *et al.*, 2019)

Previous elegant work showed that RNAs such as EGFRvIII mRNA can be transferred from GBM cells to surrounding normal brain microvascular endothelial cells via microvesicles (exosomes) and translated by these recipient cells (Skog *et al.*, 2008). Another evidence showed that GBM exosomes can alter gene expression of endothelial cells (Li *et al.*, 2013). Additionally, ectopic expression of the oncogenic transcription factors SRY-related box 2 (SOX2), oligodendrocyte lineage transcription factor 2 (OLIG2) and zinc-finger E-box binding homeobox 1 (ZEB1), can transform tumour-suppressor-deficient astrocytes and activate the transcription machinery that initiates gliomagenesis (Singh *et al.*, 2017). The role of extracellular microvesicles and tumour microtubule networks in cancer pathogenesis have become more evident in the recent years (Lynch, Panagopoulou and Gregory, 2017; Jabalee, Towle and Garnis, 2018; Han, Lam and Sun, 2019; Venkataramani *et al.*, 2019). This evidence, coupled with the upregulation of viral translation and foreign DNA cytosolic sensor immune pathways, observed in both the co-cultured astrocytes from Gliomasphere Matrices and tumour associated astrocytes, has implications for GBM propagation and treatment. One hypothesis states that GBM cells can reprogram the surrounding astrocytes by hijacking the host translation machinery and stress response pathways via NS1, resulting in translation of neoplastic foreign RNA transferred from GBM via ‘oncosomes’ (Valadi *et al.*, 2007; Minciacchi *et al.*, 2015; Tkach and Théry, 2016; Maas, Breakefield and Weaver, 2017), or Gap-junctional-1 (Hong *et al.*, 2015), and microtubules network channels which is prevalently expressed in GBM (Osswald *et*

al., 2019). In this context, astrocytes may be responding to exogenous GBM mRNA as if these molecules were 'viral'. Such reprogramming of astrocytes may be an adaptive characteristic of infiltrative GBM cells to modulate and/or co-opt the peri-tumour microenvironment to facilitate tumour recurrence. In future work, this hypothesis could be tested by CRISPR-Cas9-mediated knock-out of NS1 (or components of the protein translation pathway) in YFP-astrocytes, prior to co-culture within Gliomasphere Matrices and transcriptomic profiling after FACS-isolation of astrocytes. This would falsify whether activation of viral translation and foreign DNA cytosolic sensor immune pathways is abrogated.

A further hypothesis states that GBM can be treated using oncolytic viral therapy predicated on the overexpression of NS1. As NS1 is a potent translation initiator of viral mRNA, cell death signals carried by these engineered viruses would be expected to be efficiently translated. In support of this hypothesis, a phase I/IIa GBM parvovirus oncolytic trial reported that Parvovirus RNA abundance was directly correlated with NS1expression in GBM cells. This was histologically confirmed by clustering of viral RNA expression within tumour regions and was further validated by the co-localisation of NS1 protein and GBM markers such as GFAP and EGFR (Geletneky *et al.*, 2017).

Although NS1 was proposed to have antagonizing effect on interferons studied by Garcia-Sastre group (García-Sastre *et al.*, 1998; García-Sastre, 2001, 2004) via NF-κB (Wang *et al.*, 2000) and IRF3 (Talon *et al.*, 2000), the co-cultured astrocytes (Day 10) and the 5-ALA negative tumour associated astrocytes showed significant upregulation of interferon pathway genes. These contrasting results could be due to the nature of the triggering factor of NS1. Whereas the previously studies described NS1 activation in relation to the viral infections, we hypothesise that the GBM cells (by transfer of tumour mRNA) are the cause for activating NS1 in the co-cultured astrocytes and tumour associated astrocytes.

Considerable previous evidence shows that foreign genetic material found in the host cytoplasm (from tissue damage or intracellular pathogens) can trigger recognition machinery to activate type I interferon signalling in both immune and non-immune cells (Okabe *et al.*, 2005; Yasuda *et al.*, 2005; Ishii and Akira, 2006; Ishii *et al.*, 2006; Martin and Elkon, 2006; Shirota *et al.*, 2006; Stetson and Medzhitov, 2006; Takaoka *et al.*, 2007; Cai, Chiu and Chen, 2014). This recognition can either be mediated by Toll-like receptors 9 (TLR9) in a sequence (CpG)-dependant manner (Klinman, 2004;

Wagner, 2004; Krieg, 2006), or via Z-DNA-Binding Protein 1 (ZBP1; also known as DLM-I) (Ishii and Akira, 2006). Although the TLR9 pathway was not significantly upregulated in both the 5-ALA negative GBM-associated astrocytes and co-cultured astrocytes, the ZBP1-recognition (STING) pathway mediated by TBK1 and IRF3, were both significantly upregulated. The STING pathway can be activated when the cytosolic sensor ZBP1 dimerizes with double-stranded (dsDNA) to recruit TBK1, which phosphorylates IRF3. Consequently, IRF3 translocates to the nucleus, which results in the production of type I interferon (Ishii and Akira, 2006, Chen *et al.*, 2016). Foreign genetic material transferred from cancer cells have been reported to activate the STING pathway in peritoneal macrophages and peritoneal lining cells in mice with tumour ascites (Fu *et al.*, 1999). Additionally, a recent elegant study that metastatic lung and breast cancer cell dsDNA activated the STING pathway in co-cultured astrocytes via the secondary messenger cGAMP in a GJA1-dependent manner. The authors suggested that secreted interferon and TNF by co-cultured astrocytes might aid cancer cell survival and chemoresistance mediated by NF-κB (Chen *et al.*, 2016). In our study, we found that both the interferon and NF-κB pathways are highly and significantly upregulated in the co-cultured astrocytes and 5-ALA negative tumour associated astrocytes. This raises the question of whether this activation occurred in response to autocrine signalling of interferons or due to other activated signalling pathways expressed by the co-cultured astrocytes, such as Notch and MAPK which are also known to activate NF-κB (Oswald *et al.*, 1998; Cheng *et al.*, 2001; Nickoloff *et al.*, 2002; Hyun *et al.*, 2006). The activation of NF-κB can also be involved in tumourigenesis and inflammation reviewed in (Taniguchi and Karin, 2018). The cross-talk between IRF3, which promotes anticancer behaviour via type I interferons (Honda and Taniguchi, 2006; Zitvogel *et al.*, 2015), and the activated NF-κB, may contribute to the anti-GBM inflammatory environment around the tumour (Taniguchi and Karin, 2018). Analysis of TCGA data using the Xena TCGA computational tool shows that IFTIM2, an interferon-induced anti-viral/tumour gene, is downregulated in LGGs, whereas it is upregulated in GBM, as compared to non-malignant brain GTEX samples. IFTIM2 upregulation in GBM may be explained by TCGA samples being representative of the contrast-enhanced core of the tumour, where infiltrative immune cells may activate interferon signalling. Furthermore, GTEX RNA-seq samples are likely derived from normal brain regions where astrocytes were not in close proximity to malignant GBM cells and therefore not induced to express interferon pathway genes in response to cross-talk with GBM cells.

Heiland et al. (2019) showed that astrocytes failed to express interferons, when

injected in a microglia-depleted orthotopic brain slice model for 6 days (Henrik Heiland *et al.*, 2019). In the same study however, analysis of a tumour associated astrocytic RNA-seq dataset publicly available from (Zhang *et al.*, 2016), showed overexpression of interferon pathways in the tumour –associated astrocytes and thus suggested that interferon pathways can merely activated in the astrocytes via the interaction with the microglia. Based on our findings, we propose that interferon inactivation observed in (Henrik Heiland *et al.*, 2019) was due to the duration of astrocyte culture within the orthotopic brain slide model, as the co-cultured YFP-astrocytes in our Gliomasphere Matrices did not show significant upregulation of interferon pathways after 6 days, whereas the interferon signals were significantly upregulated at day 10, relative to astrocyte-only controls. Heiland et al. (2019) also found that CD247 (PDL1; Programmed Death Ligand 1) of the co-cultured astrocytes is overexpressed in tumour-associated astrocytes. Based on this finding, the authors suggested that astrocytes enhance the immune-suppressive environment within GBM as interferon type II (gamma), but not type I (alpha and beta), is responsible for T-cell inactivation through PD1-PDL1 and PDL2 (Garcia-Diaz *et al.*, 2017). In our study, the tumour-associated astrocytes showed significant upregulation of the CD28 co-stimulation pathway represented by T-cell stimulatory molecules such as CD28, ICOS and others, despite the expression of type I (alpha and beta) and II (gamma) interferons, in addition to the T-call inhibitory molecules such as PD1, and CTLA4. Our results are supported by previous studies which have shown that signals induced by T-cell engagement with co-stimulatory CD28 and ICOS molecules, is counter-balanced by the inhibitory signals when the same T-cells engage with PD1 and CTLA4 molecules (Slavik, Hutchcroft and Bierer, 1999; Alegre, Frauwirth and Thompson, 2001; Acuto and Michel, 2003). It is proposed that this balance is harmonious between and required to maximize a defensive immune response while maintaining tolerability to avoid autoimmunity (Slavik, Hutchcroft and Bierer, 1999; Alegre, Frauwirth and Thompson, 2001; Acuto and Michel, 2003).

Interferon therapy has can also exert anti-cancer effects via different mechanisms (Parker, Rautela and Hertzog, 2016) such as the modulation of the MHC type I (Yang *et al.*, 2004) and found to be experimentally (Fujita *et al.*, 2010) beneficial as a monotherapy to treat in GBM treatment alone to decrease resistance (Happold *et al.*, 2014), or in combination with TNFα (Ehtesham *et al.*, 2002), TMZ (KAWAJI *et al.*, 2015; Park *et al.*, 2015), and PD1/PD-L1 axis inhibitors (Qian *et al.*, 2018). A case report also descried the improved clinical outcome of a patient with recurrent GBM who was treated with interferon plus Nimustine (Utsuki *et al.*, 2011). Our results and

those described from supporting literature, therefore encourage the consideration of interferon therapy, especially type I, in treating GBM via the activation of stimulatory receptors of T-cell populations at the GBM invasive margin (Petrecca *et al.*, 2013; Lemée, Clavreul and Menei, 2015) or combining interferon therapy with PD1/PD-L1 axis inhibitors. Equally important, the interferon gene expression pattern (higher expression in the non-tumoural brain (GTEX samples) as compared to LGG specimens obtained from TCGA data analysis) suggests that type I interferon therapy could be initiated at early disease (time of diagnosis of LGG) to maximize the benefit via stimulation of T-cell immune response within the healthy peri-tumoural edge during early disease that is predominantly composed of reactive astrocytes upregulating the interferon pathway.

The validation of such studies *in vitro* and *in vivo* however, remains experimentally challenging. For example, it is technically difficult to culture normal astrocytes, GBM cells and immune cells (T-cells) within the same *in vitro* model due to different culture condition requirements for each cell type. *In vivo* models also present considerable challenges as immune-competent models are not suitable for orthotopic injection of human cells and immune-compromised models cannot respond to interferon therapy. The use of syngeneic mouse allografts could alternatively be used to assess mammalian immune response to interferon therapy in this context, with the caveat of extrapolating findings to the clinic.

Using Gliomasphere Matrices, the comparison of astrocyte transcriptome profiles after co-culture with each of ten different patient-derived invasive primary GBM cells, relative to six astrocyte monoculture controls at Day 6 and Day 10 collectively, resulted in the identification of differentially expressed genes yet to be fully characterized in the scientific literature, including C1orf61 and Gap43. Although the ImmuNet bioinformatics tool shows that C1orf61 is associated with several immune mechanisms in many cancers including glial tumours, only 3/100 genes from these large immune gene networks had statistical significance in our data generated from astrocyte co-cultures and 5-ALA negative tumour associated astrocytes. This suggests that C1orf61 is unlikely to be involved in immune reactions mediated by astrocytes within these two experimental contexts. Alternatively, C1orf61 has been reported to be involved in oncogenesis and tumour formation process. C1orf61 was shown to activate the c-fos proto-oncogene (Jeffrey *et al.*, 2000), which is a typical example of group of transcription factors for genes known as immediate-early genes (IEGS). These IEGS encode a variety of proteins and enzymes (Jeffrey *et al.*, 2000),

which can alter cellular phenotype and function by governing transcription and cell signalling (Qian *et al.*, 1993; Yamagata *et al.*, 1993, 1994; Kohmura *et al.*, 1995; Lyford *et al.*, 1995; Papa *et al.*, 1995). C-fos was also linked to signal transduction pathways via the phosphorylation of CREB and MAPK kinases via its P-loop motif and SH3-domain, which can lead to feedback transcription activation at the promoter of c-fos via specific regulatory elements (Marais, Wynne and Treisman, 1993; Ghosh *et al.*, 1994; Xing, Ginty and Greenberg, 1996; Ahn *et al.*, 1998). C-fos is involved in cellular proliferation (Bravo *et al.*, 1987; Fisch, Prywes and Roeder, 1987), differentiation (Gubits, Hazelton and Simantov, 1988; Bardoscia, Amstad and Honegger, 1992; Didier *et al.*, 1992), programmed cell death (Visvader, Sassone-Corsi and Verma, 1988; Colotta *et al.*, 1992), and resistance to chemotherapeutic agents (Kaina, Haas and Kappes, 1997). In general, C1orf61 is distinctly overexpressed by different brain tissues as compared to other somatic tissues (Jeffrey *et al.*, 2000). Furthermore, another study showed that C1orf61 is predominantly expressed by the radial glia (Nowakowski *et al.*, 2017). This is in accordance with our analysis of TCGA data, which intriguingly reveals significantly elevated expression of C1orf61 in normal brain tissue and astrocytomas (both LGG and GBM), relative to all other human somatic cancers. Ultimately, this may influence future diagnostic and therapeutic approaches considering C1orf61. For example, the brain tissue-specific expression of C1orf61 may offer a new transgenic approach selective for gliomas. Specifically, genetic designing of a vector containing the C1orf61 promoter followed by a sequence encoding for a death/immune signal, could lead to selective therapeutic (viral oncolytic therapy) targeting of glioma cells (Russell and Peng, 2007).

C1orf61 expression has also been identified in proliferative stem cells within supraventricular and olfactory rostral regions during neurodevelopment of mouse embryos (Jeffrey *et al.*, 2000). *c1orf61* was upregulated by the co-cultured YFP-astrocytes throughout the days of the experiment (Day 6 and Day 10) and found to be the top upregulated gene when collectively comparing all 6 YFP-astrocytes controls to all 20 co-cultured YFP-astrocytes at both time points. However, *c1orf61* was upregulated in 5-ALA positive invasive GBM cells relative to 5-ALA negative tumour-associated astrocytes. This can be explained by the remarkable direct proportional relationship between the upregulation of the *c1orf61* gene with malignant character in the 5-ALA positive (GBM) cells as compared to the 5-ALA tumour-associated astrocytes, which may eventually transform into, or to exhibit, oncogenic features to foster GBM growth. This relationship has become more

evident within the last decade. *c1orf61* expression is associated with the proneural subtype according to Verhaak's GBM classification (Verhaak *et al.*, 2010). Additionally, *c1orf61* appears in gene regulatory analysis (ARACNE) as one of the transcription factor networks of CCAAT enhancer-binding protein-β, which acts synergistically with signal transducer and activator of transcription 3 (STAT-3) to regulate and initiate the mesenchymal signature of glioma (Carro *et al.*, 2010; Bhat *et al.*, 2011). Cai and colleagues also suggested that *c1orf61* is expressed in diffuse astrocytoma and GBM according to rules 3 and 15 respectively, when they tried to classify glioma into multiple subtypes according to gene expression (Cai *et al.*, 2018). Moreover, *c1orf61* is one of the genes expressed by Temozolomide-sensitive GBM cells (Meyer *et al.*, 2015). Furthermore, *c1orf61* was shown to be associated with GSC gene expression profiles (Marziali, Signore, Buccarelli, Grande, Palma, Biffoni, Rosi, Q. G. D'Alessandris, *et al.*, 2016; Taiwo, Mahlokozera and Kim, 2018). While studying the reciprocal changes between GSC and differentiated tumour cells, *c1orf61* was overexpressed in both of these cell archetypes (Wang *et al.*, 2018). Parallel to the significant up-regulation of *sox2* observed in the transcription profiles of the co-cultured astrocytes and tumour-associated astrocytes of our study, *c1orf61* was previously found to be positively correlated with *sox2* which enhanced GBM pathogenesis by orchestrating plasticity and the differentiation of astrocytes (Berezovsky *et al.*, 2014). In addition, *c1orf61* was listed as one of the top genes that was associated with β3 integrins that modulate *glut3* expression to satisfy the requirements of GBM glucose metabolism (Cosset *et al.*, 2017). Additionally, *c1orf61* and *gap43*, (also identified as significantly upregulated in the co-cultured astrocytes), are reported to be associated with the formation and functionality of tumour microtubules (Osswald *et al.*, 2015), and with other genes which also promote glioma microtubule formation (Jung *et al.*, 2017). In addition to the significant association between *c1orf61* and gliomas, considerable literature evidence suggests its correlation with many other cancer types. For example, Jeffery et al studied the translocation of *c1orf61* into the cytoplasm during the differentiation of rat neuroblastoma cells after inhibiting cellular proliferation using dibutyryl cyclic AMP (Jeffrey *et al.*, 2000). Recently, the expression of *c1orf61* has been revealed in many somatic cancers such as melanoma (Berger *et al.*, 2010; Nsengimana *et al.*, 2018), lung (Dalvi *et al.*, 2017), and colorectal (Zheng, Zhou and Tong, 2015; Tanaka *et al.*, 2018). *c1orf61* is overexpressed particularly in $CD133^+$ hepatic tumour initiating cells (Tang *et al.*, 2012). In addition, important studies showed the and several studies highlight the essential role of *c1orf61* in tumourigenesis, progression and metastasis of hepatocellular carcinoma (Hu *et al.*, 2013; Lowdon and Wang, 2017; J. *et al.*,

2019). Hu et al. has proposed that *c1orf61* acts as a tumour initiator, as C1orf61ectopic expression in a normal liver cell line induced malignant features including proliferation, colony formation, cell cycle progression, invasion and epithelial to mesenchymal transition (Hu *et al.*, 2013). This together with results obtained from the co-relation of GBM methylation status of 20 CpG islands of *c1orf61* and *fam50b* to GBM patient survival data from TCGA, led to a recent hypothesis that *c1orf61* is a key genetic element in the initiation and development GBM (Jia *et al.*, 2019). Based on this collective evidence and the significant upregulation of *c1orf61* observed in Gliomasphere Matrix astrocytes upon co-culture with invasive GBM cells, we hypothesise that GBM cells can reprogram the surrounding astrocytes to support GBM survival and/or invasion by (transiently) acquiring malignant features. However, this needs to be investigated using reverse genetics. For example, overexpressing *c1orf61* in primary healthy astrocytes and assessing for classical malignant features (e.g. enhanced proliferation, migration and invasion).

The association of primary brain malignancies with viral infection is neither a new topic nor hypothesis as Cobbs and colleagues suggested the possible association of cytomegalovirus (CMV) and gliomas 2001 (Cobbs *et al.*, 2002). In 2012, a consensus between oncologists and virologists was reached, where sufficient evidence suggested that "*CMV sequences and viral gene expression do exist in most, if not all, malignant glioma*" and CMV can modulate glioma malignant phenotypes (Dziurzynski *et al.*, 2012). Despite the controversial role of viruses in glioma pathogenesis (Saddawi-Konefka and Crawford, 2010; Kofman *et al.*, 2011), many studies have presented evidence linking brain cancers to the presence of viruses, reviewed in (Akhtar *et al.*, 2018), whereas viruses can modulate pathways to enhance oncogenic processes (Kofman *et al.*, 2011). The modulation of genetic and biochemical pathways within the host cells by viruses, may lead to immune-suppression, translating oncoproteins and increasing gene expression at viral integration sites (White, Pagano and Khalili, 2014; Elgui de Oliveira, Müller-Coan and Pagano, 2016). In a recent open clinical trial for personalised therapy, scientists are using viral epitopes as a vaccine component to sensitize patients' immune cells (Hilf *et al.*, 2019). This reflects the significant role of viral infections in brain cancers. It is noteworthy to mention that *c1orf61* was found to be considerably overexpressed in hepatomas as compared with normal liver tissue. Moreover, this upregulation was significantly higher in liver cancer patients who also presented with hepatitis E virus (HEV) infection (Hu *et al.*, 2013). The association of HEV with glioma remains unclear, although HEV is known to be linked to central and peripheral nervous

system symptoms (Kamar *et al.*, 2011, 2014, 2016; Van Eijk *et al.*, 2014; Bandyopadhyay *et al.*, 2015; Bazerbachi *et al.*, 2015; Dalton *et al.*, 2016; Silva *et al.*, 2016; Pischke *et al.*, 2017) and also *c1orf61* is distinctly overexpressed in brain tissue relative to any other tissue-type in the body (Jeffrey *et al.*, 2000). Host C1orf61 was shown to interact with the open read frame 3 (ORF3) and X proteins of HEV (Subramani *et al.*, 2018). Furthermore, the replication, assembly, and release of HEV were successfully supported in neuronal cells (Drave *et al.*, 2016), despite the known difficulty to propagated this virus. Moreover, the U87 GBM cell line supported the long-term replication and production of HEV (Zhou *et al.*, 2017). Thus, we argue that the association of HEV with glioma must be excluded by screening blood samples of glioma patients for HEV antigens, immunohistochemical detection of HEV antigens using formalin-fixed paraffin-embedded sections and scanning of tissue samples for HEV-specific genomic sequences using PCR. If a unique predilection of HEV to glioma cells is identified, the use of HEV in viral oncolytic therapy may be a viable therapeutic option. The HEV backbone contains an open-reading frame (ORF)-3 sequence, which may facilitate viral internalisation into GBM cells and thereby, selective delivery of therapeutics.

In conclusion, studying Glioma/astrocytes interaction remains scientifically and technically challenging. To address this knowledge gap, we generated and validated the utility of Gliomasphere Matrices, a multi-component model to assess physiologically-accurate molecular cross-communication between human astrocytes and invasive GBM cells. MDS analyses of the RNA-sequencing data demonstrated the consistency and the high degree of reproducibility of this 3D culture system, which reflects the stringency of experimentally controlling the biological conditions. We identified putative reprogramming events within astrocytes induced by the infiltration of malignant cells within Gliomasphere Matrices. RNA sequencing after FACS-isolation of co-cultured astrocytes based on YFP transgene expression, highlighted important canonical pathways such as NOTCH and PI3K-AKT/mTOR, which are known to contribute intrinsically to glioma pathogenesis. However, the roles of these pathways in tumour associated astrocytes within brain parenchyma harbouring residual, invasive GBM cells post-surgery, are unknown, and are identified here for the first time. Surprisingly, co-cultured astrocytes also significantly upregulated pathways which typically contribute to anti-viral and anti-tumour behaviours, such as the type I interferon pathway. This may suggest that these astrocytes are in a fluctuating state between malignant transformation process induced by GBM signalling and an intrinsic defence based on activated immune

mechanisms. Confirmation of whether co-cultured astrocytes within Gliomasphere Matrices are transformed, would require isolation of the cells and orthotopic injection into the brains of immune-compromised rodents, to determine if these cells are tumourigenic. Finally, our results led us to hypothesise several therapeutic approaches using, for example, the use of type I interferon-based therapy. This approach could also be further potentiated if combined with repurposed oncogenic pathway blockers such as Notch (especially Notch1) inhibitors or thePD1-PDL1 inhibitor is to maximise the immune response.

Chapter (7)

Conclusion

Chapter 7: Conclusion

Gliomas are the commonest adult brain cancer and remain therapeutically challenging, despite considerable researches and efforts that have been conducted so far to unravel the complexity of disease pathogenesis and tumour cell behaviours. Many large-scale studies analysing thousands of tumour samples in the TCGA data were conducted (McLendon *et al.*, 2008b; Verhaak *et al.*, 2010; Sturm, Witt, Hovestadt, Khuong-Quang, David T W Jones, *et al.*, 2012; Bhat *et al.*, 2013; Brennan *et al.*, 2013; Brat *et al.*, 2015; Korshunov *et al.*, 2015; Ceccarelli *et al.*, 2016), and many intricate models (Hubert *et al.*, 2016; Bian *et al.*, 2018; Chekhonin *et al.*, 2018; Broekman *et al.*, 2018; Ogawa *et al.*, 2018; Yi *et al.*, 2019; Linkous *et al.*, 2019; Robertson *et al.*, 2019; Sood *et al.*, 2019; Wolf *et al.*, 2019; Jacob *et al.*, 2020), were sophisticatedly designed to bridge this scientific gap, which in turn could improve patients' prognostic outcome. However, the bulk of GBM tumour mass has historically been the scope of these models and transcriptome/(epi)genome-wide studies. For example, these recent modelling studies focused on how to best model GBM tumours. Furthermore, genome-wide studies usually involve analysing RNA-sequencing data of glioma samples deposited in TCGA which have been conventionally obtained from surgical specimens resected from the centrally enhanced core, where maximum heterogeneity and necrosis occur, to diagnose a GBM tumour. An individual study has sought to study tumour associated astrocytes located at the peri-tumour region (Zhang *et al.*, 2016). However, the isolation of these tumour-associated astrocytes is questionable as these "reactive astrocytes" were isolated based on the HepaCam molecular marker, which is a non-discriminative marker expressed in both malignant (WHO grade IV astrocytoma) and non-malignant astrocytes. Moreover, the non-enhanced peri-tumour region, from where the HepaCAM positive cells were isolated, was not discriminated as to whether it was oedematous or infiltrated with GBM cells, and the ultimate isolated cell population (HepaCam positive) was therefore a cell-population mixture of both malignant (astrocytoma) and non-malignant astrocytes. Indeed, the sequenced HepaCam positive cells expressed transcriptomic profiles of mature astrocytes as well as astrocytes progenitor cells, representing gene expression of a mixed, rather than pure population of astrocytes.

Intercellular communications which occur at the GBM peri-tumour region and which lead to deadly GBM recurrence, should be comprehensively studied and well characterised. Whereas the GBM bulk mass (including the central contrast-enhanced

region) is resected during debulking surgery, the remaining tumour edge harbours residual infiltrative GBM cells which inevitably results in tumour recurrence within 2-3cm beyond the surgical margin (Wallner *et al.*, 1989; Pennington *et al.*, 2006; Konishi *et al.*, 2012; Petrecca *et al.*, 2013; Lemée, Clavreul and Menei, 2015; Rapp *et al.*, 2017). This renders the invasive margin more clinically-relevant to patient outcome and for the identification of viable molecular therapeutic targets.

Consequently, we hypothesised that accurate modelling of the peri-tumour GBM invasive region and studying the transcriptomic alterations within normal YFP-astrocytes upon co-culture with different GIN lines, could reveal the genetic intercellular communication essential for GBM recurrence and may provide insights on designing novel therapeutic approaches. To achieve this, we designed an invasion model (described in Chapter 5), which we termed “Gliomasphere Matrix”, to simulate a GBM infiltrative microenvironment, predominated by a normal astrocytic population, invaded by a minority of GIN cells, thus mimicking residual disease post-surgery.

The H1-NSC line was genetically-labelled with a YFP reporter gene to allow differentiated YFP-astrocytic cell-tracking and isolation upon co-culture with primary cell lines derived from the invasive margins of each of 10 different GBMs. Using sequential protocols, YFP-astrocytes and GIN cells were co-cultured within a 3D physiologically-accurate brain-mimic microenvironment, which was composed of dhb-ECM reconstructed using a defined material known as PEGDA hydrogel, to avoid the utilization of commercially available animal sarcomatous products. Two Gliomasphere Matrix phenotypes were created in line with the principles of good manufacturing practice of drug screening and cell-based therapy systems, which include high-throughput, provision of a 3D microenvironment, reproducibility, feasibility, multi-faceting, consistency and scalability. Peripherally-located co-cultured YFP-astrocytes were FACS-isolated at two time points (Day 6 and Day 10) to represent two transcriptomic alteration snapshots as a result of cross-talk with malignant GIN cells. The results were computationally validated with RNA sequencing data obtained from surgically obtained samples using 5-ALA based FACS-isolation, and TCGA. However, we had some limitations and technical challenges when conducting this study; for example, we created three Crispr-mediated knock-in stable cell lines as we aimed to increase the power of the study and to reduce interpersonal variability; however, we couldn’t use two of these cell lines due to cost issue including differentiation, cell-culture, and sequencing costs.

Although knock-in of the YFP-gene in the AAVS1 site has several advantages discussed in chapter 3, this approach does not facilitate studying the transcriptome of the astrocytes had these astrocytes acquired stem characteristics, as the GFAP promoter will stop transcription of YFP that allowed the isolation of YFP-expressing astrocytes. In chapter 4 of this study, a remarkable limitation was the inability to identify the full components of mouse and human brain ECM which are poorly studied in the literature in general, more specifically when analysing and comparing the ions of the components of dhb-ECM data produced by TOS-SIMS; i.e., there are only three papers conducted 10-15 years ago, in which only major proteins like collagen, fibronectin and laminin were characterised. Although we have physically showed consistency and reproducibility in the creation of our Gliomasphere matrix model, more quantitative data could have provided more confidence about the efficiency and reproducibility of results. However, we could not quantify these microwells as there are 300 microwells in each macrowell and there are replicates of each sample. This means thousands of microwells, which makes quantifying Gliomasphere Matrices within these microwells technically and practically not possible. It can be also argued that imaging techniques could facilitate counting spheres in the microwells. However, the lowest possible magnification (10X) only allows the visualisation of 8 microwells, and thus imaging 300 small Gliomasphere Matrices, each composed of the least amount of cells (1500 cells) at once, is not possible nor accurate.

It is novel and advantageous to generate a Gliomasphere Matrix model which is a xeno-free product and derived from decellularised human brain plus a well-defined PEGDA material with high standards. However, the lack of an ideal method to confirm even distribution of the dhb-ECM within the full depth of PEGDA hydrogel in microwells remains technically challenging. To anticipate this, we characterised the main components of dhb-ECM solution, using a sensitive analytical instrument (ToF-SIMS), before mixing it with PEGDA hydrogel, which resembles many of the widely-used products available in the market such as Hystem. Future studies may assess the rheological modulus of this dhb-ECM within the full depth of PEGDA hydrogel as this may affect cellular behaviour.

Using the Gliomasphere Matrix model, the comparison of YFP-astrocyte transcriptome profiles after co-culture with each of ten patient-derived invasive primary GBM cells, relative to six astrocyte monoculture controls at Day 6 and Day 10 individually and/or collectively, resulted in the identification of important genetic signatures and molecular pathways, which were previously found to be involved in

GBM tumorigenesis, recurrence and resistance to treatment such as NOTCH, AKT/mTOR pathways. Furthermore, these YFP-astrocyte upregulated an interesting gene, known as *c1orf61,* after co-culture with ten patient-derived invasive primary GBM cells. Using well known bioinformatics platforms, we aimed to corroborate/validate our *in-vitro* findings with RNA-sequencing data generated from 20 patient samples previously isolated using 5-ALA fluorescence, that differentiate malignant (positive) and non-malignant (negative) cells, as well as TCGA data. However, transcriptome profiles of 5-ALA negative cells, which represent the peri-tumour astrocytes showed less expression of *c1orf61* relative to 5-ALA positive cells, which represents infiltrative tumour cells, and the result of this patient sample analysis can give the impression of contradiction to our results in our *in-vitro* experiment. However, we argued that *c1orf61* is rather upregulated in 5-ALA positive invasive GBM cells relative to 5-ALA negative tumour-associated astrocytes. Furthermore, the comparison occurred between malignant and non-malignant cells, unlike our experiment in which we compared YFP-astrocytes after co-culture with malignant cells to mono-cultured astrocytes controls with no previous contact with malignant cells. Moreover, TCGA data analysis also showed the distinct upregulation of this developmental gene in the tumour samples as compared to normal brain samples. Based on these genome-based analyses discussed above, *c1orf61* seems to be expressed in GBM cells and to a lesser extent in the peritumour astrocytes located in direct contact with GBM cells.

Unlike previous evidence which describes astrocytes as a contributor to GBM pathogenesis, our *In-vitro* experiment reveals a potential trigger of an innate immune response (STING) pathway in the co-cultured YFP-astrocytes when co-cultured in direct contact with GIN cells as compared to monocultured astrocyte controls. This pathway is known to be activated in cells with direct physical contact with malignant tumour cells, this has been cross-validated with independent analysis in 5-ALA negative (tumour-associated astrocytes; peritumoural astrocytes) cells as compared to their matching 5-ALA positive (GBM) cells of the 10 individual patients. The upregulation of the STING pathway in macrophages and peritoneal lining cells in mice with tumour ascites (Fu *et al.*, 1999), and when astrocytes were co-cultured with metastatic breast and lung cancer cells (Chen *et al.*, 2016). Arwert *et. al* (2020) also showed that upregulation of the STING pathway in stromal fibroblasts which were in direct contact with tumour cells, led to inhibition of both viral infection of malignant cells and intracellular viral replication, as interferon has wide-spectral anti-viral effects that undermine oncolytic viral therapy (Samuel, 2001; Sen, 2001; Arwert

et al., 2020). In this context, we may hypothesise that the efficacy of a viral oncolytic approach designed to target GBM cells in previous studies, is likely to be compromised by the anti-viral effect of activated interferon (STING) pathway expressed by surrounding peri-tumour astrocytes as part of their innate anti-tumour defence. This together with our finding of *c1orf61* expression in GBM tumour cells and tumour-associated astrocytes may indicate the future potential of new therapeutic strategy; i.e., upregulating suicidal genes under the genetic promoter of *c1orf61* using viral therapy in an orthotopic GBM mouse model will probably allow oncolytic viral-targeting of GBM tumour cells directly and enhance the reduction of an interferon anti-viral effect primed by *STING*$^{+}$/*c1orf61*$^{+}$-expressing peri-tumoural astrocytes indirectly. In general, this evidence may highlight the defence (anti-tumour) response triggered in normal parenchymal cells of various tissues in response to malignant cells, which are in direct contact. Based on the fact that STING activation represents an innate immune response exhibited by normal cells towards malignant cells in contact, many studies have been advocating the importance of designing novel immunotherapies targeting this pathway to combat cancers (Bose, 2017; Yum *et al.*, 2019). Recent elegant evidence sought to enhance anti-tumour activity by engineering STING-agonist producing bacteria (Leventhal *et al.*, 2020).

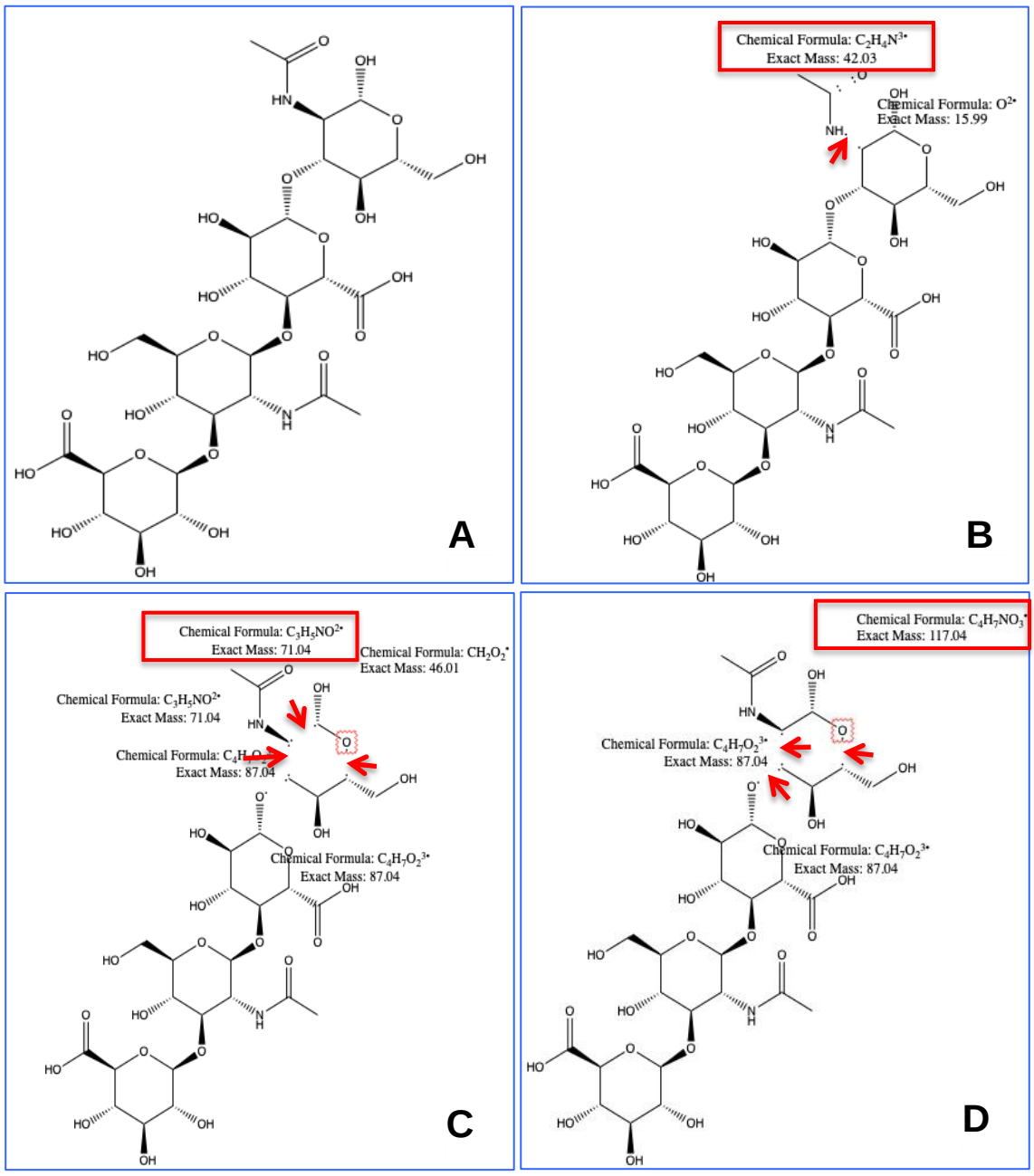
Conducting this project has provided significant learning and experience in multi-disciplinary research fields (cloning, genetic-editing using CRISPR-cas9 technology, bioinformatics RNA-sequencing data analysis, decellularisation of tissues, biomaterials, and TOF-SIMS surface analysis). All of these skills were invested to model and interrogate the genetic alterations of the astrocytes located in close vicinity of GBM cells in the invasive margin environment of GBM tumours, which is a novel research area that has not been investigated so far due to many ethical and technical barriers. We were able to generate a model to study this region; however we have faced technical challenges that have also been limiting for many other studies in general in the research field. For example, it will be of considerable scientific value if we can confirm our main genetic findings (*c1orf61* and STING) at the protein level using commonly used techniques such as antibody hybridization techniques on GBM invasive margin histopathology sections or western blotting. However, re-isolating high numbers of YFP-astrocytes after co-culture with GBM cells using FACS is not possible using our Gliomasphere Matrix model and needs further studies to optimize the experiment to harvest higher numbers of astrocytes after differentiation and after co-culture re-isolation; i.e., we initially seeded 350000

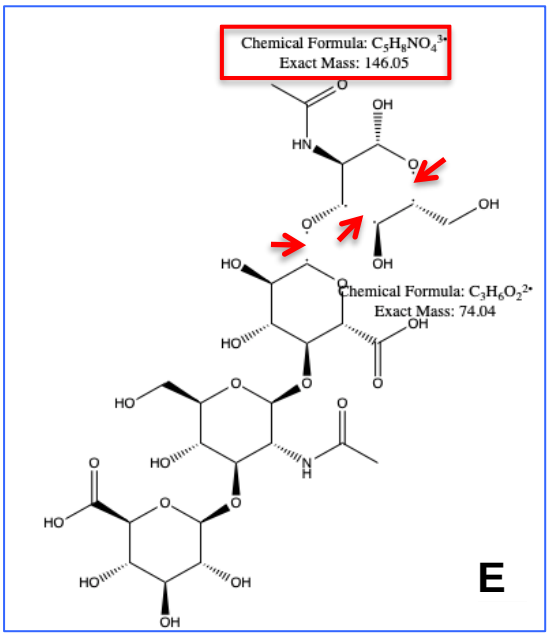
YFP-astrocytes in each macrowell of an Aggrewell plate and we were only able to re-isolate few hundreds to thousands of cells after 6 and 10 days of the co-culture. It is not clear why this has occurred, however there are two possible causes for this; firstly, YFP-astrocyte apoptosis as reveled by the Reactome pathway analysis of the top expressed gene list of RNA-sequencing data, and secondly, due to probable dedifferentiation of the terminally differentiated astrocytes, which has resulted in losing the YFP fluorescence due to underexpression of the knocked-in YFP-gene downstream to the astrocyte-specific GFAP promoter. Isolation of small number of cells hampers western bloating validation that requires millions of cells to harvest the protein of interest. It could be argued that hybridization and staining techniques would be more feasible and convenient for validation of gene-expression results, however there is no clear boarders separating the GBM from normal parenchymal brain tissue, which makes the assessment of the expression of proteins such as *c1orf61* and interferons of STING pathway in peritumoural astrocytes not accurate, nor valid. Furthermore, GBM is heavily infiltrated by immune cells which express high levels of interferon, which also give inaccurate results, and can be confused with interferon expressed by the tumour associated astrocytes. This is the rationale for choosing to validate our RNA-sequencing results using bioinformatics by comparing them to previous RNA-sequencing patient samples and TCGA data.

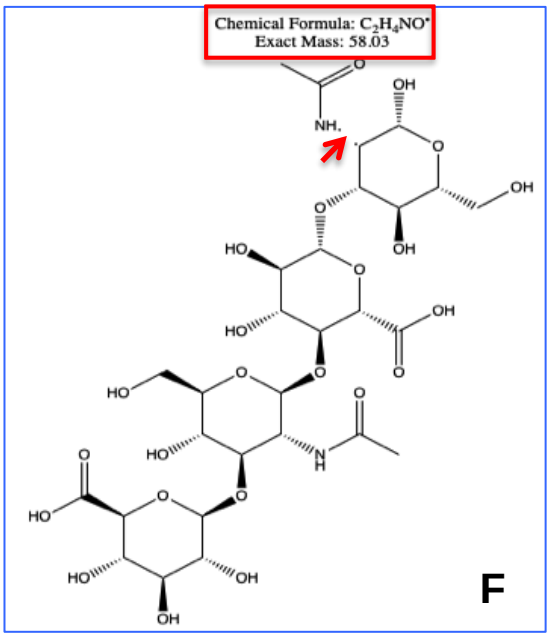
8. Appendix

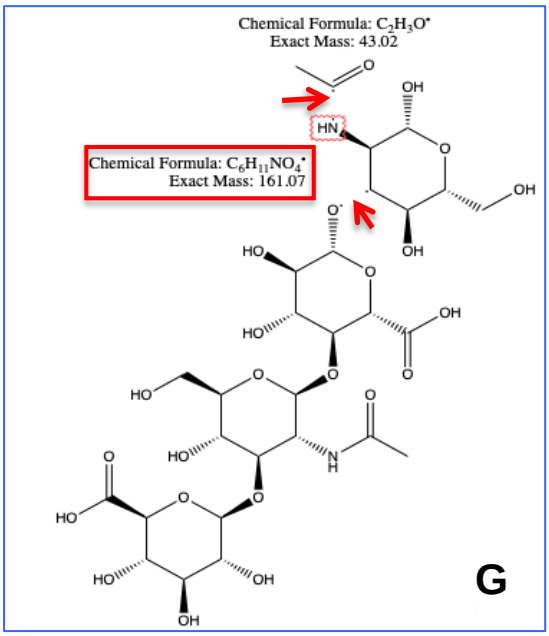
Appendix of chapter four

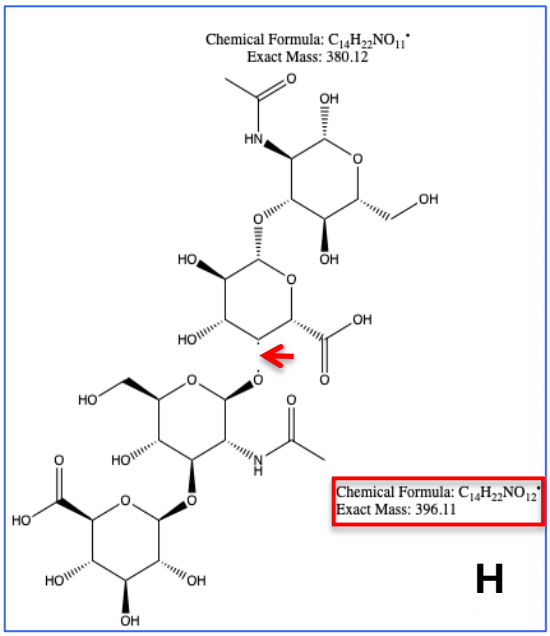
Random fragmentation figures showing methods used to obtain ions of HA, and sulfated-GAGs (keratan sulfate and chondroitin sulfate).

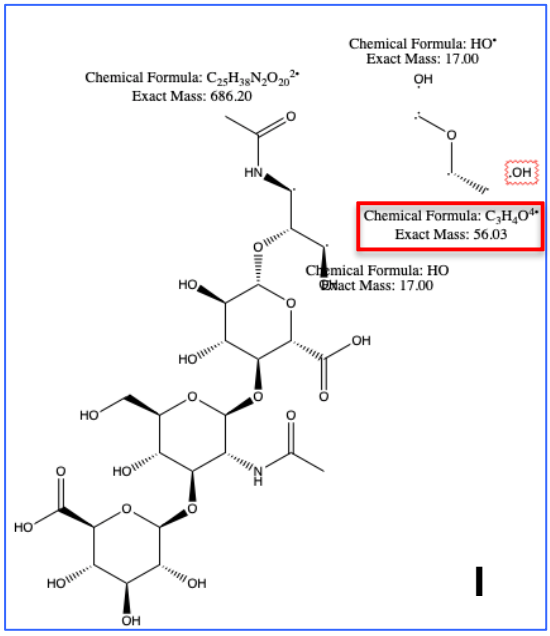


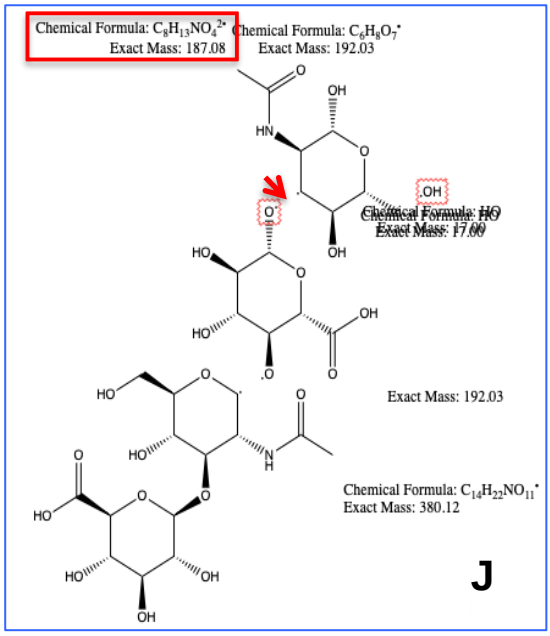

Chemical Formula: $C_5H_8NO_4^{3+}$
Exact Mass: 146.05
Chemical Formula: $C_3H_6O_2^{2+}$
Exact Mass: 74.04
E


Chemical Formula: $C_2H_4NO^{+}$
Exact Mass: 58.03
F


Chemical Formula: $C_2H_3O^{+}$
Exact Mass: 43.02
Chemical Formula: $C_6H_{11}NO_4^{+}$
Exact Mass: 161.07
G


Chemical Formula: $C_{14}H_{22}NO_{11}^{+}$
Exact Mass: 380.12
Chemical Formula: $C_{14}H_{22}NO_{12}^{+}$
Exact Mass: 396.11
H


Chemical Formula: $C_{25}H_{38}N_2O_{20}^{2+}$
Exact Mass: 686.20
Chemical Formula: HO^{+}
Exact Mass: 17.00
Chemical Formula: $C_3H_4O^{+}$
Exact Mass: 56.03
Chemical Formula: HO
Exact Mass: 17.00
I


Chemical Formula: $C_8H_{13}NO_4^{2+}$
Exact Mass: 187.08
Chemical Formula: $C_6H_8O_7^{+}$
Exact Mass: 192.03
Exact Mass: 192.03
Chemical Formula: $C_{14}H_{22}NO_{11}^{+}$
Exact Mass: 380.12
J

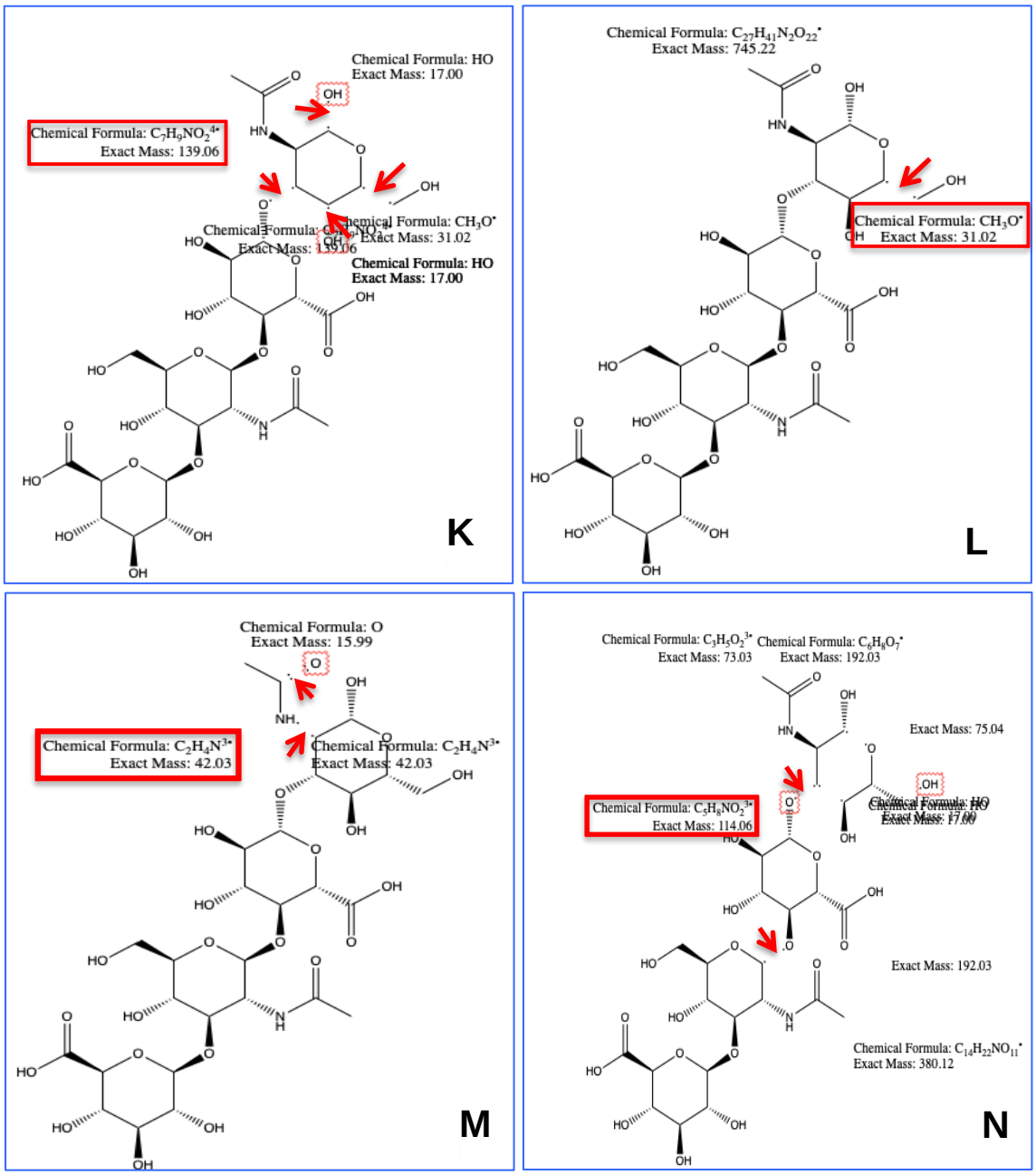


Figure 8. 1. Random Fragmentation method of the HA molecule. HA compound (A) was fragmented at random sites (indicated by red arrows) to generate ions (red rectangles) with a specific molecular mass for each ion (B-N).

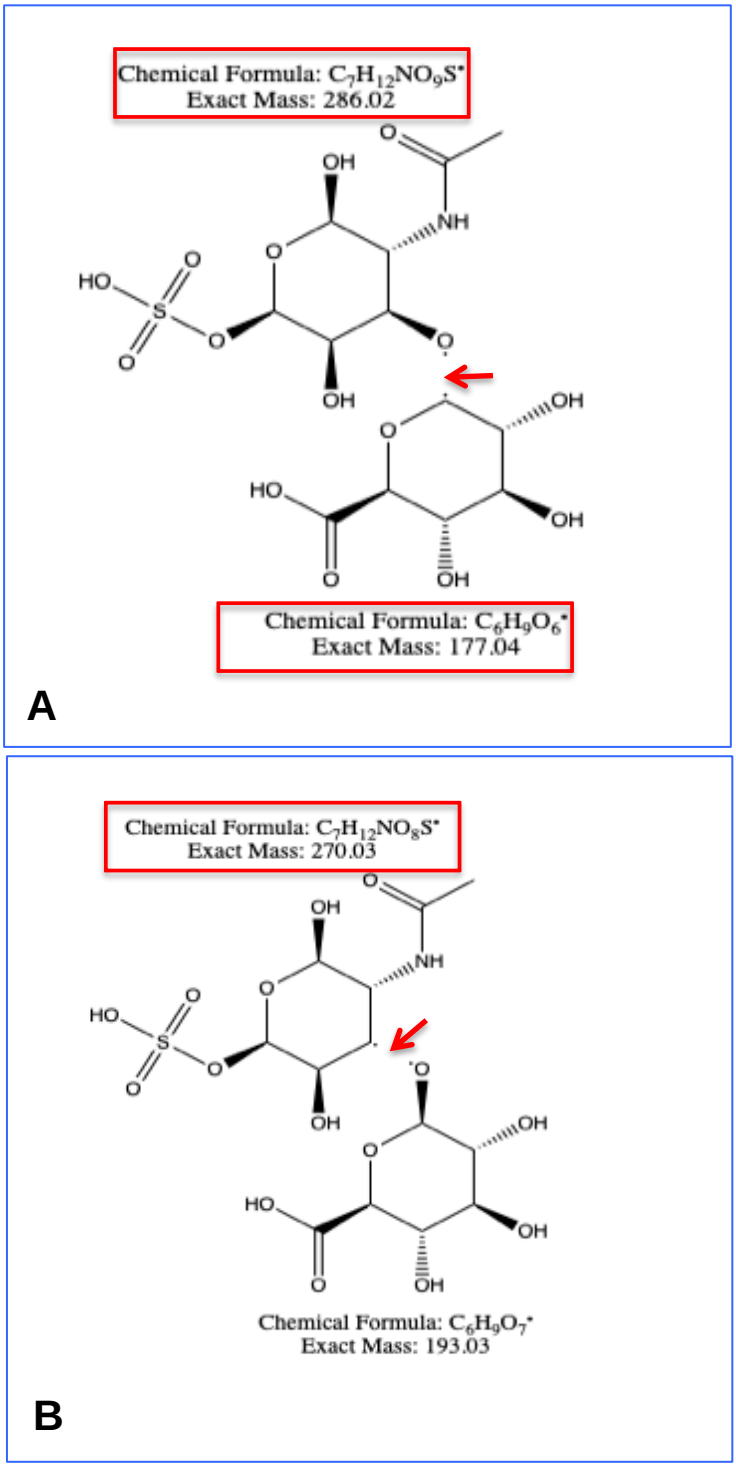


Figure 8. 2. Random Fragmentation method of chondroitin sulfate molecules. Chondroitin sulfate compound was fragmented at random sites (red arrows) to generate ions(red rectangles) with a specific molecular mass for each ion (A-B).

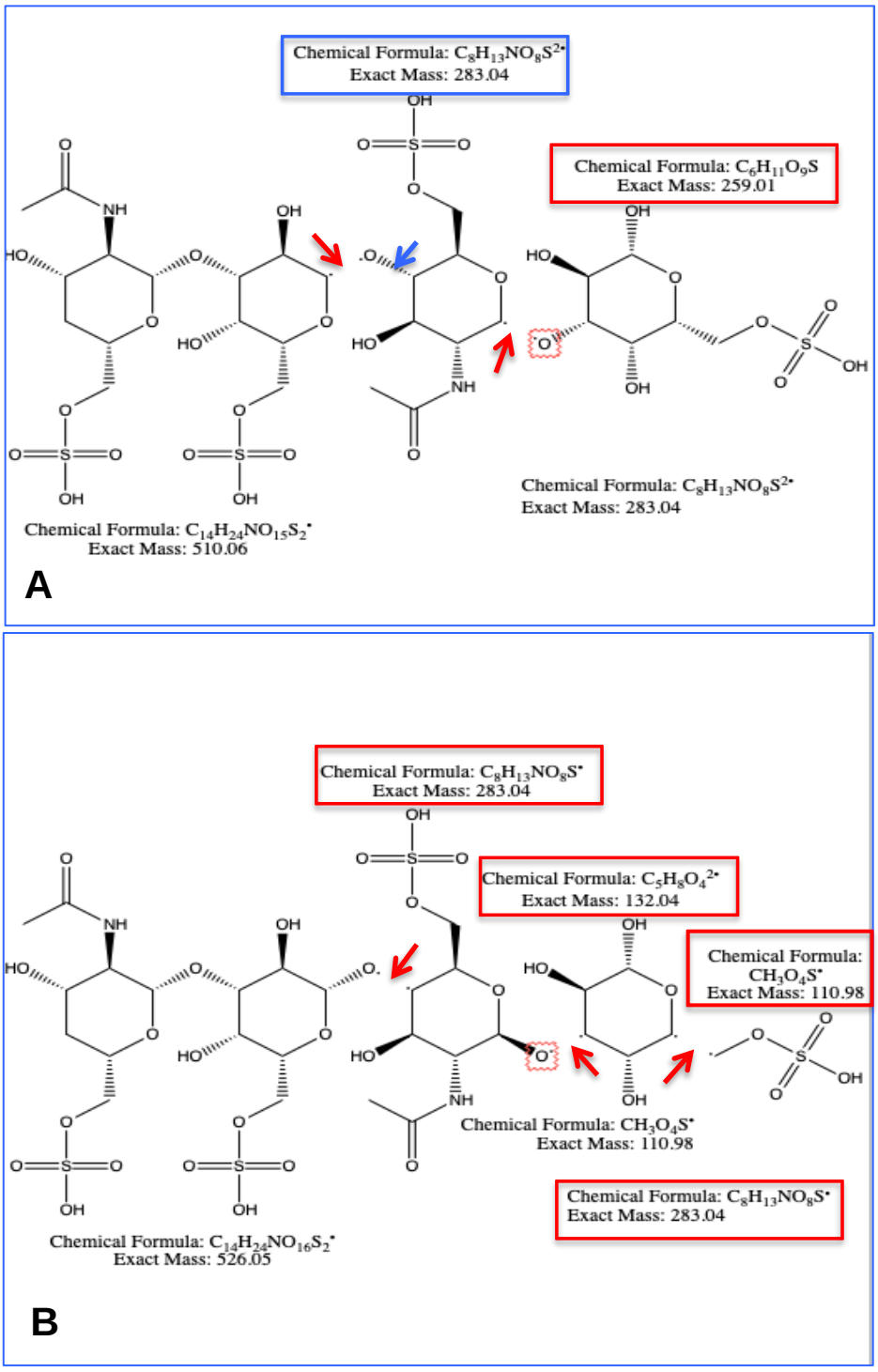


Figure 8. 3. Random Fragmentation method of keratan sulfate molecules. Keratan sulfate compound was fragmented at random sites (red arrows) to generate ions (red rectangles and blue rectangle) with a specific molecular mass for each ion (A-B).

Determining the unknown concentration of sulphated-GAGs in dhb-ECM using a Blyscan colorimetric assay.

A

MD IDs:

96	1	2	3	4	5	6	7	8	9	10	11	12
A	0.043	0.069	0.125	0.150	0.169	0.235	0.254	0.344	0.331	0.373	0.409	0.024
B	0.311	0.405	0.403	0.408	0.296	0.024	0.024	0.024	0.023	0.023	0.023	0.024
C	0.038	0.077	0.135	0.172	0.195	0.271	0.287	0.365	0.355	0.422	0.469	0.024
D	0.045	0.080	0.130	0.168	0.194	0.266	0.280	0.358	0.386	0.420	0.472	0.023
E	0.039	0.078	0.129	0.167	0.192	0.260	0.280	0.359	0.357	0.417	0.469	0.024
F	0.025	0.036	0.025	0.025	0.025	0.025	0.024	0.024	0.024	0.025	0.024	0.024
G	0.025	0.025	0.026	0.025	0.025	0.024	0.024	0.025	0.025	0.025	0.025	0.024
H	0.026	0.026	0.025	0.025	0.025	0.025	0.025	0.025	0.027	0.024	0.024	0.029

Finished cycle: 1
Display cycles: 1 ... 1
Absorbance values [OD]

B

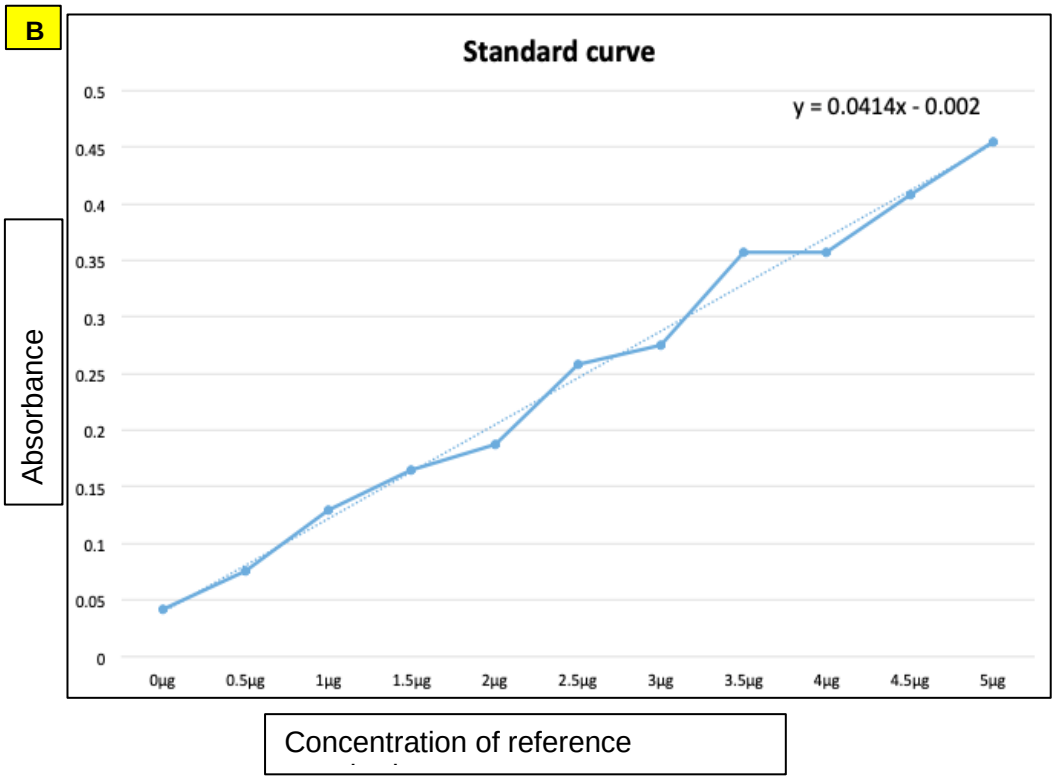


Figure 8. 4. Determining the unknown concentration of sulphated-GAGs in **dhb-ECM using Blyscan colorimetric assay.** The absorbance results layout obtained from a 96-well plate absorbance reader (A). A spectrophotometer was used to obtain the absorbance of known concentrations of reference standards of sulfated GAGs (red underline) and five unknown (unknown sulphated-GAGs concentration) replicate samples of dhb-ECM (blue underline) (A). The absorbance results of reference standards were plotted against their known concentrations using a standard curve (B), to obtain the equation (y=0.0414x-0.002). This equation was used to calculate the unknown concentration of sulphated-GAGs in dhb-ECM using the measured absorbance of each sample (blue underline in A) as determined by values on the x-axis.

Appendix of chapter five

Table 8. 1. Description of GIN cell lines utilised for Gliomasphere Matrix modelling

Tissue sample number & region	Regions	5-ALA (Y/N)	IDH-1	ATRX	Recurrence status	Treatment RT/CT
GBM 28.5	Invasive margin	Y	wild-type	wild-type	Primary GBM	No neoadjuvant
GBM 37.5	Invasive margin	Y	wild-type	wild-type	Primary GBM	No neoadjuvant
GBM 39.5	Invasive margin	Y	wild-type	wild-type	Primary GBM	No neoadjuvant
GBM 40.5	Invasive margin	Y	wild-type	wild-type	Primary GBM	No neoadjuvant
GBM 46.5	Invasive margin	Y	wild-type	wild-type	Primary GBM	No neoadjuvant
GBM 55.4	Invasive margin	Y	wild-type	wild-type	Primary GBM	No neoadjuvant
GBM 58.5	Invasive margin	Y	wild-type	wild-type	Primary GBM	No neoadjuvant
GBM 38.5	Invasive margin	Y	wild-type	wild-type	Primary GBM	No neoadjuvant
GBM 41.5	Invasive margin	Y	wild-type	wild-type	Primary GBM	No neoadjuvant
GBM 52.6	Invasive margin	Y	wild-type	wild-type	Primary GBM	No neoadjuvant

PCA analysis performed by Qiagen show a variance of 26% and 12% between the co-cultured astrocytes and the astrocyte controls after 6 and 10 days co-culture respectively **(Figure 8. 5)**.

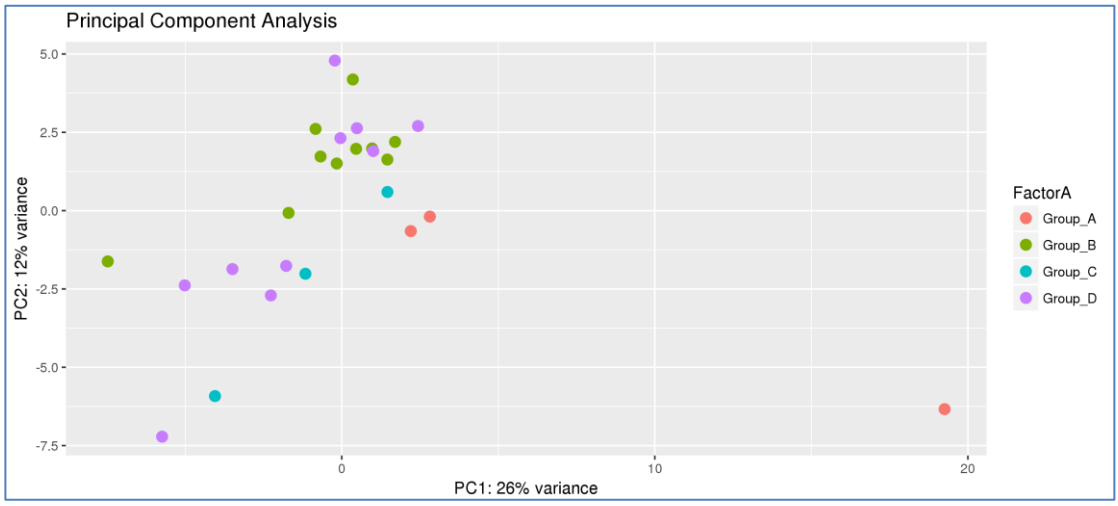


Figure 8. 5. Qiagen PCA analysis of *in-vitro* all samples across both time points. The PCA was performed on all samples using the DESeq2 transformed counts of all genes. PCA analysis of all sample genes show a variance of 26% and 12% between the co-cultured astrocytes and the YFP-controls after 6 (PCA1) and 10 (PCA10) days respectively. *Group_A and Group_B are the YFP-controls of first and second time point respectively, whereas Group_C and Group_D are the co-cultured astrocytes of the first and second time points respectively.*

Table 8. 2. Reactome pathway analysis of DEG expressed by YFP-astrocytes after co-culture with primary GBM cells for 6 days. The DEG list has been generated using EdgeR software.

Pathway Name	Entities Found	Entities Total	Entities Ratio	Entities P-value	Entities FDR	Reactions Found	Reactions Total	Reactions Ratio	Species Name
tRNA processing in the mitochondrion	14	45	0.003	1.81E-07	2.29E-04	*3*	*3*	*0*	Homo sapiens
rRNA processing in the mitochondrion	12	40	0.003	1.95E-06	1.23E-03	*1*	*6*	*0*	Homo sapiens
tRNA processing	19	182	0.013	3.96E-03	6.99E-01	*11*	*54*	*0.004*	Homo sapiens
Relaxin receptors	3	8	0.001	8.83E-03	6.99E-01	*3*	*4*	*0*	Homo sapiens
Intraflagellar transport	8	56	0.004	1.01E-02	6.99E-01	*9*	*12*	*0.001*	Homo sapiens
Integration of energy metabolism	15	145	0.01	1.05E-02	6.99E-01	*35*	*62*	*0.005*	Homo sapiens
Regulation of insulin secretion	12	106	0.007	1.10E-02	6.99E-01	*21*	*34*	*0.003*	Homo sapiens
NOTCH3 Intracellular Domain Regulates Transcription	6	36	0.002	1.24E-02	6.99E-01	*6*	*22*	*0.002*	Homo sapiens
Reversible hydration of carbon dioxide	4	17	0.001	1.27E-02	6.99E-01	*4*	*8*	*0.001*	Homo sapiens
Growth hormone receptor signalling	5	29	0.002	1.90E-02	6.99E-01	*4*	*28*	*0.002*	Homo sapiens
ROBO receptors bind AKAP5	3	11	0.001	2.05E-02	6.99E-01	*4*	*7*	*0.001*	Homo sapiens
G beta:gamma signalling through CDC42	4	21	0.001	2.52E-02	6.99E-01	*6*	*6*	*0*	Homo sapiens

Adrenaline,noradrenaline inhibits insulin secretion	5	32	0.002	2.74E-02	6.99E-01	*5*	*6*	*0*	Homo sapiens
Cooperation of PDCL (PhLP1) and TRiC/CCT in G-protein beta folding	6	45	0.003	3.22E-02	6.99E-01	*10*	*11*	*0.001*	Homo sapiens
Semaphorin interactions	8	70	0.005	3.25E-02	6.99E-01	*12*	*40*	*0.003*	Homo sapiens
Recruitment of NuMA to mitotic centrosomes	10	97	0.007	3.33E-02	6.99E-01	*2*	*2*	*0*	Homo sapiens
Ephrin signalling	4	23	0.002	3.35E-02	6.99E-01	*11*	*11*	*0.001*	Homo sapiens
G beta:gamma signalling through PLC beta	4	23	0.002	3.35E-02	6.99E-01	*2*	*2*	*0*	Homo sapiens
Presynaptic function of Kainate receptors	4	23	0.002	3.35E-02	6.99E-01	*1*	*2*	*0*	Homo sapiens
Opioid Signalling	11	111	0.008	3.37E-02	6.99E-01	*27*	*58*	*0.005*	Homo sapiens
Activation of RAC1	3	15	0.001	4.47E-02	6.99E-01	*1*	*4*	*0*	Homo sapiens
Glucagon-like Peptide-1 (GLP1) regulates insulin secretion	6	49	0.003	4.54E-02	6.99E-01	*7*	*11*	*0.001*	Homo sapiens
Thromboxane signalling through TP receptor	4	26	0.002	4.86E-02	6.99E-01	*6*	*7*	*0.001*	Homo sapiens
NOTCH4 Intracellular Domain Regulates Transcription	4	26	0.002	4.86E-02	6.99E-01	*2*	*9*	*0.001*	Homo sapiens

Table 8. 3. Reactome pathway analysis of DEG expressed by YFP-astrocytes after co-culture with primary GBM cells 10 days. The DEG list has been generated using EdgeR software.

Pathway Name	Entities Found	Entities Total	Entities Ratio	Entities P-value	Entities FDR	Reactions Found	Reactions Total	Reactions Ratio	Species Name
L13a-mediated translational silencing of Ceruloplasmin expression	25	120	0.008	8.42E-05	6.69E-02	*3*	*3*	*0*	Homo sapiens
Formation of a pool of free 40S subunits	23	106	0.007	8.86E-05	6.69E-02	*2*	*2*	*0*	Homo sapiens
Signalling by NOTCH3	16	63	0.004	1.85E-04	6.69E-02	*35*	*37*	*0.003*	Homo sapiens
GTP hydrolysis and joining of the 60S ribosomal subunit	24	120	0.008	2.09E-04	6.69E-02	*3*	*3*	*0*	Homo sapiens
Eukaryotic Translation Initiation	25	130	0.009	2.78E-04	6.69E-02	*16*	*21*	*0.002*	Homo sapiens
Cap-dependent Translation Initiation	25	130	0.009	2.78E-04	6.69E-02	*13*	*18*	*0.001*	Homo sapiens
Nonsense Mediated Decay (NMD) independent of the Exon Junction Complex (EJC)	21	101	0.007	3.07E-04	6.69E-02	*1*	*1*	*0*	Homo sapiens
NOTCH3 Intracellular Domain Regulates Transcription	11	36	0.002	4.09E-04	7.81E-02	*20*	*22*	*0.002*	Homo sapiens
Peptide chain elongation	20	97	0.007	4.67E-04	7.93E-02	*4*	*5*	*0*	Homo sapiens
Nonsense-Mediated Decay (NMD)	23	124	0.009	7.68E-04	1.07E-01	*6*	*6*	*0*	Homo sapiens
Nonsense Mediated Decay (NMD) enhanced by the Exon Junction Complex (EJC)	23	124	0.009	7.68E-04	1.07E-01	*5*	*5*	*0*	Homo sapiens
Eukaryotic Translation Elongation	20	102	0.007	8.56E-04	1.07E-01	*4*	*9*	*0.001*	Homo sapiens

Constitutive Signalling by NOTCH1 HD+PEST Domain Mutants	15	68	0.005	1.19E-03	1.07E-01	*16*	*21*	*0.002*	Homo sapiens
Signalling by NOTCH1 PEST Domain Mutants in Cancer	15	68	0.005	1.19E-03	1.07E-01	*16*	*21*	*0.002*	Homo sapiens
Signalling by NOTCH1 HD+PEST Domain Mutants in Cancer	15	68	0.005	1.19E-03	1.07E-01	*16*	*21*	*0.002*	Homo sapiens
Constitutive Signalling by NOTCH1 PEST Domain Mutants	15	68	0.005	1.19E-03	1.07E-01	*16*	*21*	*0.002*	Homo sapiens
Signalling by NOTCH1 in Cancer	15	68	0.005	1.19E-03	1.07E-01	*22*	*39*	*0.003*	Homo sapiens
Eukaryotic Translation Termination	20	106	0.007	1.34E-03	1.12E-01	*3*	*5*	*0*	Homo sapiens
Oncogene Induced Senescence	11	42	0.003	1.40E-03	1.12E-01	*14*	*19*	*0.002*	Homo sapiens
Regulation of expression of SLITs and ROBOs	29	183	0.013	1.91E-03	1.45E-01	*6*	*20*	*0.002*	Homo sapiens
SRP-dependent co-translational protein targeting to membrane	21	119	0.008	2.28E-03	1.64E-01	*5*	*5*	*0*	Homo sapiens
Selenocysteine synthesis	20	113	0.008	2.76E-03	1.89E-01	*2*	*7*	*0.001*	Homo sapiens
Respiratory electron transport, ATP synthesis by chemiosmotic coupling, and heat production by uncoupling proteins.	24	146	0.01	2.86E-03	1.89E-01	*16*	*29*	*0.002*	Homo sapiens
Viral mRNA Translation	20	114	0.008	3.05E-03	1.92E-01	*2*	*2*	*0*	Homo sapiens
Signalling by NOTCH1	16	83	0.006	3.15E-03	1.92E-01	*28*	*37*	*0.003*	Homo sapiens
Response of EIF2AK4 (GCN2) to amino acid deficiency	20	115	0.008	3.35E-03	1.94E-01	*4*	*16*	*0.001*	Homo sapiens

Signalling by NOTCH4	17	92	0.006	3.63E-03	2.03E-01	*13*	*20*	*0.002*	Homo sapiens
NOTCH1 Intracellular Domain Regulates Transcription	12	56	0.004	4.40E-03	2.32E-01	*15*	*16*	*0.001*	Homo sapiens
Signalling by NOTCH	36	257	0.018	4.46E-03	2.32E-01	*120*	*152*	*0.012*	Homo sapiens
Major pathway of rRNA processing in the nucleolus and cytosol	28	189	0.013	5.55E-03	2.83E-01	*7*	*7*	*0.001*	Homo sapiens
Translation initiation complex formation	12	62	0.004	9.42E-03	4.62E-01	*2*	*2*	*0*	Homo sapiens
rRNA processing in the nucleus and cytosol	29	207	0.014	9.89E-03	4.65E-01	*9*	*15*	*0.001*	Homo sapiens
Notch-HLH transcription pathway	7	28	0.002	1.24E-02	5.71E-01	*2*	*2*	*0*	Homo sapiens
Loss of MECP2 binding ability to 5hmC-DNA	2	2	0	1.35E-02	5.89E-01	*1*	*1*	*0*	Homo sapiens
AKT phosphorylates targets in the cytosol	5	16	0.001	1.39E-02	5.89E-01	*9*	*9*	*0.001*	Homo sapiens
Respiratory electron transport	18	115	0.008	1.40E-02	5.89E-01	*13*	*19*	*0.002*	Homo sapiens
Activation of the mRNA upon binding of the cap-binding complex and eIFs, and subsequent binding to 43S	12	66	0.005	1.47E-02	6.02E-01	*5*	*6*	*0*	Homo sapiens
Formation of ATP by chemiosmotic coupling	6	23	0.002	1.65E-02	6.61E-01	*3*	*3*	*0*	Homo sapiens
Signalling by NOTCH2	8	38	0.003	1.98E-02	7.36E-01	*13*	*20*	*0.002*	Homo sapiens
p53-Dependent G1/S DNA damage checkpoint	12	70	0.005	2.19E-02	7.36E-01	*11*	*22*	*0.002*	Homo sapiens

p53-Dependent G1 DNA Damage Response	12	70	0.005	2.19E-02	7.36E-01	*11*	*22*	*0.002*	Homo sapiens
Formation of the ternary complex, and subsequently, the 43S complex	10	54	0.004	2.20E-02	7.36E-01	*1*	*3*	*0*	Homo sapiens
IRF3 mediated activation of type 1 IFN	3	7	0	2.40E-02	7.36E-01	*5*	*5*	*0*	Homo sapiens
Cyclin E associated events during G1/S transition	14	88	0.006	2.47E-02	7.36E-01	*12*	*20*	*0.002*	Homo sapiens
G1/S DNA Damage Checkpoints	12	72	0.005	2.64E-02	7.36E-01	*13*	*26*	*0.002*	Homo sapiens
Ribosomal scanning and start codon recognition	11	64	0.004	2.70E-02	7.36E-01	*2*	*2*	*0*	Homo sapiens
AUF1 (hnRNP D0) binds and destabilizes mRNA	10	56	0.004	2.72E-02	7.36E-01	*3*	*4*	*0*	Homo sapiens
NOTCH4 Intracellular Domain Regulates Transcription	6	26	0.002	2.79E-02	7.36E-01	*8*	*9*	*0.001*	Homo sapiens
Cyclin A:Cdk2-associated events at S phase entry	14	90	0.006	2.90E-02	7.36E-01	*13*	*19*	*0.002*	Homo sapiens
Transcriptional regulation by RUNX3	17	118	0.008	3.28E-02	7.36E-01	*15*	*47*	*0.004*	Homo sapiens
The role of GTSE1 in G2/M progression after G2 checkpoint	13	83	0.006	3.29E-02	7.36E-01	*5*	*10*	*0.001*	Homo sapiens
Loss of MECP2 binding ability to the NCoR/SMRT complex	3	8	0.001	3.36E-02	7.36E-01	*1*	*1*	*0*	Homo sapiens
Regulation of mRNA stability by proteins that bind AU-rich elements	14	93	0.006	3.65E-02	7.36E-01	*10*	*26*	*0.002*	Homo sapiens
Stabilization of p53	10	59	0.004	3.66E-02	7.36E-01	*8*	*15*	*0.001*	Homo sapiens
NOTCH3 Activation and Transmission of Signal to the	6	28	0.002	3.78E-02	7.36E-01	*15*	*15*	*0.001*	Homo sapiens

Nucleus									
Signalling by ROBO receptors	29	235	0.016	4.19E-02	7.36E-01	*6*	*60*	*0.005*	Homo sapiens
rRNA processing	30	245	0.017	4.25E-02	7.36E-01	*10*	*21*	*0.002*	Homo sapiens
Presynaptic depolarization and calcium channel opening	4	15	0.001	4.35E-02	7.36E-01	*2*	*2*	*0*	Homo sapiens
GLI3 is processed to GLI3R by the proteasome	10	62	0.004	4.82E-02	7.36E-01	*5*	*5*	*0*	Homo sapiens
Degradation of GLI2 by the proteasome	10	62	0.004	4.82E-02	7.36E-01	*5*	*5*	*0*	Homo sapiens
SCF(Skp2)-mediated degradation of p27/p21	10	62	0.004	4.82E-02	7.36E-01	*6*	*7*	*0.001*	Homo sapiens
Diseases of Cellular Senescence	2	4	0	4.82E-02	7.36E-01	*3*	*3*	*0*	Homo sapiens
Vpr-mediated induction of apoptosis by mitochondrial outer membrane permeabilization	2	4	0	4.82E-02	7.36E-01	*1*	*2*	*0*	Homo sapiens
Ubiquitin-dependent degradation of Cyclin D	9	54	0.004	4.99E-02	7.36E-01	*3*	*5*	*0*	Homo sapiens

Table 8. 4. Reactome pathway analysis of DEG by comparing all (20) co-cultured astrocyte samples to all six astrocyte-only controls of both time points. The DEG list has been generated using EdgeR software.

Pathway Name	Entities Found	Entities Total	Entities Ratio	Entities P-value	Entities FDR	Reactions Found	Reactions Total	Reactions Ratio	Species Name
NOTCH3 Intracellular Domain Regulates Transcription	9	36	0.002	1.36E-03	8.33E-01	*20*	*22*	*0.002*	Homo sapiens
Signalling by NOTCH3	11	63	0.004	6.55E-03	8.33E-01	*22*	*37*	*0.003*	Homo sapiens
APC truncation mutants have impaired AXIN binding	4	14	0.001	1.89E-02	8.33E-01	*1*	*1*	*0*	Homo sapiens
Truncations of AMER1 destabilize the destruction complex	4	14	0.001	1.89E-02	8.33E-01	*1*	*1*	*0*	Homo sapiens
AXIN missense mutants destabilize the destruction complex	4	14	0.001	1.89E-02	8.33E-01	*1*	*1*	*0*	Homo sapiens
truncated APC mutants destabilize the destruction complex	4	14	0.001	1.89E-02	8.33E-01	*1*	*2*	*0*	Homo sapiens
Mis-spliced GSK3beta mutants stabilize beta-catenin	4	15	0.001	2.36E-02	8.33E-01	*1*	*1*	*0*	Homo sapiens
AMER1 mutants destabilize the destruction complex	4	15	0.001	2.36E-02	8.33E-01	*1*	*2*	*0*	Homo sapiens
AXIN mutants destabilize the destruction complex, activating WNT signalling	4	15	0.001	2.36E-02	8.33E-01	*1*	*2*	*0*	Homo sapiens
CD28 co-stimulation	7	39	0.003	2.37E-02	8.33E-01	*7*	*19*	*0.002*	Homo sapiens
tion site mutants of CTNNB1 are to the proteasome by the complex	4	16	0.001	2.89E-02	8.33E-01	*4*	*4*	*0*	Homo sapiens

T41 mutants of beta-catenin aren't phosphorylated	4	16	0.001	2.89E-02	8.33E-01	*1*	*1*	*0*	Homo sapiens
S45 mutants of beta-catenin aren't phosphorylated	4	16	0.001	2.89E-02	8.33E-01	*1*	*1*	*0*	Homo sapiens
S33 mutants of beta-catenin aren't phosphorylated	4	16	0.001	2.89E-02	8.33E-01	*1*	*1*	*0*	Homo sapiens
S37 mutants of beta-catenin aren't phosphorylated	4	16	0.001	2.89E-02	8.33E-01	*1*	*1*	*0*	Homo sapiens
Reversible hydration of carbon dioxide	4	17	0.001	3.49E-02	8.33E-01	*4*	*8*	*0.001*	Homo sapiens
NOTCH4 Intracellular Domain Regulates Transcription	5	26	0.002	4.05E-02	8.33E-01	*8*	*9*	*0.001*	Homo sapiens
CD28 dependent PI3K/Akt signalling	5	26	0.002	4.05E-02	8.33E-01	*6*	*9*	*0.001*	Homo sapiens
VEGFR2 mediated vascular permeability	7	44	0.003	4.10E-02	8.33E-01	*11*	*15*	*0.001*	Homo sapiens
Beta-catenin phosphorylation cascade	4	19	0.001	4.89E-02	8.33E-01	*4*	*4*	*0*	Homo sapiens
Protein methylation	4	19	0.001	4.89E-02	8.33E-01	*4*	*9*	*0.001*	Homo sapiens

Table 8. 5. Reactome pathway analysis of DEG expressed by 5-ALA negative samples (tumour associated astrocytes) when compared to 5-ALA positive (GBM cells). The DEG list has been generated using EdgeR software.

Pathway Name	Entities Found	Entities Total	Entities Ratio	Entities P-value	Entities FDR	Reactions Found	Reactions Total	Reactions Ratio	Species Name
Nonsense Mediated Decay (NMD) independent of the Exon Junction Complex (EJC)	66	101	0.007	1.11E-16	7.55E-15	*1*	*1*	*0*	Homo sapiens
Endosomal/Vacuolar pathway	52	82	0.006	1.11E-16	7.55E-15	*4*	*4*	*0*	Homo sapiens
Formation of a pool of free 40S subunits	66	106	0.007	1.11E-16	7.55E-15	*2*	*2*	*0*	Homo sapiens
Viral mRNA Translation	66	114	0.008	1.11E-16	7.55E-15	*2*	*2*	*0*	Homo sapiens
SRP-dependent co-translational protein targeting to membrane	67	119	0.008	1.11E-16	7.55E-15	*5*	*5*	*0*	Homo sapiens
GTP hydrolysis and joining of the 60S ribosomal subunit	66	120	0.008	1.11E-16	7.55E-15	*3*	*3*	*0*	Homo sapiens
L13a-mediated translational silencing of Ceruloplasmin expression	66	120	0.008	1.11E-16	7.55E-15	*3*	*3*	*0*	Homo sapiens
Nonsense-Mediated Decay (NMD)	67	124	0.009	1.11E-16	7.55E-15	*5*	*6*	*0*	Homo sapiens
Peptide chain elongation	66	97	0.007	1.11E-16	7.55E-15	*4*	*5*	*0*	Homo sapiens
Nonsense Mediated Decay (NMD) enhanced by the Exon Junction Complex (EJC)	67	124	0.009	1.11E-16	7.55E-15	*4*	*5*	*0*	Homo sapiens
Interferon gamma signalling	91	250	0.017	1.11E-16	7.55E-15	*12*	*15*	*0.001*	Homo sapiens
Response of EIF2AK4 (GCN2) to amino acid deficiency	70	115	0.008	1.11E-16	7.55E-15	*12*	*16*	*0.001*	Homo sapiens

Immunoregulatory interactions between a Lymphoid and a non-Lymphoid cell	100	316	0.022	1.11E-16	7.55E-15	*32*	*43*	*0.003*	Homo sapiens
Eukaryotic Translation Initiation	66	130	0.009	1.11E-16	7.55E-15	*13*	*21*	*0.002*	Homo sapiens
Eukaryotic Translation Termination	66	106	0.007	1.11E-16	7.55E-15	*3*	*5*	*0*	Homo sapiens
Cap-dependent Translation Initiation	66	130	0.009	1.11E-16	7.55E-15	*10*	*18*	*0.001*	Homo sapiens
Eukaryotic Translation Elongation	66	102	0.007	1.11E-16	7.55E-15	*4*	*9*	*0.001*	Homo sapiens
Regulation of expression of SLITs and ROBOs	72	183	0.013	1.11E-16	7.55E-15	*8*	*20*	*0.002*	Homo sapiens
Selenocysteine synthesis	66	113	0.008	1.11E-16	7.55E-15	*2*	*7*	*0.001*	Homo sapiens
Antigen Presentation: Folding, assembly and peptide loading of class I MHC	51	102	0.007	2.22E-16	1.42E-14	*13*	*16*	*0.001*	Homo sapiens
Influenza Viral RNA Transcription and Replication	67	175	0.012	2.44E-15	1.49E-13	*3*	*14*	*0.001*	Homo sapiens
Interleukin-10 signalling	45	86	0.006	2.89E-15	1.67E-13	*13*	*15*	*0.001*	Homo sapiens
Translocation of ZAP-70 to Immunological synapse	31	42	0.003	9.88E-15	5.53E-13	*4*	*4*	*0*	Homo sapiens
Influenza Life Cycle	68	188	0.013	2.15E-14	1.16E-12	*4*	*51*	*0.004*	Homo sapiens
Major pathway of rRNA processing in the nucleolus and cytosol	68	189	0.013	2.75E-14	1.40E-12	*6*	*7*	*0.001*	Homo sapiens
Selenoamino acid metabolism	66	181	0.013	3.63E-14	1.78E-12	*2*	*33*	*0.003*	Homo sapiens

Antigen processing-Cross presentation	67	187	0.013	5.14E-14	2.47E-12	*16*	*23*	*0.002*	Homo sapiens
PD-1 signalling	31	45	0.003	5.91E-14	2.60E-12	*4*	*4*	*0*	Homo sapiens
Phosphorylation of CD3 and TCR zeta chains	31	45	0.003	5.91E-14	2.60E-12	*6*	*7*	*0.001*	Homo sapiens
Generation of second messenger molecules	35	59	0.004	1.04E-13	4.49E-12	*13*	*17*	*0.001*	Homo sapiens
ER-Phagosome pathway	61	165	0.011	1.89E-13	7.77E-12	*6*	*10*	*0.001*	Homo sapiens
Influenza Infection	68	199	0.014	2.82E-13	1.13E-11	*4*	*59*	*0.005*	Homo sapiens
Signalling by ROBO receptors	74	235	0.016	1.21E-12	4.74E-11	*21*	*60*	*0.005*	Homo sapiens
rRNA processing in the nucleus and cytosol	68	207	0.014	1.60E-12	6.09E-11	*7*	*15*	*0.001*	Homo sapiens
Interferon alpha/beta signalling	61	184	0.013	1.56E-11	5.76E-10	*6*	*20*	*0.002*	Homo sapiens
Interferon Signalling	100	392	0.027	2.83E-11	1.02E-09	*21*	*66*	*0.005*	Homo sapiens
rRNA processing	68	245	0.017	1.73E-09	6.04E-08	*7*	*21*	*0.002*	Homo sapiens
Neutrophil degranulation	109	480	0.033	2.32E-09	7.89E-08	*10*	*10*	*0.001*	Homo sapiens
Co-stimulation by the CD28 family	36	97	0.007	1.42E-08	4.68E-07	*23*	*34*	*0.003*	Homo sapiens
Formation of the ternary complex, and subsequently, the 43S complex	25	54	0.004	4.02E-08	1.29E-06	*1*	*3*	*0*	Homo sapiens
Cytokine Signalling in Immune system	221	1,261	0.087	1.31E-07	4.07E-06	*238*	*699*	*0.056*	Homo sapiens

Interleukin-4 and Interleukin-13 signalling	56	211	0.015	1.90E-07	5.69E-06	*20*	*46*	*0.004*	Homo sapiens
Chemokine receptors bind chemokines	24	57	0.004	3.99E-07	1.20E-05	*13*	*19*	*0.002*	Homo sapiens
Translation initiation complex formation	25	62	0.004	5.02E-07	1.46E-05	*2*	*2*	*0*	Homo sapiens
Ribosomal scanning and start codon recognition	25	64	0.004	8.81E-07	2.47E-05	*2*	*2*	*0*	Homo sapiens
TCR signalling	42	147	0.01	1.03E-06	2.88E-05	*29*	*52*	*0.004*	Homo sapiens
Activation of the mRNA upon binding of the cap-binding complex and eIFs, and subsequent binding to 43S	25	66	0.005	1.51E-06	4.07E-05	*2*	*6*	*0*	Homo sapiens
Translation	72	339	0.023	1.14E-05	3.07E-04	*36*	*99*	*0.008*	Homo sapiens
Immune System	420	2,822	0.196	1.74E-05	4.53E-04	*736*	*1,597*	*0.128*	Homo sapiens
Downstream TCR signalling	34	124	0.009	2.37E-05	5.94E-04	*6*	*24*	*0.002*	Homo sapiens
Signalling by Interleukins	117	639	0.044	2.39E-05	5.98E-04	*184*	*490*	*0.039*	Homo sapiens
Cellular responses to stress	121	690	0.048	1.04E-04	2.49E-03	*103*	*227*	*0.018*	Homo sapiens
Adaptive Immune System	165	999	0.069	1.20E-04	2.88E-03	*166*	*261*	*0.021*	Homo sapiens
Cellular responses to external stimuli	121	708	0.049	2.80E-04	6.72E-03	*103*	*258*	*0.021*	Homo sapiens
Attenuation phase	16	47	0.003	3.50E-04	8.04E-03	*3*	*5*	*0*	Homo sapiens
Innate Immune System	204	1,328	0.092	8.54E-04	1.96E-02	*360*	*696*	*0.056*	Homo sapiens

DAP12 interactions	15	53	0.004	3.10E-03	6.82E-02	*31*	*33*	*0.003*	Homo sapiens
HSF1 activation	13	43	0.003	3.30E-03	7.26E-02	*1*	*7*	*0.001*	Homo sapiens
HSF1-dependent transactivation	16	59	0.004	3.46E-03	7.27E-02	*4*	*8*	*0.001*	Homo sapiens
RUNX1 and FOXP3 control the development of regulatory T lymphocytes (Tregs)	7	17	0.001	5.83E-03	1.22E-01	*20*	*20*	*0.002*	Homo sapiens
Complement cascade	30	156	0.011	1.36E-02	2.86E-01	*44*	*71*	*0.006*	Homo sapiens
Regulation of Complement cascade	27	139	0.01	1.65E-02	3.30E-01	*25*	*42*	*0.003*	Homo sapiens
Interleukin-1 processing	4	8	0.001	1.82E-02	3.65E-01	*5*	*5*	*0*	Homo sapiens
CLEC7A/inflammasome pathway	4	8	0.001	1.82E-02	3.65E-01	*3*	*4*	*0*	Homo sapiens
Antimicrobial peptides	24	123	0.009	2.17E-02	4.12E-01	*34*	*58*	*0.005*	Homo sapiens
Nef and signal transduction	4	9	0.001	2.66E-02	5.05E-01	*4*	*5*	*0*	Homo sapiens
Initial triggering of complement	23	120	0.008	2.88E-02	5.46E-01	*12*	*21*	*0.002*	Homo sapiens
RUNX3 Regulates Immune Response and Cell Migration	4	10	0.001	3.69E-02	7.00E-01	*5*	*5*	*0*	Homo sapiens
Alternative complement activation	3	6	0	3.93E-02	7.08E-01	*4*	*9*	*0.001*	Homo sapiens
Class I MHC mediated antigen processing & presentation	71	465	0.032	4.34E-02	7.81E-01	*36*	*48*	*0.004*	Homo sapiens
Alpha-defensins	4	11	0.001	4.91E-02	8.84E-01	*9*	*12*	*0.001*	Homo sapiens

Modulation by Mtb of host immune system	4	11	0.001	4.91E-02	8.84E-01	*4*	*6*	*0*	Homo sapiens

Table 8. 6. The association of C1orf61 in immune processes according to the IMMUNET website:

C1orf61 in Antigen processing and presentation
C1orf61 in B cell receptor signalling pathway
C1orf61 in Chemokine signalling pathway
C1orf61 in Complement and coagulation cascades
C1orf61 in Cytosolic DNA sensing pathway
C1orf61 in DC Network
C1orf61 in Fc epsilon RI signalling pathway
C1orf61 in Fc gamma R mediated phagocytosis
C1orf61 in Hematopoietic cell lineage
C1orf61 in Intestinal immune network for IgA production
C1orf61 in Leukocyte transendothelial migration
C1orf61 in Natural killer cell mediated cytotoxicity
C1orf61 in NOD like receptor signalling pathway
C1orf61 in RIG I like receptor signalling pathway
C1orf61 in T cell receptor signalling pathway
C1orf61 in Toll like receptor signalling pathway
C1orf61 in Immune Global
C1orf61 in BC-Antigen processing and presentation
C1orf61 in BC-B cell receptor signalling pathway
C1orf61 in BC-Chemokine signalling pathway
C1orf61 in BC-Complement and coagulation cascades
C1orf61 in BC-Cytosolic DNA sensing pathway
C1orf61 in BC-DC Network
C1orf61 in BC-Fc epsilon RI signalling pathway
C1orf61 in BC-Fc gamma R mediated phagocytosis
C1orf61 in BC-Hematopoietic cell lineage
C1orf61 in BC-Intestinal immune network for IgA production
C1orf61 in BC-Leukocyte transendothelial migration
C1orf61 in BC-Natural killer cell mediated cytotoxicity
C1orf61 in BC-NOD like receptor signalling pathway
C1orf61 in BC-RIG I like receptor signalling pathway
C1orf61 in BC-T cell receptor signalling pathway
C1orf61 in BC-Toll like receptor signalling pathway
C1orf61 in BC-Immune Global

Outputs

Published Papers

- Review paper: Diksin, M., Smith, S. J. and Rahman, R. (2017) 'The molecular and phenotypic basis of the glioma invasive perivascular niche', *International Journal of Molecular Sciences*. doi: 10.3390/ijms18112342.

- Smith, S. J. *et al.* (2017) 'The invasive region of glioblastoma defined by 5ALA guided surgery has an altered cancer stem cell marker profile compared to central Tumour', *International Journal of Molecular Sciences*, 18(11). doi: 10.3390/ijms18112452.

- Smith, S. J. *et al.* (2020) 'Metabolism based isolation of invasive glioblastoma cells with specific gene signatures and tumorigenic potential' *Neuro-Oncology Advances,* 2(1), pp. 1-12.

Submitted papers:

- "Genome wide expression and anti-proliferative effects of electronic field therapy on pediatric and adult brain tumours" was submitted to *Neuro-Oncology Advances*

Paper in preparation for *Nature Communications*:

- "Characterization of Invasive glioma niche using astrocyte-glioblastoma organoids and decellularised human brain (Gliomasphere matrices)"

Published Abstracts

- SNO conference

  Diksin, M., et al. Characterisation of The Post-Surgical Invasive Tumour Niche Using Astrocyte-Glioblastoma Organoids And Decellularised Human Brain. *Neuro Oncol*, Volume 21, Issue Supplement_6, November 2019, Pages vi264–vi265 https://doi.org/10.1093/neuonc/noz175.1110

- BNOS conference

  Diksin, M., et al., Characterisation of the invasive tumour niche using astrocyte-glioblastoma organoids and decellularised human brain. *Neuro Oncol*, Volume 21, Issue Supplement_4, October 2019, Page iv7, https://doi.org/10.1093/neuonc/noz167.028.

References

Acuto, O. and Michel, F. (2003) 'CD28-mediated co-stimulation: A quantitative support for TCR signalling', *Nature Reviews Immunology*. 3, pp. 939–951. doi: 10.1038/nri1248.

Adam, I. *et al.* (2018) 'Upregulation of tryptophanyl-tRNA synthethase adapts human cancer cells to nutritional stress caused by tryptophan degradation', *OncoImmunology*. 7(12), e1486353. doi: 10.1080/2162402X.2018.1486353.

Ahn, S. *et al.* (1998) ' A Dominant-Negative Inhibitor of CREB Reveals that It Is a General Mediator of Stimulus-Dependent Transcription of c- fos ', *Molecular and Cellular Biology*. 18, pp. 967 – 977. doi: 10.1128/mcb.18.2.967.

Akhtar, S. *et al.* (2018) 'Epstein-barr virus in gliomas: Cause, association, or artifact?', *Frontiers in Oncology*. 8, pp. 123. doi: 10.3389/fonc.2018.00123.

Al-Hajj, M. and Clarke, M. F. (2004) 'Self-renewal and solid tumor stem cells', *Oncogene*. 23, pp. 7274–7282. doi: 10.1038/sj.onc.1207947.

Albini, A. *et al.* (1992) 'Matrigel promotes retinoblastoma cell growth in vitro and in vivo', *International Journal of Cancer*. 9, pp. 234–240. doi: 10.1002/ijc.2910520214.

Aldape, K. *et al.* (2015) 'Glioblastoma: pathology, molecular mechanisms and markers', *Acta Neuropathologica*. 129(6), pp. 829-48. doi: 10.1007/s00401-015-1432-1.

Alegre, M. L., Frauwirth, K. A. and Thompson, C. B. (2001) 'T-cell regulation by CD28 and CTLA-4', *Nature Reviews Immunology*. 1, pp. 220–228. doi: 10.1038/35105024.

Alifieris, C. and Trafalis, D. T. (2015) 'Glioblastoma multiforme: Pathogenesis and treatment', *Pharmacology and Therapeutics*. 152, pp. 63-82 doi: 10.1016/j.pharmthera.2015.05.005.

Allen, R. A. *et al.* (2010) 'Adrenal extracellular matrix scaffolds support adrenocortical cell proliferation and function in vitro', *Tissue Engineering - Part A*. 16(11), pp. 3363-3374. doi: 10.1089/ten.tea.2010.0005.

Angelucci, C., Lama, G. and Sica, G. (2019) 'Multifaceted functional role of semaphorins in glioblastoma', *International Journal of Molecular Sciences*. 20(9), pii, E2144. doi: 10.3390/ijms20092144.

Arita, H. *et al.* (2013) 'Upregulating mutations in the TERT promoter commonly occur in adult malignant gliomas and are strongly associated with total 1p19q loss', *Acta Neuropathologica*. 126(2), pp. 267-76. doi: 10.1007/s00401-013-1141-6.

Arwert, E. N. *et al.* (2020) 'STING and IRF3 in stromal fibroblasts enable sensing of genomic stress in cancer cells to undermine oncolytic viral therapy', *Nature Cell Biology*. 22, pp. 758–766. doi: 10.1038/s41556-020-0527-7.

Azari, H. *et al.* (2011) 'Isolation and expansion of human glioblastoma multiforme tumor cells using the neurosphere assay.', *Journal of visualized experiments : JoVE*. (56), pp. e3633. doi: 10.3791/3633.

Badylak, S. F., Freytes, D. O. and Gilbert, T. W. (2009) 'Extracellular matrix as a biological scaffold material: Structure and function', *Acta Biomaterialia*. 5(1), pp. 1-13. doi: 10.1016/j.actbio.2008.09.013.

Baek, K. H. and Ryeom, S. (2017) 'Detection of oncogene-induced senescence in vivo', *Methods in Molecular Biology*. 1534, pp. 185-198. doi: 10.1007/978-1-4939-6670-7_18.

Baki, A. *et al.* (2017) 'Surface modification of PDLLGA microspheres with gelatine methacrylate: Evaluation of adsorption, entrapment, and oxygen plasma treatment approaches', *Acta Biomaterialia*. 15(53), pp. 450-459. doi: 10.1016/j.actbio.2017.01.042.

Bandyopadhyay, D. *et al.* (2015) 'Two Uncommon Causes of Guillain-Barré Syndrome: Hepatitis E and Japanese Encephalitis', *Case Reports in Neurological Medicine*. 2015, 759495. doi: 10.1155/2015/759495.

Barani, I. J. and Larson, D. A. (2015) 'Radiation therapy of glioblastoma', *Cancer Treatment and Research*. 20(5), pp. 1375–1382. doi: 10.1007/978-3-319-12048-5_4.

Bardoscia, M. T., Amstad, P. and Honegger, P. (1992) 'Expression of the proto-oncogene c-fos in three-dimensional fetal brain cell cultures and the lack of correlation with maturation-inducing stimuli', *Molecular Brain Research*. 12, pp. 23-30. doi: 10.1016/0169-328X(92)90064-I.

Barkan, D., Green, J. E. and Chambers, A. F. (2010) 'Extracellular matrix: A gatekeeper in the transition from dormancy to metastatic growth', *European Journal of Cancer*. 46(7), pp. 1181-8. doi: 10.1016/j.ejca.2010.02.027.

Barnes, T. J., Kempson, I. M. and Prestidge, C. A. (2011) 'Surface analysis for compositional, chemical and structural imaging in pharmaceutics with mass spectrometry: A ToF-SIMS perspective', *International Journal of Pharmaceutics*. 417(1-2), pp. 61-9. doi: 10.1016/j.ijpharm.2011.01.043.

Bartsch, D. *et al.* (1995) 'Frequent mutations of CDKN2 in primary pancreatic adenocarcinomas', *Genes, Chromosomes and Cancer*. 14(3), pp. 189-195 doi: 10.1002/gcc.2870140306.

Battiston, K. G. *et al.* (2014) 'Biomaterials in co-culture systems: Towards optimizing tissue integration and cell signaling within scaffolds', *Biomaterials*. 35(15), PP. 4465-76.doi: 10.1016/j.biomaterials.2014.02.023.

Baysan, M. *et al.* (2014) 'Micro-environment causes reversible changes in DNA methylation and mRNA expression profiles in patient-derived glioma stem cells', *PLoS ONE*. 9(4):e94045. doi: 10.1371/journal.pone.0094045.

Bazerbachi, F. *et al.* (2015) 'Extra-hepatic manifestations associated with hepatitis E virus infection: a comprehensive review of the literature', *Gastroenterology Report*. 4(1), pp. 1-15. doi: 10.1093/gastro/gov042.

Bazzoni, R. and Bentivegna, A. (2019) 'Role of Notch Signaling Pathway in Glioblastoma Pathogenesis', *Cancers*. 11(3). doi: 10.3390/cancers11030292.

Beauchesne, P. (2011) 'Extra-neural metastases of malignant gliomas: Myth or reality?', *Cancers*, 3(1), pp. 461–477. doi: 10.3390/cancers3010461.

Becker, T. M. *et al.* (2005) 'Impaired inhibition of NF-κB activity by melanoma-associated p16INK4a mutations', *Biochemical and Biophysical Research Communications*. 332(3), pp. 873-879. doi: 10.1016/j.bbrc.2005.05.032.

Beenken, A. and Mohammadi, M. (2009) 'The FGF family: biology, pathophysiology and therapy', *Nature Reviews Drug Discovery*, 8(3), pp. 235–253. doi: 10.1038/nrd2792.

Behm-Ansmant, I. *et al.* (2007) 'mRNA quality control: An ancient machinery recognizes and degrades mRNAs with nonsense codons', *FEBS Letters*. 581, pp. 2845–2853. doi: 10.1016/j.febslet.2007.05.027.

Belu, A. M. *et al.* (2000) 'TOF-SIMS characterization and imaging of controlled-release drug delivery systems', *Analytical Chemistry*. 72(22), pp. 5625–5638. doi: 10.1021/ac000450+.

Ben-David, U. *et al.* (2017) 'Patient-derived xenografts undergo mouse-specific tumor evolution', *Nature Genetics*. 49, pp. 1567–1575. doi: 10.1038/ng.3967.

Van Den Bent, M. J. *et al.* (2010) 'IDH1 and IDH2 mutations are prognostic but not predictive for outcome in anaplastic oligodendroglial tumors: A report of the European Organization for Research and Treatment of Cancer Brain Tumor Group', *Clinical Cancer Research*. 16(5), pp. 1597-604. doi: 10.1158/1078-0432.CCR-09-2902.

Van Den Bent, M. J. (2010) 'Interobserver variation of the histopathological diagnosis in clinical trials on glioma: A clinician's perspective', *Acta Neuropathologica*. 120, pp. 297–304. doi: 10.1007/s00401-010-0725-7.

Berezovsky, A. D. *et al.* (2014) 'Sox2 promotes malignancy in glioblastoma by regulating plasticity and astrocytic differentiation', *Neoplasia (United States)*. 206.e19-25. doi: 10.1016/j.neo.2014.03.006.

Berger, M. F. *et al.* (2010) 'Integrative analysis of the melanoma transcriptome', *Genome Research*. 20(4), pp. 413-27. doi: 10.1101/gr.103697.109.

Bernard, M. P. *et al.* (1983) 'Nucleotide Sequences of Complementary Deoxyribonucleic Acids for the Proal Chain of Human Type I Procollagen. Statistical Evaluation of Structures That Are Conserved during Evolution', *Biochemistry*. 22 (5), pp. 1139-1145. doi: 10.1021/bi00291a023.

Bettegowda, C. *et al.* (2011) 'Mutations in CIC and FUBP1 contribute to human oligodendroglioma', *Science*. 333(6048), pp. 1453-5. doi: 10.1126/science.1210557.

Beutler, A. S. *et al.* (1999) 'Tumor gene therapy made easy: Allogeneic major histocompatibility complex in the C6 rat glioma model', *Human Gene Therapy*. 10:95–101. doi: 10.1089/10430349950019228.

Bhat, K. P. L. *et al.* (2011) 'The transcriptional coactivator TAZ regulates mesenchymal differentiation in malignant glioma', *Genes and Development*. 25(24), pp. 2594-609. doi: 10.1101/gad.176800.111.

Bhat, K. P. L. *et al.* (2013) 'Mesenchymal Differentiation Mediated by NF-κB Promotes Radiation Resistance in Glioblastoma', *Cancer Cell*. 24, pp. 331–346. doi: 10.1016/j.ccr.2013.08.001.

Bhaya, D., Davison, M. and Barrangou, R. (2011) 'CRISPR-Cas Systems in Bacteria and Archaea: Versatile Small RNAs for Adaptive Defense and Regulation', *Annual Review of Genetics*. 45, pp. 273-97. doi: 10.1146/annurev-genet-110410-132430.

Bhuvanagiri, M. *et al.* (2010) 'NMD: RNA biology meets human genetic medicine', *Biochemical Journal*. 430(3), pp. 365–377. doi: 10.1042/BJ20100699.

Bian, S. *et al.* (2018) 'Genetically engineered cerebral organoids model brain tumor formation', *Nature Methods*. 15(8), pp. 631-639. doi: 10.1038/s41592-018-0070-7.

Biankin, A. V. *et al.* (2012) 'Pancreatic cancer genomes reveal aberrations in axon guidance pathway genes', *Nature*. 491(7424), pp. 399-405. doi: 10.1038/nature11547.

Biasoli, D. *et al.* (2014) 'Glioblastoma cells inhibit astrocytic p53-expression favoring cancer malignancy', *Oncogenesis*. 3, e123. doi: 10.1038/oncsis.2014.36.

Bigner, S. H., Mark, J. and Bigner, D. D. (1987) 'Chromosomal progression of malignant human gliomas from biopsy to establishment as permanent lines in vitro', *Cancer Genetics and Cytogenetics*. 24(1), pp. 163-176 .doi: 10.1016/0165-4608(87)90094-X.

Blaisdell, F. W. (2002) 'The pathophysiology of skeletal muscle ischemia and the reperfusion syndrome: A review', *Vascular*. 10(6), pp. 620-30. doi: 10.1177/096721090201000620.

Bloch, O. *et al.* (2012) 'Impact of extent of resection for recurrent glioblastoma on overall survival: Clinical article', *Journal of Neurosurgery*. 117(6), pp. 1032-8. doi: 10.3171/2012.9.JNS12504.

Bodzon-Kulakowska, A. and Suder, P. (2016) 'Imaging mass spectrometry: Instrumentation, applications, and combination with other visualization techniques', *Mass Spectrometry Reviews*. 35, pp. 147–169 doi: 10.1002/mas.21468.

Bornstein, P. and Sage, E. H. (2002) 'Matricellular proteins: Extracellular modulators of cell function', *Current Opinion in Cell Biology*. 14, pp. 608–616. doi: 10.1016/S0955-0674(02)00361-7.

Bose, D. (2017) 'CGAS/STING pathway in cancer: Jekyll and hyde story of cancer immune response', *International Journal of Molecular Sciences*. 18(11), pii. E2459. doi: 10.3390/ijms18112459.

Bosnakovski, D. *et al.* (2006) 'Chondrogenic differentiation of bovine bone marrow mesenchymal stem cells (MSCs) in different hydrogels: Influence of collagen type II extracellular matrix on MSC chondrogenesis', *Biotechnology and Bioengineering*. 93 (6), pp. 1152–63. doi: 10.1002/bit.20828.

Boström, J. *et al.* (2001) 'Alterations of the tumor suppressor genes CDKN2A (p16INK4a), p14ARF, CDKN2B (p15INK4b), and CDKN2C (p18INK4c) in atypical and anaplastic meningiomas', *American Journal of Pathology*. 159, pp. 661–669. doi: 10.1016/S0002-9440(10)61737-3.

Brafman, D. A. *et al.* (2009) 'Defining long-term maintenance conditions of human embryonic stem cells with arrayed cellular microenvironment technology', *Stem Cells and Development*. 18(8), pp. 1141-54. doi: 10.1089/scd.2008.0410.

Brandao, M. *et al.* (2019) 'Astrocytes, the rising stars of the glioblastoma microenvironment', *GLIA*. 67(5), pp. 779-790. doi: 10.1002/glia.23520.

Brandes, A. A., Bartolotti, M. and Franceschi, E. (2013) 'Second surgery for recurrent glioblastoma: Advantages and pitfalls', *Expert Review of Anticancer Therapy*. 13(5), pp. 583–587. doi: 10.1586/era.13.32.

Brat, D. J. *et al.* (2015) 'Comprehensive, integrative genomic analysis of diffuse lower-grade gliomas', *New England Journal of Medicine*. 372(26), pp. 2481-98. doi: 10.1056/NEJMoa1402121.

Bravo, R. *et al.* (1987) 'Involvement of common and cell type-specific pathways in c-fos gene control: Stable induction by cAMP in macrophages', *Cell*. 51(5), pp. 721-32. doi: 10.1016/0092-8674(87)90428-4.

Brennan, C. W. *et al.* (2013) 'The somatic genomic landscape of glioblastoma', *Cell*, 155(2), pp. 462–477. doi: 10.1016/j.cell.2013.09.034.

Broekman, Marike L *et al.* (2018) 'Multidimensional communication in the microenvirons of glioblastoma', *Nature Reviews Neurology*. 14, pp. 482–495. doi: 10.1038/s41582-018-0025-8.

Brown, A. and Vickerman, J. C. (1984) 'Static SIMS for applied surface analysis', *Surface and Interface Analysis*. 25(11), pp. 1897-1907. doi: 10.1002/sia.740060102.

Brown, B. N. *et al.* (2009) 'Macrophage phenotype and remodeling outcomes in response to biologic scaffolds with and without a cellular component', *Biomaterials*. 30(8), pp. 1482-91 doi: 10.1016/j.biomaterials.2008.11.040.

Byrne, S. M. *et al.* (2015) 'Multi-kilobase homozygous targeted gene replacement in human induced pluripotent stem cells', *Nucleic Acids Research*. 43(3), e21.doi: 10.1093/nar/gku1246.

Cai, X., Chiu, Y. H. and Chen, Z. J. (2014) 'The cGAS-cGAMP-STING pathway of cytosolic DNA sensing and signaling', *Molecular Cell*. 54, pp. 289 – 296. doi: 10.1016/j.molcel.2014.03.040.

Cai, Y.-D. *et al.* (2018) 'Identification of the Gene Expression Rules That Define the Subtypes in Glioma', *Journal of Clinical Medicine*. 7(10), pii: E350. doi: 10.3390/jcm7100350.

Canavan, H. E. *et al.* (2007) 'Comparison of native extracellular matrix with adsorbed protein films using secondary ion mass spectrometry', *Langmuir*. 29 (3), pp. 902-912. doi: 10.1021/la062330o.

Carro, M. S. *et al.* (2010) 'The transcriptional network for mesenchymal transformation of brain tumours', *Nature*. 463(7279). pp.318-25. doi: 10.1038/nature08712.

Castellano, M. *et al.* (1997) 'CDKN2A/p16 is inactivated in most melanoma cell lines', *Cancer Research*. 57(21), pp. 4868-4875.

Ceccarelli, M. *et al.* (2016) 'Molecular Profiling Reveals Biologically Discrete Subsets and Pathways of Progression in Diffuse Glioma', *Cell*, 164(3), pp. 550–563. doi: 10.1016/j.cell.2015.12.028.

Chang, H. H. Y. *et al.* (2017) 'Non-homologous DNA end joining and alternative pathways to double-strand break repair', *Nature Reviews Molecular Cell Biology*. 18(8), pp. 495-506. doi: 10.1038/nrm.2017.48.

Chang, Y.-F., Imam, J. S. and Wilkinson, M. F. (2007) 'The Nonsense-Mediated Decay RNA Surveillance Pathway', *Annual Review of Biochemistry*. 76, pp. 51–74. doi: 10.1146/annurev.biochem.76.050106.093909.

Charles, N. *et al.* (2010) 'Perivascular Nitric Oxide Activates Notch Signaling and Promotes Stem-like Character in PDGF-Induced Glioma Cells', *Cell Stem Cell*. 6(2), pp. 141-52. doi: 10.1016/j.stem.2010.01.001.

Chastain, S. R. *et al.* (2006) 'Adhesion of mesenchymal stem cells to polymer scaffolds occurs via distinct ECM ligands and controls their osteogenic differentiation', *Journal of Biomedical Materials Research - Part A*, 78(1), pp. 73–85. doi: 10.1002/jbm.a.30686.

Chédotal, A. (2019) 'Roles of axon guidance molecules in neuronal wiring in the developing spinal cord', *Nature Reviews Neuroscience*. 20(7), pp. 380-396. doi: 10.1038/s41583-019-0168-7.

Chédotal, A., Kerjan, G. and Moreau-Fauvarque, C. (2005) 'The brain within the tumor: New roles for axon guidance molecules in cancers', *Cell Death and Differentiation*. 12, pp. 1044–1056. doi: 10.1038/sj.cdd.4401707.

Chekhonin, I. V. *et al.* (2018) 'Glioma Cell and Astrocyte Co-cultures As a Model to Study Tumor–Tissue Interactions: A Review of Methods', *Cellular and Molecular Neurobiology*. 38(6), pp. 1179-95. doi: 10.1007/s10571-018-0588-3.

Chen, C. *et al.* (2018) 'Promoter-Operating Targeted Expression of Gene Therapy in Cancer: Current Stage and Prospect', *Molecular Therapy - Nucleic Acids*. 27(10), pp. 1816-1823. doi: 10.1016/j.omtn.2018.04.003.

Chen, J. W. E. *et al.* (2018) 'Influence of hyaluronic acid transitions in tumor microenvironment on glioblastoma malignancy and invasive behavior', *Frontiers in Materials*. 5, 39. doi: 10.3389/fmats.2018.00039.

Chen, L. *et al.* (2014) 'Predicting the likelihood of an isocitrate dehydrogenase 1 or 2 mutation in diagnoses of infiltrative glioma', *Neuro-Oncology*. 16, pp. 1478–1483. doi: 10.1093/neuonc/nou097.

Chen, Q. *et al.* (2016) 'Carcinoma-astrocyte gap junctions promote brain metastasis by cGAMP transfer', *Nature*. 533, pp. 493–498. doi: 10.1038/nature18268.

Chen, Y. and Swanson, R. A. (2003) 'Astrocytes and brain injury', *Journal of Cerebral Blood Flow and Metabolism*. 23, pp. 137–149. doi: 10.1097/01.WCB.0000044631.80210.3C.

Cheng, M. H. *et al.* (2010) 'Dermis-derived hydrogels support adipogenesis in vivo', *Journal of Biomedical Materials Research - Part A*. 92(3), pp. 852-8. doi: 10.1002/jbm.a.32410.

Cheng, N. C. *et al.* (2009) 'Chondrogenic differentiation of adipose-derived adult stem cells by a porous scaffold derived from native articular cartilage extracellular matrix', *Tissue Engineering - Part A*. 15(2), pp. 231-41. doi: 10.1089/ten.tea.2008.0253.

Cheng, P. *et al.* (2001) 'Notch-1 Regulates NF-κB Activity in Hemopoietic Progenitor Cells', *The Journal of Immunology*. 58, pp. 8097–109. doi: 10.4049/jimmunol.167.8.4458.

Childs, B. G. *et al.* (2015) 'Cellular senescence in aging and age-related disease: From mechanisms to therapy', *Nature Medicine*. 21(12), pp. 1424-35. doi: 10.1038/nm.4000.

Christopher Beadle *et al.* (2008) 'The Role of Myosin II in Glioma Invasion of the Brain', *Molecular Biology of the Cell*, 19, pp. 3357–3368. doi: 10.1091/mbc.E08.

Cobbs, C. S. *et al.* (2002) 'Human cytomegalovirus infection and expression in human malignant glioma', *Cancer Research*. 62(12), pp. 3347-50.

Cohen, M. H. *et al.* (2009) 'FDA Drug Approval Summary: Bevacizumab (Avastin®) as Treatment of Recurrent Glioblastoma Multiforme', *The Oncologist*. 14(11), pp. 1131-8. doi: 10.1634/theoncologist.2009-0121.

Colak, D. *et al.* (2013) 'XRegulation of axon guidance by compartmentalized nonsense-mediated mRNA decay', *Cell*. 153(6), pp. 1252-65. doi: 10.1016/j.cell.2013.04.056.

Colotta, F. *et al.* (1992) 'Expression and involvement of c-fos and c-jun protooncogenes in programmed cell death induced by growth factor deprivation in lymphoid cell lines', *Journal of Biological Chemistry*. 267, pp. 18278-18283.

Conti, L. *et al.* (2005) 'Niche-independent symmetrical self-renewal of a mammalian tissue stem cell', *PLoS Biology*. 3, e283. doi: 10.1371/journal.pbio.0030283.

Cooper, S. T. *et al.* (2004) 'C2C12 co-culture on a fibroblast substratum enables sustained survival of contractile, highly differentiated myotubes with peripheral nuclei and adult fast myosin expression', *Cell Motility and the Cytoskeleton*. 58, pp. 200–211. doi: 10.1002/cm.20010.

Cortiella, J. *et al.* (2010) 'Influence of acellular natural lung matrix on murine embryonic stem cell differentiation and tissue formation', *Tissue Engineering - Part A*. 16, pp. 2565–2580. doi: 10.1089/ten.tea.2009.0730.

Cosset, É. *et al.* (2017) 'Glut3 Addiction Is a Druggable Vulnerability for a Molecularly Defined Subpopulation of Glioblastoma', *Cancer Cell*. 21(2), pp. 256-263. doi: 10.1016/j.ccell.2017.10.016.

Crapo, P. M. *et al.* (2012) 'Biologic scaffolds composed of central nervous system extracellular matrix', *Biomaterials*. 33(13), pp. 3539-47. doi: 10.1016/j.biomaterials.2012.01.044.

Crapo, P. M., Gilbert, T. W. and Badylak, S. F. (2011) 'An overview of tissue and whole organ decellularization processes', *Biomaterials*. 32, pp. 3233–43. doi: 10.1016/j.biomaterials.2011.01.057.

Cuddapah, V. A. *et al.* (2014) 'A neurocentric perspective on glioma invasion', *Nature Reviews Neuroscience*. Nature Publishing Group, 15(7), pp. 455–465. doi: 10.1038/nrn3765.

D'Abaco, G. M. and Kaye, A. H. (2007) 'Integrins: Molecular determinants of glioma invasion', *Journal of Clinical Neuroscience*, 14(11), pp. 1041–1048. doi: 10.1016/j.jocn.2007.06.019.

Dalton, H. R. *et al.* (2016) 'Hepatitis E virus and neurological injury', *Nature Reviews Neurology*. 12, pp. 77–85. doi: 10.1038/nrneurol.2015.234.

Dalvi, M. P. *et al.* (2017) 'Taxane-Platin-Resistant Lung Cancers Co-develop Hypersensitivity to JumonjiC Demethylase Inhibitors', *Cell Reports*. 19(8), pp. 1669-1684. doi: 10.1016/j.celrep.2017.04.077.

Davis, M. E. (2016) 'Glioblastoma: Overview of disease and treatment', *Clinical Journal of Oncology Nursing*. 20(5 Suppl), S2-8. doi: 10.1188/16.CJON.S1.2-8.

Davis, M. E. and Stoiber, A. M. M. (2011) 'Glioblastoma multiforme: Enhancing survival and quality of life', *Clinical Journal of Oncology Nursing*. 15(3), pp. 291-297. doi: 10.1188/11.CJON.291-297.

DeKelver, R. C. *et al.* (2010) 'Functional genomics, proteomics, and regulatory DNA analysis in isogenic settings using zinc finger nuclease-driven transgenesis into a safe harbor locus in the human genome', *Genome Research*, 20(8), pp. 1133–1142. doi: 10.1101/gr.106773.110.

Delacôte, F. and Lopez, B. S. (2008) 'Importance of the cell cycle phase for the choice of the appropriate DSB repair pathway, for genome stability maintenance: The trans-S double-strand break repair model', *Cell Cycle*. 7(1), pp. 33-38 doi: 10.4161/cc.7.1.5149.

Demuth, T. and Berens, M. E. (2004) 'Molecular mechanisms of glioma cell migration and invasion', *Journal of Neuro-Oncology*, 70(2), pp. 217–228. doi: 10.1007/s11060-004-2751-6.

Depner, C. *et al.* (2016) 'EphrinB2 repression through ZEB2 mediates tumour invasion and anti-angiogenic resistance', *Nature Communications*. 7, pp. 12329. doi: 10.1038/ncomms12329.

Dequach, J. A. *et al.* (2011) 'Decellularized porcine brain matrix for cell culture and tissue engineering scaffolds', *Tissue Engineering - Part A*. 17(5-6), pp. 799-807. doi: 10.1089/ten.tea.2010.0724.

DeQuach, J. A. *et al.* (2010) 'Simple and high yielding method for preparing tissue specific extracellular matrix coatings for cell culture', *PLoS ONE*. 5(9), e13039. doi: 10.1371/journal.pone.0013039.

DeQuach, J. A. *et al.* (2011) 'Decellularized Porcine Brain Matrix for Cell Culture and Tissue Engineering Scaffolds', *Tissue Engineering Part A*, 17(21–22), pp. 2583–2592. doi: 10.1089/ten.tea.2010.0724.

DeQuach, J. A. *et al.* (2012) 'Injectable skeletal muscle matrix hydrogel promotes neovascularization and muscle cell infiltration in a hindlimb ischemia model', *European Cells and Materials*. 23, pp. 400–412.doi: 10.22203/eCM.v023a31.

Dereymaker, A. *et al.* (2017) 'Controlling the release of indomethacin from glass solutions layered with a rate controlling membrane using fluid-bed processing. Part 1: Surface and cross-sectional chemical analysis', *Molecular Pharmaceutics*. 14(4), pp. 959–973. doi: 10.1021/acs.molpharmaceut.6b01023.

Deryugina, E. I. *et al.* (1997) 'Matrix metalloproteinase-2 activation modulates glioma cell migration.', *Journal of cell science*, 110 Pt 1, pp. 2473–82. Available at: http://www.ncbi.nlm.nih.gov/pubmed/9410885.

Didier, M. *et al.* (1992) 'Long-term expression of the c-fos protein during the in vitro differentiation of cerebellar granule cells induced by potassium or NMDA', *Molecular Brain Research*. 12(1-3), 249-258. doi: 10.1016/0169-328X(92)90091-O.

Diksin, M., Smith, S. J. and Rahman, R. (2017) 'The molecular and phenotypic basis of the glioma invasive perivascular niche', *International Journal of Molecular Sciences*. 18(11), pii: E2342. doi: 10.3390/ijms18112342.

Ding, L. *et al.* (2012) 'Clonal evolution in relapsed acute myeloid leukaemia revealed by whole-genome sequencing', *Nature*. 481(7382), pp. 506-10. doi: 10.1038/nature10738.

Dobin, A. *et al.* (2013) 'STAR: Ultrafast universal RNA-seq aligner', *Bioinformatics*. 29(1), pp. 15-21. doi: 10.1093/bioinformatics/bts635.

Drave, S. A. *et al.* (2016) 'Extra-hepatic replication and infection of hepatitis E virus in neuronal-derived cells', *Journal of Viral Hepatitis*. 23(7), pp. 512-521. doi: 10.1111/jvh.12515.

Dunbar, E. and Yachnis, A. T. (2010) 'Glioma diagnosis: Immunohistochemistry and beyond', *Advances in Anatomic Pathology*. 17, pp. 187–201. doi: 10.1097/PAP.0b013e3181d98cd9.

Dwyer, C. and Matthews, R. (2011) 'The Neural Extracellular Matrix, Cell Adhesion Molecules and Proteolysis in Glioma Invasion and Tumorigenicity', in *Molecular Targets of CNS Tumors*. doi: 10.5772/21709.

Dziurzynski, K. *et al.* (2012) 'Consensus on the role of human cytomegalovirus in glioblastoma', *Neuro-Oncology*. 14(3), pp. 246–255. doi: 10.1093/neuonc/nor227.

Eckel-Passow, J. E. *et al.* (2015) 'Glioma groups based on 1p/19q, IDH, and TERT promoter mutations in tumors', *New England Journal of Medicine*. 372(26), pp. 2499-508. doi: 10.1056/NEJMoa1407279.

Ehtesham, M. *et al.* (2002) 'Treatment of intracranial glioma with in situ interferon-gamma and tumor necrosis factor-alpha gene transfer', *Cancer Gene Therapy*. 9, pp. 925–934. doi: 10.1038/sj.cgt.7700516.

Van Eijk, J. J. J. *et al.* (2014) 'Neuralgic amyotrophy and hepatitis E virus infection', *Neurology*. 82, pp. 498–503. doi: 10.1212/WNL.0000000000000112.

Eischen, C. M. *et al.* (1999) 'Disruption of the ARF-Mdm2-p53 tumor suppressor pathway in Myc-induced lymphomagenesis', *Genes and Development*. 13(20), pp. 2658–2669.doi: 10.1101/gad.13.20.2658.

Elgui de Oliveira, D., Müller-Coan, B. G. and Pagano, J. S. (2016) 'Viral Carcinogenesis Beyond Malignant Transformation: EBV in the Progression of Human Cancers', *Trends in Microbiology*. 24(8), pp. 649-664. doi: 10.1016/j.tim.2016.03.008.

Elliott, R. A. and Hoehn, J. G. (1973) 'Use of commercial porcine skin for wound dressings', *Plastic and Reconstructive Surgery*. 58(1), pp. 51–56. doi: 10.1097/00006534-197352040-00013.

Ellisen, L. W. *et al.* (1991) 'TAN-1, the human homolog of the Drosophila Notch gene, is broken by chromosomal translocations in T lymphoblastic neoplasms', *Cell*. 66(4), pp. 649–661. doi: 10.1016/0092-8674(91)90111-B.

Ellor, S. V., Pagano-Young, T. A. and Avgeropoulos, N. G. (2014) 'Glioblastoma: Background, standard treatment paradigms, and supportive care considerations', *Journal of Law, Medicine and Ethics*. 42(2), 171-82.doi: 10.1111/jlme.12133.

Everitt, E. A., Malik, A. B. and Hendey, B. (1996) 'Fibronectin enhances the migration rate of human neutrophils in vitro', *Journal of Leukocyte Biology*. 60(2), pp. 199-206. doi: 10.1002/jlb.60.2.199.

Fael Al-Mayhani, T. M. *et al.* (2009) 'An efficient method for derivation and propagation of glioblastoma cell lines that conserves the molecular profile of their original tumours', *Journal of Neuroscience Methods*. 176(2), pp. 192-9. doi: 10.1016/j.jneumeth.2008.07.022.

Farin, A. *et al.* (2006) 'Transplanted glioma cells migrate and proliferate on host brain vasculature: A dynamic analysis', *GLIA*, 53(8), pp. 799–808. doi: 10.1002/glia.20334.

Farnebo, S. *et al.* (2014) 'Design and characterization of an injectable tendon hydrogel: A novel scaffold for guided tissue regeneration in the musculoskeletal system', *Tissue Engineering - Part A*. 20(9–10), pp. 1550–1561. doi: 10.1089/ten.tea.2013.0207.

Fisch, T. M., Prywes, R. and Roeder, R. G. (1987) 'c-fos sequence necessary for basal expression and induction by epidermal growth factor, 12-O-tetradecanoyl phorbol-13-acetate and the calcium ionophore.', *Molecular and Cellular Biology*. 7(10), pp. 3490-3502. doi: 10.1128/mcb.7.10.3490.

Fisher, M. B. *et al.* (2012) 'Potential of healing a transected anterior cruciate ligament with genetically modified extracellular matrix bioscaffolds in a goat model', *Knee Surgery, Sports Traumatology, Arthroscopy*. 20(7), pp. 1357-65. doi: 10.1007/s00167-011-1800-x.

Flaim, C. J. *et al.* (2008) 'Combinatorial signaling microenvironments for studying stem cell fate', *Stem Cells and Development*. 17(1), pp. 29–39. doi: 10.1089/scd.2007.0085.

Fletcher, J. S. *et al.* (2008) 'A new dynamic in mass spectral imaging of single biological cells', *Analytical Chemistry*. 80(23), pp. 9058-64. doi: 10.1021/ac8015278.

Flynn, L. E. (2010) 'The use of decellularized adipose tissue to provide an inductive microenvironment for the adipogenic differentiation of human adipose-derived stem cells', *Biomaterials*. 31(17), pp. 4715-24. doi: 10.1016/j.biomaterials.2010.02.046.

Franceschi, E. *et al.* (2009) 'Treatment options for recurrent glioblastoma: Pitfalls and future trends', *Expert Review of Anticancer Therapy*. 9(5), pp. 613-9. doi: 10.1586/ERA.09.23.

Franceschi, E. *et al.* (2015) 'The effect of re-operation on survival in patients with recurrent glioblastoma', *Anticancer Research*. 35(3), pp. 1743-8.

Freytes, D. O. *et al.* (2008) 'Preparation and rheological characterization of a gel form of the porcine urinary bladder matrix', *Biomaterials*. 29(11), pp. 1630-7 doi: 10.1016/j.biomaterials.2007.12.014.

Fu, Y. *et al.* (1999) 'Cloning of DLM-1, a novel gene that is up-regulated in activated macrophages, using RNA differential display', *Gene*. 241(1), pp. 3–17. doi: 10.1016/S0378-1119(99)00419-9.

Fu, Y. *et al.* (2016) 'Decellularization of porcine skeletal muscle extracellular matrix for the formulation of a matrix hydrogel: A preliminary study', *Journal of Cellular and Molecular Medicine*. 20(4), pp. 740-9. doi: 10.1111/jcmm.12776.

Fujita, M. *et al.* (2010) 'Role of type 1 IFNs in antiglioma immunosurveillance - Using mouse studies to guide examination of novel prognostic markers in humans', *Clinical Cancer Research*. 16, pp. 3409–19. doi: 10.1158/1078-0432.CCR-10-0644.

Galli, R. *et al.* (2004) 'Isolation and characterization of tumorigenic, stem-like neural precursors from human glioblastoma', *Cancer Research*. 64, pp. 7011–7021. doi: 10.1158/0008-5472.CAN-04-1364.

Garcia-Diaz, A. *et al.* (2017) 'Interferon Receptor Signaling Pathways Regulating PD-L1 and PD-L2 Expression', *Cell Reports*. 19(6), pp. 1189-1201. doi: 10.1016/j.celrep.2017.04.031.

García-Sastre, A. *et al.* (1998) 'Influenza A virus lacking the NS1 gene replicates in interferon- deficient systems', *Virology*. 252, pp. 324–330. doi: 10.1006/viro.1998.9508.

García-Sastre, A. (2001) 'Inhibition of interferon-mediated antiviral responses by influenza A viruses and other negative-strand RNA viruses', *Virology*. 279, pp. 375–384. doi: 10.1006/viro.2000.0756.

García-Sastre, A. (2004) 'Identification and characterization of viral antagonists of type I interferon in negative-strand RNA viruses', *Current Topics in Microbiology and Immunology*. 283, 249-280. doi: 10.1007/978-3-662-06099-5_7.

Gatenby, R. A. *et al.* (2009) 'Adaptive therapy', *Cancer Research*. 69(11), pp. 4894–4903. doi: 10.1158/0008-5472.CAN-08-3658.

Geletneky, K. *et al.* (2017) 'Oncolytic H-1 Parvovirus Shows Safety and Signs of Immunogenic Activity in a First Phase I/IIa Glioblastoma Trial', *Molecular Therapy*. 25(12), pp. 2620-2634. doi: 10.1016/j.ymthe.2017.08.016.

Genander, M. *et al.* (2009) 'Dissociation of EphB2 Signaling Pathways Mediating Progenitor Cell Proliferation and Tumor Suppression', *Cell*. 139(4), pp. 679-92. doi: 10.1016/j.cell.2009.08.048.

Gerlinger, M. *et al.* (2012) 'Intratumor heterogeneity and branched evolution revealed by multiregion sequencing', *New England Journal of Medicine*. 366(10), pp. 883–92. doi: 10.1056/NEJMoa1113205.

Gersey, Z. *et al.* (2019) 'Therapeutic Targeting of the Notch Pathway in Glioblastoma Multiforme', *World Neurosurgery*. 131, pp. 252-263. doi: 10.1016/j.wneu.2019.07.180.

Ghosh, A. *et al.* (1994) 'Calcium regulation of gene expression in neuronal cells', *Journal of Neurobiology*. 25(3), pp. 294-303. doi: 10.1002/neu.480250309.

Ghuman, H. *et al.* (2016) 'ECM hydrogel for the treatment of stroke: Characterization of the host cell infiltrate', *Biomaterials*. 91, pp. 166–181. doi: 10.1016/j.biomaterials.2016.03.014.

Gilbert, M. R. *et al.* (2014) 'A Randomized Trial of Bevacizumab for Newly Diagnosed Glioblastoma', *New England Journal of Medicine*, 370(8), pp. 699–708. doi: 10.1056/NEJMoa1308573.

Gilbert, T. W., Sellaro, T. L. and Badylak, S. F. (2006) 'Decellularization of tissues and organs', *Biomaterials*. 27(19), pp. 3515-3690. doi: 10.1016/j.biomaterials.2006.02.014.

Goff, S. L. *et al.* (2019) 'Pilot trial of adoptive transfer of chimeric antigen receptor-Transduced t cells targeting egfrviii in patients with glioblastoma', *Journal of Immunotherapy*. 42(4), pp. 126-135. doi: 10.1097/CJI.0000000000000260.

Greaves, M. and Maley, C. C. (2012) 'Clonal evolution in cancer', *Nature*. 481, pp. 306–313.doi: 10.1038/nature10762.

Griffin, C. A. *et al.* (2006) 'Identification of der(1;19)(q10;p10) in five oligodendrogliomas suggests mechanism of concurrent 1p and 19q loss', *Journal of Neuropathology and Experimental Neurology*. 65, pp. 988–994. doi: 10.1097/01.jnen.0000235122.98052.8f.

Gubits, R. M., Hazelton, J. L. and Simantov, R. (1988) 'Variations in c-fos gene expression during rat brain development', *Molecular Brain Research*. 3(2), pp. 197-201. doi: 10.1016/0169-328X(88)90067-8.

Hackam, D. G., Goodman, S. G. and Anand, S. S. (2005) 'Management of risk in peripheral artery disease: Recent therapeutic advances', *American Heart Journal*. 150 (1), pp. 35–40. doi: 10.1016/j.ahj.2005.01.008.

Haferkamp, S. *et al.* (2008) 'p16INK4a-induced senescence is disabled by melanoma-associated mutations', *Aging Cell*. 7, pp. 733–745. doi: 10.1111/j.1474-9726.2008.00422.x.

El Hallani, S. *et al.* (2010) 'A new alternative mechanism in glioblastoma vascularization: Tubular vasculogenic mimicry', *Brain*, 133(4), pp. 973–982. doi: 10.1093/brain/awq044.

Hambardzumyan, D. *et al.* (2011) 'Genetic modeling of gliomas in mice: New tools to tackle old problems', *GLIA*. 59(8), pp. 1155-68. doi: 10.1002/glia.21142.

Han, L., Lam, E. W. F. and Sun, Y. (2019) 'Extracellular vesicles in the tumor microenvironment: Old stories, but new tales', *Molecular Cancer*. 18, 59. doi: 10.1186/s12943-019-0980-8.

Han, Y. *et al.* (2015) 'Advanced applications of RNA sequencing and challenges', *Bioinformatics and Biology Insights*. 9(Suppl1), pp. 29-46. doi: 10.4137/BBI.S28991.

Happold, C. *et al.* (2014) 'Interferon-β induces loss of spherogenicity and overcomes therapy resistance of glioblastoma stem cells', *Molecular Cancer Therapeutics*. 13, pp. 948–961. doi: 10.1158/1535-7163.MCT-13-0772.

Hara, M. *et al.* (2017) 'Interaction of reactive astrocytes with type i collagen induces astrocytic scar formation through the integrin-N-cadherin pathway after spinal cord injury', *Nature Medicine*. 23(7), pp. 818-828. doi: 10.1038/nm.4354.

Harland, M. *et al.* (2000) 'Mutation screening of the CDKN2A promoter in melanoma families', *Genes Chromosomes and Cancer*. 28(1), pp. 45-57. doi: 10.1002/(SICI)1098-2264(200005)28:1<45::AID-GCC6>3.0.CO;2-F.

Harland, M. (2001) 'A deep intronic mutation in CDKN2A is associated with disease in a subset of melanoma pedigrees', *Human Molecular Genetics*. 10(23), pp. 2679-2686. doi: 10.1093/hmg/10.23.2679.

Hartmann, C. *et al.* (2010) 'Patients with IDH1 wild type anaplastic astrocytomas exhibit worse prognosis than IDH1-mutated glioblastomas, and IDH1 mutation

status accounts for the unfavorable prognostic effect of higher age: Implications for classification of gliomas', *Acta Neuropathologica*. 120(6), pp. 707-18. doi: 10.1007/s00401-010-0781-z.

Hashimoto, H. *et al.* (2004) 'Quantitative TOF-SIMS imaging of DNA microarrays produced by bubble jet printing technique and the role of TOF-SIMS in life science industry', in *Applied Surface Science*. 231, pp. 385-391. doi: 10.1016/j.apsusc.2004.03.106.

Hatzistavrou, T. *et al.* (2009) 'ErythRED, a hESC line enabling identification of erythroid cells', *Nature Methods*. 6(9), pp. 659–662. doi: 10.1038/nmeth.1364.

Hayat, M. A. (2011) *Tumors of the Central Nervous System, Volume 2: Gliomas: glioblastoma*, *Tumors of the Central Nervous System*. USA: Springer, Dordrecht. doi: 10.1007/978-94-007-0618-7.

He, S. and Sharpless, N. E. (2017) 'Senescence in Health and Disease', *Cell*. 169(6), pp. 1000-1011. doi: 10.1016/j.cell.2017.05.015.

Hemmati, H. D. *et al.* (2003) 'Cancerous stem cells can arise from pediatric brain tumors', *Proceedings of the National Academy of Sciences of the United States of America*. 100, pp. 15178–15183. doi: 10.1073/pnas.2036535100.

Henrik Heiland, D. *et al.* (2019) 'Tumor-associated reactive astrocytes aid the evolution of immunosuppressive environment in glioblastoma', *Nature Communications*. 10(1), 2541. doi: 10.1038/s41467-019-10493-6.

Herman, J. G. *et al.* (1995) 'Inactivation of the CDKN2/pl6/MTS1 Gene Is Frequently Associated with Aberrant DNA Methylation in All Common Human Cancers', *Cancer Research*. 55(20), pp. 4525-4530.

Hilf, N. *et al.* (2019) 'Actively personalized vaccination trial for newly diagnosed glioblastoma', *Nature*. 565(7738), pp. 240-245. doi: 10.1038/s41586-018-0810-y.

Hoadley, K. A. *et al.* (2018) 'Cell-of-Origin Patterns Dominate the Molecular Classification of 10,000 Tumors from 33 Types of Cancer', *Cell*. 173(2), pp. 291-304. doi: 10.1016/j.cell.2018.03.022.

Hockemeyer, D. *et al.* (2009) 'Efficient targeting of expressed and silent genes in human ESCs and iPSCs using zinc-finger nucleases', *Nature Biotechnology*, 27(9), pp. 851–857. doi: 10.1038/nbt.1562.

Hockemeyer, D. *et al.* (2011) 'Genetic engineering of human pluripotent cells using TALE nucleases', *Nature Biotechnology*. 29, pp. 731–734. doi:

10.1038/nbt.1927.

Honda, K. and Taniguchi, T. (2006) 'IRFs: Master regulators of signalling by Toll-like receptors and cytosolic pattern-recognition receptors', *Nature Reviews Immunology*. 6, pp. 644–658. doi: 10.1038/nri1900.

Hong, X. *et al.* (2015) 'Gap junctions modulate glioma invasion by direct transfer of microRNA', *Oncotarget*. 6, pp. 15566–15577. doi: 10.18632/oncotarget.3904.

Hong, X., Chedid, K. and Kalkanis, S. N. (2012) 'Glioblastoma cell line-derived spheres in serum-containing medium versus serum-free medium: A comparison of cancer stem cell properties', *International Journal of Oncology*. 41(5), pp. 1693–1700. doi: 10.3892/ijo.2012.1592.

Horvath, P. *et al.* (2016) 'Screening out irrelevant cell-based models of disease', *Nature Reviews Drug Discovery*. 15(11), pp. 751-769. doi: 10.1038/nrd.2016.175.

Horvath, P. and Barrangou, R. (2010) 'CRISPR/Cas, the immune system of Bacteria and Archaea', *Science*. 327(5962), pp. 167-70. doi: 10.1126/science.1179555.

Hottinger, A. F., Pacheco, P. and Stupp, R. (2016) 'Tumor treating fields: A novel treatment modality and its use in brain tumors', *Neuro-Oncology*. 18, pp. 1338–1349. doi: 10.1093/neuonc/now182.

Hu, B. *et al.* (2008) 'The proteoglycan brevican binds to fibronectin after proteolytic cleavage and promotes glioma cell motility', *Journal of Biological Chemistry*, 283(36), pp. 24848–24859. doi: 10.1074/jbc.M801433200.

Hu, H. M. *et al.* (2013) 'C1orf61 acts as a tumor activator in human hepatocellular carcinoma and is associated with tumorigenesis and metastasis', *FASEB Journal*. 27, pp. 163–173. doi: 10.1096/fj.12-216622.

Hubert, C. G. *et al.* (2016) 'A three-dimensional organoid culture system derived from human glioblastomas recapitulates the hypoxic gradients and cancer stem cell heterogeneity of tumors found in vivo', *Cancer Research*. 76(8), pp. 2465-77. doi: 10.1158/0008-5472.CAN-15-2402.

Hydbring, P., Malumbres, M. and Sicinski, P. (2016) 'Non-canonical functions of cell cycle cyclins and cyclin-dependent kinases', *Nature Reviews Molecular Cell Biology*. 17, pp. 280-292. doi: 10.1038/nrm.2016.27.

Hyun, M. S. *et al.* (2006) 'Notch1 augments NF-κB activity by facilitating its nuclear retention', *EMBO Journal*. 25, 129–138. doi: 10.1038/sj.emboj.7600902.

Ignatova, T. N. *et al.* (2002) 'Human cortical glial tumors contain neural stem-like cells expressing astroglial and neuronal markers in vitro', *GLIA*. 39, pp. 193–206. doi: 10.1002/glia.10094.

Ishii, K. J. *et al.* (2006) 'A toll-like receptor-independent antiviral response induced by double-stranded B-form DNA', *Nature Immunology*. 7, pp. 40–48. doi: 10.1038/ni1282.

Ishii, K. J. and Akira, S. (2006) 'Innate immune recognition of, and regulation by, DNA', *Trends in Immunology*. 27(11), pp. 525-32. doi: 10.1016/j.it.2006.09.002.

Isken, O. and Maquat, L. E. (2007) 'Quality control of eukaryotic mRNA: Safeguarding cells from abnormal mRNA function', *Genes and Development*. 21, pp. 1833–1856. . doi: 10.1101/gad.1566807.

Itahana, K. and Zhang, Y. (2008) 'Mitochondrial p32 Is a Critical Mediator of ARF-Induced Apoptosis', *Cancer Cell*. 13(6), pp. 542-53. doi: 10.1016/j.ccr.2008.04.002.

J., Y. *et al.* (2019) 'LncRNA CACNA1G-AS1 facilitates hepatocellular carcinoma progression through the miR-2392/C1orf61 pathway', *Journal of Cellular Physiology*. 243 (10), pp. 18415-18422. doi: 10.1002/jcp.28477.

Jabalee, J., Towle, R. and Garnis, C. (2018) 'The Role of Extracellular Vesicles in Cancer: Cargo, Function, and Therapeutic Implications', *Cells*. 7(8), 93. doi: 10.3390/cells7080093.

Jacob, F. *et al.* (2020) 'A Patient-Derived Glioblastoma Organoid Model and Biobank Recapitulates Inter- and Intra-tumoral Heterogeneity', *Cell*. 180(1), pp. 188-204. doi: 10.1016/j.cell.2019.11.036.

Jahani-As, A. *et al.* (2016) 'Control of glioblastoma tumorigenesis by feed-forward cytokine signaling', *Nature Neuroscience*. 19, pp. 798-806. doi: 10.1038/nn.4295.

Jeanblanc, M. *et al.* (2012) 'Parallel pathways in RAF-induced senescence and conditions for its reversion', *Oncogene*. 31(25), pp. 3072-85. doi: 10.1038/onc.2011.481.

Jeffrey, P. L. *et al.* (2000) 'CROC-4: A novel brain specific transcriptional activator of c-fos expressed from proliferation through to maturation of multiple neuronal cell types', *Molecular and Cellular Neurosciences*. 16(3), pp. 185–196. doi: 10.1006/mcne.2000.0866.

Jenkins, R. B. *et al.* (2006) 'A t(1;19)(q10;p10) mediates the combined deletions of 1p and 19q and predicts a better prognosis of patients with oligodendroglioma', *Cancer Research*. 66, pp. 9852–9861. doi: 10.1158/0008-5472.CAN-06-1796.

Jesson, D. A. and Watts, J. F. (2012) 'The interface and interphase in polymer matrix composites: Effect on mechanical properties and methods for identification', *Polymer Reviews*. 52(3), 321-354. doi: 10.1080/15583724.2012.710288.

Jia, D. *et al.* (2019) 'Integrative analysis of DNA methylation and gene expression to identify key epigenetic genes in glioblastoma', *Aging*. 11(15), pp. 5579-5592. doi: 10.18632/aging.102139.

Jiao, Y. *et al.* (2012) 'Frequent ATRX, CIC, FUBP1 and IDH1 mutations refine the classification of malignant gliomas', *Oncotarget*. 3, pp. 709–722. doi: 10.18632/oncotarget.588.

Johnson, B. E. (2014a) 'Mutational Analysis Reveals the', 189(January), pp. 189–194. doi: 10.1126/science.1239947.

Johnson, B. E. (2014b) 'Mutational Analysis Reveals the Origin and Therapy-Driven Evolution of Reccurent Glioma', *Science*, 189(January), pp. 189–194. doi: 10.1126/science.1239947.

Johnson, D. R. *et al.* (2015) 'Case-based review: Newly diagnosed glioblastoma', *Neuro-Oncology Practice*. 2(3), pp. 106-121. doi: 10.1093/nop/npv020.

Jung, E. *et al.* (2017) 'Tweety-homolog 1 drives brain colonization of gliomas', *Journal of Neuroscience*. 37(13), pp. 3532-3543. doi: 10.1523/JNEUROSCI.3532-16.2017.

Kaina, B., Haas, S. and Kappes, H. (1997) 'A general role for c-Fos in cellular protection against DNA-damaging carcinogens and cytostatic drugs', *Cancer Research*. 57, pp. 2721-2731.

Kamar, N. *et al.* (2011) 'Hepatitis E virus and neurologic disorders', *Emerging Infectious Diseases*. 17(2), pp. 173-9. doi: 10.3201/eid1702.100856.

Kamar, N. *et al.* (2014) 'Hepatitis E virus infection', *Clinical Microbiology Reviews*. 27(1), pp. 116-138. doi: 10.1128/CMR.00057-13.

Kamar, N. *et al.* (2016) 'Extrahepatic manifestations of hepatitis E virus', *Liver International*. 36(4), pp. 667-472. doi: 10.1111/liv.13037.

Kamb, A. *et al.* (1994) 'A cell cycle regulator potentially involved in genesis of many tumor types', *Science*. 264(5157), pp. 436-440 doi: 10.1126/science.8153634.

Kaneko, Sadahiro and Kaneko, Sadao (2016) 'Fluorescence-guided resection of malignant glioma with 5-ALA', *International Journal of Biomedical Imaging*. 2016, 6135293. doi: 10.1155/2016/6135293.

Karabekmez, F. E., Duymaz, A. and Moran, S. L. (2009) 'Early clinical outcomes with the use of decellularized nerve allograft for repair of sensory defects within the hand', *Hand*. 4, pp. 245–9. doi: 10.1007/s11552-009-9195-6.

Karzbrun, E. *et al.* (2018) 'Human brain organoids on a chip reveal the physics of folding', *Nature Physics*. 14(5), pp. 515-522. doi: 10.1038/s41567-018-0046-7.

Kash, J. C. *et al.* (2006) 'Hijacking of the host-cell response and translational control during influenza virus infection', *Virus Research*. 119(1), pp. 111–120. doi: 10.1016/j.virusres.2005.10.013.

KAWAJI, H. *et al.* (2015) 'Interferon-β and temozolomide combination therapy for temozolomide monotherapy-refractory malignant gliomas', *Molecular and Clinical Oncology*. 3, pp. 909–913. doi: 10.3892/mco.2015.542.

Keane, T. J. *et al.* (2012) 'Consequences of ineffective decellularization of biologic scaffolds on the host response', *Biomaterials*. 33(6), pp. 1771-81. doi: 10.1016/j.biomaterials.2011.10.054.

Keane, T. J., Dziki, J., Castelton, A., *et al.* (2017) 'Preparation and characterization of a biologic scaffold and hydrogel derived from colonic mucosa', *Journal of Biomedical Materials Research - Part B Applied Biomaterials*. 105(2), pp. 291-306. doi: 10.1002/jbm.b.33556.

Keane, T. J., Dziki, J., Sobieski, E., *et al.* (2017) 'Restoring Mucosal Barrier Function and Modifying Macrophage Phenotype with an Extracellular Matrix Hydrogel: Potential Therapy for Ulcerative Colitis', *Journal of Crohn's & colitis*. 11(3), pp. 360-368. doi: 10.1093/ecco-jcc/jjw149.

Keane, T. J., Swinehart, I. T. and Badylak, S. F. (2015) 'Methods of tissue decellularization used for preparation of biologic scaffolds and in vivo relevance', *Methods*. 84, pp. 25–34. doi: 10.1016/j.ymeth.2015.03.005.

Keats, J. J. *et al.* (2012) 'Clonal competition with alternating dominance in multiple myeloma', *Blood*. 120(5), pp. 1067-76. doi: 10.1182/blood-2012-01-405985.

Keles, G. E., Anderson, B. and Berger, M. S. (1999) 'The effect of extent of resection on time to tumor progression and survival in patients with glioblastoma multiforme of the cerebral hemisphere', *Surgical Neurology*. 52, pp. 371–379. doi: 10.1016/S0090-3019(99)00103-2.

Killela, P. J. *et al.* (2014) 'Mutations in IDH1, IDH2, and in the TERT promoter define clinically distinct subgroups of adult malignant gliomas', *Oncotarget*. 5(6), pp. 1515–1525.doi: 10.18632/oncotarget.1765.

Kim, E. J. *et al.* (2016) 'Injectable and Thermosensitive Soluble Extracellular Matrix and Methylcellulose Hydrogels for Stem Cell Delivery in Skin Wounds', *Biomacromolecules*. 17(1), pp. 4-11. doi: 10.1021/acs.biomac.5b01566.

Kim, H. and Kim, J. S. (2014) 'A guide to genome engineering with programmable nucleases', *Nature Reviews Genetics*. 15(5), pp. 321-34. doi: 10.1038/nrg3686.

Kim, M. Y. *et al.* (2014) 'Augmentation of tendon healing with an injectable tendon hydrogel in a rat achilles tendon model', *Plastic and Reconstructive Surgery*. 133(5), 645e-653e. doi: 10.1097/PRS.0000000000000106.

Kim, S. S., Pirollo, K. F. and Chang, E. H. (2015) 'Isolation and culturing of glioma cancer stem cells', *Current Protocols in Cell Biology*. 67(1), pp. doi: 10.1002/0471143030.cb2310s67.

Kleinman, H. K. and Martin, G. R. (2005) 'Matrigel: Basement membrane matrix with biological activity', *Seminars in Cancer Biology*. 15, pp. 378–386. doi: 10.1016/j.semcancer.2005.05.004.

Klinman, D. M. (2004) 'Immunotherapeutic uses of CpG oligodeoxynucleotides', *Nature Reviews Immunology*. 4, pp. 249–258. doi: 10.1038/nri1329.

Knobbe, C. B., Reifenberger, J. and Reifenberger, G. (2004) 'Mutation analysis of the Ras pathway genes NRAS, HRAS, KRAS and BRAF in glioblastomas', *Acta Neuropathologica*. 1, pp. 467–470. doi: 10.1007/s00401-004-0929-9.

Kofman, A. *et al.* (2011) 'The roles of viruses in brain tumor initiation and oncomodulation', *Journal of Neuro-Oncology*. 105(3), pp. 451-66. doi: 10.1007/s11060-011-0658-6.

Koh, I. *et al.* (2018) 'The mode and dynamics of glioblastoma cell invasion into a decellularized tissue-derived extracellular matrix-based three-dimensional tumor model', *Scientific Reports*. 15;8(1), 4608. doi: 10.1038/s41598-018-

22681-3.

Kohmura, E. *et al.* (1995) 'Expression of c-fos mRNA after cortical ablation in rat brain is modulated by basic fibroblast growth factor (bFGF) and the NMDA receptor is involved in c-fos expression', *Molecular Brain Research*. 29:177–184. doi: 10.1016/0169-328X(94)00198-N.

Koivunen, P. *et al.* (2012) 'Transformation by the (R)-enantiomer of 2-hydroxyglutarate linked to EGLN activation', *Nature*. 483(7390), pp. 484–488.doi: 10.1038/nature10898.

Konishi, Y. *et al.* (2012) 'Patterns of intracranial glioblastoma recurrence after aggressive surgical resection and adjuvant Management: Retrospective Analysis of 43 Cases', *Neurologia Medico-Chirurgica*. 52, pp. 577 – 86. doi: 10.2176/nmc.52.577.

Koochekpour, S., Merzak, a and Pilkington, G. J. (1995) 'Extracellular matrix proteins inhibit proliferation, upregulate migration and induce morphological changes in human glioma cell lines.', *European journal of cancer (Oxford, England : 1990)*, 31A(3), pp. 375–80.

Korshunov, A. *et al.* (2015) 'Integrated analysis of pediatric glioblastoma reveals a subset of biologically favorable tumors with associated molecular prognostic markers', *Acta Neuropathologica*. 129, pp. 669–678. doi: 10.1007/s00401-015-1405-4.

Kotin, R. M., Linden, R. M. and Berns, K. I. (1992) 'Characterization of a preferred site on human chromosome 19q for integration of adeno-associated virus DNA by non-homologous recombination.', *The EMBO Journal*. 11, pp. 5071–5078. doi: 10.1002/j.1460-2075.1992.tb05614.x.

Kraft, M. L. and Klitzing, H. A. (2014) 'Imaging lipids with secondary ion mass spectrometry', *Biochimica et Biophysica Acta - Molecular and Cell Biology of Lipids*. 1841(8), pp. 1108-1119. doi: 10.1016/j.bbalip.2014.03.003.

Krieg, A. M. (2006) 'Therapeutic potential of toll-like receptor 9 activation', *Nature Reviews Drug Discovery*. 5, pp. 471–84. doi: 10.1038/nrd2059.

Kuhnt, D. *et al.* (2011) 'Correlation of the extent of tumor volume resection and patient survival in surgery of glioblastoma multiforme with high-field intraoperative MRI guidance', *Neuro-Oncology*. 13, pp. 1339–1348. doi: 10.1093/neuonc/nor133.

Kumar, V., Abbas, A. K. and Aster, J. C. (2013) *Robbins Basic Pathology Ninth Edition*, *Robbins basic pathology*. USA:Elsevier Saunders. doi: 10.1021/ja108313u.

Kwiatkowska, A. and Symons, M. (2013) 'Signaling determinants of glioma cell invasion', *Advances in Experimental Medicine and Biology*, 986, pp. 121–141. doi: 10.1007/978-94-007-4719-7-7.

Labussière, M. *et al.* (2014) 'TERT promoter mutations in gliomas, genetic associations and clinico-pathological correlations', *British Journal of Cancer*. 111, pp. 2024-2032. doi: 10.1038/bjc.2014.538.

Lacroix, M. *et al.* (2001) 'A multivariate analysis of 416 patients with glioblastoma multiforme: Prognosis, extent of resection, and survival', *Journal of Neurosurgery*. 95(2), pp. 190-198. doi: 10.3171/jns.2001.95.2.0190.

LaPak, K. M. and Burd, C. E. (2014) 'The molecular balancing act of p16ink4a in cancer and aging', *Molecular Cancer Research*. 12(2), pp. 167-83. doi: 10.1158/1541-7786.MCR-13-0350.

Law, J. W. S. and Lee, A. Y. W. (2012) 'The Role of Semaphorins and Their Receptors in Gliomas', *Journal of Signal Transduction*. 2012, 902854. doi: 10.1155/2012/902854.

Lee, J. S. *et al.* (2014) 'Liver extracellular matrix providing dual functions of two-dimensional substrate coating and three-dimensional injectable hydrogel platform for liver tissue engineering', *Biomacromolecules*. 15(1), pp. 206-218. doi: 10.1021/bm4015039.

Lee, S. Y. *et al.* (2009) 'Gain-of-function mutations and copy number increases of Notch2 in diffuse large B-cell lymphoma', *Cancer Science*. 100(25), pp. 920-926. doi: 10.1111/j.1349-7006.2009.01130.x.

Lee, W., Lim, S. and Kim, Y. (2017) *The role of myosin II in glioma invasion: A mathematical model*, *PLoS ONE*. 12(2):e0171312. doi: 10.1371/journal.pone.0171312.

LemCrossed D Sign©e, J. M., Clavreul, A. and Menei, P. (2015) 'Intratumoral heterogeneity in glioblastoma: Don't forget the peritumoral brain zone', *Neuro-Oncology*. 17(10), pp. 1322-32.doi: 10.1093/neuonc/nov119.

Leventhal, D. S. *et al.* (2020) 'Immunotherapy with engineered bacteria by targeting the STING pathway for anti-tumor immunity', *Nature Communications*. 11(1):2739. doi: 10.1038/s41467-020-16602-0.

Li, C. C. Y. *et al.* (2013) 'Glioma microvesicles carry selectively packaged coding and noncoding RNAs which alter gene expression in recipient cells', *RNA Biology*. 10(8), pp. 1333-44. doi: 10.4161/rna.25281.

Li, F. *et al.* (2016) 'Rapid reprogramming of primary human astrocytes into potent tumor-initiating cells with defined genetic factors', *Cancer Research*. 76(17), pp. 5143-50. doi: 10.1158/0008-5472.CAN-16-0171.

Lieber, M. R. *et al.* (2014) 'Nonhomologous DNA end joining (NHEJ) and chromosomal translocations in humans', *Subcellular Biochemistry*. 50, pp. 279-96. doi: 10.1007/978-90-481-3471-7_14.

Liesi, P. (1984) 'Laminin and fibronectin in normal and malignant neuroectodermal cells', *Medical Biology*. 62(3), pp. 163-80.

Lietz, C. B., Gemperline, E. and Li, L. (2013) 'Qualitative and quantitative mass spectrometry imaging of drugs and metabolites', *Advanced Drug Delivery kReviews*. 65(8), pp. 1074-85. doi: 10.1016/j.addr.2013.04.009.

Linkous, A. *et al.* (2019) 'Modeling Patient-Derived Glioblastoma with Cerebral Organoids', *Cell Reports*. 26(12), pp. 3203-3211. doi: 10.1016/j.celrep.2019.02.063.

Lino, M. M., Merlo, A. and Boulay, J. L. (2010) 'Notch signaling in glioblastoma: A developmental drug target?', *BMC Medicine*. 8, 72. doi: 10.1186/1741-7015-8-72.

Liu, L. *et al.* (1999) 'Mutation of the CDKN2A 5' UTR creates an aberrant initiation codon and predisposes to melanoma', *Nature Genetics*. 21, pp. 128–32. doi: 10.1038/5082.

Louis, D. N. *et al.* (2014) 'International Society Of Neuropathology--Haarlem consensus guidelines for nervous system tumor classification and grading', in *Brain pathology (Zurich, Switzerland)*. 24(5), pp. 429-35. doi: 10.1111/bpa.12171.

Love, M. I., Huber, W. and Anders, S. (2014) 'Moderated estimation of fold change and dispersion for RNA-seq data with DESeq2', *Genome Biology*. 15, 550. doi: 10.1186/s13059-014-0550-8.

Lowdon, R. F. and Wang, T. (2017) 'Epigenomic annotation of noncoding mutations identifies mutated pathways in primary liver cancer', *PLoS ONE*. 23;12(3), e0174032. doi: 10.1371/journal.pone.0174032.

Luo, Y. *et al.* (2006) 'Effects of growth factors on extracellular matrix production by vocal fold fibroblasts in 3-dimensional culture', in *Tissue Engineering*. 12(2), pp. 3365-3374. doi: 10.1089/ten.2006.12.3365.

Lutolf, M. P. and Hubbell, J. A. (2005) 'Synthetic biomaterials as instructive extracellular microenvironments for morphogenesis in tissue engineering', *Nature Biotechnology*. 23, pp. 47-55. doi: 10.1038/nbt1055.

Lyford, G. L. *et al.* (1995) 'Arc, a growth factor and activity-regulated gene, encodes a novel cytoskeleton-associated protein that is enriched in neuronal dendrites', *Neuron*. 14, pp. 433–445. doi: 10.1016/0896-6273(95)90299-6.

Lynch, C., Panagopoulou, M. and Gregory, C. D. (2017) 'Extracellular vesicles arising from apoptotic cells in tumors: Roles in cancer pathogenesis and potential clinical applications', *Frontiers in Immunology*. 8, 1174. doi: 10.3389/fimmu.2017.01174.

Ma, F. *et al.* (2019) 'A comparison between whole transcript and 3' RNA sequencing methods using Kapa and Lexogen library preparation methods 06 Biological Sciences 0604 Genetics', *BMC Genomics*. 20(1), 9 doi: 10.1186/s12864-018-5393-3.

Maas, S. L. N., Breakefield, X. O. and Weaver, A. M. (2017) 'Extracellular Vesicles: Unique Intercellular Delivery Vehicles', *Trends in Cell Biology*. 27(3), pp. 172-188. doi: 10.1016/j.tcb.2016.11.003.

MacDonald, S. M. *et al.* (2007) 'Intensity modulated radiation therapy versus three-dimensional conformal radiation therapy for the treatment of high grade glioma: A dosimetric comparison', *Journal of Applied Clinical Medical Physics*. 8(2), pp. 47-60. doi: 10.1120/jacmp.v8i2.2423.

Mali, P. *et al.* (2013) 'RNA-guided human genome engineering via Cas9.', *Science (New York, N.Y.)*, 339(6121), pp. 823–6. doi: 10.1126/science.1232033.

Mali, P., Esvelt, K. M. and Church, G. M. (2013) 'Cas9 as a versatile tool for engineering biology', *Nature Methods*. 10(10, pp. :957-63. doi: 10.1038/nmeth.2649.

Manfredi, A. A. *et al.* (2009) 'Regulation of dendritic- and T-cell fate by injury-associated endogenous signals', *Critical Reviews in Immunology*. 29(1), pp. 69-86. doi: 10.1615/critrevimmunol.v29.i1.30.

Marais, R., Wynne, J. and Treisman, R. (1993) 'The SRF accessory protein Elk-1 contains a growth factor-regulated transcriptional activation domain', *Cell*.

73(2), pp. 381-393. doi: 10.1016/0092-8674(93)90237-K.

Marina, D. *et al.* (2019) 'Relevance of Translation Initiation in Diffuse Glioma Biology and its Therapeutic Potential', *Cells*. 8(12), pii: E1542. doi: 10.3390/cells8121542.

Martin, D. A. and Elkon, K. B. (2006) 'Intracellular mammalian DNA stimulates myeloid dendritic cells to produce type I interferons predominantly through a Toll-like receptor 9-independent pathway', *Arthritis and Rheumatism*. 54(3), pp. 951-962. doi: 10.1002/art.21677.

Marziali, G., Signore, M., Buccarelli, M., Grande, S., Palma, A., Biffoni, M., Rosi, A., D'Alessandris, Q. G., *et al.* (2016) 'Metabolic/Proteomic Signature Defines Two Glioblastoma Subtypes with Different Clinical Outcome', *Scientific Reports*. 6, 21557. doi: 10.1038/srep21557.

Marziali, G., Signore, M., Buccarelli, M., Grande, S., Palma, A., Biffoni, M., Rosi, A., D'Alessandris, Q.G., *et al.* (2016) 'Metabolic/Proteomic Signature Defines Two Glioblastoma Subtypes With Different Clinical Outcome', *Scientific Reports*, 6(21557), pp. 1–13. doi: 10.1038/srep21557.

Massensini, A. R. *et al.* (2015) 'Concentration-dependent rheological properties of ECM hydrogel for intracerebral delivery to a stroke cavity', *Acta Biomaterialia*. 75, pp. 254-72. doi: 10.1016/j.actbio.2015.08.040.

Masui, K. *et al.* (2013) 'MTOR complex 2 controls glycolytic metabolism in glioblastoma through FoxO acetylation and upregulation of c-Myc', *Cell Metabolism*. 18(5), pp. 726-39. doi: 10.1016/j.cmet.2013.09.013.

Masui, K. *et al.* (2015) 'Glucose-dependent acetylation of Rictor promotes targeted cancer therapy resistance', *Proceedings of the National Academy of Sciences of the United States of America*. 112(30), pp. 9406-11. doi: 10.1073/pnas.1511759112.

Masui, K., Cavenee, W. K. and Mischel, P. S. (2014) 'MTORC2 in the center of cancer metabolic reprogramming', *Trends in Endocrinology and Metabolism*. 25(7), pp. 364-73doi: 10.1016/j.tem.2014.04.002.

Masui, K., Mischel, P. S. and Reifenberger, G. (2016a) 'Molecular classification of gliomas', in *Handbook of Clinical Neurology*. 134, pp. 97-120. doi: 10.1016/B978-0-12-802997-8.00006-2.

Masui, K., Mischel, P. S. and Reifenberger, G. (2016b) *Molecular classification of gliomas*. 1st edn, *Handbook of Clinical Neurology*. 1st edn. Elsevier B.V. 134,

pp. 97-120. doi: 10.1016/B978-0-12-802997-8.00006-2.

Mazor, T. *et al.* (2015) 'DNA Methylation and Somatic Mutations Converge on the Cell Cycle and Define Similar Evolutionary Histories in Brain Tumors', *Cancer Cell*. Elsevier Inc., 28(3), pp. 307–317. doi: 10.1016/j.ccell.2015.07.012.

McGirt, M. J. *et al.* (2009) 'Independent association of extent of resection with survival in patients with malignant brain astrocytoma: Clinical article', *Journal of Neurosurgery*. 110(1), pp. 156-62. doi: 10.3171/2008.4.17536.

McLendon, R. *et al.* (2008a) 'Comprehensive genomic characterization defines human glioblastoma genes and core pathways', *Nature*. 455, pp. 1061-1068. doi: 10.1038/nature07385.

McLendon, R. *et al.* (2008b) 'Comprehensive genomic characterization defines human glioblastoma genes and core pathways', *Nature*, 455(7216), pp. 1061–1068. doi: 10.1038/nature07385.

McPhail, D. S. (2006) 'Applications of Secondary Ion Mass Spectrometry (SIMS) in materials science', *Journal of Materials Science*. 41, pp. 873-903. doi: 10.1007/s10853-006-6568-x.

Meeus, J. *et al.* (2012) 'Nanoscale surface characterization and miscibility study of a spray-dried injectable polymeric matrix consisting of poly(lactic-co-glycolic acid) and polyvinylpyrrolidone', *Journal of Pharmaceutical Sciences*. 101(9), pp. 3473-4385. doi: 10.1002/jps.23131.

Meeus, J., Scurr, D. J., *et al.* (2015) 'Combination of (M)DSC and surface analysis to study the phase behaviour and drug distribution of ternary solid dispersions', *Pharmaceutical Research*. 32(4), pp. 1407-16. doi: 10.1007/s11095-014-1543-8.

Meeus, J., Lenaerts, M., *et al.* (2015) 'The Influence of Spray-Drying Parameters on Phase Behavior, Drug Distribution, and in Vitro Release of Injectable Microspheres for Sustained Release', *Journal of Pharmaceutical Sciences*. 104(4), pp. 1451-1460. doi: 10.1002/jps.24361.

Mehlen, P., Delloye-Bourgeois, C. and Chédotal, A. (2011) 'Novel roles for Slits and netrins: Axon guidance cues as anticancer targets?', *Nature Reviews Cancer*. 11(3), pp. 188-97. doi: 10.1038/nrc3005.

Merlo, A. *et al.* (1995) '5' CpG Island méthylation is associated with transcriptional silencing of the tumour suppressor p16/CDKN2/MTS1 in human cancers', *Nature Medicine*. 1, pp. 686–692. doi: 10.1038/nm0795-686.

Merlo, A. (2003) 'Genes and pathways driving glioblastomas in humans and murine disease models', *Neurosurgical Review*. 26, pp. 145-158. doi: 10.1007/s10143-003-0267-8.

Meyer, M. *et al.* (2015) 'Single cell-derived clonal analysis of human glioblastoma links functional and genomic heterogeneity', *Proceedings of the National Academy of Sciences of the United States of America*. 112(3), pp. 851-6. doi: 10.1073/pnas.1320611111.

Middeldorp, J. and Hol, E. M. (2011) 'Progress in Neurobiology GFAP in health and disease', *Progress in Neurobiology*. Elsevier Ltd, 93(3), pp. 421–443. doi: 10.1016/j.pneurobio.2011.01.005.

Minciacchi, V. R. *et al.* (2015) 'Large oncosomes contain distinct protein cargo and represent a separate functional class of tumor-derived extracellular vesicles', *Oncotarget*. 6(13), pp. 11327–11341. doi: 10.18632/oncotarget.3598.

Molenaar, R. J. *et al.* (2014) 'The driver and passenger effects of isocitrate dehydrogenase 1 and 2 mutations in oncogenesis and survival prolongation', *Biochimica et Biophysica Acta - Reviews on Cancer*. 1846(2), pp. 326–41. doi: 10.1016/j.bbcan.2014.05.004.

Montana, V. and Sontheimer, H. (2011) 'Bradykinin Promotes the Chemotactic Invasion of Primary Brain Tumors', *Journal of Neuroscience*, 31(13), pp. 4858–4867. doi: 10.1523/JNEUROSCI.3825-10.2011.

Mun, E. J. *et al.* (2018) 'Tumor-treating fields: A fourth modality in cancer treatment', *Clinical Cancer Research*. 24(2), pp. 266-275. doi: 10.1158/1078-0432.CCR-17-1117.

Nagao, M., Sugimori, M. and Nakafuku, M. (2007) 'Cross Talk between Notch and Growth Factor/Cytokine Signaling Pathways in Neural Stem Cells', *Molecular and Cellular Biology*. 27(11), pp. 3982–3994. doi: 10.1128/mcb.00170-07.

Nagata, S., Hanayama, R. and Kawane, K. (2010) 'Autoimmunity and the Clearance of Dead Cells', *Cell*. 140, pp. 619–630. doi: 10.1016/j.cell.2010.02.014.

Nakada, M. *et al.* (2005) 'EphB2/R-ras signaling regulates glioma cell adhesion, growth, and invasion', *American Journal of Pathology*. 167(2), pp. 565-576. doi: 10.1016/S0002-9440(10)62998-7.

Nakada, M. *et al.* (2007) 'Molecular targets of glioma invasion', *Cellular and Molecular Life Sciences*, 64, pp. 458–478. doi: 10.1007/s00018-007-6342-5.

Narayana, A. *et al.* (2006) 'Intensity-modulated radiotherapy in high-grade gliomas:

Clinical and dosimetric results', *International Journal of Radiation Oncology Biology Physics*. 64, pp. 892–897. doi: 10.1016/j.ijrobp.2005.05.067.

Natsume, T. *et al.* (2016) 'Rapid Protein Depletion in Human Cells by Auxin-Inducible Degron Tagging with Short Homology Donors', *Cell Reports*. 15(1), pp. 210-218. doi: 10.1016/j.celrep.2016.03.001.

Neu-Yilik, G. and Kulozik, A. E. (2008) 'Chapter 4 NMD. Multitasking Between mRNA Surveillance and Modulation of Gene Expression', *Advances in Genetics*. 62, pp. 185-243. doi: 10.1016/S0065-2660(08)00604-4.

Nicholson, P. *et al.* (2010) 'Nonsense-mediated mRNA decay in human cells: Mechanistic insights, functions beyond quality control and the double-life of NMD factors', *Cellular and Molecular Life Sciences*. 67(5), pp. 677-700. doi: 10.1007/s00018-009-0177-1.

Nickoloff, B. J. *et al.* (2002) 'Jagged-1 mediated activation of notch signaling induces complete maturation of human keratinocytes through NF-κB and PPARγ', *Cell Death and Differentiation*. 9, pp. 842–855. doi: 10.1038/sj.cdd.4401036.

Niyazi, M. *et al.* (2016) 'Bevacizumab and radiotherapy for the treatment of glioblastoma: Brothers in arms or unholy alliance?', *Oncotarget*. 7(3), pp. 2313-28. doi: 10.18632/oncotarget.6320.

Noushmehr, H. *et al.* (2010) 'Identification of a CpG Island Methylator Phenotype that Defines a Distinct Subgroup of Glioma', *Cancer Cell*. 17(5), pp. 510–522.doi: 10.1016/j.ccr.2010.03.017.

Nowakowski, T. J. *et al.* (2017) 'Spatiotemporal gene expression trajectories reveal developmental hierarchies of the human cortex', *Science*. 358(6368), pp. 1318-1323. doi: 10.1126/science.aap8809.

Nsengimana, J. *et al.* (2018) 'β-Catenin-mediated immune evasion pathway frequently operates in primary cutaneous melanomas', *Journal of Clinical Investigation*. 128(5), pp. 2048-2063. doi: 10.1172/JCI95351.

O'Driscoll, M. and Jeggo, P. A. (2006) 'The role of double-strand break repair - Insights from human genetics', *Nature Reviews Genetics*. 7, pp. 45–54.doi: 10.1038/nrg1746.

O'Rourke, D. M. *et al.* (2017) 'A single dose of peripherally infused EGFRvIII-directed CAR T cells mediates antigen loss and induces adaptive resistance in patients with recurrent glioblastoma', *Science Translational Medicine*. 9 (399), eaaa0984. doi: 10.1126/scitranslmed.aaa0984.

Obacz, J. *et al.* (2017) 'Endoplasmic reticulum proteostasis in glioblastoma - From molecular mechanisms to therapeutic perspectives', *Science Signaling*. 10(470). pii: eaal2323. doi: 10.1126/scisignal.aal2323.

Oceguera-yanez, F. *et al.* (2016) 'Engineering the AAVS1 locus for consistent and scalable transgene expression in human iPSCs and their differentiated derivatives', *Methods*. Elsevier Inc., 101, pp. 43–55. doi: 10.1016/j.ymeth.2015.12.012.

Ogata, T., Kozuka, T. and Kanda, T. (2003) 'Identification of an Insulator in AAVS1, a Preferred Region for Integration of Adeno-Associated Virus DNA', *Journal of Virology*. 77, pp. 9000–9007. doi: 10.1128/jvi.77.16.9000-9007.2003.

Ogawa, J. *et al.* (2018) 'Glioblastoma Model Using Human Cerebral Organoids', *Cell Reports*. 23(4), pp. 1220-1229 doi: 10.1016/j.celrep.2018.03.105.

Oh, T. *et al.* (2014) 'Immunocompetent murine models for the study of glioblastoma immunotherapy', *Journal of Translational Medicine*. 12, 107. doi: 10.1186/1479-5876-12-107.

Ohgaki, H. and Kleihues, P. (2013) 'The definition of primary and secondary glioblastoma', *Clinical Cancer Research*. 19, pp. 764–772. doi: 10.1158/1078-0432.CCR-12-3002.

Okabe, Y. *et al.* (2005) 'Toll-like receptor-independent gene induction program activated by mammalian DNA escaped from apoptotic DNA degradation', *Journal of Experimental Medicine*. 202, pp. 1333–1339. doi: 10.1084/jem.20051654.

Osswald, M. *et al.* (2015) 'Brain tumour cells interconnect to a functional and resistant network', *Nature*. 528(7580), pp. 93-8. doi: 10.1038/nature16071.

Osswald, M. *et al.* (2019) 'Tunneling nanotube-like structures in brain tumors', *CANCER REPORTS*. 2(6), e1181. doi: 10.1002/cnr2.1181.

Ostrom, Q. T. *et al.* (2014) 'The epidemiology of glioma in adults: A state of the science review', *Neuro-Oncology*. 16(7), pp. 896-913. doi: 10.1093/neuonc/nou087.

Ostrowski, S. G. *et al.* (2005) 'Secondary ion MS imaging of lipids in picoliter vials with a buckminsterfullerene ion source', *Analytical Chemistry*. 77(19), pp.

6190-6196. doi: 10.1021/ac0508189.

Oswald, F. *et al.* (1998) 'NF-κB2 Is a Putative Target Gene of Activated Notch-1 via RBP-Jκ', *Molecular and Cellular Biology*. 18, pp. 2077–2088. doi: 10.1128/mcb.18.4.2077.

Ott, H. C. *et al.* (2010) 'Regeneration and orthotopic transplantation of a bioartificial lung', *Nature Medicine*. 16(8), pp. 927-33. doi: 10.1038/nm.2193.

Papa, M. *et al.* (1995) 'Immediate early genes and brain DNA remodeling in the Naples High- and Low-excitability rat lines following exposure to a spatial novelty', *Brain Research Bulletin*. 37(2), pp. 111-118. doi: 10.1016/0361-9230(94)00254-X.

Park, J. H. *et al.* (2015) 'Combination therapy for gliomas using temozolomide and interferon-beta secreting human bone marrow derived mesenchymal stem cells', *Journal of Korean Neurosurgical Society*. 57(5), pp. 323-8. doi: 10.3340/jkns.2015.57.5.323.

Parker, B. S., Rautela, J. and Hertzog, P. J. (2016) 'Antitumour actions of interferons: Implications for cancer therapy', *Nature Reviews Cancer*. 16(3), pp. 131-44. doi: 10.1038/nrc.2016.14.

Parsons, D. W. *et al.* (2008) 'An integrated genomic analysis of human glioblastoma multiforme', *Science*. 321(5897), pp. 1807-12. doi: 10.1126/science.1164382.

Pasquale, E. B. (2010) 'Eph receptors and ephrins in cancer: Bidirectional signalling and beyond', *Nature Reviews Cancer*. 10(3), pp. 165-80. doi: 10.1038/nrc2806.

Passarelli, M. K. and Winograd, N. (2011) 'Lipid imaging with time-of-flight secondary ion mass spectrometry (ToF-SIMS)', *Biochimica et Biophysica Acta - Molecular and Cell Biology of Lipids*. 1811(11), pp. 976-90 doi: 10.1016/j.bbalip.2011.05.007.

Patel, A. P. *et al.* (2014) 'Single-cell RNA-seq highlights intratumoral heterogeneity in primary glioblastoma', *Science*. 344(6190), pp. 1396-401. doi: 10.1126/science.1254257.

Pennington, C. *et al.* (2006) 'A pilot study of brain tumour growth between radiotherapy planning and delivery', *Clinical Oncology*. 18(2), pp. 104-108. doi: 10.1016/j.clon.2005.09.004.

Perego, C. *et al.* (2002) 'Invasive behaviour of glioblastoma cell lines is associated with altered organisation of the cadherin-catenin adhesion system', *Journal of*

Cell Science. 115, pp. 3331-3340.

Perry, A. and Wesseling, P. (2016) *Histologic classification of gliomas*. 1st edn, *Handbook of Clinical Neurology*. 1st edn. Elsevier B.V. 134, pp. 71–95. doi: 10.1016/B978-0-12-802997-8.00005-0.

Perry, J. *et al.* (2006) 'The use of prophylactic anticonvulsants in patients with brain tumours - A systematic review', *Current Oncology*. 13(6), pp. 222–229.doi: 10.3747/co.v13i6.107.

Petersen, T. H. *et al.* (2010) 'Tissue-engineered lungs for in vivo implantation', *Science*. 329(5991), pp. 538-41. doi: 10.1126/science.1189345.

Petrecca, K. *et al.* (2013) 'Failure pattern following complete resection plus radiotherapy and temozolomide is at the resection margin in patients with glioblastoma', *Journal of Neuro-Oncology*. 111(1), pp. 19–23. doi: 10.1007/s11060-012-0983-4.

Pinyol, M. *et al.* (2000) 'INK4a/ARF locus alterations in human non-Hodgkin's lymphomas mainly occur in tumors with wild-type p53 gene', *American Journal of Pathology*. 156(6), pp. 1987–1996. doi: 10.1016/S0002-9440(10)65071-7.

Pischke, S. *et al.* (2017) 'Hepatitis E virus: Infection beyond the liver?', *Journal of Hepatology*. 66(5), pp. 1082-1095. doi: 10.1016/j.jhep.2016.11.016.

Pollard, S. M. *et al.* (2006) 'Adherent neural stem (NS) cells from fetal and adult forebrain', *Cerebral Cortex*. 16 (Suppl 1), i112–i120. doi: 10.1093/cercor/bhj167.

Pollard, S. M. *et al.* (2009) 'Glioma Stem Cell Lines Expanded in Adherent Culture Have Tumor-Specific Phenotypes and Are Suitable for Chemical and Genetic Screens', *Cell Stem Cell*. 4(6), pp. 568-80. doi: 10.1016/j.stem.2009.03.014.

Poon, C. J. *et al.* (2013) 'Preparation of an adipogenic hydrogel from subcutaneous adipose tissue', *Acta Biomaterialia*. 9(3), pp. 5609-20. doi: 10.1016/j.actbio.2012.11.003.

Popp, M. W. and Maquat, L. E. (2018) 'Nonsense-mediated mRNA Decay and Cancer', *Current Opinion in Genetics and Development*. 48, pp. 44-50. doi: 10.1016/j.gde.2017.10.007.

Pouliot, R. A. *et al.* (2016) 'Development and characterization of a naturally derived lung extracellular matrix hydrogel', *Journal of Biomedical Materials Research - Part A*. 104(8), pp. 1922-1935. doi: 10.1002/jbm.a.35726.

Prah, J. *et al.* (2019) 'A novel serum free primary astrocyte culture method that mimic quiescent astrocyte phenotype', *Journal of Neuroscience Methods*. 320, pp. 50-63. doi: 10.1016/j.jneumeth.2019.03.013.

Prestidge, C. A., Barnes, T. J. and Skinner, W. (2007) 'Time-of-flight secondary-ion mass spectrometry for the surface characterization of solid-state pharmaceuticals', *Journal of Pharmacy and Pharmacology*. 59(2), pp. 251-259. doi: 10.1211/jpp.59.2.0011.

Qian, J. *et al.* (2018) 'The IFN-γ/PD-L1 axis between T cells and tumor microenvironment: Hints for glioma anti-PD-1/PD-L1 therapy', *Journal of Neuroinflammation*. 15(1), 290. doi: 10.1186/s12974-018-1330-2.

Qian, Z. *et al.* (1993) 'Tissue-plasminogen activator is induced as an immediate-early gene during seizure, kindling and long-term potentiation', *Nature*. 361, pp. 453–457.doi: 10.1038/361453a0.

Radisic, M. *et al.* (2008) 'Pre-treatment of synthetic elastomeric scaffolds by cardiac fibroblasts improves engineered heart tissue', *Journal of Biomedical Materials Research - Part A*. 86, pp. 713–724. doi: 10.1002/jbm.a.31578.

Raghu, H. *et al.* (2011) 'Specific knockdown of uPA/uPAR attenuates invasion in glioblastoma cells and xenografts by inhibition of cleavage and trafficking of Notch -1 receptor', *Molecular Cancer*. 10, 130. doi: 10.1186/1476-4598-10-130.

Ran, F. A. *et al.* (2013) 'Genome engineering using the CRISPR-Cas9 system', 8(11), pp. 2281–2308. doi: 10.1038/nprot.2013.143.

Rao, J. S. (2003) 'Molecular mechanisms of glioma invasiveness: the role of proteases', *Nature Reviews Cancer*, 3(7), pp. 489–501. doi: 10.1038/nrc1121.

Rapp, M. *et al.* (2017) 'Recurrence Pattern Analysis of Primary Glioblastoma', *World Neurosurgery*. 103, pp. 733-740. doi: 10.1016/j.wneu.2017.04.053.

Rebbapragada, I. and Lykke-Andersen, J. (2009) 'Execution of nonsense-mediated mRNA decay: what defines a substrate?', *Current Opinion in Cell Biology*. 21(3), pp. 394-402. doi: 10.1016/j.ceb.2009.02.007.

Reuss, D. E. *et al.* (2015) 'ATRX and IDH1-R132H immunohistochemistry with subsequent copy number analysis and IDH sequencing as a basis for an "integrated" diagnostic approach for adult astrocytoma, oligodendroglioma and glioblastoma', *Acta Neuropathologica*. 129(1), pp. 133-46. doi: 10.1007/s00401-014-1370-3.

Reynolds, B. A. and Rietze, R. L. (2005) 'Neural stem cells and neurospheres - Re-evaluating the relationship', *Nature Methods*. 2, pp. 333–336. doi: 10.1038/nmeth758.

Reynolds, B. A. and Weiss, S. (1992) 'Generation of neurons and astrocytes from isolated cells of the adult mammalian central nervous system', *Science*. 255(5052), pp. 1707-1710. doi: 10.1126/science.1553558.

Robertson, F. L. *et al.* (2019) 'Experimental models and tools to tackle glioblastoma', *DMM Disease Models and Mechanisms*. 12(9), pii: dmm040386. doi: 10.1242/dmm.040386.

Robinson, G. W., Orr, B. A. and Gajjar, A. (2014) 'Complete clinical regression of a BRAF V600E-mutant pediatric glioblastoma multiforme after BRAF inhibitor therapy', *BMC Cancer*. 14, 258. doi: 10.1186/1471-2407-14-258.

Roder, C. *et al.* (2014) 'Maximizing the extent of resection and survival benefit of patients in glioblastoma surgery: High-field iMRI versus conventional and 5-ALA-assisted surgery', *European Journal of Surgical Oncology*. 40(3), pp. 297-304. doi: 10.1016/j.ejso.2013.11.022.

Ruas, M. *et al.* (1999) 'Functional evaluation of tumour-specific variants of p16(INK4a)/CDKN2A: Correlation with protein structure information', *Oncogene*. 18, pp. 5423-34. doi: 10.1038/sj.onc.1202918.

Ruoslahti, E. (1996) 'Brain extracellular matrix.', *Glycobiology*, 6(5), pp. 489–492. doi: 10.1093/glycob/6.5.489.

Russell, S. J. and Peng, K. W. (2007) 'Viruses as anticancer drugs', *Trends in Pharmacological Sciences*. 28(7), pp. 326-333. doi: 10.1016/j.tips.2007.05.005.

Saddawi-Konefka, R. and Crawford, J. R. (2010) 'Chronic viral infection and primary central nervous system malignancy', *Journal of Neuroimmune Pharmacology*. 5, pp. 387–403. doi: 10.1007/s11481-010-9204-0.

Sadelain, M., Papapetrou, E. P. and Bushman, F. D. (2011) 'Safe harbours for the integration of new DNA in the human genome', *Nature Reviews Cancer*. Nature Publishing Group, 12(1), pp. 51–58. doi: 10.1038/nrc3179.

Sahm, F. *et al.* (2014) 'Farewell to oligoastrocytoma: in situ molecular genetics favor classification as either oligodendroglioma or astrocytoma', *Acta Neuropathologica*. 128(4), pp. 551-9. doi: 10.1007/s00401-014-1326-7.

Sakata, T., Kamahori, M. and Miyahara, Y. (2004) 'Immobilization of oligonucleotide

probes on Si3N4 surface and its application to genetic field effect transistor', in *Materials Science and Engineering C*. 24(6), pp. 827-832. doi: 10.1016/j.msec.2004.08.042.

Sakuma, T. and Woltjen, K. (2014) 'Nuclease-mediated genome editing: At the front-line of functional genomics technology', *Development Growth and Differentiation*, 56, pp. 2–13. doi: 10.1111/dgd.12111.

Salacz, M. E., Watson, K. R. and Schomas, D. A. (2011) 'Glioblastoma: Part I. Current state of affairs.', *Missouri medicine*. 108(3), pp. 187-94.

Samuel, C. E. (2001) 'Antiviral actions of interferons', *Clinical Microbiology Reviews*. 14(4), pp. 778–809. doi: 10.1128/CMR.14.4.778-809.2001.

Samuel, N. T. and Castner, D. G. (2004) 'ToF-SIMS characterization of hybridization onto self-assembled single-stranded DNA monolayers', in *Applied Surface Science*. 231, pp. 397-401. doi: 10.1016/j.apsusc.2004.03.146.

Sandmann, T. *et al.* (2015) 'Patients with proneural glioblastoma may derive overall survival benefit from the addition of bevacizumab to first-line radiotherapy and temozolomide: Retrospective analysis of the AVAglio trial', *Journal of Clinical Oncology*. 33(25), pp. 2735-44. doi: 10.1200/JCO.2015.61.5005.

Sanson, M. *et al.* (2009) 'Isocitrate dehydrogenase 1 codon 132 mutation is an important prognostic biomarker in gliomas', *Journal of Clinical Oncology*. 27(25), pp. 4150-4. doi: 10.1200/JCO.2009.21.9832.

Sasaki, M. *et al.* (2012) 'D-2-hydroxyglutarate produced by mutant Idh1 perturbs collagen maturation and basement membrane function', *Genes and Development*. 26(18), pp. 2038–2049. doi: 10.1101/gad.198200.112.

Scheithauer, B. W. (2009) 'Development of the WHO classification of tumors of the central nervous system: A historical perspective', *Brain Pathology*. 19(4), pp. 551-64. doi: 10.1111/j.1750-3639.2008.00192.x.

Scheithauer, B. W., Fuller, G. N. and VandenBerg, S. R. (2008) 'The 2007 WHO Classification of Tumors of the Nervous System: Controversies in surgical neuropathology', *Brain Pathology*. 18(3), pp. 307-16. doi: 10.1111/j.1750-3639.2008.00179.x.

Scherer, H. J. (1938) 'Structural development in gliomas', *American Journal of Cancer*, 34(3), pp. 333–351. doi: 10.1158/ajc.1938.333.

Schiff, D. *et al.* (2015) 'Medical management of brain tumors and the sequelae of treatment', *Neuro-Oncology*. 17, pp. 488–504. doi: 10.1093/neuonc/nou304.

Schmitt, C. A. *et al.* (1999) 'INK4a/ARF mutations accelerate lymphomagenesis and promote chemoresistance by disabling p53', *Genes and Development*. 13(20), pp. 2670–2677. doi: 10.1101/gad.13.20.2670.

Schurch, N. J. *et al.* (2016) 'How many biological replicates are needed in an RNA-seq experiment and which differential expression tool should you use?', *RNA*. 22(6), pp. 839-51. doi: 10.1261/rna.053959.115.

Seif-Naraghi, S. B. *et al.* (2011) 'Patient-to-patient variability in autologous pericardial matrix scaffolds for cardiac repair', *Journal of Cardiovascular Translational Research*. 4(5), pp. 545-56. doi: 10.1007/s12265-011-9293-z.

Seif-Naraghi, S. B. *et al.* (2012) 'Injectable extracellular matrix derived hydrogel provides a platform for enhanced retention and delivery of a heparin-binding growth factor', *Acta Biomaterialia*. 8(10), pp. 3695-703. doi: 10.1016/j.actbio.2012.06.030.

Seif-Naraghi, S. B. *et al.* (2013) 'Safety and efficacy of an injectable extracellular matrix hydrogel for treating myocardial infarction', *Science Translational Medicine*. 5(173), 173ra25. doi: 10.1126/scitranslmed.3005503.

Sellaro, T. L. *et al.* (2010) 'Maintenance of human hepatocyte function in vitro by liver-derived extracellular matrix gels', *Tissue Engineering - Part A*. 16(3), pp. 1075-82. doi: 10.1089/ten.tea.2008.0587.

Sen, G. C. (2001) 'Viruses and Interferons', *Annual Review of Microbiology*. 55, pp. 255–281. doi: 10.1146/annurev.micro.55.1.255.

Shard, A. G. *et al.* (1997) 'X-ray photoelectron spectroscopy and time-of-flight SIMS investigations of hyaluronic acid derivatives', *Langmuir*. 13(10), pp. 1808-2814.

Shima, K. *et al.* (2011) 'Prognostic significance of CDKN2A (p16) promoter methylation and loss of expression in 902 colorectal cancers: Cohort study and literature review', *International Journal of Cancer*. 128(5), pp. 1080-94. doi: 10.1002/ijc.25432.

Shirota, H. *et al.* (2006) 'Contribution of interferon-β to the immune activation induced by double-stranded DNA', *Immunology*. 118, pp. 302–10. doi: 10.1111/j.1365-2567.2006.02367.x.

Silva, M. *et al.* (2016) 'Hepatitis E virus infection as a direct cause of neuralgic

amyotrophy', *Muscle and Nerve*. 54(2), pp. 325-7. doi: 10.1002/mus.25096.

Simon-Assmann, P. *et al.* (1995) 'Extracellular matrix components in intestinal development', *Experientia*, 51, pp. 883–900. doi: 10.1007/BF01921739.

Singelyn, J. M. *et al.* (2009) 'Naturally derived myocardial matrix as an injectable scaffold for cardiac tissue engineering', *Biomaterials*. 30(29), pp. 5409-5416. doi: 10.1016/j.biomaterials.2009.06.045.

Singelyn, J. M. *et al.* (2012) 'Catheter-deliverable hydrogel derived from decellularized ventricular extracellular matrix increases endogenous cardiomyocytes and preserves cardiac function post-myocardial infarction', *Journal of the American College of Cardiology*. 59(8), pp. 751-63. doi: 10.1016/j.jacc.2011.10.888.

Singh, D. *et al.* (2012) 'Transforming fusions of FGFR and TACC genes in human glioblastoma', *Science*. 337(6099), pp. 1231-5. doi: 10.1126/science.1220834.

Singh, D. K. *et al.* (2017) 'Oncogenes Activate an Autonomous Transcriptional Regulatory Circuit That Drives Glioblastoma', *Cell Reports*. Elsevier, 18(4), pp. 961–976. doi: 10.1016/j.celrep.2016.12.064.

Singh, Sheila K *et al.* (2004) 'Cancer stem cells in nervous system tumors', *Oncogene*, 23(43), pp. 7267–7273. doi: 10.1038/sj.onc.1207946.

Singh, Sheila K. *et al.* (2004) 'Identification of human brain tumour initiating cells', *Nature*. 432, pp. 396–401. doi: 10.1038/nature03128.

Skog, J. *et al.* (2008) 'Glioblastoma microvesicles transport RNA and proteins that promote tumour growth and provide diagnostic biomarkers', *Nature Cell Biology*. 10(12), pp. 1470-6. doi: 10.1038/ncb1800.

Slavik, J. M., Hutchcroft, J. E. and Bierer, B. E. (1999) 'CD28/CTLA-4 and CD80/CD86 families: signaling and function', *Immunol Res*. 19, pp. 1–24. doi: 10.1007/BF02786473.

Smith, J. R. *et al.* (2008) 'Robust, Persistent Transgene Expression in Human Embryonic Stem Cells Is Achieved with AAVS1-Targeted Integration', *Stem Cells*, 26(2), pp. 496–504. doi: 10.1634/stemcells.2007-0039.

Smith, S. J. *et al.* (2015) 'Endothelial-like malignant glioma cells in dynamic three dimensional culture identifies a role for VEGF and FGFR in a tumor-derived angiogenic response.', *Oncotarget*, 6(26), pp. 22191–205. doi: 10.18632/oncotarget.4339.

Smith, S. J. *et al.* (2020) 'Metabolism based isolation of invasive glioblastoma cells with specific gene signatures and tumorigenic potential' *Neuro-Oncology Advances,* 2(1), pp. 1-12.

Sood, D. *et al.* (2019) '3D extracellular matrix microenvironment in bioengineered tissue models of primary pediatric and adult brain tumors', *Nature Communications*. 10(1), 4529. doi: 10.1038/s41467-019-12420-1.

Sottoriva, A. *et al.* (2013) 'Intratumor heterogeneity in human glioblastoma reflects cancer evolutionary dynamics.', *Proceedings of the National Academy of Sciences of the United States of America*, 110(10), pp. 4009–14. doi: 10.1073/pnas.1219747110.

Stern, M. M. *et al.* (2009) 'The influence of extracellular matrix derived from skeletal muscle tissue on the proliferation and differentiation of myogenic progenitor cells ex vivo', *Biomaterials*. 30(12), pp. 2393-2399. doi: 10.1016/j.biomaterials.2008.12.069.

Stetson, D. B. and Medzhitov, R. (2006) 'Recognition of cytosolic DNA activates an IRF3-dependent innate immune response', *Immunity*. 24, pp. 93–103. doi: 10.1016/j.immuni.2005.12.003.

Stockhausen, M. T., Kristoffersen, K. and Poulsen, H. S. (2010) 'The functional role of Notch signaling in human gliomas', *Neuro-Oncology*. 12(2), pp. 199-211. doi: 10.1093/neuonc/nop022.

Stummer, W. *et al.* (2006) 'Fluorescence-guided surgery with 5-aminolevulinic acid for resection of malignant glioma: a randomised controlled multicentre phase III trial', *Lancet Oncology*. 7(5), pp. 392-401. doi: 10.1016/S1470-2045(06)70665-9.

Stupp, R. *et al.* (2005) 'Radiotherapy plus Concomitant and Adjuvant Temozolomide for Glioblastoma', *New England Journal of Medicine*, 352(10), pp. 987–996. doi: 10.1056/NEJMoa043330.

Stupp, R. *et al.* (2009) 'Effects of radiotherapy with concomitant and adjuvant temozolomide versus radiotherapy alone on survival in glioblastoma in a randomised phase III study: 5-year analysis of the EORTC-NCIC trial', *The Lancet Oncology*. 10(5), pp. 459-66. doi: 10.1016/S1470-2045(09)70025-7.

Stupp, R. *et al.* (2012) 'NovoTTF-100A versus physician's choice chemotherapy in recurrent glioblastoma: A randomised phase III trial of a novel treatment modality', *European Journal of Cancer*. 48, pp. 2192–2202. doi:

10.1016/j.ejca.2012.04.011.

Stupp, R. *et al.* (2015) 'Maintenance therapy with tumor-Treating fields plus temozolomide vs temozolomide alone for glioblastoma a randomized clinical trial', *JAMA - Journal of the American Medical Association*. 314(23), pp. 2535-43. doi: 10.1001/jama.2015.16669.

Sturm, D., Witt, H., Hovestadt, V., Khuong-Quang, D. A., Jones, David T.W., *et al.* (2012) 'Hotspot Mutations in H3F3A and IDH1 Define Distinct Epigenetic and Biological Subgroups of Glioblastoma', *Cancer Cell*. 22, pp. 425–437. doi: 10.1016/j.ccr.2012.08.024.

Sturm, D., Witt, H., Hovestadt, V., Khuong-Quang, D. A., Jones, David T W, *et al.* (2012) 'Hotspot Mutations in H3F3A and IDH1 Define Distinct Epigenetic and Biological Subgroups of Glioblastoma', *Cancer Cell*, 22(4), pp. 425–437. doi: 10.1016/j.ccr.2012.08.024.

Subramani, C. *et al.* (2018) 'Host-Virus Protein Interaction Network Reveals the Involvement of Multiple Host Processes in the Life Cycle of Hepatitis E Virus', *mSystems*. 3(1), pii: e00135-17. doi: 10.1128/msystems.00135-17.

Suh, Y. and Lee, S.-J. (2015) 'Radiation treatment and cancer stem cells.', *Archives of pharmacal research*, 38(3), pp. 408–13. doi: 10.1007/s12272-015-0563-1.

Sullivan, S. M. (2014) 'GFAP variants in health and disease: Stars of the brain and gut', *Journal of Neurochemistry*. 130, pp. 729-732. doi: 10.1111/jnc.12754.

Suter, T. A. C. S. and Jaworski, A. (2019) 'Cell migration and axon guidance at the border between central and peripheral nervous system', *Science*. 365(6456), pii: eaaw8231. doi: 10.1126/science.aaw8231.

Suzuki, H. *et al.* (2015) 'Mutational landscape and clonal architecture in grade II and III gliomas', *Nature Genetics*. Nature Publishing Group, 47(5), pp. 458–468. doi: 10.1038/ng.3273.

Svendsen, C. N. *et al.* (1998) 'A new method for the rapid and long term growth of human neural precursor cells', *Journal of Neuroscience Methods*. 85, pp. 141–152. doi: 10.1016/S0165-0270(98)00126-5.

Taal, W. *et al.* (2014) 'Single-agent bevacizumab or lomustine versus a combination of bevacizumab plus lomustine in patients with recurrent glioblastoma (BELOB trial): A randomised controlled phase 2 trial', *The Lancet Oncology*. 15(11), pp. 484-92. doi: 10.1016/S1470-2045(14)70314-6.

Taiwo, R., Mahlokozera, T. and Kim, A. H. (2018) 'Stem nourished by branches:

Glioblastomas co-opt classic neurotrophic factor signaling to maintain stem-like cell pool', *Stem Cell Investigation*. 5, 22. doi: 10.21037/sci.2018.07.01.

Takaoka, A. *et al.* (2007) 'DAI (DLM-1/ZBP1) is a cytosolic DNA sensor and an activator of innate immune response', *Nature*. 448, pp. 501–505. doi: 10.1038/nature06013.

Talon, J. *et al.* (2000) 'Activation of Interferon Regulatory Factor 3 Is Inhibited by the Influenza A Virus NS1 Protein', *Journal of Virology*. 74, pp. 7989–7996. doi: 10.1128/jvi.74.17.7989-7996.2000.

Tamayo-Orrego, L. *et al.* (2016) 'Evasion of Cell Senescence Leads to Medulloblastoma Progression', *Cell Reports*. 14(12), pp. 2925-37. doi: 10.1016/j.celrep.2016.02.061.

Tanaka, H. *et al.* (2018) '*ZNF350* promoter methylation accelerates colon cancer cell migration', *Oncotarget*. 9(95), pp. 36750-36769. doi: 10.18632/oncotarget.26353.

Tanaka, K. *et al.* (2011) 'Oncogenic EGFR signaling activates an mTORC2-NF-κB pathway that promotes chemotherapy resistance', *Cancer Discovery*. 1(6), pp. 524-38.doi: 10.1158/2159-8290.CD-11-0124.

Tang, K. H. *et al.* (2012) 'CD133 + liver tumor-initiating cells promote tumor angiogenesis, growth, and self-renewal through neurotensin/interleukin-8/CXCL1 signaling', *Hepatology*. 55(3), pp. 807-20. doi: 10.1002/hep.24739.

Taniguchi, K. and Karin, M. (2018) 'NF-B, inflammation, immunity and cancer: Coming of age', *Nature Reviews Immunology*. 18(5), pp. 309-324. doi: 10.1038/nri.2017.142.

TCW, J. *et al.* (2017) 'An Efficient Platform for Astrocyte Differentiation from Human Induced Pluripotent Stem Cells', *Stem Cell Reports*. 9(2), pp. 600-614. doi: 10.1016/j.stemcr.2017.06.018.

Tenzen, T., Zembowicz, F. and Cowan, C. A. (2010) 'Genome modification in human embryonic stem cells', *Journal of Cellular Physiology*, 222(2), pp. 278–281. doi: 10.1002/jcp.21948.

Teodorczyk, M. and Schmidt, M. H. H. (2014) 'Notching on cancer's door: Notch signaling in brain tumors', *Frontiers in Oncology*. 4, 341. doi: 10.3389/fonc.2014.00341.

Thakkar, J. P. *et al.* (2014) 'Epidemiologic and molecular prognostic review of glioblastoma', *Cancer Epidemiology Biomarkers and Prevention*. 23(1), pp.

1985–96. doi: 10.1158/1055-9965.EPI-14-0275.

Tiyaboonchai, A. *et al.* (2014) 'Utilization of the AAVS1 safe harbor locus for hematopoietic specific transgene expression and gene knockdown in human ES cells', *Stem Cell Research*. 12(3), pp. 630-7. doi: 10.1016/j.scr.2014.02.004.

Tkach, M. and Théry, C. (2016) 'Communication by Extracellular Vesicles: Where We Are and Where We Need to Go', *Cell*. 164(6), pp. 1226-1232. doi: 10.1016/j.cell.2016.01.043.

Tomlins, P. (2015) *Characterisation and Design of Tissue Scaffolds*, *Characterisation and Design of Tissue Scaffolds*. pp. 1-21. doi: 10.1016/c2013-0-16452-5.

Touboul, D. *et al.* (2004) 'Tissue Molecular Ion Imaging by Gold Cluster Ion Bombardment', *Analytical Chemistry*. 76(6), 1550-1559. doi: 10.1021/ac035243z.

Tukmachev, D. *et al.* (2016) 'Injectable Extracellular Matrix Hydrogels as Scaffolds for Spinal Cord Injury Repair', *Tissue Engineering - Part A*. 21(5-6), pp. 1047-54. doi: 10.1089/ten.tea.2015.0422.

Tunici, P. *et al.* (2004) 'Genetic alterations and in vivo tumorigenicity of neurospheres derived from an adult glioblastoma', *Molecular Cancer*. 3, 25. doi: 10.1186/1476-4598-3-25.

Ueno, H. *et al.* (2001) 'Evaluation effects of chitosan for the extracellular matrix production by fibroblasts and the growth factors production by macrophages', *Biomaterials*. 22, pp. 2125–2130. doi: 10.1016/S0142-9612(00)00401-4.

Ungerleider, J. L. *et al.* (2016) 'Extracellular Matrix Hydrogel Promotes Tissue Remodeling, Arteriogenesis, and Perfusion in a Rat Hindlimb Ischemia Model', *JACC: Basic to Translational Science*. 1(1-2), pp. 32–44. doi: 10.1016/j.jacbts.2016.01.009.

Uriel, S. *et al.* (2008) 'The role of adipose protein derived hydrogels in adipogenesis', *Biomaterials*. 29(27), pp. 3712-9. doi: 10.1016/j.biomaterials.2008.05.028.

Uriel, S. *et al.* (2009) 'Extraction and assembly of tissue-derived gels for cell culture and tissue engineering', *Tissue Engineering - Part C: Methods*. 17, pp. 1201–1208.doi: 10.1089/ten.tec.2008.0309.

Uriel, S., Brey, E. M. and Greisler, H. P. (2006) 'Sustained low levels of fibroblast growth factor-1 promote persistent microvascular network formation', *American Journal of Surgery*, 192(5 SPEC. ISS.), pp. 604–609. doi:

10.1016/j.amjsurg.2006.08.012.

Utsuki, S. *et al.* (2011) 'Effectiveness of interferon-beta therapy for recurrent glioblastoma: A case report', *Tumori*. 97(1), pp. 119-22. doi: 10.1700/611.7149.

Uygun, B. E. *et al.* (2010) 'Organ reengineering through development of a transplantable recellularized liver graft using decellularized liver matrix', *Nature Medicine*. 16, pp. 814–20. doi: 10.1038/nm.2170.

Valadi, H. *et al.* (2007) 'Exosome-mediated transfer of mRNAs and microRNAs is a novel mechanism of genetic exchange between cells', *Nature Cell Biology*. 9(6), pp. 654–659. doi: 10.1038/ncb1596.

Venkataramani, V. *et al.* (2019) 'Glutamatergic synaptic input to glioma cells drives brain tumour progression', *Nature*. 573(7775), pp. 532-538. doi: 10.1038/s41586-019-1564-x.

Venkatesh, H. S. *et al.* (2019) 'Electrical and synaptic integration of glioma into neural circuits', *Nature*. 573(7775), pp. 539-545. doi: 10.1038/s41586-019-1563-y.

Verhaak, R. G. W. *et al.* (2010) 'Integrated Genomic Analysis Identifies Clinically Relevant Subtypes of Glioblastoma Characterized by Abnormalities in PDGFRA, IDH1, EGFR, and NF1', *Cancer Cell*. Elsevier Ltd, 17(1), pp. 98–110. doi: 10.1016/j.ccr.2009.12.020.

Verma, P. and Greenberg, R. A. (2016) 'Noncanonical views of homology-directed DNA repair', *Genes and Development*. 30(10), pp. 1138-54. doi: 10.1101/gad.280545.116.

Vincentelli, C. *et al.* (2012) 'The use of neuroimaging to guide the histologic diagnosis of central nervous system lesions', *Advances in Anatomic Pathology*. 19(2), pp. 97-107. doi: 10.1097/PAP.0b013e318248b747.

Visvader, J., Sassone-Corsi, P. and Verma, I. M. (1988) 'Two adjacent promoter elements mediate nerve growth factor activation of the c-fos gene and bind distinct nuclear complexes', *Proceedings of the National Academy of Sciences of the United States of America*. 85(24), pp. 9373-9377. doi: 10.1073/pnas.85.24.9474.

Vogazianou, A. P. *et al.* (2010) 'Distinct patterns of 1p and 19q alterations identify subtypes of human gliomas that have different prognoses', *Neuro-Oncology*. 12(7), pp. 664-78. doi: 10.1093/neuonc/nop075.

Vorotnikova, E. *et al.* (2010) 'Extracellular matrix-derived products modulate endothelial and progenitor cell migration and proliferation in vitro and stimulate regenerative healing in vivo', *Matrix Biology*. 29(8), pp. 690-700. doi: 10.1016/j.matbio.2010.08.007.

Vukicevic, V. *et al.* (2010) 'Genetic instability and diminished differentiation capacity in long-term cultured mouse neurosphere cells', *Mechanisms of Ageing and Development*. 131, pp. 124–132. doi: 10.1016/j.mad.2010.01.001.

Wagner, H. (2004) 'The immunobiology of the TLR9 subfamily', *Trends in Immunology*. 25(7), pp. 381-6. doi: 10.1016/j.it.2004.04.011.

Wagner, M. S. and Castner, D. G. (2001) 'Characterization of adsorbed protein films by time-of-flight secondary ion mass spectrometry with principal component analysis', *Langmuir*. 17(15), 4649-4660. doi: 10.1021/la001209t.

Wagner, M. S., Horbett, T. A. and Castner, D. G. (2003) 'Characterizing multicomponent adsorbed protein films using electron spectroscopy for chemical analysis, time-of-flight secondary ion mass spectrometry, and radiolabeling: Capabilities and limitations', *Biomaterials*. 24(11), pp. 1897-1809. doi: 10.1016/S0142-9612(02)00612-9.

Wagner, M. S., Tyler, B. J. and Castner, D. G. (2002) 'Interpretation of static time-of-flight secondary ion mass spectra of adsorbed protein films by multivariate pattern recognition', *Analytical Chemistry*. 74(8), 1824-1835. doi: 10.1021/ac0111311.

Wallner, K. E. *et al.* (1989) 'Patterns of failure following treatment for glioblastoma multiforme and anaplastic astrocytoma', *International Journal of Radiation Oncology, Biology, Physics*. 16, pp. 1405–9. doi: 10.1016/0360-3016(89)90941-3.

Wang, L., Gundelach, J. H. and Bram, R. J. (2017) 'Cycloheximide promotes paraptosis induced by inhibition of cyclophilins in glioblastoma multiforme', *Cell death & disease*. 8(5), e2807. doi: 10.1038/cddis.2017.217.

Wang, R. M. and Christman, K. L. (2016) 'Decellularized myocardial matrix hydrogels: In basic research and preclinical studies', *Advanced Drug Delivery Reviews*. 96, pp. 77-82. doi: 10.1016/j.addr.2015.06.002.

Wang, X. *et al.* (2000) 'Influenza A Virus NS1 Protein Prevents Activation of NF-kappa B and Induction of Alpha/Beta Interferon', *Journal of Virology*. 74, pp.

11566–11573. doi: 10.1128/jvi.74.24.11566-11573.2000.

Wang, X. *et al.* (2018) 'Reciprocal Signaling between Glioblastoma Stem Cells and Differentiated Tumor Cells Promotes Malignant Progression', *Cell Stem Cell*. 22(4), pp. 514–528. doi: 10.1016/j.stem.2018.03.011.

Wang, Z., Gerstein, M. and Snyder, M. (2009) 'RNA-Seq: A revolutionary tool for transcriptomics', *Nature Reviews Genetics*. 10, pp. 57–63. doi: 10.1038/nrg2484.

Wassenaar, J. W., Gaetani, R., *et al.* (2016) 'Evidence for mechanisms underlying the functional benefits of a myocardial matrix hydrogel for post-MI treatment', *Journal of the American College of Cardiology*. 67(9), pp. 1074-86. doi: 10.1016/j.jacc.2015.12.035.

Wassenaar, J. W., Braden, R. L., *et al.* (2016) 'Modulating: In vivo degradation rate of injectable extracellular matrix hydrogels', *Journal of Materials Chemistry B*. 4(16), 2794-2802. doi: 10.1039/c5tb02564h.

Watkins, S. *et al.* (2014) 'Disruption of astrocyte–vascular coupling and the blood–brain barrier by invading glioma cells', *Nature Communications*, 5, 4196. doi: 10.1038/ncomms5196.

Watkins, S. and Sontheimer, H. (2011) 'Hydrodynamic Cellular Volume Changes Enable Glioma Cell Invasion', *Journal of Neuroscience*, 31(47), pp. 17250–17259. doi: 10.1523/JNEUROSCI.3938-11.2011.

Weiler, M. *et al.* (2014) 'MTOR target NDRG1 confers MGMT-dependent resistance to alkylating chemotherapy', *Proceedings of the National Academy of Sciences of the United States of America*. 111(1), pp. 409–414. doi: 10.1073/pnas.1314469111.

Weller, M. *et al.* (2009) 'Molecular predictors of progression-free and overall survival in patients with newly diagnosed glioblastoma: A prospective translational study of the German Glioma Network', *Journal of Clinical Oncology*. 27(34), 5743-5750. doi: 10.1200/JCO.2009.23.0805.

Weller, M. *et al.* (2015) 'Glioma', *Nature Reviews Disease Primers*. 1,15017. doi: 10.1038/nrdp.2015.17.

Weng, A. P. *et al.* (2004) 'Activating mutations of NOTCH1 in human T cell acute lymphoblastic leukemia', *Science*. 306(5694), pp. 269-271. doi: 10.1126/science.1102160.

White, L. J. *et al.* (2017) 'The impact of detergents on the tissue decellularization process: A ToF-SIMS study', *Acta Biomaterialia*. 50, pp. 207-219**.** doi: 10.1016/j.actbio.2016.12.033.

White, M. K., Pagano, J. S. and Khalili, K. (2014) 'Viruses and human cancers: A long road of discovery of molecular paradigms', *Clinical Microbiology Reviews*. 27(3), pp. 463-81. doi: 10.1128/CMR.00124-13.

Wicha, M. S. *et al.* (1982) 'Extracellular matrix promotes mammary epithelial growth and differentiation in vitro', *Proceedings of the National Academy of Sciences of the United States of America*. 79(10), 3213–3217. doi: 10.1073/pnas.79.10.3213.

Wick, W. *et al.* (2009) 'NOA-04 randomized phase III trial of sequential radiochemotherapy of anaplastic glioma with Procarbazine, Lomustine, and Vincristine or Temozolomide', *Journal of Clinical Oncology*. 27(35), pp. 5874-5880. doi: 10.1200/JCO.2009.23.6497.

Wiedenheft, B., Sternberg, S. H. and Doudna, J. A. (2012) 'RNA-guided genetic silencing systems in bacteria and archaea', *Nature*. 482(7385), pp. 331-8. doi: 10.1038/nature10886.

William, D. *et al.* (2017) 'Optimized creation of glioblastoma patient derived xenografts for use in preclinical studies', *Journal of Translational Medicine*. 15(1), 27. doi: 10.1186/s12967-017-1128-5.

Williams, C. M. *et al.* (2008) 'Fibronectin expression modulates mammary epithelial cell proliferation during acinar differentiation', *Cancer Research*, 68(9), pp. 3185–3192. doi: 10.1158/0008-5472.CAN-07-2673.

Wilson, T. A., Karajannis, M. A. and Harter, D. H. (2014) 'Glioblastoma multiforme: State of the art and future therapeutics', *Surgical Neurology International*. 5, 64. doi: 10.4103/2152-7806.132138.

Witkiewicz, A. K. *et al.* (2011) ' The meaning of p16 ink4a expression in tumors ', *Cell Cycle*. 10, pp. 2497–2503. doi: 10.4161/cc.10.15.16776.

Wolf, K. J. *et al.* (2019) 'Dissecting and rebuilding the glioblastoma microenvironment with engineered materials', *Nature Reviews Materials*. 4, pp. 651-668. doi: 10.1038/s41578-019-0135-y.

Wolf, M. T. *et al.* (2012) 'A hydrogel derived from decellularized dermal extracellular matrix', *Biomaterials*. 33(29), pp. 7028-38. doi:

10.1016/j.biomaterials.2012.06.051.

Wolfenson, H., Lavelin, I. and Geiger, B. (2013) 'Dynamic Regulation of the Structure and Functions of Integrin Adhesions', *Developmental Cell*. Elsevier Inc., 24(5), pp. 447–458. doi: 10.1016/j.devcel.2013.02.012.

Wong, D. J. *et al.* (1997) 'p16(INK4a) promoter is hypermethylated at a high frequency in esophageal adenocarcinomas', *Cancer Research*. 57(13), pp. 2619-22.

Wua, J. *et al.* (2015) 'An injectable extracellular matrix derived hydrogel for meniscus repair and regeneration', *Acta Biomaterialia*. 16, pp. 49-59. doi: 10.1016/j.actbio.2015.01.027.

Xing, J., Ginty, D. D. and Greenberg, M. E. (1996) 'Coupling of the RAS-MAPK pathway to gene activation by RSK2, a growth factor-regulated CREB kinase', *Science*. 273, pp. 959–963. doi: 10.1126/science.273.5277.959.

Xu, W. *et al.* (2011) 'Oncometabolite 2-hydroxyglutarate is a competitive inhibitor of α-ketoglutarate-dependent dioxygenases', *Cancer Cell*. 19(1), pp. 17-30. doi: 10.1016/j.ccr.2010.12.014.

Xu, Z. *et al.* (2018) 'Orthotopic patient-derived glioblastoma xenografts in mice', in *Methods in Molecular Biology*. 1741, pp. 183-190. doi: 10.1007/978-1-4939-7659-1_14.

Yamagata, K. *et al.* (1993) 'Expression of a mitogen-inducible cyclooxygenase in brain neurons: Regulation by synaptic activity and glucocorticoids', *Neuron*. 11 (2), pp. 371–386. doi: 10.1016/0896-6273(93)90192-T.

Yamagata, K. *et al.* (1994) 'rheb, a growth factor- and synaptic activity-regulated gene, encodes a novel ras-related protein', *Journal of Biological Chemistry*. 269(23), pp. 16333-9.

Yan, H. *et al.* (2009) 'IDH1 and IDH2 mutations in gliomas', *New England Journal of Medicine*. 360(8), pp. 765-73. doi: 10.1056/NEJMoa0808710.

Yang, I. *et al.* (2004) 'Modulation of major histocompatibility complex Class I molecules and major histocompatibility complex-bound immunogenic peptides induced by interferon-α and interferon-γ treatment of human glioblastoma multiforme', *Journal of Neurosurgery*. 100(2), pp. 310-9. doi: 10.3171/jns.2004.100.2.0310.

Yap, T. A. *et al.* (2012) 'Intratumor heterogeneity: Seeing the wood for the trees', *Science Translational Medicine*. 4(127), 127ps10. doi:

10.1126/scitranslmed.3003854.

Yasuda, K. *et al.* (2005) 'Endosomal Translocation of Vertebrate DNA Activates Dendritic Cells via TLR9-Dependent and -Independent Pathways', *The Journal of Immunology*. 174(10), pp. 6129-36. doi: 10.4049/jimmunol.174.10.6129.

Ye, J. *et al.* (2010) 'The GCN2-ATF4 pathway is critical for tumour cell survival and proliferation in response to nutrient deprivation', *EMBO Journal*. 29, pp. 2082–2096. doi: 10.1038/emboj.2010.81.

Yi, H. G. *et al.* (2019) 'A bioprinted human-glioblastoma-on-a-chip for the identification of patient-specific responses to chemoradiotherapy', *Nature Biomedical Engineering*. 3(7), pp. 509-519. doi: 10.1038/s41551-019-0363-x.

Yoganarasimha, S. *et al.* (2014) 'Peracetic acid: A practical agent for sterilizing heat-labile polymeric tissue-engineering scaffolds', *Tissue Engineering - Part C: Methods*. 20(9), pp. 714-23. doi: 10.1089/ten.tec.2013.0624.

Young, D. A. *et al.* (2011) 'Injectable hydrogel scaffold from decellularized human lipoaspirate', *Acta Biomaterialia*. 7(3), pp. 1040-9. doi: 10.1016/j.actbio.2010.09.035.

Young, R. M. *et al.* (2015) 'Current trends in the surgical management and treatment of adult glioblastoma', *Annals of Translational Medicine*. 3(9), 121. doi: 10.3978/j.issn.2305-5839.2015.05.10.

Yu, Q. *et al.* (2018) 'Fibronectin promotes the malignancy of glioma stem-like cells via modulation of cell adhesion, differentiation, proliferation and chemoresistance', *Frontiers in Molecular Neuroscience*. 11, 130. doi: 10.3389/fnmol.2018.00130.

Yuan, X. *et al.* (2004) 'Isolation of cancer stem cells from adult glioblastoma multiforme', *Oncogene*. 23(58), 9392–9400. doi: 10.1038/sj.onc.1208311.

Yue, W. and Brodie, A. (1993) 'MCF-7 human breast carcinomas in nude mice as a model for evaluating aromatase inhibitors', *Journal of Steroid Biochemistry and Molecular Biology*. 44(4–6), pp. 671–673. doi: 10.1016/0960-0760(93)90278-5.

Yum, S. *et al.* (2019) 'Roles of the cGAS-STING Pathway in Cancer Immunosurveillance and Immunotherapy', *Annual Review of Cancer Biology*. 3, pp. 323-344. doi: 10.1146/annurev-cancerbio-030518-055636.

Zagzag, D. *et al.* (2008) 'Hypoxia- and Vascular Endothelial Growth Factor-Induced Stromal Cell-Derived Factor-1α/CXCR4 Expression in Glioblastomas', *The American Journal of Pathology*, 173(2), pp. 545–560. doi: 10.2353/ajpath.2008.071197.

Zhang, L. *et al.* (2013) 'Effect of an inductive hydrogel composed of urinary bladder matrix upon functional recovery following traumatic brain injury', *Tissue Engineering - Part A*. 19(17-18), pp. 1909–1918. doi: 10.1089/ten.tea.2012.0622.

Zhang, P. *et al.* (2015) 'Generation of GFAP :: GFP Astrocyte Reporter Lines from Human Adult Fibroblast-Derived iPS Cells Using Zinc-Finger Nuclease Technology'. 64(1), pp. 63-75. doi: 10.1002/glia.22903.

Zhang, Q. *et al.* (2010) 'Circulating mitochondrial DAMPs cause inflammatory responses to injury', *Nature*. 464(7285), pp. 104-7. doi: 10.1038/nature08780.

Zhang, Y. *et al.* (2016) 'Purification and Characterization of Progenitor and Mature Human Astrocytes Reveals Transcriptional and Functional Differences with Mouse', *Neuron*. 89(1), pp. 37-53. doi: 10.1016/j.neuron.2015.11.013.

Zhang, Y. and Xiong, Y. (1999) 'Mutations in human ARF exon 2 disrupt its nucleolar localization and impair its ability to block nuclear export of MDM2 and p53', *Molecular Cell*. 3(5), pp. 579-591. doi: 10.1016/S1097-2765(00)80351-2.

Zhao, S. *et al.* (2013) 'Intraoperative Fluorescence-Guided Resection of High-Grade Malignant Gliomas Using 5-Aminolevulinic Acid-Induced Porphyrins: A Systematic Review and Meta-Analysis of Prospective Studies', *PLoS ONE*. 8, e63682 doi: 10.1371/journal.pone.0063682.

Zheng, P. S. *et al.* (2004) 'Versican/PG-M G3 domain promotes tumor growth and angiogenesis.', *The FASEB journal : official publication of the Federation of American Societies for Experimental Biology*. 18(6), 754-756. doi: 10.1096/fj.03-0545fje.

Zheng, Y., Zhou, J. and Tong, Y. (2015) 'Gene signatures of drug resistance predict patient survival in colorectal cancer', *Pharmacogenomics Journal*. 15(2), pp. 135-43. doi: 10.1038/tpj.2014.45.

Zhou, X. *et al.* (2017) 'Hepatitis E virus infects neurons and brains', *Journal of Infectious Diseases*. 215(8), pp. 1197-1206. doi: 10.1093/infdis/jix079.

Zitvogel, L. *et al.* (2015) 'Type I interferons in anticancer immunity', *Nature Reviews*

Immunology. 15(7), pp. 405-14. doi: 10.1038/nri3845.

Zufferey, R. *et al.* (1999) 'Woodchuck hepatitis virus posttranscriptional regulatory element enhances expression of transgenes delivered by retroviral vectors.', *Journal of virology*, 73(4), pp. 2886–92. doi: 10.1038/nn.2751.